

Nicolaus Copernicus University in Toruń  
Faculty of Physics, Astronomy and Informatics  
Department of Atomic, Molecular and Optical Physics

# COLLISIONS OF SIMPLE MOLECULES AND ATOMS IN FUNDAMENTAL STUDIES



HUBERT JÓŹWIAK

Dissertation submitted in partial fulfillment  
of the requirements for the degree of  
DOCTOR OF PHILOSOPHY

Thesis supervised by dr hab. Piotr Wcisło, prof. NCU  
Department of Atomic, Molecular and Optical Physics  
Institute of Physics, Nicolaus Copernicus University in Toruń



Toruń 2025







## ABSTRACT

The subject of this dissertation is a comprehensive study of the interplay between molecular collisions and spectroscopy. In particular, the dissertation provides key reference data, such as rate coefficients, collisional line-shape parameters, and the positions and intensities of hyperfine components of rovibrational transitions for various diatomic molecules. The work is firmly grounded in quantum theory: the reference data are determined using rigorous quantum scattering calculations performed on state-of-the-art potential energy surfaces. The results are discussed in the context of applications in astrophysics, terrestrial atmosphere research, and high-precision spectroscopy of molecular hydrogen.

In addition to providing practical reference data, this dissertation addresses fundamental challenges at the intersection of quantum scattering and line-shape theory. In particular, we investigate how subtle collisional effects manifest in astrophysical observations, we explore the role of the accuracy of potential energy surfaces in providing accurate reference data for remote sensing applications, and we demonstrate the feasibility of performing large-scale *ab initio* calculations for populating spectroscopic databases. Finally, we explore how hyperfine interactions and external magnetic fields affect precision measurements of molecular hydrogen, and we propose novel methods to push the experimental accuracy further, allowing for more stringent tests of quantum theory through spectroscopy of the simplest neutral diatomic molecule.





## STRESZCZENIE

Przedmiotem niniejszej rozprawy są szerokie badania zależności pomiędzy zderzeniami cząsteczek a spektroskopią. W ramach przedstawionej pracy wyznaczono kluczowe dane referencyjne: współczynniki szybkości przejść zderzeniowych, parametry kształtu linii widmowych oraz położenia i natężenia komponentów nadsubtelnych przejść rotacyjno-wibracyjnych w różnych cząsteczkach dwuatomowych. Podejście zastosowane w rozprawie jest mocno osadzone w teorii kwantowej: wszystkie dane zderzeniowe uzyskano poprzez ścisłe obliczenia kwantowego rozpraszania, przeprowadzone z wykorzystaniem najnowocześniejszych powierzchni energii potencjalnej. Przedstawione wyniki omówiono w kontekście ich zastosowań w astrofizyce, badaniach atmosfery ziemskiej oraz wysokorozdzielczej spektroskopii cząsteczkowego wodoru.

Oprócz dostarczenia praktycznych danych referencyjnych, celem rozprawy jest zmierzenie się z kluczowymi wyzwaniem leżącymi na styku teorii zderzeń kwantowych i teorii kształtu linii widmowych. W szczególności badane są subtelne efekty zderzeniowe ujawniające się w obserwacjach astrofizycznych, analizowana jest rola dokładności powierzchni energii potencjalnej w uzyskiwaniu wiarygodnych danych referencyjnych dla zastosowań teledetekcyjnych, a także wykazana zostaje możliwość przeprowadzania wielkoskalowych obliczeń wychodzących z zasad pierwszych w celu populowania spektroskopowych baz danych. Ponadto, w rozprawie badany jest wpływ oddziaływań nadsubtelnych oraz zewnętrznych pól magnetycznych na precyzyjne pomiary spektroskopowe cząsteczki wodoru. W pracy zaproponowano także nowe metody zwiększania dokładności eksperymentalnej, które umożliwią bardziej rygorystyczne testy teorii kwantowej oparte na spektroskopii najprostszej neutralnej cząsteczki dwuatomowej.



# ACKNOWLEDGMENTS

I would like to express my deepest gratitude to my supervisor, Piotr Wcisło, for his exceptional guidance, unwavering support, and mentorship over the course of nearly nine years of collaboration. His dedication, insight, and encouragement have been pivotal throughout my entire academic journey.

I am grateful to all my co-authors and collaborators on the papers constituting this dissertation, with special thanks to the authors from the Institute of Physics at Nicolaus Copernicus University in Toruń, for their contributions and insights. In particular, I would like to mention Roman Ciuryło, Daniel Lisak, Szymon Wójtewicz, Grzegorz Kowzan, Michał Słowiński, Nikodem Stolarczyk, Michał Żółtowski, Kamil Stankiewicz, Maciej Gancewski and Artur Olejnik.

I extend my heartfelt thanks to Franck Thibault for his invaluable discussions on line-shape theory and for his hospitality during my stays in Rennes. My gratitude also goes to the entire scientific community at the Université de Rennes 1 for the fruitful collaboration, especially François Lique, who warmly introduced me to his group.

Similarly, I am deeply grateful to Timur Tscherbul for stimulating discussions on quantum scattering theory and for his hospitality during my visits to Reno. My thanks also go to Balakrishnan Naduvalath, who graciously welcomed me in Las Vegas and provided guidance that was crucial to my professional development. I would like to acknowledge Michał Tomza for his consistent mentorship and encouragement throughout my academic career.

Lastly, I extend my heartfelt gratitude to my wife Alicja, for her unwavering support, patience, and encouragement throughout this journey; her belief in me has been my greatest strength.

The research presented within this dissertation was supported by the National Science Centre (projects 2018/31/B/ST2/00720 and 2019/35/B/ST2/01118) as well as by the budgetary funds on science projected for 2019-2023 as a research project under the “Diamantowy Grant” program. It was also co-financed by the Polish National Agency for Academic Exchange under the PHC Polonium program (Grant No. dec. PPN/X/PS/318/2018) and was co-funded by the European Union (Grant Nos. ERC-2022-STG, H2TRAP, and 101075678). Views and opinions expressed are, however, those of the author(s) only and do not necessarily reflect those of the European Union or the European Research Council Executive Agency. Neither the European Union nor the granting authority can be held responsible for them. The author was also supported by the Foundation for Polish Science (FNP). The research is a part of the program of the National Laboratory FAMO in Toruń, Poland.

Calculations have been partially carried out using resources provided by the Wrocław Centre for Networking and Supercomputing (<http://wcss.pl>), Grant No. 546. We gratefully acknowledge Poland's high-performance computing infrastructure PLGrid (HPC Centers: ACK Cyfronet AGH, PCSS, CI TASK) for providing computer facilities and support within computational Grants No. PLG/2022/015576, PLG/2023/016409, PLG/2023/016279, PLG/2024/017252, PLG/2024/017376.







# CONTENTS

	PAGE
<b>PUBLICATIONS CONSTITUTING THE DISSERTATION</b>	<b>1</b>
<b>INTRODUCTION</b>	<b>4</b>
<b>AUTHOR CONTRIBUTION STATEMENT</b>	<b>49</b>
<b>PUBLICATIONS</b>	<b>52</b>
ARTICLE A . . . . .	53
ARTICLE B . . . . .	61
ARTICLE C . . . . .	75
ARTICLE D . . . . .	85
ARTICLE E . . . . .	100
ARTICLE F . . . . .	107
ARTICLE G . . . . .	112
ARTICLE H . . . . .	117
ARTICLE I . . . . .	126
ARTICLE J . . . . .	141
ARTICLE K . . . . .	149
ARTICLE L . . . . .	156
<b>CONCLUSIONS</b>	<b>170</b>
<b>Co-AUTHOR CONTRIBUTION STATEMENTS</b>	<b>174</b>
<b>ALL PUBLISHED ARTICLES</b>	<b>210</b>
<b>NOTATION</b>	<b>218</b>
<b>APPENDIX</b>	<b>221</b>
A. QUANTUM SCATTERING CALCULATIONS OF COLLISIONAL RATE COEF- FICIENTS . . . . .	221
B. <i>Ab initio</i> DESCRIPTION OF THE SPECTRAL LINE SHAPE . . . . .	232



C. THE ROLE OF QUANTUM INDISTINGUISHABILITY IN SPECTRAL LINE SHAPE THEORY . . . . .	250
D. PRESSURE BROADENING AND SHIFT COEFFICIENTS FOR HYPERFINE COMPONENTS OF ROVIBRATIONAL TRANSITIONS . . . . .	255
<b>BIBLIOGRAPHY</b>	<b>262</b>





## PUBLICATIONS

### CONSTITUTING THE DISSERTATION

- A** Revisiting the rovibrational (de-)excitation of molecular hydrogen by helium

**Hubert Jóźwiak**, Franck Thibault, Alexandra Viel, Piotr Wcisło, François Lique

*Astronomy & Astrophysics* 685, A113 (2024)

DOI: 10.1051/0004-6361/202348645

- B** Accurate reference spectra of HD in an H<sub>2</sub>–He bath for planetary applications

**Hubert Jóźwiak**, Nikodem Stolarczyk, Kamil Stankiewicz, Mikołaj Zaborowski, Daniel Lisak, Szymon Wójtewicz, Piotr Jankowski, Konrad Patkowski, Krzysztof Szalewicz, Franck Thibault, Iouli E. Gordon, Piotr Wcisło

*Astronomy & Astrophysics* 687, A69 (2024)

DOI: 10.1051/0004-6361/202449889

- C** The first comprehensive dataset of beyond-Voigt line-shape parameters from *ab initio* quantum scattering calculations for the HITRAN database: He-perturbed H<sub>2</sub> case study

Piotr Wcisło, Franck Thibault, Nikodem Stolarczyk, **Hubert Jóźwiak**, Michał Słowiński, Maciej Gancewski, Kamil Stankiewicz, Magdalena Konefał, Samir Kassi, Alain Campargue, Yan Tan, Jin Wang, Konrad Patkowski, Roman Ciuryło, Daniel Lisak, Roman Kochanov, Laurence S. Rothman, Iouli E. Gordon

*Journal of Quantitative Spectroscopy and Radiative Transfer* 260, 107477 (2021)

DOI: 10.1016/j.jqsrt.2020.107477



- D** *Ab initio* investigation of the CO–N<sub>2</sub> quantum scattering: The collisional perturbation of the pure rotational R(0) line in CO  
**Hubert Jóźwiak**, Franck Thibault, Hubert Cybulski, Piotr Wcisło  
*The Journal of Chemical Physics* 154, 054314 (2021)  
DOI: 10.1063/5.0040438
- E** Stimulated Raman scattering metrology of molecular hydrogen  
Marco Lamperti, Lucile Rutkowski, Daniele Ronchetti, Davide Gatti, Riccardo Gotti, Giulio Cerullo, Franck Thibault, **Hubert Jóźwiak**, Szymon Wójtewicz, Piotr Masłowski, Piotr Wcisło, Dario Polli, Marco Marangoni  
*Communications Physics* 6, 67 (2023)  
DOI: 10.1038/s42005-023-01187-z
- F** Hyperfine components of rovibrational dipole transitions in HT and DT  
**Hubert Jóźwiak**, Hubert Cybulski, Piotr Wcisło  
*Journal of Quantitative Spectroscopy and Radiative Transfer* 270, 107662 (2021)  
DOI: 10.1016/j.jqsrt.2021.107662
- G** Hyperfine structure of rovibrational quadrupole transitions in HD  
**Hubert Jóźwiak**, Hubert Cybulski, Piotr Wcisło  
*Journal of Quantitative Spectroscopy and Radiative Transfer* 272, 107753 (2021)  
DOI: 10.1016/j.jqsrt.2021.107753
- H** Hyperfine structure of the  $EF^1\Sigma_g^+$  state in H<sub>2</sub>  
**Hubert Jóźwiak**, Hubert Cybulski, Antoni Grabowski, Piotr Wcisło  
*Physical Review A* 104, 012808 (2021)  
DOI: 10.1103/PhysRevA.104.012808



- I** Lack of hyperfine shifts in Doppler-limited spectra of molecular hydrogen  
**Hubert Jóźwiak**, Piotr Wcisło  
*Physical Review A* 107, 012802 (2023)  
DOI: 10.1103/PhysRevA.107.012802
- J** Relative intensities of hyperfine components of rovibrational transitions in molecular hydrogen  
**Hubert Jóźwiak**, Piotr Wcisło  
*Physical Review A* 105, 062812 (2022)  
DOI: 10.1103/PhysRevA.105.062812
- K** Magic wavelength for a rovibrational transition in molecular hydrogen  
**Hubert Jóźwiak**, Piotr Wcisło  
*Scientific Reports* 12, 14529 (2023)  
DOI: 10.1038/s41598-022-18159-y
- L** Hyperfine and Zeeman interactions in ultracold collisions of molecular hydrogen with atomic lithium  
**Hubert Jóźwiak**, Timur V. Tscherbul, Piotr Wcisło  
*The Journal of Chemical Physics* 160, 094304 (2024)  
DOI: 10.1063/5.0193148



# INTRODUCTION

This dissertation focuses on the structure and dynamics of simple molecules, specifically on how molecular collisions influence their interactions with electromagnetic fields.

The interactions of molecules with electromagnetic fields form the foundation of spectroscopy—a field that has driven scientific discovery for centuries. From Isaac Newton’s pioneering experiments with light through the 19th-century discovery that spectra reveal discrete energy levels, spectroscopy has consistently pushed the boundaries of knowledge. Today, it remains at the forefront of precision science, defining primary time standards [1], enabling stringent tests of quantum theory [2–6], and contributing to searches for physics beyond the Standard Model (SM) [7–10].

Accurate studies of molecular spectra must account for the significant influence of molecular collisions. Occurring on timescales ranging from tens of femtoseconds to picoseconds, collisions perturb interactions between molecules and electromagnetic fields, producing observable effects such as broadening, shifting, and asymmetry of spectral lines [11]. Yet, these effects also present an opportunity: by analyzing collision-perturbed spectra through *ab initio* calculations, we can uncover the molecular dynamics [12, 13] and validate quantum chemical models of intermolecular interactions [14, 15].

The objective of this dissertation is to bridge these two perspectives. On one hand, it provides accurate reference data—collisional rate coefficients and spectral line-shape parameters—for three major fields where collisions play a critical role: astrophysics, atmospheric science, and high-precision spectroscopy of simple molecules for fundamental studies. On the other hand, it examines subtle effects that shape collisional dynamics and perturb interactions with electromagnetic fields, such as the accuracy of intermolecular potentials, quantum indistinguishability, hyperfine structure, and external magnetic fields. These goals are firmly grounded in quantum theory: the approach employed in this work relies on *ab initio* potential energy surfaces (PESs), rigorous quantum scattering calculations, and a line-shape model derived from the quantum Boltzmann equation.



This dissertation is organized thematically into three main parts. The first part explores the influence of molecular collisions in two vastly different astrophysical environments: the interstellar medium (ISM) and planetary atmospheres. The second part focuses on the role of collisions in studies of the terrestrial atmosphere and ongoing efforts to develop comprehensive databases of collisional parameters. Finally, the third part shifts to high-precision spectroscopy of the simplest neutral diatomic molecule—hydrogen—addressing various factors that contribute to uncertainties in transition frequency measurements. This part concludes by discussing recent proposals to push precision spectroscopy toward its fundamental limits, including the concept of trapping molecular hydrogen and exploring the potential for sympathetic cooling.

The Introduction is followed by 12 peer-reviewed publications that constitute the core of this work. The Conclusions section summarizes the achievements and presents potential future research directions. The Notation section includes descriptions of key nomenclature used throughout the thesis and a list of acronyms for reference. For interested readers, appendices provide additional details on methodology, technical aspects, and unpublished results.

## **Part I. Astrophysics: Interstellar Medium and Planetary Atmospheres**

Our knowledge of remote astronomical objects relies fundamentally on spectroscopy [16]. The positions of spectral lines reveal the chemical composition of the observed celestial object, while their relative intensities, reflecting the population distribution of atomic or molecular energy levels, carry information about its temperature. Accurate determination of line intensities, when combined with laboratory measurements or theoretical calculations of intrinsic line strengths, allows determination of the abundance of atoms or molecules in the observed environment. Doppler shifts in astronomical spectra reveal the motion of distant objects relative to the observer. If the spectra are taken with high resolution, the shape of individual spectral lines can provide information about the pressure and density of the emitting region. Spectra can even provide information about magnetic fields in remote environments, as these lead to the splitting of spectral lines.



## Interstellar medium

Spectroscopic observations of the ISM began with Hartmann's 1904 discovery [17]. While examining the binary system  $\delta$ -Orionis—the westernmost star of Orion's belt—Hartmann identified "*extraordinarily weak, but almost perfectly sharp*" ionized calcium line at 393.4 nm. Interestingly, this absorption line did not exhibit the periodic Doppler shift variations, that are characteristic for lines associated with a rotating binary system. This indicated that the line originated from "*clouds of atoms*" along the line of sight to the stellar source. The presence of molecules in the ISM was confirmed in the 1940s [18] with the detection of radicals such as CH [19, 20],  $\text{CH}^+$  [21], and CN [22, 23]. The advent of radio astronomy after World War II significantly accelerated the detection of interstellar molecules [18]. Modern telescopes enable the acquisition of high-resolution spectra across a wide range of wavelengths, from the millimeter and sub-millimeter regime (e.g., the ground-based Atacama Large Millimeter/sub-millimeter Array, ALMA [24, 25]) to the infrared (e.g., the Stratospheric Observatory for Infrared Astronomy, SOFIA [26, 27], and the James Webb Space Telescope, JWST [28, 29]). As of December 2024, over 320 molecular species have been identified in the interstellar medium.<sup>1</sup>

The ISM is composed of various phases, each characterized by distinct densities and temperatures [30]. The hottest and most tenuous phase, the ionized medium, consists of plasma at temperatures exceeding  $10^6$  K and densities as low as  $10^{-4} \text{ cm}^{-3}$ , often found in regions heated by supernova explosions. Cooler phases include the warm neutral (atomic) medium, with temperatures around  $10^4$  K and densities of  $0.1\text{--}1 \text{ cm}^{-3}$ , and the cold neutral medium, where temperatures drop to  $10\text{--}100$  K and densities increase to  $10\text{--}100 \text{ cm}^{-3}$ . The densest regions are found in molecular clouds, where temperatures range from  $10$  to  $100$  K and densities can reach up to  $10^6 \text{ cm}^{-3}$ .<sup>2</sup> Molecular clouds are of particular interest – this is precisely the environment in which stars are formed and these regions are particularly rich in chemistry.

Interpreting ISM spectra is far from straightforward. A key quantity in spectral analysis is the specific intensity,  $I_\nu$ , defined as the amount of energy passing through a surface normal to the line of sight, per unit time, surface area, frequency, and solid angle. The propagation of specific intensity through an

<sup>1</sup><https://cdms.astro.uni-koeln.de/classic/molecules>

<sup>2</sup>To add some perspective, the densities of air at sea level and in laboratory high-vacuum chambers are  $10^{19} \text{ cm}^{-3}$  and  $10^{10} \text{ cm}^{-3}$ , respectively.



absorbing and emitting medium is governed by the radiative transfer equation [31]

$$\frac{dI_v}{ds} = -\alpha_v(\mathbf{r})I_v + j_v, \quad (1)$$

where  $s$  is the distance along the line of sight  $\alpha_v$  is the absorption coefficient, and  $j_v$  is the emission coefficient.  $\alpha_v$  and  $j_v$  depend on Einstein coefficients for stimulated emission and absorption, and spontaneous emission, respectively, and on the populations of molecular levels. However, in the low-density environments of the ISM, local thermodynamic equilibrium (LTE) is often not achieved, and molecular populations deviate from the Boltzmann distribution [32]. Instead, the level populations are determined by an interplay between radiative and collisional processes.

### Radiative transfer calculations

To compute molecular populations, a set of rate equations must be solved, incorporating both radiative and collisional transitions. For a simple two-level system, the rate equations are [31]

$$\begin{aligned} \frac{dn_1}{dt} &= \left( -n_1 B_{12} + n_2 B_{21} \right) \rho_\nu + n_2 A_{21} - n_1 C_{12} + n_2 C_{21} \\ \frac{dn_2}{dt} &= -\frac{dn_1}{dt}. \end{aligned} \quad (2)$$

The first two terms describe radiative transitions proportional to the spectral energy density,  $\rho_\nu$ : absorption from level 1 to level 2, governed by the Einstein  $B_{12}$  coefficient (in units of  $\text{m}^3 \text{s}^{-2} \text{J}^{-1}$ ), and stimulated emission from level 2 to level 1, described by the Einstein coefficient  $B_{21}$  (same units). The third term,  $n_2 A_{21}$ , represents spontaneous emission from level 2 to level 1, where  $A_{21}$  (in  $\text{s}^{-1}$ ) is the Einstein coefficient for spontaneous emission. The last two terms account for collisional transitions between levels, where  $C_{ij}$  are the collisional rates (in  $\text{s}^{-1}$ ), proportional to the density of the perturbing species  $n^{\text{col}}$  (in  $\text{cm}^{-3}$ ) and the collisional rate coefficients  $k_{ij}$  (in  $\text{cm}^3 \text{s}^{-1}$ )

$$C_{ij} = n^{\text{col}} k_{ij}. \quad (3)$$

In molecular clouds, where hydrogen ( $\text{H}_2$ ) is the most abundant species,  $k_{ij}$  quantifies the rate of collisional excitation of the radiatively active molecule from state  $i$  to  $j$  upon collision with  $\text{H}_2$ .



## Rate coefficients

Accurate determination of collisional rate coefficients is essential for interpreting molecular spectra and understanding the physical and chemical processes in the ISM [32, 33]. Experimental measurements of state-specific collisional rates are notoriously challenging due to the difficulty of isolating individual transitions and covering the temperature range relevant to ISM studies ( $T < 100$  K). Instead, rate coefficients can be calculated theoretically. The most accurate approach relies on rigorous quantum scattering calculations, which use *ab initio* potential energy surfaces (PESs) to predict state-to-state collisional dynamics.

A typical procedure begins with the calculation of the PES (within the Born-Oppenheimer approximation), for the system involving *target* species and the *projectile* – which is typically the  $\text{H}_2$  molecule.<sup>3</sup> The PES is used to solve the Schrödinger equation for the nuclear motion of the colliding partners. From the boundary conditions imposed on the scattering wavefunction, the  $S$ -matrix is obtained, which describes the state-to-state cross-sections for collisional transitions. To derive rate coefficients, these cross-sections are computed over a grid of collision energies and averaged over the thermal distribution of collision energies at a given temperature. A detailed description of this procedure is provided in Appendix A.

Given the increasing number of molecular species detected in the ISM, providing a comprehensive dataset of collisional rate coefficients for each molecular species becomes a well-defined, but challenging goal of the molecular astrophysics community. For the large, polyatomic organic molecules frequently detected in the ISM or systems with deep potential wells, rigorous quantum scattering calculations are computationally infeasible [34, 35]. Instead, decoupling approximations [36–38], mixed quantum/classical theory [39–41], or statistical approaches [42, 43] are employed to estimate rate coefficients, though these often give an order of magnitude estimate for the actual rate coefficients. For simpler systems, such as  $\text{H}_2\text{-H}$  [44],  $\text{HD-H}$  [45] or  $\text{HD-H}_2$  [46], revisiting older calculations with modern PESs allows for broader coverage of molecular levels and temperatures with improved accuracy.

<sup>3</sup>Due to its overall simplicity, helium atom is frequently used as a proxy for  $\text{H}_2$ , and rate coefficients are usually rescaled by the proper reduced mass ratio,  $k^{\text{X-H}_2} = \sqrt{\frac{\mu_{\text{X-H}_2}}{\mu_{\text{X-He}}}} k^{\text{X-He}}$ .





## Revisiting rate coefficients with improved PESs

Article **A** follows this trend, focusing on one of the simplest systems in the ISM:  $\text{H}_2$ -He. Rate coefficients for rovibrational transitions of  $\text{H}_2$  in collisions with He are crucial for modeling various astrophysical environments. In the early Universe, collisional excitation of  $\text{H}_2$  followed by infrared emission was one of the dominant cooling mechanisms of the primordial gas [47]. Beyond the cosmological context,  $\text{H}_2$ -He rate coefficients play a significant role in modeling turbulent diffuse interstellar clouds [48] and protoplanetary disk chemistry [49].

Historically, the most commonly adopted rate coefficients for the  $\text{H}_2$ -He system were computed by Flower [50] using the PES of Muchnick and Russek (MR) [51]. While pioneering for its time, the accuracy of this PES has been a matter of debate. Inelastic rate coefficients calculated using this surface were considered robust in the early 2000s [52, 53]. However, a recent comparative study of interaction potentials [54] revealed that even an improved version of the MR PES fails to accurately model the shapes of optical resonances, which are more susceptible to the fine details of the interaction potential than inelastic rate coefficients [14].

This raises an important question: how reliable are the existing datasets? Could a new PES introduce significant corrections to rate coefficients, potentially altering astrophysical models?

In light of this, Paper **A** revisited the  $\text{H}_2$ -He system using the state-of-the-art PES [55] to perform rigorous quantum scattering calculations and reassess the 26-year-old data. The revised rate coefficients showed excellent agreement with the earlier results [50, 56, 57] for pure rotational transitions. However, significant discrepancies were observed for excited vibrational transitions, which were attributed to the superior quality of the new PES. Unlike its predecessor, the new PES accurately describes  $\text{H}_2$ -He interactions across a wider range of  $\text{H}_2$  bond lengths, which is particularly important for transitions involving highly excited vibrational states.

To assess the astrophysical implications, the revised data were incorporated into radiative transfer calculations [31], simulating excitation conditions in the early Universe ( $T = 5000$  K, He density of  $10^3 \text{ cm}^{-3}$ ) and warm molecular clouds ( $T = 1000$  K, He density of  $10^5 \text{ cm}^{-3}$ ). While the updated rates had a negligible effect on the populations of  $\text{H}_2$  within the ground vibrational



state, a significant reduction was observed for the populations of excited vibrational states ( $v > 0$ ). This finding demonstrates the importance of using the updated collisional data in astrophysical models, particularly those involving vibrationally excited  $\text{H}_2$  in high-temperature astrophysical environments.

## Planetary atmospheres

In stark contrast to the ISM, planetary atmospheres are characterized by high densities and frequent molecular collisions. Under these conditions, local thermodynamic equilibrium is achieved, and molecular populations follow the Boltzmann distribution. However, the high frequency of collisions significantly perturbs the shape of spectral lines through two main effects: collisional broadening and collisional shifting. Before delving into their specific impact on planetary spectra, it is essential to briefly outline the fundamental factors that shape the observed spectral profiles.

### Fundamental Factors Contributing to the Spectral Line Shape

**Collisional broadening and shift.** The most direct effect of collisions is the energy transfer between the *active molecule* and the *perturber*, which includes vibrational, rotational, and relative translational motions [11]. These energy exchanges limit the lifetimes  $\Delta t$  of molecular states involved in a spectral transition,  $b \leftarrow a$ . According to Heisenberg's uncertainty principle, the collisional width for this line is approximately  $(\Delta t_a)^{-1} + (\Delta t_b)^{-1}$ .<sup>4</sup> Since the energy transfer occurs during collisions, the lifetimes can be approximated by the free-flight duration—the time between successive collisions,  $\tau_0$ . This is estimated as the ratio of the mean free path,  $l_0$ , to the average relative velocity of colliding species. For common diatomic molecules ( $\text{CO}$ ,  $\text{N}_2$ ,  $\text{O}_2$ ) at standard temperature and pressure,  $\tau_0 \approx 10^{-10}$  s. Consequently, the half-width at half-maximum (HWHM) is  $\Gamma \approx 1/\tau_0$ , which agrees within an order of magnitude with typical collisional widths—approximately 1 GHz at pressure  $p = 1$  atm and room temperature.

The collisional shift occurs because the interactions between colliding molecules modify their energy levels—the transition frequency  $\nu_0 = (E_b - E_a)/h$ ,

---

<sup>4</sup>Even in the absence of collisions, spectral lines possess an inherent width, *the natural width*, arising from finite lifetimes of states  $a$  and  $b$  due to spontaneous emission. Natural widths for rovibrational transitions in most diatomic molecules are below the best spectral resolutions; however, the concept of natural linewidth will be revisited in the final section of this thesis.



becomes a function of intermolecular distance. First-order perturbation theory relates the collisional shift  $\Delta$  to the difference in averaged interaction energies between states  $b$  and  $a$  [11]

$$\Delta \approx h^{-1} \left( \langle V \rangle_b - \langle V \rangle_a \right), \quad (4)$$

where  $\langle V \rangle_i$  is the averaged interaction between the active molecule and the perturber when the former is in state  $i$ , and  $h$  is the Planck constant. A significant collisional shift occurs only if the interaction energies differ substantially between the two states coupled by electromagnetic radiation. Conversely, collisional broadening is related to the *sum* of the perturbations in the two states [11]. As a result, in most molecular systems collisional shifts are at least an order of magnitude smaller than collisional broadening. An important exception is self- and foreign-gas perturbed molecular hydrogen lines [15, 58], also discussed in this thesis.

In the absence of other broadening and shifting mechanisms, the spectral line shape induced by collisional effects is Lorentzian [59]

$$L(\nu; \Gamma, \Delta) = \frac{1}{\pi} \frac{\Gamma}{\Gamma^2 + (\nu - \nu_0 - \Delta)^2}, \quad (5)$$

where  $\Gamma = p\gamma$  is the collisional HWHM,  $\Delta = p\delta$  is the collisional shift (both in  $\text{s}^{-1}$ ),  $p$  is the pressure,  $\nu_0$  is the unperturbed transition frequency, and  $\gamma$  and  $\delta$  are the pressure broadening and shift coefficients, respectively. While the SI unit for  $\gamma$  and  $\delta$  is  $\text{Pa}^{-1} \text{s}^{-1}$ , it is customary to express them as  $\text{cm}^{-1} \text{atm}^{-1}$ , as done in this work.

**Doppler broadening** In addition to collisional effects, the motion of molecules relative to incoming light introduces another important broadening mechanism: Doppler broadening. Molecules in a gas are constantly in motion, with their velocities ( $v$ ) distributed according to the Maxwell-Boltzmann distribution

$$f(v)dv = \left( \frac{1}{\sqrt{\pi}v_m} \right)^3 \exp \left( -\frac{v^2}{v_m^2} \right) dv, \quad (6)$$

where  $v = |v|$  is the speed and  $v_m = \sqrt{2k_B T/m}$  denotes the most probable speed. Here,  $m$  is the molecular mass,  $k_B$  is the Boltzmann constant and  $T$  is the temperature. When a molecule moves relative to the propagation of light, the frequency of the absorbed or emitted photon is shifted by an amount pro-



portional to the molecule's velocity along the line of sight,  $\nu_0 v_k/c$ , where  $v_k$  is the velocity component of the molecule along the direction of light propagation,  $\mathbf{v} \cdot \hat{\mathbf{k}}$ ,  $\hat{\mathbf{k}}$  is the unit vector along  $\mathbf{k}$ , and  $c$  is the speed of light. Summing the contributions from all molecular velocity classes gives the frequency distribution of absorbed or emitted light. The resulting line shape is a Gaussian

$$G(\nu; \nu_D) = \frac{1}{\sqrt{\pi}\nu_D} \exp\left(-\frac{(\nu - \nu_0)^2}{\nu_D^2}\right), \quad (7)$$

where the Doppler width (in  $\text{s}^{-1}$ ) is given by

$$\nu_D = \nu_0 \frac{v_m}{c}. \quad (8)$$

$\nu_D$  corresponds to the standard deviation of the frequency distribution and is related to the HWHM of the Gaussian profile by

$$\Gamma_D = \sqrt{\ln 2} \nu_D. \quad (9)$$

At room temperature, the Doppler broadening for typical diatomic molecules in the infrared range is of an order of  $10^2$  MHz.

**Voigt profile** The Lorentzian (Eq. (5)) and Gaussian (Eq. (7)) functions describe collisional and Doppler broadening mechanisms, respectively, under the assumption that no other factors perturb the line shape. This assumption rarely holds, since at standard atmospheric conditions collisional and Doppler broadening have comparable magnitudes. How, then, should the spectral line be described to account for both collisional and motional effects? A common approach is to assume that these effects are statistically independent. The resulting spectral line shape is given by the convolution of the Gaussian and Lorentzian profiles, referred to as the *Voigt profile* [60]

$$I_V(\nu; \nu_D, \Gamma, \Delta) = \int_{-\infty}^{+\infty} G(\nu'; \nu_D) L(\nu - \nu'; \Gamma, \Delta) d\nu'. \quad (10)$$

The Voigt profile is widely used in spectral analysis and serves as a reference for more sophisticated line-shape models [11]. It provides an intuitive description of what happens in two limiting regimes: the low-pressure case with negligible collisional contribution reduces to the Doppler-broadened Gaussian, and the high-pressure limiting case provides the collision-perturbed Lorentzian.



**Beyond-Voigt line-shape effects** However, accurate interpretation of molecular spectra—particularly in atmospheric contexts—requires consideration of subtle effects that arise from the interplay between thermal motion and molecular collisions. These effects, collectively referred to as *beyond-Voigt line-shape effects*, include two prominent phenomena: speed dependence of collisional parameters [61–63] and line narrowing due to velocity-changing collisions [64, 65].

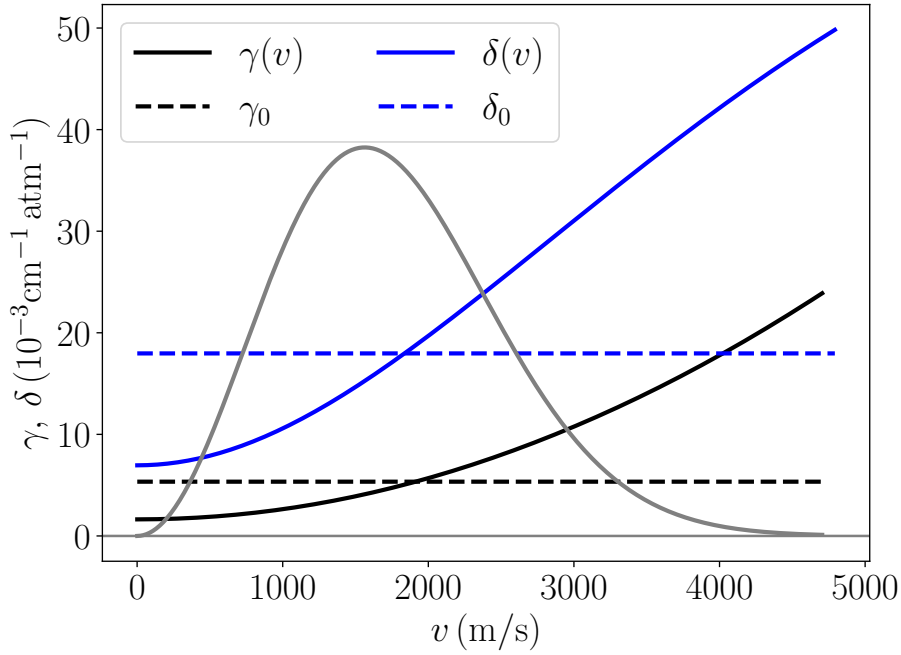


Figure 1: Speed-dependence of pressure broadening ( $\gamma(v)$ , black curve), and pressure shift coefficients ( $\delta(v)$ , blue curve) of the He-perturbed 2-0 Q(1) line in  $\text{H}_2$  at  $T = 296$  K. The speed-averaged values ( $\gamma_0$  and  $\delta_0$ ) are given as black and blue dashed lines, respectively. The grey curve corresponds to the Maxwell-Boltzmann distribution of molecular speeds at  $T = 296$  K. The plots are generated based on generalized spectroscopic cross-sections published in Article **C**.

The first effect refers to the variation of collisional broadening,  $\Gamma$ , and shift,  $\Delta$ , with the molecule’s speed. Figure 1 illustrates the speed dependence of the pressure broadening ( $\gamma = \Gamma/p$ ) and shift ( $\delta = \Delta/p$ ) coefficients for the He-perturbed 2-0 Q(1) transition in  $\text{H}_2$ , calculated *ab initio* at  $T = 296$  K. This is an example of the spectral line, for which the speed-averaged pressure shift coefficient is three times larger than the pressure broadening coefficient. Both  $\gamma$  and  $\delta$  exhibit a strong speed dependence, varying by factors of 14 and 7, respectively, across the range of molecular speeds described by the Maxwell-Boltzmann distribution.

To understand how these variations influence the eventual spectral line shape, Fig. 2 demonstrates the distribution of Lorentzian profiles simulated for different molecular speeds, with  $\Gamma$  and  $\Delta$  values substituted by their speed-dependent counterparts presented in Fig. 1. The analysis separates the effects of speed-dependent broadening and shift. In the left panel, the simulated Lorentzians incorporate the actual speed dependence of  $\Gamma(v)$  while keeping the shift fixed at the speed-averaged value,  $\Delta_0 = 1.797 \times 10^{-2} \text{ cm}^{-1}$ . In the right panel, the simulated Lorentzians include the speed dependence of  $\Delta(v)$ , while the width is held constant at the speed-averaged value,  $\Gamma_0 = 5.34 \times 10^{-3} \text{ cm}^{-1}$ .<sup>5</sup>

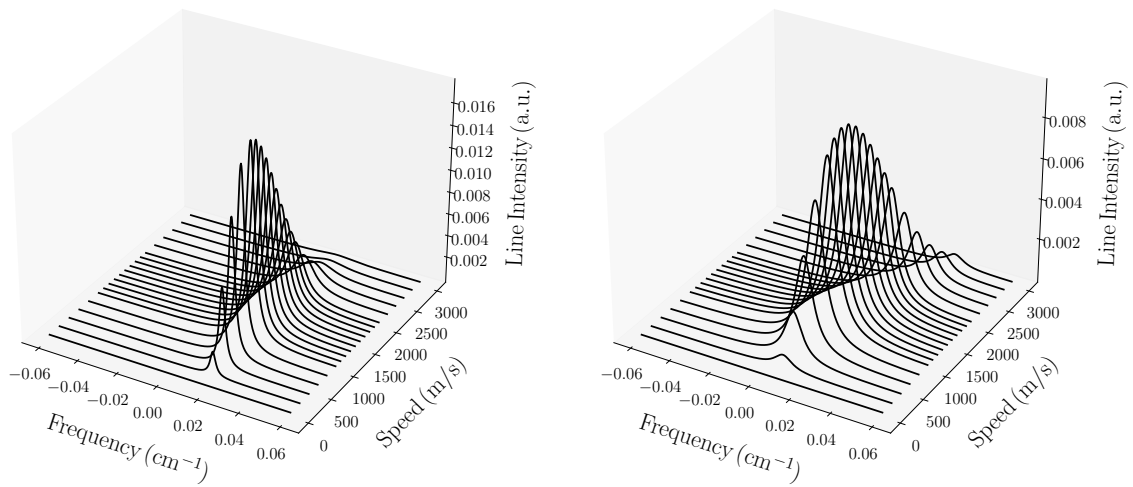


Figure 2: Simulation of the He-perturbed 2-0 Q(1) line in H<sub>2</sub> at  $T = 296 \text{ K}$  and  $p = 1 \text{ atm}$ , using Lorentzian profiles (Eq. (5)) for different H<sub>2</sub> speeds. In the left panel, the collisional shift is fixed to its speed-averaged value, while the HWHM varies with  $\gamma(v)$  from Fig. 1. In the right panel, the collisional HWHM is fixed to its speed-averaged value, while the shifts vary with  $\delta(v)$  from Fig. 1.

The left panel clearly shows that most of the most intense Lorentzians have widths smaller than the speed-averaged collisional HWHM: they are narrower than Lorentzians in the right panel, which are simulated with widths fixed at  $\Gamma_0$ . This effect can be deduced from the previous figure, where  $\gamma(v)$  intersects  $\gamma_0$  at a speed higher than the most probable speed. When averaged over speeds, these Lorentzians will lead to a symmetric and narrowed profile.

The right panel presents the impact of speed dependence of collisional shift, showing a distribution of Lorentzians where the shifts vary with  $\delta(v)$  from Fig. 1. When averaged over the speed distribution, these Lorentzians produce an asymmetric and strongly broadened profile.

<sup>5</sup>Values of  $\Gamma_0$ ,  $\Delta_0$ , along with the generalized spectroscopic cross-sections used to derive the speed-dependent counterparts, are taken from Article **C**.

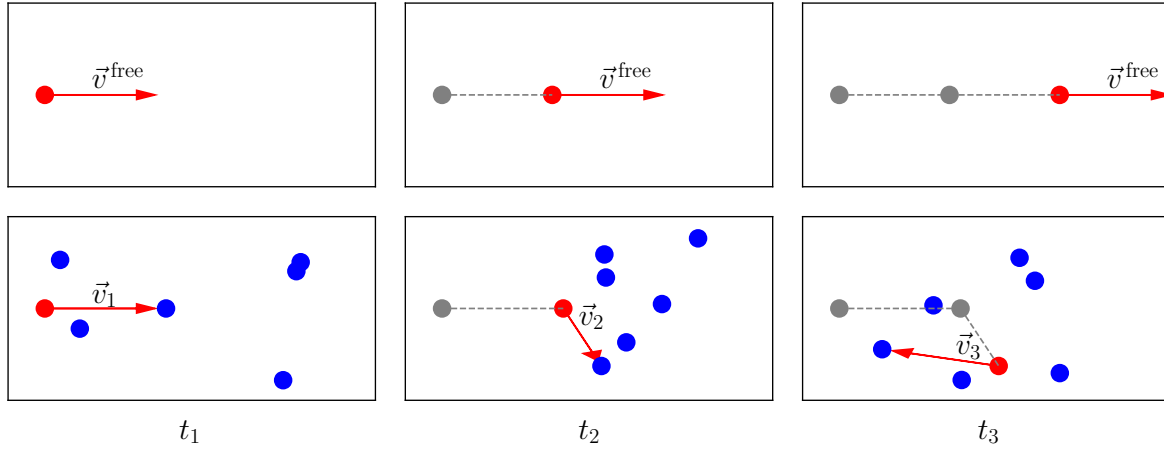


Figure 3: A simple illustration of the origin of the Dicke narrowing effect. The top panels represent the free-streaming motion of an active molecule (red dot) without collisions, where the molecule travels at a constant velocity ( $v^{\text{free}}$ ) across three consecutive timestamps ( $t_1$ ,  $t_2$ ,  $t_3$ ). The bottom panels depict velocity-changing (VC) collisions of the active molecule, the trajectory of which is altered by collisions with perturbers. The current position of the active molecule at timestamp  $t_i$  is shown in red, while its past positions are marked as gray dots, connected by dashed gray lines to indicate its history. The blue markers represent perturber molecules.

The second effect involves collisions in which the active molecule remains in the same quantum state but experiences changes in its velocity. Frequent velocity changes lead to *Dicke narrowing*. Fig. 3 illustrates an intuitive explanation of this effect. In the absence of collisions (top panel), a free-streaming molecule moves with velocity  $v^{\text{free}} = \Delta r^{\text{free}} / \Delta t$ , where  $\Delta r^{\text{free}}$  is the displacement during time interval  $\Delta t = t_3 - t_1$ . When velocity-changing (VC) collisions occur (bottom panel), the effective displacement  $r^{\text{VC}}$  is reduced compared to the free-streaming case ( $r^{\text{VC}} < r^{\text{free}}$ ). Consequently, the Doppler broadening contribution is also reduced, as  $\hat{k} \cdot v^{\text{VC}} < \hat{k} \cdot v^{\text{free}}$ , leading to a narrowing of the spectral line.

The phenomenon of Dicke narrowing, first detected in light molecules [66–69], has now been identified in more than 20 species [11, 65]. The theoretical basis was first described in the 1950s by Dicke [64], who developed a model to account for velocity-changing collisions. In his framework, VC collisions reduce the effective displacement of a molecule during its free flight, confining its motion and thereby narrowing the Doppler broadening contribution. The





resulting line shape is Lorentzian, with a HWHM given by [70]

$$\Gamma_{\text{Dicke}} = p\gamma + k^2 \frac{D_0}{p}, \quad (11)$$

where  $D_0$  is the diffusion coefficient. This formula predicts a pressure dependence of the HWHM: it initially decreases as Dicke narrowing dominates, reaches a minimum, and then increases as collisional broadening ( $p\gamma$ ) becomes the dominant effect. However, at low pressures, Dicke's model fails to converge to the Doppler limit.

The ultimate goal of line-shape theory is to develop a model that correctly predicts spectral line profiles across both limiting regimes—low pressures dominated by Doppler broadening and high pressures dominated by collisions—while also accurately describing the intermediate regime where these effects coexist. Over the decades, numerous phenomenological models have been proposed to address this challenge [71–73]. A detailed review of these models is beyond the scope of this introduction. Interested readers are directed to comprehensive discussions available in the literature [11, 74].

A fundamental limitation of phenomenological line-shape models is their reliance on adjustable parameters: collisional width, shift, their speed dependence, and the parameter quantifying the frequency of velocity-changing collisions, which are determined through spectral fitting. This approach presents two challenges: first, different line-shape models can fit the same spectra equally well; second, the fitted parameters may be correlated with one another. In both cases, this raises concerns about the physical interpretation and reliability of the extracted parameters.

An alternative approach is to predict spectral line shapes from first principles, based on rigorous quantum mechanical calculations. These *ab initio* approaches eliminate reliance on fitting and provide a direct connection between the microscopic properties of the system and the observed spectra. This framework [75, 76] forms the foundation of the work presented in this dissertation. For a brief overview of the theoretical approach, the interested reader is referred to Appendix B.

The key advantage of *ab initio* approaches is their ability to link collisional widths and shifts, their speed dependences, and parameters quantifying velocity-changing collisions directly to the scattering  $S$ -matrix. The same rigorous quantum scattering calculations used to determine collisional rate coef-





ficients (Eq. (3)) can thus be employed to derive collisional line-shape parameters. This provides a powerful tool for detailed studies of mechanisms driving collisional perturbation of spectral lines.

In this dissertation, specifically in Papers **B**, **C**, and **E**, beyond-Voigt spectra are modeled using a line-shape profile that accounts for the Doppler effect, velocity-changing collisions, the speed dependence of collisional broadening and shift, and the correlations between velocity- and state-changing collisions. The model approximates the speed dependence of collisional width and shift as a quadratic function

$$\Gamma(v) - i\Delta(v) \approx (\Gamma_0 - i\Delta_0) + (\Gamma_2 - i\Delta_2) \left( \frac{v^2}{v_{m_A}^2} - \frac{3}{2} \right), \quad (12)$$

where  $v_{m_A}$  is the most probable speed of the active molecule. Additionally, the velocity-changing collisions are treated using the hard-collision model, in which post-collisional velocity is randomly sampled from a Maxwell-Boltzmann distribution, independent of the pre-collisional value.

This model is commonly referred to as the quadratic speed-dependent hard-collision (qSDHC) profile. However, in Article **B**, it is referred to for the first time as the modified Hartmann-Tran (mHT) profile. The name stems from the Hartmann-Tran (HT) profile [77], which was recommended by the International Union of Pure and Applied Chemistry Water-Vapor Task Group for water line analysis [78]. The most significant difference between the HT and mHT profiles is that the HT profile includes the real-valued frequency of velocity-changing collision and an additional correlation parameter  $\eta$ , which quantifies the correlation between velocity- and state-changing collisions [73]. The mHT profile replaces the velocity-changing collision frequency with a complex Dicke parameter and does not involve the  $\eta$  parameter.

It is important to note that the mHT profile has phenomenological roots [72, 73, 79, 80]. However, its mathematical form closely resembles the high-pressure limit of the *ab initio* Hess profile [75] (see Appendix B). The Hess profile, in contrast to the mHT, is derived rigorously and involves parameters that can be determined directly from quantum scattering calculations. Leveraging this resemblance, the adjustable parameters of the mHT profile are assigned to correspond to the parameters that define the Hess profile, grounding the phenomenological model in a rigorous theoretical framework.

For systems exhibiting strong Dicke narrowing, it is recommended to apply



the so-called  $\beta$ -correction [58, 81], which enhances the hard-collision model of velocity-changing collisions, making it more similar to the speed-dependent billiard ball (SDBB) profile [82]. The SDBB profile is recognized as the most accurate line-shape model for representing spectra of molecular hydrogen [15, 83], although it is significantly more computationally demanding.  $\beta$ -correction, however, offers a computationally efficient alternative that is applicable to any molecular system, as it depends only on the perturber-to-absorber mass ratio. In this dissertation, the  $\beta$ -corrected version of the mHT or HT profile was used in Papers **B**, **C**, and **E**.

### **Collisional perturbation of planetary spectra**

An important question arises—since we are in the astrophysical section—to what extent do collisional effects perturb the shape of planetary spectra? Are beyond-Voigt effects relevant for planetary atmosphere observations? At first glance, the reader might find this claim dubious, given that planetary spectra are often recorded with signal-to-noise ratios on the order of  $10^1$ . This very question is addressed in Paper **B**, which focuses on the atmospheric studies of the giant planets in the Solar System: Jupiter, Saturn, Uranus, and Neptune.

The atmospheres of these gas giants are dominated by significant amounts of hydrogen and helium. Molecular hydrogen spectra, in particular, exhibit exceptionally strong beyond-Voigt line shape effects [58, 84]. First, due to the large rotational constant ( $B = 60.453 \text{ cm}^{-1}$  [85]), inelastic collisions are inhibited at  $T < 1000 \text{ K}$ , and velocity-changing collisions dominate, leading to significant Dicke narrowing of hydrogen lines. Second, hydrogen spectra exhibit an unusually strong speed-dependence of line shifts, resulting in strong inhomogeneous broadening and pronounced asymmetry [86]. These factors have made the proper interpretation of hydrogen spectra a significant challenge for more than 25 years [83, 84, 87–92]. The need for incorporating beyond-Voigt spectral line shape parameters in astrophysical models has been previously raised in the context of populating *ab initio* databases, particularly for analyzing planetary spectra [58].

Paper **B** highlights the significance of these effects for conditions relevant to the atmospheres of gas giants. Figure 2 in Paper **B**, for instance, graphically represents the errors introduced by using the Voigt profile in analyzing the three strongest pure rotational transitions of hydrogen deuteride (HD), compared to the mHT profile, which incorporates beyond-Voigt effects. Even



under moderate conditions, these errors can reach up to 70%, demonstrating the critical need for accurate line shape modeling.

To address this, Paper **B** provides reference collisional line-shape parameters for H<sub>2</sub>- and He-perturbed pure rotational transitions in HD. Calculations are performed using a new, *ab initio* PES for the H<sub>2</sub>-H<sub>2</sub> system, validated against high-precision cavity-enhanced spectra. These results have been coupled with HITRAN's [93] Application Programming Interface (HAPI) [94], enabling users to simulate beyond-Voigt line profiles directly from the data provided in the paper.

A careful reader might wonder why this study focuses on hydrogen deuteride, which is less abundant than H<sub>2</sub>. While this is true, HD spectra are still detected in planetary atmospheres because the molecule possesses a small dipole moment, permitting electric dipole rovibrational transitions [95]. Observations of HD are essential for determining the deuterium-to-hydrogen (D/H) ratio, a key marker in planetary evolution models [96].

A vast body of literature has been dedicated to measuring and interpreting the D/H ratio across the Solar System (see references in Paper **B**). Since deuterium is lost in the <sup>3</sup>He synthesis inside the Sun, it is expected that the D/H ratio decreased monotonically in time from the *protosolar value* ( $(2.1 \pm 0.5) \times 10^{-5}$  [97]) to the contemporary D/H ratio observed in the local interstellar medium ( $(1.5 \pm 0.1) \times 10^{-5}$  [98]). For Jupiter and Saturn, however, planetary models predict that the D/H ratio should be close to the protosolar value [96] or slightly larger, due to the accretion of deuterium-rich icy grains and planetesimals [99].

Recent observations revealed that the deuterium fraction is smaller on Saturn than on Jupiter [100], raising the possibility of an unknown deuterium depletion mechanism in Saturn's atmosphere. The most accurate values of the D/H ratio in gas giants are derived from the analysis of pure rotational lines in HD and H<sub>2</sub> [96, 101]. As shown in Paper **B**, proper treatment of molecular collisions, including beyond-Voigt effects, is crucial for the accurate determination of these ratios.

Interestingly, a few months ago, a group of astronomers revisited the HD spectra of Jupiter using *ab initio* line-shape parameters determined in our group [102]. The revised D/H ratio was found to be in agreement with the previously determined value for Saturn, suggesting that no additional depletion mechanisms are present after all.



**A demand for collisional datasets for exoplanetary studies** So far, I have highlighted an important application of *ab initio* calculations of spectral line-shape parameters in the study of giant planet atmospheres within the Solar System. A natural question arises: are these calculations also needed for exoplanetary studies? This issue has indeed been raised by many authors [103–106], highlighting the need for accurate line-shape modeling of exoplanetary spectra. With the launch of the JWST in 2021 [29], exoplanetary research has entered a new era, enabling the acquisition of spectra at high spectral resolutions. It is crucial to ensure that no factors on the spectroscopic side introduce biases into the interpretation of these spectra.

Although beyond-Voigt effects are not yet significantly influencing exoplanetary spectral analyses, a recent study suggests that pressure broadening coefficients for the molecules detected in exoplanetary atmospheres should be known to within 10% uncertainty to avoid potential biases [107]. The same study highlights a gap in existing databases, such as HITRAN [93] and ExoMol [108], which currently provide limited information on pressure broadening coefficients, particularly for molecules critical to exoplanetary research. This shows a growing demand for accurate line-shape parameters—not only to refine the interpretation of exoplanetary spectra today but also to account for more subtle effects that will become increasingly important in future missions.

## **Part II. Terrestrial Atmospheric Studies: Toward *ab initio* Spectroscopic Databases**

The demand for accurate spectral line-shape parameters is more pressing in the context of terrestrial atmospheric science. Applications such as climate modeling and pollution tracking rely on remote sensing—spectroscopic observations of the atmosphere from satellites and ground-based instruments. Concentrations of greenhouse gases (e.g., CO<sub>2</sub>, CH<sub>4</sub>) and atmospheric pollutants (e.g., CO, HCl, HF) are retrieved by fitting line-shape models to observed spectra. With the high spectral resolution and signal-to-noise ratios typical of these measurements ( $\sim 10^2$ ), the simple Voigt profile fails to accurately reproduce the observed spectra. The resulting errors in spectral fitting can propagate to errors in the derived quantities, such as the abundance of absorbing species.



To reduce systematic errors in the analysis of atmospheric spectra, accurate reference line-shape parameters are essential. However, providing such parameters *experimentally* is infeasible given the vast number of species of interest, the multitude of spectral transitions to cover, and the broad range of thermodynamic conditions encountered in the atmosphere. This parallels the challenges faced in providing reference collisional rate coefficients for interstellar medium studies. An alternative approach is to rely on theoretical methods to produce accurate reference datasets.

## **Benchmark system: H<sub>2</sub>-He**

The previous section—specifically, Paper **B**—demonstrated the feasibility of using *ab initio* calculations to generate accurate reference datasets for the strongest pure rotational transitions in hydrogen deuteride. This naturally raises the question: is it possible to extend these methods to produce comprehensive databases of collisional line-shape parameters entirely through theory? Achieving this goal would fill a critical gap in atmospheric spectroscopy, enabling more precise interpretations of molecular spectra across a wide range of applications.

As a first step toward this ambitious objective, we focused on the benchmark system: He-perturbed H<sub>2</sub> lines. The H<sub>2</sub>-He system has been a focal point of our group’s research for nearly a decade. A detailed assessment of various potential energy surfaces [14] identified the PES of Bakr, Smith, and Patkowski (BSP) [109] as the most reliable for predicting pressure broadening and shift coefficients for various rovibrational transitions in He-perturbed lines of H<sub>2</sub> and D<sub>2</sub>. This PES was subsequently refined to cover an extended range of bond stretches in H<sub>2</sub> and supplemented with additional *ab initio* points at large He-H<sub>2</sub> separations [55].

The improved PES has since been used to calculate beyond-Voigt line-shape parameters for selected rovibrational transitions in He-perturbed H<sub>2</sub> [55, 110], HD [111, 112], and D<sub>2</sub> [113], as well as rate coefficients for these systems (see Article **A**, and Refs. [114, 115]). A significant milestone was achieved when purely theoretical spectra derived from these calculations were superimposed on experimental spectra, yielding sub-percent agreement [15]. Further studies underscored the importance of accounting for more subtle effects, such as the centrifugal distortion of the PES, to maintain sub-percent accuracy in collision-



nal line-shape parameters for transitions involving highly excited rovibrational levels [54, 112].

Building on this extensive body of work, Paper **C** provides the first comprehensive dataset of beyond-Voigt line-shape parameters for this benchmark system. Using the state-of-the-art potential energy surface [55], we performed rigorous quantum scattering calculations for the lowest-lying states of  $\text{H}_2$ , covering rotational levels up to  $N = 7$  and vibrational manifolds up to  $v = 5$ . The resulting scattering  $S$ -matrices were used to compute beyond-Voigt line-shape parameters for the 321 strongest rovibrational transitions in  $\text{H}_2$ . The results were extrapolated to weaker transitions, including higher overtones, high- $N$  lines, and hot bands. The entire dataset involves a total of 3480 transitions in  $\text{H}_2$ .

To make this vast dataset computationally efficient, we employed a simple parametrization of the temperature dependence of spectroscopic line-shape parameters [116, 117]. Instead of storing extensive tabulated data, this method requires only four coefficients per line-shape parameter, to accurately represent the temperature dependence of collisional line-shape parameters in the temperature range of 20 to 1000 K.

An essential validation step involved comparing the simulated spectra, based on the new dataset, with high-precision cavity-enhanced spectra for two selected rovibrational transitions. The results demonstrated sub-percent agreement (in terms of the relative root-mean-square error) between theoretical and experimental spectra. This compact yet precise dataset has since been incorporated into the HITRAN spectroscopic database, which, as of December 2024, serves an active user base of 34 000 researchers and practitioners worldwide.

## **Towards databases for atmospherically-relevant species**

From the perspective of atmospheric studies, constructing *ab initio* databases for key atmospheric species— $\text{CO}$ ,  $\text{CO}_2$ ,  $\text{CH}_4$ , and  $\text{O}_2$ —perturbed by the most abundant atmospheric molecules,  $\text{N}_2$  and  $\text{O}_2$ , is of critical importance. However, this task is significantly more challenging than for He-perturbed molecular hydrogen lines. The complexity arises at every step of the process.

First, potential energy surfaces for diatom-atom systems are inherently simpler, depending on three coordinates: the internuclear distance within the





diatomic molecule (bond stretch), the distance between the diatomic molecule's center of mass and the atom, and the angle between the intra- and intermolecular axes. In contrast, PESs for diatom-diatom systems are significantly more complex, depending on six coordinates: two angles describing the relative orientations of the intramolecular axes with respect to the intermolecular axis, the dihedral angle, two bond stretches (one for each diatomic molecule), and the intermolecular distance between the centers of mass of the two molecules. This results in a 6-dimensional PES for diatom-diatom systems, compared to the 3-dimensional PES for diatom-atom systems. The complexity increases exponentially with the addition of more atoms—for instance, the PES for two water molecules involves 12 dimensions [118].

As a result, constructing a PES for diatom-diatom systems requires a significantly larger number of *ab initio* points to achieve an accurate analytical fit. Additionally, as outlined in Appendix A, the PES must be expanded in an appropriate angular basis to express the interaction energy as a function of the intermolecular distance for quantum scattering calculations. This expansion is computationally more demanding for diatom-diatom systems due to the larger number of angular terms involved. Table 1 provides the number of terms used in the expansion of the PES ( $N_{\text{PES}}$ ) for several systems studied in our group. Details on how this value is determined are given in Appendix A.

Next, the computational effort required for rigorous quantum scattering calculations grows dramatically as we study heavier molecules. The approach involves expanding the unknown sought wave function of the system into scattering channels—a known basis of eigenvectors combining the internal states of the colliding molecules and the relative orbital angular momentum (partial waves). The Schrödinger equation is then reduced to a system of  $N$  coupled ordinary differential equations, where  $N$  is the number of scattering channels. Solving these equations numerically involves matrix multiplication and inversion, the computational cost of which scales as  $N^3$ .

Significant simplifications arise from exploiting conserved quantities. For instance, total angular momentum  $J$  is conserved (in the absence of external fields), allowing the equations to be solved independently for each  $J$  value [119]. Furthermore, the equations are block-diagonal with respect to spatial parity, enabling additional decoupling. As a result, the coupled equations can be solved separately for each  $J$ , parity pair.

Despite these simplifications, the unfavorable  $N^3$  scaling poses significant



challenges for molecule-molecule systems [120]. The number of scattering channels,  $N$ , is determined by the combination of rotational states for each diatomic molecule and the partial waves contributing to the scattering process. Achieving numerical convergence of the cross-sections requires increasing both the number of rotational states and partial waves until the cross-sections stabilize within a chosen convergence threshold.

For diatom-atom systems, the rotational states involve only the active molecule, as the atom is treated as a structureless perturber. In contrast, for diatom-diatom systems, if  $N_{\max}^{(1)}$  rotational states are needed for the active molecule, a similarly large number,  $N_{\max}^{(2)}$ , is required for the perturber to achieve convergence. This leads to  $N_{\text{basis}} = N_{\max}^{(1)} N_{\max}^{(2)}$  pair combinations. Additionally, the number of partial waves required to converge the cross-sections increases with the reduced mass of the scattering system.

Table 1 summarizes the number of rotational level combinations,  $N_{\text{basis}}$ , and the number of partial waves,  $l_{\max}$ , needed to converge the pressure broadening (PBXS) and pressure shift (PSXS) cross-sections at a collision energy of  $200 \text{ cm}^{-1}$  for various systems studied in our group. Note that Table 1 demonstrates that the pressure shift cross-sections converge more slowly with the number of partial waves compared to the pressure broadening cross-sections, highlighting the additional computational challenge associated with obtaining converged collisional shifts.

System	$N_{\text{PES}}$	$N_{\text{basis}}$	$l_{\max}$		Reference
			PBXS	PSXS	
H <sub>2</sub> -He	4	5	13	32	Paper <b>C</b>
HD-H <sub>2</sub>	19	15	13	30	Paper <b>B</b>
CO-N <sub>2</sub>	205	44	94	–	Paper <b>D</b>
HCl-O <sub>2</sub>	271	36	91	186	[121]

Table 1: Overview of computational complexity for various systems studied in our group. The first molecule in each system is the active species undergoing a spectral transition, while the second molecule acts as the perturber.  $N_{\text{PES}}$  is the number of terms in the PES expansion required to fit *ab initio* interaction energies accurately.  $N_{\text{basis}}$  represents the number of rotational level combinations for the colliding molecules.  $l_{\max}$  is the maximum number of partial waves required to converge the pressure broadening (PBXS) and pressure shift (PSXS) cross-sections within 1% at a collision energy of  $200 \text{ cm}^{-1}$ . Note that converged PSXS was not reported for the CO-N<sub>2</sub> system. For homonuclear active molecules, the S(0) line is studied, while for heteronuclear molecules, the R(0) line is considered. Perturbers are assumed to be in their ground vibrational ( $v = 0$ ) and rotational ( $N = 0$ ) states, except for O<sub>2</sub>, where  $N = 1$ .





An additional complication arises because, unlike a structureless perturbing atom, molecules occupy different rotational levels at a given temperature, following the Boltzmann distribution. The scattering cross-sections depend on the rotational state of the perturbing molecule, requiring calculations to be performed for each rotational level and subsequently averaged according to the Boltzmann distribution.

This raises an important question: are quantum scattering calculations for atmospherically relevant systems feasible, and at what computational cost can we provide reliable line-shape parameters for the atmospheric science community?

### **N<sub>2</sub>-perturbed pure rotational transition in CO**

Paper **D** presents the first fully quantum calculations of collisional perturbation for a molecular line in an atmospherically relevant system: the N<sub>2</sub>-perturbed pure rotational transition in carbon monoxide (CO). Remarkably, three *ab initio* PESs for the CO-N<sub>2</sub> system were published within just six months, between December 2017 and April 2018 [122–124]. This unusual coincidence provided an opportunity to evaluate how the choice of PES affects collisional line-shape parameters, an important secondary goal of this study, inspired by earlier investigations on the He-H<sub>2</sub> system [14, 54]. The central focus of Paper **D**, however, was to demonstrate the feasibility of applying quantum scattering calculations to this system and achieving good agreement with experimental data.

The study focused on the first rotational transition of CO in its ground vibrational state,  $v_b = 0, N_b = 1 \leftarrow v_a = 0, N_a = 0$ , commonly denoted as 0-0 R(0). The line shape of this transition is predominantly determined by pressure broadening, as the collisional shift is at least two orders of magnitude smaller [125]. Therefore, Paper **D** reports the pressure broadening coefficient for this spectral transition.

Due to the computational challenges of fully quantum coupled-channel (CC) calculations, the coupled states approximation (CSA) [126] was employed. This method simplifies the problem by creating sub-block structures within each  $J$ , parity block, grouping channels with the same projection of the total angular momentum onto the intermolecular axis. While CSA significantly accelerates calculations, it can reduce the accuracy of predicted cross-sections.

Despite these approximations, the calculated pressure broadening coeffi-



cients agree well with experimental values, with discrepancies lying within the estimated error bars. Two notable findings should be emphasized. First, the beyond-Voigt effect—specifically, the speed dependence of collisional broadening—narrowed the line by approximately 4%, which brought the theoretical broadening coefficient closer to experimental results. Second, the three PESs produced nearly identical results, making it difficult to identify the most accurate surface. This is not surprising, as collisional broadening in this system is primarily governed by inelastic transitions. The broadening coefficient is effectively a half-sum of inelastic coefficients from  $v_a = 0, N_a = 0$  and  $v_b = 0, N_b = 1$  [14], which are relatively insensitive to subtle differences in the PES. Recall that Paper **A** demonstrated that the improved H<sub>2</sub>-He PES led to rate coefficients for pure rotational transitions in H<sub>2</sub> that were nearly identical to those obtained with the 26-year-old PES, which was calculated using a lower-level *ab initio* theory. Additionally, Paper **D** study focused on room-temperature collisions, whereas finer details of the PES are more discernible in low-temperature regimes (see Appendix C of Ref. [55]).

Pressure shift could serve as a better discriminator for PES quality, but this was beyond the scope of Paper **D**. First, the collisional shift for this transition is exceptionally small [125]. From a first-order perturbation theory perspective, the pressure shift is related to the difference in CO-N<sub>2</sub> interaction energies between the ground and excited states (Eq. (4)), which, in this case, belong to the same vibrational manifold. Second, the CSA is known to perform poorly for pressure shift calculations [127]. Tests for the N<sub>2</sub>-perturbed pure rotational R(0) line in CO have shown that CSA pressure shift cross-sections can even have opposite signs compared to CC results. Finally, even if CC calculations were computationally feasible, achieving convergence for the pressure shift cross-section would remain extraordinarily challenging. This difficulty remains a persistent challenge that our group continues to address, as discussed further in the next section.

## How far can we go?

The inability of the decoupling approximation to provide accurate pressure shifts, combined with additional uncertainty introduced to pressure broadening, emphasizes the importance of advancing fully rigorous quantum scattering calculations for systems of atmospheric interest. This raises an important



question: how far can we push the limits of rigorous quantum scattering calculations, and what challenges must we overcome to achieve this?

This question motivated the development of a custom scattering code within our group. While this was partly driven by intellectual curiosity and a desire to gain hands-on experience with computational complexity, it was primarily a response to practical challenges encountered while performing coupled-channel calculations for the CO–N<sub>2</sub> system using the widely used `MOLSCAT` code [128]. The most critical issue stemmed from `MOLSCAT`'s use of static memory allocation. Before compilation, the user must specify the size of the largest matrix to be stored in memory, corresponding to an order of magnitude less than the product of the number of channels and the number of anisotropies in the interaction potential included in the calculation. During my attempts to perform converged CO–N<sub>2</sub> calculations at high collision energies, I encountered fatal memory errors, which we attributed to architecture-related limitations of four-byte integers used in defining matrix sizes. Attempts to naively redefine this variable as an eight-byte integer were unsuccessful and the calculations could not be completed.

Since 2019, our group has been developing a custom scattering code, codenamed `BIGOS`. The `BIGOS` package comprises five modules, enabling users to: (1) calculate energy levels and wavefunctions of bound states for isolated diatomic molecules, (2) expand the interaction potential in the angular basis and average expansion coefficients over monomer bond lengths, (3) solve the quantum scattering equations, (4) compute generalized spectroscopic cross-sections, and (5) average these cross-sections over the Maxwell-Boltzmann collision energy distribution to obtain line-shape parameters. The codes are written in modern `Fortran` and incorporate dynamic memory allocation, eliminating the need for users to predefine the size of matrices.<sup>6</sup> Contrary to other quantum scattering codes, the calculations are performed in the body-fixed basis (see Appendix A for details). This approach reduces memory usage and provides a modest improvement in computational speed. Additionally, the package supports calculations involving two vibrating molecules—a feature missing in `MOLSCAT` and available, to our knowledge, only in the `TwoBC` code [129].

Parts of the `BIGOS` package already utilize object-oriented programming, with plans to extend this approach to the entire package. The diatom–atom

---

<sup>6</sup>Users must still ensure adequate random-access memory is available for calculations.



scattering module is publicly available on GitHub [130], and the complete package will eventually be released. I am the lead contributor to this project, having designed and implemented nearly the entire codebase.

This custom code has enabled us to overcome MOLSCAT's limitations and represents a significant step forward in the development of spectroscopic line-shape databases for atmospheric species. In a series of studies, our group has demonstrated excellent agreement between theoretical predictions and experimental results for several systems of atmospheric relevance. These include O<sub>2</sub>-perturbed pure rotational transitions in CO [131], N<sub>2</sub>-perturbed fine structure transitions in O<sub>2</sub> [132], and fully converged calculations of six beyond-Voigt line-shape parameters for O<sub>2</sub>-perturbed transitions in HCl [121]. The latter study warrants special attention, as it represents the first atmospheric system for which a fully converged value of the pressure shift has been obtained. Additionally, it provides a significant contribution to the understanding of the physical meaning of the Dicke parameter—previously determined through phenomenological fits to experimental spectra, which often led to questionable physical interpretations. These achievements mark the first steps toward generating comprehensive spectroscopic databases for molecules of atmospheric interest.

## **Part III. Spectroscopy of Simple Molecules for Fundamental Studies**

Accurate knowledge of collisional line-shape parameters is crucial for the proper analysis of laboratory spectra, where signal-to-noise ratios can exceed  $10^5$  [133, 134]. In these cases, fitting simple line-shape models (Eq. (5)-(10)) leads to large systematic errors in the determined transition frequency, as beyond-Voigt effects can significantly perturb the spectra. This is particularly true for molecular hydrogen [58], but before delving into the details of this system, let us explore the broader importance of precision spectroscopy in Atomic, Molecular and Optical (AMO) physics and its role in testing the fundamental laws of physics.



## Testing Fundamental Physics

Unlike large-scale collaborations in particle physics, such as those surrounding the Large Hadron Collider or Fermilab, precision experiments in AMO physics often go unnoticed by the general public. This is despite the fact that these experiments provide some of the most accurate validations of the Standard Model [9]. A prime example is the measurement of the electron magnetic moment, determined with an extraordinary precision of 1.3 parts in  $10^{13}$  [135]. Optical atomic clocks are another remarkable example, achieving relative uncertainties below the  $10^{-18}$  level in atomic transition frequencies [136]. These clocks not only push the boundaries of metrology but also enable searches for temporal variations in the fine-structure constant and the proton-to-electron mass ratio [137, 138], or signatures of dark matter [139, 140].

Molecules also play a pivotal role in precision tests of the SM, particularly in searches for new symmetry-violating forces mediated by massive particles [10]. While the SM predicts the existence of charge- and parity-violating (CP) forces, their magnitude is far too small to explain the observed matter-antimatter asymmetry in the Universe. Several beyond-Standard Model theories propose new CP-violating forces, which would manifest as a permanent electric dipole moment (EDM) of the electron, far larger than the SM prediction [141, 142].

Searches for the electron EDM are conducted using molecules with strong internal electric fields, such as thorium monoxide (ThO) molecules [143] and hafnium fluoride ions ( $\text{HfF}^+$ ) [144], which are particularly sensitive to EDM effects. While still several orders of magnitude above the SM predictions, recent experiments have put constraints on the electron EDM value, effectively ruling out many beyond-Standard Model theories that predict CP-violating physics at the tera-electronvolt (TeV) scale [144]—well beyond the energy reach of the Large Hadron Collider.

A separate category of precision measurements involves few-electron systems, for which the energy structure can be accurately predicted by theory. These experiments embody the quote often attributed to Albert A. Michelson, who suggested that "*new physics awaits at the next decimal place*" [145]: any experimentally observed discrepancy between theoretical and measured values can indicate the presence of previously unknown physics. An important role in this context has been played by atomic hydrogen: the detection of the Lamb shift [146], which contradicted Dirac's theory, drove the development



of quantum electrodynamics (QED) [147]. Today, atomic hydrogen remains a cornerstone of precision metrology, providing the energy scale for *ab initio* calculations through the Rydberg constant and contributing to the global adjustment of fundamental physical constants [148].

Studies of muonic hydrogen, formed by replacing the electron in a hydrogen atom with a muon, have been pivotal in refining the determination of the proton's charge radius [2]. Spectroscopic measurements of this exotic system revealed a discrepancy with the proton's charge radius determined from ordinary atomic hydrogen spectroscopy [149] and electron-proton scattering experiments [150]. This unexpected result, known as the proton radius puzzle, prompted a thorough reexamination of previous measurements and stimulated new theoretical approaches aimed at resolving the issue [151]. Another key two-body system is positronium—a bound state of an electron and a positron. Being free of nuclear structure, positronium provides an excellent platform for high-precision tests of QED [152].

Beyond these, three-body calculable systems such as helium atoms [153, 154], molecular hydrogen ions [4, 5], and exotic helium atoms further expand the scope of precision measurements. A notable example is antiprotonic helium, an exotic atom formed by a helium nucleus, an antiproton, and an electron. Spectroscopy of antiprotonic helium enables precise determinations of the antiproton-to-electron mass ratio, allowing comparisons to the proton-to-electron mass ratio that test the charge, parity and time reversal (CPT) symmetry [3].

## Molecular hydrogen

Molecular hydrogen and its isotopologues extend the family of simple systems used for precision studies to four-body systems. Among few-body systems, hydrogen holds a unique advantage: its ground electronic state,  $X^1\Sigma_g^+$ , hosts 302 long-lived rovibrational states, with natural lifetimes extending up to several weeks [155]. The ratio of the natural linewidth to the transition frequencies is on the order of  $10^{-20}$ . Given the ability to resolve spectral lines down to approximately  $10^{-4}$  of their linewidth, this implies a theoretical ultimate limit for testing fundamental physics with  $H_2$  at a relative accuracy of  $10^{-24}$ .

Figure 4 provides a historical perspective on the relative accuracy of measurements of rovibrational lines in hydrogen. The steady improvement in





the precision of hydrogen measurements (black points [156–159]) was dramatically accelerated with the advent of optical frequency combs (blue points) [160–175]. Recent measurements have achieved relative uncertainties below the  $10^{-10}$  level [176, 177]. Theoretical predictions (red points) have similarly progressed, with accuracy advancing alongside experimental techniques [139, 156, 159, 161, 178]. The leading nonrelativistic contribution to the rovibrational energies of molecular hydrogen (the orange dot) is now determined to 13 significant digits [179], paving the way for further theoretical advances.

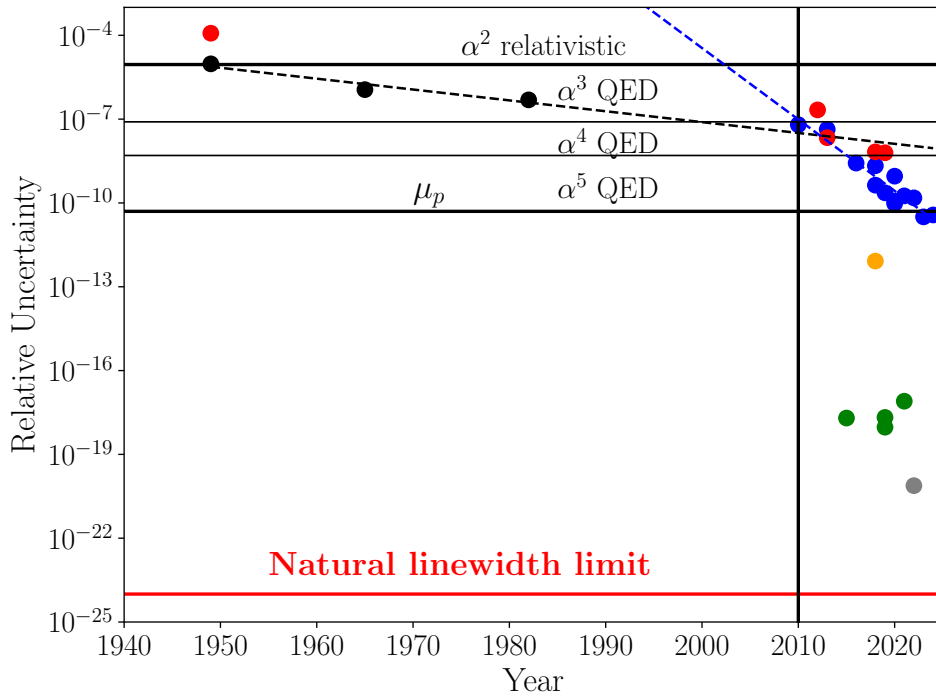


Figure 4: Historical overview of the relative accuracy of measured (black and blue) and calculated (red) rovibrational transition frequencies in molecular hydrogen. Further details are provided in the text.

The comparison between experimental and theoretical transition frequencies in hydrogen has already provided stringent tests of relativistic and leading QED corrections to energy levels (horizontal black lines). The black line below the  $10^{-10}$  level indicates the regime where the proton-to-electron mass ratio begins to significantly influence energy levels.

Despite the remarkable progress in both theoretical and experimental investigations of rovibrational transitions in hydrogen [180], an enormous gap of 8 orders of magnitude remains between these and the best spectroscopic measurements achieved using atomic clocks [136, 140, 181–183] (green points). Recent advances, such as the resolution of gravitational redshifts on an



atomic scale (grey dot) [184], hint at further progress in this field. The fundamental limit for hydrogen spectroscopy, lying 14 orders of magnitude below the state-of-the-art measurements in  $H_2$ , is represented by the red horizontal line.

This enormous gap serves as a driving force for pursuing ever more precise spectroscopy of  $H_2$ . Progress in this field opens up exciting possibilities for testing higher-order QED corrections [178], putting constraints on hypothetical beyond-Standard Model physics [8], involving higher dimensions [7] and long-range hadron-hadron forces [185], and contributing to the global adjustment of fundamental constants [186].

How do we bridge this enormous gap between current experimental capabilities and the fundamental limit in hydrogen spectroscopy? To answer this, we must address the challenges inherent in achieving the best measurements of rovibrational transitions in hydrogen.

The very feature that makes hydrogen advantageous for precision studies—long lifetimes of its rovibrational states—also presents a significant experimental challenge. Rovibrational transitions in  $H_2$  are dipole-forbidden, occurring only via weak electric quadrupole [155] or magnetic dipole transitions [187].<sup>7</sup> As a result, exceptionally long absorption paths, such as those used in Herzberg’s experiments [156], or highly sensitive detection techniques, like those employing optical cavities, are required to observe these transitions. Indeed, the vast majority of the most accurate experiments on hydrogen involve optical cavities [163, 165, 166, 169, 170, 176, 177].

An important class of experiments is based on Doppler-limited spectroscopy [162–164, 166, 167, 171]. Within this approach, the accuracy is constrained primarily by large Doppler broadening, reaching up to 1.5 GHz at room temperature. Another significant contribution to uncertainty arises from collisional effects [188]. As discussed in previous sections, hydrogen spectra are notably perturbed by beyond-Voigt effects [58, 84, 86]. Paper **E**, as well as Refs. [166, 189], shows an example of how these effects can be mitigated by providing reference theoretical collisional data.

High precision can be achieved through saturation spectroscopy. However, the inherent weakness of hydrogen transitions demands large laser powers to achieve saturation. Once saturation was finally achieved for hydrogen isotopo-

---

<sup>7</sup>Magnetic dipole transitions between rovibrational levels in molecular hydrogen have never been detected.





logues [186, 190], the observed spectra exhibited unexpected asymmetric shapes [165, 170], making it challenging to determine transition frequencies accurately. A significant effort has gone into investigating whether the underlying hyperfine structure of rovibrational transitions plays a role in causing these asymmetries. My contributions to these efforts are provided Refs. [191–193] and Papers **F–J**.

Another approach to increasing the accuracy of spectroscopic measurements is cooling the hydrogen sample. Cooling primarily mitigates Doppler broadening and increases peak absorption by collapsing the population into the ground rovibrational state. Many research groups have pursued this strategy [173–177], but ensuring uniform cooling of the entire setup—not just the gas sample—poses a significant challenge [194]. My contribution to the pioneering work in this area by our group—the first spectroscopy of  $\text{H}_2$  at temperatures as low as 5 K—is highlighted toward the end of this section.

Despite these advancements, even the most optimistic estimates place the relative accuracy of current techniques at the  $10^{-11}$  level. This remains 13 orders of magnitude above the fundamental limit shown in Fig. 4. In the final part of this section, I discuss ongoing efforts to trap cold  $\text{H}_2$  samples and the theoretical proposals detailed in Papers **K** and **L**, which outline promising pathways to further narrow this gap.

## **Doppler-limited spectra: collisional effects**

Modern cavity-enhanced spectroscopy techniques allow for routine measurements of rovibrational quadrupole transitions in molecular hydrogen [180, 195]. Due to the weak nature of these transitions, and to reduce statistical errors, measurements are typically conducted at pressures of 0.1–1 atm, placing them in a regime where collisional effects are significant [188]. Collision-perturbed spectral lines in hydrogen exhibit pronounced beyond-Voigt effects [58], including the speed dependence of collisional shifts [86], which induces line asymmetry, and velocity-changing collisions, which cause Dicke narrowing [64]. These effects present significant challenges for accurate spectral analysis.

A recent study demonstrated that fitting hydrogen spectra with simplified line-shape profiles, which neglect the speed dependence of collisional broadening and shifts, introduces substantial systematic errors when extracting the



unperturbed transition frequency by linear extrapolation to zero pressure. The asymmetry caused by the speed-dependent collisional shift leads to an apparent nonlinear scaling of the line position with pressure at low values of  $p$ . Consequently, collisional effects represent the largest contribution to the systematic error budget in Doppler-limited spectroscopy of molecular hydrogen [188].

To minimize these systematic errors, accurate theoretical reference data are essential. The methodology outlined earlier—combining *ab initio* potential energy surfaces, rigorous quantum scattering calculations, and a physically justified line-shape model—provides the most reliable approach for modeling collision-perturbed spectra of  $\text{H}_2$ . During my master’s thesis, I applied this methodology to the self-perturbed 2-0 S(2) transition in molecular deuterium, significantly reducing systematic errors in experimental measurements conducted by our group [166]. This work resulted in the most accurate determination of a transition frequency in molecular deuterium at that time.

During my PhD, I conducted analogous calculations for the self-perturbed 1-0 Q(1) Raman transition in  $\text{H}_2$ , which forms the basis of Paper **E**. This work represents the first demonstration of stimulated Raman scattering (SRS) metrology. SRS is a nonlinear spectroscopic technique that uses two laser fields—the pump and Stokes fields—to excite a spectral transition with a frequency corresponding to the difference between the pump and Stokes laser frequencies. The novelty of this work lies in enhancing the precision of SRS measurements by introducing an optical frequency comb. The comb-assisted SRS metrology was applied to study the fundamental Q(1) transition in  $\text{H}_2$ , improving the accuracy of the determined transition frequency by a factor of 20 compared to the previous experimental determination [196].

An essential factor in reducing the uncertainty of the transition frequency was the use of *ab initio* collisional line-shape parameters for this line, which constituted my primary contribution. Using the  $\text{H}_2$ - $\text{H}_2$  PES from Ref. [197], I performed quantum scattering calculations to determine six collisional line-shape parameters of the  $\beta$ -corrected Hartmann-Tran profile [81] for this transition. Details of the fitting procedures are provided in Paper **E**. Notably, various fits, where some parameters were fixed to *ab initio* values while others were allowed to vary, revealed a significant discrepancy—a factor of approximately two—in the pressure shift coefficient and the imaginary part of the Dicke narrowing parameter, the origin of which is currently unknown.



## The role of quantum indistinguishability

A careful reader might note that in Article **E**, the colliding molecules were treated as distinguishable species. Indeed, the role of quantum indistinguishability has received relatively little attention in line-shape theory [198–203]. It is generally acknowledged that effects related to quantum indistinguishability can be significant for pure rotational transitions. This is because the active molecule, in both the ground and excited states, shares the same energy structure as the perturber [200].

For rovibrational transitions, however, these effects are expected to be less pronounced. Molecules in different vibrational states are effectively distinguishable due to slight differences in their rotational constants between the  $v_a = 0$  and  $v_b > 0$  states. Additionally, the so-called exchange effects in self-broadening rely on vibrational energy transfer, which is orders of magnitude less efficient than rotational energy transfer.

This dissertation addresses this topic in Appendix C. My findings indicate that quantum indistinguishability significantly affects *pure rotational* transitions of molecular hydrogen at low temperatures. Unfortunately, the absence of pure rotational spectra with signal-to-noise ratios comparable to rovibrational spectra limits experimental validation of these effects. One promising avenue for testing these results lies in the pressure shift. Calculations that include or neglect quantum indistinguishability effects predict different temperatures at which the pressure shift changes sign from negative to positive. Measuring spectra near these transition temperatures could provide a direct test of the theory.

The potential role of indistinguishability in rovibrational transitions will be revisited later in this dissertation.

## Saturated absorption spectroscopy

It was mentioned earlier that the weakness of hydrogen’s quadrupole transitions poses a significant challenge for saturating these lines. Readers unfamiliar with the term and the principles of saturated absorption spectroscopy are referred to classical texts on the subject [204, 205]. For completeness, a brief explanation of saturated absorption spectroscopy is provided here.

Saturated absorption spectroscopy is a technique designed to overcome Doppler broadening of spectral lines. It uses two counter-propagating laser



beams: a strong "pump" beam and a weaker "probe" beam. The pump beam selectively excites molecules moving at a velocity such that their Doppler-shifted resonance frequency matches the laser frequency. The probe beam, on the other hand, detects the absorption at this frequency. When the two beams interact with molecules moving at the same velocity class, a saturation effect occurs, reducing absorption. This creates a narrow, symmetric "Lamb dip" at the center of the Doppler-broadened line, allowing the precise determination of transition frequencies.

In 2018, groups in Amsterdam and Hefei reported the first successful saturation of the 2-0 transitions in hydrogen deuteride [186, 190]. To give the reader an appreciation of the drastic reduction in spectral width achieved through saturation, the observed full widths at half maxima (FWHM) of these transitions were reduced from Doppler-broadened widths on the order of 1 GHz to sub-MHz levels. Despite claiming relative uncertainties in the determined transition frequencies at the level of 20 kHz, the reported values differed by as much as 1 MHz. This unexpected discrepancy prompted numerous investigations into potential sources of error.

One hypothesis tied the observed discrepancies to the hyperfine structure of the investigated transitions [165]. Hyperfine structure arises from interactions involving nuclear magnetic and electric moments, creating substructure within molecular energy levels [206, 207]. In molecular hydrogen and its isotopologues, three primary hyperfine interactions are relevant: the interaction of nuclear spin magnetic moments with the magnetic field generated by molecular rotation (nuclear spin-rotation interaction), the dipolar interaction between the nuclear magnetic moments, and the interaction of the electric quadrupole moment of the deuteron with the molecular electric field gradient (present only in isotopologues involving deuterium) [208]. At the time, the strengths of these interactions were well-characterized for the absolute ground states of  $\text{H}_2$ , HD, and  $\text{D}_2$ , thanks to the pioneering work of Norman Ramsey [209–212]. However, hyperfine coupling constants vary significantly across rotational and vibrational levels, and these values were largely unknown for excited rovibrational states. This was crucial for the accurate simulation of positions and intensities of all 21 hyperfine components of the 2-0 R(1) level investigated in Hefei and Amsterdam.



## Hyperfine structure of molecular hydrogen

This knowledge gap prompted multiple theoretical studies [213–215], to which I contributed during my master’s thesis. I provided hyperfine coupling constants, as well as positions and intensities for 985 534 hyperfine components of 60 179 electric quadrupole rovibrational transitions in  $\text{H}_2$  and  $\text{D}_2$  [192], tritium-bearing isotopologues [193], and electric dipole transitions in HD [191]. These results proved instrumental in interpreting molecular spectra in Amsterdam [175, 177, 216], Hefei [170, 174, 217], and the most accurate determination of a rovibrational transition frequency in  $\text{D}_2$  [172].

As part of this dissertation, the work was extended to cover the remaining transitions in hydrogen isotopologues. Paper **F** explores hyperfine interactions in the tritiated heteronuclear isotopologues of molecular hydrogen (HT and DT) and provides positions and intensities of 331 892 hyperfine components of all 18 585 rovibrational dipole transitions in these isotopologues.

Spectroscopy of tritium-bearing species is crucial for comprehensive tests of QED in four-body systems, extending the theoretical framework to heavier isotopologues less affected by mass-dependent non-adiabatic corrections. The results of Paper **F** were used in the analysis of the first saturation spectra of HT [218]. The authors measured the P(1), R(0) and R(1) lines from the first overtone. A particularly remarkable feature of the 2-0 R(0) transition in HT is the presence of a single isolated hyperfine component, predicted to be shifted by +444 kHz relative to the hyperfine-less position. This prediction was experimentally confirmed in Ref. [218], with the measured position of the component in excellent agreement with my calculations.

Paper **G** presents the positions and intensities of 185 631 hyperfine components for 7 251 electric quadrupole transitions within the ground electronic state of HD. Although weaker than electric dipole transitions, quadrupole transitions have been the subject of precision spectroscopy, achieving uncertainties on the order of several MHz [219, 220]. While the hyperfine structure of these transitions has not yet been resolved experimentally, the data provided in this work offers a crucial reference for future experimental studies. Additionally, for the sake of completeness, this work includes hyperfine splittings for all six isotopologues of hydrogen, serving as a practical resource for the analysis of experimental data.



## The asymmetric line shape puzzle

The story of the frequency discrepancy took another turn when the Amsterdam group remeasured the 2-0 R(1) transition in HD [165]. Unexpectedly, instead of the anticipated symmetric Lamb dip, they observed an asymmetric, dispersive line shape. By developing a theoretical model based on optical Bloch equations, they successfully reproduced the observed shape. The authors attributed this phenomenon to the manifestation of *crossover resonances*, a feature characteristic of saturation spectroscopy.

Earlier, the basic principles of saturated absorption were introduced under the implicit assumption of a two-level system. However, this is rarely the case in practical experiments. Specifically, in these measurements, each rovibrational state involves multiple hyperfine levels, resulting in numerous hyperfine components (for the 2-0 R(1) line in HD, there are 21 hyperfine components). When multiple transitions lie within the same Doppler-broadened line and share a common ground (or excited) state, crossover peaks (or dips) can appear at frequencies between two transitions. This occurs because molecules interact with pump and probe beams that are resonant with two separate transitions.

The model developed by the Amsterdam group implied a reassessment of the uncertainty in the transition frequency of the 2-0 R(1) line, which increased to 50kHz [165]. Additionally, the model predicted a dispersive-like line shape for all transitions in the 2-0 band of HD, with two notable exceptions: the P(1) and R(0) lines. These transitions exhibit drastically simpler hyperfine structures. In the case of the P(1) line, the excited ( $v_b = 2, N_b = 0$ ) state, and for the R(0) line, the ground ( $v_a = 0, N_a = 0$ ) state, each contain two nearly degenerate hyperfine states separated by approximately 40Hz [215]. This degeneracy reduces the number of distinct components from 9 to 5 [191], leading to a simplified structure of crossover resonances. As a result, these lines were expected to exhibit *symmetric* line shapes. Indeed, a symmetric Lamb peak was observed for the 2-0 P(1) line [169]. However, surprisingly, a dispersive-like line shape was observed for the R(0) line [175].

This inconsistency highlighted the challenges in fully understanding and accounting for crossovers between hyperfine components of rovibrational lines under saturated absorption conditions. Further evidence that the observed asymmetry was *not* caused by hyperfine structure came from the same group,





which investigated a similarly weak transition in carbon dioxide—a molecule without hyperfine structure. Despite the absence of hyperfine components, a similar dispersive-like line shape was observed [175].

Simultaneously, the group in Hefei confirmed the asymmetric line shape of the R(1) line using three different spectroscopic techniques [170]. Their analysis showed that the spectra could be fit using a Fano profile [221]. The Hefei group hypothesized that the continuum responsible for the Fano profile could arise from collisional effects or the far wings of strong electronic transitions to the  $B^1\Sigma^+$  state. However, this model fails to explain why Fano-type resonances have not been observed for the 2-0 P(1) line [169] or in molecular beam experiments [168, 172].

The one clear difference between the setups that observed asymmetric line shapes [165, 170, 175] and those using molecular beam experiments [168, 172] or Doppler-limited measurements [164] is the presence of a strong, standing-wave electromagnetic field in the former, generated by the pump beam used in the saturated absorption experiments.

The Hefei group hypothesized that molecules passing through the standing wave could experience simultaneous periodic excitation and modulation to a far electronic state, resulting in the Fano resonance. This model was tested on various weak transitions in  $\text{CO}_2$  [222].

The Amsterdam group, on the other hand, proposed that the dipole force induced by the strong pump beam could alter the velocity distribution of hydrogen molecules, slowing them down or even trapping them along the beam path.<sup>8</sup> This effect could lead to a peak observed at the center of the transition [205]. By tuning the intracavity power across two orders of magnitude, the group observed a gradual transition in the line shape—from a symmetric Lamb dip at low powers, through a dispersive-like shape, to a central peak at the highest powers for the hyperfine-free 2-0 S(0) transition in  $\text{H}_2$  [176].

While significant progress has been made, the origin of the asymmetric line shape remains unresolved and demands further theoretical and experimental exploration. A deeper understanding of these effects is crucial for reliably and more accurately testing quantum theory on hydrogen using saturated absorption spectroscopy.

---

<sup>8</sup>The largest power used in the Amsterdam experiments [176] should be sufficient to create a trapping potential for  $\text{H}_2$  molecules with a depth of 5  $\mu\text{K}$ .



## Hyperfine structure in the excited electronic states

The exploration of hyperfine structure in molecular hydrogen and its isotopologues is far from complete. Until recently, most studies focused on the ground electronic  $X^1\Sigma_g^+$  state. However, much less is known about the hyperfine structure of excited electronic states. In principle, excited  $^1\Sigma$  states should have hyperfine coupling constants different than those of the  $X^1\Sigma_g^+$  ground state, while states with non-zero projections of the electronic orbital angular momentum on the internuclear axis (such as  $\Pi$  or  $\Delta$  states) involve additional hyperfine couplings. These include interactions between nuclear magnetic moments and the magnetic fields generated by electron orbital motion. Excited metastable *triplet* states introduce yet another layer of complexity due to their non-zero electronic spin, giving rise to Fermi contact and magnetic dipole-dipole interactions.

Some early work on hyperfine structure in metastable  $^3\Pi_u$  was carried out by Brooks, Lichten and Reno [223]. Additionally, knowledge of hyperfine structure in Rydberg states is known from the combination of millimeter spectroscopy and multichannel quantum defect theory (MQDT) [224, 225]. However, there is a notable gap in understanding key excited  $^1\Sigma$  states, such as the double-well EF and GK states, which are essential for precise determination of the dissociation energy of molecular hydrogen via multiphoton ionization spectroscopy [226, 227]. The unknown hyperfine structure of these states contributes to the uncertainty in dissociation energy measurements.

In Paper **H**, we investigated the leading hyperfine interactions in the EF  $^1\Sigma_g^+$  state of  $H_2$ , focusing on rovibrational states within the double-well potential of this electronic state ( $v = 0 - 6$ ). Our results revealed that hyperfine coupling constants differ significantly from those in the ground state, primarily due to the extended internuclear separation in the EF state's double-well structure. Since hyperfine couplings scale as  $R^{-3}$ , their overall strength is reduced by a factor of 2 for states in the inner well and by an order of magnitude for states in the outer well. These findings have already been used to estimate the hyperfine structure of the GK  $^1\Sigma_g^+$  state in HD in the revised determination of the dissociation energy of HD [227].





## **The influence of hyperfine interactions on Doppler-limited spectra**

Studies of hyperfine structure in hydrogen have also played a role in Doppler-limited spectroscopy of its ground electronic  $X^1\Sigma_g^+$  state. In 2021, the Caserta group revisited [171, 228] their earlier [164] cavity-enhanced measurements of the 2-0 R(1) transition in HD. Contrary to the measurements reported by Amsterdam and Hefei groups [186, 190] around the same time as their 2018 result [164], the spectra measured in Caserta are Doppler-broadened, meaning that the underlying 21 hyperfine components of this transition are not expected to be resolved in their experiment—these components overlap within a spectral range of 0.5 MHz while being broadened by 1.5 GHz. Despite this, the group attempted to refit the spectra using the known positions and relative intensities of these components from one of our works. Their analysis led to a shifted line position by approximately 350 kHz, raising the question: is this shift real, or an artifact of overfitting?

Paper **I** addressed this question using spherical tensor analysis. It demonstrated that, for all rovibrational transitions in molecular hydrogen isotopologues, the first moment of the spectrum—the sum of the product of hyperfine component positions and their relative intensities—vanishes. This result aligns with the expectation that, at low resolution, overlapping hyperfine components blend into a single line centered at the unperturbed transition frequency. An important factor enabling this cancellation is hydrogen’s large rotational constant, which effectively decouples hyperfine-induced interactions between neighboring rotational levels.

The paper further quantified the conditions under which hyperfine-induced shifts could appear in Doppler-limited spectra. It demonstrated that the ratio of the linewidth to the mean-square hyperfine splitting, which determines the detectability of such shifts, is too large for any hyperfine shift to be observed in all Doppler-limited experiments reported at that time [164, 166, 167, 171, 173]. The study concluded that detectable hyperfine shifts in Doppler-limited spectroscopy would only emerge at much lower temperatures, well below 1 K.

This analysis does not suggest that the Caserta group’s findings are erroneous. Paper **I** neglected collisional effects, assuming that the linewidth of each hyperfine component is determined solely by Doppler broadening (Eq. (7)). A natural extension of this work would be to investigate the existence of a



net hyperfine shift in collision-perturbed spectra. In such cases, hyperfine components could exhibit distinct linewidths and line shifts, as demonstrated for the hyperfine structure of rotational transitions in  $\text{CH}_3\text{I}$  [229]. Collisional broadening and shift coefficients for each hyperfine component of the 2-0 R(1) transition could be calculated *ab initio*, using the formalism outlined earlier. Appendix D details how collisional parameters can be obtained for hyperfine components of a rovibrational transition in  $\text{H}_2$  molecule. Although these results indicate a limited significance of such effects, further investigation—specific to individual transitions—is needed to fully understand their impact on Doppler-limited spectra of molecular hydrogen isotopologues.

Paper **J** extended the investigation of hyperfine effects in the ground electronic state of the six hydrogen isotopologues studied in Refs. [191–193] and Papers **F** and **G**, revealing an intriguing property. Using spherical tensor analysis, we demonstrated that the hyperfine components of rovibrational transitions can be categorized into four distinct groups based on the vibrational dependence of their relative intensities. Remarkably, a significant subset of hyperfine components exhibits identical relative intensities across different vibrational bands. This effect is attributed to hydrogen’s large rotational constant, which effectively decouples hyperfine and rotational degrees of freedom. Consequently, despite variations in hyperfine coupling constants between vibrational bands, the relative intensities of these specific hyperfine components remain independent of  $v$ .

These findings provide a systematic framework for analyzing hyperfine-resolved spectra in the six hydrogen isotopologues and may also apply to other diatomic molecules with rotational constants significantly larger than their strongest hyperfine coupling constants.

## **Into the cryogenic regime**

As mentioned earlier, another approach to improving the accuracy of molecular hydrogen measurements is cooling the gas sample to cryogenic temperatures. This offers multiple advantages: reduced Doppler broadening, enhanced peak absorption due to the collapse of population into the ground vibrational state, and the elimination of unwanted molecular species with strong dipole transitions, which can complicate hydrogen spectral analysis [164]. At these temperatures, such species are completely frozen out.



Our group has recently developed a cryogenic spectrometer capable of operating at temperatures as low as 4 K. Unlike other setups [194], this system ensures uniform cooling of the entire cavity, including the mirrors and cavity length actuator. This design eliminates temperature gradients and ensures thermodynamic equilibrium across the gas sample.

The spectrometer will be described in detail in a forthcoming publication [230]. Among its many applications, it enables precise measurements of transitions in the fundamental band of  $\text{H}_2$  under cryogenic conditions. By conducting measurements across a temperature range of 5 to 8 K, we determined the transition frequency of the 1-0 S(0) line in  $\text{H}_2$  with a relative uncertainty of  $10^{-10}$ . This result represents a three-order-of-magnitude improvement over the best previous measurement of this line [158], and an order-of-magnitude improvement over the best measurements for homonuclear hydrogen isotopologues achieved using Doppler-limited spectroscopy (Ref. [166] and Paper **E**). The accuracy achieved in this work allows us to test relativistic and QED corrections to the transition frequency at the fifth significant digit.

The experiments were performed in the saturated vapor regime, allowing studying hydrogen spectra below its boiling point (20.271 K). In this regime, pressure changes drastically with temperature—by approximately four orders of magnitude as  $\text{H}_2$  is cooled from 10 K to 5 K. This allows the experimental setup to probe both the collision-free regime (at 5 K, the pressure is below  $10^{-2}$  Pa) and the regime where collisions remain significant (at 10 K, the pressure exceeds  $10^2$  Pa).

The latter regime provides an intriguing opportunity to test theoretical models of collision-perturbed spectral line shapes under cryogenic conditions. To this end, I performed quantum scattering calculations on the state-of-the-art  $\text{H}_2\text{-H}_2$  PES reported in Paper **B** to provide collisional line-shape parameters for the self-perturbed 1-0 S(0) line in  $\text{H}_2$ . Compared to previous examples of providing reference data for experiments (Paper **E** and Refs. [166, 189]), this work includes a significant advancement: for the first time, quantum indistinguishability effects, as described in Appendix C, are incorporated into the calculations.

Figure 5 presents the calculated speed-averaged pressure broadening and shift coefficients for this line below  $T = 20$  K. Apart from drastic changes of  $\gamma_0$  and  $\delta_0$  as a function of temperatures, Fig. 5 shows a pronounced sensitivity of line-shape parameters to quantum indistinguishability effects at temperatures

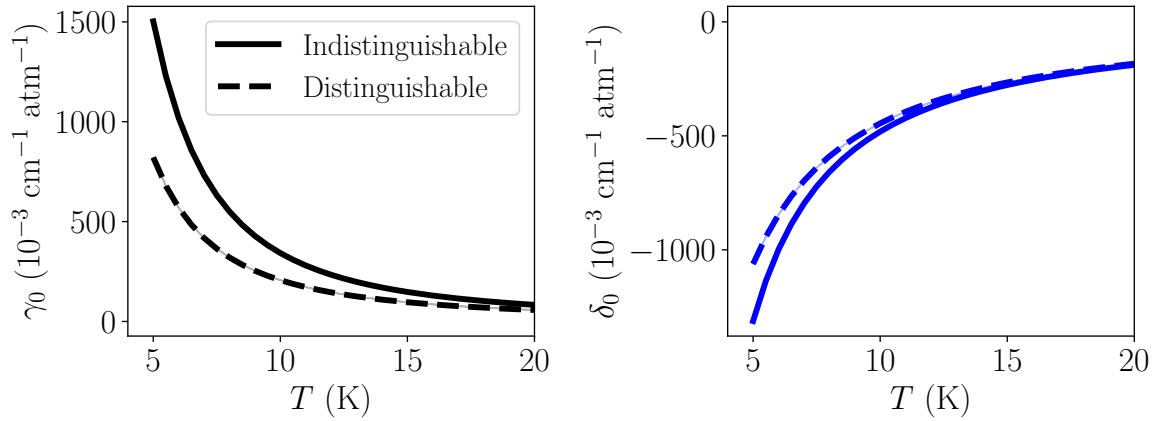


Figure 5: Temperature dependence of the speed-averaged pressure broadening coefficient ( $\gamma_0$ , left panel), and pressure shift coefficient ( $\delta_0$ , right panel) for the self-perturbed 1-0 S(0) transition in  $\text{H}_2$  in the cryogenic regime. Results are shown for calculations in which colliding molecules are treated as indistinguishable molecules (solid lines) and distinguishable (dashed lines).

below 15 K. For example, the pressure shift coefficient differs up to 30% at  $T = 5$  K when quantum indistinguishability was neglected.

An important theoretical insight gained from treating molecules as indistinguishable relates to the partial waves contributing to the generalized spectroscopic cross-sections (see Fig. 6). In collisions involving two identical ground-state bosonic molecules, such as  $\text{H}_2$ , only even partial waves contribute to the scattering cross-section. Interestingly, treating the molecules as distinguishable introduces contributions from odd partial waves, resulting in incorrect cross-section values. This highlights the necessity of properly accounting for indistinguishability when modeling such systems.

Interestingly, the collisional broadening and shifting cross-sections for this transition are dominated by a single partial wave—the  $d$ -wave ( $l = 2$ ) resonance. Even after thermal averaging, this resonance remains the primary contributor to the pressure broadening and shift coefficients, demonstrating that the measurements are effectively conducted in the single-partial-wave regime.

While the initial measurements were performed at sufficiently low temperatures to minimize collisional effects, a new measurement campaign is currently underway in our group at higher temperatures. These experiments aim to provide detailed data for a comprehensive collisional analysis, which will validate the theoretical calculations and deepen our understanding of collisional dynamics in the cryogenic regime.

## Towards the fundamental limit

Current spectroscopic measurements of molecular hydrogen are estimated to approach a relative uncertainty of  $10^{-11}$ , which is thirteen orders of magnitude above the fundamental natural linewidth limit (see Fig. 4). To bridge this enormous gap and push the boundaries of precision further, a paradigm shift in methodology is required, similar to the impact of optical frequency combs that accelerated hydrogen measurements in the last decade.

Our group has proposed that the next major breakthrough in hydrogen spectroscopy could be achieved by trapping a cold  $\text{H}_2$  sample. However, manipulating molecular hydrogen presents significant challenges. As a homonuclear molecule,  $\text{H}_2$  lacks a permanent dipole moment and interacts weakly with electric fields. Similarly, its lack of electronic spin means it interacts with magnetic fields only through its nuclear spin, making magnetic trapping challenging. Additionally, strong electronic transitions in  $\text{H}_2$  lie in the extreme ultraviolet, a spectral range difficult to access with current laser technology. The absence of a cycling transition [231] further precludes direct laser cooling.

The proposed trapping scheme, to be detailed in an upcoming publication, involves two approaches: a superconducting magnetic trap and an ultra-high-power optical dipole trap (ODT), with trap depths on the order of 1 mK. The initial stage of cooling (down to 5 K) will be achieved using standard refrigeration techniques. The trap zone will then be filled *in situ* with a thermal

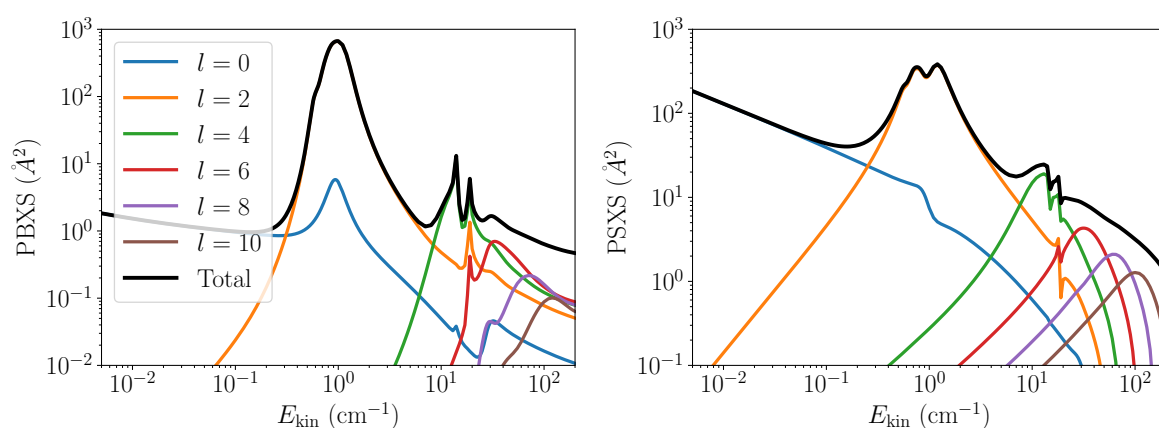


Figure 6: Partial wave decomposition of the pressure broadening (PBXS, left panel) and the pressure shift (PSXS, right panel) cross-sections for the self-perturbed 1-0 S(0) line in  $\text{H}_2$ . Results are shown for calculations in which colliding molecules are treated as indistinguishable species.



distribution of  $\text{H}_2$  molecules at 5 K. Since no current technology can cool hydrogen between 5 K and 1 mK, we propose that only the coldest fraction of the sample will be trapped by dynamically activating the trap within the timescale of the molecules' flight through the trap region. This method exploits time-dependent potentials to confine the coldest  $10^{-7}$  fraction of the molecular population within the shallow trap.

Recent advancements at UC Berkeley [232] have demonstrated the feasibility of generating high-intensity laser fields, paving the way for sub-Kelvin ODTs capable of trapping a significantly larger fraction of the molecular population. These developments mark the first step in pushing the accuracy of future hydrogen measurements towards the fundamental limit.

### **Mitigating Stark shifts in the optical dipole traps**

While the technical details of the trapping mechanism will be discussed in a forthcoming paper, an important question arises: How can precise spectroscopy be performed on  $\text{H}_2$  molecules in an ODT?

The key challenge lies in addressing the dynamic Stark shift caused by the strong laser field forming the trap. This laser field shifts molecular energy levels due to differences in isotropic polarizabilities between the ground and excited states. For instance, the polarizability of  $\text{H}_2$  differs by approximately 10% between the  $v_a = 0$  and  $v_b = 1$  vibrational states [233]. This differential shift will not only displace the effective position of the spectral resonance but also will induce significant inhomogeneous broadening, as the Stark shift varies with the molecule's position within the trap, posing a major limitation to measurement accuracy.

Paper **K** proposes a strategy to mitigate Stark shift effects and enable precise spectroscopy of the 1-0 S(0) transition in  $\text{H}_2$  within an ODT. First, we demonstrate that coupling the ground state to a specific Stark component of the excited states—leveraging polarizability anisotropy in the  $v_a = 1, N_b = 2$  states—can reduce the differential Stark shift from 10% to 0.1%. Next, we propose a method inspired by atomic spectroscopy, where *magic wavelengths* are employed to eliminate differential Stark shifts [234]. This concept exploits the frequency dependence of polarizabilities: at certain wavelengths, the Stark shifts of the ground and excited states are identical, resulting in no net line shift. However, applying this concept to  $\text{H}_2$  is challenging, as the two rovibrational levels involved in the 1-0 S(0) transition belong to the same electronic





state, with minimal polarizability differences in the infrared range.

Paper **K** provides an alternative solution, exploiting drastic changes in polarizability induced by weak quadrupole transitions that lie in the infrared. Through this approach, we identified 44 magic wavelengths for the 1-0 S(0) transition in  $\text{H}_2$ . This result paves the way for Stark-shift-free hydrogen spectroscopy in ODTs, enabling more precise tests of quantum theory in this fundamental system.

## Sympathetic cooling of molecular hydrogen

While the optical dipole trapping proposal is well-suited for para- $\text{H}_2$ , alternative mechanisms could be employed to trap ortho- $\text{H}_2$ . Since *ortho*- $\text{H}_2$  possesses a non-zero nuclear magnetic moment, it can, in principle, be confined using strong inhomogeneous magnetic fields.

Figure 3 in Paper **L** illustrates the Zeeman structure of the ground state in ortho- $\text{H}_2$ . The dominant contribution to the Zeeman splitting arises from the coupling of the nuclear spin magnetic moment with the external magnetic field, grouping the Zeeman levels into three sets based on the projection of the nuclear spin quantum number,  $M_I$ . A secondary, weaker interaction—approximately six times smaller—stems from the rotational magnetic moment, further subdividing each  $M_I$  group into triplets characterized by the projection of the rotational quantum number,  $M_N$ . Out of the nine resulting states, three are low-field-seeking, meaning their energy increases with the magnetic field strength. These states can be confined using magnetic traps. Fig. 3 in Paper **L** indicates that a magnetic field strength of approximately 0.4 T is sufficient to create a 1 mK deep magnetic trap.

Paper **L** builds upon this magnetic trapping concept by investigating the feasibility of sympathetically cooling trapped *ortho*- $\text{H}_2$  to sub-millikelvin temperatures via collisions with lithium atoms. Sympathetic cooling involves cooling a molecular system through elastic collisions with a colder atomic gas, ideally of similar mass. Elastic collisions transfer momentum from the gas to the molecules, effectively cooling them. Conversely, inelastic collisions can transfer molecules to high-field-seeking states, leading to heating and trap loss. The feasibility of sympathetic cooling is often evaluated by the ratio of elastic-to-inelastic cross-sections or rate coefficients, with a ratio exceeding 100 being a benchmark for efficient cooling.

In Paper **L**, we explore the feasibility of sympathetic cooling of molecular



hydrogen through collisions with  $^6\text{Li}$  atoms. Using an *ab initio*  $\text{H}_2\text{-Li}$  potential energy surface, we determine the ratio of elastic-to-inelastic collisions through rigorous scattering calculations. These calculations explicitly incorporate the hyperfine structure of molecular hydrogen, the magnetic dipolar interaction between the nuclear magnetic moment of  $\text{H}_2$ , and the electron spin magnetic moment of lithium. This represents the first study of molecular hydrogen collisions that accounts for hyperfine and external field degrees of freedom, as well as intermolecular hyperfine interactions. The paper demonstrates propensity rules for collisional nuclear spin relaxation in  $^1\Sigma$  molecules colliding with  $^2S$  atoms, provides a discussion of the feasibility of sympathetic cooling of molecular hydrogen by lithium, and paves the way for further collisional studies involving molecular hydrogen in external fields.





# AUTHOR CONTRIBUTION STATEMENT

## Article A

I was responsible for developing all computer codes used in the quantum scattering calculations, with a primary focus on the scattering code, the key element of the BIGOS software package published alongside this paper (including preparation of its documentation). I also prepared the H<sub>2</sub>-He potential energy surface for quantum scattering calculations, performed all quantum scattering calculations, calculated state-to-state cross-sections and rate coefficients, and prepared the majority of the draft (apart from Sec. 4), figures, and supplementary materials. As the corresponding author, I coordinated the project, led the submission process, and prepared responses to the reviewers.

## Article B

I was responsible for developing all computer codes used in the quantum scattering calculations. I prepared the new H<sub>2</sub>-H<sub>2</sub> potential energy surface for quantum scattering calculations in the HD-H<sub>2</sub> and D<sub>2</sub>-H<sub>2</sub> systems, performed almost all quantum scattering calculations in these systems, and calculated the six line-shape parameters of the modified Hartmann-Tran profile. I prepared the majority of the draft (including Appendices B and C), Figure 3, and supplementary materials. As the corresponding author, I coordinated the project, led the submission process, and prepared responses to the reviewers.

## Article C

I was responsible for developing all computer codes used in the quantum scattering calculations, preparing the H<sub>2</sub>-He potential energy surface for quantum scattering calculations, and performing the entire computational campaign that resulted in determining the six line-shape parameters of the modified Hartmann-Tran profile for 321 He-perturbed H<sub>2</sub> lines. I contributed to writing parts of the manuscript (Section 3) and preparing part of the supplementary materials.



## **Article D**

I prepared the three CO-N<sub>2</sub> potential energy surfaces for quantum scattering calculations, performed quantum scattering calculations, calculated the pressure broadening coefficient for the N<sub>2</sub>-perturbed CO line under study, and prepared the original draft of the manuscript. As the corresponding author, I led the submission process and prepared responses to the reviewers.

## **Article E**

I prepared the H<sub>2</sub>-H<sub>2</sub> potential energy surfaces for quantum scattering calculations, performed part of the quantum scattering calculations, calculated the six line-shape parameters of the modified Hartmann-Tran profile for the self-perturbed H<sub>2</sub> line under study, and prepared the manuscript section regarding the scattering calculations (Section S3).

## **Article F**

I calculated rovibrationally-averaged hyperfine coupling constants as well as positions and intensities of all hyperfine components of the rovibrational dipole transitions in HT and DT molecules reported in this work. I prepared the original draft of the manuscript and supplementary materials. As the corresponding author, I coordinated the project, led the submission process, and prepared responses to the reviewers.

## **Article G**

I calculated rovibrationally-averaged hyperfine coupling constants as well as positions and intensities of all hyperfine components of the rovibrational quadrupole transitions in the HD molecule reported in this work. I prepared the original draft of the manuscript and supplementary materials. As the corresponding author, I coordinated the project, led the submission process, and prepared responses to the reviewers.



## **Article H**

I calculated rovibrationally-averaged hyperfine coupling constants and hyperfine splittings of the rovibrational levels of  $\text{H}_2$  considered in this work. I prepared the original draft of the manuscript. As the corresponding author, I coordinated the project, led the submission process, and prepared responses to the reviewers.

## **Article I**

I derived all the formulas reported in the manuscript, drew conclusions regarding the lack of hyperfine shifts in Doppler-limited spectra, and prepared the original draft of the manuscript. As the corresponding author, I coordinated the project, led the submission process, and prepared responses to the reviewers.

## **Article J**

I derived all the formulas reported in the manuscript and prepared the original draft of the manuscript. As the corresponding author, I coordinated the project, led the submission process, and prepared responses to the reviewers.

## **Article K**

I derived all the formulas reported in the manuscript, performed calculations of the magic wavelengths in the perturbative approach, and conducted the non-perturbative analysis of the problem. I prepared parts of the original draft, including all figures and supplementary materials. As the corresponding author, I led the submission process and prepared responses to the reviewers.






## **Article L**

I prepared the  $\text{H}_2\text{-Li}$  potential energy surface for quantum scattering calculations, adapted the scattering code to the case considered in this work, performed all quantum scattering calculations, and prepared the original draft. As the corresponding author, I led the submission process and prepared responses to the reviewers.



# PUBLICATIONS

# Revisiting the rovibrational (de-)excitation of molecular hydrogen by helium<sup>★</sup>

Hubert Jóźwiak<sup>1</sup> , Franck Thibault<sup>2</sup> , Alexandra Viel<sup>2</sup> , Piotr Wcisło<sup>1</sup> , and François Lique<sup>2</sup> 

<sup>1</sup> Institute of Physics, Faculty of Physics, Astronomy and Informatics, Nicolaus Copernicus University in Toruń, Grudziądzka 5, 87-100 Toruń, Poland

e-mail: [hubert.jozwiak@doktorant.umk.pl](mailto:hubert.jozwiak@doktorant.umk.pl)

<sup>2</sup> Univ Rennes, CNRS, IPR (Institut de Physique de Rennes) – UMR 6251, 35000 Rennes, France

Received 17 November 2023 / Accepted 24 February 2024

## ABSTRACT

**Context.** The collisional (de-)excitation of H<sub>2</sub> by He plays an important role in the thermal balance and chemistry of various astrophysical environments, making accurate rate coefficients essential for interpreting observations of the interstellar medium.

**Aims.** Our goal is to utilize a state-of-the-art potential energy surface (PES) to provide comprehensive state-to-state rate coefficients for He-induced transitions among rovibrational levels of H<sub>2</sub>.

**Methods.** We performed quantum scattering calculations for the H<sub>2</sub>–He system. Thus, we were able to provide state-to-state rate coefficients for 1059 transitions between rovibrational levels of H<sub>2</sub>, with internal energies up to  $\approx 15\,000\text{ cm}^{-1}$ , for temperatures ranging from 20 to 8000 K.

**Results.** Our results demonstrate a good agreement with previous calculations for pure rotational transitions between low-lying rotational levels. However, we do find significant discrepancies for rovibrational processes involving highly-excited rotational and vibrational states. We attribute these differences to two key factors: (1) the broader range of intramolecular distances covered by ab initio points and (2) the superior accuracy of the PES, resulting from the utilization of the state-of-the-art quantum chemistry methods, compared to previous lower-level calculations.

**Conclusions.** Radiative transfer calculations performed with the new collisional data indicate that the population of rotational levels in excited vibrational states experiences significant modifications, highlighting the critical need for this updated dataset in models of high-temperature astrophysical environments.

**Key words.** molecular data – radiative transfer – scattering – ISM: molecules

## 1. Introduction

As the most abundant molecule in the Universe, H<sub>2</sub> plays a crucial role in the chemistry and thermal balance of various astrophysical environments, as a result of collisions. For instance, when a shock wave passes through a molecular gas, heating the medium to temperatures of a few hundred degrees kelvin (or above), inelastic collisions with H<sub>2</sub> determine the rate of cooling of the gas at temperatures in the range of 100–1000 K (Aannestad & Field 1973; Shull & Beckwith 1982; Le Bourlot et al. 1999). The collisional excitation of H<sub>2</sub> and subsequent infrared emission was also one of the important cooling mechanisms in the post-recombination era, after the first molecules were formed. Despite its low abundance in the early Universe, collisions of H<sub>2</sub> and its deuterated isotopologue (HD) dominated the cooling process, leading to the gravitational collapse of inhomogeneities in the primordial gas and to the formation of the first stars (Flower & Pineau des Forêts 2001).

Although it is less abundant than molecular hydrogen, He is one of the most important collisional partners for H<sub>2</sub> (along with H, H<sup>+</sup>, and H<sub>2</sub> itself) across a broad variety of astrophysical environments, such as diffuse clouds, dense molecular clouds, protoplanetary disks, and in the early Universe. It is essential

to note that typical densities in these environments are not sufficient to achieve local thermodynamic equilibrium (LTE). In such cases, the evolution of molecular populations is determined by two processes: radiative transitions and inelastic collisions. Thus, accurate rate coefficients for collisional processes involving H<sub>2</sub> are crucial for a reliable interpretation of observations of the interstellar medium. For instance, rate coefficients for rovibrational excitation and de-excitation of H<sub>2</sub> in collisions with He have been used in calculations of the cooling rate of the primordial gas (Flower et al. 2000; Glover & Abel 2008), as well as analyses of populations of H<sub>2</sub> in turbulent diffuse interstellar clouds (Cecchi-Pestellini et al. 2005) and the evolution of molecular gas in dark, dense clouds following the passage of C-type shocks (Yuan & Neufeld 2010; Nesterenok 2018), and in studies of protoplanetary disk chemistry (Ruaud 2021).

The astrophysical community typically uses the H<sub>2</sub>–He rate coefficients calculated by Flower et al. (1998, hereafter, F98), which are available in the BASECOL database (Dubernet et al. 2013). These rate coefficients were obtained from quantum scattering calculations performed on the potential energy surface (PES) reported by Muchnick & Russek (1994). The authors included rovibrational levels up to  $v = 3, j = 8$  in their calculations and provided rate coefficients for temperatures ranging from 100 to 6000 K. Theoretical rate coefficients for vibrational relaxation from rotational levels in the  $v = 1$  manifold are in satisfactory agreement (within a factor of 2) with experimental

<sup>★</sup> The ortho- and para-H<sub>2</sub> data are available at the CDS via anonymous ftp to [cdsarc.cds.unistra.fr](ftp://cdsarc.cds.unistra.fr) (130.79.128.5) or via <https://cdsarc.cds.unistra.fr/viz-bin/cat/J/A+A/685/A113>

data of Dove & Teitelbaum (1974) and Audibert et al. (1976). Independent quantum scattering calculations performed on the same PES by Balakrishnan et al. (1999a,b), but using a different approach to performing a rovibrational average of the PES led to a good agreement with the results of Flower et al. (1998) for transitions involving  $|\Delta j| = 0, 2$ , and 4. Importantly, the calculations of Balakrishnan et al. (1999b) extended the original dataset of Flower et al. (1998) to  $v = 4, 5$  and 6.

The quality of theoretical rate coefficients is largely determined by the potential energy surface (PES) employed. Since the works of Flower et al. (1998) and Balakrishnan et al. (1999a,b), new PESs have been published that should, in principle, provide a more accurate description of H<sub>2</sub>–He interaction energies. Lee et al. (2005) conducted a comparative study between the rate coefficients derived from the Muchnick & Russek (1994) (MR) PES and the then most recent PES reported by Boothroyd et al. (2003, BMP). Surprisingly, they discovered that the total quenching rate from the  $v = 1, j = 0$  state calculated with the BMP PES was three orders of magnitude larger than that calculated with the MR PES and the experimental data reported by Audibert et al. (1976). In a joint experimental and theoretical study of low-temperature (between 22 and 180 K), inelastic collisions of H<sub>2</sub> and He, Tejeda et al. (2008) found that the rate coefficients for pure rotational de-excitation,  $k_{v=0, j=2 \rightarrow v'=0, j'=0}$ , obtained from quantum scattering calculations based on the MR PES were in better agreement with the experimental data than those derived from the BMP PES. The two papers confirmed the quality of the MR PES and (indirectly) the rate coefficients calculated by Flower et al. (1998).

However, studies comparing rate coefficients may not be sensitive enough to discern the differences between various PESs. A much more stringent test of the PES can be performed by comparing spectroscopic parameters of molecular lines, such as pressure broadening and shift coefficients (Thibault et al. 2016). Recently, we have shown that the most recent H<sub>2</sub>–He PES (Thibault et al. 2017, hereafter, BSP3) leads to a sub-percent agreement between experimental and theoretical line profiles of molecular hydrogen perturbed in collisions with He (Słowiński et al. 2020). In particular, we have demonstrated that quantum scattering calculations based on the older PESs, such as the improved version from Muchnick & Russek (1994, mMR), fail to reproduce the cavity-enhanced spectra of the 3–0 S(1) and 2–0 Q(1) He-perturbed lines of H<sub>2</sub> (Słowiński et al. 2022). The most recent PES has been successfully used in comprehensive calculations of line-shape parameters for He-perturbed H<sub>2</sub> (Jóźwiak et al. 2018) and HD (Thibault et al. 2020; Stankiewicz et al. 2020) lines, which provided a basis for the construction of a new generation of line-shape parameters databases based on ab initio calculations (Wcisło et al. 2021; Stankiewicz et al. 2021). The BSP3 PES has also been used in studies of stereodynamics of cold He-HD (Morita & Balakrishnan 2020a,b) and He-D<sub>2</sub> (Jambrina et al. 2022) collisions.

In this paper, we use the most recent PES (Thibault et al. 2017) to perform quantum scattering calculations for the H<sub>2</sub>–He system and to revise the state-to-state rate coefficients calculated by Flower et al. (1998). The paper is organized as follows. In Sect. 2, we briefly describe the quantum scattering calculations. We present examples of cross-sections and rate coefficients and compare the results with available theoretical and experimental data in Sect. 3. In Sect. 4, we discuss the potential implications of our results on astrophysical models before giving our concluding remarks in Sect. 5. The complete dataset with all state-to-state coefficients will be available online from the BASECOL (Dubernet et al. 2013) website.

## 2. Methods

We studied the inelastic collisions in the H<sub>2</sub>–He systems by solving the close-coupling equations in the body-fixed (BF) frame of reference. The theory of non-reactive scattering in systems with arbitrary angular momenta in the BF frame was developed by Launay (1977). It was recently recalled by some of the present authors in the context of scattering calculations for He-perturbed shape of HD rovibrational resonances (Stankiewicz et al. 2020). We chose the BF frame of reference because the coupling matrix exhibits a predominantly block-diagonal structure with blocks interconnected by centrifugal terms (see Fig. 3 in Rabitz 1975), which significantly reduces computational time and memory requirements.

We employed the H<sub>2</sub>–He potential energy surface reported by Thibault et al. (2017), which extends the PES calculated by Bakr et al. (2013). The PES was computed using the coupled-cluster method with single, double, and perturbative triple excitations [CCSD(T)], supplemented by full configuration interaction corrections. In comparison to the previous version, which covered H–H distances in the range of  $r_{\text{HH}} \in [1.1, 1.7] a_0$ , this PES encompasses a broader range of intramolecular H–H distances ( $r_{\text{HH}} \in [0.65, 3.75] a_0$ ). This serves as a critical aspect for accurately studying inelastic transitions between excited vibrational states of H<sub>2</sub>.

The PES is expanded in the Legendre polynomials:

$$V(R, r_{\text{HH}}, \theta) = \sum_{\lambda=0,2,4,6} A_{\lambda}(R, r_{\text{HH}}) P_{\lambda}(\cos \theta), \quad (1)$$

where  $R$  denotes the distance between He and the center of mass of H<sub>2</sub>, while  $\theta$  is the angle between the intra- and intermolecular axis. Since H<sub>2</sub> is a homonuclear molecule,  $\lambda$  takes only even values. We use the analytical representation of the expansion terms,  $A_{\lambda}(R, r_{\text{HH}})$ , provided in Eq. (2) of Thibault et al. (2017). The dependence of the expansion coefficients on the stretching coordinate,  $r_{\text{HH}}$ , is ruled out by averaging the PES over rovibrational wave functions of isolated H<sub>2</sub> molecule,  $\chi_{vj}(r_{\text{HH}})$ :

$$v_{\lambda,v,j,v',j'}(R) = \int dr_{\text{HH}} \chi_{vj}(r_{\text{HH}}) A_{\lambda}(R, r_{\text{HH}}) \chi_{v'j'}(r_{\text{HH}}). \quad (2)$$

We used 703 coupling terms,  $v_{\lambda,v,j,v',j'}(R)$ , for each  $\lambda$  value. These terms describe couplings between all 37 (see below) rovibrational states included in the calculations. Rovibrational wave functions of H<sub>2</sub>,  $\chi_{v'j'}(r_{\text{HH}})$ , are obtained by solving the Schrödinger equation for nuclear motion of H<sub>2</sub> molecule with the potential energy curve of Schwenke (1988), using the discrete variable representation-finite basis representation method.

We recall that the close-coupling equations are diagonal with respect to the total angular momentum ( $J$ ) and parity ( $p$ ), namely, they can be solved for each value of  $J$  and  $p$  separately. Since the PES does not couple states with different nuclear spins ( $I$ ), we considered the scattering of para-H<sub>2</sub> ( $I = 0$ , rotational states with even  $j$  values) and ortho-H<sub>2</sub> ( $I = 1$ , rotational states with odd  $j$  values) separately. The coupled equations are solved using renormalized Numerov's algorithm implemented in the in-house scattering code BIGOS (Jóźwiak 2024)<sup>1</sup>. The log-derivative matrix is transformed to the space-fixed (SF) frame of reference at a sufficiently large value of  $R$ , and the boundary conditions, imposed on the scattering wave functions allow us to

<sup>1</sup> The scattering code, optimized for H<sub>2</sub>–He calculations, is publicly available at [https://github.com/hjozwiak-umk/bigos\\_h2he](https://github.com/hjozwiak-umk/bigos_h2he)



obtain the S-matrix elements. The state-to-state cross-sections are calculated from the S-matrix elements as follows

$$\sigma_{vj \rightarrow v'j'}(E_{\text{kin}}) = \frac{\pi}{k_{vj}^2(2j+1)} \times \sum_{J,l,l'} (2J+1) \left| \delta_{vv'} \delta_{jj'} \delta_{ll'} - S_{vj l \rightarrow v' j' l'}^J(E) \right|^2, \quad (3)$$

where  $v$  and  $j$  denote pre-collisional vibrational and rotational quantum numbers of  $\text{H}_2$ ,  $l$  is the angular momentum of the relative motion in the colliding system,  $E = E_{\text{kin}} + E_{vj}$  is the total energy (the sum of the relative kinetic energy and the internal energy of  $\text{H}_2$  in the given rovibrational state),  $k_{vj} = \hbar^{-1} \sqrt{2\mu(E - E_{vj})}$ ,  $\mu$  is the reduced mass of the  $\text{H}_2$ –He system, and  $\hbar$  is the reduced Planck constant. Primed symbols denote post-collisional values. The sum over  $J$  is truncated at a value  $J_{\text{max}}$  large enough to ensure convergence of the elastic and the largest inelastic cross-sections at the level of  $10^{-4} \text{ \AA}^2$ . The range of the sum over  $l$  (and  $l'$ ) is determined by the triangular rule resulting from adding two angular momenta  $\mathbf{j} + \mathbf{l} = \mathbf{J}$  (and  $\mathbf{j}' + \mathbf{l}' = \mathbf{J}$ ).

In this study, we are interested in rovibrational transitions between  $\text{H}_2$  levels with internal energies lower than  $15\,000 \text{ cm}^{-1}$ . There are 26 such levels in ortho- $\text{H}_2$ , and 27 such levels in para- $\text{H}_2$ . When all these levels are energetically accessible, there are 676 possible transitions for ortho- $\text{H}_2$  and 729 for para- $\text{H}_2$ . The cross-sections were calculated for total energies ranging between  $10^{-6}$  and  $40\,000 \text{ cm}^{-1}$  with various energy steps, in order to accurately describe the channel-opening effects and resonances. We tested the convergence of the cross-sections with respect to the parameters of the propagator and the size of the rovibrational basis. The specific values for these parameters, including the range of propagation ( $R_{\text{min}}$  and  $R_{\text{max}}$ ) and the number of steps per half-de Broglie wavelength, are presented in Table 1. The convergence with respect to the size of the rovibrational basis is tested through a series of calculations at the largest collision energy ( $40\,000 \text{ cm}^{-1}$ ). The basis is incrementally expanded by adding rovibrational levels of  $\text{H}_2$  in order of increasing energy until the state-to-state cross-sections of the 676 (ortho- $\text{H}_2$ ) and 729 (para- $\text{H}_2$ ) transitions differ by less than 1%. This basis (which we refer to as a “fully converged basis”) involves all rovibrational levels of  $\text{H}_2$  up to  $v = 5, j = 6$  and  $v = 5, j = 7$  for para- $\text{H}_2$ –He and ortho- $\text{H}_2$ –He collisions, respectively. After establishing a fully-converged basis, we compared the cross-sections derived from smaller basis sets to this benchmark. We set an acceptable level of convergence at 10% when comparing these cross-sections against those obtained from the fully converged basis. Ultimately, the basis set involved 37 rovibrational levels (up to the  $v = 2, j = 14$  for para- $\text{H}_2$  and  $v = 5, j = 1$  for ortho- $\text{H}_2$ ), which ensured convergence better than 10% with respect to the fully-converged basis for 539 (out of 729) cross-sections in the para- $\text{H}_2$  case and 520 (out of 676) cross-sections in the ortho- $\text{H}_2$  case related to transitions between levels with internal energies lower than  $15\,000 \text{ cm}^{-1}$ , leading to the total number of 1 059 transitions.

We calculated the thermal rate coefficients by averaging the state-to-state cross-sections over the distribution of relative kinetic energy as follows:

$$k_{vj \rightarrow v'j'}(T) = \langle v_r \rangle \left( \frac{1}{k_B T} \right)^2 \int_0^\infty \sigma_{vj \rightarrow v'j'}(E_{\text{kin}}) E_{\text{kin}} e^{-E_{\text{kin}}/k_B T} dE_{\text{kin}}, \quad (4)$$

**Table 1.** Parameters ensuring convergence in scattering calculations.

Parameter	Value
$R_{\text{min}}$	$1 a_0$
$R_{\text{max}}$	$100 a_0$
Number of steps per half-de Broglie wavelength	15
Number of rovibrational levels of $\text{H}_2$ in the basis	37

**Notes.** See text for details regarding the construction of the basis set.

where  $\langle v_r \rangle = \sqrt{8k_B T / (\pi \mu)}$  is the mean relative speed of the colliding partners at a given temperature. The range of total energies covered by the scattering calculations (from  $10^{-6}$  to  $40\,000 \text{ cm}^{-1}$ ) allows us to determine thermal rate coefficients ranging from 20 to 8000 K for the 1059 considered transitions.

### 3. Results

In this section, we discuss the calculated cross-sections and thermal rate coefficients.

#### 3.1. Pure rotational ( $v' = v$ ) (de-)excitation

We began with the inelastic processes between rotational levels within the ground vibrational state, which are the most populated states in  $\text{H}_2$  in the 100–1000 K temperature range. Since the PES does not couple ortho- and para- $\text{H}_2$ ,  $\Delta j = \pm 1$  transitions are forbidden. The dominant inelastic processes are the ones that change the rotational quantum number by  $\Delta j = \pm 2$ . These are mostly driven by the  $\lambda = 2$  term in the expansion in Eq. (1), which is the largest anisotropic term in the expansion of the PES. Figure 1 presents the state-to-state cross-sections for pure rotational de-excitation with  $\Delta j = -2$  of  $\text{H}_2$  upon collisions with helium up to  $j = 7$ . At ultra-low kinetic energies (below  $10^{-3} \text{ cm}^{-1}$ , the cross-sections obey the Wigner threshold law (Wigner 1948) for de-excitation cross-section ( $\sigma \sim k^{-1/2}$ ). As the kinetic energy increases, more partial waves contribute to the inelastic scattering, the cross-sections pass through a minimum near  $20 \text{ cm}^{-1}$  and gradually increase at higher kinetic energies. For the majority of considered kinetic energies, the cross-sections decrease with increasing initial rotational state. This property is translated to thermal rate coefficients (bottom panel in Fig. 1), which also decrease with increasing rotational quantum numbers. This is related to the fact that the rotational spacing between levels increases with  $j$ , thus reducing the de-excitation process.

Pure rotational de-excitation (with  $\Delta j = -2$ ) within excited vibrational states looks similar to the de-excitation within  $v = 0$ . The only difference is that the cross-sections (and corresponding rate coefficients) increase with the increasing value of  $v$ . Figure 2 presents a comparison between the  $\sigma_{v,2 \rightarrow v,0}$  (in the top panel) and  $k_{v,2 \rightarrow v,0}$  (in the bottom panel) for different vibrational quantum numbers. The observed trend is explained by the fact that the energy interval between rotational states decreases with increasing  $v$ , thus enhancing rotational transitions within the same vibrational level. This is in line with an increased contribution from inelastic processes to pressure broadening of rovibrational lines as  $v$  increases (Hartmann et al. 2021), as observed in He-perturbed Q (Thibault et al. 2017), and S and O (Jóźwiak et al. 2018) lines of  $\text{H}_2$ .

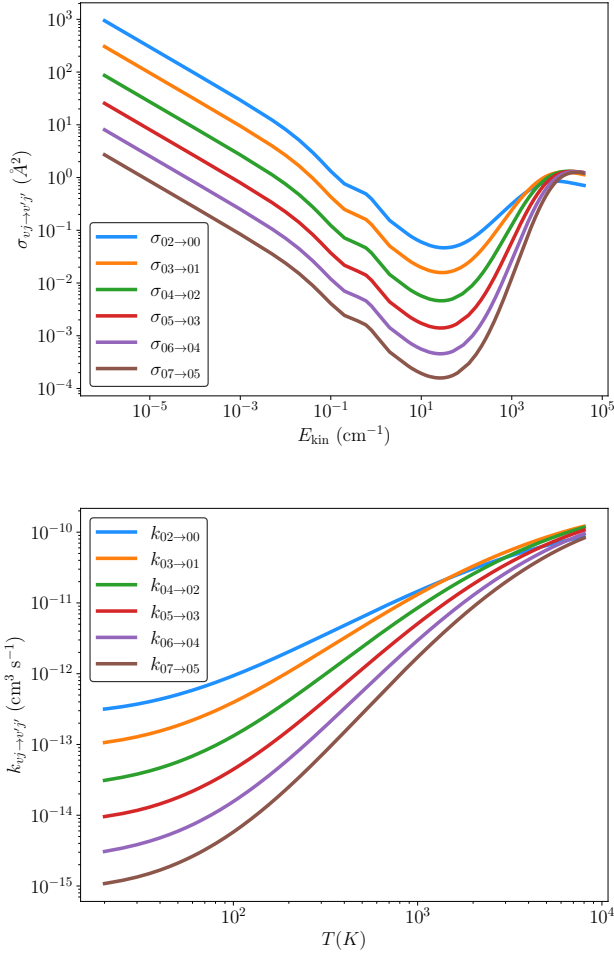


**Fig. 1.** State-to-state cross-sections (top panel) and corresponding thermal rate coefficients (bottom panel) for pure rotational de-excitation in  $v = 0$  with  $\Delta_j = -2$ .

### 3.2. Rovibrational (de-)excitation

Figure 3 presents a comparison of the state-to-state cross-sections and corresponding rate coefficients for  $\Delta v, \Delta j = 0$  transitions. For reference, we put the elastic scattering cross-section in the  $v = 0, j = 0$  state (dark blue color), which is at least three orders of magnitude larger than the cross-sections for vibrationally inelastic processes. We recover the expected asymptotic behavior of the elastic cross-section at ultra-low kinetic energies, where it converges to the constant value. The dependence of  $v$ -changing cross-sections follows a trend similar to pure rotational de-excitation, with a minimum near  $20 \text{ cm}^{-1}$ , but the increase in the orders of magnitude of the cross-sections at high ( $>10^3 \text{ cm}^{-1}$ ) is more drastic. For instance, the  $\sigma_{1,0 \rightarrow 0,0}$  cross-section increases by eight orders of magnitude for kinetic energies in the range from 20 to  $40\,000 \text{ cm}^{-1}$ . Overall, the cross-sections and the corresponding thermal rate coefficient decrease rapidly with increasing  $\Delta v$ , owing to the fact that the off-diagonal (in terms of vibrational quantum numbers) radial coupling terms of the potential decrease with  $\Delta v$ . This trend is transferred to thermal rate coefficients. We note that the rate coefficients for vibrational-state-changing collisions are at least three orders of magnitude smaller (at  $T = 8000 \text{ K}$ ) than the rate coefficients for pure rotational de-excitation presented in the top panels of Figs. 1 and 2.

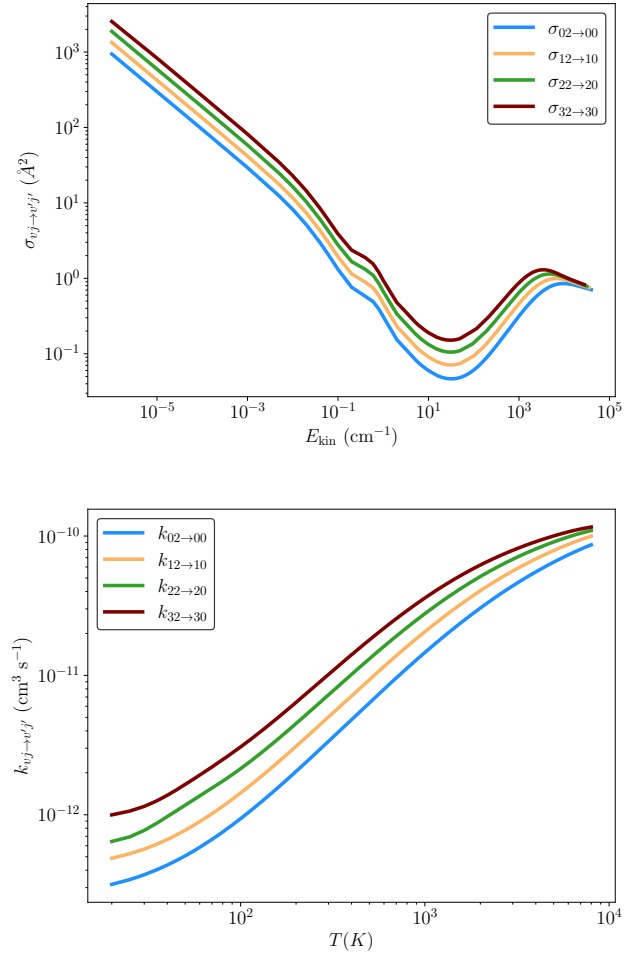


**Fig. 2.** State-to-state cross-sections (top panel) and corresponding thermal rate coefficients (bottom panel) for  $v, j = 2 \rightarrow v', j' = 0$  de-excitation with  $v = 0, 1, 2, 3$ .

Rate coefficients for simultaneous quenching of both rotational and vibrational excitation are even smaller. Figure 4 presents state-to-state cross-sections and thermal rate coefficients for the  $v, j = 2 \rightarrow v' = 0, j' = 0$  transitions. Contrary to  $v, j = 0 \rightarrow v' = 0, j' = 0$  transitions from Fig. 3, driven only by  $\lambda = 0$  terms which are off-diagonal in vibrational quantum numbers, transitions in Fig. 4 owe their strength to the anisotropic  $\lambda = 2$  terms which are off-diagonal in  $v, v'$ . Due to the reasons discussed above, the cross-sections and rate coefficients rapidly decrease with increasing  $\Delta v$ .

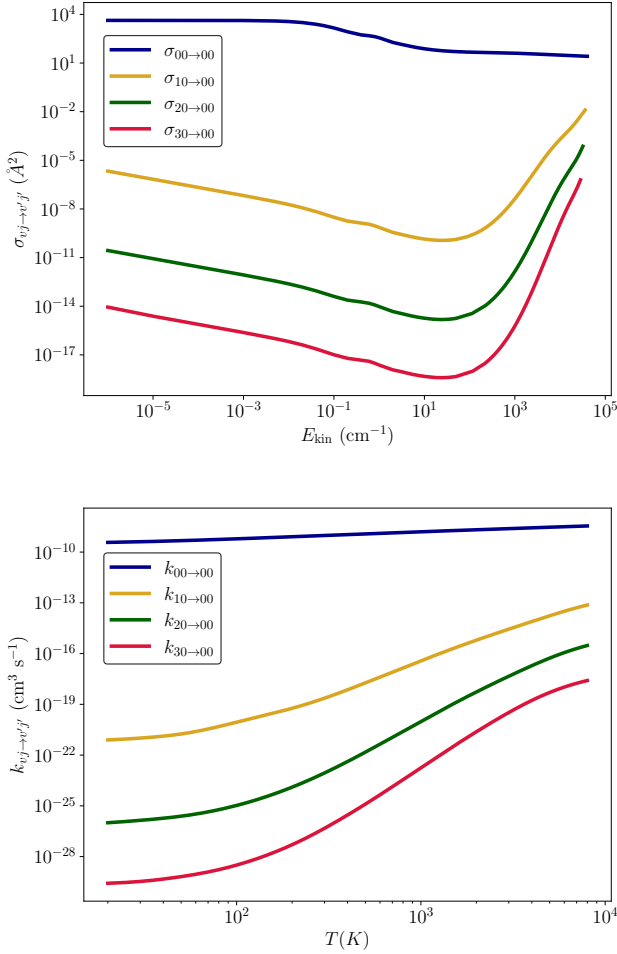
For the sake of brevity, we do not discuss the analogous ( $v, j = 1 \rightarrow v' = 0, j' = 1$  and  $v, j = 3 \rightarrow v' = 0, j' = 1$ ) transitions in ortho- $\text{H}_2$ . The dependence of the cross-sections and rate coefficients on  $\Delta v$  and the overall relation with respect to kinetic energy and temperature remains similar.

### 3.3. Comparison with previous results

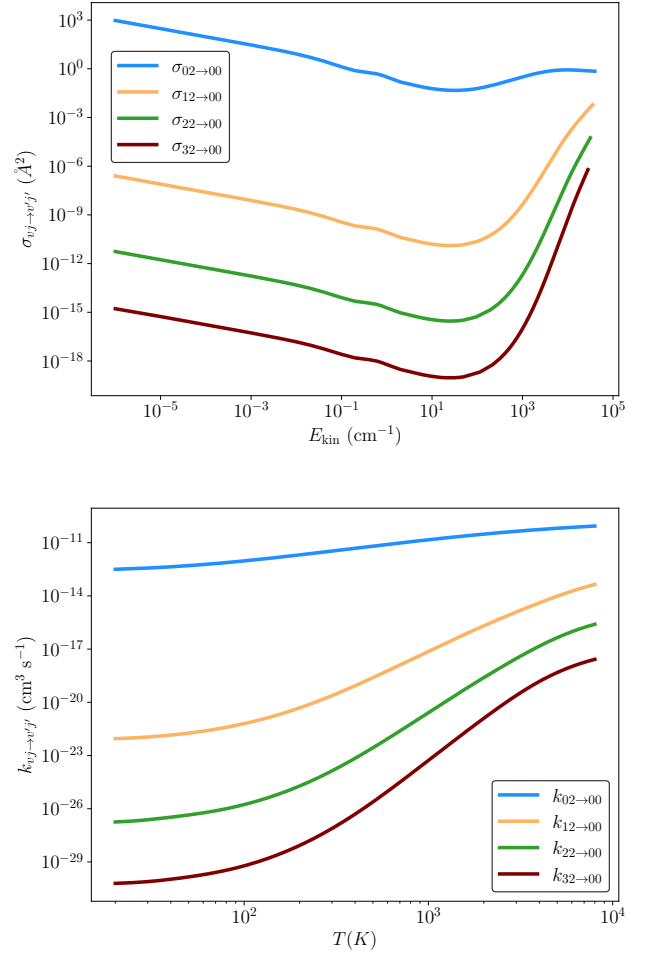
Here, we compare the new rate coefficients with the available literature data. Due to the large size of the dataset, we begin with a discussion of a few representative rovibrational transitions that highlight the differences and similarities between our results and previous findings.

We begin with the comparison of rate coefficients for pure rotational de-excitation of  $\text{H}_2$  in the  $v = 0$  state upon collisions with He. In the top left ( $k_{0,2 \rightarrow 0,0}$ ) and right ( $k_{0,3 \rightarrow 0,1}$ ) panels of





**Fig. 3.** State-to-state cross-sections (top panel) and corresponding thermal rate coefficients (bottom panel) for  $v, j = 0 \rightarrow v' = 0, j' = 0$  de-excitation with  $v = 0, 1, 2, 3$ .



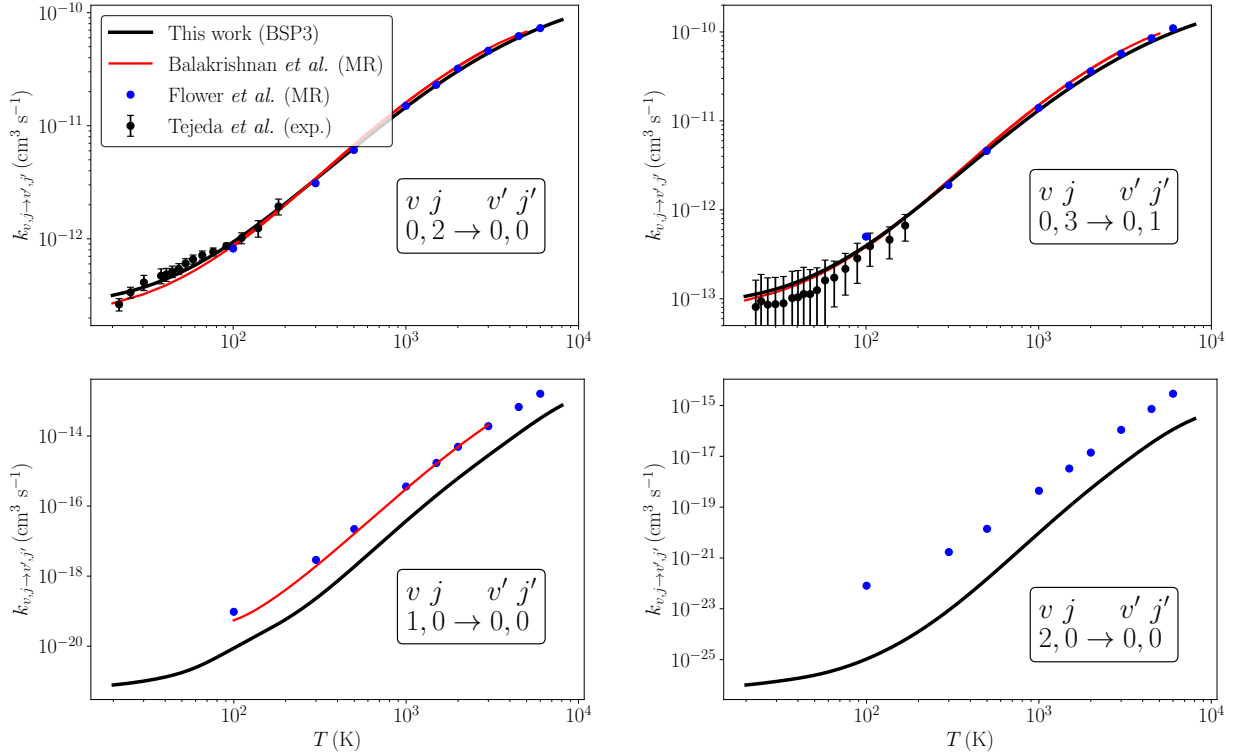
**Fig. 4.** State-to-state cross-sections (top panel) and corresponding thermal rate coefficients (bottom panel) for  $v, j = 2 \rightarrow v' = 0, j' = 0$  de-excitation from the four considered vibrational states.

Fig. 5 we gathered theoretical rate coefficients calculated in this work, those reported by Flower et al. (1998) and Balakrishnan et al. (1999a), as well as experimental results (Tejeda et al. 2008) determined using Raman spectroscopy in supersonic jets of  $\text{H}_2$ –He mixtures. For theoretical results, we use abbreviations of the names of PESs employed in quantum scattering calculations. We note that both Flower et al. (1998) and Balakrishnan et al. (1999a) performed quantum scattering calculations on the same PES, but used different approach to the rovibrational average in Eq. (2). Flower et al. (1998) approximated the  $\text{H}_2$  wave functions as harmonic oscillator wave functions (independent of  $j$ ), while Balakrishnan et al. (1999a,b) obtained  $\chi_{vj}(r_{\text{HH}})$  as expansions in Hermite polynomials using the potential energy curve for  $\text{H}_2$  taken from Schwenke (1988).

We observe a very good agreement with all previous theoretical calculations, both in the cold ( $\approx 10$  K) regime, as well as at temperatures of an order of 1000 K. For the  $v = 0, j = 2 \rightarrow v' = 0, j' = 0$  transitions, our low-temperature results reproduce the experimental datapoints slightly better than other theoretical rate coefficients. We note that Tejeda et al. (2008) also reported results of extensive scattering calculations for the two transitions using the MR PES, its modified (mMR) version (Boothroyd et al. 2003), and the BMP PES. We do not add these results to the top panels in Fig. 5 to maintain the readability of the plot. For the  $v = 0, j = 2 \rightarrow v' = 0, j' = 0$

de-excitation, using MR and mMR PESs, Tejeda et al. (2008) obtained a perfect agreement with the results of Balakrishnan et al. (1999a), but rate coefficients obtained using the BMP PES deviated significantly from both theoretical and experimental datapoints. A similar agreement between theoretical calculations from the MR and mMR PESs was found for rate coefficients for the  $v = 0, j = 3 \rightarrow v' = 0, j' = 1$  de-excitations, with results derived from the BMP PES being  $\approx 50\%$  smaller. We also note that rate coefficients for pure rotational de-excitation of  $\text{H}_2$  by He were studied by Zhou & Chen (2017) who conducted quantum scattering calculations on the BSP PES (Bakr et al. 2013). From Fig. 5 in their paper, we can deduce that rate coefficients for the  $v = 0, j = 2 \rightarrow v' = 0, j' = 0$  transitions calculated in the range 25 to 150 K are slightly lower than the experimental datapoints and are closer to the results of Balakrishnan et al. (1999a).

Now, looking at transitions with  $v > 0$ , we generally obtain a good agreement with the results of Flower et al. (1998) and Balakrishnan et al. (1999a) for transitions with  $\Delta v = 0$ , and  $\Delta j = \pm 2, \pm 4$ . As the difference in vibrational and rotational quantum numbers increases, we observe significant differences between our results and previous theoretical calculations. In particular, as shown in the bottom-left (for de-excitation from the  $v = 1, j = 0$  state) and bottom-right (for a de-excitation from the  $v = 2, j = 0$  state) of Fig. 5, we observe that rate coefficients for vibrational de-excitation are significantly (by between one and two orders of magnitude) lower than the results of



**Fig. 5.** Comparison between the rate coefficients for pure rotational  $v = 0, j = 2 \rightarrow v = 0, j = 0$  (top left panel),  $v = 0, j = 3 \rightarrow v = 0, j = 1$  (top-right), and rovibrational  $v = 1, j = 0 \rightarrow v' = 0, j' = 0$  (bottom left panel) and  $v = 2, j = 0 \rightarrow v' = 0, j' = 0$  (bottom-right) de-excitation provided in this work and the available literature data.

Flower et al. (1998) and Balakrishnan et al. (1999a). We attribute the discrepancies between the results to the quality of the PESs. We recall that the most recent PES was calculated using coupled-cluster method with single, double, and perturbative triple excitations [CCSD(T)], supplemented by full configuration interaction corrections. On the other hand, the MR PES was obtained using much smaller Gaussian basis sets and a lower level of electronic structure theory. Moreover, the BSP3 PES covered a significantly larger range of intramolecular distances ( $r_{\text{HH}} \in [0.65, 3.75] a_0$ ), which is crucial for the accuracy of quantum scattering calculations involving vibrationally excited  $\text{H}_2$ .

#### 4. Astrophysical applications

As previously mentioned, in the early Universe, as well as in interstellar clouds, the  $\text{H}_2$  molecules can be excited by collisions with He, H,  $\text{H}_2$ , and  $\text{H}^+$  which are the dominant heavy projectiles in such media. It is then of interest to compare and discuss the efficiency of all projectiles for (de-)exciting  $\text{H}_2$  by collisions. Hence, we compare in Fig. 6 the new  $\text{H}_2$ –He collisional data for the rovibrational relaxation of  $\text{H}_2(v = 1, j = 0)$  to  $\text{H}_2(v' = 0, j' = 0)$  to those for  $\text{H}_2$ –H (Lique 2015),  $\text{H}_2$ – $\text{H}^+$  (González-Lezana et al. 2021), and  $\text{H}_2$ –p- $\text{H}_2$  (Flower & Roueff 1998) as a function of the temperature.

As one can see,  $\text{H}^+$  is by far the most efficient projectile to (de-)excite  $\text{H}_2$ , especially at low temperatures. Such dominance is not surprising and can be explained by the charge of  $\text{H}^+$  leading to a strong interaction between  $\text{H}_2$  and  $\text{H}^+$  and, thus, to an efficient energy transfer during collisions.

For the (de-)excitation induced by neutral projectiles, H is significantly dominating over He and  $\text{H}_2$  because of its lighter mass and the reactive nature of the system ( $\text{H}_2$  can be excited

by H via inelastic and reactive processes, Lique 2015). Over all the temperature ranges explored in this work, He- and p- $\text{H}_2$ -rate coefficients exhibit similar magnitude showing that the He: $\text{H}_2$  abundance ratio will not be a crucial parameter for determining the excitation conditions of  $\text{H}_2$  in both the early universe and in interstellar clouds. When modeling of the interstellar spectra, it is customary to use He as a proxy to estimate rate coefficients for the para- $\text{H}_2(j = 0)$  collider, based on the assumption that their cross sections are equal. Indeed, both He and para- $\text{H}_2(j = 0)$  possess two electrons and have a spherical shape. One can then use a mass-scaling relation to model para- $\text{H}_2(j = 0)$  collisional data from He ones:

$$k^{\text{p-H}_2}(T) = \left( \frac{\mu_{\text{H}_2-\text{He}}}{\mu_{\text{H}_2-\text{H}_2}} \right)^{1/2} k^{\text{He}}(T), \quad (5)$$

where  $\mu$  is the reduced mass of the collisional system. In the present case,  $\left( \frac{\mu_{\text{H}_2-\text{He}}}{\mu_{\text{H}_2-\text{H}_2}} \right)^{1/2} \simeq 1.1$  and this approximation seems indeed to aptly justified since He and para- $\text{H}_2(j = 0)$  collisional data agree well. It should however be mentioned that both sets of collisional data were not performed at the same level of accuracy. It would be desirable, in order to confirm this global agreement, to obtain a new set of para- $\text{H}_2(j = 0)$  collisional data with a similar level of accuracy to the present He ones.

Moreover, as a second application and in order to test the impact of the new rate coefficients compared to those of F98 widely used in the astrophysical community, we performed radiative transfer calculations to determine the population of  $\text{H}_2$  induced by He collisions. Non-local thermodynamic equilibrium (non-LTE) calculations were performed with the RADEX code (van der Tak et al. 2007). Both collisional and radiative processes

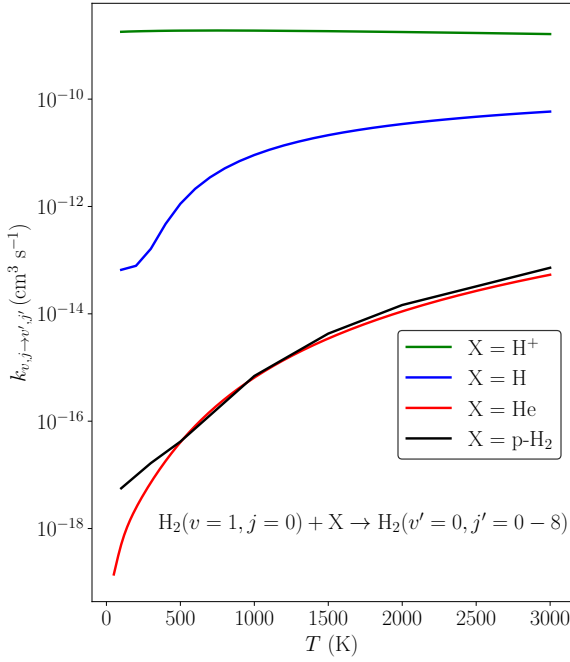


**Fig. 6.** Comparison between the rate coefficients for rovibrational  $v = 1, j = 0 \rightarrow v' = 0, \sum_0^8 j'$  de-excitation provided in this work and the available literature data (see text).

**Table 2.** Comparison between para-H<sub>2</sub> fractional population,  $p_{v,j}$ , obtained using present and F98 collisional data.

Level	$T = 5000 \text{ K}, n(\text{He}) = 10^3 \text{ cm}^{-3}$	
	$p_{v,j}$ (this work)	$p_{v,j}$ (F98)
$v = 0, j = 2$	$2.542 \times 10^{-1}$	$2.381 \times 10^{-1}$
$v = 0, j = 4$	$3.585 \times 10^{-1}$	$3.405 \times 10^{-1}$
$v = 0, j = 6$	$2.648 \times 10^{-1}$	$2.753 \times 10^{-1}$
$v = 1, j = 0$	$6.574 \times 10^{-6}$	$2.470 \times 10^{-5}$
$v = 1, j = 2$	$3.646 \times 10^{-5}$	$1.233 \times 10^{-4}$
$v = 1, j = 4$	$7.594 \times 10^{-5}$	$2.132 \times 10^{-4}$
$v = 2, j = 0$	$9.924 \times 10^{-9}$	$1.641 \times 10^{-7}$
$v = 2, j = 2$	$6.026 \times 10^{-8}$	$8.365 \times 10^{-7}$
$v = 3, j = 0$	$4.233 \times 10^{-11}$	$3.060 \times 10^{-9}$

are taken into account. Only the He projectiles were taken into account. We simulate the excitation conditions of both para- and ortho-H<sub>2</sub> induced by He for physical conditions corresponding to the early Universe (Flower et al. 2021) and typical warm molecular clouds where rovibrational lines of H<sub>2</sub> are detected (Neufeld & Yuan 2008). Tables 2–3 and 4–5 show a comparison of the H<sub>2</sub> fractional population,  $p_{v,j}$ , obtained using present and F98 collisional data for a temperature of 5000 K and a He density of  $10^3 \text{ cm}^{-3}$  (typical physical conditions in the early Universe) and for a temperature of 1000 K and a He density of  $10^5 \text{ cm}^{-3}$  (typical physical conditions in warm molecular clouds), respectively. We note that the fractional populations in Tables 2–5 are normalized separately for para-H<sub>2</sub> and ortho-H<sub>2</sub> species. The relative ortho-to-para ratio is maintained at 3:1, which is consistent with the fact that collisions with He do not induce transitions between para and ortho states.

We can clearly see the population of the different rotational levels in  $v = 0$  vibrational manifold is weakly impacted by the

**Table 3.** Comparison between ortho-H<sub>2</sub> fractional population,  $p_{v,j}$ , obtained using present and F98 collisional data.

Level	$T = 5000 \text{ K}, n(\text{He}) = 10^3 \text{ cm}^{-3}$	
	$p_{v,j}$ (this work)	$p_{v,j}$ (F98)
$v = 0, j = 3$	$3.226 \times 10^{-1}$	$3.031 \times 10^{-1}$
$v = 0, j = 5$	$3.440 \times 10^{-1}$	$3.361 \times 10^{-1}$
$v = 0, j = 7$	$1.510 \times 10^{-1}$	$1.748 \times 10^{-1}$
$v = 1, j = 1$	$2.044 \times 10^{-5}$	$7.409 \times 10^{-5}$
$v = 1, j = 3$	$5.569 \times 10^{-5}$	$1.703 \times 10^{-4}$
$v = 1, j = 5$	$8.754 \times 10^{-5}$	$2.338 \times 10^{-4}$
$v = 2, j = 1$	$3.230 \times 10^{-8}$	$4.979 \times 10^{-7}$
$v = 2, j = 3$	$9.804 \times 10^{-8}$	$1.161 \times 10^{-6}$
$v = 3, j = 1$	$1.493 \times 10^{-10}$	$1.600 \times 10^{-8}$

**Table 4.** Comparison between para-H<sub>2</sub>  $p_{v,j}$  obtained using present and F98 collisional data.

Level	$T = 1000 \text{ K}, n(\text{He}) = 10^5 \text{ cm}^{-3}$	
	$p_{v,j}$ (this work)	$p_{v,j}$ (F98)
$v = 0, j = 2$	$4.951 \times 10^{-1}$	$4.942 \times 10^{-1}$
$v = 0, j = 4$	$2.753 \times 10^{-1}$	$2.749 \times 10^{-1}$
$v = 0, j = 6$	$6.106 \times 10^{-2}$	$6.191 \times 10^{-2}$
$v = 0, j = 8$	$3.612 \times 10^{-3}$	$4.337 \times 10^{-3}$
$v = 1, j = 0$	$7.374 \times 10^{-8}$	$2.692 \times 10^{-7}$
$v = 1, j = 2$	$2.425 \times 10^{-7}$	$8.941 \times 10^{-7}$
$v = 1, j = 4$	$2.257 \times 10^{-7}$	$7.768 \times 10^{-7}$
$v = 1, j = 6$	$1.370 \times 10^{-7}$	$2.257 \times 10^{-7}$

**Table 5.** Comparison between ortho-H<sub>2</sub>  $p_{v,j}$  obtained using present and F98 collisional data.

Level	$T = 1000 \text{ K}, n(\text{He}) = 10^5 \text{ cm}^{-3}$	
	$p_{v,j}$ (this work)	$p_{v,j}$ (F98)
$v = 0, j = 3$	$4.181 \times 10^{-1}$	$4.174 \times 10^{-1}$
$v = 0, j = 5$	$1.457 \times 10^{-1}$	$1.458 \times 10^{-1}$
$v = 0, j = 7$	$1.864 \times 10^{-2}$	$1.983 \times 10^{-2}$
$v = 0, j = 9$	$4.103 \times 10^{-4}$	$5.944 \times 10^{-4}$
$v = 1, j = 1$	$1.909 \times 10^{-7}$	$7.033 \times 10^{-7}$
$v = 1, j = 3$	$2.397 \times 10^{-7}$	$8.864 \times 10^{-7}$
$v = 1, j = 5$	$2.095 \times 10^{-7}$	$5.850 \times 10^{-7}$
$v = 1, j = 7$	$5.440 \times 10^{-8}$	$1.267 \times 10^{-7}$

use of the new rate coefficients. A deviation of less than 5% is typically observed for these levels. The effect is the same for both para- and ortho-H<sub>2</sub>. Such a weak impact can be explained by the good overall agreement between present and F98 pure rotational data. When the vibrational quantum number increases, substantial differences, greater than an order of magnitude, start to appear. These significant deviations reflect the large deviation between present and F98 rovibrational rate coefficients. Globally, the population of rovibrationally excited levels of H<sub>2</sub> induced by He collisional is weaker when using present data than when using F98 ones, reflecting new collisional data weaker in magnitude than the former ones.

The magnitude of the line intensities of rovibrational transitions detected by telescopes is directly proportional to the population of the energy levels. The significant deviations seen are likely to modify the observations analysis and the final determination of the abundance of  $\text{H}_2$  in molecular clouds, even if He is not the dominant collider. The population of  $v = 1$  energy levels when using the new data are a factor of 3–5 lower than when using the F98 data. We anticipate an increase in the  $\text{H}_2$  abundance derived from the observations since modeling observational spectra with a weaker population will require to increase in the  $\text{H}_2$  column density.

Such differences are also likely to modify the cooling function of  $\text{H}_2$ , which is strongly dependent on the  $\text{H}_2$  populations (Flower et al. 2021). Nevertheless, we note that the largest deviations in the fractional populations are seen for weakly populated levels and we anticipate that the global impact on the cooling function will be moderate.

## 5. Conclusions

We used the state-of-the-art PES (Thibault et al. 2017) to perform quantum scattering calculations for the  $\text{H}_2$ –He system and to revise the state-to-state rate coefficients calculated by Flower et al. (1998). The revised rates are consistent with the results of previous studies for pure rotational transitions within the ground vibrational state, as reported by Flower et al. (1998) and Balakrishnan et al. (1999a). However, significant discrepancies emerge for rovibrational transitions involving highly-excited rotational and vibrational states. We attribute these discrepancies to the superior accuracy of the PES and the broader range of intramolecular distances in  $\text{H}_2$  covered by ab initio points, which is crucial for accurate description of inelastic processes involving excited rovibrational states.

The new collisional data have been introduced in a radiative transfer code in order to simulate the excitation conditions of  $\text{H}_2$  in the early Universe and in warm molecular clouds. We have found that the population of rotational levels in  $v = 0$  vibrational manifold is weakly impacted by the use of the new collisional data. On the contrary, the population of rotational levels in  $v > 0$  vibrational manifold is significantly reduced demonstrating the need of using the new set of data in astrophysical models.

**Acknowledgements.** We acknowledge financial support from the European Research Council (Consolidator Grant COLLEXISM, Grant Agreement No. 811363), and the financial support of the University of Rennes via a grant project dedicated to international collaborations and via the CNRS IRN MCTDH grant. H.J. is supported by the Foundation for Polish Science (FNP) and by the National Science Centre in Poland through Project No. 2019/35/B/ST2/01118. P.W. is supported by the National Science Centre in Poland through Project No. 2022/46/E/ST2/00282. For the purpose of Open Access, the author has applied a CC-BY public copyright license to any Author Accepted Manuscript (AAM) version arising from this submission.

## References

- Aannestad, P. A., & Field, G. B. 1973, *ApJ*, **186**, L29
- Audibert, M.-M., Vilaseca, R., Lukasiak, J., & Ducuing, J. 1976, *Chem. Phys. Lett.*, **37**, 408
- Bakr, B. W., Smith, D. G., & Patkowski, K. 2013, *J. Chem. Phys.*, **139**, 144305
- Balakrishnan, N., Forrey, R. C., & Dalgarno, A. 1999a, *ApJ*, **514**, 520
- Balakrishnan, N., Vieira, M., Babb, J. F., et al. 1999b, *ApJ*, **524**, 1122
- Boothroyd, A. I., Martin, P. G., & Peterson, M. R. 2003, *J. Chem. Phys.*, **119**, 3187
- Cecchi-Pestellini, C., Casu, S., & Dalgarno, A. 2005, *MNRAS*, **364**, 1309
- Dove, J. E., & Teitelbaum, H. 1974, *Chem. Phys.*, **6**, 431
- Dubernet, M.-L., Alexander, M. H., Ba, Y. A., et al. 2013, *A&A*, **553**, A50
- Flower, D. R., & Pineau des Forêts, G. 2001, *MNRAS*, **323**, 672
- Flower, D. R., & Roueff, E. 1998, *J. Phys. B At. Mol. Phys.*, **31**, 2935
- Flower, D. R., Roueff, E., & Zeppen, C. J. 1998, *J. Phys. B-At. Mol. Opt.*, **31**, 1105
- Flower, D. R., Le Bourlot, J., Pineau des Forêts, G., & Roueff, E. 2000, *MNRAS*, **314**, 753
- Flower, D. R., Pineau des Forêts, G., Hily-Blant, P., et al. 2021, *MNRAS*, **507**, 3564
- Glover, S. C. O., & Abel, T. 2008, *MNRAS*, **388**, 1627
- González-Lezana, T., Hily-Blant, P., & Faure, A. 2021, *J. Chem. Phys.*, **154**, 054310
- Hartmann, J.-M., Boulet, C., & Robert, D. 2021, *Collisional Effects on Molecular Spectra* (Elsevier)
- Jambrina, P. G., Morita, M., Croft, J. F. E., Aoiz, F. J., & Balakrishnan, N. 2022, *J. Phys. Chem.*, **13**, 4064
- Jóźwiak, H. 2024, *The SCATTERING code adjusted for diatom-atom calculations*
- Jóźwiak, H., Thibault, F., Stolarczyk, N., & Wcisło, P. 2018, *JQSRT*, **219**, 313
- Launay, J. M. 1977, *J. Phys. B-At. Mol. Opt.*, **10**, 3665
- Le Bourlot, J., Pineau des Forêts, G., & Flower, D. R. 1999, *MNRAS*, **305**, 802
- Lee, T.-G., Rochow, C., Martin, R., et al. 2005, *J. Chem. Phys.*, **122**, 024307
- Lique, F. 2015, *MNRAS*, **453**, 810
- Morita, M., & Balakrishnan, N. 2020a, *J. Chem. Phys.*, **153**, 091101
- Morita, M., & Balakrishnan, N. 2020b, *J. Chem. Phys.*, **153**, 184307
- Muchnick, P., & Russek, A. 1994, *J. Chem. Phys.*, **100**, 4336
- Nesterenok, A. V. 2018, *Astrophys. Space Sci.*, **363**, 151
- Neufeld, D. A., & Yuan, Y. 2008, *ApJ*, **678**, 974
- Rabitz, H. 1975, *J. Chem. Phys.*, **63**, 5208
- Ruud, M. 2021, *ApJ*, **916**, 103
- Schwenke, D. W. 1988, *J. Chem. Phys.*, **89**, 2076
- Shull, J. M., & Beckwith, S. 1982, *ARA&A*, **20**, 163
- Słowiński, M., Thibault, F., Tan, Y., et al. 2020, *Phys. Rev. A*, **101**, 052705
- Słowiński, M., Jóźwiak, H., Gancewski, M., et al. 2022, *JQSRT*, **277**, 107951
- Stankiewicz, K., Jóźwiak, H., Gancewski, M., et al. 2020, *JQSRT*, **254**, 107194
- Stankiewicz, K., Stolarczyk, N., Jóźwiak, H., Thibault, F., & Wcisło, P. 2021, *JQSRT*, **276**, 107911
- Tejeda, G., Thibault, F., Fernández, J. M., & Montero, S. 2008, *J. Chem. Phys.*, **128**, 224308
- Thibault, F., Wcisło, P., & Ciuryło, R. 2016, *Eur. Phys. J. D*, **70**, 236
- Thibault, F., Patkowski, K., Żuchowski, P. S., et al. 2017, *JQSRT*, **202**, 308
- Thibault, F., Martínez, R. Z., Bermejo, D., & Wcisło, P. 2020, *Mol. Astrophys.*, **19**, 100063
- van der Tak, F. F. S., Black, J. H., Schöier, F. L., Jansen, D. J., & van Dishoeck, E. F. 2007, *A&A*, **468**, 627
- Wcisło, P., Thibault, F., Stolarczyk, N., et al. 2021, *JQSRT*, **260**, 107477
- Wigner, E. P. 1948, *Phys. Rev.*, **73**, 1002
- Yuan, Y., & Neufeld, D. A. 2010, *ApJ*, **726**, 76
- Zhou, B., & Chen, M. 2017, *Mol. Phys.*, **115**, 2442

# Accurate reference spectra of HD in an H<sub>2</sub>–He bath for planetary applications<sup>★</sup>

H. Jóźwiak<sup>1</sup>, N. Stolarczyk<sup>1</sup>, K. Stankiewicz<sup>1</sup>, M. Zaborowski<sup>1</sup>, D. Lisak<sup>1</sup>, S. Wójtewicz<sup>1</sup>, P. Jankowski<sup>2</sup>,  
K. Patkowski<sup>3</sup>, K. Szalewicz<sup>4</sup>, F. Thibault<sup>5</sup>, I. E. Gordon<sup>6</sup>, and P. Wcisło<sup>1</sup>

<sup>1</sup> Institute of Physics, Faculty of Physics, Astronomy and Informatics, Nicolaus Copernicus University in Toruń, Grudziądzka 5, 87-100 Toruń, Poland

e-mail: [hubert.jozwiak@doktorant.umk.pl](mailto:hubert.jozwiak@doktorant.umk.pl); [piotr.wcislo@umk.pl](mailto:piotr.wcislo@umk.pl)

<sup>2</sup> Faculty of Chemistry, Nicolaus Copernicus University in Toruń, Gagarina 7, 87-100 Toruń, Poland

<sup>3</sup> Department of Chemistry and Biochemistry, Auburn University, Auburn, Alabama 36849, USA

<sup>4</sup> Department of Physics and Astronomy, University of Delaware, Newark, DE 19716, USA

<sup>5</sup> Univ Rennes, IPR (Institut de Physique de Rennes) – UMR 6251, 35000 Rennes, France

<sup>6</sup> Harvard-Smithsonian Center for Astrophysics, Atomic and Molecular Physics Division, Cambridge, MA 02138, USA

Received 7 March 2024 / Accepted 17 April 2024

## ABSTRACT

**Context.** The hydrogen deuteride (HD) molecule is an important deuterium tracer in astrophysical studies. The atmospheres of gas giants are dominated by molecular hydrogen, and the simultaneous observation of H<sub>2</sub> and HD lines provides reliable information on the D/H ratios on these planets. The reference spectroscopic parameters play a crucial role in such studies. Under the thermodynamic conditions encountered in these atmospheres, spectroscopic studies of HD require not only the knowledge of line intensities and positions but also accurate reference data on pressure-induced line shapes and shifts.

**Aims.** Our aim is to provide accurate collision-induced line-shape parameters for HD lines that cover any thermodynamic conditions relevant to the atmospheres of giant planets, namely any relevant temperature, pressure, and perturbing gas composition (the H<sub>2</sub>–He mixture).

**Methods.** We performed quantum-scattering calculations on our new, highly accurate ab initio potential energy surface (PES), and we used scattering S matrices obtained in this way to determine the collision-induced line-shape parameters. We used cavity ring-down spectroscopy to validate our theoretical methodology.

**Results.** We report accurate collision-induced line-shape parameters for the pure rotational R(0), R(1), and R(2) lines, the most relevant HD lines for investigations of the atmospheres of the giant planets. Besides the basic Voigt-profile collisional parameters (i.e., the broadening and shift parameters), we also report their speed dependences and the complex Dicke parameter, which can influence the effective width and height of the HD lines up to almost a factor of 2 for giant planet conditions. The sub-percent-level accuracy reached in this work is a considerable improvement over previously available data. All the reported parameters (and their temperature dependences) are consistent with the HITRAN database format, hence allowing for the use of the HITRAN Application Programming Interface (HAPI) for generating the beyond-Voigt spectra of HD.

**Key words.** atomic data – line: profiles – molecular data – scattering – planets and satellites: atmospheres

## 1. Introduction

Hydrogen deuteride (HD), the second most abundant isotopolog of molecular hydrogen, is an important tracer of deuterium in the Universe. The small and constant primordial fraction of deuterium to hydrogen, D/H ( $(2.8 \pm 0.2) \times 10^{-5}$ ; Pettini et al. 2008), is one of the key arguments supporting the Big Bang theory. Measurements of the D/H ratio in the Solar System provide information about planetary formation and evolution. The standard ratio on Earth is considered to be Vienna Standard Mean Ocean Water (VSMOW; D/H =  $1.5576 \times 10^{-4}$ ; Araguás-Araguás et al. 1998). Employing it, Donahue et al. (1982) found the D/H ratio in the Venusian atmosphere to be  $(1.6 \pm 0.2) \times 10^{-2}$  (i.e., two orders of magnitude higher than VSMOW). This higher ratio is attributed to the evaporation of oceans and the subsequent photodissociation of H<sub>2</sub>O in the upper parts of the

atmosphere (Donahue & Pollack 1983). A comparison of the D/H ratios on Earth and Mars with those determined for various comets indicates the role of this ratio in the volatile accretion on these two planets (Drake & Righter 2002; Hartogh et al. 2011). The two largest gas giants, Jupiter and Saturn, are incapable of nuclear fusion; thus, planetary models predict that the D/H ratio in their atmospheres should be close to the primordial value for the Solar System (Lellouch et al. 2001) or slightly larger due to the accretion of deuterium-rich icy grains and planetesimals (Guillot 1999). The abundance of deuterium is larger by a factor of 2.5 in the atmospheres of Uranus and Neptune (Feuchtergruber et al. 2013), owing to their ice-rich interiors (Guillot 1999). Additionally, the determination of the D/H ratio in comets and moons provides information about the formation of ices in the early Solar System (Hersant et al. 2001; Gautier & Hersant 2005; Horner et al. 2006).

The D/H ratio in planets, moons, or comets can be derived from either in situ mass spectrometry (Eberhardt et al. 1995; Mahaffy et al. 1998; Niemann et al. 2005;

<sup>★</sup> Data are available at the CDS via anonymous ftp to [cdsarc.cds.unistra.fr](https://cdsarc.cds.unistra.fr) (130.79.128.5) or via <https://cdsarc.cds.unistra.fr/viz-bin/cat/J/A+A/687/A69>



Altwegg et al. 2015) or spectroscopic observations of various molecules and their deuterated isotopologs in the millimeter and infrared range (Bockelée-Morvan et al. 1998; Meier et al. 1998; Crovisier et al. 2004; Fletcher et al. 2009; Pierel et al. 2017; Krasnopolsky et al. 2013; Blake et al. 2021). Interestingly, as pointed out by Krasnopolsky et al. (2013), the ratios determined from spectra of different molecules can differ substantially. Moreover, even on Earth, the HDO/H<sub>2</sub>O ratio in the atmosphere can vary substantially across the globe (Araguás-Araguás et al. 1998). In this context, the observation of isotopologs of molecular hydrogen can be a reliable benchmark for determining D/H ratios. The most accurate values of the D/H ratio in gas giants stem from analyses of the pure rotational R(0), R(1), R(2), and R(3) lines of HD and S(0) and S(1) lines in H<sub>2</sub>. Lellouch et al. (2001) determined the D/H ratio in the Jovian atmosphere using the Short Wavelength Spectrometer (SWS) on board the Infrared Space Observatory to be  $(2.25 \pm 0.35) \times 10^{-5}$ . Pierel et al. (2017) analyzed the far-infrared spectra of Saturn's atmosphere gathered by Cassini's Composite Infrared Spectrometer. Interestingly, the Pierel et al. result suggests that the D/H ratio on Saturn is lower than that of Jupiter, which contradicts predictions based on interior models (Guillot 1999; Owen & Encrenaz 2006) and points to an unknown mechanism of deuterium fractionating in Saturn's atmosphere. The D/H ratio in the atmospheres of Uranus and Neptune was determined from measurements of the pure rotational R(0), R(1), and R(2) lines in HD using the Photoconductor Array Camera and Spectrometer (PACS) on board the *Herschel* space observatory (Feuchtgruber et al. 2013). The analysis revealed similar values for these two giants –  $(4.4 \pm 0.4) \times 10^{-5}$  and  $(4.1 \pm 0.4) \times 10^{-5}$ , respectively – confirming the expected deuterium enrichment with respect to the protosolar value.

Atmospheric models of the Solar System's gas giants, from which the relative abundance of HD with respect to H<sub>2</sub> is retrieved (and consequently, the D/H ratio), require knowledge about the line parameters of HD and H<sub>2</sub>. The temperature profiles considered in the models cover seven orders of magnitude of pressure (1  $\mu$ bar–10 bar; see for instance Pierel et al. 2017). Thus, in addition to line position and intensity, knowledge about collisional effects that perturb the shape of observed lines is crucial for the accurate determination of the relative HD abundance. Furthermore, the incorporation of non-Voigt line-shape effects (such as Dicke narrowing and speed-dependent effects) allows for reducing the systematic errors in atmospheric models, as shown for Jupiter (Smith 1989) and for Uranus and Neptune (Baines et al. 1995). Indeed, although the spectral lines of most molecules observed in planetary atmospheres are not sensitive to non-Voigt effects, considering the resolving power of available telescopes, the lines of molecular hydrogen and its isotopologs are (Smith 1989; Baines et al. 1995).

In this article we report accurate collision-induced line-shape parameters for the rotational transitions R(0), R(1), and R(2) within the ground vibrational state. These HD lines are most frequently used for studies of the atmospheres of the giant planets. The results cover all thermodynamic conditions relevant to the atmospheres of giant planets in the Solar System, that is, all relevant temperatures, pressures, and H<sub>2</sub>–He perturbing gas compositions (the HD–H<sub>2</sub> data are provided in this work, while the HD–He data are taken from Stankiewicz et al. 2020, 2021). Besides the basic Voigt-profile collisional parameters (i.e., the broadening and shift parameters), we also report their speed dependences and the complex Dicke parameter, which, as we will show, can influence the effective width and height of the HD lines up to almost a factor of 2 for giant planet conditions.

For the R(0) line, the non-Voigt regime coincides with the maximum of the monochromatic contribution function (see Fig. 1 in Feuchtgruber et al. 2013), which has a direct influence on the abundance of HD inferred from observations.

We performed quantum-scattering calculations on our new, highly accurate ab initio 6D potential energy surface (PES), and we used the scattering S matrices obtained in this way to determine the collision-induced line-shape parameters. We used the cavity ring-down spectroscopy to validate our theoretical methodology, demonstrating a sub-percent-level accuracy that considerably surpasses the accuracy of any previous theoretical (Schaefer & Monchick 1992) or experimental study of line-shape parameters of pure rotational lines in HD (Ulivi et al. 1989; Lu et al. 1993; Sung et al. 2022) and offers valuable input for the HITRAN database (Gordon et al. 2022). This work represents significant methodological and computational progress; calculations at this level of theory and accurate experimental validation have already been performed for a molecule-atom system (3D PES; Słowiński et al. 2020, 2022), but in this work we extend it to a molecule-molecule system (6D PES). All the reported parameters (and their temperature dependences) are consistent with the HITRAN database format, hence allowing for the use of the HITRAN Application Programming Interface (HAPI; Kochanov et al. 2016) for generating the beyond-Voigt spectra of HD for any H<sub>2</sub>–He perturbing gas composition and thermodynamic condition.

## 2. Ab initio calculations of the line-shape parameters

In recent years, the methodology for accurate ab initio calculations of the line-shape parameters (including the beyond-Voigt parameters) was developed and experimentally tested for He-perturbed H<sub>2</sub> and HD rovibrational lines, starting from accurate ab initio H<sub>2</sub>–He PES calculations (Bakr et al. 2013; Thibault et al. 2017), through the state-of-the-art quantum scattering calculations and line-shape parameter determination (Thibault et al. 2017; Józwiak et al. 2018), up to accurate experimental validation (Słowiński et al. 2020, 2022) and using the results for populating the HITRAN database (Weislo et al. 2021; Stankiewicz et al. 2021).

In this work, we extend the entire methodology to a much more complex system of a diatomic molecule colliding with another diatomic molecule. First, we calculated an accurate 6D H<sub>2</sub>–H<sub>2</sub> PES. Second, we performed state-of-the-art quantum-scattering calculations. Third, we calculated the full set of the six line-shape parameters in a wide temperature range. Finally, we report the results in a format consistent with the HITRAN database.

The 6D PES was obtained using the supermolecular approach based on the level of theory similar to that used to calculate the 4D H<sub>2</sub>–H<sub>2</sub> surface (Patkowski et al. 2008). The crucial contributions involve: (1) interaction energy calculated at the Hartree–Fock (HF) level, (2) the correlation contribution to the interaction energy calculated using the coupled-cluster method with up to perturbative triple excitations, CCSD(T), with the results extrapolated to the complete basis set limit (Halkier et al. 1999), (3) electron correlation effects beyond CCSD(T) up to full configuration interaction (FCI), and (4) the diagonal Born–Oppenheimer correction (DBOC; Handy et al. 1986). The details regarding the basis sets used in calculations of each contribution and the analytical fit to the interaction energies are given in

Appendix A. The PES is expected to be valid for intramolecular distances  $r_i \in [0.85, 2.25] a_0$ .

For the purpose of performing quantum scattering calculations, the 6D PES was expanded over a set of appropriate angular functions and the resulting 3D numerical function in radial coordinates was then expanded in terms of rovibrational wave functions of isolated molecules (see Appendix B for details). The close-coupling equations were solved in the body-fixed frame using a renormalized Numerov's algorithm, for the total number of 3 014 energies ( $E_T = E_{\text{kin}} + E_{v_1 j_1} + E_{v_2 j_2}$ , where  $E_{\text{kin}}$  is the relative kinetic energy of the colliding pair, and  $E_{v_1 j_1}$  and  $E_{v_2 j_2}$  are the rovibrational energies of the two molecules at large separations) in a range from  $10^{-3} \text{ cm}^{-1}$  to  $4000 \text{ cm}^{-1}$ . Calculations were performed using the quantum scattering code from the BIGOS package developed in our group (Jóźwiak et al. 2024; Jóźwiak 2024). The scattering S matrix elements were obtained from boundary conditions imposed on the radial scattering function. Convergence of the calculated S matrix elements was ensured by a proper choice of the integration range, propagator step, and the size of the rovibrational basis (see Appendix C for details).

Next, we calculated the generalized spectroscopic cross-sections,  $\sigma_\lambda^q$  (Monchick & Hunter 1986; Schaefer & Monchick 1992), which describe how collisions perturb the shape of molecular resonance. Contrary to the state-to-state cross-sections, which give the rate coefficients (see, for instance, Wan et al. 2019), the  $\sigma_\lambda^q$  cross-sections are complex. For  $\lambda = 0$ , real and imaginary parts of this cross-section correspond to the pressure broadening and shift cross-section, respectively. For  $\lambda = 1$ , the complex cross-section describes the collisional perturbation of the translational motion and is crucial for the proper description of the Dicke effect. The index  $q$  is the tensor rank of the spectral transition operator and equals 1 for electric dipole lines considered here.

We used the  $\sigma_0^1$  and  $\sigma_1^1$  cross-sections to calculate the six line-shape parameters relevant to collision-perturbed HD spectra, the collisional broadening, and the shift,

$$\gamma_0 - i\delta_0 = \frac{1}{2\pi c} \frac{1}{k_B T} \langle v_r \rangle \int_0^\infty x e^{-x} \sigma_0^1(x) dx, \quad (1)$$

the speed dependences of collisional broadening and shift,

$$\begin{aligned} \gamma_2 - i\delta_2 &= \frac{1}{2\pi c} \frac{1}{k_B T} \frac{\langle v_r \rangle \sqrt{M_a}}{2} e^{-y^2} \\ &\times \int_0^\infty \left( 2\bar{x} \cosh(2\bar{x}y) - \left( \frac{1}{y} + 2y \right) \sinh(2\bar{x}y) \right) \bar{x}^2 e^{-\bar{x}^2} \sigma_0^1(\bar{x} \bar{v}_p) d\bar{x}, \end{aligned} \quad (2)$$

and the real and imaginary parts of the complex Dicke parameter,

$$\tilde{\gamma}_{\text{opt}}^r - i\tilde{\gamma}_{\text{opt}}^i = \frac{1}{2\pi c} \frac{\langle v_r \rangle M_a}{k_B T} \int_0^\infty x e^{-x} \left[ \frac{2}{3} x \sigma_1^1(x k_B T) - \sigma_0^1(x k_B T) \right] dx, \quad (3)$$

where  $v_r$  is the relative (absorber to perturber) speed of the colliding molecules,  $\langle v_r \rangle$  is its mean value at temperature  $T$ ,  $\bar{v}_p$  is the most probable speed of the perturbed distribution,  $M_a = \frac{m_a}{m_a + m_p}$ ,

$x = \frac{E_{\text{kin}}}{k_B T}$ ,  $\bar{x} = \frac{2v_r}{\sqrt{\pi M_a \langle v_r \rangle}}$ ,  $y = \sqrt{\frac{m_p}{m_a}}$  and  $m_a$  and  $m_p$  are the masses of the active and perturbing molecules, respectively (Wcisło et al. 2021). We estimate the uncertainty of the calculated line-shape parameters in Appendix C. The six line-shape parameters define the modified Hartmann–Tran (mHT) profile (see

Appendix D), which encapsulates the relevant beyond-Voigt effects. To make the outcome of this work consistent with the HITRAN database (Gordon et al. 2022), we provide temperature dependences of the calculated line-shape parameters within the double-power-law (DPL) format (Gamache & Vispoel 2018; Stolarczyk et al. 2020):

$$\begin{aligned} \gamma_0(T) &= g_0(T_{\text{ref}}/T)^n + g'_0(T_{\text{ref}}/T)^{n'}, \\ \delta_0(T) &= d_0(T_{\text{ref}}/T)^m + d'_0(T_{\text{ref}}/T)^{m'}, \\ \gamma_2(T) &= g_2(T_{\text{ref}}/T)^j + g'_2(T_{\text{ref}}/T)^{j'}, \\ \delta_2(T) &= d_2(T_{\text{ref}}/T)^k + d'_2(T_{\text{ref}}/T)^{k'}, \\ \tilde{\gamma}_{\text{opt}}^r(T) &= r(T_{\text{ref}}/T)^p + r'(T_{\text{ref}}/T)^{p'}, \\ \tilde{\gamma}_{\text{opt}}^i(T) &= i(T_{\text{ref}}/T)^q + i'(T_{\text{ref}}/T)^{q'}, \end{aligned} \quad (4)$$

where  $T_{\text{ref}} = 296 \text{ K}$ .

### 3. Results: Line-shape parameters for the R(0), R(1), and R(2) lines in HD perturbed by a mixture of H<sub>2</sub> and He

In Fig. 1, we show the main result of this work: all six line-shape parameters for the R(0), R(1), and R(2) 0–0 lines in H<sub>2</sub>-perturbed HD calculated as a function of temperature. Figure 1 covers the temperature range relevant for the giant planets, 50 to 200 K (Lellouch et al. 2001; Feuchtgruber et al. 2013; Pierel et al. 2017; for our full temperature range, 20 to 1000 K, see the data available at CDS). In Fig. 1, we also recall the corresponding He-perturbed data calculated with the same methodology at the same accuracy level (Stankiewicz et al. 2021). The difference between the two perturbors is not negligible, and for many cases the line-shape parameters differ by a factor of 2 or even more.

The data shown in Fig. 1 are given in Table 1 in a numerical form within the HITRAN DPL format (see Eq. (4)). The accuracy of our ab initio line-shape parameters is within 1% of the magnitude of each parameter (see Appendix C for details). The DPL approximation of the temperature dependences introduces additional errors. For  $\gamma_0(T)$  and  $\tilde{\gamma}_{\text{opt}}^r(T)$ , the DPL error is negligible, for  $\delta_0(T)$  the DPL error is at the 1 % level, and for other line-shape parameters it can be even higher, but their impact on the final line profile is much smaller (see Appendix E for details). For applications that require the full accuracy of our ab initio line-shape parameters, we provide the line-shape parameter values explicitly on a dense temperature grid in the data available at CDS.

The set of parameters in Table 1 contains all the information necessary to simulate the collision-perturbed shapes of the three HD lines at a high level of accuracy at any conditions relevant to the atmospheres of giant planets (pressure, temperature, and He/H<sub>2</sub> relative concentration). In Fig. 2, we show an example of simulated spectra based on the data from Table 1. It should be emphasized that at the conditions relevant to giant planets, the shapes of the HD lines may considerably deviate from the simple Voigt profile. In Fig. 2a, we show the difference between the Voigt profile and a more physical profile, which includes the relevant beyond-Voigt effects such as Dicke narrowing and the dependence on the speed of the broadening and shift (the mHT profile; see Appendix D). For the moderate pressures, the error introduced by the Voigt-profile approximation can reach almost 70%. The orange, yellow, red, and black lines in Fig. 2a are the temperature-pressure profiles for Jupiter (Seiff et al. 1998), Saturn (Lindal et al. 1985), Uranus (Lindal et al. 1987), and

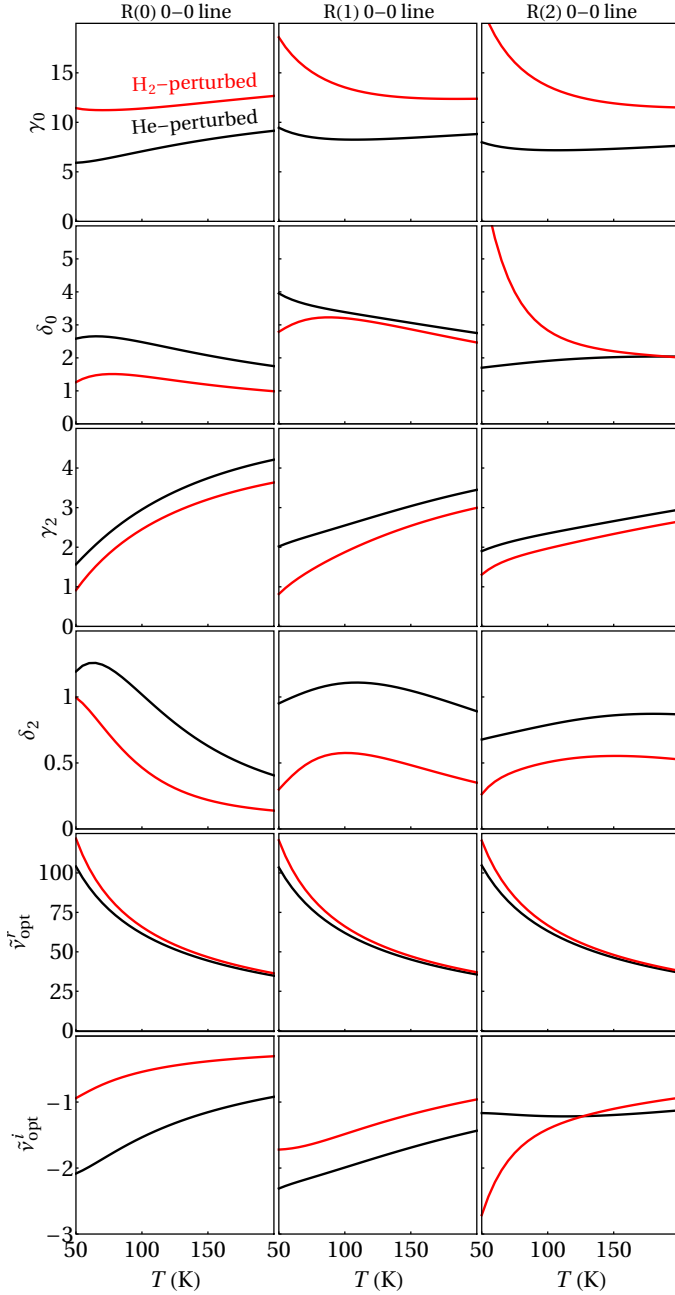


**Fig. 1.** Ab initio temperature dependences of the collisional line-shape parameters (in units of  $10^{-3} \text{ cm}^{-1} \text{ atm}^{-1}$ ) of the first three electric dipole lines of HD perturbed by  $\text{H}_2$  (red curves) and He (black curves).

Neptune (Lindal et al. 1990), respectively. We illustrate this with spectra simulations for the case of Neptune’s atmosphere (panels b–d corresponds to the black dots in Fig. 2a). Panels b–d illustrate three different regimes. Panel b is the low-pressure regime with a small collisional contribution in which the line shape collapses to Gaussian, and hence the beyond-Voigt effects are small. Panel d is the opposite: the shape of a resonance is dominated by the collisional effects, but the simple Lorentzian broadening dominates over other collisional effects and again the beyond-Voigt effects are small. Panel c illustrates the nontrivial situation in which the shape of resonance is dominated by the beyond-Voigt effects (see the green horizontal ridges in Fig. 2a). The discrepancies between the beyond-Voigt line-shape model and the Voigt profile are also clearly seen as a difference between

the blue lines and blue shadows in panel c. In the context of the giant planet studies, it should be noted that the beyond-Voigt regions marked in panel a (the green horizontal ridges) coincide well with the maxima of the monochromatic contribution functions for these three HD lines (see Fig. 1 in Feuchtgruber et al. 2013 for the case of the atmospheres of Neptune and Uranus).

Panels b–d of Fig. 2 also illustrate the influence of atmosphere composition on the collision-induced shapes of the HD lines for the example of Neptune atmosphere. The differences between the He- and  $\text{H}_2$ -perturbers are negligible in the low-pressure regime (panel b) since at these conditions the line shape is mainly determined by thermal Doppler broadening. In moderate- and high-pressure ranges (panels c and d), the profiles differ at the peak by a factor of 2. Hence, including both perturbing species is important for spectra analyses of the atmospheres of giant planets, especially for the R(0) line, whose contribution function dominates at moderate and high pressures (Feuchtgruber et al. 2013).

The data reported in this article (see Table 1) account for three factors that are necessary for reaching sub-percent-level accuracy: (1) separate ab initio data for both perturbers (which allows one to simulate perturbation by any  $\text{H}_2$ –He mixture), (2) accurate representation of temperature dependences, and (3) parametrization of the beyond-Voigt line-shape effects. In general, simulating the beyond-Voigt line-shape profiles is a complex task (see Appendix D). In this work, we used HAPI (Kochanov et al. 2016) to generate the beyond-Voigt spectra shown in Fig. 2 (based on the DPL parameters from Table 1):

```
from hapi import *
db_begin('hitran_data')
nu,coef = absorptionCoefficient_mHT(
    SourceTables='HD',
    Diluent={'He':0.2,'H2':0.8},
    WavenumberRange=[xmin,xmax],
    WavenumberStep=step,
    Environment={'p':press,'T':temp},
    HITRAN_units=True)
```

The combination of the data reported in Table 1 and the Python-based HAPI constitutes a powerful tool that allows one to efficiently generate accurate HD spectra (based on advanced beyond-Voigt model, the mHT profile) for arbitrary temperature, pressure, and mixture composition.

At low temperatures, relevant for studies of giant planet atmospheres and the chemistry and dynamics of the interstellar medium and protoplanetary disks, the spin isomer (para/ortho) concentration ratio of  $\text{H}_2$  at thermal equilibrium (eq- $\text{H}_2$ ) deviates from 1:3 (the ratio of so-called normal  $\text{H}_2$ , n- $\text{H}_2$ ). Moreover, various processes, such as diffusion between atmospheric layers in gas giants, might result in the sub-equilibrium distribution of  $\text{H}_2$ . These nontrivial para/ortho distributions play a key role in atmospheric models that involve collision-induced absorption (Karman et al. 2019) and spectral features originating from hydrogen dimers (Fletcher et al. 2018), as well as in isotope chemistry of the interstellar medium, where para/ortho ratio controls the deuterium fractionation process (Flower et al. 2006; Nomura et al. 2022). In Fig. 3, we show the influence of the spin isomer concentration on the line-shape parameters. Spin isomer concentration has a large impact at low temperatures. All the line-shape parameters reported in this work are calculated for the thermal equilibrium spin isomer concentration.



**Table 1.** DPL parameterization of the temperature dependences of the line-shape parameters of HD perturbed by He and H<sub>2</sub>.

He-perturbed HD				
R(0) 0–0 line				
$\gamma_0(T)$	$g_0 = 218.905$	$g'_0 = -209.398$	$n = 0.0929083$	$n' = 0.105086$
$\delta_0(T)$	$d_0 = 76.1358$	$d'_0 = -74.6225$	$m = -0.102987$	$m' = -0.116673$
$\gamma_2(T)$	$g_2 = 210.682$	$g'_2 = -206.11$	$j = -0.862904$	$j' = -0.876244$
$\delta_2(T)$	$d_2 = 7.77569$	$d'_2 = -7.45369$	$k = 1.43509$	$k' = 1.45106$
$\tilde{\nu}_{\text{opt}}^r(T)$	$r = 157.867$	$r' = -132.815$	$p = 0.569778$	$p' = 0.512484$
$\tilde{\nu}_{\text{opt}}^i(T)$	$i = -0.0148171$	$i' = -0.732168$	$q = 0.589866$	$q' = 0.589866$
R(1) 0–0 line				
$\gamma_0(T)$	$g_0 = 8.98598$	$g'_0 = 0.07062$	$n = -0.116463$	$n' = 1.83834$
$\delta_0(T)$	$d_0 = 3.27647$	$d'_0 = -0.997538$	$m = 0.171067$	$m' = -0.548127$
$\gamma_2(T)$	$g_2 = 5.47783$	$g'_2 = -1.63047$	$j = -0.540645$	$j' = -1.19601$
$\delta_2(T)$	$d_2 = 64.7968$	$d'_2 = -64.0672$	$k = -0.314427$	$k' = -0.325103$
$\tilde{\nu}_{\text{opt}}^r(T)$	$r = 39.7564$	$r' = -13.9988$	$p = 0.652375$	$p' = 0.276761$
$\tilde{\nu}_{\text{opt}}^i(T)$	$i = -0.0600157$	$i' = -1.04666$	$q = 0.478987$	$q' = 0.478987$
R(2) 0–0 line				
$\gamma_0(T)$	$g_0 = 7.91606$	$g'_0 = 0.106818$	$n = -0.158512$	$n' = 1.59926$
$\delta_0(T)$	$d_0 = 60.8755$	$d'_0 = -59.1362$	$m = -0.560989$	$m' = 0.57118$
$\gamma_2(T)$	$g_2 = 3.44668$	$g'_2 = -0.0918827$	$j = -0.351514$	$j' = -2.42064$
$\delta_2(T)$	$d_2 = 48.9743$	$d'_2 = -48.2166$	$k = -0.522538$	$k' = -0.53522$
$\tilde{\nu}_{\text{opt}}^r(T)$	$r = 33.4337$	$r' = -6.77194$	$p = 0.682741$	$p' = 0.0477307$
$\tilde{\nu}_{\text{opt}}^i(T)$	$i = -0.160883$	$i' = -0.705905$	$q = 0.278356$	$q' = 0.278356$
H <sub>2</sub> -perturbed HD				
R(0) 0–0 line				
$\gamma_0(T)$	$g_0 = 13.1538$	$g'_0 = -0.0209275$	$n = -0.102409$	$n' = -4.47666$
$\delta_0(T)$	$d_0 = 21.8124$	$d'_0 = -21.0255$	$m = 1.06916$	$m' = 1.08444$
$\gamma_2(T)$	$g_2 = 215.242$	$g'_2 = -211.197$	$j = -1.0114$	$j' = -1.02533$
$\delta_2(T)$	$d_2 = 17.5611$	$d'_2 = -17.4505$	$k = 0.41528$	$k' = 0.405624$
$\tilde{\nu}_{\text{opt}}^r(T)$	$r = 25.0013$	$r' = 0.0005783$	$p = 0.889907$	$p' = 4.16595$
$\tilde{\nu}_{\text{opt}}^i(T)$	$i = -0.0049349$	$i' = -0.257607$	$q = 0.64352$	$q' = 0.64352$
R(1) 0–0 line				
$\gamma_0(T)$	$g_0 = 11.5582$	$g'_0 = 0.165258$	$n = 0.0781601$	$n' = 1.89474$
$\delta_0(T)$	$d_0 = 133.353$	$d'_0 = -131.231$	$m = -0.244838$	$m' = -0.257492$
$\gamma_2(T)$	$g_2 = 131.359$	$g'_2 = -128.602$	$j = 0.484966$	$j' = 0.495567$
$\delta_2(T)$	$d_2 = 35.3179$	$d'_2 = -35.0081$	$k = -0.330198$	$k' = -0.33988$
$\tilde{\nu}_{\text{opt}}^r(T)$	$r = 12.373$	$r' = 12.3606$	$p = 1.02771$	$p' = 0.755534$
$\tilde{\nu}_{\text{opt}}^i(T)$	$i = -0.307423$	$i' = -0.307142$	$q = 0.656905$	$q' = 0.656905$
R(2) 0–0 line				
$\gamma_0(T)$	$g_0 = 5.05367$	$g'_0 = 5.04862$	$n = 0.767269$	$n' = -0.528791$
$\delta_0(T)$	$d_0 = 1.10007$	$d'_0 = 0.346535$	$m = 0.0896926$	$m' = 1.57482$
$\gamma_2(T)$	$g_2 = 4.9771$	$g'_2 = -1.86783$	$j = -0.69627$	$j' = -1.38558$
$\delta_2(T)$	$d_2 = 63.3239$	$d'_2 = -62.865$	$k = -0.627633$	$k' = -0.634526$
$\tilde{\nu}_{\text{opt}}^r(T)$	$r = 26.3022$	$r' = 0.0004301$	$p = 0.856557$	$p' = 4.29539$
$\tilde{\nu}_{\text{opt}}^i(T)$	$i = -0.208711$	$i' = -0.208511$	$q = 1.07071$	$q' = 1.07071$

**Notes.** Coefficients 1 and 2 are in  $10^{-3} \text{ cm}^{-1} \text{ atm}^{-1}$ . Exponents 1 and 2 are dimensionless.

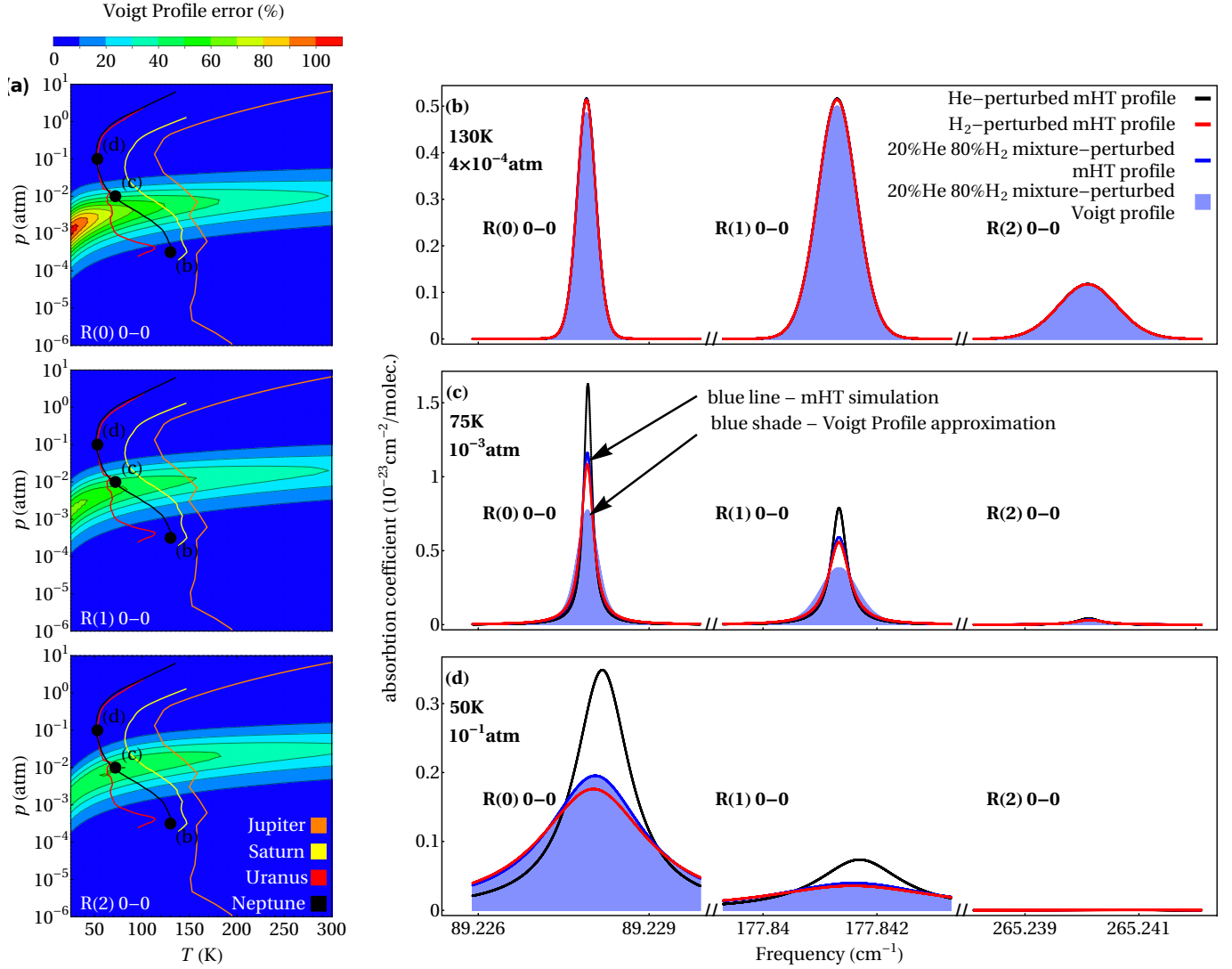


**Fig. 2.** Impact of the beyond-Voigt effects and bath mixture composition on collision-perturbed spectra of HD at conditions relevant for giant planet atmospheres. Panel a: relative error of the Voigt-profile approximation as a function of pressure and temperature, shown as the relative difference between the Voigt and mHT profiles at profile maximum. The panels show, from top to bottom, the R(0), R(1), and R(2) lines. Panels b–d: simulations of the HD spectra (blue lines) at conditions relevant for the Neptune atmosphere (the perturbing bath is 80% H<sub>2</sub> and 20% He). The spectra are generated with the mHT profile using HAPI based on the DPL temperature parametrization. As a reference, we show the same lines for the cases of pure H<sub>2</sub> and pure He perturbers (see the red and black lines, respectively). The blue shadows show the same simulations as the blue lines but generated with the simple Voigt profile. Panels b–d correspond to points b–d shown in the temperature–pressure maps in panel a (the three selected points lie on the Neptune temperature–pressure line). The three cases illustrate three different line-shape regimes. The first one, (b), is the low-pressure case in which the lines are broadened mainly by the Doppler effect, and the pressure-induced collisional effects do not dominate the line shapes. The intermediate-pressure case, panel c, illustrates the extreme non-Voigt regime (the differences between the blue curves and blue shadows reach almost a factor of 2; see also the green ridge in the maps in the bottom panel). The third case, panel d, illustrates the high-pressure regime at which the HD lines are well described by a simple Voigt profile (the blue shadows almost overlap with the blue lines), but setting a proper composition of the perturber gas components plays an important role.

#### 4. Experimental validation

In Fig. 4, we show a comparison between our ab initio calculations (black lines) and the experimental data available in the literature. Fourier-transformed scans from the Michelson interferometer were used to obtain the high-pressure spectra reported in the works of Ulivi et al. (1989) and Lu et al. (1993); the spectra were collected in a temperature range from 77 to 296 K. Recently, the same lines were measured at low pressures (<1 bar) with the Fourier transform spectrometer coupled to the Soleil-synchrotron far-infrared source (Sung et al. 2022) in a temperature range from 98 to 296 K (see the olive lines in

Fig. 4). The discrepancy between these experimental data is by far too large to test our theoretical results at the one percent level.

To validate our ab initio calculations at the estimated accuracy level, we performed accurate measurements using a frequency-stabilized cavity ring-down spectrometer linked to an optical frequency comb, referenced to a primary frequency standard (Cygan et al. (2016, 2019); Zaborowski et al. (2020)). Our 73.5-cm-long ultrahigh finesse ( $\mathcal{F} = 637\,000$ ) optical cavity operates in the frequency-agile rapid scanning spectroscopy mode (Truong et al. 2013; Cygan et al. 2016, 2019; see Zaborowski et al. 2020 for details regarding the experimental setup). Since our spectrometer operates at 1.6  $\mu\text{m}$ , we chose

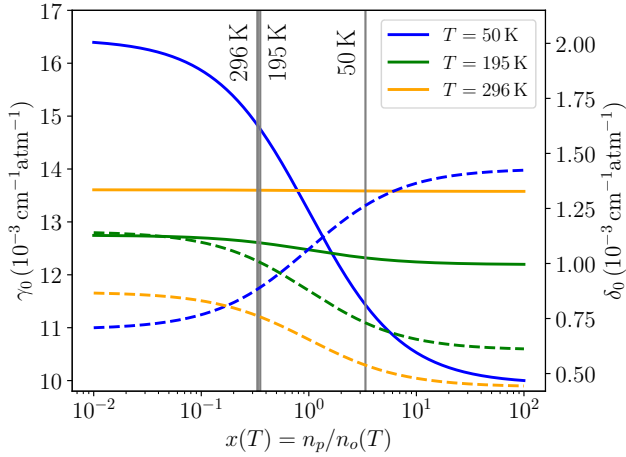


**Fig. 3.** Dependence of pressure broadening,  $\gamma_0$  (solid lines), and shift,  $\delta_0$  (dashed lines), on the spin isomer concentration ratio ( $x = n_p/n_o$ ) for the  $\text{H}_2$ -perturbed R(0) line in HD at different temperatures. The vertical gray lines correspond to the value of  $x$  for normal  $\text{H}_2$ ,  $x = 1/3$ , and  $x_{eq}(T)$ , as determined by the Boltzmann distribution at  $T = 50$ , 195, and 296 K.

the S(2) 2–0 line in the  $\text{H}_2$ -perturbed  $\text{D}_2$  (we repeated all the ab initio calculations for this case). From the perspective of theoretical methodology, the  $\text{H}_2$ -perturbed  $\text{D}_2$  and  $\text{H}_2$ -perturbed HD are equivalent and either can be used for validating the theoretical methodology (for both cases two distinguishable diatomic molecules are considered and the PES is the same except for the almost negligible DBOC term; see Appendix A). We used a sample of 2%  $\text{D}_2$  and 98% of  $\text{H}_2$  mixture and collected the spectra at four pressures (0.5, 1, 1.5, and 2 atm) and two temperatures (296 and 330 K; see the black dots in Fig. 5). The corresponding theoretical spectra are the red curves. The methodology for simulating the collision-perturbed shapes of molecular lines (based on the line-shape parameters calculated from Eqs. (1)–(3)) is described in our previous works (Wcisło et al. 2018; Słowiński et al. 2020, 2022). The two sets of residuals depicted in Fig. 5 show comparisons with two line-shape models, the speed-dependent billiard-ball (SDBB) profile and the mHT profile. The SDBB profile (Shapiro et al. 2002; Ciuryło et al. 2002) is the state-of-the-art approach that gives the most realistic description of the underlying collisional processes. As expected it gives the best agreement with experimental spectra (the mean residuals are 0.65%; see Fig. 5), but it is computationally very expensive (Wcisło et al. 2013). The mHT profile is slightly less accurate (the mean residuals are 1.23%) but it is highly efficient from a computational perspective and, hence, well suited for practical spectroscopic applications. In conclusion, the ab initio line-shape parameters reported in this work (Fig. 1 and Table 1) lead to profiles that are in excellent agreement with accurate experimental spectra, and the theory-experiment comparison is limited by a choice of a line-shape model used to simulate the experimental spectra.

## 5. Conclusion

We have computed accurate collision-induced line-shape parameters for the three pure rotational HD lines (R(0), R(1), and

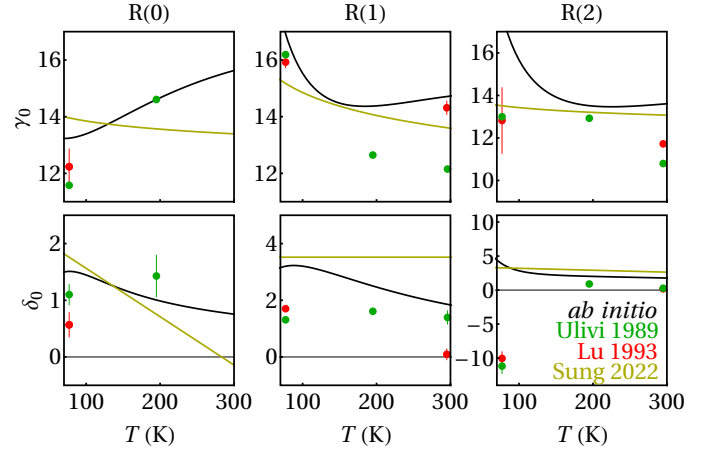


**Fig. 4.** Comparison of the experimental and theoretical values of the pressure broadening and shift parameters,  $\gamma_0$  and  $\delta_0$  (in units of  $10^{-3} \text{ cm}^{-1} \text{ atm}^{-1}$ ). Black curves correspond to the ab initio calculations performed in this work, while green and red points report the experimental measurements from Ulivi et al. (1989) and Lu et al. (1993), respectively. The olive curves are the single-power-law (for  $\gamma_0$ ) and linear (for  $\delta_0$ ) temperature dependences retrieved from the measurements of Sung et al. (2022).

R(2)) that are currently employed for the analysis of the giant planets' atmospheres. To this end, we investigated HD– $\text{H}_2$  collisions using coupled channel quantum scattering calculations on a new, highly accurate ab initio PES. Scattering S matrices determined from these calculations allowed us to obtain the collisional width and shift, as well as their speed dependences and the complex Dicke parameter of  $\text{H}_2$ -perturbed HD lines. By integrating data from our previous work on the HD–He system (Stankiewicz et al. 2020, 2021), we provide comprehensive results that cover a wide range of thermodynamic conditions, including temperature, pressure, and  $\text{H}_2$ –He concentration, relevant to the atmospheres of giant planets. We validated our theoretical methodology using cavity ring-down spectroscopy, demonstrating a sub-percent-level accuracy that surpasses the accuracy of previous theoretical and experimental studies of line-shape parameters in HD.

All the reported line-shape parameters and their temperature dependences are consistent with the HITRAN database format. Utilizing HAPI, we demonstrated how our results can be applied to simulate HD spectra under various conditions pertinent to giant planets in the Solar System.

Until now, the analysis of observed collision-perturbed spectra in astrophysical studies has predominantly relied on the simple Voigt profile. We have introduced a methodology and provided a comprehensive dataset that enables the simulation of beyond-Voigt shapes for HD in  $\text{H}_2$ –He atmospheres. Our work demonstrates that accounting for the speed dependence of collisional width and shift, along with the complex Dicke parameter, is crucial. These factors can alter the effective width and height of HD lines by up to a factor of 2. To quantitatively assess the impact of these results on the D/H ratio on giant planets, radiative transfer modeling is necessary. Given that the beyond-Voigt effects result in a narrower line width (Fig. 2c), the previously inferred HD abundance from astrophysical observations may be underestimated.

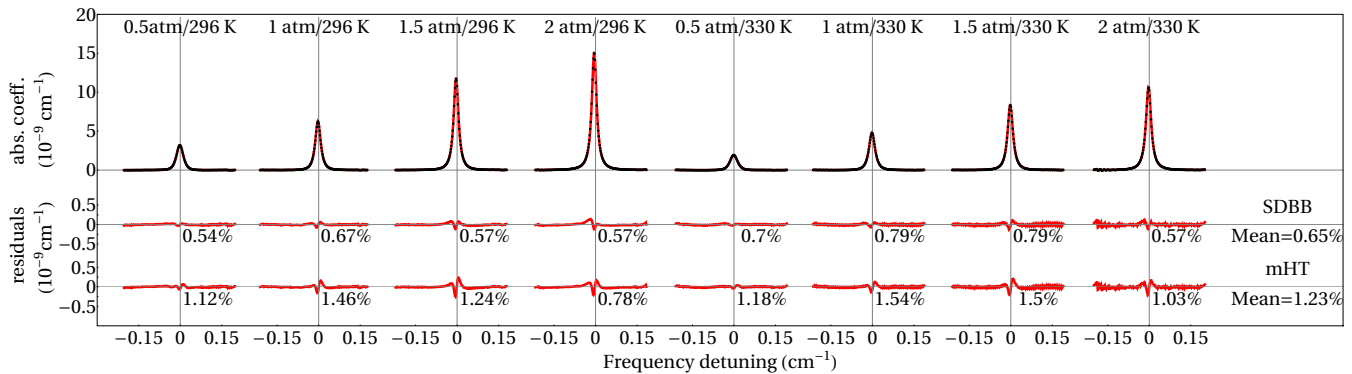


**Fig. 5.** Direct validation of the ab initio quantum-scattering calculations on the accurate experimental spectra of the S(2) 2–0 line of D<sub>2</sub> perturbed by collisions with H<sub>2</sub> molecules (see the main text for details). The black dots are the experimental spectra, and the red lines are the ab initio profiles. Below each profile, we show the absolute residuals of two models: the SDBB profile and the mHT profile. To quantify how well theory agrees with experiments, we report the relative (with respect to the profile peak value) root mean square errors (rRMSEs) of the experiment-theory differences calculated within the  $\pm$ FWHM range around the line center (see the percentages below the residuals). The mean rRMSEs are also summarized for each of the models (see the numbers on the right side of the figure).

**Acknowledgements.** H.J. and N.S. were supported by the National Science Centre in Poland through Project No. 2019/35/B/ST2/01118. H.J. was supported by the Foundation for Polish Science (FNP). K.S. contribution is supported by budgetary funds within the Minister of Education and Science program “Perły Nauki”, Project No. PN/01/0196/2022. D.L. was supported by the National Science Centre in Poland through Project No. 2020/39/B/ST2/00719. S.W. was supported by the National Science Centre in Poland through Project No. 2021/42/E/ST2/00152. P.J. was supported by the National Science Centre in Poland through Project No. 2017/25/B/ST4/01300. K.P. was supported by the U.S. National Science Foundation award CHE-1955328. K.Sz. was supported by the US NSF award CHE-2313826. I.E.G.’s contribution was supported through NASA grant 80NSSC24K0080. P.W. was supported by the National Science Centre in Poland through Project No. 2022/46/E/ST2/00282. For the purpose of Open Access, the author has applied a CC-BY public copyright licence to any Author Accepted Manuscript (AAM) version arising from this submission. We gratefully acknowledge Polish high-performance computing infrastructure PLGrid (HPC Centers: ACK Cyfronet AGH, CI TASK) for providing computer facilities and support within the computational grant, Grant No. PLG/2023/016409. Calculations have been carried out using resources provided by the Wrocław Centre for Networking and Supercomputing (<http://wcss.pl>), Grant No. 546. The research is a part of the program of the National Laboratory FAMO in Toruń, Poland.

## References

- Altwegg, K., Balsiger, H., Bar-Nun, A., et al. 2015, *Science*, **347**, 1261952
- Araguás-Araguás, L., Froehlich, K., & Rozanski, K. 1998, *J. Geophys. Res. Atmos.*, **103**, 28721
- Babin, V., Leforestier, C., & Paesani, F. 2013, *J. Chem. Theory Comput.*, **9**, 5395
- Baines, K. H., Mickelson, M. E., Larson, L. E., & Ferguson, D. W. 1995, *Icarus*, **114**, 328
- Bakr, B. W., Smith, D. G. A., & Patkowski, K. 2013, *J. Chem. Phys.*, **139**, 144305
- Blake, J. S. D., Fletcher, L. N., Greathouse, T. K., et al. 2021, *A&A*, **653**, A66
- Bockelée-Morvan, D., Gautier, D., Lis, D., et al. 1998, *Icarus*, **133**, 147
- Braams, B. J., & Bowman, J. M. 2009, *Intern. Rev. Phys. Chem.*, **28**, 577
- Ciuryło, R., Shapiro, D. A., Drummond, J. R., & May, A. D. 2002, *Phys. Rev. A*, **65**, 012502
- Crovisier, J., Bockelée-Morvan, D., Colom, P., et al. 2004, *A&A*, **418**, 1141
- Cygan, A., Wójtewicz, S., Kowzan, G., et al. 2016, *J. Chem. Phys.*, **144**, 214202
- Cygan, A., Wcisło, P., Wójtewicz, S., et al. 2019, *Opt. Express*, **27**, 21810
- Donahue, T. M., & Pollack, J. B. 1983, in *Venus* (University of Arizona Press), 1003
- Donahue, T. M., Hoffman, J. H., Hodges, R. R., & Watson, A. J. 1982, *Science*, **216**, 630
- Drake, M. J., & Righter, K. 2002, *Nature*, **416**, 39
- Dubernet, M.-L., & Tuckey, P. 1999, *Chem. Phys. Lett.*, **300**, 275
- Eberhardt, P., Reber, M., Krankowsky, D., & Hodges, R. 1995, *A&A*, **302**, 301
- Fernández, B., Koch, H., & Makarewicz, J. 1999, *J. Chem. Phys.*, **110**, 8525
- Feuchtgruber, H., Lellouch, E., Orton, G., et al. 2013, *A&A*, **551**, A126
- Fletcher, L., Orton, G., Teanby, N., Irwin, P., & Bjoraker, G. 2009, *Icarus*, **199**, 351
- Fletcher, L. N., Gustafsson, M., & Orton, G. S. 2018, *ApJS*, **235**, 24
- Flower, D., Pineau des Forêts, G., & Walmsley, C. 2006, *A&A*, **449**, 621
- Gamache, R. R., & Vispoel, B. 2018, *JQSRT*, **217**, 440
- Gancewski, M., Józwiak, H., Quintas-Sánchez, E., et al. 2021, *J. Chem. Phys.*, **155**, 124307
- Gauss, J., A.Tajti, Kállay, M., & Szalay, J. F. S. P. G. 2006, *J. Chem. Phys.*, **125**, 144111
- Gautier, D., & Hersant, F. 2005, *SSR*, **116**, 25
- Gordon, I., Rothman, L., Hargreaves, R., et al. 2022, *JQSRT*, **277**, 107949
- Green, S., Blackmore, R., & Monchick, L. 1989, *J. Chem. Phys.*, **91**, 52
- Guillot, T. 1999, *P&SS*, **47**, 1183
- Halkier, A., Klopper, W., Helgaker, T., Jørgensen, P., & Taylor, P. R. 1999, *J. Chem. Phys.*, **111**, 9157
- Handy, N. C., Yamaguchi, Y., & Schaefer III, H. F. 1986, *J. Chem. Phys.*, **84**, 4481
- Hartogh, P., Lis, D. C., Bockelée-Morvan, D., et al. 2011, *Nature*, **478**, 218
- Hersant, F., Gautier, D., & Hure, J.-M. 2001, *ApJ*, **554**, 391
- Hornor, J., Mousis, O., & Hersant, F. 2006, *Earth Moon Planets*, **100**, 43
- Józwiak, H. 2024, <https://doi.org/10.5281/zenodo.10776727>
- Józwiak, H., Thibault, F., Stolarczyk, N., & Wcisło, P. 2018, *JQSRT*, **219**, 313
- Józwiak, H., Thibault, F., Cybulski, H., & Wcisło, P. 2021, *J. Chem. Phys.*, **154**, 054314
- Józwiak, H., Thibault, F., Viel, A., Wcisło, P., & Lique, F. 2024, *A&A*, **685**, A113
- Karman, T., Gordon, I. E., van der Avoird, A., et al. 2019, *Icarus*, **328**, 160
- Kendall, R. A., Dunning, Jr., T. H., & Harrison, R. J. 1992, *J. Chem. Phys.*, **96**, 6796
- Kochanov, R., Gordon, I., Rothman, L., et al. 2016, *JQSRT*, **177**, 15
- Konefał, M., Słowiński, M., Zaborowski, M., et al. 2020, *JQSRT*, **242**, 106784
- Krasnopolsky, V., Belyaev, D., Gordon, I., Li, G., & Rothman, L. 2013, *Icarus*, **224**, 57
- Lellouch, E., Bézard, B., Fouchet, T., et al. 2001, *A&A*, **370**, 610
- Lindal, G. F., Sweetnam, D. N., & Eshleman, V. R. 1985, *AJ*, **90**, 1136
- Lindal, G. F., Lyons, J. R., Sweetnam, D. N., et al. 1987, *J. Geophys. Res. Space Phys.*, **92**, 14987
- Lindal, G. F., Lyons, J. R., Sweetnam, D. N., et al. 1990, *Geophys. Res. Lett.*, **17**, 1733
- Lu, Z., Tabisz, G. C., & Ulivi, L. 1993, *Phys. Rev. A*, **47**, 1159
- Mahaffy, P. R., Donahue, T. M., Atreya, S. K., Owen, T. C., & Niemann, H. B. 1998, *SSR*, **251**
- Meier, R., Owen, T. C., Matthews, H. E., et al. 1998, *Science*, **279**, 842
- Monchick, L., & Hunter, L. W. 1986, *J. Chem. Phys.*, **85**, 713
- Niemann, H., Atreya, S., Bauer, S., et al. 2005, *Nature*, **438**, 779
- Nomura, H., Furuya, K., Cordiner, M., et al. 2022, arXiv preprint [arXiv:2203.10863]
- Owen, T., & Encrenaz, T. 2006, *P&SS*, **54**, 1188
- Patkowski, K., Cencek, W., Jankowski, P., et al. 2008, *J. Chem. Phys.*, **129**, 094304

- Pettini, M., Zych, B. J., Murphy, M. T., Lewis, A., & Steidel, C. C. 2008, [MNRAS](#), **391**, 1499
- Pierel, J. D. R., Nixon, C. A., Lellouch, E., et al. 2017, [ApJ](#), **154**, 178
- Schaefer, J., & Monchick, L. 1992, [A&A](#), **265**, 859
- Schwenke, D. W. 1988, [J. Chem. Phys.](#), **89**, 2076
- Seiff, A., Kirk, D. B., Knight, T. C. D., et al. 1998, [J. Geophys. Res. Planets](#), **103**, 22857
- Shafer, R., & Gordon, R. G. 1973, [J. Chem. Phys.](#), **58**, 5422
- Shapiro, D. A., Ciuryło, R., Drummond, J. R., & May, A. D. 2002, [Phys. Rev. A](#), **65**, 012501
- Słowiński, M., Thibault, F., Tan, Y., et al. 2020, [Phys. Rev. A](#), **101**, 052705
- Słowiński, M., Józwiak, H., Gancewski, M., et al. 2022, [JQSRT](#), **277**, 107951
- Smith, W. H. 1989, [Icarus](#), **81**, 429
- Stankiewicz, K., Józwiak, H., Gancewski, M., et al. 2020, [JQSRT](#), **254**, 107194
- Stankiewicz, K., Stolarczyk, N., Józwiak, H., Thibault, F., & Wcisło, P. 2021, [JQSRT](#), **276**, 107911
- Stolarczyk, N., Thibault, F., Cybulski, H., et al. 2020, [JQSRT](#), **240**, 106676
- Sung, K., Wishnow, E. H., Drouin, B. J., et al. 2022, [JQSRT](#), 108412
- Thibault, F., Patkowski, K., Żuchowski, P. S., et al. 2017, [JQSRT](#), **202**, 308
- Thibault, F., Wcisło, P., & Ciuryło, R. 2016, [EPJD](#), **70**, 236
- Truong, G.-W., Douglass, K. O., Maxwell, S. E., et al. 2013, [Nat. Photonics](#), **7**, 532
- Ullivi, L., Lu, Z., & Tabisz, G. C. 1989, [Phys. Rev. A](#), **40**, 642
- Valeev, E. F., & Sherrill, C. D. 2003, [J. Chem. Phys.](#), **118**, 3921
- Wan, Y., Balakrishnan, N., Yang, B. H., Forrey, R. C., & Stancil, P. C. 2019, [MNRAS](#), **488**, 381
- Wcisło, P., Cygan, A., Lisak, D., & Ciuryło, R. 2013, [Phys. Rev. A](#), **88**, 12517
- Wcisło, P., Gordon, I., Tran, H., et al. 2016, [JQSRT](#), **177**, 75
- Wcisło, P., Thibault, F., Zaborowski, M., et al. 2018, [JQSRT](#), **213**, 41
- Wcisło, P., Thibault, F., Stolarczyk, N., et al. 2021, [JQSRT](#), **260**, 107477
- Zaborowski, M., Słowiński, M., Stankiewicz, K., et al. 2020, [Opt. Lett.](#), **45**, 1603
- Zadrozny, A., Józwiak, H., Quintas-Sánchez, E., Dawes, R., & Wcisło, P. 2022, [J. Chem. Phys.](#), **157**, 174310
- Zuo, J., Croft, J. F. E., Yao, Q., Balakrishnan, N., & Guo, H. 2021, [J. Chem. Theory Comput.](#), **17**, 6747



## Appendix A: Details of the PES calculations

The 6D PES for the H<sub>2</sub>-H<sub>2</sub> system was calculated at the following level of theory;

$$E_{\text{int}} = E_{\text{int}}^{\text{HF}}[5] + \delta E_{\text{int}}^{\text{CCSD(T)}}[Q5] + \delta E_{\text{int}}^{\text{T(Q)}}[Q] + \delta E_{\text{int}}^{\text{FCI}}[T] + \delta E_{\text{int}}^{\text{DBOC}}[T]. \quad (\text{A.1})$$

In all cases, the aug-cc-pVXZ basis sets (Kendall et al. 1992) were employed with the cardinal number  $X$  taking values 2 (D), 3 (T), 4 (Q), and 5. The consecutive terms are defined in the following way:  $E_{\text{int}}^{\text{HF}}[5]$  is the interaction energy calculated at the HF level using the aug-cc-pV5Z basis set,  $\delta E_{\text{int}}^{\text{CCSD(T)}}[Q5]$  is the correlation contribution to the interaction energy calculated using the coupled-cluster method with up to perturbative triple excitations, CCSD(T), with the results extrapolated to complete basis set limits using the  $1/X^3$  formula (Halkier et al. 1999) from the calculations in the aug-cc-pVQZ and aug-cc-pV5Z basis sets. The next contribution,  $\delta E_{\text{int}}^{\text{T(Q)}}[Q] = E_{\text{int}}^{\text{CCSDT(Q)}}[Q] - E_{\text{int}}^{\text{CCSD(T)}}[Q]$ , accounts for the electron correlation effects beyond CCSD(T) included in the CC method with up to perturbative quadruple excitations, CCSDT(Q), computed with the aug-cc-pVQZ basis set, whereas  $\delta E_{\text{int}}^{\text{FCI}}[T] = E_{\text{int}}^{\text{FCI}}[T] - E_{\text{int}}^{\text{CCSDT(Q)}}[T]$  describes the electron correlation effects beyond CCSDT(Q), calculated with the aug-cc-pVTZ basis set. The DBOC (Handy et al. 1986),  $\delta E_{\text{int}}^{\text{DBOC}}[T]$ , was calculated with the masses of <sup>1</sup>H with the CCSD densities (Valeev & Sherrill 2003; Gauss et al. 2006) obtained with the aug-cc-pVTZ basis set. The  $\delta E_{\text{int}}^{\text{DBOC}}$  term is the only one that depends on masses. However, it is small compared to other terms and would be even smaller if calculated for HD-H<sub>2</sub> instead of H<sub>2</sub>-H<sub>2</sub>. Thus, the resulting surface can be applied to the former system with full confidence.

The interaction energies were fitted by an analytic function that consisted of short- and long-range parts, with a smooth switching at  $R$  values between 9 and 10  $a_0$ , using the switching function from Babin et al. (2013). The short-range part was taken in the form of a sum of products of exponentials  $e^{-\alpha r_{ab}}$ , where  $r_{ab}$  are atom-atom distances (Fernández et al. 1999; Braams & Bowman 2009). In contrast to most published work that uses the same  $\alpha$  for all terms, we used four different optimized values. The form of the long-range part was taken from Patkowski et al. (2008), but the parameters  $C_n^{l_1 l_2 l}$  were multiplied by linear combinations of symmetry-invariant polynomials of  $r_1$ ,  $r_2$ , and of magnitudes of their differences. The linear coefficients are determined from the fit to the ab initio energies obtained at the same level of theory as for the short-range part. The PES is expected to be valid for  $r_i \in [0.85, 2.25] a_0$ . Zuo et al. (2021) recently published a 6D PES for the H<sub>2</sub> dimer obtained from the complete active space self-consistent field calculations combined with the multi-reference configuration interaction calculations. According to Zuo et al. (2021), the potential is valid up to  $r_i = 3.45 a_0$ , beyond the upper limit of our PES. However, in the region of validity of both PESs, our surface should be more accurate due to the higher level of theory used.

## Appendix B: Quantum scattering calculation details

The dependence of the 6D PES on the three Jacobi angles was separated from the radial and intramolecular distances by the expansion of the PES over the bi-spherical harmonics,  $I_{l_1 l_2 l}(\theta_1, \theta_2, \phi)$ :

$$V(R, r_1, r_2, \theta_1, \theta_2, \phi) = \sum_{l_1, l_2, l} A_{l_1 l_2 l}(R, r_1, r_2) I_{l_1 l_2 l}(\theta_1, \theta_2, \phi), \quad (\text{B.1})$$

where the bi-spherical harmonics are defined as

$$I_{l_1 l_2 l}(\theta_1, \theta_2, \phi = \phi_1 - \phi_2) = \sqrt{\frac{2l+1}{4\pi}} \sum_m (l_1 m l_2 -m | l_1 l_2 l 0) Y_{l_1 m}(\theta_1, \phi_1) Y_{l_2 -m}(\theta_2, \phi_2). \quad (\text{B.2})$$

If the  $i$ -th ( $i = 1, 2$ ) molecule is homo-nuclear, the  $l_i$  index in the expansion in Eq. (B.1) takes only even values. The  $A_{l_1 l_2 l}(R, r_1, r_2)$  expansion coefficients were obtained by integrating the product of the PES and the corresponding bi-spherical harmonic, over Jacobi angles (see, for instance, Eq. (3) in Zdrożny et al. (2022) and the discussion therein). We employed a 19-point Gauss-Legendre quadrature to integrate over  $\theta_1$  and  $\theta_2$  and a 19-point Simpson's rule for the integral over  $\phi$ . The integration resulted in a tabular representation of the  $A_{l_1 l_2 l}(R, r_1, r_2)$  expansion coefficients, calculated for  $R$  in the range of 2.5 to 200  $a_0$  with a step of 0.1  $a_0$ , and for intramolecular distances ranging from 0.85 to 2.25  $a_0$  with a step of 0.1  $a_0$ .

In this work we used terms up to the  $I_{448}(\theta_1, \theta_2, \phi)$  bi-spherical harmonic, which corresponds to a total of 19 and 32 terms in the D<sub>2</sub>-H<sub>2</sub> and HD-H<sub>2</sub> case, respectively. Such numbers of terms represent an intermediate complexity of the problem – the number of terms in the HD-H<sub>2</sub> case is larger by a factor of 4 in comparison to the HD-He case (Stankiewicz et al. (2020, 2021)), but significantly smaller in comparison to more anisotropic PESs, studied in our previous works (85 for O<sub>2</sub>-N<sub>2</sub> (Gancewski et al. (2021)), and 205 for CO-N<sub>2</sub> and CO-O<sub>2</sub> (Jóźwiak et al. (2021); Zdrożny et al. (2022))). The error introduced by the truncation of the PES expansion is discussed in Appendix C.

The dependence of the expansion coefficients on  $r_1$  and  $r_2$  was reduced by averaging  $A_{l_1 l_2 l}(R, r_1, r_2)$  over rovibrational wave functions of isolated molecules,  $(\chi_{\eta_i}(r_i))$ :

$$A_{l_1 l_2 l, \eta_1, \eta_1', \eta_2, \eta_2'}(R) = \int dr_2 \chi_{\eta_2}(r_2) \left( \int dr_1 \chi_{\eta_1}(r_1) A_{l_1 l_2 l}(R, r_1, r_2) \chi_{\eta_1'}(r_1) \right) \chi_{\eta_2'}(r_2), \quad (\text{B.3})$$

where  $\eta_i = (v_i, j_i)$  denotes the quantum numbers of a rovibrational state of the  $i$ -th molecule. The wave functions of H<sub>2</sub>, HD, and D<sub>2</sub> were obtained by solving the nuclear Schrödinger equation for isolated molecules using the potential energy curve of Schwenke

(1988). We used the standard trapezoidal rule to perform the integration in Eq. (B.3), and we obtain  $A_{l_1 l_2, \eta_1, \eta'_1, \eta_2, \eta'_2}(R)$  coupling terms for  $R$  within the range 2.5 to 200  $a_0$ , with a step size of 0.1  $a_0$ .

The average in Eq. (B.3) provides a large number of possible coupling terms. In the HD-H<sub>2</sub> case, we considered pure rotational transitions (up to 1000 K); thus, we neglected the terms that couple excited vibrational states ( $v'_{\text{HD}} \neq v_{\text{HD}}$ ,  $v'_{\text{H}_2} \neq v_{\text{H}_2}$ ). In the D<sub>2</sub>-H<sub>2</sub> case, we observe that the terms that couple different vibrational levels are three orders of magnitude smaller than terms diagonal in  $v$ . Since we performed quantum scattering calculations in the  $v_{\text{D}_2} = 0$  and  $v_{\text{D}_2} = 2$  states separately (while maintaining  $v_{\text{H}_2} = 0$ ), we neglected radial coupling terms off-diagonal in vibrational quantum numbers. This approximation is additionally justified by the fact that the 2-0 S(2) line in H<sub>2</sub>-perturbed deuterium is measured at room temperature, where the population of H<sub>2</sub> in vibrationally excited states is negligible.

The dependence of the coupling terms in Eq. (B.3) on rotational quantum numbers (usually at the level of a few percent) is one of the key factors that affect theoretical predictions of the pressure shift of pure rotational lines in light molecules (Shafer & Gordon 1973; Dubernet & Tuckey 1999; Thibault et al. 2016; Jóźwiak et al. 2018). This is due to the fact that the line shift is sensitive to the difference in the scattering amplitude in the two rotational states that participate in an optical transition. Some authors neglect the  $j$  dependence of the radial coupling terms (the centrifugal distortion of the PES) in scattering calculations for rovibrational transitions (Green et al. 1989; Thibault et al. 2017) and average the expansion coefficients for a given vibrational  $v$  over the rovibrational wave function  $v, j = 0$ . This approximation is invoked either to save computational resources or due to a lack of information about the dependence of the PES on the stretching coordinates but works well for Q( $j$ ) lines. We have shown that taking the centrifugal distortion of the PES into account is crucial for achieving a sub-percent agreement with the experimental spectra in He-perturbed vibrational lines in H<sub>2</sub> (Słowiński et al. 2022) and HD (Stankiewicz et al. 2020). Thus, in both the HD-H<sub>2</sub> and D<sub>2</sub>-H<sub>2</sub> cases, we included centrifugal distortion of the PES in the scattering calculations. This leads to a large number of coupling terms (22 960 for  $v = 0$  state in HD, 16 359 in  $v = 0$  of D<sub>2</sub> and 17 157 for  $v = 2$ ), which is an order of magnitude more than in the case of HD-He (1 029). Similar to the HD-He case, this effect is crucial for achieving a sub-percent agreement with the cavity-enhanced spectra.

## Appendix C: Convergence of quantum scattering calculations and uncertainty budget for line-shape parameters

**Table C.1.** Uncertainties associated with each convergence parameter in the quantum scattering calculations. The values with slashes in the “Basis set size” line correspond to the case of collisions with *para*-H<sub>2</sub> and *ortho*-H<sub>2</sub>, respectively. See the main text for details.

Parameter	Value	Reference value	Maximum relative uncertainty (%)					
			$\gamma_0$	$\delta_0$	$\gamma_2$	$\delta_2$	Re( $v_{\text{opt}}$ )	Im( $v_{\text{opt}}$ )
$R_{\text{max}}$	100 $a_0$	200 $a_0$	0.01	1	0.01	1	0.001	0.5
$N_{\text{steps}}$	200/100/50	500	0.4	1	0.5	3	0.1	5
$(j_1^{\text{max}}, j_2^{\text{max}}, l_2^{\text{max}})$ in Eq. (B.1)	(4,4,8)	(6,6,12)	0.01	0.1	0.02	1	0.01	0.2
Basis set size ( $j_{\text{HD}}^{\text{max}}, j_{\text{H}_2}^{\text{max}}$ )	see text	(6,6)/(7,7)	0.01	0.2	0.01	0.2	0.01	0.2
Total			0.4	1.4	0.5	3.5	0.1	5

In this appendix we provide a detailed analysis of the convergence of generalized spectroscopic cross-sections with respect to specific parameters and how these parameters influence the uncertainty of the line-shape parameters. They include the range of propagation, the propagator step, the number of terms in the expansion of the PES (B.1), the size of the rotational basis set, and the number of partial waves. The uncertainties were estimated by calculating six line-shape parameters for the R(0) line at temperatures ranging from 20 to 1000 K. These values were then compared with those obtained from the generalized spectroscopic cross-sections calculated with the reference values of each parameter, which are significantly larger than the ones used in the final calculations. The stated uncertainties represent the maximum error observed within this temperature range. We assume that a similar level of accuracy is maintained for all other transitions considered in this paper. The results are summarized in Table C.1.

The range of propagation is defined by the starting and ending points ( $R_{\text{min}}$  and  $R_{\text{max}}$ ). The smallest  $R$  value that can be reliably calculated using quantum chemistry methods was employed as  $R_{\text{min}}$ , which in this case (taking into account the coordinate transformation from the H<sub>2</sub>-H<sub>2</sub> to HD-H<sub>2</sub> system) was 3  $a_0$ . On the other hand,  $R_{\text{max}}$  should be large enough to apply boundary conditions to the scattering equations (i.e., in the range of  $R$  where the PES becomes negligible compared to the centrifugal barrier). We tested the sensitivity of our results to  $R_{\text{max}}$  by performing calculations with  $R_{\text{max}} = 50 a_0, 75 a_0, 100 a_0, 150 a_0$ , and 200  $a_0$ . After assessing the tradeoff between computational cost and accuracy, we chose  $R_{\text{max}} = 100 a_0$  for the final calculations. Table C.1 provides uncertainties for six line-shape parameters impacted by this choice, estimated with respect to the reference calculations with  $R_{\text{max}} = 200 a_0$ .

The step size of the propagation directly affects the precision and the computational cost of the quantum scattering calculations. We performed tests with a varying number of steps per half-de Broglie wavelength ( $N_{\text{steps}}$ ), including 10, 20, 30, 50, 100, 200, and 500. Based on these tests, we chose a step size of 50 for  $E_{\text{kin}} > 3 \text{ cm}^{-1}$ , 100 for  $E_{\text{kin}} \in (1.5, 3) \text{ cm}^{-1}$ , and 200 for  $E_{\text{kin}} \leq 1.5 \text{ cm}^{-1}$ . Uncertainties introduced by the choice of the number of steps, estimated with respect to the reference calculations with 500 steps per half-de Broglie wavelength, are gathered in Table C.1.

We tested the convergence of the results with respect to the number of terms in the PES expansion (Eq. (B.1)), comparing line-shape parameters for the R(0) line obtained from cross-sections calculated using a truncated expansion of the PES (with terms up to

the  $I_{448}(\theta_1, \theta_2, \phi)$  bi-spherical harmonic) and an expanded set of expansion coefficients describing higher anisotropies of the system (up to the  $I_{6612}(\theta_1, \theta_2, \phi)$  term). The results are gathered in Table C.1.

The number of partial waves (or equivalently, blocks with given total angular momentum  $J$ ) necessary to converge the scattering equations was determined based on a criterion of stability in the calculated cross-sections. We solved the coupled equations for an increasing number of  $J$ -blocks until four consecutive  $J$ -blocks contributed to the largest elastic and inelastic state-to-state cross-sections by less than  $10^{-4} \text{ \AA}^2$ . The convergence criterion ensured that the estimated error introduced by the number of partial waves was smaller than the smallest uncertainty attributable to the other parameters in our study. This implies that the uncertainty in the number of partial waves did not significantly contribute to the overall uncertainty in our results; thus, we do not consider this factor in Table C.1.

The size of the rotational basis set is a critical factor in quantum scattering calculations, and it was chosen with great care to ensure a consistent level of accuracy across different rotational states. For each calculation, we checked that the basis set included all energetically accessible (open) levels of the colliding pair, as well as a certain number of asymptotically energetically inaccessible (closed) levels. We gradually increased the size of the basis set until the calculated cross-sections did not show appreciable differences, identifying a fully converged basis set. We then determined the smallest basis set that ensured convergence to better than 1% with respect to the fully converged basis. This was done for each initial state of the HD-H<sub>2</sub> system in a way that the estimated error for all transitions ( $R(j_{\text{HD}})$ ,  $j_{\text{HD}}=0, 1, 2$ ), including those involving rotationally excited states, remained within the specified limit.

The tests were conducted separately for collisions with *para*-H<sub>2</sub> (which involves only even rotational quantum numbers) and *ortho*-H<sub>2</sub> (which involves only odd rotational quantum numbers). In the case of *para*-H<sub>2</sub>, all rotational levels of HD and H<sub>2</sub> with  $j \leq j_{\text{max}}^{\text{max}} = 4$  were consistently included in the calculations. For specific calculations with H<sub>2</sub> initially in the  $j_{\text{H}_2} = 4$  state, or HD initially in the  $j_{\text{HD}} = 3$  state, the basis set was expanded to incorporate all rotational levels of HD and H<sub>2</sub> with  $j \leq 6$ . For *ortho*-H<sub>2</sub>, the basis set consistently included all rotational levels of HD and H<sub>2</sub> with  $j \leq j_{\text{max}}^{\text{max}} = 5$ . We extended the basis set to cover  $j_{\text{HD}}^{\text{max}} = 6$  and  $j_{\text{H}_2}^{\text{max}} = 5$  for cases where HD and H<sub>2</sub> were initially in the  $(j_{\text{HD}}, j_{\text{H}_2}) = (0,3), (1,3)$ , or  $(2,1)$  states. The largest basis set, with  $j_{\text{HD}}^{\text{max}} = j_{\text{H}_2} = 7$ , was employed in all calculations involving HD and H<sub>2</sub> in  $(j_{\text{HD}}, j_{\text{H}_2}) = (0,5), (1,5), (2,3), (2,5), (3,1), (3,3)$ , and  $(3,5)$  states.

Assuming the uncertainties associated with each parameter as independent, we estimated the maximum total uncertainty of each line-shape parameter using the root-sum-square method. The results are gathered in the last line of Table C.1.

## Appendix D: Modified Hartmann-Tran profile

This appendix describes the mHT profile, which we used to simulate the spectra. We considered the mHT profile to be the best compromise between the accurate but computationally demanding SDBB profile and the simple Voigt profile. The mHT profile can be expressed as a quotient of two quadratic speed-dependent Voigt (qSDV) profiles,

$$\tilde{I}_{\text{mHT}}(f) = \frac{\tilde{I}_{\text{qSDV}}^*(f)}{1 - (\nu_{\text{opt}}^r + i\nu_{\text{opt}}^i)\pi\tilde{I}_{\text{qSDV}}^*(f)}, \quad (\text{D.1})$$

which are directly linked to the spectral line-shape parameters from Eqs (1)-(3),

$$\tilde{I}_{\text{qSDV}}^*(f) = \frac{1}{\pi} \int d^3v f_m(v) \frac{1}{\Gamma_0 + i\Delta_0 + (\Gamma_2 + i\Delta_2)(v^2/v_m^2 - 3/2) + \nu_{\text{opt}}^r + i\nu_{\text{opt}}^i - i(f - f_0 - f_D v_z/v_m)}. \quad (\text{D.2})$$

The line-shape profile uses the parameters in the pressure-dependent form:

$$\begin{aligned} \Gamma_0 &= \gamma_0 \cdot p, \quad \Delta_0 = \delta_0 \cdot p \\ \Gamma_2 &= \gamma_2 \cdot p, \quad \Delta_2 = \delta_2 \cdot p \\ \nu_{\text{opt}}^r &= \tilde{\nu}_{\text{opt}}^r \cdot p, \quad \nu_{\text{opt}}^i = \tilde{\nu}_{\text{opt}}^i \cdot p. \end{aligned} \quad (\text{D.3})$$

The  $f_m(v)$  is the Maxwell-Boltzmann distribution of the active molecule velocity,  $v_m$  is its most probable speed, and  $v_z$  is one of the three Cartesian components of the  $v$  vector. The  $f$ ,  $f_0$ , and  $f_D$  are the frequency of light, the central frequency of the transition, and the Doppler frequency, respectively.

The hard-collision model of the velocity-changing collisions, which is used in the mHT profile, suffices to describe the velocity-changing line-shape effects (such as the Dicke narrowing) in the majority of the molecular species. However, in the cases with a significant Dicke narrowing, such as molecular hydrogen transitions, the hard-collision model does not reproduce the line shapes at the required accuracy level. To overcome this problem, a simple analytical correction (the  $\beta$  correction function) was introduced (Wcislo et al. 2016; Konefal et al. 2020), which mimics the behavior of the billiard ball model and, hence, considerably improves the accuracy of the mHT profile for hydrogen, at negligible numerical cost. The correction is made by replacing the  $\nu_{\text{opt}}^r$  with  $\beta_\alpha(\chi)\nu_{\text{opt}}^r$ , where  $\alpha$  is the perturber-to-absorber mass ratio and  $\chi = \nu_{\text{opt}}^r/\Gamma_D$  (where  $\Gamma_D$  is the Doppler width; see Konefal et al. (2020) for details). It should be emphasized that the  $\beta$  correction does not require any additional transition-specific parameters (it depends only on the perturber-to-absorber mass ratio  $\alpha$ ). The  $\beta$  correction was applied every time the mHT profile was used in this work.



## Appendix E: DPL representation of the temperature dependences

In this appendix, we discuss the details of the DPL representation of the temperature dependences of the spectral line-shape parameters. The DPL function is used to convert the exact temperature dependence of the line-shape parameters into a simple, analytical expression, suitable for storing in spectroscopic databases (Stolarczyk et al. (2020)). This conversion is done by fitting the DPL function to the actual ab initio temperature dependence data.

Within this work, we calculated the ab initio values at temperatures ranging from 50 to 1000 K. Due to its relevance to the atmospheres of giant planets, we chose to prioritize the 50-200 K temperature range and use the data only from this range to generate the DPL coefficients (Stolarczyk et al. 2020). Projection of the ab initio data on the DPL representation is performed by fitting the DPL function in the selected temperature range. For the most faithful reconstruction of the temperature dependence, we performed several different fitting procedures (i.e., Newton, Quasi-Newton, Levenberg-Marquardt, global optimization, and gradient methods) and selected the one that gives the best result (i.e., the lowest relative root mean square error; see the next paragraph). This selection was done separately for each of the line-shape parameters and molecular transitions. Mathematically, the two terms of the DPL functions are identical. Thus, to avoid swapping them, we followed the convention that the first base coefficients should always be greater than second base coefficients. Furthermore, to reduce the number of significant digits, if the two base coefficients have opposite signs, we required that their absolute values differ at least by 1‰.

**Table E.1.** Relative root mean square error of the DPL representation. We fitted the DPL function (see Eq. (4)) to the ab initio data at the temperature range of 50-200 K. This table presents the root mean square differences between the actual ab initio data and the DPL representation in this range (see Fig. E.1), divided by the value of the line-shape parameter at 296 K.

parameter	R(0)	R(1)	R(2)
$\gamma_0$	0.04%	0.04%	0.03%
$\delta_0$	0.48%	1.04%	0.29%
$\gamma_2$	0.29%	0.20%	0.21%
$\delta_2$	2.36%	4.40%	1.20%
$\tilde{\nu}_{\text{opt}}^r$	0.03%	0.03%	0.03%
$\tilde{\nu}_{\text{opt}}^i$	1.51%	1.39%	0.53%

The DPL coefficients listed in Table 1 can be used to retrieve the temperature dependence of the line-shape parameters through Eq. (4). The efficiency of the DPL representation is depicted in Fig. E.1. The red curves show the results of the ab initio calculations, while the black curves (covered by the red ones in some cases) are the values reconstructed from the DPL coefficients from Table 1. The corresponding residuals are presented under each of the plots. Table E.1 quantifies the accuracy of the DPL representation by presenting the values of the relative root mean square error (rRMSE) of the differences between the ab initio data and the DPL fit. The values of the rRMSE are normalized with respect to the value of the corresponding line-shape parameter at 296 K. Even though the rRMSE values for some parameters are on the level of several percent, the overall error of the shape of the line is much smaller because the two parameters that impose the highest impact on the line width,  $\gamma_0$  and  $\tilde{\nu}_{\text{opt}}^r$ , are reproduced with high accuracy. A detailed discussion of the propagation of errors from the parameters to the final shape of the line is provided in Słowiński et al. (2022).

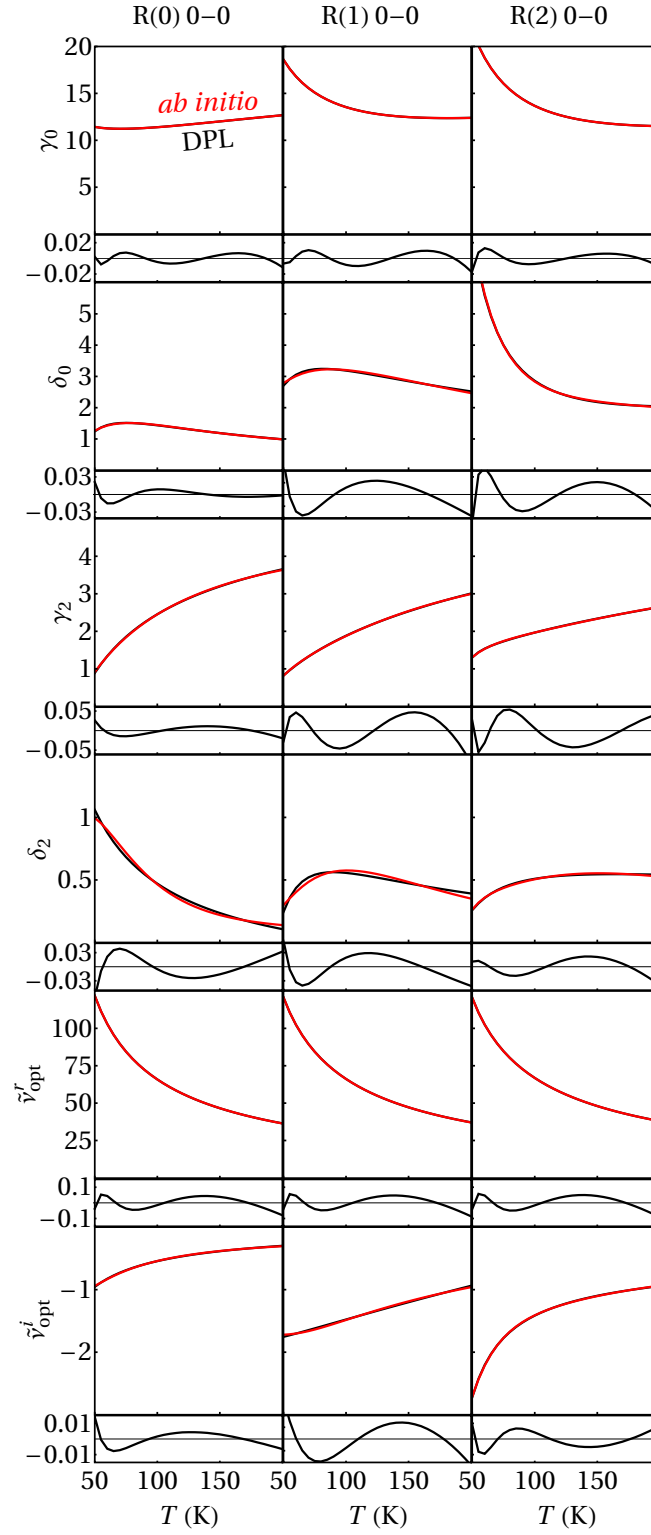


**Fig. E.1.** Temperature dependences of the six collisional line-shape parameters,  $\gamma_0$ ,  $\delta_0$ ,  $\gamma_2$ ,  $\delta_2$ ,  $\tilde{\nu}_{\text{opt}}^r$ , and  $\tilde{\nu}_{\text{opt}}^i$ , of the R(0) 0-0, R(1) 0-0, and R(2) 0-0 lines of HD perturbed by H<sub>2</sub>. The red and black curves are the *ab initio* results and DPL approximations, respectively. The small panels show the residuals from the DPL fits. The vertical axes for all the panels (including residuals) are in  $10^{-3} \text{ cm}^{-1} \text{ atm}^{-1}$ .



# The first comprehensive dataset of beyond-Voigt line-shape parameters from *ab initio* quantum scattering calculations for the HITRAN database: He-perturbed H<sub>2</sub> case study



P. Wcisło<sup>a,\*</sup>, F. Thibault<sup>b</sup>, N. Stolarczyk<sup>a</sup>, H. Jóźwiak<sup>a</sup>, M. Słowiński<sup>a</sup>, M. Gancewski<sup>a</sup>, K. Stankiewicz<sup>a</sup>, M. Konefał<sup>a,c</sup>, S. Kassı<sup>c</sup>, A. Campargue<sup>c</sup>, Y. Tan<sup>d</sup>, J. Wang<sup>d</sup>, K. Patkowski<sup>e</sup>, R. Ciuryło<sup>a</sup>, D. Lisak<sup>a</sup>, R. Kochanov<sup>f,g</sup>, L.S. Rothman<sup>f</sup>, I.E. Gordon<sup>f</sup>

<sup>a</sup> Institute of Physics, Faculty of Physics, Astronomy and Informatics, Nicolaus Copernicus University in Toruń, Grudziadzka 5, 87-100 Toruń, Poland

<sup>b</sup> Univ Rennes, CNRS, IPR (Institut de Physique de Rennes)-UMR 6251, F-35000 Rennes, France

<sup>c</sup> University of Grenoble Alpes, CNRS, LIPhy, F-38000 Grenoble, France

<sup>d</sup> Hefei National Laboratory for Physical Sciences at Microscale, iChEM, University of Science and Technology of China, Hefei, 230026 China

<sup>e</sup> Department of Chemistry and Biochemistry, Auburn University, Auburn, AL 36849, USA

<sup>f</sup> Harvard-Smithsonian Center for Astrophysics, Atomic and Molecular Physics Division, Cambridge, MA, USA

<sup>g</sup> QUAMER laboratory, Tomsk State University, 36 Lenin Avenue, 634050 Tomsk, Russia

## ARTICLE INFO

### Article history:

Received 15 September 2020

Revised 9 December 2020

Accepted 9 December 2020

Available online 11 December 2020

### Keywords:

Beyond-Voigt line-shape parameters

HITRAN

H<sub>2</sub>-He

*Ab initio* quantum scattering calculations

## ABSTRACT

We demonstrate a new method for populating line-by-line spectroscopic databases with beyond-Voigt line-shape parameters, which is based on *ab initio* quantum scattering calculations. We report a comprehensive dataset for the benchmark system of He-perturbed H<sub>2</sub> (we cover all the rovibrational bands that are present in the HITRAN spectroscopic database). We generate the entire dataset of the line-shape parameters (broadening and shift, their speed dependence, and the complex Dicke parameter) from fully *ab initio* quantum-scattering calculations. We extend the previous calculations by taking into account the centrifugal distortion for all the bands and by including the hot bands. The results are projected on a simple structure of the quadratic speed-dependent hard-collision profile. We report a simple and compact formula that allows the speed-dependence parameters to be calculated directly from the generalized spectroscopic cross sections. For each line and each line-shape parameter, we provide a full temperature dependence within the double-power-law (DPL) representation, which makes the dataset compatible with the HITRAN database. The temperature dependences cover the range from 20 to 1000 K, which includes the low temperatures relevant for the studies of the atmospheres of giant planets. The final outcome from our dataset is validated on highly accurate experimental spectra collected with cavity ring-down spectrometers. The methodology can be applied to many other molecular species important for atmospheric and planetary studies.

© 2020 Elsevier Ltd. All rights reserved.

## 1. Introduction

The collisional line-shape effects, including the beyond-Voigt effects [1–8], play an important role in atomic and molecular physics [9–13]. On one hand, they give access to studying the molecular interactions [14–16] and dynamics [17], but on the other hand they can affect the accuracy of optical metrology based on molecular spectroscopy [18]. In particular, insufficient modeling of the line-

shape effects can limit the accuracy of simulations of atmospheric measurements of the Earth [19] and other planets [20] and even modify the retrieved opacity of exoplanetary atmospheres [21,22]. To address this problem, a new relational structure [23] was introduced into the most widely used line-by-line spectroscopic database, HITRAN [24], allowing the beyond-Voigt line-shape effects to be represented [25]. It is, however, remarkably challenging to populate the entire database (all the molecules and their isotopologues over a great spectral range and thermodynamic conditions) with purely experimental beyond-Voigt line-shape parameters, not only due to a large number of transitions to be measured at different conditions and different spectral ranges, but

\* Corresponding author.

E-mail addresses: [piotr.wcislo@fizyka.umk.pl](mailto:piotr.wcislo@fizyka.umk.pl), [piotr.wcislo@umk.pl](mailto:piotr.wcislo@umk.pl) (P. Wcisło).

also due to strong numerical correlations between the line-shape parameters.

In this article, we demonstrate a new method for populating line-by-line spectroscopic databases with beyond-Voigt line-shape parameters that is based on *ab initio* quantum scattering calculations. We report a comprehensive dataset for the benchmark system of He-perturbed  $H_2$  lines. We cover all the rovibrational bands (with their branches) that are present in HITRAN. We generate the values of the line-shape parameters (broadening and shift, their speed dependence, and the complex Dicke parameter) from fully *ab initio* quantum-scattering calculations. We extend the calculations of the generalized spectroscopic cross sections reported in Refs. [15,26] by taking into account the centrifugal distortion for all the bands and by including the hot bands. We extrapolate the *ab initio* results to populate very weak lines, i.e., higher overtones,  $\nu' \geq 6$ , higher rotational numbers,  $J' \geq 8$ , and high- $\nu'$  hot bands,  $\nu' \geq 6$ ; following the standard HITRAN notation, we denote the final and initial states of a transition with primes and double primes, respectively. The results are projected on a simple structure of the quadratic speed-dependent hard-collision (qSDHC) profile [27–29] that is consistent with the recently recommended HITRAN parametrization [30]. We also report a simple and compact formula that allows the speed-dependence parameters (within the quadratic model) to be calculated directly from the generalized spectroscopic cross sections, which considerably speeds up the calculations and makes them numerically more stable. For each line and each line-shape parameter we provide a full temperature dependence within the double-power-law (DPL) representation, which was recently recommended for the HITRAN database [30]. The results are valid for a wide temperature range from 20 to 1000 K, with the 50–200 K range prioritized (in this range the DPL fits have 10 times larger weights), which is relevant for the studies of the atmospheres of giant planets. The final outcome from our dataset is validated on highly accurate experimental spectra collected with cavity ring-down spectrometers [31] demonstrating sub-percent agreement. Incorporation of beyond-Voigt line-shape parameters reported in this paper together with their DPL temperature dependences into the HITRAN database is possible thanks to the recently developed flexible relational structure of HITRAN [23]. The complex structure of this dataset is easily accessible for non-expert HITRAN users thanks to the HITRAN Application Programming Interface (HAPI) [32] that automatically generates spectra at the desired spectral range and thermodynamic conditions chosen by the user.

The atmospheres of the giant planets in the Solar System are greatly dominated by a mixture of molecular hydrogen and atomic helium. Moreover, atmospheres of some types of super-Earth exoplanets are predicted to be dominated by the  $H_2$ -He mixture [21]. The spectroscopic studies of giant planet atmospheres are naturally based on the main isotopologue of molecular hydrogen [33]. However, although the abundance of hydrogen deuteride is 4–5 orders of magnitude smaller, HD is noticeable in the spectroscopic studies of giant planets [20,33] due to the much larger intensity of the dipole transitions compared to the weak quadrupole lines in  $H_2$ . In total, four combinations of collision partners should be considered to provide a complete reference data for the planetary studies: self-perturbed  $H_2$ , He-perturbed  $H_2$ ,  $H_2$ -perturbed HD and He-perturbed HD. In this article, we consider the simplest benchmark case of He-perturbed  $H_2$ .

In Section 2, we discuss the general methodology of generating beyond-Voigt line-shape parameters from *ab initio* calculations. Section 3 illustrates the methodology on the examples of two rovibrational lines in He-perturbed  $H_2$ . The full comprehensive dataset for He-perturbed  $H_2$  is discussed in Section 4 and the complete dataset is provided in the supplementary material [34].

## 2. Methodology of generating datasets of the beyond-Voigt line-shape parameters based on the *ab initio* calculations

A typical approach to populating the HITRAN database with the beyond-Voigt line-shape parameters [24,32] uses the data that were obtained from fitting the advanced profiles to the high-quality experimental spectra [25,35–39], see the red boxes in the flowchart in Fig. 1. It is a challenging task to populate the entire database with the purely experimental approach due to the large number of transitions required to be accurately measured at different conditions. Another difficulty is related to strong numerical correlations between the line-shape parameters, which often results in large systematic errors in the retrieved line-shape parameters. The numerical correlation can be considerably reduced by implementing the multispectrum fitting approach [40–42] which is, however, very demanding from a technical point of view and is still difficult to automatically apply to large experimental datasets.

In this article, we present a new methodology for populating the spectroscopic databases based on *ab initio* calculations. A key factor that enables development of this approach was a demonstration that the fully *ab initio* quantum-scattering calculations can reproduce the shapes of the high-quality collision-perturbed experimental spectra at the subpercent level [31], including the deep non-Voigt regime (by subpercent agreement we mean that the root-mean-square error of the *ab initio* model relative to profile peak (rRMSE) calculated within  $\pm FWHM$  is smaller than 1%). The flowchart in Fig. 1 illustrates our methodology (see the yellow boxes). The chain of the *ab initio* calculations starts with the quantum-chemical calculations of the PESs [14,15]. In the second step, the PESs are used to perform the quantum-scattering calculations by solving the close-coupling equations, which provide the scattering S-matrices as a function of relative kinetic energy of the collision,  $E_{kin}$ . The S-matrices allow us to calculate the generalized spectroscopic cross-sections,  $\sigma_{\lambda}^q(E_{kin})$ , that describe the collision perturbation of the optical coherence associated with the considered molecular transition. This approach also allows for the calculations of off-diagonal generalized spectroscopic cross-sections. Thus, for instance, the well-known case of overlapping lines could be considered. However, in this study we limit the discussion to the case of isolated lines, which is relevant for the molecular system considered here at pressures typical for the atmospheres of gas giants. We consider two types of generalized cross-sections that differ by the rank of the velocity tensor,  $\lambda$ . For the zero rank,  $\lambda = 0$ ,  $\sigma_{\lambda}^q$  describes perturbation of internal motion of the

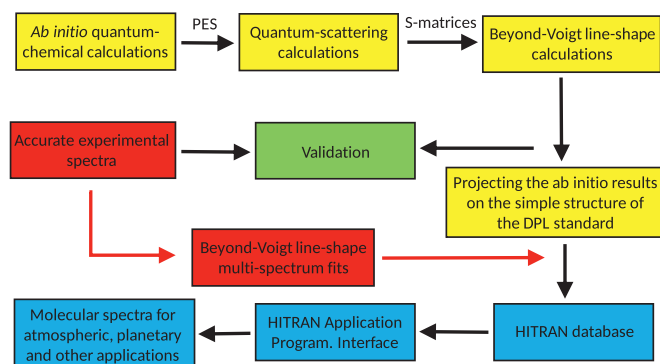


**Fig. 1.** Diagram illustrating our approach to generating the experimentally validated *ab initio* dataset of the beyond-Voigt line-shape parameters and its incorporation into the HITRAN database. The red arrows show the usual way of populating the database based on experimental spectra analysis only. (For interpretation of the references to color in this figure legend, the reader is referred to the web version of this article.)

molecule, and its real and imaginary parts have spectroscopic interpretation of the pressure broadening and shift cross-sections (PBXS and PSXS, respectively) [43–46]. For  $\lambda = 1$ ,  $\sigma_\lambda^q$  describes perturbation of translational motion (including the correlations with dephasing and state-changing collisions) and it has spectroscopic interpretation of the complex Dicke cross-section (its real and imaginary parts are denoted as RDXS and IDXS, respectively) [26,47–50].  $q$  is the tensor rank of the spectral transition operator (equal to 1 and 2 for dipole and quadrupole lines, respectively). In principle,  $\sigma_\lambda^q$  should also be labeled with the quantum numbers specifying the ground and excited levels of the transition (a diagonal cross-section in Liouville space); for the sake of notation clarity we skip them in this article. The two complex cross sections,  $\sigma_0^q$  and  $\sigma_1^q$ , allow us to calculate the collisional quantities that are needed for modeling the beyond-Voigt shapes of molecular lines, as depicted in the third yellow box in Fig. 1. The basic quantities are the collisional broadening,  $\gamma$ , and shift,  $\delta$ , of molecular lines expressed as a function of active molecule speed,  $v$ , which can be calculated as [3,51]

$$\gamma(v) + i\delta(v) = \frac{1}{2\pi c} \frac{1}{k_B T} \frac{2}{\sqrt{\pi} \bar{v}_p} \int_0^\infty dv_r v_r^2 e^{-\frac{v^2 + v_r^2}{\bar{v}_p^2}} \sinh\left(\frac{2vv_r}{\bar{v}_p^2}\right) \sigma_0^q(v_r), \quad (1)$$

where  $\bar{v}_p$  and  $v_r$  are the most probable speed of the perturber distribution and relative absorber-perturber speed, respectively.  $k_B$  and  $T$  are the Boltzmann constant and temperature. Two other line-shape parameters, which quantify the rate of the velocity-changing collisions, are the real,  $\tilde{v}_{\text{opt}}^r$ , and imaginary,  $\tilde{v}_{\text{opt}}^i$ , parts of the complex Dicke parameter,  $\tilde{v}_{\text{opt}}$ , which is calculated as

$$\tilde{v}_{\text{opt}} = \tilde{v}_{\text{opt}}^r + i\tilde{v}_{\text{opt}}^i = \frac{1}{2\pi c} \frac{1}{k_B T} \langle v_r \rangle M_2 \times \int_0^\infty dx x e^{-x} \left[ \frac{2}{3} \sigma_1^q(E_{\text{kin}} = xk_B T) - \sigma_0^q(E_{\text{kin}} = xk_B T) \right], \quad (2)$$

where  $M_2 = m_2/(m_1 + m_2)$ , and  $m_1$  and  $m_2$  are the masses of the active and perturbing molecules (or atoms),  $\langle v_r \rangle = \sqrt{8k_B T/\pi\mu}$  is the average relative speed and  $\mu$  is the reduced mass of the colliding partners. The variable of integration,  $x$ , is a dimensionless kinetic energy of a collision,  $x = E_{\text{kin}}/(k_B T)$ . The quantities expressed by Eqs. (1) and (2) [i.e.,  $\gamma(v)$ ,  $\delta(v)$ ,  $\tilde{v}_{\text{opt}}^r$  and  $\tilde{v}_{\text{opt}}^i$ ] carry all the collisional information that comes from our *ab initio* calculations and enters the beyond-Voigt line-shape models. The details of the line-shape calculations based on these quantities can be found in Ref. [6,52,53].

From the perspective of spectroscopy applications and populating the HITRAN database, the full speed dependences, given by Eq. (1), and full *ab initio* line-shape models [53] are far too complex to be stored in the database and are computationally too demanding to be used to analyze large sets of molecular spectra. Therefore, following Ref. [30], we project the full *ab initio* line-shape model on a simple structure of the quadratic speed-dependent hard-collision model (qSDHC) [27–29], in which the speed dependence is approximated with a quadratic function [54]

$$\gamma(v) + i\delta(v) \approx \gamma_0 + i\delta_0 + (\gamma_2 + i\delta_2)(v^2/v_m^2 - 3/2), \quad (3)$$

where  $v_m$  is the most probable absorber speed. The speed-averaged broadening and shift,  $\gamma_0$  and  $\delta_0$ , are calculated as real and imaginary parts of a simple average of  $\sigma_0^q$  over the Maxwellian  $E_{\text{kin}}$  distribution [3,51]

$$\gamma_0 + i\delta_0 = \frac{1}{2\pi c} \frac{1}{k_B T} \langle v_r \rangle \int_0^\infty dx x e^{-x} \sigma_0^q(E_{\text{kin}} = xk_B T). \quad (4)$$

Alternatively,  $\gamma_0$  and  $\delta_0$  can be calculated by averaging  $\gamma(v)$  and  $\delta(v)$  over the Maxwell distribution of active molecule speed,  $v$ , yielding exactly the same result as Eq. (4). The two parameters

quantifying the speed dependence of the broadening and shift,  $\gamma_2$  and  $\delta_2$ , are calculated by demanding that the slope of the quadratic approximation equals the slope of the actual speed dependences at  $v = v_m$  [53],

$$\gamma_2 + i\delta_2 = \frac{v_m}{2} \frac{d}{dv} (\gamma(v) + i\delta(v))|_{v=v_m}. \quad (5)$$

Following the generalized Hess method [4,48,50], we directly take the complex Dicke parameter,  $\tilde{v}_{\text{opt}} = \tilde{v}_{\text{opt}}^r + i\tilde{v}_{\text{opt}}^i$ , as a complex rate of the velocity-changing collisions in the qSDHC model [30]. In the cases of molecules for which the Dicke narrowing is pronounced, we recommend the use of the  $\beta$  correction [25,55] that improves the hard-collision approximation without increasing the cost of the line-shape computations. Note that the  $\beta$  correction is a generic concept valid for any molecular system and does not require any additional parameter to be stored (it depends only on the perturber-to-absorber mass ratio [55]). In total, the most general form of the qSDHC profile requires six line-shape parameters to be stored:

$$\gamma_0, \delta_0, \gamma_2, \delta_2, \tilde{v}_{\text{opt}}^r, \tilde{v}_{\text{opt}}^i. \quad (6)$$

The recent approach adopted in HITRAN [30] allows the temperature dependences of all the six line-shape parameter to be represented with the double-power-law (DPL):

$$\begin{aligned} \gamma_0(T) &= g_0(T_{\text{ref}}/T)^n + g'_0(T_{\text{ref}}/T)^{n'}, \\ \delta_0(T) &= d_0(T_{\text{ref}}/T)^m + d'_0(T_{\text{ref}}/T)^{m'}, \\ \gamma_2(T) &= g_2(T_{\text{ref}}/T)^j + g'_2(T_{\text{ref}}/T)^{j'}, \\ \delta_2(T) &= d_2(T_{\text{ref}}/T)^k + d'_2(T_{\text{ref}}/T)^{k'}, \\ \tilde{v}_{\text{opt}}^r(T) &= r(T_{\text{ref}}/T)^p + r'(T_{\text{ref}}/T)^{p'}, \\ \tilde{v}_{\text{opt}}^i(T) &= i(T_{\text{ref}}/T)^q + i'(T_{\text{ref}}/T)^{q'}, \end{aligned} \quad (7)$$

where  $T_{\text{ref}} = 296$  K. The full parametrization of the collisional line-shape effects requires 24 coefficients per single line, i.e., four coefficients per each of the six line-shape parameters, see Eq. (7). It should be noted that Eq. (7) represent the most general case of the DPL representation adopted in HITRAN [30]. For many molecular systems, not all the collisional effects are important at the considered accuracy level and, for a given experimental temperature range, a simple single-power law suffices. In such cases, one of the two approaches will be adopted in HITRAN. Either a single-power law and a smaller number of line-shape parameters will be stored (e.g.,  $\gamma_0$  and  $\delta_0$  for the simple Voigt profile or  $\gamma_0$ ,  $\delta_0$ ,  $\gamma_2$  and  $\delta_2$  for the quadratic speed-dependent Voigt profile) or the full DPL parametrization will be adopted but some of the 24 coefficients will be set to zero.

In this article, we show that our approach based on *ab initio* calculations allows us to fully benefit from the DPL parametrization given by Eq. (7). We generated a comprehensive dataset of the beyond-Voigt line-shape parameters for a system for which all the six line-shape parameters are necessary to represent the shapes of molecular lines (i.e., He-perturbed  $\text{H}_2$ ) and we use the DPL parametrization to represent these parameters in a wide temperature range, see Section 3.3 for details.

The HITRAN DPL parametrization, see Eq. (7) and Ref. [30], does not use the exact form of the Hartmann-Tran profile (HT profile) [56] but its modified version, the qSDHC profile. The main difference between these profiles is that for the description of the velocity-changing collisions the HT profile uses the frequency of the velocity-changing collisions,  $\tilde{v}_{\text{vc}}$ , and the correlation parameter,  $\eta$  (first introduced by Rautian and Sobelmann [2]), while the qSDHC profile uses an explicit parametrization with the real,  $\tilde{v}_{\text{opt}}^r$ , and imaginary,  $\tilde{v}_{\text{opt}}^i$ , parts of the complex Dicke parameter. The major advantage of the parametrization used in this work [30] is that it avoids singularities in temperature dependences of the complex Dicke parameter that may appear when the HT parametrization is used [30]. Another advantage of the qSDHC profile is that it



does not require to introduce unphysical speed dependence of the complex Dicke parameter, in contrast to the original formulation of the HT profile. For details refer to the Appendices A and B in Ref. [30]; see also Ref. [57].

Hartmann proposed a different approach to populating spectroscopic databases with line-shape parameters based on *ab initio* calculations [58] (see also Section 2 in Ref. [30]). In his approach, the *ab initio* line-shape parameters are used with one of the sophisticated line-shape models to generate reference shapes in a wide range of pressures, and then the reference spectra are fitted with some simpler phenomenological model. In his scheme the fitted line-shape parameters lose their physical meaning but, in principle, the shapes of molecular lines should better agree with experiment. Similar tests were done before, for instance see Ref. [59] (in that work, due to a lack of *ab initio* parameters, a sophisticated line-shape model was used with parameters determined experimentally). Recently, this approach was tested for the requantized Classical Molecular Dynamics Simulations corrected with the use of experimental spectra [60]. However, in the case of the He-perturbed  $H_2$  lines considered here, the difference between the qSDHC profile and the more sophisticated ones are much smaller than the difference with experimental data. Hence that approach [58] would not improve the accuracy of the dataset reported here.

### 3. Illustration of the methodology for the case of 2-0 Q(1) and 3-0 S(1) lines

In this section, we use an example of two rovibrational lines in He-perturbed  $H_2$  to illustrate the methodology described in Section 2 and shown in Fig. 1. We consider the 2-0 Q(1) and 3-0 S(1) quadrupole lines that were recently accurately measured with the cavity enhanced techniques [31]; in this article we refer to them as reference lines. These measurements were used for accurate validation of the *ab initio* collisional line-shape calculations [31] and more recently these spectra were used for validation of improved quantum-scattering calculations that include centrifugal distortion [61].

#### 3.1. Ab initio quantum scattering calculations

The  $H_2$ -He PES is three-dimensional, i.e., it depends on the distance between the center of mass of the hydrogen molecule and the helium atom,  $R$ , the distance between the two hydrogen atoms,  $r$ , and the angle between the intra- and intermolecular axes,  $\theta$ . The quantum-scattering calculations [15,26] that we used to generate the line-shape parameter dataset are based on the recent state-of-the-art PES that is an extension of the PES published by Bakr, Smith and Patkowski [14] (this PES will be referred to as BSP). The BSP PES was calculated using the coupled-cluster method with single, double and perturbative triple (CCSD(T)) excitations, taking into account also the contributions from the higher coupled-cluster excitations. It was determined for ten intramolecular separations, between 1.1 and 1.75  $a_0$ , which was shown to be insufficient for the detailed studies of processes involving the vibrationally excited  $H_2$  molecule (see Section 2 of Ref. [46] and Appendix C of [15] for details). This issue was addressed in the second version of this PES, BSP2, which extended the range of *ab initio* data points to  $r \in [0.65, 3.75] a_0$ . The final version of this PES, BSP3 [15], which was used in this work, has improved asymptotic behavior of the  $H_2$ -He interaction energy at large  $R$ . The quantum scattering calculations based on the BSP3 PES were recently tested on highly accurate cavity-enhanced measurements of the shapes of He-perturbed  $H_2$  2-0 Q(1) and 3-0 S(1) lines [31] resulting in unprecedented agreement between experimental and theoretical collision-induced line shapes. Furthermore, the BSP3 PES was em-

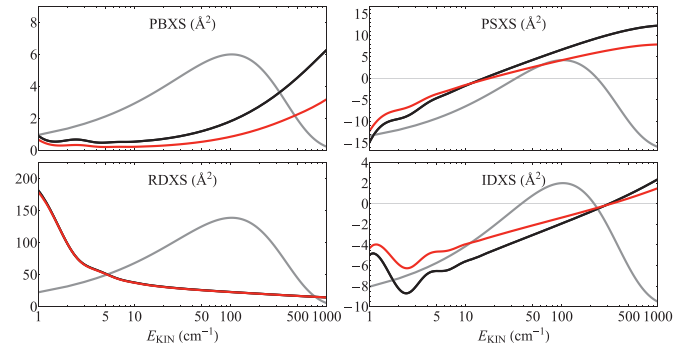


**Fig. 2.** Examples of the generalized spectroscopic cross sections for the case of 2-0 Q(1) and 3-0 S(1) lines in helium-perturbed  $H_2$ , see the red and black lines, respectively. The four panels show the pressure broadening (PBXS), pressure shift (PSXS), and real (RDXS) and imaginary (IDXS) parts of the complex Dicke cross-sections as a function of collision energy. The gray line is the Maxwell-Boltzmann distribution at 296 K in arbitrary units. (For interpretation of the references to color in this figure legend, the reader is referred to the web version of this article.)

ployed in the studies of purely rotational lines of He-perturbed isotopologues of molecular hydrogen:  $D_2$  [47,62] and HD [63,64].

For the purpose of dynamical calculations [15,26], the three-dimensional  $H_2$ -He PES is projected over Legendre polynomials,  $P_\xi$  [15,26,46]:

$$V(R, r, \theta) = \sum_{\xi} v_{\xi}(R, r) P_{\xi}(\cos \theta). \quad (8)$$

In the case of homonuclear molecules like  $H_2$ , the  $\xi$  index takes only even values. Due to the small overall anisotropy of the  $H_2$ -He PES, only the first four  $\xi$  values are retained throughout the calculations. The  $v_{\xi}(R, r)$  terms are averaged over rovibrational wavefunctions of the unperturbed molecule,  $\chi_{v,J}(r)$ , leading to the radial coupling terms,  $A_{\xi,v,J,v',J'}(R)$ , which enter the close-coupled equations. At room temperature the vibrational coupling ( $v \neq v'$ ) can be neglected [15,26]. The influence of the centrifugal distortion (the  $J$  dependence of the radial coupling terms) was usually neglected in the scattering calculations for the rovibrational transitions [15,26], as it was suggested that this effect might be masked due to the large contribution from the vibrational dephasing [46]. However, it was shown recently [61,64] that if one aims for sub-percent accuracy of the line-shape parameters, the centrifugal distortion of the potential energy surface must be taken into account. Therefore, the  $J$ -dependence of the radial coupling terms  $A_{\xi,v,J,v',J'}(R)$  was included in the following analysis.

The scattering calculations were performed using the recently developed BIGOS code [65] for a wide range of relative kinetic energies. The BIGOS code solves the coupled equations in the body-fixed frame of reference using the renormalized Numerov's algorithm [66]. Calculations were carried out for intermolecular distances ranging from 1 to 200  $a_0$  and three asymptotically closed levels were kept in the basis set. Fig. 2 presents an example of the generalized spectroscopic cross sections for the 2-0 Q(1) and 3-0 S(1) lines.

#### 3.2. Speed dependence of the broadening and shift, and the quadratic approximation

The calculations of the  $\gamma_0$ ,  $\delta_0$ ,  $\tilde{\nu}_{\text{opt}}^r$  and  $\tilde{\nu}_{\text{opt}}^i$  parameters are straightforward and require only performing the averaging (with proper weights) of the generalized spectroscopic cross sections over the Maxwell distribution of the relative kinetic energy of a collision, see Eqs. (2) and (4). Calculations of the speed-dependence parameters,  $\gamma_2$  and  $\delta_2$ , are, in principle, more complex and require a few additional steps. First, the *ab initio* speed-dependent broadening and shift are calculated from Eq. (1); Fig. 3

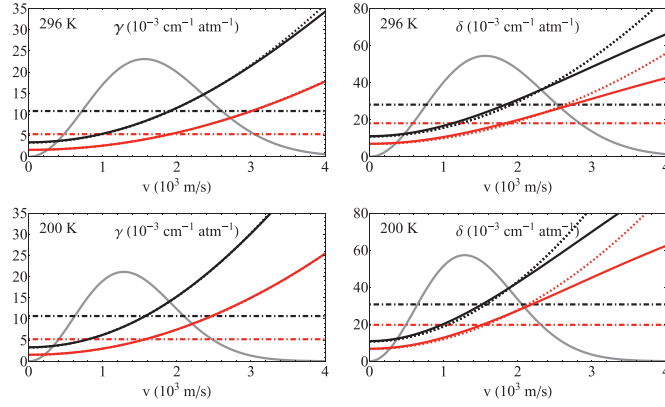


**Fig. 3.** Examples of the speed dependences of the broadening,  $\gamma$ , and shift,  $\delta$ , parameters. The red and black lines correspond to the 2-0 Q(1) and 3-0 S(1) lines in helium-perturbed  $H_2$ , respectively. The solid lines show the full *ab initio* results and the dotted lines show the quadratic approximations. The dash-dotted lines show the corresponding speed-averaged values. The calculations were done for  $T = 296$  K (upper panels) and 200 K (lower panels); the corresponding Maxwell-Boltzmann distributions (in arbitrary units) are plotted as a gray lines. (For interpretation of the references to color in this figure legend, the reader is referred to the web version of this article.)

shows the result for the case of the 2-0 Q(1) and 3-0 S(1) lines. The full speed dependences are approximated with a quadratic function, see Eq. (3). The choice of how the  $\gamma_2$  and  $\delta_2$  parameters are determined is not unique [67,68]. In our methodology we demand that the slopes of the *ab initio* and quadratic speed dependences are equal at the most probable speed, see Eq. (5). This approach is very efficient from a computational perspective. The derivative from Eq. (5) can be done analytically before the integration in Eq. (1) and, hence, the  $\gamma_2$  and  $\delta_2$  parameters can be evaluated directly by averaging the  $\sigma_0^q$  cross section with proper weights

$$\gamma_2 + i\delta_2 = \frac{1}{2\pi c} \frac{1}{k_B T} \frac{\bar{v}_p}{\sqrt{\pi}} e^{-y^2} \times \int_0^\infty \left( 2x \cosh(2xy) - \left( \frac{1}{y} + 2y \right) \sinh(2xy) \right) \times x^2 e^{-x^2} \sigma_0^q(x\bar{v}_p) dx, \quad (9)$$

where  $x = v_r/\bar{v}_p$  and  $y = v_m/\bar{v}_p$ , with  $v_r$ ,  $v_m$  and  $\bar{v}_p$  being the relative absorber to perturber speed, most probable absorber speed and most probable perturber speed, respectively. Note that  $y = \sqrt{\alpha}$ , where  $\alpha$  is the perturber-to-absorber mass ratio. The quadratic approximations for the 2-0 Q(1) and 3-0 S(1) transitions are shown in Fig. 3 as dotted lines. The results from Fig. 3 were calculated for  $T = 296$  K. The accuracy of the quadratic approximation depends on the choice of transition and line-shape parameter. In the cases considered in Fig. 3, the approximation works better for the  $\gamma$  parameter.

### 3.3. Temperature dependences of the line-shape parameters

The values of the six collisional line-shape parameters,  $\gamma_0$ ,  $\delta_0$ ,  $\gamma_2$ ,  $\delta_2$ ,  $\bar{v}_{opt}^r$  and  $\bar{v}_{opt}^i$ , were calculated in the temperature range from 20 to 1000 K using Eqs. (4), (9) and (2). The examples of these results, for the case of our reference lines, are shown in Fig. 4. To represent these temperature dependences in the HITRAN database, we use the recently recommended DPL approximation [30] for all the six line-shape parameters, see Eq. (7). The DPL fits were done for the 20 – 1000 K temperature range enforcing ten times larger fitting weights for the prioritized temperature range from 50 to 200 K (see the gray shadows in Fig. 4), which is relevant for the atmospheres of giant planets. The examples of the DPL

**Table 1**

Examples of the complete records from our DPL line-shape parameter dataset for the cases of the Q(1) 2-0 and S(1) 3-0 lines in  $H_2$  perturbed by He. Coefficients 1 and 2 are in  $\text{cm}^{-1}\text{atm}^{-1}$ . Exponents 1 and 2 are dimensionless. All the DPL coefficients are defined by Eq. (7), following the original formulation from Ref. [30].

Q(1) 2-0 line				
	Coefficient 1	Coefficient 2	Exponent 1	Exponent 2
$\gamma_0(T)$	$g_0 = 0.29611$	$g'_0 = -0.29076$	$n = -0.30724$	$n' = -0.31188$
$\delta_0(T)$	$d_0 = 1.29146$	$d'_0 = -1.27385$	$m = 0.617$	$m' = 0.622$
$\gamma_2(T)$	$g_2 = 0.114102$	$g'_2 = -0.111618$	$j = 0.2396$	$j' = 0.2453$
$\delta_2(T)$	$d_2 = 0.091305$	$d'_2 = -0.083861$	$k = -0.0013$	$k' = -0.0383$
$\bar{v}_{opt}^r(T)$	$r = 0.04277$	$r' = -0.00417$	$p = 0.6856$	$p' = -0.1236$
$\bar{v}_{opt}^i(T)$	$i = -0.27435$	$i' = 0.26376$	$q = 0.07106$	$q' = 0.05273$
S(1) 3-0 line				
	Coefficient 1	Coefficient 2	Exponent 1	Exponent 2
$\gamma_0(T)$	$g_0 = 0.012847$	$g'_0 = -0.001465$	$n = -0.11276$	$n' = -0.92775$
$\delta_0(T)$	$d_0 = 1.87405$	$d'_0 = -1.84585$	$m = 0.61066$	$m' = 0.61600$
$\gamma_2(T)$	$g_2 = 0.0493132$	$g'_2 = -0.0440504$	$j = -0.34485$	$j' = -0.38797$
$\delta_2(T)$	$d_2 = 1.5985$	$d'_2 = -1.5867$	$k = -0.01288$	$k' = -0.01602$
$\bar{v}_{opt}^r(T)$	$r = 0.05173$	$r' = -0.01689$	$p = 0.6530$	$p' = 0.2554$
$\bar{v}_{opt}^i(T)$	$i = -0.4136$	$i' = 0.39691$	$q = 0.08613$	$q' = 0.06746$

fits are shown in Fig. 4 as green lines. The DPL approximation performs best when the temperature dependence is monotonic; when an extremum is clearly seen then the accuracy is worse, see the  $\delta_0$  panels in Fig. 4. The amplitude of the residuals for most of the cases is smaller than 1%; their exact values are taken into account in the estimations of the line-shape parameter uncertainties reported in our dataset, see the supplementary materials [34].

### 3.4. Examples of a complete dataset record

In Table 1, we show examples of complete records from our line-shape parameter dataset for the cases of the two reference lines. All the coefficients are defined by Eqs. (7), following the original formulation from Ref. [30]. A set of 24 coefficients per a single molecular transition is required for a full DPL description of the six line-shape parameters. The values of the coefficients gathered in Table 1 are directly taken from the fits shown in Fig. 4. Note that at  $T = T_{ref}$ , Eqs. (7) simplify and a given line-shape parameter is simply a sum of the corresponding Coefficient 1 and Coefficient 2; for instance  $\gamma_0(T_{ref}) = g_0 + g'_0$ .

### 3.5. Experimental validation

In this section, we show experimental validation of our line-shape parameter dataset for the cases of the two reference lines. We use the experimental data reported in Ref. [31]. The 2-0 Q(1) line was measured in the Grenoble laboratory at nine pressures from 0.39 to 1.05 atm and at a temperature of 294.2 K. The 3-0 S(1) line was measured in the Hefei laboratory at four pressures from 0.36 to 1.35 atm and at temperature of 296.6 K. The experimental spectra are shown as black dots in Fig. 5. Both experiments are based on high-finesse cavity ring-down spectrometers; the experimental details are given in Ref. [31].

It was demonstrated in Ref. [31] that the synthetic profiles based on the fully *ab initio* calculations agree exceptionally well with the experimental profiles without fitting any of the line-shape parameters. The relative root mean square error (rRMSE) averaged over the pressures calculated within  $\pm$ FWHM around the line center was 0.33% and 0.99% for the 2-0 Q(1) and 3-0 S(1) lines, respectively [31]. Recently, the agreement with these experimental profiles was confirmed with an improved theoretical approach that includes the centrifugal distortion in the quantum-scattering calculation; rRMSE was 0.38% and 0.86% for the 2-0 Q(1) and 3-0 S(1) lines, respectively [61]. In this section, we show that we can reach an almost equally good agreement if we replace the



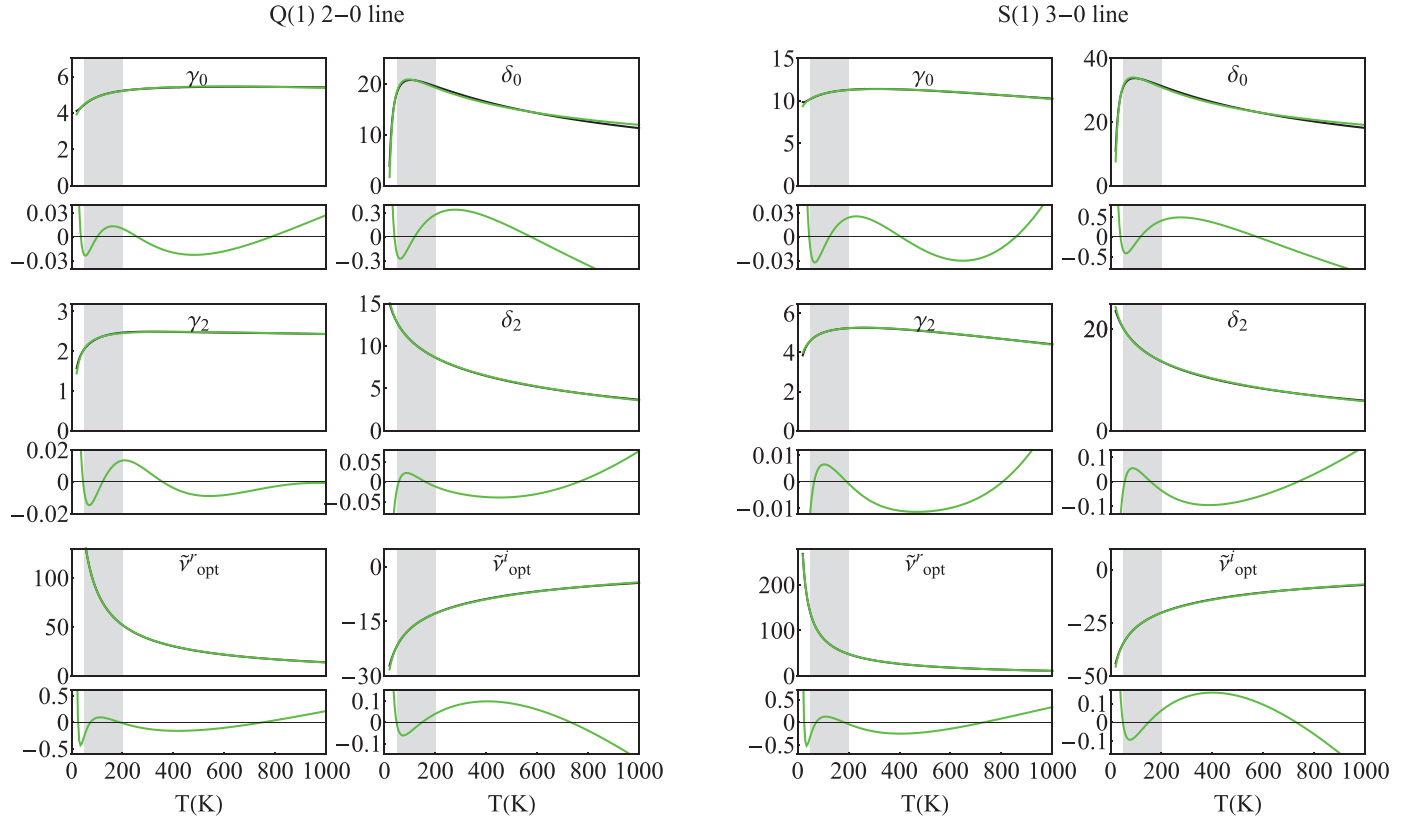


**Fig. 4.** Examples of the temperature dependences of the six collisional line-shape parameters,  $\gamma_0$ ,  $\delta_0$ ,  $\gamma_2$ ,  $\delta_2$ ,  $\tilde{\gamma}_{\text{opt}}^r$  and  $\tilde{\gamma}_{\text{opt}}^i$ , for the cases of the Q(1) 2-0 and S(1) 3-0 lines in  $\text{H}_2$  perturbed by He. The black and green lines are the *ab initio* results and DPL approximations, respectively. The small panels show the residuals from the DPL fits. The vertical axes for all the panels (including residuals) are in  $10^{-3}\text{cm}^{-1}\text{atm}^{-1}$ . The gray shadows indicate the temperature range prioritized in the DPL fits; this temperature range is relevant for the atmospheres of giant planets. (For interpretation of the references to color in this figure legend, the reader is referred to the web version of this article.)

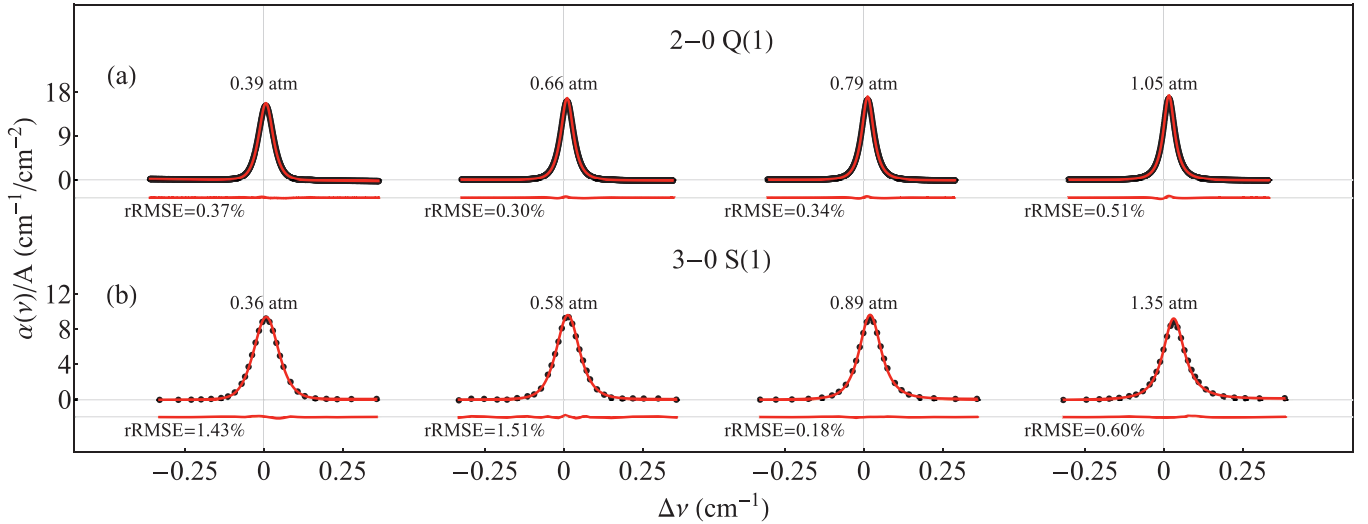


**Fig. 5.** Comparison of the synthetic spectra of the He-perturbed  $\text{H}_2$  lines generated from our DPL HITRAN-format line-shape dataset (red lines) with experimental spectra (black points) collected with cavity ring-down spectrometers. Temperatures for the experimental and synthetic spectra are 294.2 K and 296.6 K for the 2-0 Q(1) and 3-0 S(1) lines, respectively. The red lines below the profiles show the differences between the experimental and synthetic spectra; rRMSE is the corresponding relative root mean square error calculated within  $\pm\text{FWHM}$  around line center (relative means that RMSE is divided by the absorption coefficient at the line peak). (For interpretation of the references to color in this figure legend, the reader is referred to the web version of this article.)

full *ab initio* model with the approximate approach presented in this article, consistent with the HITRAN-format DPL parametrization [30]. The approximation is twofold. First, the full line-shape model [31,53,69] is replaced with a quadratic speed-dependent hard-collision (qSDHC) model. Second, the full *ab initio* tempera-

ture dependences are approximated with DPL. The comparison is shown in Fig. 5. The average rRMSE is 0.46% and 0.93% for the 2-0 Q(1) and 3-0 S(1) lines, respectively. It should be emphasized that none of the line-shapes were fitted in this comparison (all of them were taken from our dataset). For this comparison, we only fitted

the line area, baseline, background slope and line center (all the pressures were fitted simultaneously and the fitted line center was constrained to be the same for all the pressures). The profiles from Fig. 5 were calculated using the  $\beta$  correction [25,55] to the qSDHC profile, see Section 2 for details. Without the  $\beta$  correction, the average rRMSE considerably deteriorates and equals 1.43% and 1.08% for the 2-0 Q(1) and 3-0 S(1) lines, respectively.

#### 4. Comprehensive dataset of beyond Voigt line-shape parameters for the helium-perturbed H<sub>2</sub> lines

In this section, we discuss the main result of the present paper, i.e., the complete dataset of the beyond-Voigt line-shape parameters for the He-perturbed H<sub>2</sub> rovibrational lines. We provide a full set of the line-shape parameters for all the 3480 H<sub>2</sub> rovibrational electric quadrupole lines present in the HITRAN database [24]. For our basic set of 321 lines (that contains the strongest lines) we directly perform *ab initio* calculations of the generalized spectroscopic cross sections, see Section 3.1. For all the other lines (higher overtones, high- $J$  lines and high- $\nu'$  hot bands) we extrapolate the *ab initio* data. The majority of the extrapolated data concerns the hot bands. In this work, we extended the *ab initio* calculations from Refs. [15,26] by taking into account the centrifugal distortion for all the bands and by including the hot bands. We also performed *ab initio* calculations for several dozen other lines with high  $\nu$  or  $J$  numbers, which we use to adjust and validate our extrapolation scheme.

We use our *ab initio* generalized spectroscopic cross sections to calculate the line-shape parameters and their temperature dependences within the HITRAN DPL parametrization [30]. Our *ab initio* calculations of the cross sections were performed for:

- 105 lines from the Q-branches ( $J''$  ranging from 1 to 7; Q(0) is forbidden) from the  $\nu' - \nu''$  bands, with  $\nu'' = 0, \dots, 4$  and  $\Delta\nu = \nu' - \nu'' = 1, \dots, 5$ ,
- 126 lines from the S-branches ( $J''$  ranging from 0 to 5) from the  $\nu' - \nu''$  bands, with  $\nu'' = 0, \dots, 5$  and  $\Delta\nu = \nu' - \nu'' = 0, \dots, 5$ ,
- 90 lines from the O-branches ( $J''$  ranging from 2 to 7) from the  $\nu' - \nu''$  bands, with  $\nu'' = 0, \dots, 4$  and  $\Delta\nu = \nu' - \nu'' = 1, \dots, 5$ .

For each of these 321 lines, we employ the methodology introduced in Section 2 to populate a complete dataset record defined by Eqs. (7) and illustrated in Table 1.

In Fig. 6, we show an example of the vibrational,  $\nu'$ , and rotational,  $J''$ , quantum number dependences of the line-shape parameters generated from our dataset at 150 K and 296 K (the plots do not show the raw *ab initio* data, but the line-shape parameters already reconstructed from our HITRAN-format DPL dataset). We observe a strong dependence of all the six line-shape parameters on the vibrational number  $\nu'$ , and much weaker dependence on the rotational number  $J''$ , which is consistent with the phenomenological dataset for self-perturbed H<sub>2</sub> [25]. In Fig. 7, we show the results for different hot bands; the colors indicate the change of the vibrational quantum number  $\Delta\nu = \nu' - \nu''$ . In contrast to the simplest assumption that for a fixed  $\Delta\nu$  the line-shape parameters should hardly depend on  $\nu''$  (this was assumed, for instance, in the phenomenological database for the self-perturbed H<sub>2</sub> [25]), we observe a strong dependence on  $\nu''$ , especially for small  $\Delta\nu$  for the  $\gamma_0$  parameter.

The rovibrational lines in H<sub>2</sub> are exceptionally weak; the strongest line at  $T = T_{\text{ref}} = 296$  K is the 1-0 S(1) line with a line intensity of  $3.2 \times 10^{-26}$  cm/molecule. The intensity quickly decreases with  $J''$  and  $\nu'$ . For instance, the intensity of the 1-0 S(5) line is as small as  $2.2 \times 10^{-29}$  cm/molecule, and the intensity of the 5-0 S(1) line is  $0.95 \times 10^{-29}$  cm/molecule. At lower temperatures that are relevant for giant planet atmospheres, the line intensity decreases with  $J''$  and  $\nu'$  even faster. For this reason, we limit our full line-shape calculations based on the *ab initio* generalized spectroscopic cross sections to  $J' < 8$  and  $\nu' < 6$ . For the completeness of the dataset, we extrapolate our calculations for higher  $J''$  and  $\nu'$  lines that are present in HITRAN (in fact, in this procedure we combine extrapolation and interpolation). The extrapolation scheme is as follows. For every branch (O, Q and S), we calculated the values of the line-shape parameters for one high- $\nu'$  line per cold/hot band, i.e., we performed additional *ab initio* calculations for the following lines: Q(1) 9-x, S(1) 9-x, O(3) 9-x, with  $x = 0, \dots, 5$ . We assumed in our extrapolation that the proportions of the values of the line-shape parameters between the 9-0 and 5-0 bands for other  $J''$  are the same as for the three cases mentioned above (i.e.,

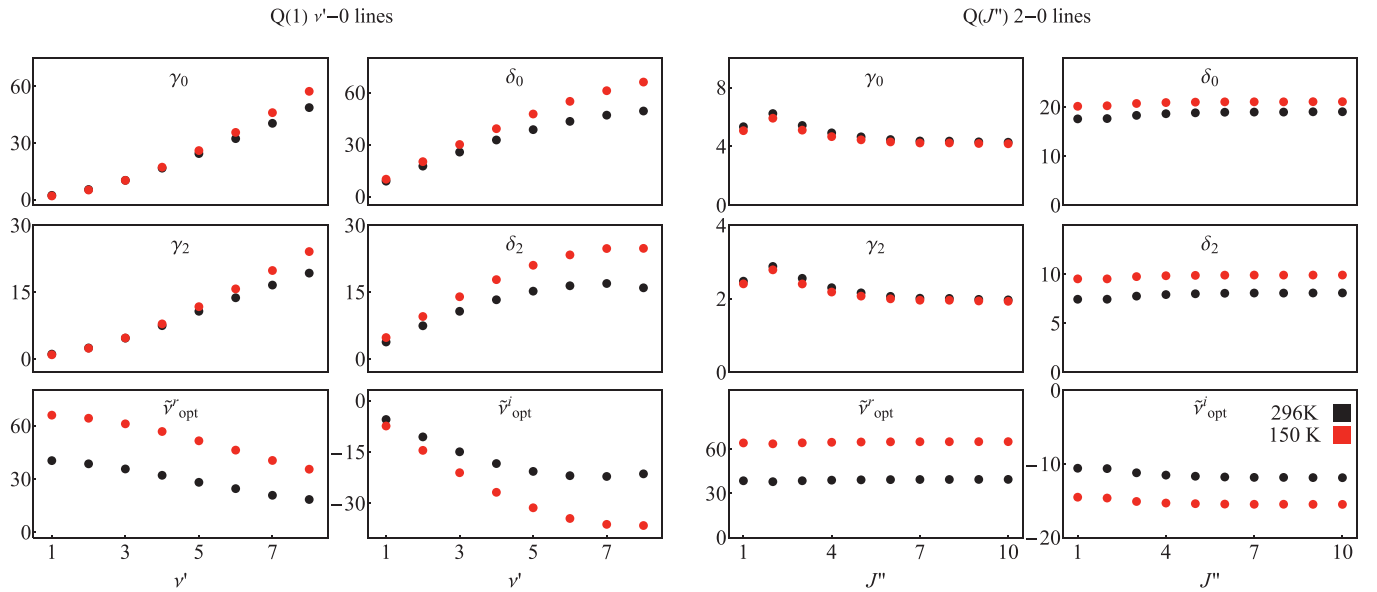


**Fig. 6.** An excerpt from our dataset illustrating the structure of the dataset and the examples of the vibrational and rotational dependences of all six line-shape parameters. The line-shape parameters are determined for the He-perturbed H<sub>2</sub> rovibrational lines at  $T = 150$  and  $296$  K; refer to red and black colors, respectively. All the parameters are expressed in units of  $10^{-3} \text{ cm}^{-1} \text{ atm}^{-1}$ . The values of the line-shape parameters shown in this plot are not directly taken from *ab initio* calculations, but reconstructed from the DPL relations, Eqs. (7), based on the coefficients from our dataset [34]. (For interpretation of the references to color in this figure legend, the reader is referred to the web version of this article.)

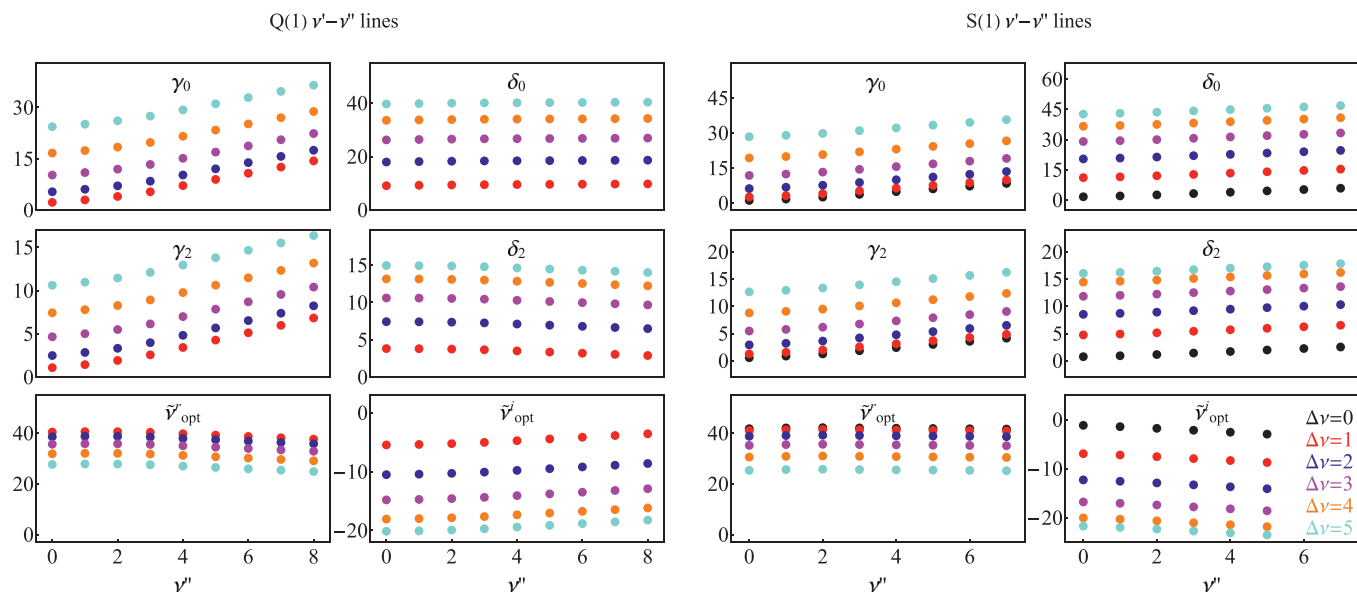


**Fig. 7.** An excerpt from our dataset illustrating the values of the beyond-Voigt line-shape parameters for different hot bands. The left and right sides of the figure show the results for the Q(1) and S(1) lines, respectively. All the parameters are expressed in units of  $10^{-3} \text{ cm}^{-1} \text{ atm}^{-1}$ . The values of the line-shape parameters shown in this plot are not directly taken from *ab initio* calculations, but reconstructed from the DPL relations, Eqs. (7), based on the coefficients from our dataset [34]. The data for  $v' = v'' + \Delta v \geq 6$  come from extrapolation.

the same within each branch). In the next step, we interpolated the line-shape parameters for the bands between 5-0 and 9-0 using a quadratic function fitted (separately for every  $J''$ ) to 4-0, 5-0 and 9-0 data. The same approach was applied to extrapolate the data for hot bands. To populate the dataset for higher  $J''$ , we performed fully *ab initio* calculations for the six high- $J''$  transitions belonging to the 2-0 band: O(10), O(13), Q(8), Q(11), S(8) and S(11) lines. We constrained the same proportions of the line-shape parameters between  $J'' = 5, 8$  and 11 (10 and 13 for O branches) for other bands, and we interpolated the values of the line-shape parameters between  $J'' = 5$  and 11 (13 for the O bands) with a quadratic function. For  $J'' > 11$  ( $J'' > 13$  for the O bands) we used linear extrapolation based on the last two  $J''$ . This approach (based on the data for the 2-0 band) was used to extrapolate the data for higher  $J''$  for all cold and hot bands. The scheme of data interpolation and extrapolation described above was implemented directly to the raw *ab initio* data before fitting the DPL temperature dependences. The reason for this is that the four DPL coefficients are strongly correlated with each other, and even for neighboring  $J''$  and  $v'$  quantum numbers their fitted values can be very different despite similar temperature dependences.

Due to a strong numerical correlation between the DPL coefficients, the uncertainties of the DPL coefficients do not suffice and a full covariance matrix would be needed. For this reason, we do not report an individual uncertainty for every DPL coefficient, but a single uncertainty for the entire DPL function for a given line-shape parameter. The uncertainty consists of two contributions, the first one comes from the DPL approximation, and the second one from *ab initio* calculations. We calculate the DPL contribution as a standard deviation of the difference between the full *ab initio* values of the line-shape parameter and their DPL approximation calculated in the range from 50 to 200 K, see the small panels in Fig. 4. We estimate the uncertainty of our *ab initio* calculations at 1%.

The complete dataset of the line-shape parameters within the DPL representation [30] for the He-perturbed  $\text{H}_2$  lines is given in the supplementary materials [34]; the definition of the reported coefficients is given by Eqs. (7). The lines are ordered with increas-

ing transition energy. The above described format of the uncertainties reported in this work does not fit the standard HITRAN uncertainty codes. For this reason, the error codes in HITRAN will be set to *unreported* (code = 0). Nevertheless, all the uncertainties are reported in the supplementary materials [34] in the columns labelled *DPL-err*. In the supplementary materials [34], we also provide the source *ab initio* data that were used to generate the DPL dataset, i.e., the generalized spectroscopic cross sections and line-shape parameters as a function of temperature.

## 5. Conclusion

We demonstrated a methodology for populating line-by-line spectroscopic databases with beyond-Voigt line-shape parameters that is based on *ab initio* quantum scattering calculations. We provided a comprehensive dataset for the benchmark system of He-perturbed  $\text{H}_2$  (we cover all the rovibrational bands that are present in HITRAN). We extended the previous quantum-scattering calculations by taking into account the centrifugal distortion for all the bands and by including the hot bands. The results were projected on a simple structure of the quadratic speed-dependent hard-collision profile. For each line and each line-shape parameter, we provided a full temperature dependence within the double-power-law (DPL) representation. The temperature dependences cover the range from 20 to 1000 K, which also includes the low temperatures relevant for the studies of the atmospheres of giant planets. We demonstrated that the synthetic spectra generated from our dataset agree with highly accurate experimental spectra collected with cavity ring-down spectrometers at a subpercent accuracy level. The methodology can be applied to many other molecular species important for atmospheric and planetary studies.

## Declaration of Competing Interest

The authors declare that they have no known competing financial interests or personal relationships that could have appeared to influence the work reported in this paper.

## CRediT authorship contribution statement

**P. Wcisło:** Conceptualization, Methodology, Validation, Writing - original draft, Writing - review & editing. **F. Thibault:** Conceptualization, Methodology, Software, Validation, Writing - original draft, Writing - review & editing. **N. Stolarczyk:** Investigation, Visualization, Methodology, Software, Validation, Data curation, Writing - original draft, Writing - review & editing. **H. Jóźwiak:** Investigation, Methodology, Software, Validation, Data curation, Writing - original draft, Writing - review & editing. **M. Słowiński:** Investigation, Visualization, Methodology, Software, Validation, Data curation, Writing - original draft, Writing - review & editing. **M. Gancewski:** Investigation, Software, Validation, Data curation, Writing - original draft, Writing - review & editing. **K. Stankiewicz:** Investigation, Software, Validation, Data curation, Writing - original draft, Writing - review & editing. **M. Konefał:** Validation. **S. Kassi:** Investigation. **A. Campargue:** Investigation. **Y. Tan:** Investigation. **J. Wang:** Investigation. **K. Patkowski:** Investigation, Software, Writing - review & editing. **R. Ciuryło:** Conceptualization, Methodology, Writing - review & editing. **D. Lisak:** Conceptualization, Methodology, Writing - review & editing. **R. Kochanov:** Conceptualization, Methodology, Data curation. **L.S. Rothman:** Conceptualization, Methodology, Data curation, Validation, Writing - review & editing. **I.E. Gordon:** Conceptualization, Methodology, Data curation, Validation, Writing - review & editing.

## Acknowledgements

P.W. was supported by Polish National Science Centre Project No. 2019/35/B/ST2/01118. N.S. and H.J. were supported by Polish National Science Centre Project No. 2018/31/B/ST2/00720. M.S., M.G. and K.S. were supported by the A next-generation worldwide quantum sensor network with optical atomic clocks project carried out within the TEAM IV Programme of the Foundation for Polish Science cofinanced by the European Union under the European Regional Development Fund. S.K. and A.C. acknowledge funding support from the Agence Nationale de la Recherche (Equipex REFIMEVE+ANR-11-EQPX-0039). M.K. and D.L. were supported by Polish National Science Centre Project No. 2015/18/E/ST2/00585. K.P. was supported by U.S. National Science Foundation CAREER award CHE-1351978. The project was cofinanced by the Polish National Agency for Academic Exchange under the PHC Polonium program (dec. PPN/X/PS/318/2018). The research was part of the program of the National Laboratory FAMO in Toruń, Poland. The HITRAN database is supported by NASA AURA NNX17AI78G and NASA PDART NNX16AG51G grants.

## Supplementary material

Supplementary material associated with this article can be found, in the online version, at doi:[10.1016/j.jqsrt.2020.107477](https://doi.org/10.1016/j.jqsrt.2020.107477).

## References

- [1] Dicke R. The effect of collisions upon the Doppler width of spectral lines. *Phys Rev* 1953;89:472–3. doi:[10.1103/PhysRev.89.472](https://doi.org/10.1103/PhysRev.89.472).
- [2] Rautian SG, Sobelman IL. The effect of collisions on the doppler broadening of spectral lines. *Usp Fiz Nauk* 1966;90:209. [*Sov Phys Usp* 1967;9:701]
- [3] Berman PR. Speed-dependent collisional width and shift parameters in spectral profiles. *J Quant Spectrosc Radiat Transf* 1972;12(9):1331–42. doi:[10.1016/0022-4073\(72\)90189-6](https://doi.org/10.1016/0022-4073(72)90189-6).
- [4] Hess S. Kinetic theory of spectral line shapes. The transition between Doppler broadening and collisional broadening. *Physica* 1972;61(1):80–94. doi:[10.1016/0031-8914\(72\)90035-3](https://doi.org/10.1016/0031-8914(72)90035-3).
- [5] Blackmore R. A modified Boltzmann kinetic equation for line shape functions. *J Chem Phys* 1987;87(2):791–800. doi:[10.1063/1.453286](https://doi.org/10.1063/1.453286).
- [6] Ciuryło R, Bielski A, Drummond JR, Lisak D, May AD, Pine AS, et al. Spectral line shapes. In: Back CA, editor. (AIP, Melville, NY); 2002a. p. 151.
- [7] May AD, Liu W-K, McCourt FRW, Ciuryło R, Sanchez-FortStoker J, Shapiro D, et al. The impact theory of spectral line shapes: a paradigm shift. *Can J Phys* 2013;91(11):879–95. doi:[10.1139/cjp-2012-0345](https://doi.org/10.1139/cjp-2012-0345).
- [8] Hartmann J-M, Tran H, Ngo NH, Landsheere X, Chelin P, Lu Y, et al. *Ab initio* calculations of the spectral shapes of CO<sub>2</sub> isolated lines including non-Voigt effects and comparisons with experiments. *Phys Rev A* 2013;87:013403. doi:[10.1103/PhysRevA.87.013403](https://doi.org/10.1103/PhysRevA.87.013403).
- [9] De Vizia MD, Castrillo A, Fasci E, Amodio P, Moretti L, Gianfrani L. Experimental test of the quadratic approximation in the partially correlated speed-dependent hard-collision profile. *Phys Rev A* 2014;90:022503. doi:[10.1103/PhysRevA.90.022503](https://doi.org/10.1103/PhysRevA.90.022503).
- [10] Devi VM, Benner DC, Smith MAH, Mantz AW, Sung K, Crawford TJ, et al. Self- and air-broadened line shape parameters in the  $\nu_2+\nu_3$  band of <sup>12</sup>CH<sub>4</sub>: 4500–4630 cm<sup>-1</sup>. *J Quant Spectrosc Radiat Transf* 2015;152:149–65. doi:[10.1016/j.jqsrt.2014.11.011](https://doi.org/10.1016/j.jqsrt.2014.11.011).
- [11] Campargue A, Karlovets EV, Kassi S. The 4–0 band of carbon monoxide by high sensitivity cavity ring down spectroscopy near 8200 cm<sup>-1</sup>. *J Quant Spectrosc Radiat Transf* 2015;154:113–19. doi:[10.1016/j.jqsrt.2014.12.011](https://doi.org/10.1016/j.jqsrt.2014.12.011).
- [12] Wójtewicz S, Maślowski P, Cygan A, Wcisło P, Zaborowski M, Piwiński M, et al. Speed-dependent effects and Dicke narrowing in nitrogen-broadened oxygen. *J Quant Spectrosc Radiat Transf* 2015;165:68–75. doi:[10.1016/j.jqsrt.2015.06.022](https://doi.org/10.1016/j.jqsrt.2015.06.022).
- [13] Sironneau VT, Hodges JT. Line shapes, positions and intensities of water transitions near 1.28  $\mu$ m. *J Quant Spectrosc Radiat Transf* 2015;152:1–15. doi:[10.1016/j.jqsrt.2014.10.020](https://doi.org/10.1016/j.jqsrt.2014.10.020).
- [14] Bakr BW, Smith DGA, Patkowski K. Highly accurate potential energy surface for the He-H<sub>2</sub> dimer. *J Chem Phys* 2013;139(14):144305. doi:[10.1063/1.4824299](https://doi.org/10.1063/1.4824299).
- [15] Thibault F, Patkowski K, Żuchowski PS, Jóźwiak H, Ciuryło R, Wcisło P. Rovibrational line-shape parameters for H<sub>2</sub> in He and new H<sub>2</sub>-He potential energy surface. *J Quant Spectrosc Radiat Transf* 2017;202:308–20. doi:[10.1016/j.jqsrt.2017.08.014](https://doi.org/10.1016/j.jqsrt.2017.08.014).
- [16] Wcisło P, Ciuryło R. Influence of the interaction potential shape on the Dicke narrowed spectral line profiles affected by speed-dependent collisional broadening and shifting. *J Quant Spectrosc Radiat Transf* 2013;120(0):36–43. doi:[10.1016/j.jqsrt.2013.02.023](https://doi.org/10.1016/j.jqsrt.2013.02.023).
- [17] Wcisło P, Thibault F, Cybulski H, Ciuryło R. Strong competition between velocity-changing and phase- or state-changing collisions in H<sub>2</sub> spectra perturbed by Ar. *Phys Rev A* 2015;91:052505. doi:[10.1103/PhysRevA.91.052505](https://doi.org/10.1103/PhysRevA.91.052505).
- [18] Wcisło P, Gordon IE, Cheng C-F, Hu S-M, Ciuryło R. Collision-induced line-shape effects limiting the accuracy in Doppler-limited spectroscopy of H<sub>2</sub>. *Phys Rev A* 2016a;93:022501. doi:[10.1103/PhysRevA.93.022501](https://doi.org/10.1103/PhysRevA.93.022501).
- [19] Miller CE, Brown LR, Toth RA, Benner DC, Devi VM. Spectroscopic challenges for high accuracy retrievals of atmospheric CO<sub>2</sub> and the orbiting carbon observatory (OCO) experiment. *C R Phys* 2005;6(8):876–87. doi:[10.1016/j.crhy.2005.09.005](https://doi.org/10.1016/j.crhy.2005.09.005).
- [20] Feuchtgruber H, Lellouch E, Orton G, de Graauw T, Vandenbussche B, Swinyard B, et al. The D/H ratio in the atmospheres of Uranus and Neptune from Herschel-PACS observations. *A&A* 2013;551:A126. doi:[10.1051/0004-6361/201220857](https://doi.org/10.1051/0004-6361/201220857).
- [21] Miller-Ricci E, Seager S, Sasselov D. The atmospheric signatures of super-Earths: how to distinguish between hydrogen-rich and hydrogen-poor atmospheres. *Astrophys J* 2008;690(2):1056–67. doi:[10.1088/0004-637x/690/2/1056](https://doi.org/10.1088/0004-637x/690/2/1056).
- [22] Fortney JJ, Robinson T.D., Domagal-Goldman S., Genio A.D.D., Gordon I.E., Gharib-Nezhad E., et al. The need for laboratory measurements and *ab initio* studies to aid understanding of exoplanetary atmospheres. *arXiv:1905.07064* 2019;URL <https://arxiv.org/abs/1905.07064>.
- [23] Hill C, Gordon IE, Kochanov RV, Barrett L, Wilzewski JS, Rothman LS. HITRAN-Nonline: An online interface and the flexible representation of spectroscopic data in the HITRAN database. *J Quant Spectrosc Radiat Transf* 2016;177:4–14. doi:[10.1016/j.jqsrt.2015.12.012](https://doi.org/10.1016/j.jqsrt.2015.12.012).
- [24] Gordon I, Rothman L, Hill C, Kochanov R, Tan Y, Bernath P, et al. The HITRAN2016 molecular spectroscopic database. *J Quant Spectrosc Radiat Transf* 2017;203:3–69. doi:[10.1016/j.jqsrt.2017.06.038](https://doi.org/10.1016/j.jqsrt.2017.06.038).
- [25] Wcisło P, Gordon I, Tran H, Tan Y, Hu S-M, Campargue A, et al. The implementation of non-Voigt line profiles in the HITRAN database: H<sub>2</sub> case study. *J Quant Spectrosc Radiat Transf* 2016b;177:75–91. doi:[10.1016/j.jqsrt.2016.01.024](https://doi.org/10.1016/j.jqsrt.2016.01.024).
- [26] Jóźwiak H, Thibault F, Stolarczyk N, Wcisło P. *Ab initio* line-shape calculations for the S and O branches of H<sub>2</sub> perturbed by He. *J Quant Spectrosc Radiat Transf* 2018;219:313–22. doi:[10.1016/j.jqsrt.2018.08.023](https://doi.org/10.1016/j.jqsrt.2018.08.023).
- [27] Pine AS. Asymmetries and correlations in speed-dependent Dicke-narrowed line shapes of argon-broadened HF. *J Quant Spectrosc Radiat Transf* 1999;62(4):397–423. doi:[10.1016/S0022-4073\(98\)00112-5](https://doi.org/10.1016/S0022-4073(98)00112-5).
- [28] Ngo N, Lisak D, Tran H, Hartmann J-M. An isolated line-shape model to go beyond the Voigt profile in spectroscopic databases and radiative transfer codes. *J Quant Spectrosc Radiat Transf* 2013;129:89–100. doi:[10.1016/j.jqsrt.2013.05.034](https://doi.org/10.1016/j.jqsrt.2013.05.034).
- [29] Tennyson J, Bernath PF, Campargue A, Császár AG, Daumont L, Gamache RR, et al. Recommended isolated-line profile for representing high-resolution spectroscopic transitions (IUPAC technical report). *Pure Appl Chem* 2014;86(12):1931–43. doi:[10.1515/pac-2014-0208](https://doi.org/10.1515/pac-2014-0208).
- [30] Stolarczyk N, Thibault F, Cybulski H, Jóźwiak H, Kowzan G, Vispoel B, et al. Evaluation of different parameterizations of temperature dependences of the line-shape parameters based on *ab initio* calculations: Case study for the HITRAN database. *J Quant Spectrosc Radiat Transf* 2020;240:106676. doi:[10.1016/j.jqsrt.2019.106676](https://doi.org/10.1016/j.jqsrt.2019.106676).
- [31] Showiński M, Thibault F, Tan Y, Wang J, Liu A-W, Hu S-M, et al. H<sub>2</sub>-He collisions: *ab initio* theory meets cavity-enhanced spectra. *Phys Rev A* 2020;101:052705. doi:[10.1103/PhysRevA.101.052705](https://doi.org/10.1103/PhysRevA.101.052705).



- [32] Kochanov R, Gordon I, Rothman L, Wcisło P, Hill C, Wilzewski J. HITRAN Application Programming Interface (HAPI): a comprehensive approach to working with spectroscopic data. *J Quant Spectrosc Radiat Transf* 2016;177:15–30. doi:[10.1016/j.jqsrt.2016.03.005](https://doi.org/10.1016/j.jqsrt.2016.03.005).
- [33] Lellouch E, Bézard B, Fouchet T, Feuchtgruber H, Encrenaz T, de Graauw T. The deuterium abundance in Jupiter and Saturn from ISO-SWS observations. *A&A* 2001;370(2):610–22. doi:[10.1051/0004-6361:20010259](https://doi.org/10.1051/0004-6361:20010259).
- [34] Wcisło P, Thibault F, Stolarczyk N, Jóźwiak H, Słowiński M., Gancewski M., et al. Supplementary material 2020. doi:[10.1016/j.jqsrt.2020.107477](https://doi.org/10.1016/j.jqsrt.2020.107477).
- [35] Long D, Havey D, Okumura M, Miller C, Hodges J. O<sub>2</sub> A-band line parameters to support atmospheric remote sensing. *J Quant Spectrosc Radiat Transf* 2010;111(14):2021–36. doi:[10.1016/j.jqsrt.2010.05.011](https://doi.org/10.1016/j.jqsrt.2010.05.011).
- [36] Devi VM, Benner DC, Smith M, Mantz A, Sung K, Brown L, et al. Spectral line parameters including temperature dependences of self- and air-broadening in the 2-0 band of CO at 2.3  $\mu\text{m}$ . *J Quant Spectrosc Radiat Transf* 2012a;113:1013–33. doi:[10.1016/j.jqsrt.2012.02.010](https://doi.org/10.1016/j.jqsrt.2012.02.010).
- [37] Devi VM, Benner DC, Smith MAH, Mantz AW, Sung K, Brown LR. Spectral line parameters including temperature dependences of air-broadening for the 2-0 bands of <sup>13</sup>C<sup>18</sup>O and <sup>12</sup>C<sup>18</sup>O at 2.3  $\mu\text{m}$ . *J Mol Spectrosc* 2012b;276–277:33–48. doi:[10.1016/j.jms.2012.05.005](https://doi.org/10.1016/j.jms.2012.05.005).
- [38] Li G, Gordon IE, Hajigeorgiou PG, Coxon JA, Rothman LS. Reference spectroscopic data for hydrogen halides, Part II: The line lists. *J Quant Spectrosc Radiat Transf* 2013;130:284–95. doi:[10.1016/j.jqsrt.2013.07.019](https://doi.org/10.1016/j.jqsrt.2013.07.019).
- [39] Domysławska J, Wójtewicz S, Masłowski P, Cygan A, Bielska K, Trawiński RS, et al. A new approach to spectral line shapes of the weak oxygen transitions for atmospheric applications. *J Quant Spectrosc Radiat Transf* 2016;169:111–21. doi:[10.1016/j.jqsrt.2015.10.019](https://doi.org/10.1016/j.jqsrt.2015.10.019).
- [40] Benner DC, Rinsland CP, Devi VM, Smith MAH, Atkins D. A multispectrum nonlinear least squares fitting technique. *J Quant Spectrosc Radiat Transf* 1995;53(6):705–21. doi:[10.1016/0022-4073\(95\)00015-D](https://doi.org/10.1016/0022-4073(95)00015-D).
- [41] Pine A, Ciuryło R. Multispectrum fits of Ar-broadened HF with a generalized asymmetric lineshape: effects of correlation, hardness, speed dependence, and collision duration. *J Mol Spectrosc* 2001;208(2):180–7. doi:[10.1006/jmsp.2001.8375](https://doi.org/10.1006/jmsp.2001.8375).
- [42] Amodio P, Moretti L, Castrillo A, Gianfrani L. Line-narrowing effects in the near-infrared spectrum of water and precision determination of spectroscopic parameters. *J Chem Phys* 2014;140(4):044310. doi:[10.1063/1.4862482](https://doi.org/10.1063/1.4862482).
- [43] Ben-Reuven A. Symmetry considerations in pressure-broadening theory. *Phys Rev* 1966a;141:34–40. doi:[10.1103/PhysRev.141.34](https://doi.org/10.1103/PhysRev.141.34).
- [44] Ben-Reuven A. Impact broadening of microwave spectra. *Phys Rev* 1966b;145:7–22. doi:[10.1103/PhysRev.145.7](https://doi.org/10.1103/PhysRev.145.7).
- [45] Shafer R, Gordon RG. Quantum scattering theory of rotational relaxation and spectral line shapes in H<sub>2</sub>-He gas mixtures. *J Chem Phys* 1973;58(12):5422–43. doi:[10.1063/1.1679162](https://doi.org/10.1063/1.1679162).
- [46] Thibault F, Wcisło P, Ciuryło R. A test of H<sub>2</sub>-He potential energy surfaces. *Eur Phys J D* 2016;70:236. doi:[10.1140/epjd/e2016-70114-9](https://doi.org/10.1140/epjd/e2016-70114-9).
- [47] Martínez RZ, Bermejo D, Thibault F, Wcisło P. Testing the *ab initio* quantum-scattering calculations for the D<sub>2</sub>-He benchmark system with stimulated Raman spectroscopy. *J Raman Spectrosc* 2018;49(8):1339–49. doi:[10.1002/jrs.5391](https://doi.org/10.1002/jrs.5391).
- [48] Monchick L, Hunter LW. Diatomic diatomic molecular collision integrals for pressure broadening and Dicke narrowing: a generalization of Hess's theory. *J Chem Phys* 1986;85(2):713–18. doi:[10.1063/1.451277](https://doi.org/10.1063/1.451277).
- [49] Schaefer J, Monchick L. Line shape cross sections of HD immersed in He and H<sub>2</sub> gas. I. Pressure broadening cross sections. *J Chem Phys* 1987;87(1):171–81. doi:[10.1063/1.453612](https://doi.org/10.1063/1.453612).
- [50] Corey GC, McCourt FR. Dicke narrowing and collisional broadening of spectral lines in dilute molecular gases. *J Chem Phys* 1984;81(5):2318–29. doi:[10.1063/1.447930](https://doi.org/10.1063/1.447930).
- [51] Ward J, Cooper J, Smith EW. Correlation effects in the theory of combined Doppler and pressure broadening - I. Classical theory. *J Quant Spectrosc Radiat Transf* 1974;14(7):555–90. doi:[10.1016/0022-4073\(74\)90036-3](https://doi.org/10.1016/0022-4073(74)90036-3).
- [52] Lisak D, Hodges JT, Ciuryło R. Comparison of semiclassical line-shape models to rovibrational H<sub>2</sub>O spectra measured by frequency-stabilized cavity ring-down spectroscopy. *Phys Rev A* 2006;73:012507. doi:[10.1103/PhysRevA.73.012507](https://doi.org/10.1103/PhysRevA.73.012507).
- [53] Wcisło P, Thibault F, Zaborowski M, Wójtewicz S, Cygan A, Kowzan G, et al. Accurate deuterium spectroscopy for fundamental studies. *J Quant Spectrosc Radiat Transf* 2018;213:41–51. doi:[10.1016/j.jqsrt.2018.04.011](https://doi.org/10.1016/j.jqsrt.2018.04.011).
- [54] Rohart F, Włodarczak G, Colmont J-M, Cazzoli G, Dore L, Puzzarini C. Galatry versus speed-dependent Voigt profiles for millimeter lines of O<sub>3</sub> in collision with N<sub>2</sub> and O<sub>2</sub>. *J Mol Spectrosc* 2008;251(1):282–92. doi:[10.1016/j.jms.2008.03.005](https://doi.org/10.1016/j.jms.2008.03.005).
- [55] Konefał M, Słowiński M, Zaborowski M, Ciuryło R, Lisak D, Wcisło P. Analytical-function correction to the Hartmann Tran profile for more reliable representation of the Dicke-narrowed molecular spectra. *J Quant Spectrosc Radiat Transf* 2020;242:106784. doi:[10.1016/j.jqsrt.2019.106784](https://doi.org/10.1016/j.jqsrt.2019.106784).
- [56] Tran H, Ngo N, Hartmann J-M. Efficient computation of some speed-dependent isolated line profiles. *J Quant Spectrosc Radiat Transf* 2013;129:199–203. doi:[10.1016/j.jqsrt.2013.06.015](https://doi.org/10.1016/j.jqsrt.2013.06.015).
- [57] Kowzan G, Wcisło P, Słowiński M, Masłowski P, Viel A, Thibault F. Fully quantum calculations of the line-shape parameters for the Hartmann-Tran profile: A CO-Ar case study. *J Quant Spectrosc Radiat Transf* 2020;243:106803. doi:[10.1016/j.jqsrt.2019.106803](https://doi.org/10.1016/j.jqsrt.2019.106803).
- [58] Private communication with J.-M. Hartmann. 2018.
- [59] Wcisło P, Lisak D, Ciuryło R, Pine AS. Multispectrum-fitting of phenomenological collisional line-shape models to a speed-dependent Blackmore profile for spectroscopic analysis and databases. *J Phys* 2017;810:012061. doi:[10.1088/1742-6596/810/1/012061](https://doi.org/10.1088/1742-6596/810/1/012061).
- [60] Ngo N, Hartmann J-M. A strategy to complete databases with parameters of refined line shapes and its test for CO in He, Ar and Kr. *J Quant Spectrosc Radiat Transf* 2017;203:334–40. doi:[10.1016/j.jqsrt.2017.01.031](https://doi.org/10.1016/j.jqsrt.2017.01.031). HITRAN2016 Special Issue
- [61] Słowiński M., et al. In preparation.
- [62] Martínez RZ, Bermejo D, Wcisło P, Thibault F. Accurate wavenumber measurements for the S<sub>0</sub>(0), S<sub>0</sub>(1), and S<sub>0</sub>(2) pure rotational Raman lines of D<sub>2</sub>. *J Raman Spectrosc* 2019;50(1):127–9. doi:[10.1002/jrs.5499](https://doi.org/10.1002/jrs.5499).
- [63] Thibault F, Martínez RZ, Bermejo D, Wcisło P. Line-shape parameters for the first rotational lines of HD in He. *Mol Astrophys* 2020;19:100063. doi:[10.1016/j.molap.2020.100063](https://doi.org/10.1016/j.molap.2020.100063).
- [64] Stankiewicz K, Jóźwiak H, Gancewski M, Stolarczyk N, Thibault F, Wcisło P. *Ab initio* calculations of collisional line-shape parameters and generalized spectroscopic cross-sections for rovibrational dipole lines in HD perturbed by He. *J Quant Spectrosc Radiat Transf* 2020;254:107194. doi:[10.1016/j.jqsrt.2020.107194](https://doi.org/10.1016/j.jqsrt.2020.107194).
- [65] Jóźwiak H., Gancewski M., Stankiewicz K., Wcisło P. BIGOS computer code, to be published.
- [66] Johnson BR. The renormalized Numerov method applied to calculating bound states of the coupled-channel Schrödinger equation. *J Chem Phys* 1978;69(10):4678–88. doi:[10.1063/1.436421](https://doi.org/10.1063/1.436421).
- [67] Rohart F, Nguyen L, Buldyreva J, Colmont J-M, Włodarczak G. Lineshapes of the 172 and 602 GHz rotational transitions of HC<sup>15</sup>N. *J Mol Spectrosc* 2007;246(2):213–27. doi:[10.1016/j.jms.2007.09.009](https://doi.org/10.1016/j.jms.2007.09.009).
- [68] Lisak D, Cygan A, Wcisło P, Ciuryło R. Quadratic speed dependence of collisional broadening and shifting for atmospheric applications. *J Quant Spectrosc Radiat Transf* 2015;151:43–8. doi:[10.1016/j.jqsrt.2014.08.016](https://doi.org/10.1016/j.jqsrt.2014.08.016).
- [69] Ciuryło R, Shapiro DA, Drummond JR, May AD. Solving the line-shape problem with speed-dependent broadening and shifting and with Dicke narrowing. II. Application. *Phys Rev A* 2002b;65:012502. doi:[10.1103/PhysRevA.65.012502](https://doi.org/10.1103/PhysRevA.65.012502).

# *Ab initio* investigation of the CO–N<sub>2</sub> quantum scattering: The collisional perturbation of the pure rotational R(0) line in CO

Cite as: J. Chem. Phys. **154**, 054314 (2021); <https://doi.org/10.1063/5.0040438>

Submitted: 13 December 2020 • Accepted: 14 January 2021 • Published Online: 05 February 2021

 Hubert Jóźwiak,  Franck Thibault,  Hubert Cybulski, et al.



View Online



Export Citation



CrossMark

## ARTICLES YOU MAY BE INTERESTED IN

Fully quantum calculations of O<sub>2</sub>–N<sub>2</sub> scattering using a new potential energy surface:  
Collisional perturbations of the oxygen 118#GHz fine structure line

The Journal of Chemical Physics **155**, 124307 (2021); <https://doi.org/10.1063/5.0063006>

$\Delta$ -machine learning for potential energy surfaces: A PIP approach to bring a DFT-based PES  
to CCSD(T) level of theory

The Journal of Chemical Physics **154**, 051102 (2021); <https://doi.org/10.1063/5.0038301>

Rate constants for the H<sup>+</sup> + H<sub>2</sub> reaction from 5 K to 3000 K with a statistical quantum  
method

The Journal of Chemical Physics **154**, 054310 (2021); <https://doi.org/10.1063/5.0039629>



# *Ab initio* investigation of the CO–N<sub>2</sub> quantum scattering: The collisional perturbation of the pure rotational R(0) line in CO

Cite as: J. Chem. Phys. 154, 054314 (2021); doi: 10.1063/5.0040438

Submitted: 13 December 2020 • Accepted: 14 January 2021 •

Published Online: 5 February 2021



Hubert Jóźwiak,<sup>1,a)</sup> Franck Thibault,<sup>2</sup> Hubert Cybulski,<sup>3</sup> and Piotr Wcisło<sup>1,b)</sup>

## AFFILIATIONS

<sup>1</sup>Institute of Physics, Faculty of Physics, Astronomy and Informatics, Nicolaus Copernicus University in Toruń, Grudziadzka 5, 87-100 Toruń, Poland

<sup>2</sup>Univ. Rennes, CNRS, IPR (Institut de Physique de Rennes)-UMR 6251, Rennes F-35000, France

<sup>3</sup>Institute of Physics, Kazimierz Wielki University, ul. Powstańców Wielkopolskich 2, 85-090 Bydgoszcz, Poland

<sup>a)</sup>Author to whom correspondence should be addressed: [hubert.jozwiak@doktorant.umk.pl](mailto:hubert.jozwiak@doktorant.umk.pl)

<sup>b)</sup>Electronic mail: [piotr.wcislo@umk.pl](mailto:piotr.wcislo@umk.pl)

## ABSTRACT

We report fully quantum calculations of the collisional perturbation of a molecular line for a system that is relevant for Earth's atmosphere. We consider the N<sub>2</sub>-perturbed pure rotational R(0) line in CO. The results agree well with the available experimental data. This work constitutes a significant step toward populating the spectroscopic databases with *ab initio* collisional line-shape parameters for atmosphere-relevant systems. The calculations were performed using three different recently reported potential energy surfaces (PESs). We conclude that all three PESs lead to practically the same values of the pressure broadening coefficients.

Published under license by AIP Publishing. <https://doi.org/10.1063/5.0040438>

## I. INTRODUCTION

Detailed knowledge about the interaction energy in molecular systems is crucial for understanding a variety of physical phenomena. An accurate potential energy surface (PES) is important for the calculations of bound states of molecular complexes,<sup>1</sup> understanding the dynamics of the interstellar medium,<sup>2</sup> proper interpretation of collisionally induced spectra,<sup>3</sup> and determination of shapes of the optical molecular resonances.<sup>4</sup> Nitrogen molecule, as the main constituent of Earth's atmosphere, is of particular importance for the spectroscopic community. Collisions with N<sub>2</sub> can perturb the absorption lines of less abundant molecules in the atmosphere, leading to the pressure broadening (and shift) of the spectra, and constitute the primary broadening mechanism in the troposphere.<sup>5</sup> Accurate values of pressure broadening and shift coefficients are essential for reducing atmospheric-spectra fit residuals,<sup>6</sup> which might affect values of the quantities retrieved from the fit, such as the volume mixing ratio (VMR)<sup>6,7</sup> of the absorbing compound. This is especially important in terms of remote sensing applications, as

subpercent accuracy of the VMR is needed to reliably identify the sources and sinks of the greenhouse gases.<sup>8,9</sup> Carbon monoxide is a trace gas in Earth's atmosphere, which has an indirect impact on the concentration of methane. Indeed, CO reacts with hydroxyl radicals (·OH) and reduces their abundance in the atmosphere, which, in turn, leads to higher concentration of the CH<sub>4</sub> molecules.<sup>10,11</sup> Carbon monoxide is also an important gaseous pollutant and a useful tracer of various anthropogenic activities, such as fossil fuel combustion.<sup>12–14</sup>

Apart from remote sensing measurements, accurate pressure broadening coefficients of the nitrogen-perturbed CO lines are of particular importance in the analysis of the atmospheres of various objects in the outer solar system. The atmosphere of Titan, the largest moon of Saturn, is dominated by nitrogen (94.2%) and methane (5.65%).<sup>15,16</sup> Trace amounts of the CO molecule were discovered there by Lutz *et al.*,<sup>17</sup> who identified several P and R lines of the 3–0 band from ground-based measurements. To accurately determine the CO concentration in Titan's atmosphere, several studies were pursued, where pure rotational transitions,<sup>18,19</sup> in



particular the R(0),<sup>20–23</sup> R(1),<sup>23,24</sup> and R(2)<sup>23,25</sup> lines, as well as transitions from the fundamental band, were investigated.<sup>26–28</sup> Currently,<sup>29</sup> the most accurate values of the VMR of carbon monoxide come from ground-based measurements using the Submillimeter Array,<sup>25</sup> from the SPIRE instrument on the Herschel satellite,<sup>30</sup> and the Composite Infrared Spectrometer (CIRS) on board the Cassini probe<sup>19</sup> and are given by  $(5.1 \pm 0.4) \times 10^{-5}$ ,  $(4.0 \pm 0.5) \times 10^{-5}$ , and  $(4.7 \pm 0.8) \times 10^{-5}$ , respectively. In all these investigations, the experimental values<sup>31–34</sup> of the pressure broadening coefficients of the N<sub>2</sub>-perturbed CO lines were necessary to properly interpret the measured spectra.

Carbon monoxide was also detected in the nitrogen-dominated<sup>35</sup> atmosphere of Triton, the largest moon of Neptune.<sup>36</sup> The ground-based spectroscopic observations of Triton in the 2.32  $\mu\text{m}$ –2.37  $\mu\text{m}$  region, using the European Southern Observatory Very Large Telescope (ESO VLT), determined the abundance of CO and CH<sub>4</sub> to be at a level of a few hundredths of a percent of that of nitrogen. Accurate information about the relative abundance of CO and CH<sub>4</sub> is especially needed for the analysis of seasonal changes in Triton's atmosphere<sup>37</sup> and could be a subject of interest for future orbital missions to Neptune.<sup>38</sup> The atmosphere of Pluto shares some similarities to those of Triton and Titan, as it consists mostly of nitrogen, with trace amounts of methane (0.25%) and carbon monoxide.<sup>39</sup> Searches for the CO features in the atmospheric spectra of Pluto were subjects of various investigations in the millimeter<sup>40–43</sup> and near-IR ranges.<sup>44,45</sup> The analysis of the pure rotational R(2) line by Lellouch *et al.* indicated a CO mole fraction of  $515 \pm 40$  ppm for a surface pressure of 12  $\mu\text{bars}$ .<sup>43</sup>

As a molecular complex, the CO–N<sub>2</sub> system was a subject of thorough theoretical and experimental investigations throughout the past years. The first pure rotational spectra of the CO–N<sub>2</sub> complex were observed in 1996<sup>46,47</sup> in the IR region. These works were followed by studies of the microwave and millimeter transitions in the complex,<sup>48–52</sup> and several studies devoted to the transitions in the IR region.<sup>53,54</sup> We recall also two very recent studies of this complex in the millimeter range,<sup>55,56</sup> which provided an accurate test of the recently reported PESs.<sup>55,57,58</sup>

The theoretical investigations on the CO–N<sub>2</sub> complex were reviewed in more detail in a previous paper.<sup>57</sup> Here, we only recall the importance of the study conducted by Fišer and Polák,<sup>59</sup> who investigated multiple orientations of the complex using the coupled-cluster singles and doubles including connected triple corrections [CCSD(T)] and the Møller–Plesset (MP) perturbation theory up to fourth order. The first four-dimensional (4D) PES was reported by Karimi-Jafari *et al.*,<sup>60</sup> who employed the MP4 method with a basis set obtained from Dunning's aug-cc-pVQZ basis set. In this investigation, the g and f functions were removed from the original basis set and, additionally, a set of 3s3p2d1f midbond functions was used. Nonetheless, as it was stated in Ref. 57, due to the method used, reduction in the basis set, and too small number of grid points chosen by the authors, this PES should not be considered reliable enough to study various physical phenomena. Recently, three highly accurate PESs were reported.<sup>55,57,58</sup> Liu *et al.*<sup>58</sup> calculated a 5D PES using the CCSD(T)-F12 method and the aug-cc-pVQZ basis set, claiming the discrepancies between theoretical and experimental energies of the IR transitions of the CO–N<sub>2</sub> complex to be smaller than  $0.068 \text{ cm}^{-1}$ . Surin *et al.*<sup>55</sup> reported a 4D

PES calculated using the standard CCSD(T) method and the aug-cc-pVQZ basis set, supplemented with 3s2p1d midbond functions. The accompanying experimental results enabled the authors to assign several newly detected transitions. However, some significant discrepancies between the calculated and experimental rotational states were observed. The third, more recent potential,<sup>57</sup> was calculated using the CCSD(T) method with the aug-cc-pVQZ basis set, extended with the 3s3p2d1f1g midbond functions. This 4D PES was fit to an analytical expression,<sup>57</sup> which performs well for geometries where the interaction energy does not exceed  $100 \mu\text{E}_h$ . The agreement between the theoretical and experimental values of the energy levels is significantly better than that for all the aforementioned PESs.

Collisional broadening of the CO lines by nitrogen molecules has been studied in detail both theoretically and experimentally. A majority of the experimental data refers to the lines in the fundamental band of CO.<sup>33,34,61–89</sup> N<sub>2</sub>-perturbed CO lines were also measured for the first<sup>84,90–94</sup> and second overtones.<sup>65,95–97</sup> In the case of pure rotational transitions, the pressure broadening coefficients of the N<sub>2</sub>-perturbed lines were determined for the first five R lines of CO. The first measurements of the nitrogen-, oxygen-, and air-broadened widths of the R(0) line were reported by Connor and Radford<sup>98</sup> and by Colmont and Monnanteuil.<sup>31</sup> These results were refined by Nissen *et al.*<sup>99</sup> in a comparative study of foreign-gas pressure broadening of the R(0) line, using Fourier-transform and radio-acoustical detection spectrometers. There are also a few papers regarding foreign-gas broadening of the R(1),<sup>32</sup> R(2)<sup>100</sup>, and R(4)<sup>101,102</sup> CO lines, in which a temperature dependence of the N<sub>2</sub> broadening coefficients was determined. Puzzarini *et al.*<sup>103</sup> reported a thorough study of various line-shape models in the analysis of the N<sub>2</sub>- and O<sub>2</sub>-broadened R(0–3) lines at 296 K. The pressure broadening coefficients of the N<sub>2</sub>-perturbed CO lines from the S branch were also determined using coherent anti-Stokes Raman scattering (CARS) spectroscopy.<sup>104</sup>

It has been recently shown for a benchmark system of helium-perturbed H<sub>2</sub> that a full *ab initio* description of the shapes of rovibrational transitions leads to subpercent agreement with experimentally measured spectra.<sup>105</sup> This successful theoretical approach is based on a very accurate PES, determined from first principles,<sup>106,107</sup> quantum-scattering calculations, and a state-of-the-art model of collision-perturbed shape of rovibrational resonance,<sup>108–111</sup> which includes the speed-dependence of line broadening and shift<sup>112</sup> and the influence of velocity changing collisions.<sup>113</sup> Helium-perturbed H<sub>2</sub> lines were subjects of several recent investigations. In Ref. 114, the influence of PESs' quality on shapes of particular rovibrational lines was studied in detail. The most accurate PES for this system and line-shape parameters for the rovibrational Q lines were reported in Ref. 107. Shapes of optical resonances from the O and S branches were determined in Ref. 115. Importance of centrifugal distortion (the dependence of the radial coupling terms of the PES on the rotational quantum number) was studied in Ref. 116. Finally, the first comprehensive database of the line-shape parameters (broadening, shift, their speed-dependence, and the complex Dicke parameter), generated from *ab initio* calculations, was reported in Ref. 117. The same methodology was applied to the cases of helium-perturbed lines of HD<sup>118,119</sup> and D<sub>2</sub>.<sup>120,121</sup> Recently, subpercent agreement with the experimental shapes of Ar-perturbed rovibrational lines in CO was achieved.<sup>122</sup>

Here, we report the *ab initio* quantum-scattering calculations of the collision-perturbed shape of the molecular line for a system that is relevant for the terrestrial atmosphere. We investigate the width of the N<sub>2</sub>-perturbed pure rotational R(0) line in CO. Scattering calculations are performed using three PESs.<sup>55,57,58</sup> Our results are in good agreement with the available experimental data.<sup>31,98,99,103</sup> The shape of the pure rotational R(0) line is dominated by the collisional broadening, which is two orders of magnitude larger than the pressure induced shift. Hence, in this paper, we do not consider the pressure shift coefficient. Due to the complex structure of the close-coupled (CC) equations and a large number of channels that must be taken into account, the equations are solved using the coupled states approximation (CSA).<sup>123</sup>

This paper is organized as follows: in Sec. II, we briefly describe the PESs used in the calculations. In Sec. III, we discuss the details of the scattering calculations and we analyze the obtained generalized spectroscopic cross sections. In Sec. IV, we describe the calculations of the pressure broadening coefficient, and in Sec. V, we compare our results with the experimental data. We discuss the accuracy of our calculations in Sec. VI, and in Sec. VII, we summarize our results.

## II. POTENTIAL ENERGY SURFACE

The PES for a system consisting of two rigid diatomic molecules (A and B) depends on four variables: the intermolecular distance between the centers of mass of the molecules,  $R$ , the angles between each of the molecular axes and the intermolecular axis,  $\theta_A$  and  $\theta_B$ , and the dihedral angle,  $\phi$ . Let us identify subscripts A and B with CO and N<sub>2</sub> molecules, respectively. The definition of the angles is presented in Fig. 1. Contrary to the PESs of Surin *et al.*<sup>55</sup> and Cybulski *et al.*,<sup>57</sup> which are 4D, the PES of Liu *et al.*<sup>58</sup> additionally takes into account the stretching of the CO molecule. However, for the purpose of these calculations (we investigate a pure rotational transition in the ground vibrational state of CO), we do not consider any changes in the intramolecular distance of the molecule.

In order to reduce the potential to a form suitable for the scattering calculations, the 4D PES is expanded over bispherical harmonics:

$$V(R, \theta_A, \theta_B, \phi) = \sum_{l_A, l_B, l} A_{l_A, l_B, l}(R) I_{l_A, l_B, l}(\theta_A, \theta_B, \phi). \quad (1)$$

The radial terms of the potential are denoted as  $A_{l_A, l_B, l}$ , and the bispherical harmonics,  $I_{l_A, l_B, l}$ , are defined as

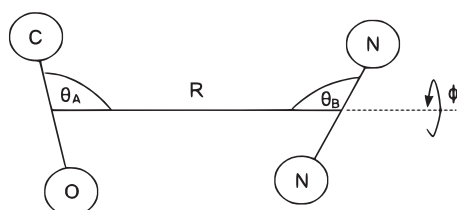


FIG. 1. Geometry of the CO–N<sub>2</sub> system.

$$I_{l_A, l_B, l}(\theta_A, \theta_B, \phi) = \sqrt{\frac{2l+1}{4\pi}} \sum_m (l_A m l_B - m | l_A l_B l 0) \times Y_{l_A, m}(\theta_A, \phi_A) Y_{l_B, -m}(\theta_B, \phi_B), \quad (2)$$

where  $Y_{l, m}(\theta_i, \phi_i)$  are spherical harmonics and  $(l_i m l_j - m | l_i l_j l 0)$  are the Clebsch–Gordan coefficients. In the case of the CO–N<sub>2</sub> system,  $l_A$  is a non-negative integer,  $l_B$  is a non-negative integer that takes only even values, and  $l$  satisfies the triangular condition  $|l_A - l_B| \leq l \leq l_A + l_B$ . Additionally, the sum of these three indices is an even integer.

The radial terms of the potential,  $A_{l_A, l_B, l}(R)$ , are obtained by the integration of the product of the bispherical harmonics and the full PES, over the angles  $\theta_A$ ,  $\theta_B$ , and  $\phi$ .<sup>124</sup>

$$A_{l_A, l_B, l}(R) = \frac{8\pi^2}{2l+1} \int_0^{2\pi} d\phi \int_0^\pi d\theta_A \sin \theta_A \int_0^\pi d\theta_B \sin \theta_B \times V(R, \theta_A, \theta_B, \phi) I_{l_A, l_B, l}(\theta_A, \theta_B, \phi). \quad (3)$$

In the cases of Liu's<sup>58</sup> and Surin's<sup>55</sup> PESs, we used their analytical fits. In the case of Cybulski's PES,<sup>57</sup> the reliable fit is limited to energies smaller than 100  $\mu\text{E}_h$ ; hence, we interpolated the original 10 000 energy points (which covered the intermolecular distances from 5.0 to 30.0  $a_0$ ) with the reproducing kernel Hilbert space method (RKHS).<sup>125</sup> The values of the smoothness parameter,  $n$ , and the parameter that determines the long-range behavior of the radial terms,  $m$ , were set to the same values as the ones used in the paper of Surin *et al.*<sup>55</sup>

Finally, all the three PESs were prepared in a form of 205 radial terms, up to the term with  $l_A = 10$ ,  $l_B = 8$ , and  $l = 18$ . The grid of the intermolecular distances for which the radial terms were calculated consisted of 230 points, from 4.25  $a_0$  to 50  $a_0$ . Figure 2 presents a comparison between isotropic and (two) anisotropic contributions to the three PESs in the vicinity of the minimum of the isotropic component.

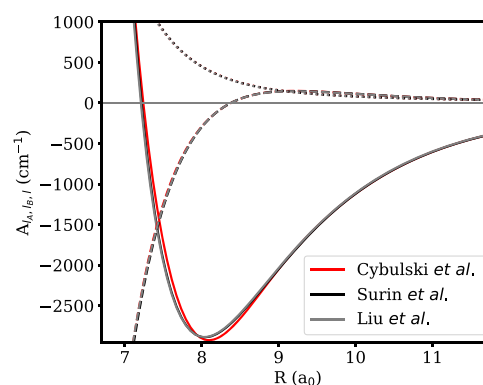


FIG. 2. Comparison between isotropic ( $l_A, l_B, l = 0, 0, 0$ , solid lines) and anisotropic ( $l_A, l_B, l = 1, 0, 1$ , dashed lines and  $l_A, l_B, l = 2, 2, 4$ , dotted lines) radial terms of the three considered PESs.<sup>55,57,58</sup> The two curves corresponding to the isotropic terms of Surin's and Liu's PES, as well as the curves representing the anisotropic terms for all the three PESs, are overlapping.

## III. QUANTUM-SCATTERING CALCULATIONS

The quantum-scattering theory of two rigid diatomic molecules in a  $^1\Sigma$  electronic state is well-known and thoroughly discussed in the literature.<sup>124,126–129</sup> Here, we briefly summarize the issue and we connect the results of the scattering calculations with the generalized spectroscopic cross section.

The total wavefunction of the system is expanded in a basis set discussed in Ref. 124 or in Ref. 129. The expansion separates the intermolecular distance and the angles describing the geometry of the two diatomics. A substitution of the expanded form of the wavefunction into the Schrödinger equation leads to a set of CC equations for the radial part of the total wavefunction [see Eq. (9) in Ref. 124]. The equations are solved numerically for a wide range of kinetic energies. Boundary conditions on the radial part of the total wavefunction connect the solutions of the coupled equations with the scattering S-matrix [see Eq. (11) of Ref. 128]. The elements of the scattering S-matrix enter the formulas for the generalized spectroscopic cross section, whose real and imaginary parts are called the pressure broadening and shift cross section, respectively.<sup>130,131</sup>

In contrast to simpler systems of molecule–atom<sup>107,115,120,132</sup> or molecule–molecule with large rotational constants,<sup>109</sup> for a system of two diatomic molecules typical for Earth's atmosphere, the number of basis levels (necessary to converge numerical calculations) grows considerably with the relative kinetic energy of the colliding pair. At present, this effectively hinders the possibility to study the room-temperature collisions. The memory resources and the CPU time required to perform such calculations exceed capabilities of typical work stations. It has enforced us to use an approximate method of solving the CC equations.

There are several well-known methods for simplifying the coupled equations.<sup>123,133–141</sup> In this work, we have made use of the widely used coupled states (CS) approximation.<sup>123</sup> The theory behind the formulas is well-known, and the review of the literature can be found in Chap. 9 of Ref. 142.

In the body-fixed frame of reference, the relative angular momentum operator,  $\mathbf{I}^2$ , couples channels with different values of the projection of the  $\mathbf{j}_{12}$  angular momentum,  $\Omega$ , on the intermolecular axis, where  $\mathbf{j}_{12}$  is the result of coupling of the rotational angular momentum of the two diatomic molecules,  $\mathbf{j}_{12} = \mathbf{j}_1 + \mathbf{j}_2$ . Within the most common version of the CS approximation, the off-diagonal matrix elements of the relative angular momentum operator,  $\mathbf{I}^2$ , coupling different values of  $\Omega$ , are neglected. This leads to the coupled equations that are diagonal with respect to this quantum number and immensely speeds up the calculations. Additionally, a new quantum number,  $\bar{l}$ , which approximates the diagonal matrix elements of the relative angular momentum operator as  $\bar{l}(\bar{l} + 1)$ , is introduced. This quantum number is used instead of the total angular momentum,  $J$ . Finally, within the CS approximation, the coupled equations are block-diagonal with respect to  $\bar{l}$  and  $\Omega$ .

The rest of the procedure is similar to the case without the approximations. The S-matrix elements [connected with the space-fixed S-matrix elements by a unitary transformation, see Eq. (44) of Ref. 143 and the discussion therein] are obtained, and the generalized spectroscopic cross section is calculated. Due to the unitary transformation between the S-matrix elements

obtained within the CS approximation and calculated exactly in the space-fixed frame of reference, the formula for the generalized spectroscopic cross section is quite different [see Eq. (96) of Ref. 144],

$$\begin{aligned} \sigma_0^q(j_i, j_f, j'_i, j'_f, j_2, E_{\text{kin}}) &= \frac{\pi}{k^2} \sqrt{\frac{2j'_i + 1}{2j_i + 1}} \sum_{\bar{l}, \Omega, \Omega'} \sum_{j_2, j_{12}, j'_{12}, j'_{12}} (-1)^{j_{12} + j'_{12} + \bar{j}_{12} + j'_{12}} \\ &\times (2\bar{l} + 1) \sqrt{[j_{12}][j'_{12}][\bar{j}_{12}][\bar{j}'_{12}]} \begin{pmatrix} j'_{12} & \bar{j}'_{12} & q \\ -\Omega' & -\Omega' & \Omega' - \Omega \end{pmatrix} \\ &\times \begin{pmatrix} j_{12} & \bar{j}_{12} & q \\ \Omega & -\Omega' & \Omega' - \Omega \end{pmatrix} \begin{pmatrix} j'_{12} & \bar{j}'_{12} & q \\ j'_i & j'_f & j'_2 \end{pmatrix} \begin{pmatrix} j_{12} & \bar{j}_{12} & q \\ j_i & j_f & j_2 \end{pmatrix} \\ &\times [\delta_{j_{12}j'_{12}} \delta_{\bar{j}_{12}\bar{j}'_{12}} \delta_{j_2j'_2} \delta_{j_{12}j'_2} - \langle j_{12}j_{12} | S_{\Omega}^{\text{CS}}(E_T) | j'_i j'_f j'_2 \rangle \\ &\times \langle j_f j_2 \bar{j}_{12} | S_{\Omega'}^{\text{CS}*}(E_T) | j'_f j'_2 \bar{j}'_{12} \rangle], \end{aligned} \quad (4)$$

where  $[x] = 2x + 1$ , the quantities in parentheses are Wigner 3- $j$  symbols, and the quantities in braces are Wigner 6- $j$  symbols. If line-mixing effects are not considered, the cross sections are calculated with  $j_i = j'_i$  and  $j_f = j'_f$ , which denote the initial and final states, respectively, of the spectroscopic transition. For the dipole R line analyzed in this work, the tensor order of the radiation–matter interaction,  $q$ , is equal to 1.

The results presented here were obtained by solving the coupled equations, within the CS approximation, using the MOLSCAT code.<sup>145</sup> The modified log-derivative algorithm of Manolopoulos<sup>146</sup> was used, with propagation beginning deeply in the repulsive wall of the potential at  $R = 4.25 a_0$  and ending at  $R = 100 a_0$ . The radial coupling terms of the PES were extrapolated for  $R > 50 a_0$  in a  $C_n/R^n$  form, where  $C_n$  and  $n$  were obtained from the fit using the long-range part of the  $A_{\text{A},\text{B},\text{J}}(R)$  terms. We took advantage of the fact that there are two spin isomers of the nitrogen molecule, which give rise to two different symmetries of the rotational wavefunction. *ortho*-N<sub>2</sub>, with total nuclear spin  $I = 0$  or  $I = 2$ , exhibits a rotational structure, which involves only even  $j$  values, while *para*-N<sub>2</sub>, with  $I = 1$ , yields rotational levels, which correspond to odd  $j$  values. This allowed us to perform scattering calculations with these two species independently and, thus, to reduce the basis set. At least two asymptotically closed levels  $[(j_1; j_2)$  states, the energy of which is larger than the total energy of the scattering system and are, thus, energetically inaccessible at large intermolecular distances] were kept throughout the calculations. The rotational energy levels of both molecules were taken from the HITRAN database.<sup>147</sup> The generalized spectroscopic cross sections were obtained using the newly developed FORTRAN code.<sup>148</sup>

It is difficult to obtain, for a given relative kinetic energy, converged values of the imaginary part of  $\sigma_0^1$ . The pressure shift cross section is very sensitive to the range and step of the propagator and the number of asymptotically closed channels in the basis set (see Sec. 5 of Ref. 115 and Sec. 4 of Ref. 119). The susceptibility of  $\text{Im}(\sigma_0^1)$  to these factors is especially pronounced in the molecule–molecule scattering systems and might lead to relatively large uncertainties of the resulting pressure shift coefficients. This is the case for, analyzed here, the N<sub>2</sub>-perturbed pure rotational R(0) line in CO. However, the pressure shift is at least two orders of magnitude smaller than

the collisional broadening of this particular line, and it has not been detected in any experiment.<sup>31,98,99,103</sup> Thus, in this study, we focus on the real part of  $\sigma_0^1$  and the resulting pressure broadening coefficient,  $\gamma$  [see Eq. (6)].

We begin the discussion with a comparison of the pressure broadening cross sections obtained using three different PESs. Figure 3 presents the dependence of  $\sigma_0^1$  on kinetic energy for  $j_2 = 0$ . For this particular value of  $j_2$ , we were able to calculate the cross sections for the widest range of relative kinetic energies. As it can be seen in Fig. 3, all the three PESs result in almost the same values of the pressure broadening cross sections (the largest relative difference between the cross sections is at a level of 1.5%). The same situation occurs for higher values of  $j_2$ , with relative differences between the values of  $\sigma_0^1$  obtained with different PESs being at the level of 1%. Due to very small differences between the pressure broadening cross sections, in the following analysis, we will focus on the results obtained with the PES of Cybulski *et al.*<sup>57</sup>

Figure 4 presents the kinetic energy dependence of the calculated generalized spectroscopic cross sections for various rotational levels of the perturber,  $j_2$ . The range of the kinetic energies, for which the calculations of  $\sigma_0^1$  are feasible, strongly depends on  $j_2$ . For example, for  $j_2 = 0$ , we were able to calculate the cross sections up to kinetic energy values of 400  $\text{cm}^{-1}$ ; for  $j_2 = 7$ , up to 250  $\text{cm}^{-1}$ ; and for  $j_2 = 12$ , up to 120  $\text{cm}^{-1}$ . We note that, at large kinetic energies, the dependencies are linear on the log-log plot. This type of relation has already been reported in the studies of the argon-perturbed CO lines,<sup>122,149,150</sup> as well as in the studies of the Ar-perturbed CO<sub>2</sub><sup>151</sup> or H<sub>2</sub>-perturbed N<sub>2</sub><sup>152</sup> isotropic Raman lines. Moreover, it is seen from Fig. 4 that, for a given relative kinetic energy, the pressure broadening cross sections become  $j_2$ -independent for larger  $j_2$ . A tentative explanation for such behavior of the cross sections is as follows. The PBXS for this system is essentially determined by the contribution from the inelastic state-to-state cross sections (fact that we have checked making use of the random phase approximation<sup>151,153,154</sup>). This is even more evident for larger  $j_2$  values since the N<sub>2</sub> molecule rotates faster and averages the long-range anisotropic components of the PES, resulting in a small elastic dephasing

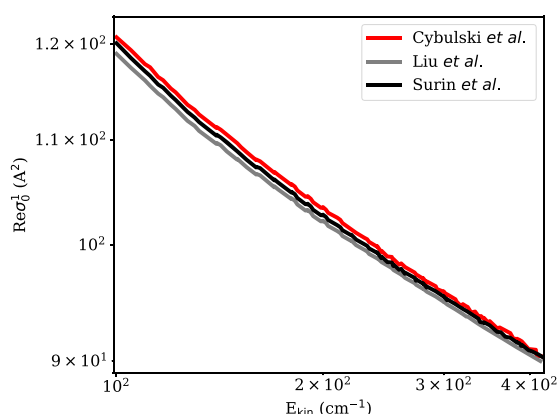


FIG. 3. Comparison between pressure broadening cross sections for  $j_2 = 0$  calculated using three different PESs.<sup>55,57,58</sup>

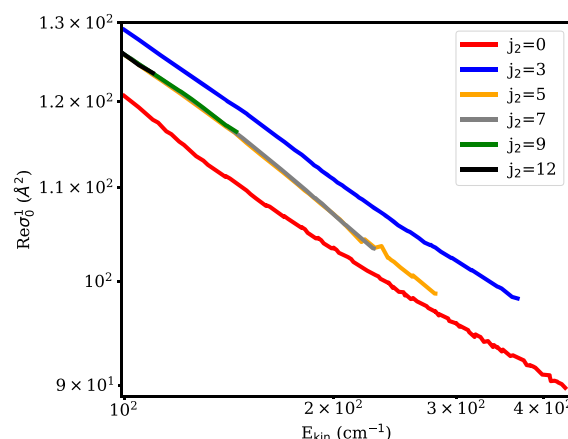


FIG. 4. Pressure broadening cross sections as a function of relative kinetic energy for several values of  $j_2$ . The cross sections were calculated using the PES of Cybulski *et al.*<sup>57</sup>

contribution. Therefore, large  $j_2$  values mostly sample the same, short-range (repulsive) part of the PES. We, thus, observe small differences between the PBXS for large  $j_2$  values. This phenomenon was already noticed for several molecule-molecule systems.<sup>152–154</sup> For instance, in the study of the C<sub>2</sub>H<sub>2</sub>-H<sub>2</sub> system,<sup>153</sup> a very weak  $j_2$ -dependence of the cross sections for kinetic energies larger than 500  $\text{cm}^{-1}$  was reported (see Fig. 3 in Ref. 153 and the discussion therein). In fact, during the calculations of the thermally averaged pressure broadening coefficient at temperatures larger than 500 K, the cross sections for  $j_2 > 3$  were taken as the mean value of  $\sigma_0^q$  with  $j_2 = 1, 2$ , and 3. Similar observations about less pronounced  $j_2$ -dependence of  $\sigma_0^q$  at large relative kinetic energies were reported in the studies of the N<sub>2</sub>-H<sub>2</sub> and N<sub>2</sub>-N<sub>2</sub> systems (see Fig. 1 of Ref. 152 and Fig. 3 of Ref. 154, respectively).

The conclusion that  $\sigma_0^1(E_{\text{kin}})$  obeys the power law allows us to extrapolate it for large kinetic energies. We fit the *ab initio* values of  $\sigma_0^1$  to the single power law,

$$\sigma_0^1(E_{\text{kin}}) = A \left( \frac{E_0}{E_{\text{kin}}} \right)^b, \quad (5)$$

where  $E_0 = 100 \text{ cm}^{-1}$ . The cutoff energies are set from 30  $\text{cm}^{-1}$  to 180  $\text{cm}^{-1}$ , depending on the value of  $j_2$ . In the case of the extrapolation with respect to the rotational quantum numbers of the perturber, we make use of another observation that, for large values of  $j_2$ , for a given kinetic energy, the  $\sigma_0^1$  cross section converges to a constant value. Thus, we use the following procedure to determine  $\sigma_0^1$  for the given  $j_2$  and  $E_{\text{kin}}$ : for  $j_2 < 12$ ,  $\sigma_0^1(E_{\text{kin}}, j_2)$  is obtained by fitting the expression given in Eq. (5) to the results of the quantum-scattering calculations. For  $j_2$  values larger than 12, we assume that  $\sigma_0^1(E_{\text{kin}}, j_2) = \sigma_0^1(E_{\text{kin}}, j_2 = 12)$ .

Figures 5 and 6 demonstrate the extrapolation procedure for the given  $j_2$  and  $E_{\text{kin}}$ , respectively. In Fig. 5, we present the *ab initio* and fitted values of  $\sigma_0^1$  for  $j_2 = 0$  and  $j_2 = 7$ . As noticed earlier, the power-law fit works well at sufficiently large values of  $E_{\text{kin}}$ . In Fig. 6, we show the values of the cross sections as a function of the

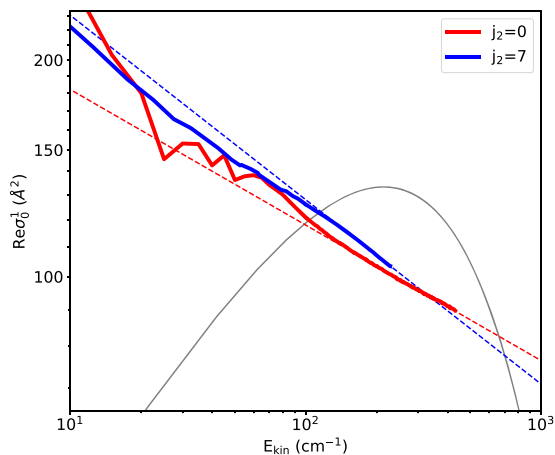


**FIG. 5.** Kinetic energy dependence of  $\sigma_0^1$  for  $j_2 = 0$  and  $j_2 = 7$ . The solid and dashed curves correspond to the *ab initio* and fitted [see Eq. (5)] values, respectively. For reference, we put the Maxwell-Boltzmann distribution at 298.15 K (gray curve).

rotational levels of the perturber, for three kinetic energies:  $E_{\text{kin}} = 100 \text{ cm}^{-1}$ ,  $200 \text{ cm}^{-1}$ , and  $300 \text{ cm}^{-1}$ . We note, following the discussion of Fig. 4, that the  $j_2$ -dependence of the cross sections becomes less pronounced as  $j_2$  increases. For these three particular values of  $E_{\text{kin}}$ , the cross sections for  $j_2 > 5$  differ from each other by less than 0.6%.

In Table I, we show the calculated parameters of the power-law fit for  $j_2 < 13$  for the three different PESs.<sup>55,57,58</sup> These data can be used to reproduce the shape of the R(0) pure rotational line with different line-shape models (not considered here). Again, we can see that the three analyzed PESs lead to almost the same generalized spectroscopic cross sections and that the dependence of the coefficient of the fit on  $j_2$  is negligible for  $j_2 > 5$ .

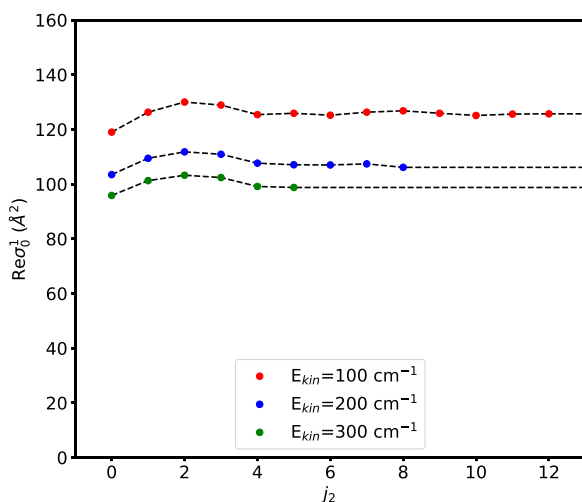


**FIG. 6.**  $j_2$ -dependence of  $\sigma_0^1$  for various kinetic energies. The points and the black dashed curves correspond to the *ab initio* and the extrapolated values, respectively.

**TABLE I.** Coefficients obtained from the fitted cross section values with the power-law expression, Eq. (5), using three analyzed PESs. Values in parentheses correspond to the standard deviation error of the parameters.

$j_2$	Cybulski <i>et al.</i> <sup>57</sup>	Surin <i>et al.</i> <sup>55</sup>	Liu <i>et al.</i> <sup>58</sup>
$A \text{ (}\text{\AA}^2\text{)}$			
0	117.5(1.7)	116.2(1.7)	115.7(2.0)
1	124.7(3.3)	124.3(3.3)	123.7(3.2)
2	127.3(2.4)	127.2(2.1)	127.2(2.2)
3	127.4(3.5)	126.9(4.2)	126.2(3.7)
4	125.4(0.8)	124.8(0.8)	124.3(0.8)
5	125.9(1.0)	125.2(0.7)	124.8(0.7)
6	125.2(0.5)	124.9(0.5)	124.4(0.5)
7	126.3(1.2)	125.9(1.2)	125.5(1.2)
8	126.8(1.2)	126.6(1.2)	125.9(1.4)
9	125.9(1.0)	125.4(1.1)	124.7(1.1)
10	125.1(1.0)	125.0(0.9)	124.4(1.3)
11	125.6(1.9)	125.3(2.2)	125.2(2.4)
12	125.7(2.1)	125.7(2.3)	125.1(3.4)
$b$			
0	0.19(2)	0.18(2)	0.18(2)
1	0.19(3)	0.19(3)	0.19(3)
2	0.19(2)	0.19(1)	0.19(2)
3	0.20(3)	0.20(4)	0.20(3)
4	0.22(1)	0.21(1)	0.22(1)
5	0.23(2)	0.23(1)	0.23(1)
6	0.23(1)	0.23(1)	0.23(1)
7	0.24(3)	0.24(3)	0.24(2)
8	0.24(2)	0.24(2)	0.24(3)
9	0.21(2)	0.21(2)	0.21(2)
10	0.21(2)	0.21(2)	0.21(2)
11	0.20(3)	0.21(3)	0.20(3)
12	0.19(4)	0.19(5)	0.19(7)

#### IV. LINE-SHAPE PARAMETERS

Generalized spectroscopic cross sections are used to calculate the pressure broadening coefficients at a given temperature  $T$ , using the following formula:<sup>109</sup>

$$\gamma(\nu) = \frac{1}{2\pi c} \frac{1}{k_B T} \sum_{j_2} p_{j_2} \frac{2}{\pi \bar{v}_p \nu} \text{Re} \int_0^\infty dv_r v_r^2 e^{-\frac{v^2 + v_r^2}{\bar{v}_p^2}} \times \sinh\left(\frac{2\nu v_r}{\bar{v}_p^2}\right) \sigma_0^1(j_i, j_f, j_2, \nu_r), \quad (6)$$

where  $\nu$  is the speed of the active molecule,  $v_p$  denotes the speed of the perturber with the most probable value  $\bar{v}_p = \sqrt{2k_B T/m_p}$ , and their relative speed is  $\nu_r$  with the mean value  $\bar{v}_r$ .  $m_p$  and  $k_B$  are the mass of the perturber and Boltzmann constant, respectively.  $p_{j_2}$  denotes the population of the perturbing molecule in a rotational state  $j_2$  (at a given temperature):

$$p_{j_2} = \frac{1}{Z(T)} w_{j_2} (2j_2 + 1) e^{-\frac{E_{j_2}}{k_B T}}, \quad (7)$$



and  $Z(T)$  is the partition function

$$Z(T) = \sum_{j_2} w_{j_2} (2j_2 + 1) e^{-\frac{E_{j_2}}{k_B T}}. \quad (8)$$

In order to cover 99% of the population of the perturber's rotational states at room temperature, one should extend the calculations up to  $j_2 = 22$ . The weight  $w_{j_2}$  comes from the symmetry of the total wavefunction of the nitrogen molecule and the degeneracy of the total nuclear spin,  $I$ . The nitrogen nucleus is a boson with the nuclear spin equal 1, which gives the resultant total nuclear spin of the  $N_2$  molecule  $I = 0, 1$ , or  $2$ . For  $I = 0$  and  $I = 2$  (*ortho*- $N_2$ ), only even values of the rotational quantum number of  $N_2$ ,  $j_2$ , are possible. This corresponds to the value of  $w_{j_2} = 6$ . *para*- $N_2$  has the total nuclear spin  $I = 1$ , with only odd values of  $j_2$  allowed. In this case,  $w_{j_2} = 3$ .

Speed-averaged values of the pressure broadening coefficients ( $\gamma_0$ ) are obtained either by averaging Eq. (6) over the velocity distribution of the active molecule or directly from the generalized spectroscopic cross sections:<sup>109</sup>

$$\gamma_0 = \frac{1}{2\pi c} \frac{1}{k_B T} \bar{v}_r \sum_{j_2} p_{j_2} \text{Re} \int_0^\infty dx x e^{-x} \sigma_0^q(j_i, j_f, j_2, x = E_{\text{kin}}/k_B T). \quad (9)$$

In Fig. 7, we compare the speed-dependent, Eq. (6), and speed-averaged, Eq. (9), values of the pressure broadening coefficient at 298.15 K. We also plot the Maxwellian distribution, which enters Eq. (9) and determines the speed-averaged value of the broadening coefficient.

To compare our calculations with the experimental data, the influence of the speed-dependence of the line broadening on the collision-perturbed profile should also be taken into account. The speed-dependence of the broadening is manifested as line narrowing, i.e., the effective width of the profile is smaller than  $\gamma_0$ . To account for this effect, we simulated the shape of the line with the weighted sum of Lorentz profiles (WSLPs) and fitted the simulated profile with a simple Lorentz profile. The fitted width of the Lorentz profile (denoted here as  $\gamma^\dagger$ ) corresponds to the values

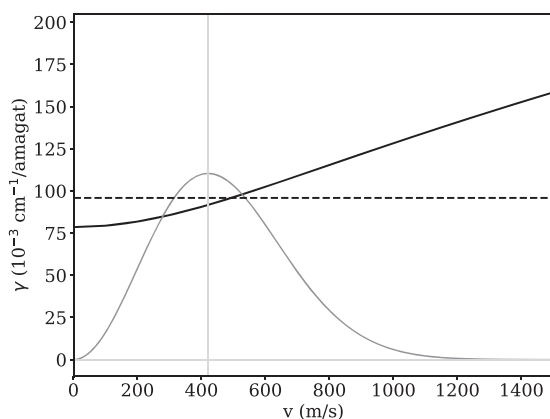


**FIG. 7.** *Ab initio* speed-dependence of the collisional broadening,  $\gamma(v)$  (black solid line), for the  $N_2$ -perturbed pure rotational R(0) line of the CO molecule at 298.15 K. The speed-averaged value,  $\gamma_0$ , is presented as the black dashed line. For reference, we put the Maxwellian distribution at this temperature (in arbitrary units), as the gray solid curve. The results were obtained using the PES of Cybulski *et al.*<sup>57</sup>

that are obtained from the experiments.<sup>31,98,99,103</sup> The influence of the speed-dependence of the collisional shift is negligible for this system.

Here, we recall that the line-shape parameters are related to the standard, pressure-dependent broadening coefficients by  $\Gamma = \gamma p$ , where  $p$  denotes the pressure.

## V. COMPARISON WITH THE EXPERIMENTAL DATA

In this section, we compare the obtained pressure broadening coefficients with the available experimental data.<sup>31,98,99,103</sup> Connor and Radford<sup>98</sup> reported pressure broadening coefficients for the  $N_2$ -,  $O_2$ -, and air-broadened R(0) lines in CO. The measurements were performed for several temperatures in the range from 202 K to 324 K, and the results were fitted to the empirical power-law relation,

$$\gamma(T) = C \left( \frac{T_0}{T} \right)^d, \quad (10)$$

where  $T_0 = 300$  K is a specific reference temperature. The study conducted by Colmont and Monnanteuil<sup>31</sup> was performed in a slightly narrower temperature range, from 220 K to 293 K. The authors derived the values of the fitting coefficients from Eq. (10) for the cases of self-,  $N_2$ -,  $O_2$ -, and air-broadened CO R(0) line, setting  $T_0 = 293$  K. Over ten years later, Nissen *et al.*<sup>99</sup> reported results of the joint study conducted by the Kiel and Nizhny Novogrod groups. In this investigation, collisional broadening of the R(0) line in CO by several buffer gases was studied by using two experimental techniques in the time and frequency domain. The frequency-domain data were obtained using a radio-acoustical detection (RAD) spectrometer for the temperature range from 230 K to 300 K, while the time-domain data were acquired

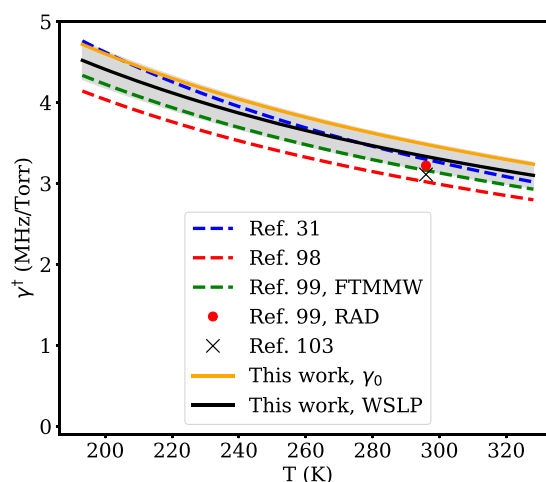


**FIG. 8.** Comparison between the effective collisional width ( $\gamma^\dagger$ ) of the pure rotational R(0) line of the  $N_2$ -perturbed CO molecule with the pressure broadening coefficient ( $\gamma_0$ ) and the available experimental data. The estimated uncertainty of  $\gamma^\dagger(T)$  is represented by the shaded area (see Sec. VI for details). The results presented here were obtained with the PES of Cybulski *et al.*<sup>57</sup>



**TABLE II.** Comparison of the theoretical and experimental power-law coefficients [Eq. (10)]. Values in parentheses correspond to the standard deviation error of the parameters.

PES	C (MHz Torr <sup>-1</sup> )	<i>d</i>
Surin <i>et al.</i> <sup>55</sup>	3.44(8)	0.71(14)
Cybulski <i>et al.</i> <sup>57</sup>	3.45(7)	0.71(14)
Liu <i>et al.</i> <sup>58</sup>	3.43(8)	0.71(14)
Surin <i>et al.</i> <sup>55 a</sup>	3.29(7)	0.71(14)
Cybulski <i>et al.</i> <sup>57 a</sup>	3.30(7)	0.71(14)
Liu <i>et al.</i> <sup>58 a</sup>	3.28(7)	0.71(14)
Experiment (Ref. 31) <sup>b</sup>	3.26(10)	0.86(12)
Experiment (Ref. 98)	2.99(+14, -10)	0.74(10)
Experiment (Ref. 99, FTMMW)	3.13(1)	0.74(2)

<sup>a</sup>The results obtained after the inclusion of the speed-dependence of the broadening (see black curve in Fig. 8).

<sup>b</sup>The C coefficient is calculated from the C and *d* values reported for *T*<sub>0</sub> = 293 K.

using a Fourier-transform spectrometer in the millimeter wave region (FTMMW) at one temperature *T* = 296 K. Puzzarini *et al.*<sup>103</sup> conducted a thorough study of self- and foreign-gas broadening of the R(0-3) lines in the CO (<sup>12</sup>CO and <sup>13</sup>CO) molecules. The authors analyzed the shapes of the measured rovibrational lines using the Voigt, Galatry,<sup>155</sup> and Rautian<sup>156</sup> profiles at 296 K.

Figure 8 presents the comparison between the theoretical and experimental collisional width of the R(0) line of CO perturbed by N<sub>2</sub> at various temperatures. In the case of the theoretical values, we present the speed-averaged pressure broadening coefficient,  $\gamma_0$ , and the effective collisional width of the line,  $\gamma^\dagger$ , as described in Sec. IV. In order to quantitatively compare the theoretical temperature dependence of the collisional width, we chose to present the power-law dependence of  $\gamma(T)$  by using coefficients fitted with Eq. (10). The theoretical and experimental values of the C and *d* coefficients are given in Table II.

The agreement between the theoretical and most of the experimental values<sup>31,99,103</sup> is very good. An exception is a slight difference between the theoretical collisional width and the results reported by Connor and Radford.<sup>98</sup> The inclusion of the speed-dependence of collisional broadening through the WSLPs leads to significantly better agreement with the experimental data.

## VI. ACCURACY OF THE CALCULATIONS

In this section, we discuss the sources of the uncertainty of the pressure broadening coefficients reported in this paper. First, we analyze the sources of the uncertainty of the calculated generalized spectroscopic cross sections, originating from the coupled states approximation, the initial parameters of the chosen propagator, and the number of the closed levels used in the calculations. In the next step, we discuss the possible error originating from extrapolation of the kinetic energy dependence of the cross sections, and finally, we discuss the influence of neglecting the resonances observed at low kinetic energies. The resulting total uncertainty of the pressure broadening coefficient corresponds to the shaded area in Fig. 8.

The most important contribution to the uncertainty of the final results comes from the coupled states approximation used while solving the coupled equations. The accuracy of the generalized spectroscopic cross sections calculated within this approximation has been thoroughly discussed in the literature.<sup>151,157–159</sup> For instance, Roche *et al.*<sup>157</sup> have reported that, for low *j* values of the active molecule and relatively small values of kinetic energies, the cross sections calculated within the CS approximation are underestimated by about 15%. However, as was confirmed in other studies using this approximation, i.e., in the cases of the molecule–molecule systems, the CS approximation works better in the domain of large kinetic energies and for larger values of *j*<sub>2</sub>.

We have made several tests to check how much the CC and CS generalized spectroscopic cross sections differ. Overall, the agreement between the approximate and exact cross sections is better than that previously reported in the literature. The largest relative difference between the CC and CS cross sections in the analyzed energy domain is about 5.8% for *E*<sub>kin</sub> = 150 cm<sup>-1</sup> and *j*<sub>2</sub> = 2. Apart from *j*<sub>2</sub> = 0, where the CS cross sections are underestimated by about 4.5%, the approximate cross sections are slightly larger than the CC values. The largest *j*<sub>2</sub> value, for which we could make such a comparison, was *j*<sub>2</sub> = 7, where we calculated the cross sections for *E*<sub>kin</sub> = 65 cm<sup>-1</sup>. Indeed, the CS works better for larger values of *j*<sub>2</sub>, although we have not observed any sign of convergence of the approximate cross sections to the exact values of  $\sigma_0^1$ . To estimate the error introduced by the CS calculations, we took the relative differences between the CC and CS cross sections from those tests and averaged them with the statistical weights coming from the population of the nitrogen molecule in the considered temperature range. This resulted in an estimated error of 2.7% coming from the approximate method of solving the coupled equations.

Another contribution to the uncertainty of the results originates from the initial parameters of the propagator that is used to solve the coupled equations. Let us recall that we have used the hybrid log-derivative propagator of Manolopoulos,<sup>146</sup> which can be controlled by choosing the starting (*R*<sub>min</sub>) and end point (*R*<sub>max</sub>) of the propagation, as well as the step size. The choice of the starting point of the propagation is driven by two factors. On the one hand, the propagation process should start possibly deep in the classically forbidden region, where the PES is strongly repulsive. On the other hand, the quantum chemical methods, such as CCSD(T), are less reliable there since in the short-range region convergence problems tend to occur. This, obviously, affects the accuracy of the radial terms of the PES that enter the coupled equations. Therefore, one needs to find a starting point, which is a compromise between these two restrictions. In this study, we set *R*<sub>min</sub> = 4.25 *a*<sub>0</sub>, which corresponds to the shortest *ab initio* distance in the *R*-grid of the PES of Surin *et al.*<sup>55</sup> We performed additional tests to check if a decrease in the value of *R*<sub>min</sub> to 4.0 *a*<sub>0</sub> or 3.5 *a*<sub>0</sub> has any significant influence on the values of the generalized spectroscopic cross sections. Since the calculated  $\sigma_0^1$  has remained unchanged in those additional runs, we can state that this parameter is chosen properly.

The propagation should end in the region where the radial terms of the PES vanish and boundary conditions can be applied, and we used *R*<sub>max</sub> = 100 *a*<sub>0</sub> in our calculations. We have also performed additional tests to check how increasing (up to 200 *a*<sub>0</sub>) or

decreasing (down 75 and even 50  $a_0$ ) this parameter influences the generalized spectroscopic cross sections. The tests confirmed that increasing this parameter does not produce any significant difference in  $\sigma_0^1$  and the decrease of this parameter to 50  $a_0$  affects the pressure broadening cross section by less than 0.01%. We conclude that the range of the propagation has been chosen properly and does not contribute to the final error of the collisional broadening reported here.

A change in the step size of the propagator mainly influences the collisional shift of the spectral line shape, which we do not consider here. Usually, the step size should be inversely proportional to the square root of the relative kinetic energy. However, an appropriate choice of the step size becomes significant for kinetic energies smaller than 40  $\text{cm}^{-1}$ , where resonant structures make obtaining the convergence of the cross sections very difficult. In the kinetic energy domain considered here, the error introduced by the step size of the propagator is insignificant.

As mentioned in Sec. III, in all the calculations, we kept at least two asymptotically closed levels. In the considered relative kinetic energy domain, this should be sufficient, but we have performed tests to check how additional closed levels (up to 6) influence the values of the pressure broadening cross section. The additional asymptotically closed levels changed the pressure broadening cross section up to about 0.7% of its referential value (for  $j_2$  values larger than 7).

To summarize, the total uncertainty of the calculated pressure broadening cross sections is estimated at a level of 3.5%.

Another important contribution to the uncertainty of the pressure broadening coefficient originates from the extrapolation of the kinetic energy dependence of  $\sigma_0^1$ . Let us recall that, for each  $j_2$ , the power-law function was fitted to the values of  $\sigma_0^1$ . The cutoff energy varied from 30  $\text{cm}^{-1}$  to 180  $\text{cm}^{-1}$ , depending on the  $j_2$  value. In order to estimate the possible error associated with the range of the *ab initio* points used in the fitting procedure, we calculated the pressure broadening coefficients using the power-law dependence of  $\sigma_0^1(E_{\text{kin}})$  fitted to the data points with  $E_{\text{kin}} = 15 \text{ cm}^{-1}$ . The largest relative difference between those values and the results presented here is at a level of 1%.

In the present study, we neglected the resonant structures observed in the kinetic energy dependence of the pressure broadening cross sections. These structures occur for kinetic energies smaller than 15  $\text{cm}^{-1}$ , although the exact range depends on  $j_2$ . An example for  $j_2 = 9$  is presented in Fig. 9. The Maxwell-Boltzmann distribution, shown in this plot, clearly justifies the neglect of the points below 15  $\text{cm}^{-1}$  in the calculations of the line-shape parameters [see Eq. (9)] at room temperature. Nonetheless, we have performed tests to quantify the influence of taking into account all the data points, including the resonant structures. We conclude that the results (at room temperature) obtained in this way differ by about 0.5% with respect to the values reported in Sec. V.

We have estimated all possible contributions to the final error of the pressure broadening coefficient. The generalized spectroscopic cross sections are calculated with  $\sim 3.5\%$  uncertainty, which originates from the coupled states approximation (2.7%) and the contribution from the number of the closed levels taken into account while solving the coupled equations (0.7%). The cutoffs for the kinetic energies used in the power-law fit introduce an estimated error of about 1%. Neglecting the resonant structures of the cross

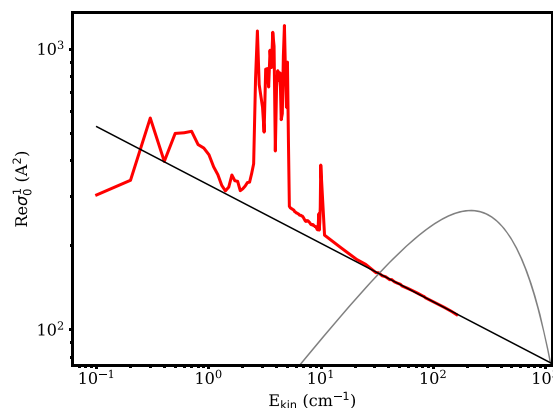


**FIG. 9.** Resonant structures observed in the pressure broadening cross sections (red curve) for kinetic energies smaller than 15  $\text{cm}^{-1}$ . The black line corresponds to the power-law function fitted to the points for which  $E_{\text{kin}} > 30 \text{ cm}^{-1}$ . As a reference, we draw the Maxwell-Boltzmann distribution at 298.15 K (gray curve). These results, corresponding to  $j_2 = 9$ , were obtained using the PES of Cybulski *et al.*<sup>57</sup>

sections for kinetic energies below 10  $\text{cm}^{-1}$  could affect the final results by 0.5%. Hence, the total uncertainty of the final pressure broadening coefficients is at the 5% level.

## VII. CONCLUSIONS

We have presented the first-ever theoretical calculations of the pressure broadening of the pure rotational R(0) line of the  $\text{N}_2$ -perturbed CO molecule. Starting from an *ab initio* PES, we performed quantum-scattering calculations. Because of the computational complexity of the coupled equations, we made use of the well-known coupled states approximation. This allowed us to obtain the generalized spectroscopic cross sections for a wide range of kinetic energies and for the values of the rotational quantum number of the perturbing molecule  $j_2 \leq 12$ . We calculated the speed-averaged and speed-dependent values of the pressure broadening coefficient, and we obtained good agreement with the experimental data.

One of the goals of this paper was to determine whether any previously reported PESs<sup>55,57,58</sup> reproduce the shape of the R(0) line significantly better than the other considered PESs. Our results suggest that all three PESs lead to almost the same results and it is impossible, at this level of accuracy of the scattering calculations, to determine which one is the most accurate.

This work constitutes a large step toward theoretical investigation of other  $\text{N}_2$ -perturbed pure rotational CO lines. Such studies are of particular importance for the physics of the terrestrial and extraterrestrial atmospheres and for populating the spectroscopic databases, such as the HITRAN database,<sup>147</sup> with *ab initio* collisional line-shape parameters.

## SUPPLEMENTARY MATERIAL

See the [supplementary material](#) associated with this article for the tabulated radial terms of the three PESs.

## ACKNOWLEDGMENTS

H.J.'s contribution was supported by the National Science Centre in Poland through Project No. 2018/31/B/ST2/00720. H.C.'s contribution was financed by the National Science Centre in Poland within the OPUS 8 Project No. 2014/15/B/ST4/04551. P.W.'s contribution was supported by the National Science Centre in Poland through Project No. 2019/35/B/ST2/01118. This project was supported by the French-Polish PHC Polonium program (Project No. 42769ZK for the French part). This project was co-financed by the Polish National Agency for Academic Exchange under the PHC Polonium program (Grant No. dec. PPN/X/PS/318/2018). This research was part of the program of the National Laboratory FAMO in Toruń, Poland.

## DATA AVAILABILITY

The data that support the findings of this study are available within the article and its [supplementary material](#).

## REFERENCES

- <sup>1</sup>P. E. S. Wormer and A. van der Avoird, "Intermolecular potentials, internal motions, and spectra of van der Waals and hydrogen-bonded complexes," *Chem. Rev.* **100**, 4109–4144 (2000).
- <sup>2</sup>D. Flower, *Molecular Collisions in the Interstellar Medium*, Cambridge Astrophysics, 2nd ed. (Cambridge University Press, 2007).
- <sup>3</sup>L. Frommhold, *Collision-Induced Absorption in Gases*, Cambridge Monographs on Atomic, Molecular and Chemical Physics (Cambridge University Press, 1994).
- <sup>4</sup>J. Hartmann, C. Boulet, and D. Robert, *Collisional Effects on Molecular Spectra* (Elsevier, 2008).
- <sup>5</sup>D. L. Hartmann, "Atmospheric radiative transfer and climate," in *Global Physical Climatology*, 2nd ed., edited by D. L. Hartmann (Elsevier, Boston, 2016), Chap. 3, pp. 49–94.
- <sup>6</sup>J.-M. Hartmann, H. Tran, R. Armante, C. Boulet, A. Campargue, F. Forget, L. Gianfrani, I. Gordon, S. Guerlet, M. Gustafsson, J. T. Hodges, S. Kass, D. Lisak, F. Thibault, and G. C. Toon, "Recent advances in collisional effects on spectra of molecular gases and their practical consequences," *J. Quantum Spectrosc. Radiat. Transfer* **213**, 178–227 (2018).
- <sup>7</sup>D. J. Jacob, *Introduction to Atmospheric Chemistry* (Princeton University Press, 1999).
- <sup>8</sup>A. Eldering, P. O. Wennberg, D. Crisp, D. S. Schimel, M. R. Gunson, A. Chatterjee, J. Liu, F. M. Schwandner, Y. Sun, C. W. O'Dell, C. Frankenberg, T. Taylor, B. Fisher, G. B. Osterman, D. Wunch, J. Hakkarainen, J. Tamminen, and B. Weir, "The Orbiting Carbon Observatory-2 early science investigations of regional carbon dioxide fluxes," *Science* **358**, eaam5745 (2017).
- <sup>9</sup>F. M. Schwandner, M. R. Gunson, C. E. Miller, S. A. Carn, A. Eldering, T. Krings, K. R. Verhulst, D. S. Schimel, H. M. Nguyen, D. Crisp, C. W. O'Dell, G. B. Osterman, L. T. Iraci, and J. R. Podolske, "Spaceborne detection of localized carbon dioxide sources," *Science* **358**, eaam5782 (2017).
- <sup>10</sup>J. C. White, W. R. Wagner, and C. N. Beale, *Global Climate Change Linkages: Acid Rain, Air Quality, and Stratospheric Ozone* (Springer Science & Business Media, 1989).
- <sup>11</sup>J. S. Daniel and S. Solomon, "On the climate forcing of carbon monoxide," *J. Geophys. Res.* **103**, 13249–13260, <https://doi.org/10.1029/98jd00822> (1998).
- <sup>12</sup>R. D. Stephens and S. H. Cadle, "Remote sensing measurements of carbon monoxide emissions from on-road vehicles," *J. Air Waste Manag. Assoc.* **41**, 39–46 (1991).
- <sup>13</sup>W. W. McMillan, R. B. Pierce, L. C. Sparling, G. Osterman, K. McCann, M. L. Fischer, B. Rappenglück, R. Newsom, D. Turner, C. Kittaka, K. Evans, S. Biraud, B. Lefer, A. Andrews, and S. Oltmans, "An observational and modeling strategy to investigate the impact of remote sources on local air quality: A Houston, Texas, case study from the Second Texas Air Quality Study (TexAQS II)," *J. Geophys. Res.* **115**, D01301, <https://doi.org/10.1029/2009jd011973> (2010).
- <sup>14</sup>C. Shan, W. Wang, C. Liu, Y. Sun, Q. Hu, X. Xu, Y. Tian, H. Zhang, I. Morino, D. W. T. Griffith, and V. A. Velasco, "Regional CO emission estimated from ground-based remote sensing at Hefei site, China," *Atmos. Res.* **222**, 25–35 (2019).
- <sup>15</sup>D. C. Catling and J. F. Kasting, "Giant planets and their satellites," in *Atmospheric Evolution on Inhabited and Lifeless Worlds* (Cambridge University Press, 2017), pp. 393–421.
- <sup>16</sup>H. B. Niemann, S. K. Atreya, J. E. Demick, D. Gautier, J. A. Haberman, D. N. Harpold, W. T. Kasprzak, J. I. Lunine, T. C. Owen, and F. Raulin, "Composition of Titan's lower atmosphere and simple surface volatiles as measured by the Cassini-Huygens probe gas chromatograph mass spectrometer experiment," *J. Geophys. Res.* **115**, E12006, <https://doi.org/10.1029/2010JE003659> (2010).
- <sup>17</sup>B. L. Lutz, C. de Bergh, and T. Owen, "Titan: Discovery of carbon monoxide in its atmosphere," *Science* **220**, 1374–1375 (1983).
- <sup>18</sup>F. M. Flasar, R. K. Achterberg, B. J. Conrath, P. J. Gierasch, V. G. Kunde, C. A. Nixon, G. L. Bjoraker, D. E. Jennings, P. N. Romani, A. A. Simon-Miller *et al.*, "Titan's atmospheric temperatures, winds, and composition," *Science* **308**, 975–978 (2005).
- <sup>19</sup>R. de Kok, P. G. J. Irwin, N. A. Teanby, E. Lellouch, B. Bézard, S. Vinatier, C. A. Nixon, L. Fletcher, C. Howett, S. B. Calcutt, N. E. Bowles, F. M. Flasar, and F. W. Taylor, "Oxygen compounds in Titan's stratosphere as observed by Cassini CIRS," *Icarus* **186**, 354–363 (2007).
- <sup>20</sup>D. O. Muhleman, G. L. Berge, and R. T. Clancy, "Microwave measurements of carbon monoxide on Titan," *Science* **223**, 393–396 (1984).
- <sup>21</sup>A. Marten, D. Gautier, L. Tanguy, A. Lecacheux, C. Rosolen, and G. Paubert, "Abundance of carbon monoxide in the stratosphere of Titan from millimeter heterodyne observations," *Icarus* **76**, 558–562 (1988).
- <sup>22</sup>M. A. Gurwell and D. O. Muhleman, "CO on Titan: Evidence for a well-mixed vertical profile," *Icarus* **117**, 375–382 (1995).
- <sup>23</sup>T. Hidayat, A. Marten, B. Bézard, D. Gautier, T. Owen, H. E. Matthews, and G. Paubert, "Millimeter and submillimeter heterodyne observations of Titan: The vertical profile of carbon monoxide in its stratosphere," *Icarus* **133**, 109–133 (1998).
- <sup>24</sup>M. A. Gurwell and D. O. Muhleman, "CO on Titan: More evidence for a well-mixed vertical profile," *Icarus* **145**, 653–656 (2000).
- <sup>25</sup>M. A. Gurwell, "Submillimeter observations of Titan: Global measures of stratospheric temperature, CO, HCN, HC<sub>3</sub>N, and the isotopic ratios <sup>12</sup>C/<sup>13</sup>C and <sup>14</sup>N/<sup>15</sup>N," *Astrophys. J.* **616**, L7–L10 (2004).
- <sup>26</sup>K. S. Noll, T. R. Geballe, R. F. Knacke, and Y. J. Pendleton, "Titan's 5 μm spectral window: Carbon monoxide and the albedo of the surface," *Icarus* **124**, 625–631 (1996).
- <sup>27</sup>E. Lellouch, A. Coustenis, B. Sebag, J.-G. Cuby, M. López-Valverde, B. Schmitt, T. Fouchet, and J. Crovisier, "Titan's 5-μm window: Observations with the very large telescope," *Icarus* **162**, 125–142 (2003).
- <sup>28</sup>M. A. López-Valverde, E. Lellouch, and A. Coustenis, "Carbon monoxide fluorescence from Titan's atmosphere," *Icarus* **175**, 503–521 (2005).
- <sup>29</sup>S. M. Hörst, "Titan's atmosphere and climate," *J. Geophys. Res.* **122**, 432–482, <https://doi.org/10.1002/2016je005240> (2017).
- <sup>30</sup>R. Courtin, B. M. Swinyard, R. Moreno, T. Fulton, E. Lellouch, M. Rengel, and P. Hartogh, "First results of Herschel-SPIRE observations of Titan," *Astron. Astrophys.* **536**, L2 (2011).
- <sup>31</sup>J. M. Colmont and N. Monnanteuil, "Self, nitrogen and oxygen broadening of the 115-GHz line of carbon monoxide," *J. Quantum Spectrosc. Radiat. Transfer* **35**, 81–85 (1986).
- <sup>32</sup>N. Semmoud-Monnanteuil and J. M. Colmont, "Pressure broadening of millimeter lines of carbon monoxide," *J. Mol. Spectrosc.* **126**, 210–219 (1987).
- <sup>33</sup>J.-P. Bouanich, R. Farrenq, and C. Brodbeck, "Direct measurements of N<sub>2</sub> broadened linewidths in the CO fundamental at low temperatures," *Can. J. Phys.* **61**, 192–197 (1983).
- <sup>34</sup>P. Varanasi, S. Chudamani, and S. Kapur, "Diode laser measurements of CO line widths at planetary atmospheric temperatures," *J. Quantum Spectrosc. Radiat. Transfer* **38**, 167–171 (1987).
- <sup>35</sup>A. L. Broadfoot, F. Herbert, J. B. Holberg, D. M. Hunten, S. Kumar, B. R. Sandel, D. E. Shemansky, G. R. Smith, R. V. Yelle, D. F. Strobel, H. W. Moos,

- T. M. Donahue, S. K. Atreya, J. L. Bertaux, J. E. Blamont, J. C. McConnell, A. J. Dessler, S. Linick, and R. Springer, "Ultraviolet spectrometer observations of Uranus," *Science* **233**, 74–79 (1986).
- <sup>36</sup>E. Lellouch, C. de Bergh, B. Sicardy, S. Ferron, and H.-U. Käufel, "Detection of CO in Triton's atmosphere and the nature of surface-atmosphere interactions," *Astron. Astrophys.* **512**, L8 (2010).
- <sup>37</sup>J. L. Elliot, H. B. Hammel, L. H. Wasserman, O. G. Franz, S. W. McDonald, M. J. Person, C. B. Olkin, E. W. Dunham, J. R. Spencer, J. A. Stansberry, M. W. Buie, J. M. Pasachoff, B. A. Babcock, and T. H. McConnochie, "Global warming on Triton," *Nature* **393**, 765–767 (1998).
- <sup>38</sup>L. N. Fletcher, R. Helled, E. Roussos, G. Jones, S. Charnoz, N. André, D. Andrews, M. Bannister, E. Bunce, T. Cavalié, F. Ferri, J. Fortney, D. Grassi, L. Griton, P. Hartogh, R. Hueso, Y. Kaspi, L. Lamy, A. Masters, H. Melin, J. Moses, O. Mousis, N. Nettleman, C. Plainaki, J. Schmidt, A. Simon, G. Tobie, P. Tortora, F. Tosi, and D. Turrini, "Ice giant systems: The scientific potential of orbital missions to Uranus and Neptune," *Planet. Space Sci.* **191**, 105030 (2020).
- <sup>39</sup>S. A. Stern, F. Bagenal, K. Ennico, G. R. Gladstone, W. M. Grundy, W. B. McKinnon, J. M. Moore, C. B. Olkin, J. R. Spencer, H. A. Weaver, L. A. Young, T. Andert, J. Andrews, M. Banks, B. Bauer, J. Bauman, O. S. Barnouin, P. Bedini, K. Beisser, R. A. Beyer, S. Bhaskaran, R. P. Binzel, E. Birath, M. Bird, D. J. Bogan, A. Bowman, V. J. Bray, M. Brozovic, C. Bryan, M. R. Buckley, M. W. Buie, B. J. Buratti, S. S. Bushman, A. Calloway, B. Carcich, A. F. Cheng, S. Conard, C. A. Conrad, J. C. Cook, D. P. Cruikshank, O. S. Custodio, C. M. Dalle Ore, C. Deboy, Z. J. B. Dischner, P. Dumont, A. M. Earle, H. A. Elliott, J. Ercol, C. M. Ernst, T. Finley, S. H. Flanigan, G. Fountain, M. J. Freeze, T. Greathouse, J. L. Green, Y. Guo, M. Hahn, D. P. Hamilton, S. A. Hamilton, J. Hanley, A. Harch, H. M. Hart, C. B. Hersman, A. Hill, M. E. Hill, D. P. Hinson, M. E. Holdridge, M. Horanyi, A. D. Howard, C. J. A. Howett, C. Jackman, R. A. Jacobson, D. E. Jennings, J. A. Kammer, H. K. Kang, D. E. Kaufmann, P. Kollmann, S. M. Krimigis, D. Kusnierkiewicz, T. R. Lauer, J. E. Lee, K. L. Lindstrom, I. R. Linscott, C. M. Lisse, A. W. Lunsford, V. A. Mallder, N. Martin, D. J. McComas, R. L. McNutt, D. Mehoke, T. Mehoke, E. D. Melin, M. Mutchler, D. Nelson, F. Schenk, J. I. Nunez, A. Ocampo, W. M. Owen, M. Paetzold, B. Page, A. H. Parker, J. W. Parker, F. Pelletier, J. Peterson, N. Pinkine, M. Piquette, S. B. Porter, S. Protopapa, J. Redfern, H. J. Reitsema, D. C. Reuter, J. H. Roberts, S. J. Robbins, G. Rogers, D. Rose, K. Runyon, K. D. Retherford, M. G. Ryschewitsch, P. Schenk, E. Schindhelm, B. Sepan, M. R. Showalter, K. N. Singer, M. Soluri, D. Stanbridge, A. J. Steffl, D. F. Strobel, T. Stryk, M. E. Summers, J. R. Szalay, M. Tapley, A. Taylor, H. Taylor, H. B. Throop, C. C. C. Tsang, G. L. Tyler, O. M. Umurhan, A. J. Verbiscer, M. H. Vestegg, M. Vincent, R. Webber, S. Weidner, G. E. Weigle, O. L. White, K. Whittenburg, B. G. Williams, K. Williams, S. Williams, W. W. Woods, A. M. Zangari, and E. Zirnstein, "The Pluto system: Initial results from its exploration by new Horizons," *Science* **350**, aad1815 (2015).
- <sup>40</sup>P. J. Barnes, "A search for CO emission from the Pluto-Charon system," *Astron. J.* **106**, 2540 (1993).
- <sup>41</sup>D. Bockelée-Morvan, E. Lellouch, N. Biver, G. Paubert, J. Bauer, P. Colom, and D. C. Lis, "Search for CO gas in Pluto, Centaurs and Kuiper Belt objects at radio wavelengths," *Astron. Astrophys.* **377**, 343–353 (2001).
- <sup>42</sup>J. S. Greaves, C. Helling, and P. Friberg, "Discovery of carbon monoxide in the upper atmosphere of Pluto," *Mon. Not. R. Astron. Soc. Lett.* **414**, L36–L40 (2011).
- <sup>43</sup>E. Lellouch, M. A. Gurwell, B. Butler, T. Fouchet, P. Lavvas, D. F. Strobel, B. Sicardy, A. Moullet, R. Moreno, D. Bockelée-Morvan, N. Biver, L. Young, D. Lis, J. Stansberry, A. Stern, H. Weaver, E. Young, X. Zhu, and J. Boissier, "Detection of CO and HCN in Pluto's atmosphere with ALMA," *Icarus* **286**, 289–307 (2017).
- <sup>44</sup>L. Young, "Upper limits on gaseous CO at Pluto and Triton from high-resolution near-IR spectroscopy," *Icarus* **153**, 148–156 (2001).
- <sup>45</sup>E. Lellouch, C. de Bergh, B. Sicardy, H. U. Käufel, and A. Smette, "High resolution spectroscopy of Pluto's atmosphere: Detection of the 2.3  $\mu\text{m}$  CH<sub>4</sub> bands and evidence for carbon monoxide," *Astron. Astrophys.* **530**, L4 (2011).
- <sup>46</sup>Y. Xu and A. R. W. McKellar, "Continuous slit-jet infrared spectrum of the CO-N<sub>2</sub> complex," *J. Chem. Phys.* **104**, 2488–2496 (1996).
- <sup>47</sup>Y. Kawashima and K. Nishiza, "Pulsed molecular beam infrared absorption spectroscopy of the N<sub>2</sub>-CO complex," *Chem. Phys. Lett.* **249**, 87–91 (1996).
- <sup>48</sup>Y. Xu, W. Jäger, L. A. Surin, I. Pak, L. A. Panfilov, and G. Winnewisser, "Microwave and millimeter wave study of *ortho*-N<sub>2</sub> states of CO-N<sub>2</sub>," *J. Chem. Phys.* **111**, 10476–10483 (1999).
- <sup>49</sup>Y. Xu and W. Jäger, "The dynamics of the CO-N<sub>2</sub> interaction: Strong Coriolis coupling in CO-*para*N<sub>2</sub>," *J. Chem. Phys.* **113**, 514–524 (2000).
- <sup>50</sup>L. A. Surin, H. S. P. Müller, E. V. Alieva, B. S. Dumes, G. Winnewisser, and I. Pak, "Detection of the bending vibration of the CO-*ortho*N<sub>2</sub> complex," *J. Mol. Struct.* **612**, 207–211 (2002).
- <sup>51</sup>L. A. Surin, A. V. Potapov, H. S. P. Müller, V. A. Panfilov, B. S. Dumes, T. F. Giesen, and S. Schlesinger, "Millimeter-wave study of the CO-N<sub>2</sub> van der Waals complex: New measurements of CO-*ortho*N<sub>2</sub> and assignments of new states of CO-*para*N<sub>2</sub>," *J. Mol. Struct.* **795**, 198–208 (2006).
- <sup>52</sup>L. A. Surin, A. Potapov, H. S. P. Müller, and S. Schlemmer, "A new millimeter-wave observation of the weakly bound CO-N<sub>2</sub> complex," *J. Mol. Spectrosc.* **307**, 54–58 (2015).
- <sup>53</sup>C. Xia, A. R. W. McKellar, and Y. Xu, "Infrared spectrum of the CO-N<sub>2</sub> van der Waals complex: Assignments for CO-*para*-N<sub>2</sub> and observation of a bending state for CO-*ortho*-N<sub>2</sub>," *J. Chem. Phys.* **113**, 525–533 (2000).
- <sup>54</sup>M. Rezaei, K. H. Michaelian, N. Moazzen-Ahmadi, and A. R. W. McKellar, "A new look at the infrared spectrum of the weakly bound CO-N<sub>2</sub> complex," *J. Phys. Chem. A* **117**, 13752–13758 (2013).
- <sup>55</sup>L. A. Surin, I. V. Tarabukin, S. Schlemmer, Y. N. Kalugina, and A. van der Avoird, "Ab initio potential and rotational spectra of the CO-N<sub>2</sub> complex," *J. Chem. Phys.* **148**, 044313 (2018).
- <sup>56</sup>I. V. Tarabukin, L. A. Surin, and S. Schlemmer, "Millimeter-wave detection of doubly excited bending mode in the CO-N<sub>2</sub> van der Waals complex," *J. Mol. Spectrosc.* **362**, 21–24 (2019).
- <sup>57</sup>H. Cybulski, C. Henriksen, R. Dawes, X.-G. Wang, N. Bora, G. Avila, T. Carrington, Jr., and B. Fernández, "Ab initio study of the CO-N<sub>2</sub> complex: A new highly accurate intermolecular potential energy surface and rovibrational spectrum," *Phys. Chem. Chem. Phys.* **20**, 12624–12636 (2018).
- <sup>58</sup>J.-M. Liu, Y. Zhai, X.-L. Zhang, and H. Li, "Intermolecular configurations dominated by quadrupole-quadrupole electrostatic interactions: Explicit correlation treatment of the five-dimensional potential energy surface and infrared spectra for the CO-N<sub>2</sub> complex," *Phys. Chem. Chem. Phys.* **20**, 2036 (2018).
- <sup>59</sup>J. Fiser and R. Polák, "An ab initio study of the CO-N<sub>2</sub> complex," *Chem. Phys. Lett.* **360**, 565–572 (2002).
- <sup>60</sup>M. H. Karimi-Jafari, A. Maghari, and A. Farjamnia, "Intermolecular potential energy surface of the N<sub>2</sub>-CO dimer: Ab initio investigation and analytical representation," *J. Phys. Chem. A* **115**, 1143–1151 (2011).
- <sup>61</sup>D. R. Eaton and H. W. Thompson, "Pressure broadening studies on vibration-rotation bands II. The effective collision diameters," *Proc. R. Soc. London, Ser. A* **251**, 475–485 (1959).
- <sup>62</sup>C. Crane-Robinson and H. W. Thompson, "Pressure broadening studies on vibration-rotation bands. IV. Optical collision diameters for foreign-gas broadening of CO and DCl bands," *Proc. R. Soc. London, Ser. A* **272**, 453–466 (1963).
- <sup>63</sup>A. T. Chai and D. Williams, "Comparison of collision cross sections for line broadening in the CO fundamental," *J. Opt. Soc. Am.* **58**, 1395 (1968).
- <sup>64</sup>D. Williams, D. C. Wenstrand, R. J. Brockman, and B. Curnutte, "Collisional broadening of infra-red absorption lines," *Mol. Phys.* **20**, 769–785 (1971).
- <sup>65</sup>J.-P. Bouanich and C. Haeusler, "Linewidths of carbon monoxide self-broadening and broadened by argon and nitrogen," *J. Quantum Spectrosc. Radiat. Transfer* **12**, 695–702 (1972).
- <sup>66</sup>P. Varanasi and S. Sarangi, "Measurements of intensities and nitrogen-broadened linewidths in the CO fundamental at low temperatures," *J. Quantum Spectrosc. Radiat. Transfer* **15**, 473–482 (1975).
- <sup>67</sup>P. L. Varghese and R. K. Hanson, "Tunable infrared diode laser measurements of line strengths and collision widths of <sup>12</sup>C<sup>16</sup>O at room temperature," *J. Quantum Spectrosc. Radiat. Transfer* **24**, 479–489 (1980).
- <sup>68</sup>J. A. Sell, "Temperature dependence of the absorption coefficient and halfwidth of the P(6) line of carbon monoxide," *J. Quantum Spectrosc. Radiat. Transfer* **23**, 595–598 (1980).
- <sup>69</sup>J. N.-P. Sun and P. R. Griffiths, "Nitrogen-broadening coefficient of vibration-rotation lines of carbon monoxide," *Appl. Opt.* **20**, 2332 (1981).



- <sup>70</sup>H. S. Lowry and C. J. Fisher, "Line parameter measurements and calculations of CO broadened by nitrogen at elevated temperatures," *J. Quantum Spectrosc. Radiat. Transfer* **27**, 585–591 (1982).
- <sup>71</sup>T. Nakazawa and M. Tanaka, "Measurements of intensities and self- and foreign-gas-broadened half-widths of spectral lines in the CO fundamental band," *J. Quantum Spectrosc. Radiat. Transfer* **28**, 409–416 (1982).
- <sup>72</sup>T. Nakazawa and M. Tanaka, "Intensities, half-widths and shapes of spectral lines in the fundamental band of CO at low temperatures," *J. Quantum Spectrosc. Radiat. Transfer* **28**, 471–480 (1982).
- <sup>73</sup>M. O. Bulanin, A. B. Dokuchaev, M. V. Tonkov, and N. N. Filippov, "Influence of line interference on the vibration-rotation band shapes," *J. Quantum Spectrosc. Radiat. Transfer* **31**, 521–543 (1984).
- <sup>74</sup>J. Bonamy, D. Robert, and C. Boulet, "Simplified models for the temperature dependence of linewidths at elevated temperatures and applications to CO broadened by Ar and N<sub>2</sub>," *J. Quantum Spectrosc. Radiat. Transfer* **31**, 23–34 (1984).
- <sup>75</sup>M. F. Le Moal and F. Severin, "N<sub>2</sub> and H<sub>2</sub> broadening parameters in the fundamental band of CO," *J. Quantum Spectrosc. Radiat. Transfer* **35**, 145–152 (1986).
- <sup>76</sup>J. M. Hartmann, M. Y. Perrin, J. Taine, and L. Rosenmann, "Diode-laser measurements and calculations of CO 1-0 P(4) line broadening in the 294- to 765-K temperature range," *J. Quantum Spectrosc. Radiat. Transfer* **35**, 357–363 (1986).
- <sup>77</sup>J.-P. Bouanich and G. Blanquet, "Pressure broadening of CO and OCS spectral lines," *J. Quantum Spectrosc. Radiat. Transfer* **40**, 205–220 (1988).
- <sup>78</sup>A. Hamdouni, A. Barbe, J.-J. Plateaux, V. Langlois, V. Dana, J.-Y. Mandin, and M. Badaoui, "Measurements of N<sub>2</sub>-induced shifts and broadening coefficients of lines in CO fundamental from Fourier transform spectra," *J. Quantum Spectrosc. Radiat. Transfer* **50**, 247–255 (1993).
- <sup>79</sup>N. Anselm, K. M. T. Yamada, R. Schieder, and G. Winnewisser, "Measurements of foreign gas pressure shift and broadening effects in the (1-0) band of CO with N<sub>2</sub> and Ar," *J. Mol. Spectrosc.* **161**, 284–296 (1993).
- <sup>80</sup>P. Duggan, P. M. Sinclair, M. P. Le Flohic, J. W. Forsman, R. Berman, A. D. May, and J. R. Drummond, "Testing the validity of the optical diffusion coefficient: Line-shape measurements of CO perturbed by N<sub>2</sub>," *Phys. Rev. A* **48**, 2077–2083 (1993).
- <sup>81</sup>J. Y. Mandin, V. Dana, M. Badaoui, A. Barbe, A. Hamdouni, and J. J. Plateaux, "Measurements of pressure-broadening and pressure-shifting coefficients from FT spectra," *J. Mol. Spectrosc.* **164**, 328–337 (1994).
- <sup>82</sup>P. Duggan, P. M. Sinclair, A. D. May, and J. R. Drummond, "Line-shape analysis of speed-dependent collisional width inhomogeneities in CO broadened by Xe, N<sub>2</sub>, and He," *Phys. Rev. A* **51**, 218–224 (1995).
- <sup>83</sup>A. Henry, D. Hurtmans, M. Margottin-Maclou, and A. Valentin, "Confinement narrowing and absorber speed dependent broadening effects on CO lines in the fundamental band perturbed by Xe, Ar, Ne, He and N<sub>2</sub>," *J. Quantum Spectrosc. Radiat. Transfer* **56**, 647–671 (1996).
- <sup>84</sup>J.-P. Bouanich, D. Bermejo, J. L. Domenech, R. Z. Martinez, and J. Santos, "Pressure-induced lineshifts in the 2 ← 0 band of CO self-perturbed and perturbed by He, Kr, O<sub>2</sub>, and N<sub>2</sub>," *J. Mol. Spectrosc.* **179**, 22–31 (1996).
- <sup>85</sup>P. M. Sinclair, P. Duggan, R. Berman, A. D. May, and J. R. Drummond, "Line broadening, shifting, and mixing in the fundamental band of CO perturbed by N<sub>2</sub> at 301 K," *J. Mol. Spectrosc.* **181**, 41–47 (1997).
- <sup>86</sup>B. Sumpf, J. P. Burrows, A. Kissel, H.-D. Kronfeldt, O. Kurtz, I. Meusel, J. Orphal, and S. Voigt, "Line shift investigations for different isotopomers of carbon monoxide," *J. Mol. Spectrosc.* **190**, 226–231 (1998).
- <sup>87</sup>T. Drascher, T. F. Giesen, T. Y. Wang, N. Schmücker, R. Schieder, G. Winnewisser, P. Joubert, and J. Bonamy, "Temperature-dependent line shift and broadening of CO infrared transitions," *J. Mol. Spectrosc.* **192**, 268–276 (1998).
- <sup>88</sup>A. Predoi-Cross, C. Luo, P. M. Sinclair, J. R. Drummond, and A. D. May, "Line broadening and the temperature exponent of the fundamental band in CO-N<sub>2</sub> mixtures," *J. Mol. Spectrosc.* **198**, 291–303 (1999).
- <sup>89</sup>M. Afzelius, P.-E. Bengtsson, and J. Bonamy, "Semiclassical calculations of collision line broadening in Raman spectra of N<sub>2</sub> and CO mixtures," *J. Chem. Phys.* **120**, 8616–8623 (2004).
- <sup>90</sup>T. C. James and E. K. Plyler, "Linewidths in the 2–0 band of carbon monoxide broadened by nitrogen and hydrogen," *J. Chem. Phys.* **40**, 221–223 (1964).
- <sup>91</sup>J.-P. Bouanich and C. Brodbeck, "Mesure des largeurs et des déplacements des raies de la bande 0 → 2 de CO autoperurbé et perturbé par N<sub>2</sub>, O<sub>2</sub>, H<sub>2</sub>, HCl, NO et CO<sub>2</sub>," *J. Quantum Spectrosc. Radiat. Transfer* **13**, 1–7 (1973).
- <sup>92</sup>J.-P. Bouanich, "Lineshifts in the first overtone band of CO self-perturbed and perturbed by N<sub>2</sub> at 298, 193, and 133 K," *Can. J. Phys.* **61**, 919–922 (1983).
- <sup>93</sup>S. Voigt, S. Dreher, J. Orphal, and J. P. Burrows, "N<sub>2</sub>-broadening in the <sup>13</sup>C<sup>16</sup>O 2–0 band around 4167 cm<sup>-1</sup>," *J. Mol. Spectrosc.* **180**, 359–364 (1996).
- <sup>94</sup>A. Predoi-Cross, J. P. Bouanich, D. C. Benner, A. D. May, and J. R. Drummond, "Broadening, shifting, and line asymmetries in the 2 ← 0 band of CO and CO-N<sub>2</sub>: Experimental results and theoretical calculations," *J. Chem. Phys.* **113**, 158–168 (2000).
- <sup>95</sup>D. E. Burch and D. A. Gryvnak, "Strengths, widths, and shapes of the lines of the 3v CO band," *J. Chem. Phys.* **47**, 4930–4940 (1967).
- <sup>96</sup>J. Henningsen, H. Simonsen, T. Mögelberg, and E. Trudso, "The 0 → 3 overtone band of CO: Precise line strengths and broadening parameters," *J. Mol. Spectrosc.* **193**, 354–362 (1999).
- <sup>97</sup>A. Predoi-Cross, C. Hnatovsky, K. Strong, J. R. Drummond, and D. Chris Benner, "Temperature dependence of self- and N<sub>2</sub>-broadening and pressure-induced shifts in the 3 ← 0 band of CO," *J. Mol. Struct.* **695–696**, 269–286 (2004).
- <sup>98</sup>B. J. Connor and H. E. Radford, "Pressure broadening of the CO J = 1–0 rotational transition by N<sub>2</sub>, O<sub>2</sub>, and air," *J. Mol. Spectrosc.* **119**, 229–231 (1986).
- <sup>99</sup>N. Nissen, J. Doose, A. Guarnieri, H. Mäder, V. N. Markov, G. Y. Golubyatnikov, I. I. Leonov, V. N. Shanin, and A. F. Krupnov, "Foreign gas broadening studies of the J' → J = 1 → 0 rotational line of CO by frequency and time domain techniques," *Z. Nat. A* **54**, 218–224 (1999).
- <sup>100</sup>D. Priem, F. Rohart, J.-M. Colmont, G. Włodarczak, and J.-P. Bouanich, "Lineshape study of the J = 3 ← 2 rotational transition of CO perturbed by N<sub>2</sub> and O<sub>2</sub>," *J. Mol. Struct.* **517–518**, 435–454 (2000).
- <sup>101</sup>V. N. Markov, G. Y. Golubyatnikov, V. A. Savin, D. A. Sergeev, A. Guarnieri, and H. Mäder, "Line broadening and shifting studies of the J = 5 ← 4 transition of carbon monoxide perturbed by CO, N<sub>2</sub>, and O<sub>2</sub>," *J. Mol. Spectrosc.* **212**, 1–5 (2002).
- <sup>102</sup>J.-M. Colmont, L. Nguyen, F. Rohart, and G. Włodarczak, "Lineshape analysis of the J = 3 ← 2 and J = 5 ← 4 rotational transitions of room temperature CO broadened by N<sub>2</sub>, O<sub>2</sub>, CO<sub>2</sub> and noble gases," *J. Mol. Spectrosc.* **246**, 86–97 (2007).
- <sup>103</sup>C. Puzzarini, L. Dore, and G. Cazzoli, "A comparison of lineshape models in the analysis of modulated and natural rotational line profiles: Application to the pressure broadening of OCS and CO," *J. Mol. Spectrosc.* **216**, 428–436 (2002).
- <sup>104</sup>P. S. Hsu, H. U. Stauffer, N. Jiang, J. R. Gord, and S. Roy, "Direct measurements of collisional Raman line broadening in the S-branch transitions of CO perturbed by CO, N<sub>2</sub>, and CO<sub>2</sub>," *Appl. Opt.* **58**, C1–C6 (2019).
- <sup>105</sup>M. Słowiński, F. Thibault, Y. Tan, J. Wang, A.-W. Liu, S.-M. Hu, S. Kass, A. Campargue, M. Konefał, H. Jóźwiak, K. Patkowski, P. Żuchowski, R. Ciuryło, D. Lisak, and P. Wcisło, "H<sub>2</sub>-He collisions: *Ab initio* theory meets cavity-enhanced spectra," *Phys. Rev. A* **101**, 052705 (2020).
- <sup>106</sup>B. W. Bakr, D. G. A. Smith, and K. Patkowski, "Highly accurate potential energy surface for the He-H<sub>2</sub> dimer," *J. Chem. Phys.* **139**, 144305 (2013).
- <sup>107</sup>F. Thibault, K. Patkowski, P. S. Żuchowski, H. Jóźwiak, R. Ciuryło, and P. Wcisło, "Rovibrational line-shape parameters for H<sub>2</sub> in He and new H<sub>2</sub>-He potential energy surface," *J. Quantum Spectrosc. Radiat. Transfer* **202**, 308–320 (2017).
- <sup>108</sup>R. Blackmore, "A modified Boltzmann kinetic equation for line shape functions," *J. Chem. Phys.* **87**, 791–800 (1987).
- <sup>109</sup>P. Wcisło, F. Thibault, M. Zaborowski, S. Wójtewicz, A. Cygan, G. Kowzan, P. Masłowski, J. Komasa, M. Puchalski, K. Pachucki, R. Ciuryło, and D. Lisak, "Accurate deuterium spectroscopy for fundamental studies," *J. Quantum Spectrosc. Radiat. Transfer* **213**, 41–51 (2018).

- <sup>110</sup>R. Ciuryło, D. A. Shapiro, J. R. Drummond, and A. D. May, "Solving the line-shape problem with speed-dependent broadening and shifting and with Dicke narrowing. II. Application," *Phys. Rev. A* **65**, 012502 (2001).
- <sup>111</sup>A. D. May, W.-K. Liu, F. R. W. McCourt, R. Ciuryło, J. Sanchez-Fortún Stoker, D. Shapiro, and R. Wehr, "The impact theory of spectral line shapes: A paradigm shift," *Can. J. Phys.* **91**, 879–895 (2013).
- <sup>112</sup>P. R. Berman, "Speed-dependent collisional width and shift parameters in spectral profiles," *J. Quantum Spectrosc. Radiat. Transfer* **12**, 1331–1342 (1972).
- <sup>113</sup>R. H. Dicke, "The effect of collisions upon the Doppler width of spectral lines," *Phys. Rev.* **89**, 472–473 (1953).
- <sup>114</sup>F. Thibault, P. Wcisło, and R. Ciuryło, "A test of H<sub>2</sub>-He potential energy surfaces," *Eur. Phys. J. D* **70**, 236 (2016).
- <sup>115</sup>H. Jóźwiak, F. Thibault, N. Stolarczyk, and P. Wcisło, "Ab initio line-shape calculations for the S and O branches of H<sub>2</sub> perturbed by He," *J. Quantum Spectrosc. Radiat. Transfer* **219**, 313–322 (2018).
- <sup>116</sup>M. Słowiński *et al.*, "Collisional line-shape effects in accurate He-perturbed H<sub>2</sub> spectra" (unpublished).
- <sup>117</sup>P. Wcisło, F. Thibault, N. Stolarczyk, H. Jóźwiak, M. Słowiński, M. Gancewski, K. Stankiewicz, M. Konefał, S. Kassi, A. Campargue, Y. Tan, J. Wang, K. Patkowski, R. Ciuryło, D. Lisak, R. Kochanov, L. Rothman, and I. Gordon, "The first comprehensive dataset of beyond-Voigt line-shape parameters from *ab initio* quantum scattering calculations for the HITRAN database: He-perturbed H<sub>2</sub> case study," *J. Quantum Spectrosc. Radiat. Transfer* **260**, 107477 (2021).
- <sup>118</sup>F. Thibault, R. Z. Martínez, D. Bermejo, and P. Wcisło, "Line-shape parameters for the first rotational lines of HD in He," *Mol. Astrophys.* **19**, 100063 (2020).
- <sup>119</sup>K. Stankiewicz, H. Jóźwiak, M. Gancewski, N. Stolarczyk, F. Thibault, and P. Wcisło, "Ab initio calculations of collisional line-shape parameters and generalized spectroscopic cross-sections for rovibrational dipole lines in HD perturbed by He," *J. Quantum Spectrosc. Radiat. Transfer* **254**, 107194 (2020).
- <sup>120</sup>R. Z. Martínez, D. Bermejo, F. Thibault, and P. Wcisło, "Testing the *ab initio* quantum-scattering calculations for the D<sub>2</sub>-He benchmark system with stimulated Raman spectroscopy," *J. Raman Spectrosc.* **49**, 1339–1349 (2018).
- <sup>121</sup>R. Z. Martínez, D. Bermejo, P. Wcisło, and F. Thibault, "Accurate wavenumber measurements for the S<sub>0</sub>(0), S<sub>0</sub>(1), and S<sub>0</sub>(2) pure rotational Raman lines of D<sub>2</sub>," *J. Raman Spectrosc.* **50**, 127–129 (2018).
- <sup>122</sup>G. Kowzan, H. Cybulski, P. Wcisło, M. Słowiński, A. Viel, P. Masłowski, and F. Thibault, "Subpercent agreement between *ab initio* and experimental collision-induced line shapes of carbon monoxide perturbed by argon," *Phys. Rev. A* **102**, 012821 (2020).
- <sup>123</sup>P. McGuire and D. J. Kouri, "Quantum mechanical close coupling approach to molecular collisions. *j<sub>z</sub>*-conserving coupled states approximation," *J. Chem. Phys.* **60**, 2488–2499 (1974).
- <sup>124</sup>S. Green, "Rotational excitation in H<sub>2</sub>-H<sub>2</sub> collisions: Close-coupling calculations," *J. Chem. Phys.* **62**, 2271–2277 (1975).
- <sup>125</sup>T.-S. Ho and H. Rabitz, "Proper construction of *ab initio* global potential surfaces with accurate long-range interactions," *J. Chem. Phys.* **113**, 3960–3968 (2000).
- <sup>126</sup>G. Gioumousis and C. F. Curtiss, "Molecular collisions. II. Diatomic molecules," *J. Math. Phys.* **2**, 96–104 (1961).
- <sup>127</sup>W. D. Davison, "Rotational energy transfer in molecular collisions: Transitions in *para*-hydrogen," *Discuss. Faraday Soc.* **33**, 71–84 (1962).
- <sup>128</sup>H. Klar, "Theory of scattering between two rigid rotors," *Z. Phys.* **228**, 59 (1969).
- <sup>129</sup>M. H. Alexander and A. E. DePristo, "Symmetry considerations in the quantum treatment of collisions between two diatomic molecules," *J. Chem. Phys.* **66**, 2166–2172 (1977).
- <sup>130</sup>L. Monchick and L. W. Hunter, "Diatomic-diatom molecular collision integrals for pressure broadening and Dicke narrowing: A generalization of Hess's theory," *J. Chem. Phys.* **85**, 713–718 (1986).
- <sup>131</sup>J. Schaefer and L. Monchick, "Line shape cross sections of HD immersed in He and H<sub>2</sub> gas. I. Pressure broadening cross sections," *J. Chem. Phys.* **87**, 171–181 (1987).
- <sup>132</sup>P. Wcisło, F. Thibault, H. Cybulski, and R. Ciuryło, "Strong competition between velocity-changing and phase- or state-changing collisions in H<sub>2</sub> spectra perturbed by Ar," *Phys. Rev. A* **91**, 052505 (2015).
- <sup>133</sup>T. P. Tsien and R. T. Pack, "Rotational excitation in molecular collisions: A strong coupling approximation," *Chem. Phys. Lett.* **6**, 54–56 (1970).
- <sup>134</sup>T. P. Tsien and R. T. Pack, "Rotational excitation in molecular collisions. Corrections to a strong coupling approximation," *Chem. Phys. Lett.* **6**, 400–402 (1970).
- <sup>135</sup>T. P. Tsien and R. T. Pack, "Rotational excitation in molecular collisions. A many-state test of the strong coupling approximation," *Chem. Phys. Lett.* **8**, 579–581 (1971).
- <sup>136</sup>R. T. Pack, "Relations between some exponential approximations in rotationally inelastic molecular collisions," *Chem. Phys. Lett.* **14**, 393–395 (1972).
- <sup>137</sup>H. Rabitz, "Effective potentials in molecular collisions," *J. Chem. Phys.* **57**, 1718–1725 (1972).
- <sup>138</sup>A. E. DePristo and M. H. Alexander, "A decoupled l-dominant approximation for ion-molecule and atom-molecule collisions," *J. Chem. Phys.* **64**, 3009–3013 (1976).
- <sup>139</sup>A. E. DePristo and M. H. Alexander, "Limits of validity of the decoupled l-dominant approximation," *Chem. Phys. Lett.* **44**, 214–218 (1976).
- <sup>140</sup>A. E. DePristo and M. H. Alexander, "Decoupling approximations for rotationally inelastic collisions between ions and polar molecules: H<sup>+</sup>-CN," *J. Phys. B: At., Mol. Opt. Phys.* **9**, 2713–2721 (1976).
- <sup>141</sup>R. Goldflam, S. Green, and D. J. Kouri, "Infinite order sudden approximation for rotational energy transfer in gaseous mixtures," *J. Chem. Phys.* **67**, 4149–4161 (1977).
- <sup>142</sup>D. G. Truhlar, J. T. Muckerman, and R. Bernstein, *Atom-Molecule Collision Theory: A Guide for the Experimentalist*, edited by R. B. Bernstein (Plenum Press, London, 1979), p. 505.
- <sup>143</sup>D. J. Kouri, T. G. Heil, and Y. Shimoni, "On the Lippmann-Schwinger equation for atom-diatom collisions: A rotating frame treatment," *J. Chem. Phys.* **65**, 226–235 (1976).
- <sup>144</sup>R. Goldflam and D. J. Kouri, "On angular momentum decoupling approximations and factorization in diatom-diatom scattering," *J. Chem. Phys.* **70**, 5076–5091 (1979).
- <sup>145</sup>J. Hutson and S. Green, Molscat computer code, version 14, Collaborative Computational Project, 1994.
- <sup>146</sup>D. E. Manolopoulos, "An improved log derivative method for inelastic scattering," *J. Chem. Phys.* **85**, 6425–6429 (1986).
- <sup>147</sup>I. E. Gordon, L. S. Rothman, C. Hill, R. V. Kochanov, Y. Tan, P. F. Bernath, M. Birk, V. Boudon, A. Campargue, K. V. Chance, B. J. Drouin, J.-M. Flaud, R. R. Gamache, J. T. Hodges, D. Jacquemart, V. I. Perevalov, A. Perrin, K. P. Shine, M.-A. H. Smith, J. Tennyson, G. C. Toon, H. Tran, V. G. Tyuterev, A. Barbe, A. G. Császár, V. M. Devi, T. Furtenbacher, J. J. Harrison, J.-M. Hartmann, A. Jolly, T. J. Johnson, T. Karman, I. Kleiner, A. A. Kyuberis, J. Loos, O. M. Lyulin, S. T. Massie, S. N. Mikhailenko, N. Moazzen-Ahmadi, H. S. P. Müller, O. V. Naumenko, A. V. Nikitin, O. L. Polyansky, M. Rey, M. Rotger, S. W. Sharpe, K. Sung, E. Starikova, S. A. Tashkun, J. V. Auwera, G. Wagner, J. Wilzewski, P. Wcisło, S. Yu, and E. J. Zak, "The HITRAN2016 molecular spectroscopic database," *J. Quantum Spectrosc. Radiat. Transfer* **203**, 3–69 (2017), special issue on: HITRAN2016.
- <sup>148</sup>F. Thibault, Pressure broadening and shift code for 2 diatomics - coupled states approximation," Mendeley Data, V1 2020, <http://dx.doi.org/10.17632/ykxz36nwry.1>.
- <sup>149</sup>R. Wehr, A. Vitcu, R. Ciuryło, F. Thibault, J. R. Drummond, and A. D. May, "Spectral line shape of the P(2) transition in CO-Ar: Uncorrelated *ab initio* calculation," *Phys. Rev. A* **66**, 062502 (2002).
- <sup>150</sup>G. Kowzan, P. Wcisło, M. Słowiński, P. Masłowski, A. Viel, and F. Thibault, "Fully quantum calculations of the line-shape parameters for the Hartmann-Trans profile: A CO-Ar case study," *J. Quantum Spectrosc. Radiat. Transfer* **243**, 106803 (2020).
- <sup>151</sup>F. Thibault, B. Calil, J. Buldyreva, M. Chrysos, J.-M. Hartmann, and J.-P. Bouanich, "Experimental and theoretical CO<sub>2</sub>-Ar pressure-broadening cross sections and their temperature dependence," *Phys. Chem. Chem. Phys.* **3**, 3924–3933 (2001).



- <sup>152</sup>L. Gomez, S. V. Ivanov, O. G. Buzykin, and F. Thibault, "Comparison of quantum, semiclassical and classical methods in hydrogen broadening of nitrogen lines," *J. Quantum Spectrosc. Radiat. Transfer* **112**, 1942–1949 (2011).
- <sup>153</sup>F. Thibault, B. Corretja, A. Viel, D. Bermejo, R. Z. Martínez, and B. Bussery-Honvault, "Linewidths of C<sub>2</sub>H<sub>2</sub> perturbed by H<sub>2</sub>: Experiments and calculations from an *ab initio* potential," *Phys. Chem. Chem. Phys.* **10**, 5419–5428 (2008).
- <sup>154</sup>F. Thibault, R. Z. Martínez, D. Bermejo, and L. Gómez, "Collisional line widths of autoperturbed N<sub>2</sub>: Measurements and quantum calculations," *J. Quantum Spectrosc. Radiat. Transfer* **112**, 2542–2551 (2011).
- <sup>155</sup>L. Galatry, "Simultaneous effect of doppler and foreign gas broadening on spectral lines," *Phys. Rev.* **122**, 1218–1223 (1961).
- <sup>156</sup>S. G. Rautian and I. I. Sobel'man, "The effect of collisions on the doppler broadening of spectral lines," *Sov. Phys. Usp.* **9**, 701–716 (1967).
- <sup>157</sup>C. F. Roche, A. S. Dickinson, and J. M. Hutson, "A failing of coupled-states calculations for inelastic and pressure-broadening cross sections: Calculations on CO<sub>2</sub>-Ar," *J. Chem. Phys.* **111**, 5824–5828 (1999).
- <sup>158</sup>F. Thibault, R. Z. Martínez, J. L. Domenech, D. Bermejo, and J.-P. Bouanich, "Raman and infrared linewidths of CO in Ar," *J. Chem. Phys.* **117**, 2523–2531 (2002).
- <sup>159</sup>R. Z. Martínez, J. L. Domenech, D. Bermejo, F. Thibault, J.-P. Bouanich, and C. Boulet, "Close coupling calculations for rotational relaxation of CO in Argon: Accuracy of energy corrected sudden scaling procedures and comparison with experimental data," *J. Chem. Phys.* **119**, 10563–10574 (2003).

## Stimulated Raman scattering metrology of molecular hydrogen

Marco Lamperti<sup>1,4✉</sup>, Lucile Rutkowski<sup>2</sup>, Daniele Ronchetti<sup>1,5,6</sup>, Davide Gatti<sup>1</sup>, Riccardo Gotti<sup>1,7</sup>, Giulio Cerullo<sup>1</sup>, Franck Thibault<sup>2</sup>, Hubert Jóźwiak<sup>3</sup>, Szymon Wójtewicz<sup>3</sup>, Piotr Maślowski<sup>3</sup>, Piotr Wcisło<sup>3</sup>, Dario Polli<sup>1</sup> & Marco Marangoni<sup>1</sup>

Frequency combs have revolutionized optical frequency metrology, allowing one to determine highly accurate transition frequencies of a wealth of molecular species. These progresses have only marginally benefited infrared-inactive transitions, due to their inherently weak cross-sections. Here we overcome this limitation by introducing stimulated-Raman-scattering metrology, where a frequency comb is exploited to calibrate the frequency detuning between the pump and Stokes excitation lasers. We apply this approach to the investigation of molecular hydrogen, which is a recognized benchmark for tests of quantum electrodynamics and of theories that describe physics beyond the standard model. Specifically, we measure the transition frequency of the Q(1) fundamental line of H<sub>2</sub> around 4155 cm<sup>-1</sup> with few parts-per-billion uncertainty, which is comparable to the theoretical benchmark of ab initio calculations and more than a decade better than the experimental state of the art. Our comb-calibrated stimulated Raman scattering spectrometer extends the toolkit of optical frequency metrology as it can be applied, with simple technical changes, to many other infrared-inactive transitions, over a 50–5000 cm<sup>-1</sup> range that covers also purely rotational bands.

<sup>1</sup>Dipartimento di Fisica - Politecnico di Milano and IFN-CNR, Via Gaetano Previati 1/C, 23900 Lecco, Italy. <sup>2</sup>Univ Rennes, CNRS, IPR (Institut de Physique de Rennes)-UMR 6251, F-35000 Rennes, France. <sup>3</sup>Institute of Physics, Faculty of Physics, Astronomy and Informatics, Nicolaus Copernicus University, Grudziadzka 5, 87-100 Toruń, Poland. <sup>4</sup>Present address: Dipartimento di Scienza e Alta tecnologia, Università degli studi dell'Insubria, 22100 Como, Italy. <sup>5</sup>Present address: Department of Physics, Universität Hamburg, Jungiusstrasse 9, 20355 Hamburg, Germany. <sup>6</sup>Present address: Max Planck School of Photonics, Friedrich-Schiller University of Jena, Albert-Einstein-Str. 6, 07745 Jena, Germany. <sup>7</sup>Present address: Dipartimento di Ingegneria Industriale e dell'Informazione, Università di Pavia, Via Ferrata 5, 27100 Pavia, Italy. ✉email: [marco.lamperti@uninsubria.it](mailto:marco.lamperti@uninsubria.it)

The invention of optical frequency combs has enabled, in the past two decades, accurate measurements of the energy values of multiple atomic and molecular transitions across a large part of the electromagnetic spectrum<sup>1–3</sup>. One of the areas where precise absolute frequency calibration plays a pivotal role for fundamental physics is the spectroscopic investigation of molecular hydrogen and its isotopologs, whose transition frequencies can be accurately predicted by theory<sup>4</sup>. The comparison between theory and experiments represents a testbed for molecular quantum electrodynamics<sup>5</sup> (QED) as well as a compelling approach to explore physics beyond the standard model<sup>6–8</sup> or to determine fundamental quantities such as the nucleon-electron mass ratios<sup>9</sup>.

A stumbling block to the accuracy of experimental determinations of transition frequencies is the intrinsic weakness of quadrupole rovibrational transitions, the only ones allowed in homonuclear species such as H<sub>2</sub> and D<sub>2</sub>. Many experiments circumvented this weakness using high-finesse optical cavities providing enhancement of the effective absorption length up to several kilometers<sup>10</sup>. Thanks to the comb referencing of the frequency of the cavity-injected laser, transition frequencies have been measured with uncertainties of few parts per billion (ppb)<sup>11–16</sup>, at the same level of *ab initio* calculations<sup>4</sup>. The main limiting factors are the signal-to-noise ratio at low pressures and the nontrivial extrapolation of the line center to zero pressure because of the complexity of absorption lineshapes<sup>17</sup>. Cavity-enhanced measurements have produced so far accurate determinations only on overtone bands in the near-infrared. Their extension to fundamental rovibrational transitions which fall in the mid-infrared is a complex task, due the decreased quality of lasers, mirrors, detectors, and modulators in this region of the spectrum.

An alternative solution for determining the frequency of fundamental transitions is resonantly-enhanced multi-photon ionization (REMPI) applied to a molecular beam: it involves state-selective ionization of the excited molecule through a pulsed ultraviolet laser and subsequent mass-selective detection of the generated ion. In 2015, Ubachs and co-workers successfully obtained by REMPI an uncertainty of  $2 \times 10^{-4} \text{ cm}^{-1}$  on the Q(0), Q(1) and Q(2) lines of the main hydrogen isotopologs<sup>18</sup>. For D<sub>2</sub>, this benchmark was improved recently, down to  $6 \times 10^{-7} \text{ cm}^{-1}$  (0.2 ppb at a frequency of  $3167 \text{ cm}^{-1}$ ) on the S(0) 1–0 transition<sup>19</sup>, primarily thanks to an efficient excitation of the molecules in the upper vibrational state and to an accurate reduction of systematic errors related to the fine structure of the transition. The excitation was fostered by a strong static electric field that induces a transition dipole moment in the molecule and thus enhances the absorption of an intense comb-referenced mid-infrared laser. The overall setup

remains quite complex and challenging to scale to purely rotational transitions, that would require far-infrared lasers<sup>20</sup>.

Here, we tackle the challenge of precision spectroscopy of infrared-inactive vibrational transitions by revitalizing and adding metrological quality to the stimulated Raman scattering (SRS) technique<sup>21</sup>. SRS is a third-order nonlinear spectroscopic process that makes use of two laser fields with proper frequency detuning, the so-called pump and Stokes fields, to excite a given vibration. It has been the approach of election in the past century to address transitions of dipole-inactive species like H<sub>2</sub><sup>22,23</sup>, but it has never benefited from the enhanced precision afforded by frequency combs. Here we introduce comb-assisted SRS metrology to study with high accuracy fundamental infrared-inactive transitions. The approach has the potential to cover a two-decade-spanning range of frequencies, from 50 to  $5000 \text{ cm}^{-1}$ , by changing the wavelength of the pump laser in the near infrared, leaving all other parts of the apparatus mostly unaltered. We apply the spectrometer to the most studied stretching mode of H<sub>2</sub> at  $\approx 4155 \text{ cm}^{-1}$ , corresponding to the Q(1) line of the 1–0 band. We improve the state of the art for H<sub>2</sub>, obtained through REMPI, by 20 times<sup>18</sup>, achieving a combined uncertainty of  $1.0 \times 10^{-5} \text{ cm}^{-1}$  (310 kHz) that challenges the theoretical benchmark<sup>4</sup>. This required the implementation of a multi-spectra fitting procedure for the extrapolation to zero pressure of the line center, with a set of fitting parameters fixed to *ab initio* values inferred from quantum-scattering calculations on H<sub>2</sub>–H<sub>2</sub> collisions<sup>24</sup>.

## Results

**Comb-calibrated coherent Raman spectrometer.** SRS requires the use of two detuned lasers (pump field at frequency  $\nu_p$  and Stokes field at frequency  $\nu_s < \nu_p$ ) to probe a rovibrational transition at frequency  $\nu_p - \nu_s$ . An energy transfer from the pump to the Stokes beam occurs when their frequency detuning is resonant with a Raman-active transition, in our case the Q(1) transition of the fundamental rovibrational band of H<sub>2</sub> around  $4155 \text{ cm}^{-1}$ . The measured quantity is the so-called Stimulated Raman Loss (SRL), which is the normalized change  $\Delta I_p / I_p$  of the pump intensity  $I_p$  induced by the Raman interaction. It is proportional, without any limitation given by phase matching, to the interaction length ( $L$ ) and to the Stokes field intensity ( $I_s$ )<sup>25</sup>:

$$\text{SRL} = \frac{\Delta I_p}{I_p} \propto \text{Im} \{ \chi^{(3)}(\nu_p - \nu_s) \} L I_s$$

The resonant third-order nonlinear susceptibility  $\chi^{(3)}$  of the medium entails the dependence of the SRL on the pump-Stokes

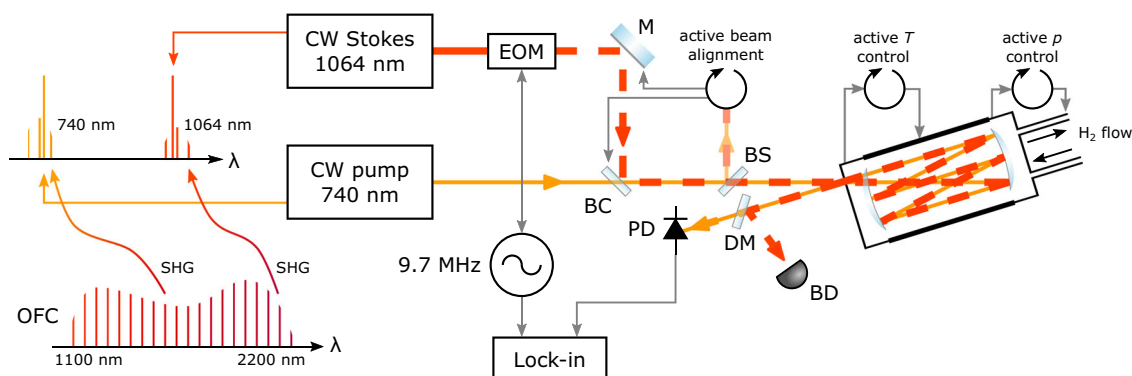


**Fig. 1 Comb-assisted stimulated Raman scattering.** EOM electro-optic modulator, M mirror, BC beam combiner, BS beam sampler, DM dichroic mirror, BD beam dumper, PD photodiode, OFC optical frequency comb, SHG second-harmonic generation. Comb referencing of pump and Stokes lasers is obtained through second-harmonic generation of selected spectral portions of an octave-spanning continuum generated by an Er:fiber comb (see “Methods” for details).

frequency detuning, which reflects in  $H_2$  a complex collisional physics. To maximize the SRL signal, we used a multi-pass cell and a high-power Stokes laser.

The spectrometer (depicted in Fig. 1) employs a pair of single-frequency lasers for the pump (2 mW at 740 nm, <300 kHz linewidth) and Stokes (5 W at 1064 nm, <100 kHz linewidth) fields, with optical frequencies calibrated on a primary frequency standard through an optical frequency comb (see “Methods” for details). The two beams are superimposed by an active alignment system (see “Methods” for details) and mode matched to a multi-pass cell filled with  $H_2$ . The cell can contain gas in a pressure range from  $10^{-3}$  to 5 bar and is equipped with broadband dielectric mirrors that guarantee a total transmission around 50% from 700 to 1100 nm upon 70 reflections inside the cell and a total optical path length of 30 m. Gas temperature and pressure are actively stabilized to user-set values (see Methods for details). At the cell output, the pump is separated from the Stokes and is sent to a photodiode to measure the SRL signal, which is at the  $10^{-4}$  level at 1 bar of  $H_2$  pressure in our experimental conditions. The signal-to-noise ratio (SNR) of the measurement is brought to the shot-noise limit (corresponding to root-mean square fluctuations of  $3.3 \times 10^{-8}$  for 1 s measurement time, see Supplementary Note 2 for details) by a modulation transfer technique that exploits high-frequency (9.7 MHz) electro-optical modulation of the Stokes intensity and synchronous detection of the SRL with a lock-in amplifier. Spectral acquisitions are carried out by measuring the SRL while repeatedly scanning the Stokes frequency over about 12 GHz around the center of the transition. The absolute frequency calibration comes from offset-locking the pump laser frequency to the nearest mode of a frequency comb and by real-time tracking of the Stokes frequency through high-speed acquisition and processing of its beat note against the same comb. A single spectral scan takes from 0.5 to 5 s depending on the gas pressure. Spectral points acquired over many subsequent scans with stable thermodynamic conditions are binned to obtain a single averaged spectrum with 1 MHz point spacing.

**Spectral measurements.** Spectral acquisitions were made at 9 pressure values in the range 0.05–4 bar and at constant temperature  $T = 303.1$  K. The exploration of such a large pressure range allows one to follow the complex collisional phenomena taking place in the ensemble of gas molecules and enables a robust determination of the transition frequency, as described in the following section and in Supplementary Note 4. A typical set of spectra is shown in Fig. 2a in an absolute SRL scale. The shape and the width of the line change considerably in the explored pressure range (see Fig. 2b for a zoom on lower pressures). Qualitatively, the most evident effect is that at high pressure the spectra are narrower and tend to exhibit a Lorentzian lineshape, whereas at lower pressure—see Fig. 2b—the lineshape tends to be broader and Gaussian. This is due to the Dicke effect<sup>26</sup>, which is the narrowing of the velocity distribution of the gas molecules and thus of the Doppler profile at increasing collision rates: this effect is prominent in  $H_2$  around 2 bar, where it leads to an almost complete extinction of Doppler broadening and to a minimum spectral width of 260 MHz. As a result, the SNR of high-pressure spectra is high even with short measurement times, reaching around 8000 over 10 min with a 1 MHz sampling. Another evident qualitative effect is a pronounced shift of the line peak with pressure, which has to be properly accounted for to extrapolate an accurate line center to zero pressure and compare it with that calculated on the isolated molecule. This calls for a refined modeling of the collisional physics of  $H_2$  and for the two-step analysis described below.

**Multi-pressure global fitting.** As a first step for data analysis we modeled the experimental spectra with the  $\beta$ -corrected Hartmann–Tran profile ( $\beta$ HTP), which is a spectral line profile optimized for  $H_2$  isotopologs<sup>27</sup>. It accounts for all main collisional phenomena at play, including velocity-changing collisions and speed-dependent effects, while exhibiting an analytical representation that can be efficiently integrated into least-square fitting procedures. To reduce the correlations among the 8 collisional parameters that define the  $\beta$ HTP profile<sup>24</sup>, we fixed a subset of them to ab initio values inferred from quantum-scattering calculations of  $H_2$ – $H_2$  collisions (described in Supplementary Note 3). For every fit we left as free parameters the unperturbed (zero-pressure) transition frequency  $\nu_0$ , which is the quantity of main interest here, and the linear pressure shift of the line center  $\delta_0$ , which is hard to be accurately predicted by theory and can be better constrained by measurements. Figure 2c, d show the residuals of two types of fitting conducted in a global form over the entire multi-pressure dataset, using just 5 (Fig. 2c) or 2 ( $\nu_0$ ,  $\delta_0$ , Fig. 2d) free parameters, respectively (details given in Supplementary Note 4). In both cases we observe structured residuals at a level of 1% of the line maximum, with similar reduced chi-square values (1.3 and 1.2) and fitted  $\delta_0$  parameters ( $-2.7$  and  $-2.69$  cm $^{-1}$ ). This is an indication of consistency between experimental spectra and lineshape model with ab initio collisional calculations. On the other hand, the two fits converge to different values of the line center  $\nu_0$ , with a discrepancy of almost 2.5 MHz. This is due to the concurrence of two effects, namely the difficulty of  $\beta$ HTP to fully model the collisional physics of  $H_2$  in such a very large pressure range<sup>24</sup> and the inclusion of high-pressure spectra in the fit. While being of key importance for the retrieval of robust collisional parameters, they introduce a strong leveraging effect that amplifies the impact on the line center of any imperfect assessment of collisional parameters.

**Extrapolation of the zero-pressure line center.** The second step in our data analysis was to develop a procedure to extrapolate the line center overcoming the limitations of the model while reducing the impact of high-pressure spectra. To this purpose, we first investigated how the inferred  $\nu_0$  changes upon restricting the fit to experimental data at lower and lower pressures (i.e., progressively discarding high-pressure spectra), down to a value  $p_{\max} = 0.2$  bar, to include in the fit at least three pressures. Figure 3a reports  $\nu_0$  as a function of  $p_{\max}$ , taking all collisional parameters except  $\delta_0$  fixed to ab initio values. Three trajectories are retrieved, corresponding to three different fixed values of  $\delta_0$ , from  $-2.7$  to  $-2.36$  cm $^{-1}$  atm $^{-1}$ , which define the limits of our confidence interval for this parameter (see Supplementary Note 4 for details on such an interval). They showcase a strong dependence of  $\nu_0$  on both  $p_{\max}$  and  $\delta_0$ , but at the same time also a clear convergence to one another while reducing  $p_{\max}$ : this suggests an extrapolation of these trajectories to  $p_{\max} = 0$  as a viable approach to infer the line center frequency of the isolated molecule, minimizing the errors introduced by the model and by the uncertainty on  $\delta_0$ . This extrapolation is shown in Fig. 3b using a quadratic fit over the last four points of the trajectories.

**Uncertainty budget.** The line center uncertainty due to  $\delta_0$  can be quantified with the help of the inset in Fig. 3, which provides a zoomed-in view of the three trajectories and their quadratic extrapolations to  $p_{\max} = 0$ . The half peak-to-peak distance between the two outer extrapolations amounts to 80 kHz, which was taken as an estimate for this systematic uncertainty term. As a second source of systematic uncertainty, we evaluated the impact on  $\nu_0$  of the uncertainty on the ab initio parameters kept fixed in the fitting. For every such parameter varied in its confidence interval (see Supplementary Notes 4 and 5 for details) we

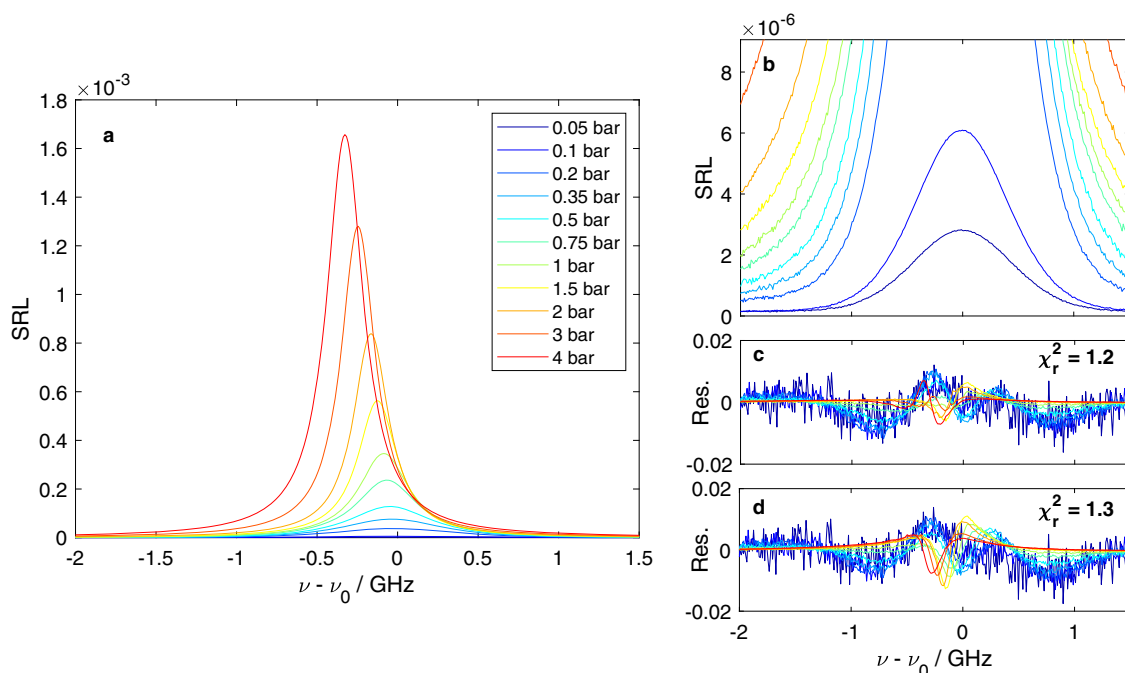


**Fig. 2 Stimulated Raman scattering metrology of H<sub>2</sub>.** **a** Set of spectra at different pressures plotted in an absolute SRL scale. Legend applies to all panels. **b** Zoom of **a** showing a detail of the spectra acquired at pressures equal to 0.05 and 0.1 bar. **c** Residuals (data—model) normalized to the corresponding spectral maxima, obtained from a global fitting with 5 free parameters and 3 fixed to ab initio value.  $\chi_r^2$  represents the reduced chi square of the fit. **d** Residuals as above, obtained from a global fitting with 2 free ( $\nu_0$ ,  $\delta_0$ ) and 6 fixed parameters.

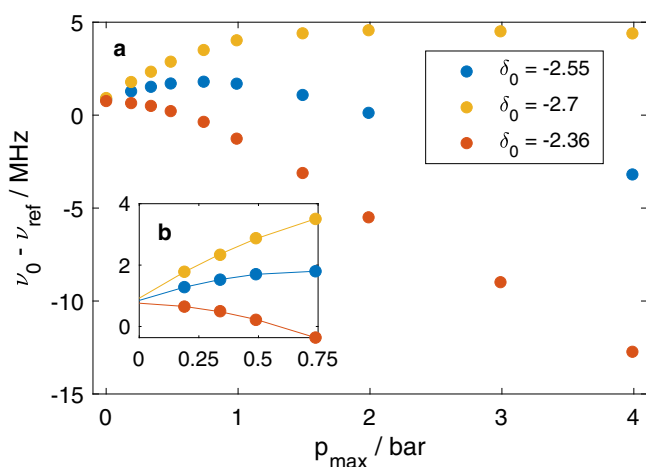


**Fig. 3 Determination of the frequency of the Q(1) 1-0 line of H<sub>2</sub>.** **a** Inferred  $\nu_0$  as a function of the maximum pressure  $p_{\max}$  considered for the global fitting. The collisional parameters are fixed to ab initio parameters except  $\delta_0$ , which is fixed to the three different values specified in the legend, generating the three trajectories shown here. **b** Zoomed-in view of the low-pressure range together with parabolic extrapolations (lines) to  $p_{\max} = 0$ . The vertical axis reports the difference between the fitted  $\nu_0$  and the ab initio value  $\nu_{\text{ref}}$  calculated by Komasa et al.<sup>4</sup>.

calculated trajectories similar to those reported in Fig. 3 and considered the half peak-to-peak distance of the outer extrapolations as the corresponding uncertainty contribution to  $\nu_0$ , to be summed up in quadrature to the other contributions. This procedure leads to an additional term of systematic uncertainty of 220 kHz. To quantify the statistical uncertainty, we applied a bootstrap procedure taking advantage of the many spectral datasets acquired, running many fits on randomly assembled spectral datasets obtained by combinations of spectra acquired in different days over several months. This allows to account not only for white noise sources on the

vertical and horizontal scales of the measurement, but also for contributions due to long-term drifts in the spectrometer or to uneven thermodynamic conditions. Differently from the systematic uncertainties above, we used here the root-mean square deviation of the different fits as an estimator for a final value of 200 kHz. The combined uncertainty budget for the extrapolated transition frequency, obtained by quadrature sum of the three contributions above, amounts to 310 kHz ( $10^{-5} \text{ cm}^{-1}$ ), thus half that of the theoretical benchmark for the transition<sup>4</sup> and 20 times better than the experimental benchmark<sup>18</sup>.

## Discussion

The measured transition frequency is  $4155.253790(10) \text{ cm}^{-1}$ . It is compared in Table 1 with the best experimental<sup>18</sup> and theoretical<sup>4</sup> determinations reported so far. For both cases, the agreement with our determination is within  $1\sigma$ , using the combined uncertainty of the two compared frequencies as an estimator for  $\sigma$ .

To put this result in a broader context, we report in Fig. 4 the deviations between theory and experiments for all transition frequencies accurately measured so far on neutral molecular hydrogen and its isotopologs. Experimental determinations are in excess of calculated values in all cases, independently of the isotopolog, of the rovibrational branch, of the experimental approach and of whether the transition is dipole or quadrupole allowed, with discrepancies from  $0.4$  up to  $2.3\sigma$ . Focusing on quadrupole lines, by far the most accurate experimental determinations were obtained on D<sub>2</sub>, with an uncertainty down to 161 kHz for lines of the 2-0 band using cavity-ring-down spectroscopy<sup>11</sup>, and of 17 kHz for lines of the 1-0 band on a molecular beam<sup>19</sup>, in both cases well below the theoretical uncertainty. For H<sub>2</sub>, the center frequency here reported is the most accurate obtained so far and the only value exhibiting an accuracy comparable with theory, thus making it of significance for QED tests. The discrepancy with theory is of the same sign and of the same order of magnitude ( $1\sigma$ ) encountered in several



measurements on D<sub>2</sub>, and is dominated by the theoretical uncertainty. Overall, experimental accuracy has grown up at a faster pace than theory in recent years, reaching and even surpassing theory in some cases, yet not at point to challenge our current QED modeling of molecules. This challenge requires further efforts, over both axes.

In conclusion, our work brings SRS metrology in the arena of available techniques for tests of fundamental physics in molecular systems. For the Q(1) 1-0 line of H<sub>2</sub> we demonstrated an improvement by more than one order of magnitude with respect to the most accurate experimental determination, and surpassed the uncertainty of state-of-the-art theoretical calculations by a factor of 2. The strength of our setup lies in the ability to target a great variety of rovibrational transitions, in the mid or far infrared, by simple tuning of a near-infrared cw laser. This metrological tool enables probing other fundamental rovibrational transitions of H<sub>2</sub> and its isotopologs. It also opens up for addressing Raman-active transitions of heavier molecules, as well as extending comb-calibration to so far unaddressed purely rotational bands.

Methods

**Absolute frequency calibration of Raman spectra.** The frequency detuning between the pump and Stokes laser fields is calibrated against a frequency comb generated by an amplified Er: fiber femtosecond oscillator (Menlo C-comb)

**Table 1 Comparison between the frequency of the Q(1) 1-0 transition obtained in this work with the best available experimental<sup>18</sup> and theoretical<sup>4</sup> data.**

	This work	Experiment <sup>18</sup>	Theory <sup>4</sup>
$\nu_0/\text{cm}^{-1}$	4155.253790(10)	4155.25400(21)	4155.253762(26)
$\nu_0/\text{MHz}$	124571374.73(31)	124571381.0(63)	124571373.89(78)
$\Delta/\text{MHz}$	-	-6.3	0.84
$\sigma/\text{MHz}$	-	6.3	0.84

The uncertainties expressed in parentheses represent one standard deviation, obtained as the quadrature sum of the statistical and systematic uncertainties (for experimental values), or the estimated systematic uncertainty (for theoretical values). The deviation  $\Delta$  between the frequencies is calculated by subtracting others' data from our value. The combined uncertainty  $\sigma$  is calculated as the quadrature sum of the uncertainties of the two measurements. Note: it is a coincidence that deviations equal uncertainties.

emitting pulses at a repetition frequency  $f_{\text{rep}} = 100$  MHz, stabilized on a GPS-disciplined Rb clock (Timing Solutions 4410 A). The experimental configuration is described in detail in Supplementary Note 1. Briefly, we first broaden the comb inside a highly nonlinear fiber, then frequency double (through second harmonic generation in periodically poled nonlinear crystals) spectral regions around 1480 nm and 2128 nm to obtain narrow frequency combs around 740 and 1064 nm. These are mixed with the pump (Toptica DL Pro) and Stokes (NKT Photonics Boostik) beams, respectively, to obtain beat notes between the comb and each cw laser. If we write the frequency of the  $n$ -th tooth of the broadened comb as  $\nu_n = nf_{\text{rep}} + f_{\text{ceo}}$ , the frequencies of the pump and Stokes lasers can be expressed as  $\nu_{p/s} = n_{p/s}f_{\text{rep}} + 2f_{\text{ceo}} \pm f_{\text{beat},p/s}$ , where the carrier-envelope frequency  $f_{\text{ceo}}$  is doubled by second harmonic generation and the beat note  $f_{\text{beat},p/s}$  is added or subtracted depending on the relative position of the pump/Stokes frequencies with respect to their closest comb tooth of index  $n_{p/s}$ . The detuning between the two cw lasers can thus be unambiguously determined from the relationship  $\nu_p - \nu_s = (n_p - n_s)f_{\text{rep}} \pm (f_{\text{beat},p} - f_{\text{beat},s})$  once the pump and Stokes beat notes are measured and the correct comb-index detuning  $\Delta n = (n_p - n_s)$  is identified, with no contribution from  $f_{\text{ceo}}$ . In our case the pump beat note is stabilized at 10 MHz while that of the Stokes beat note is measured in real time while scanning the frequency, as described in the next paragraph. The integer number  $\Delta n$  is determined by minimizing the distance between the experimental line center and its reference value from literature.

**Spectra acquisition and processing.** During spectral acquisitions the pump frequency is kept constant while the Stokes frequency is repeatedly scanned over about 12 GHz with a rate from 1 Hz at high pressure to 0.1 Hz at low pressure<sup>28</sup>. To ensure the proper calibration of spectra, we use a single digital acquisition board to synchronously measure the SRL signal and the beat note of the Stokes field. The Stokes beat note is digitized at 14 bit and 100 MSamples s<sup>-1</sup> and its frequency calculated in real-time by FFT applied at every 1024 samples via a field-programmable gate array available for on-board processing (FPGA, PXIe-7961 FPGA board and NI-5781 add-on, National Instruments). The demodulated SRL signal (from a Zurich Instruments H2FLI lock-in amplifier) is simultaneously acquired and averaged over the same 1024 samples. The absolute frequency is reconstructed in post-processing by unwrapping the measured beat note barycentre<sup>28,29</sup>. Spectral acquisition times typically vary from 10 to 30 min depending on the pressure, but longer times could be used to further enhance the SNR. The spectral points pertaining to subsequent scans are binned to produce the final averaged spectra with frequency spacing of 1 MHz. Fitted spectra and residuals are further binned with bin width of 10 MHz to help identification of non-flat residuals (see example in Fig. 2).

**Active alignment of beams.** Any angular misalignment between pump and Stokes beams during the Raman interaction was found to originate a shift of the measured frequency detuning<sup>28</sup>. Manual alignment is accurate to about 300  $\mu\text{rad}$  in our setup, corresponding to fluctuations of the measured center frequency by about 1–2 MHz from measurement to measurement. To ensure optimal superposition of

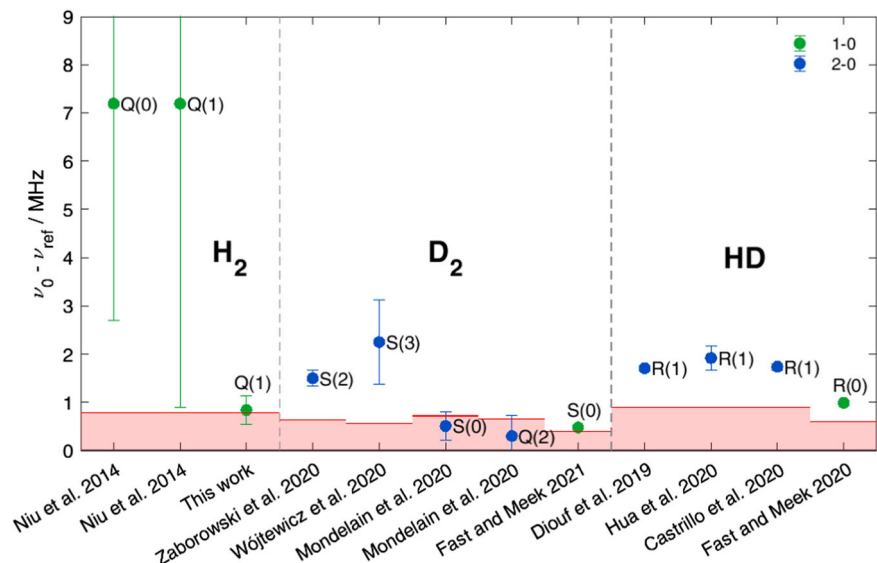


**Fig. 4 Comparison of experiment and theory for various rovibrational transitions of H<sub>2</sub> isotopologs.** Data points represent the discrepancy on the transition frequency (experiment-theory), with error bars given by the experimental uncertainty ( $1\sigma$ ) and the height of the red shaded area at the bottom representing the theoretical uncertainty. Line names are reported next to data points, while the rovibrational band is identified through the point color (see legend). The data point corresponding to this work summarizes 10 measurement series acquired over 5 months.



the laser beams, we built an active alignment system based on the imaging of the near and far fields of both beams on a camera to track any displacement and correct it in a servo loop that acts on piezo-tilt mirror holders. To this purpose, the pump and Stokes beams are sampled right after the beam combiner (BC in Fig. 2), then sent through a beam splitter to generate two replicas. The first replica impinges on the sensor of a color CMOS camera (Thorlabs CS235CU) after passing through a lens that provides imaging of the BC plane onto the sensor; we refer to this plane as the near field (NF). The second replica impinges on the sensor after a total propagation distance equal to that from the beam combiner to the center of the cell, that we refer to as the far field (FF). The differential sensitivity of the color pixels of the camera at pump and Stokes wavelengths allow disentangling the two colors and control their relative displacements in both the NF and FF. This takes place in real time thanks to a LabView software that, upon calculation of the pump and Stokes centroids from the fitting of their intensity profiles, optimizes the overlap of the Stokes beam onto the pump beam through a 4-channels proportional-integral-derivative (PID) controller followed by 4 piezoelectric tip-tilt mirror adjusters (see Supplementary Note 6 for a photograph of the apparatus). The system provides an angular root mean square (RMS) stability of  $6 \mu\text{rad}$  (corresponding to RMS fluctuations of the measured frequency detuning by 65 kHz) over few hours.

**Active stabilization of thermodynamic gas parameters.** Uniform and constant temperature of the gas inside the multipass cell is obtained by encasing the cell inside a box made with thick Styrofoam. A pair of rubber heater stripes (Minco) is placed onto the cell central cylinder, and two fans circulate the air inside the Styrofoam box to ensure temperature homogeneity better than 100 mK on the outer surface of the cell. The temperature is measured through a calibrated temperature sensor (a Pt100 probe paired to a 6  $\frac{1}{2}$  digit multimeter, Keysight 34461A) with an accuracy of 50 mK, whose output is used by a software PID controller (implemented in LabView) to regulate the current passing through the heater stripes and stabilize the temperature to 303.1 K. To compensate for small leaks of the cell, a constant flow of about  $10^{-2} \text{ L min}^{-1}$  is established in the cell using two flow controllers (Bronkhorst F-201CV-1K0-RAD-33-V), the first one installed between the  $\text{H}_2$  cylinder and the cell, the second one between the cell and the vacuum pump. The pressure inside the cell is measured via a calibrated pressure sensor (Honeywell Sensotec TJE read by a Burster 9206 interface) with relative uncertainty better than  $10^{-3}$ . Through a software PID control loop, the output flow is regulated to maintain a constant pressure inside the cell.

## Data availability

The datasets analyzed during the current study and the corresponding analysis code are available as a CodeOcean capsule, <https://doi.org/10.24433/CO.7913441.v1>.

Received: 26 September 2022; Accepted: 22 March 2023;

Published online: 11 April 2023

## References

- Holzwarth, R. et al. Optical frequency synthesizer for precision spectroscopy. *Phys. Rev. Lett.* **85**, 2264–2267 (2000).
- Diddams, S. A. et al. Direct link between microwave and optical frequencies with a 300 THz femtosecond laser comb. *Phys. Rev. Lett.* **84**, 5102–5105 (2000).
- Fortier, T. & Baumann, E. 20 Years of developments in optical frequency comb technology and applications. *Commun. Phys.* **2**, 1–16 (2019).
- Komasa, J., Puchalski, M., Czachorowski, P., Łach, G. & Pachucki, K. Rovibrational energy levels of the hydrogen molecule through nonadiabatic perturbation theory. *Phys. Rev. A* **100**, 032519 (2019).
- Salumbides, E. J., Dickenson, G. D., Ivanov, T. I. & Ubachs, W. QED effects in molecules: test on rotational quantum states of  $\text{H}_2$ . *Phys. Rev. Lett.* **107**, 2–5 (2011).
- Salumbides, E. J. et al. Bounds on fifth forces from precision measurements on molecules. *Phys. Rev. D* **87**, 112008 (2013).
- Ubachs, W., Koelemeij, J. C. J., Eikema, K. S. E. & Salumbides, E. J. Physics beyond the Standard Model from hydrogen spectroscopy. *J. Mol. Spectrosc.* **320**, 1–12 (2016).
- Biesheuvel, J. et al. Probing QED and fundamental constants through laser spectroscopy of vibrational transitions in  $\text{HD}^+$ . *Nat. Commun.* **7**, 10385 (2016).
- Patra, S. et al. Proton-electron mass ratio from laser spectroscopy of  $\text{HD}^+$  at the part-per-trillion level. *Science* **369**, 1238–1241 (2020).
- Romanini, D., Venturilli, I., Méjean, G., Morville, J. & Kerstel, E. in *Cavity-Enhanced Spectroscopy and Sensing* (eds. Gagliardi, G. & Looch, H.-P.) 1–60 (Springer, 2014).
- Zaborowski, M. et al. Ultrahigh finesse cavity-enhanced spectroscopy for accurate tests of quantum electrodynamics for molecules. *Opt. Lett.* **45**, 1603 (2020).
- Wójtewicz, S. et al. Accurate deuterium spectroscopy and comparison with ab initio calculations. *Phys. Rev. A* **101**, 052504 (2020).
- Mondelain, D., Kass, S. & Campargue, A. Transition frequencies in the (2-0) band of  $\text{D}_2$  with MHz accuracy. *J. Quant. Spectrosc. Radiat. Transf.* **253**, 107020 (2020).
- Diouf, M. L., Cozijn, F. M. J., Darquié, B., Salumbides, E. J. & Ubachs, W. Lamb-dips and Lamb-peaks in the saturation spectrum of  $\text{HD}$ . *Opt. Lett.* **44**, 4733 (2019).
- Hua, T.-P., Sun, Y. R. & Hu, S.-M. Dispersion-like lineshape observed in cavity-enhanced saturation spectroscopy of  $\text{HD}$  at  $14 \mu\text{m}$ . *Opt. Lett.* **45**, 4863 (2020).
- Castrillo, A., Fasci, E. & Gianfrani, L. Doppler-limited precision spectroscopy of  $\text{HD}$  at  $1.4 \mu\text{m}$ : an improved determination of the R (1) center frequency. *Phys. Rev. A* **103**, 22828 (2021).
- Wcisło, P., Gordon, I. E., Cheng, C. F., Hu, S. M. & Ciuryło, R. Collision-induced line-shape effects limiting the accuracy in Doppler-limited spectroscopy of  $\text{H}_2$ . *Phys. Rev. A* **93**, 022501 (2016).
- Niu, M. L., Salumbides, E. J., Dickenson, G. D., Eikema, K. S. E. & Ubachs, W. Precision spectroscopy of the  $\text{X}^1\Sigma^+, v=0 \rightarrow 1$  ( $J=0-2$ ) rovibrational splittings in  $\text{H}_2$ ,  $\text{HD}$  and  $\text{D}_2$ . *J. Mol. Spectrosc.* **300**, 44–54 (2014).
- Fast, A. & Meek, S. A. Precise measurement of the  $\text{D}_2\text{S}_1(0)$  vibrational transition frequency. *Mol. Phys.* **120**, e1999520 (2021).
- Fast, A. & Meek, S. A. Sub-ppb measurement of a fundamental band rovibrational transition in  $\text{HD}$ . *Phys. Rev. Lett.* **125**, 023001 (2020).
- Eesley, G. L. Coherent raman spectroscopy. *J. Quant. Spectrosc. Radiat. Transf.* **22**, 507–576 (1979).
- Rahn, L. A. & Rosasco, G. J. Measurement of the density shift of the  $\text{H}_2\text{Q}(0-5)$  transitions from 295 to 1000 K. *Phys. Rev. A* **41**, 3698–3706 (1990).
- Forsman, J. W., Sinclair, P. M., Duggan, P., Drummond, J. R. & May, A. D. A high-resolution Raman gain spectrometer for spectral lineshape studies. *Can. J. Phys.* **69**, 558–563 (1991).
- Wcisło, P. et al. Accurate deuterium spectroscopy for fundamental studies. *J. Quant. Spectrosc. Radiat. Transf.* **213**, 41–51 (2018).
- Polli, D., Kumar, V., Valensise, C. M., Marangoni, M. & Cerullo, G. Broadband coherent Raman scattering microscopy. *Laser Photonics Rev.* **12**, 1800020 (2018).
- Dicke, R. H. The effect of collisions upon the doppler width of spectral lines. *Phys. Rev.* **89**, 472–473 (1953).
- Konefał, M. et al. Analytical-function correction to the Hartmann–Tran profile for more reliable representation of the Dicke-narrowed molecular spectra. *J. Quant. Spectrosc. Radiat. Transf.* **242**, 106784 (2020).
- Lamperti, M., Rutkowski, L., Gatti, D., Gotti, R., Moretti, L., Polli, D., Cerullo, G. & Marangoni, M. A stimulated Raman loss spectrometer for metrological studies of quadrupole lines of hydrogen isotopologues. *Mol. Phys.*, <https://doi.org/10.1080/00268976.2023.2196353> (2023).
- Lamperti, M. et al. Optical frequency metrology in the bending modes region. *Commun. Phys.* **3**, 175 (2020).

## Acknowledgements

This work was supported by the Italian FARE-MIUR project CH2ROME (Grant no. R164WYYR8N). P.W. is supported by the National Science Centre in Poland, Project No. 2019/35/B/ST2/01118. H.J. is supported by the budgetary funds on science projected for 2019–2023 as a research project under the “Diamontowy Grant” program.

## Author contributions

M.M. conceived the experiment. M.L. and L.R. developed the spectrometer. M.L. and D.R. performed the measurements. D.G. developed the real-time acquisition system for the Stokes beat note and the SRS signal. M.L. conceived the line center extrapolation strategy to zero pressure. S.W., L.R., M.L. performed the multi-pressure HTP fitting. P.W., F.T., and H.J. performed quantum-scattering calculations of collisional parameters. D.P., G.C., P.M., P.W., D.G., and R.G. supervised the study. M.L. and M.M. wrote the manuscript with input from all authors.

## Competing interests

The authors declare no competing interests.

## Additional information

**Supplementary information** The online version contains supplementary material available at <https://doi.org/10.1038/s42005-023-01187-z>.

**Correspondence** and requests for materials should be addressed to Marco Lamperti.

**Peer review information** *Communications Physics* thanks Mikael Sjö Dahl and the other, anonymous, reviewer(s) for their contribution to the peer review of this work. Peer reviewer reports are available.

**Reprints and permission information** is available at <http://www.nature.com/reprints>

**Publisher's note** Springer Nature remains neutral with regard to jurisdictional claims in published maps and institutional affiliations.



**Open Access** This article is licensed under a Creative Commons Attribution 4.0 International License, which permits use, sharing, adaptation, distribution and reproduction in any medium or format, as long as you give appropriate credit to the original author(s) and the source, provide a link to the Creative Commons license, and indicate if changes were made. The images or other third party material in this article are included in the article's Creative Commons license, unless indicated otherwise in a credit line to the material. If material is not included in the article's Creative Commons license and your intended use is not permitted by statutory regulation or exceeds the permitted use, you will need to obtain permission directly from the copyright holder. To view a copy of this license, visit <http://creativecommons.org/licenses/by/4.0/>.

© The Author(s) 2023



Contents lists available at ScienceDirect

## Journal of Quantitative Spectroscopy &amp; Radiative Transfer

journal homepage: [www.elsevier.com/locate/jqsrt](http://www.elsevier.com/locate/jqsrt)

## Hyperfine components of rovibrational dipole transitions in HT and DT

Hubert Jóźwiak<sup>a,\*</sup>, Hubert Cybulski<sup>b</sup>, Piotr Wcisło<sup>a</sup><sup>a</sup> Institute of Physics, Faculty of Physics, Astronomy and Informatics, Nicolaus Copernicus University in Torun, Grudziadzka 5, Torun 87-100, Poland<sup>b</sup> Institute of Physics, Kazimierz Wielki University, ul. Powstańców Wielkopolskich 2, Bydgoszcz 85-090, Poland

## ARTICLE INFO

## Article history:

Received 10 February 2021

Revised 19 March 2021

Accepted 22 March 2021

Available online 8 April 2021

## Keywords:

Hydrogen molecule

Hyperfine structure

Tritium

## ABSTRACT

We report a list of positions and intensities of 331 892 hyperfine components of all 18 585 rovibrational dipole transitions in the HT and DT isotopologues of molecular hydrogen. Apart from the study of hyperfine structure, we investigate the intensities of all rovibrational dipole transitions in the two isotopologues, which were not known prior to this work. The results presented here are crucial for a reliable interpretation of accurate measurements of rovibrational transition frequencies in the tritium-bearing isotopologues of hydrogen, which are useful for tests of quantum electrodynamics for molecules and searches for new physics beyond the Standard Model.

© 2021 The Author(s). Published by Elsevier Ltd.

This is an open access article under the CC BY-NC-ND license

(<http://creativecommons.org/licenses/by-nc-nd/4.0/>)

## 1. Introduction

Rovibrational structures of tritium-bearing isotopologues of molecular hydrogen are of particular importance for the spectroscopic community. Accurate experimental data for the three tritium-bearing isotopologues broadens the perspective of recent studies of rovibrational transitions in H<sub>2</sub> [1–3], D<sub>2</sub> [4–8] and HD [9–14]. Such an abundance of experimental results has stimulated a detailed theoretical analysis of the hydrogen molecule. Since the tritiated species are significantly heavier than the three most-common isotopologues of hydrogen (H<sub>2</sub>, HD and D<sub>2</sub>), they are less susceptible to the mass-dependent contributions to the molecular binding energies, such as the adiabatic and non-adiabatic corrections to the Born-Oppenheimer energies. Three recent papers [15–17] on the Coherent Anti-Stokes Raman Spectroscopy (CARS) of T<sub>2</sub>, DT and HT constitute a perfect example of validation of theoretical results on accurate spectra of the tritium-bearing isotopologues. In Ref. [15] the Raman spectra of T<sub>2</sub> were used to test the nonrelativistic calculations from Ref. [18] and to extract the relativistic and QED corrections to the rovibrational energy levels. In a joint theoretical and experimental study from Ref. [16], the recently developed nonadiabatic perturbation theory (NAPT) [18–22], as well as the relativistic and QED corrections, were validated on the spectra of DT, leading to an excellent agreement with the experimental values. Finally, in Ref. [17],

the authors refined the data for T<sub>2</sub> and DT and measured several lines of HT. We also note that the tritiated species can be used in searches for physics beyond the Standard Model [23–25], i.e. by putting constraints on a certain form of the hypothetical fifth force parametrized by the Yukawa potential, which appear to be tighter than that of H<sub>2</sub> [16].

In general, the experimental studies of tritium-bearing isotopologues are hindered by the instability of tritium, as it undergoes a  $\beta$ -decay into <sup>3</sup>He. As pointed out in Ref. [15], a use of tritium in experimental setups is restricted to minute amounts, which rules out the possibility of molecular beam studies and might lead to material degradation. Rovibrational structures of the HT and DT molecules were studied in only a few experiments. Dieke et al. recorded emission spectra of the two heteronuclear tritium-bearing isotopologues of hydrogen [26,27]. Rovibrational structures of HT and DT were also investigated by means of Raman spectroscopy. Edwards et al. [28] reported observed pure rotational and rovibrational transitions from the first overtone in HT and DT. Veirs et al. [29], in a study of Raman spectra of the six isotopologues of hydrogen, analyzed the Q lines from the fundamental band in HT and DT. A study of the first, third and fourth overtones in HT was performed by Chuang and Zare [30] using optoacoustic spectroscopy. Finally, the two aforementioned CARS studies of the fundamental band in DT [16] and HT [17] were reported recently. The last two papers focused on several lines from the Q branch and provided an accurate test of NAPT, reaching accuracies of 12, 16 and 20 MHz for the Q lines in T<sub>2</sub>, HT and DT, respectively.

Accurate experimental measurements of the frequencies of rovibrational transitions require knowledge about the underlying (yet

\* Corresponding author.

E-mail addresses: [hubert.jozwiak@doktorant.umk.pl](mailto:hubert.jozwiak@doktorant.umk.pl) (H. Jóźwiak), [piotr.wcislo@umk.pl](mailto:piotr.wcislo@umk.pl) (P. Wcisło).

unresolved) hyperfine structure [31–36]. Recently, we have analyzed hyperfine interactions in the three tritium-bearing isotopologues and reported a set of coupling constants for the nuclear spin-rotation interaction, nuclear spin-nuclear spin dipole coupling and, in the case of DT, for the interaction between the quadrupole moment of the deuteron with molecular field gradient [35]. These three leading hyperfine interactions result in splittings of rovibrational levels, which are of an order of hundreds of kHz. We have also calculated intensities of all possible quadrupole transitions in T<sub>2</sub>, HT and DT, as well as the intensities of the respective hyperfine components.

Following our previous studies of hyperfine structure in molecular hydrogen [33–35], here, we investigate the rovibrational dipole transitions from the *P* and *R* branches in the HT and DT isotopologues. Our study results in a comprehensive list of all 331 892 hyperfine components of 18 585 rovibrational transitions in the two heteronuclear tritium-bearing isotopologues of hydrogen. Moreover, we provide the intensities of rovibrational dipole transitions in HT and DT, which, to our knowledge, were neither calculated nor measured previously. The theory behind the calculations is briefly recalled in Sections 2 and 3 and we provide two examples of the calculated dipole transitions for the two molecules in Section 4.

## 2. Hyperfine interactions in HT and DT

Hyperfine interactions in HT and DT involve the nuclear spin-rotation interaction, the nuclear spin-spin dipole coupling and, in the case of the DT molecule, the interaction of the electric quadrupole moment with the molecular electric field gradient (EFG). In Ref. [35], we reported hyperfine coupling constants, which determine the strength of these interactions, for all bound states of the three tritium-bearing isotopologues of hydrogen, in their ground electronic  $\Sigma^+$  (or  $\Sigma_g^+$ , in the case of T<sub>2</sub>) states. It was pointed out recently [36], that the slight discrepancies between the hyperfine coupling constants calculated in our previous papers [33–35] and other theoretical results [32,36] might originate from the Born-Oppenheimer (BO) potential used in our calculations. Indeed, we used the potential of Schwenke [37] to obtain the rovibrational wavefunctions of the isotopologues of hydrogen instead of the state-of-the-art potential of Pachucki [38]. However, the choice of the potential energy curve influences only the rovibrational wavefunctions which are used to calculate the hyperfine coupling constants for a given rovibrational state (see, for example Eq. (7) in Ref. [35]). The error introduced by the choice of a different potential is of an order of tens of Hz, as it can be deduced from the comparison of the nuclear spin-spin dipole constants reported in Refs. [33,34] with those given in Table 1 in Ref. [36]. Therefore, for the sake of consistency, we use the data reported by us in the previous paper [35].

Matrix elements of the effective hyperfine Hamiltonian for the HT and DT molecules were determined using a coupling scheme which is suitable for the heteronuclear molecules. The rotational angular momentum of the molecule, **N**, was coupled with one of the nuclear spins, **I**<sub>1</sub>, to form the intermediate angular momentum, **F**<sub>1</sub>, which was in turn coupled with the nuclear spin of the other nucleus, **I**<sub>2</sub>. The resulting total angular momentum and its projection on the space-fixed *z*-axis were denoted by **F** and *m<sub>F</sub>*, respectively. The coupled basis vector is denoted as  $|v; ((N I_1) F_1 I_2) F m_F\rangle$ , where *v* is the vibrational quantum number. We recall that for the HT molecule *I*<sub>1</sub> = *I*<sub>T</sub> and *I*<sub>2</sub> = *I*<sub>H</sub>, and for the DT molecule *I*<sub>1</sub> = *I*<sub>D</sub> and *I*<sub>2</sub> = *I*<sub>T</sub>.

As it was discussed in Ref. [35], the hyperfine Hamiltonian is block diagonal with respect to the total angular momentum. Energy levels of the hyperfine levels were determined by diagonalization of the *F*-labelled blocks, each of them of  $(2I_1 + 1)(2I_2 + 1) \times$

$(2I_1 + 1)(2I_2 + 1)$  size. The eigenvectors of the hyperfine Hamiltonian are denoted as  $|v; N F m_F(\pm)\rangle$ , where the  $\pm$  labels denote the eigenstates for given *N* and *F*, which are of higher (+) or lower (−) energy. The relation between the eigenbasis and the coupled basis is given by:

$$|v; N F m_F(\pm)\rangle = \sum_{F_1=|F-I_2|}^{F+I_2} \sum_{N'=|F_1-I_1|}^{F_1+I_1} a_{N'F_1}^{vNF(\pm)} |v; ((N' I_1) F_1 I_2) F m_F\rangle, \quad (1)$$

where  $a_{N'F_1}^{vNF(\pm)}$  denote the mixing coefficients.<sup>1</sup> Let us remind that the off-diagonal matrix elements, which couple different rotational states, are from 9 to 11 orders of magnitude smaller than the diagonal terms. Therefore, the mixing coefficients which couple  $N' \neq N$ , are negligibly small.

## 3. Intensities of hyperfine components of rovibrational dipole transitions

Line intensity of the dipole transition between two degenerate states (initial and final) is given [39–41] as:

$$S_{fi} = \frac{2\pi^2}{3hc\epsilon_0} \nu_0 \frac{m}{2N_i + 1} P_{fi}(T) |d_{fi}|^2, \quad (2)$$

where  $\nu_0$  is the transition frequency and  $d_{fi}$  denotes the matrix elements of the dipole moment operator. *h*, *c* and  $\epsilon_0$  are Planck's constant, the speed of light in vacuum and vacuum permittivity, respectively. The factor *m* is given by  $N_i + 1$  for the *R*(*N<sub>i</sub>*) transition and by *N<sub>i</sub>* for the *P*(*N<sub>i</sub>*) transition. The temperature-dependent factor,  $P_{fi}(T)$ , is given as:

$$P_{fi}(T) = w_i (2N_i + 1) \frac{(e^{-E_i/k_B T} - e^{-E_f/k_B T})}{Q(T)}, \quad (3)$$

with the partition function,  $Q(T)$ , defined as:

$$Q(T) = \sum_k w_k (2N_k + 1) e^{-E_k/k_B T}. \quad (4)$$

$w_k$  is the degeneracy factor of each rovibrational level due to nuclear spin statistics and equals 4 and 6 for HT and DT, respectively.  $E_k$  is the energy of the *k*th rovibrational state,  $k_B$  is the Boltzmann constant and *T* is the temperature.

Matrix elements of the dipole moment operator,  $d_{fi}$ , which couple the initial and final rovibrational states, are given by:

$$d_{fi} = \int dR \chi_f^*(R) d(R) \chi_i(R). \quad (5)$$

We used the dipole moment function reported by Pachucki and Komasa for the HD molecule [42], rescaled with the mass-dependent factor:

$$d(R) = \left( \frac{m_1 - m_2}{m_1 m_2} \right) \left( \frac{m_H m_D}{m_H - m_D} \right) d^{\text{HD}}(R), \quad (6)$$

where  $d^{\text{HD}}(R)$  denotes the dipole moment function reported in Ref. [42] and  $m_X$  is the mass of the nucleus of a particular isotope (*X* = H, D or T). Following the notation from Section 2, we set  $m_1 = m_T$  and  $m_2 = m_H$  for the HT molecule, and  $m_1 = m_D$  and  $m_2 = m_T$  for the DT molecule.

Line intensity of each hyperfine component of a rovibrational dipole transition is given as [31,33]:

$$S_{fi}^{\text{HF}} = \frac{2\pi^2}{3hc\epsilon_0} \nu_0 \frac{1}{w_i (2N_i + 1)} P_{fi}(T) |d_{fi}^{\text{HF}}|^2, \quad (7)$$

<sup>1</sup> We note that in our previous papers [33–35] we did not denote the mixing coefficients with the vibrational quantum number.

**Table 1**

Example of the calculated positions and intensities of the hyperfine transitions. The full list is provided in Supplementary Material [45]. Frequencies of the rovibrational transition are calculated with H2Spectre code of Czachorowski et al. [46] and Komasa et al. [22]. Please note that for the rovibrational transition  $d$  corresponds to  $d_{\text{fi}}$  from Eq. (2), while for the hyperfine components  $d$  denotes  $d_{\text{fi}}^{\text{HF}}$  from Eq. (7).

Band	Line	Hyperfine transition $ N'F'(\pm)\rangle \leftarrow  NF(\pm)\rangle$	Frequency (MHz)	$d$ ( $10^{-4}$ D)	Intensity (cm/molecule)	Intensity at 296 K (cm/molecule)
2-0 (DT)	P(2)	$ 1\ 3/2-\rangle \leftarrow  2\ 1/2\rangle$	158417160.5(9.3)	0.0452	$1.796 \times 10^{-26}$	$5.034 \times 10^{-27}$
		$ 1\ 3/2-\rangle \leftarrow  2\ 3/2+\rangle$	-0.22606	0.0083	$5.050 \times 10^{-29}$	$1.415 \times 10^{-29}$
		$ 1\ 3/2-\rangle \leftarrow  2\ 3/2+\rangle$	-0.21116	0.0291	$6.194 \times 10^{-28}$	$1.736 \times 10^{-28}$
		$ 1\ 5/2\rangle \leftarrow  2\ 3/2+\rangle$	-0.19570	0.0097	$6.885 \times 10^{-29}$	$1.930 \times 10^{-29}$
		$ 1\ 1/2-\rangle \leftarrow  2\ 1/2\rangle$	-0.17431	0.0250	$4.583 \times 10^{-28}$	$1.285 \times 10^{-28}$
		$ 1\ 1/2-\rangle \leftarrow  2\ 3/2+\rangle$	-0.15942	0.0061	$2.679 \times 10^{-29}$	$7.511 \times 10^{-30}$
		$ 1\ 3/2-\rangle \leftarrow  2\ 5/2+\rangle$	-0.15728	0.0078	$4.416 \times 10^{-29}$	$1.238 \times 10^{-29}$
		$ 1\ 5/2\rangle \leftarrow  2\ 5/2+\rangle$	-0.14182	0.0323	$7.649 \times 10^{-28}$	$2.144 \times 10^{-28}$
		$ 1\ 3/2-\rangle \leftarrow  2\ 3/2-\rangle$	-0.13805	0.0016	$1.888 \times 10^{-30}$	$5.292 \times 10^{-31}$
		$ 1\ 5/2\rangle \leftarrow  2\ 3/2-\rangle$	-0.12259	0.0083	$5.088 \times 10^{-29}$	$1.426 \times 10^{-29}$
		$ 1\ 1/2-\rangle \leftarrow  2\ 3/2-\rangle$	-0.08630	0.0454	$1.510 \times 10^{-27}$	$4.234 \times 10^{-28}$
		$ 1\ 3/2+\rangle \leftarrow  2\ 1/2\rangle$	-0.07205	0.0143	$1.491 \times 10^{-28}$	$4.178 \times 10^{-29}$
		$ 1\ 3/2+\rangle \leftarrow  2\ 3/2+\rangle$	-0.05716	0.0197	$2.846 \times 10^{-28}$	$7.978 \times 10^{-29}$
		$ 1\ 3/2+\rangle \leftarrow  2\ 5/2+\rangle$	-0.00328	0.0616	$2.783 \times 10^{-27}$	$7.800 \times 10^{-28}$
		$ 1\ 1/2+\rangle \leftarrow  2\ 1/2\rangle$	0.00768	0.0271	$5.394 \times 10^{-28}$	$1.512 \times 10^{-28}$
		$ 1\ 3/2+\rangle \leftarrow  2\ 3/2-\rangle$	0.01595	0.0324	$7.703 \times 10^{-28}$	$2.159 \times 10^{-28}$
		$ 1\ 1/2+\rangle \leftarrow  2\ 3/2+\rangle$	0.02257	0.0436	$1.395 \times 10^{-27}$	$3.910 \times 10^{-28}$
		$ 1\ 5/2\rangle \leftarrow  2\ 7/2\rangle$	0.05580	0.0808	$4.789 \times 10^{-27}$	$1.342 \times 10^{-27}$
		$ 1\ 3/2-\rangle \leftarrow  2\ 5/2-\rangle$	0.05617	0.0668	$3.275 \times 10^{-27}$	$9.180 \times 10^{-28}$
		$ 1\ 5/2\rangle \leftarrow  2\ 5/2-\rangle$	0.07163	0.0207	$3.126 \times 10^{-28}$	$8.762 \times 10^{-29}$
		$ 1\ 1/2+\rangle \leftarrow  2\ 3/2-\rangle$	0.09569	0.0091	$6.114 \times 10^{-29}$	$1.714 \times 10^{-29}$
		$ 1\ 3/2+\rangle \leftarrow  2\ 5/2-\rangle$	0.21018	0.0024	$4.247 \times 10^{-30}$	$1.190 \times 10^{-30}$
2-0 (HT)	R(1)	$ 2\ 1\rangle \leftarrow  1\ 0\rangle$	205380036.1(33.0)	0.2676	$1.361 \times 10^{-24}$	$5.002 \times 10^{-25}$
		$ 2\ 2-\rangle \leftarrow  1\ 1+\rangle$	-0.09442	0.2185	$1.134 \times 10^{-25}$	$4.169 \times 10^{-26}$
		$ 2\ 3\rangle \leftarrow  1\ 2\rangle$	-0.06910	0.0173	$7.090 \times 10^{-28}$	$2.606 \times 10^{-28}$
		$ 2\ 2-\rangle \leftarrow  1\ 2\rangle$	-0.06265	0.4477	$4.764 \times 10^{-25}$	$1.751 \times 10^{-25}$
		$ 2\ 2+\rangle \leftarrow  1\ 1+\rangle$	-0.02089	0.1885	$8.443 \times 10^{-26}$	$3.103 \times 10^{-26}$
		$ 2\ 2+\rangle \leftarrow  1\ 1+\rangle$	0.00035	0.3779	$3.394 \times 10^{-25}$	$1.247 \times 10^{-25}$
		$ 2\ 2-\rangle \leftarrow  1\ 1-\rangle$	0.00674	0.3277	$2.551 \times 10^{-25}$	$9.377 \times 10^{-26}$
		$ 2\ 2+\rangle \leftarrow  1\ 2\rangle$	0.04857	0.0164	$6.400 \times 10^{-28}$	$2.352 \times 10^{-28}$
		$ 2\ 2+\rangle \leftarrow  1\ 1-\rangle$	0.07620	0.0105	$2.611 \times 10^{-28}$	$9.594 \times 10^{-29}$
		$ 2\ 1\rangle \leftarrow  1\ 1+\rangle$	0.37213	0.0090	$1.920 \times 10^{-28}$	$7.057 \times 10^{-29}$
		$ 2\ 1\rangle \leftarrow  1\ 2\rangle$	0.42035	0.0489	$5.671 \times 10^{-27}$	$2.084 \times 10^{-27}$
		$ 2\ 1\rangle \leftarrow  1\ 1-\rangle$	0.44798	0.1890	$8.488 \times 10^{-26}$	$3.120 \times 10^{-26}$

where  $d_{\text{fi}}^{\text{HF}}$  is the reduced matrix element of the dipole moment tensor:

$$\begin{aligned}
 |d_{\text{fi}}^{\text{HF}}|^2 &= \left| \langle \nu_f; N_f F_f(\pm) \| T^{(1)}(\mathbf{d}) \| \nu_i; N_i F_i(\pm) \rangle \right|^2 \\
 &= \left| \sum_{F_f=|F_f-I_f|}^{F_f+I_f} \sum_{N_f'=|F_f-I_f|}^{F_f+I_f} \sum_{F_i=|F_i-I_i|}^{F_i+I_i} \sum_{N_i'=|F_i-I_i|}^{F_i+I_i} \right. \\
 &\quad a_{N_f'F_f}^{\nu_f N_f F_f(\pm)} a_{N_i'F_i}^{\nu_i N_i F_i(\pm)} \\
 &\quad \times \langle \nu_f; ((N_f' I_1) F_i I_2) F_f \| T^{(1)}(\mathbf{d}) \| \nu_i; ((N_i' I_1) F_i I_2) F_i \rangle \left. \right|^2.
 \end{aligned} \quad (8)$$

Here, we use a common representation of a dipole moment operator as a spherical tensor of rank 1,  $T^{(1)}(\mathbf{d})$  [31,33]. Matrix elements of this spherical tensor in the coupled basis are evaluated using spherical tensor algebra [43,44]:

$$\begin{aligned}
 &\langle \nu_f; ((N_f' I_1) F_i I_2) F_f \| T^{(1)}(\mathbf{d}) \| \nu_i; ((N_i' I_1) F_i I_2) F_i \rangle \\
 &= (-1)^{F_i+I_2+F_i+F_i+I_1+N_f} \sqrt{(2F_i+1)(2F_f+1)} \\
 &\quad \times \sqrt{(2F_i+1)(2F_f+1)} \begin{Bmatrix} I_2 & F_i & F_i \\ 1 & F_f & F_f \end{Bmatrix} \\
 &\quad \times \begin{Bmatrix} I_1 & F_i & N_i \\ 1 & N_f & F_f \end{Bmatrix} \langle \nu_f N_f \| T^{(1)}(\mathbf{d}) \| \nu_i N_i \rangle.
 \end{aligned} \quad (9)$$

The  $\langle \nu_f N_f \| T^{(1)}(\mathbf{d}) \| \nu_i N_i \rangle$  is further reduced to (in a  $^1\Sigma$  state):

$$\begin{aligned}
 &\langle \nu_f N_f \| T^{(1)}(\mathbf{d}) \| \nu_i N_i \rangle \\
 &= (-1)^{N_f} \sqrt{(2N_f+1)(2N_i+1)} \begin{pmatrix} N_f & 1 & N_i \\ 0 & 0 & 0 \end{pmatrix} d_{\text{fi}}.
 \end{aligned} \quad (10)$$

#### 4. Example of the complete dataset record

We calculate the positions and intensities of the hyperfine components of all dipole transitions in the ground  $^1\Sigma$  electronic state of the HT and DT molecules. Our calculations result in 331 892 hyperfine components of 18 585 dipole lines from the R and P branches. The complete dataset can be found in Supplementary Material [45].

The accuracy of the calculated transition frequencies is determined by the accuracy of the hyperfine coupling constants reported in Ref. [35]. As mentioned in our previous papers [33–35], the dominant contribution to the uncertainty of the hyperfine coupling constants originates from the quantum chemical calculations of the nuclear spin-rotation constant, which is of an order of 300 Hz. In principle, one should also consider the influence of the neglected nonadiabatic effects, which are expected to be of the order of the ratio of the electron mass to the reduced nuclear mass [32]. However, this uncertainty is significantly smaller than the one originating from the calculations of the spin-rotation coupling constant. Therefore, we claim the uncertainty of the transition frequencies to be of an order of about 0.3 kHz. The accuracy of the transition moments and line intensities is determined by the accuracy of the dipole moment function reported in Ref. [20], which, according to the authors, should be of a relative order of  $10^{-3}$ .

Table 1 presents an example of the calculated parameters for the two lines from the first overtone (2-0) band, for the DT and HT molecules. The central frequency of the rovibrational transition is taken from the H2Spectre code [22,46]. In the case of the DT molecule, we present the 2-0 P(2) line, which consists of 21 hy-



perfine components, that are spread over a range of over 400 kHz. We note that each  $\nu_f - \nu_i P(1)$  and  $R(0)$  line in DT consist of 9 hyperfine components, each  $P(2)$  and  $R(1)$  line involve 21 hyperfine components, while all the remaining rovibrational lines involve 22 components. In the case of the HT molecule, we present the 2-0  $R(1)$  line, which consists of 11 hyperfine components, that are spread over a range of over 500 kHz. Contrary to DT, this particular number of hyperfine components is characteristic for every  $\nu_f - \nu_i P$  and  $R$  line, except for the  $R(0)$  and  $P(1)$  transitions, which involve 6 components.

## 5. Conclusion

We provide a comprehensive list of positions and intensities of the 331 892 hyperfine components of 18 585 rovibrational dipole transitions from the  $P$  and  $R$  branches of HT and DT. Moreover, we have calculated the intensities of all rovibrational dipole transitions in these two isotopologues, which were not analyzed before. The results presented here can serve as reference data for future accurate measurements of transition frequencies in tritium-bearing molecules, which are useful for testing the quantum electrodynamics for molecules and searching for new physics beyond the Standard Model.

## Declaration of Competing Interest

The authors declare that they have no known competing financial interests or personal relationships that could have appeared to influence the work reported in this paper.

## CRedit authorship contribution statement

**Hubert Jóźwiak:** Conceptualization, Methodology, Software, Investigation, Writing - original draft, Writing - review & editing, Funding acquisition. **Hubert Cybulski:** Software, Investigation, Writing - original draft, Writing - review & editing. **Piotr Wcisło:** Conceptualization, Methodology, Validation, Writing - original draft, Writing - review & editing.

## Acknowledgements

The research is financed from the budgetary funds on science projected for 2019–2023 as a research project under the “Diamen-towy Grant” program. P.W. is supported by the National Science Centre in Poland, Project no. 2019/35/B/ST2/01118. The research was part of the program of the National Laboratory FAMO in Toruń, Poland.

## Supplementary material

Supplementary material associated with this article can be found, in the online version, at doi:[10.1016/j.jqsrt.2021.107662](https://doi.org/10.1016/j.jqsrt.2021.107662).

## References

- [1] Dickenson GD, Niu ML, Salumbides EJ, Komasa J, Eikema KSE, Pachucki K, et al. Fundamental vibration of molecular hydrogen. *Phys Rev Lett* 2013;110:193601. doi:[10.1103/PhysRevLett.110.193601](https://doi.org/10.1103/PhysRevLett.110.193601).
- [2] Niu M, Salumbides E, Dickenson G, Eikema K, Ubachs W. Precision spectroscopy of the  $X^1\Sigma_g^+$ ,  $v=0 \rightarrow 1$  ( $J=0-2$ ) rovibrational splittings in  $H_2$ , HD and  $D_2$ . *J Mol Spectrosc* 2014;300:44–54. doi:[10.1016/j.jms.2014.03.011](https://doi.org/10.1016/j.jms.2014.03.011).
- [3] Beyer M, Hölsch N, Hussels J, Cheng C-F, Salumbides EJ, Eikema KSE, et al. Determination of the interval between the ground states of para- and ortho- $H_2$ . *Phys Rev Lett* 2019;123:163002. doi:[10.1103/PhysRevLett.123.163002](https://doi.org/10.1103/PhysRevLett.123.163002).
- [4] Mondelain D, Kass S, Sala T, Romanini D, Gatti D, Campargue A. Sub-MHz accuracy measurement of the  $S(2)$  2-0 transition frequency of  $D_2$  by comb-assisted cavity ring down spectroscopy. *J Mol Spectrosc* 2016;326:5–8. doi:[10.1016/j.jms.2016.02.008](https://doi.org/10.1016/j.jms.2016.02.008).
- [5] Wcisło P, Thibault F, Zaborowski M, Wójtewicz S, Cygan A, Kowzan G, et al. Accurate deuterium spectroscopy for fundamental studies. *J Quant Spectrosc Radiat Transf* 2018;213:41–51. doi:[10.1016/j.jqsrt.2018.04.011](https://doi.org/10.1016/j.jqsrt.2018.04.011).
- [6] Mondelain D, Kass S, Campargue A. Transition frequencies in the (2-0) band of  $D_2$  with MHz accuracy. *J Quant Spectrosc Radiat Transf* 2020;253:107020. doi:[10.1016/j.jqsrt.2020.107020](https://doi.org/10.1016/j.jqsrt.2020.107020).
- [7] Wójtewicz S, Gotti R, Gatti D, Lamperti M, Laporta P, Jóźwiak H, et al. Accurate deuterium spectroscopy and comparison with ab initio calculations. *Phys Rev A* 2020;101:052504. doi:[10.1103/PhysRevA.101.052504](https://doi.org/10.1103/PhysRevA.101.052504).
- [8] Zaborowski M, Słowiński M, Stankiewicz K, Thibault F, Cygan A, Jóźwiak H, et al. Ultrahigh finesse cavity-enhanced spectroscopy for accurate tests of quantum electrodynamics for molecules. *Opt Lett* 2020;45(7):1603–6. doi:[10.1364/OL.389268](https://doi.org/10.1364/OL.389268).
- [9] Tao L-G, Liu A-W, Pachucki K, Komasa J, Sun YR, Wang J, et al. Toward a determination of the proton-electron mass ratio from the lamb-dip measurement of HD. *Phys Rev Lett* 2018;120:153001. doi:[10.1103/PhysRevLett.120.153001](https://doi.org/10.1103/PhysRevLett.120.153001).
- [10] Cozijn FMJ, Dupré P, Salumbides EJ, Eikema KSE, Ubachs W. Sub-Doppler frequency metrology in HD for tests of fundamental physics. *Phys Rev Lett* 2018;120:153002. doi:[10.1103/PhysRevLett.120.153002](https://doi.org/10.1103/PhysRevLett.120.153002).
- [11] Fasci E, Castrillo A, Dinesan H, Gravina S, Moretti L, Gianfrani L. Precision spectroscopy of HD at 1.38  $\mu$ m. *Phys Rev A* 2018;98:022516. doi:[10.1103/PhysRevA.98.022516](https://doi.org/10.1103/PhysRevA.98.022516).
- [12] Diouf ML, Cozijn FMJ, Darquié B, Salumbides EJ, Ubachs W. Lamb-dips and lamb-peaks in the saturation spectrum of HD. *Opt Lett* 2019;44(19):4733–6. doi:[10.1364/OL.44.004733](https://doi.org/10.1364/OL.44.004733).
- [13] Diouf ML, Cozijn FMJ, Lai K-F, Salumbides EJ, Ubachs W. Lamb-peak spectrum of the HD (2-0)  $P(1)$  line. *Phys Rev Res* 2020;2:023209. doi:[10.1103/PhysRevResearch.2.023209](https://doi.org/10.1103/PhysRevResearch.2.023209).
- [14] Fast A, Meek SA. Sub-ppb measurement of a fundamental band rovibrational transition in HD. *Phys Rev Lett* 2020;125:023001. doi:[10.1103/PhysRevLett.125.023001](https://doi.org/10.1103/PhysRevLett.125.023001).
- [15] Trivikram TM, Schlösser M, Ubachs W, Salumbides EJ. Relativistic and QED effects in the fundamental vibration of  $T_2$ . *Phys Rev Lett* 2018;120:163002. doi:[10.1103/PhysRevLett.120.163002](https://doi.org/10.1103/PhysRevLett.120.163002).
- [16] Lai K-F, Czachorowski P, Schlösser M, Puchalski M, Komasa J, Pachucki K, et al. Precision tests of nonadiabatic perturbation theory with measurements on the DT molecule. *Phys Rev Res* 2019;1:033124. doi:[10.1103/PhysRevResearch.1.033124](https://doi.org/10.1103/PhysRevResearch.1.033124).
- [17] Lai K-F, Hermann V, Trivikram TM, Diouf M, Schlösser M, Ubachs W, et al. Precision measurement of the fundamental vibrational frequencies of tritium-bearing hydrogen molecules:  $T_2$ , DT, HT. *Phys Chem Chem Phys* 2020;22:8973–87. doi:[10.1039/D0CP00596G](https://doi.org/10.1039/D0CP00596G).
- [18] Pachucki K, Komasa J. Leading order nonadiabatic corrections to rovibrational levels of  $H_2$ ,  $D_2$ , and  $T_2$ . *J Chem Phys* 2015;143(3):034111. doi:[10.1063/1.4927079](https://doi.org/10.1063/1.4927079).
- [19] Pachucki K, Komasa J. Nonadiabatic corrections to the wave function and energy. *J Chem Phys* 2008;129(3):034102. doi:[10.1063/1.2952517](https://doi.org/10.1063/1.2952517).
- [20] Pachucki K, Komasa J. Nonadiabatic corrections to rovibrational levels of  $H_2$ . *J Chem Phys* 2009;130(16):164113. doi:[10.1063/1.3114680](https://doi.org/10.1063/1.3114680).
- [21] Pachucki K, Komasa J. Rovibrational levels of HD. *Phys Chem Chem Phys* 2010;12(32):9188. doi:[10.1039/c0cp00209g](https://doi.org/10.1039/c0cp00209g).
- [22] Komasa J, Puchalski M, Czachorowski P, Łach G, Pachucki K. Rovibrational energy levels of the hydrogen molecule through nonadiabatic perturbation theory. *Phys Rev A* 2019;100:032519. doi:[10.1103/PhysRevA.100.032519](https://doi.org/10.1103/PhysRevA.100.032519).
- [23] Salumbides EJ, Koelmeij J, Komasa J, Pachucki K, Eikema KSE, Ubachs W. Bounds on fifth forces from precision measurements on molecules. *Phys Rev D* 2013;87:112008. doi:[10.1103/PhysRevD.87.112008](https://doi.org/10.1103/PhysRevD.87.112008).
- [24] Salumbides EJ, Schellekens AN, Gato-Rivera B, Ubachs W. Constraints on extra dimensions from precision molecular spectroscopy. *New J Phys* 2015;17(3):033015. doi:[10.1088/1367-2630/17/3/033015](https://doi.org/10.1088/1367-2630/17/3/033015).
- [25] Ubachs W, Koelmeij J, Eikema K, Salumbides E. Physics beyond the standard model from hydrogen spectroscopy. *J Mol Spectrosc* 2016;320:1–12. doi:[10.1016/j.jms.2015.12.003](https://doi.org/10.1016/j.jms.2015.12.003).
- [26] Dieke GH, Tomkins FS. The molecular spectrum of hydrogen. The Fulcher bands of TH and  $T_2$ . *Phys Rev* 1949;76:283–9. doi:[10.1103/PhysRev.76.283](https://doi.org/10.1103/PhysRev.76.283).
- [27] Dieke G. The molecular spectrum of hydrogen and its isotopes. *J Mol Spectrosc* 1958;2(1):494–517. doi:[10.1016/0022-2852\(58\)90095-X](https://doi.org/10.1016/0022-2852(58)90095-X).
- [28] Edwards HGM, Long DA, Mansour HR, Najm KAB. The pure rotational and vibration-rotational Raman spectra of  $^1H^3H$  and  $^2H^3H$ . *J Raman Spectrosc* 1979;8(5):251–4. doi:[10.1002/jrs.1250080507](https://doi.org/10.1002/jrs.1250080507).
- [29] Veirs D, Rosenblatt GM. Raman line positions in molecular hydrogen:  $H_2$ , HD, HT,  $D_2$ , DT, and  $T_2$ . *J Mol Spectrosc* 1987;121(2):401–19. doi:[10.1016/0022-2852\(87\)90058-0](https://doi.org/10.1016/0022-2852(87)90058-0).
- [30] Chuang M-C, Zare RN. Rotation-vibration spectrum of HT: line position measurements of the 1-0, 4-0, and 5-0 bands. *J Mol Spectrosc* 1987;121(2):380–400. doi:[10.1016/0022-2852\(87\)90057-9](https://doi.org/10.1016/0022-2852(87)90057-9).
- [31] Dupré P. Hyperfine transitions in the first overtone mode of hydrogen deuteride. *Phys Rev A* 2020;101:022504. doi:[10.1103/PhysRevA.101.022504](https://doi.org/10.1103/PhysRevA.101.022504).
- [32] Komasa J, Puchalski M, Pachucki K. Hyperfine structure in the HD molecule. *Phys Rev A* 2020;102:012814. doi:[10.1103/PhysRevA.102.012814](https://doi.org/10.1103/PhysRevA.102.012814).
- [33] Jóźwiak H, Cybulski H, Wcisło P. Positions and intensities of hyperfine components of all rovibrational dipole lines in the HD molecule. *J Quant Spectrosc Radiat Transf* 2020;253:107171. doi:[10.1016/j.jqsrt.2020.107171](https://doi.org/10.1016/j.jqsrt.2020.107171).
- [34] Jóźwiak H, Cybulski H, Wcisło P. Hyperfine components of all rovibrational quadrupole transitions in the  $H_2$  and  $D_2$  molecules. *J Quant Spectrosc Radiat Transf* 2020;253:107186. doi:[10.1016/j.jqsrt.2020.107186](https://doi.org/10.1016/j.jqsrt.2020.107186).



- [35] Jóźwiak H, Cybulski H, Wcisło P. Hyperfine structure of quadrupole rovibrational transitions in tritium-bearing hydrogen isotopologues. *J Quant Spectrosc Radiat Transf* 2020;256:107255. doi:[10.1016/j.jqsrt.2020.107255](https://doi.org/10.1016/j.jqsrt.2020.107255).
- [36] Puchalski M, Komasa J, Pachucki K. Hyperfine structure of the first rotational level in  $H_2$ ,  $D_2$  and HD molecules and the deuteron quadrupole moment. *Phys Rev Lett* 2020;125:253001. doi:[10.1103/PhysRevLett.125.253001](https://doi.org/10.1103/PhysRevLett.125.253001).
- [37] Schwenke DW. Calculations of rate constants for the three-body recombination of  $H_2$  in the presence of  $H_2$ . *J Chem Phys* 1988;89(4):2076–91. doi:[10.1063/1.455104](https://doi.org/10.1063/1.455104).
- [38] Pachucki K. Born-Oppenheimer potential for  $H_2$ . *Phys Rev A* 2010;82:032509. doi:[10.1103/PhysRevA.82.032509](https://doi.org/10.1103/PhysRevA.82.032509).
- [39] Molecular symmetry and spectroscopy. Bunker PR, editor. Academic Press; 1979. doi:[10.1016/B978-0-12-141350-7.50002-1](https://doi.org/10.1016/B978-0-12-141350-7.50002-1). ISBN 978-ISBN0-12-141350-7
- [40] Rich N, Johns J, McKellar A. Frequency and intensity measurements in the fundamental infrared band of HD. *J Mol Spectrosc* 1982;95(2):432–8. doi:[10.1016/0022-2852\(82\)90141-2](https://doi.org/10.1016/0022-2852(82)90141-2).
- [41] Kassi S, Campargue A. Electric quadrupole and dipole transitions of the first overtone band of HD by CRDS between 1.45 and 1.33  $\mu m$ . *J Mol Spectrosc* 2011;267(1):36–42. doi:[10.1016/j.jms.2011.02.001](https://doi.org/10.1016/j.jms.2011.02.001).
- [42] Pachucki K, Komasa J. Electric dipole rovibrational transitions in the HD molecule. *Phys Rev A* 2008;78:052503. doi:[10.1103/PhysRevA.78.052503](https://doi.org/10.1103/PhysRevA.78.052503).
- [43] Fano U, Racah G. *Irreducible tensorial sets*. Cambridge Molecular Science. Academic Press Inc.; 1959.
- [44] Brown JM, Carrington A. *Rotational spectroscopy of diatomic molecules*. Cambridge Molecular Science. Cambridge University Press; 2003. doi:[10.1017/CBO9780511814808](https://doi.org/10.1017/CBO9780511814808).
- [45] Jóźwiak H, Cybulski H, Wcisło P. “Supplementary material for hyperfine line positions and intensities”, [10.1016/j.jqsrt.2021.107662](https://doi.org/10.1016/j.jqsrt.2021.107662).
- [46] Czachorowski P. H2SPECTRE ver. 7.0. Fortran Source Code. University of Warsaw, Poland; 2019. Ph.D. thesis. <https://www.fuw.edu.pl/~krp/codes.html>; [http://qcg.home.amu.edu.pl/qcg/public\\_html/H2Spectre.html](http://qcg.home.amu.edu.pl/qcg/public_html/H2Spectre.html).



Contents lists available at ScienceDirect

## Journal of Quantitative Spectroscopy &amp; Radiative Transfer

journal homepage: [www.elsevier.com/locate/jqsrt](http://www.elsevier.com/locate/jqsrt)

## Hyperfine structure of rovibrational quadrupole transitions in HD

Hubert Jóźwiak<sup>a,\*</sup>, Hubert Cybulski<sup>b</sup>, Piotr Wcisło<sup>a</sup><sup>a</sup> Institute of Physics, Faculty of Physics, Astronomy and Informatics, Nicolaus Copernicus University in Toruń, Grudziadzka 5, Toruń 87-100, Poland<sup>b</sup> Institute of Physics, Kazimierz Wielki University, ul. Powstańców Wielkopolskich 2, Bydgoszcz 85-090, Poland

## ARTICLE INFO

## Article history:

Received 1 April 2021

Revised 13 May 2021

Accepted 13 May 2021

Available online 21 May 2021

## Keywords:

Hydrogen molecule

Hyperfine structure

Hydrogen deuteride

## ABSTRACT

We perform a theoretical investigation of hyperfine structure of all rovibrational quadrupole transitions in the ground electronic  $^1\Sigma^+$  state of the HD molecule. We determine positions and intensities of 185 631 hyperfine components of 7 251 quadrupole rovibrational transitions from the O, Q and S branches. Moreover, we provide a list of hyperfine splittings of all bound states in the six isotopologues of hydrogen which we considered in previous papers. The results reported here are necessary for a reliable interpretation of accurate experimental studies of rovibrational transition frequencies in the HD isotopologue, which are useful for tests of quantum electrodynamics for molecules and searches for new physics beyond the Standard Model.

© 2021 The Author(s). Published by Elsevier Ltd.

This is an open access article under the CC BY-NC-ND license (<http://creativecommons.org/licenses/by-nc-nd/4.0/>)

## 1. Introduction

Accurate experimental studies of rovibrational transitions in the ground electronic state of molecular hydrogen provide a stringent test of quantum electrodynamics for neutral molecules [1] and can be used to put constraints on hypothetical beyond-Standard-Model interactions [2,3] or higher dimensions [4]. The presence of a weak dipole moment in the HD isotopologue makes it a suitable candidate for accurate measurements using saturation spectroscopy [5–9], molecular beam spectroscopy [10] or Doppler-limited cavity-enhanced techniques [11–13]. Although the latter require careful treatment of collisional effects, which might affect the determined transition frequency [14], current state-of-the-art cavity-enhanced measurements have already achieved a sub-MHz accuracy for both dipole transitions in HD [12] and quadrupole transitions in D<sub>2</sub> [15–19].

Quadrupole transitions in HD, which are significantly weaker than dipole transitions, have been studied less frequently [11,20–23] (see Ref. [23] for a thorough review of detected absorption lines in HD). The most accurate experimental data was reported by Kassi and Campargue [11], who measured the transitions frequencies of the Q( $N = 1-4$ ) and S( $N = 0-4$ ) lines from the first overtone with an uncertainty at a level of several MHz. As the accuracy of future experiments will most likely surpass the MHz level, the un-

derlying hyperfine structure of rovibrational transitions should be taken into account. As shown recently by Castrillo et al. [13], neglecting the hyperfine splittings in the analysis of Doppler-limited spectra of the 2-0 R(1) line leads to a significant underestimation of the determined transition frequency.

Hyperfine interactions in the HD molecule were recently studied by several authors [24–27]. Dupré [24] reported the hyperfine coupling constants for the first three vibrational levels ( $v = 0, 1, 2, N = 1$ ) and studied the hyperfine components of the 2-0 P(1) and R(1) lines in HD. In our previous work [25] on the hyperfine structure of HD, we reported hyperfine coupling constants for all bound states of HD in its ground electronic state. Moreover, we provided a list of positions and intensities of 108 320 hyperfine components of 5 129 dipole transitions from the P and R branches. Komasa et al. [26] calculated coupling constants for several rovibrational states and analyzed the relative intensities of the hyperfine components of the 2-0 P(1) and R(1) transitions and of the R(0) line from the fundamental band. The authors have also provided a publicly available code, which allows the user to calculate hyperfine splittings for a given rovibrational level. Very recently, Puchalski et al. [27] have determined the value of the hyperfine coupling constants for the ( $v = 0, N = 1$ ) level, taking into account the nonadiabatic effects, which led to the most accurate determination of the quadrupole moment of the deuteron.

In this work, we extend our previous study [25] and we analyze the hyperfine structure of all rovibrational quadrupole transitions from the O, Q and S branches in the HD molecule. Our calculations result in a list of all 185 631 hyperfine components of 7 251 rovi-

\* Corresponding author.

E-mail addresses: [hubert.jozwiak@doktorant.umk.pl](mailto:hubert.jozwiak@doktorant.umk.pl) (H. Jóźwiak), [piotr.wcislo@umk.pl](mailto:piotr.wcislo@umk.pl) (P. Wcisło).

**Table 1**

Example of the calculated positions and intensities of the hyperfine components of the quadrupole transitions in the HD isotopologue. Frequencies of the rovibrational transitions are calculated with H2Spectre code of Czachorowski et al. [40] and Komasa et al. [1]. Please note that for the rovibrational transition  $Q$  corresponds to  $Q_{\text{fi}}$  from Eq. (2), while for the hyperfine components  $Q$  denotes  $Q_{\text{fi}}^{\text{HF}}$  from Eq. (9). Intensity (in the sixth column) corresponds to the temperature-independent line intensity,  $S_{\text{fi}}/P_{\text{fi}}(T)$ .

Band	Line	Hyperfine transition $ N'F'\pm\rangle \leftarrow  NF\pm\rangle$	Frequency (MHz)	$Q$ ( $10^{-2}$ a.u.)	Intensity (cm/molecule)	Intensity at 296 K (cm/molecule)
2-0	Q(1)		212 230 347.4 (5.7)	0.958	$1.935 \times 10^{-27}$	$7.556 \times 10^{-28}$
		$ 15/2\rangle \leftarrow  11/2+\rangle$	-0.2446	0.656	$1.262 \times 10^{-28}$	$4.929 \times 10^{-29}$
		$ 13/2-\rangle \leftarrow  11/2+\rangle$	-0.1893	0.550	$8.858 \times 10^{-29}$	$3.459 \times 10^{-29}$
		$ 11/2-\rangle \leftarrow  13/2+\rangle$	-0.1683	0.401	$4.720 \times 10^{-29}$	$1.843 \times 10^{-29}$
		$ 13/2+\rangle \leftarrow  11/2+\rangle$	-0.1336	0.025	$1.872 \times 10^{-31}$	$7.310 \times 10^{-32}$
		$ 11/2-\rangle \leftarrow  13/2-\rangle$	-0.1121	0.584	$9.987 \times 10^{-29}$	$3.900 \times 10^{-29}$
		$ 15/2\rangle \leftarrow  13/2+\rangle$	-0.1113	0.895	$2.348 \times 10^{-28}$	$9.168 \times 10^{-29}$
		$ 13/2-\rangle \leftarrow  13/2+\rangle$	-0.0557	0.519	$7.887 \times 10^{-29}$	$3.080 \times 10^{-29}$
		$ 11/2-\rangle \leftarrow  15/2\rangle$	-0.0556	0.482	$6.793 \times 10^{-29}$	$2.653 \times 10^{-29}$
		$ 15/2\rangle \leftarrow  13/2-\rangle$	-0.0550	0.351	$3.611 \times 10^{-29}$	$1.410 \times 10^{-29}$
		$ 13/2+\rangle \leftarrow  13/2+\rangle$	-0.0003	0.486	$6.905 \times 10^{-29}$	$2.696 \times 10^{-29}$
		$ 13/2-\rangle \leftarrow  13/2-\rangle$	0.0003	0.657	$1.264 \times 10^{-28}$	$4.935 \times 10^{-29}$
		$ 15/2\rangle \leftarrow  15/2\rangle$	0.0014	0.785	$1.806 \times 10^{-28}$	$7.052 \times 10^{-29}$
		$ 13/2+\rangle \leftarrow  13/2-\rangle$	0.0556	0.517	$7.831 \times 10^{-29}$	$3.058 \times 10^{-29}$
		$ 13/2-\rangle \leftarrow  15/2\rangle$	0.0568	0.341	$3.413 \times 10^{-29}$	$1.333 \times 10^{-29}$
		$ 15/2\rangle \leftarrow  11/2-\rangle$	0.0599	0.479	$6.727 \times 10^{-29}$	$2.627 \times 10^{-29}$
		$ 13/2+\rangle \leftarrow  15/2\rangle$	0.1125	0.899	$2.368 \times 10^{-28}$	$9.246 \times 10^{-29}$
		$ 13/2-\rangle \leftarrow  11/2-\rangle$	0.1153	0.590	$1.020 \times 10^{-28}$	$3.985 \times 10^{-29}$
		$ 11/2+\rangle \leftarrow  13/2+\rangle$	0.1261	0.018	$9.330 \times 10^{-32}$	$3.643 \times 10^{-32}$
		$ 13/2+\rangle \leftarrow  11/2-\rangle$	0.1709	0.395	$4.569 \times 10^{-29}$	$1.784 \times 10^{-29}$
		$ 11/2+\rangle \leftarrow  13/2-\rangle$	0.1823	0.552	$8.934 \times 10^{-29}$	$3.489 \times 10^{-29}$
		$ 11/2+\rangle \leftarrow  15/2\rangle$	0.2388	0.655	$1.256 \times 10^{-28}$	$4.903 \times 10^{-29}$
2-0	S(3)		232 595 960.8 (5.7)	1.025	$3.475 \times 10^{-27}$	$3.675 \times 10^{-28}$
		$ 59/2-\rangle \leftarrow  35/2+\rangle$	-0.4196	0.062	$6.429 \times 10^{-31}$	$6.798 \times 10^{-32}$
		$ 59/2-\rangle \leftarrow  37/2+\rangle$	-0.2661	0.046	$3.528 \times 10^{-31}$	$3.731 \times 10^{-32}$
		$ 511/2-\rangle \leftarrow  37/2+\rangle$	-0.2279	0.062	$6.267 \times 10^{-31}$	$6.627 \times 10^{-32}$
		$ 59/2-\rangle \leftarrow  37/2-\rangle$	-0.1078	0.567	$5.313 \times 10^{-29}$	$5.618 \times 10^{-30}$
		$ 513/2\rangle \leftarrow  39/2\rangle$	-0.0908	2.112	$7.372 \times 10^{-28}$	$7.795 \times 10^{-29}$
		$ 511/2-\rangle \leftarrow  37/2-\rangle$	-0.0696	1.875	$5.811 \times 10^{-28}$	$6.144 \times 10^{-29}$
		$ 59/2-\rangle \leftarrow  35/2-\rangle$	-0.0393	1.688	$4.707 \times 10^{-28}$	$4.977 \times 10^{-29}$
		$ 59/2-\rangle \leftarrow  39/2\rangle$	-0.0069	0.104	$1.780 \times 10^{-30}$	$1.882 \times 10^{-31}$
		$ 511/2-\rangle \leftarrow  39/2\rangle$	0.0313	0.551	$5.019 \times 10^{-29}$	$5.307 \times 10^{-30}$
		$ 511/2+\rangle \leftarrow  37/2+\rangle$	0.0442	1.892	$5.915 \times 10^{-28}$	$6.255 \times 10^{-29}$
		$ 57/2\rangle \leftarrow  35/2+\rangle$	0.0536	0.592	$5.789 \times 10^{-29}$	$6.122 \times 10^{-30}$
		$ 59/2+\rangle \leftarrow  35/2+\rangle$	0.0572	1.628	$4.379 \times 10^{-28}$	$4.631 \times 10^{-29}$
		$ 57/2\rangle \leftarrow  33/2\rangle$	0.0874	1.415	$3.310 \times 10^{-28}$	$3.500 \times 10^{-29}$
		$ 511/2+\rangle \leftarrow  37/2-\rangle$	0.2024	0.196	$6.320 \times 10^{-30}$	$6.683 \times 10^{-31}$
		$ 57/2\rangle \leftarrow  37/2+\rangle$	0.2072	0.145	$3.471 \times 10^{-30}$	$3.670 \times 10^{-31}$
		$ 59/2+\rangle \leftarrow  37/2+\rangle$	0.2108	0.632	$6.603 \times 10^{-29}$	$6.982 \times 10^{-30}$
		$ 511/2+\rangle \leftarrow  39/2\rangle$	0.3034	0.454	$3.407 \times 10^{-29}$	$3.602 \times 10^{-30}$
		$ 57/2\rangle \leftarrow  37/2-\rangle$	0.3655	0.153	$3.884 \times 10^{-30}$	$4.107 \times 10^{-31}$
		$ 59/2+\rangle \leftarrow  37/2-\rangle$	0.3691	0.326	$1.757 \times 10^{-29}$	$1.858 \times 10^{-30}$
		$ 57/2\rangle \leftarrow  35/2-\rangle$	0.4339	0.388	$2.485 \times 10^{-29}$	$2.628 \times 10^{-30}$
		$ 59/2+\rangle \leftarrow  35/2-\rangle$	0.4375	0.076	$9.630 \times 10^{-31}$	$1.018 \times 10^{-31}$
		$ 57/2\rangle \leftarrow  39/2\rangle$	0.4664	0.032	$1.672 \times 10^{-31}$	$1.768 \times 10^{-32}$
		$ 59/2+\rangle \leftarrow  39/2\rangle$	0.4700	0.157	$4.071 \times 10^{-30}$	$4.305 \times 10^{-31}$

brational quadrupole transitions. Moreover, we provide a list of hyperfine levels of all bound states in the six isotopologues of hydrogen which we have considered in previous papers. This work concludes the series of papers devoted to the hyperfine interactions and analysis of the structure of electric dipole [25,28] and electric quadrupole [29,30] transitions in the ground electronic state of the six isotopologues of hydrogen. We summarize the theory behind the calculations in Sections 2 and 3 and we provide the examples of the calculated hyperfine structure in Section 4.

## 2. Hyperfine interactions in HD

Hyperfine splittings of rovibrational states in HD originate from three leading interactions: the nuclear-spin-rotation interaction, the nuclear dipole-dipole coupling, and the interaction of the electric quadrupole moment of the deuteron with the molecular electric field gradient (EFG). Following our previous works [25,28–30], we neglect the electron-coupled spin-spin interaction [24,31–34], which is almost three orders of magnitude smaller than the leading hyperfine interactions considered here. We recall that in

Ref. [25] we reported hyperfine coupling constants for all bound states in the ground electronic  $1^1\Sigma^+$  state of HD. It was pointed out [27] that the discrepancies between the hyperfine coupling constants calculated in our previous papers [25,29] and other theoretical results [26,27] might originate from the fact that we used the Born–Oppenheimer (BO) potential of Schwenke [35] instead of the state-of-the-art potential of Pachucki [36]. We note, however, that the BO potential is used only to obtain the rovibrational wavefunctions that are employed to average the hyperfine coupling curves (see, for example Eq. (9) in Ref. [25]). The error introduced by performing the average over rovibrational wavefunctions can be estimated by comparing the quantities which depend only on such averaging, namely the nuclear dipole-dipole constants (evaluation of this constant does not require quantum-chemical calculations; it is given by a simple formula). A comparison between the values of these constants reported in Ref. [25] with those reported by Komasa et al. (see Tab. IV in Ref. [26]) and Puchalski et al. (see Tab. I in Ref. [27]) indicates that the error is of an order of tens of Hz. Therefore, we attribute the differences between our previous

**Table 2**

Example of the calculated hyperfine splittings in the three isotopologues of hydrogen.  $E_{(v,N,F,(\pm))} - E_{(v,N)}$  denotes the energy of each hyperfine level with respect to the energy of each rovibrational state. See text for details.

Isotopologue	$v$	$N$	$F$	$(\pm)$	$E_{(v,N,F,(\pm))} - E_{(v,N)}$ (MHz)	Mixing coefficients	
						$F_1/I$	$a_{F_1/I}^{v,N,F,(\pm)}$
HD	0	1	1/2	–	–0.1169	0	$-9.47737204 \times 10^{-1}$
						1	$3.19052022 \times 10^{-1}$
	0	1	5/2		–0.0584		
	0	1	3/2	–	–0.0020	1	$-7.13360400 \times 10^{-1}$
						2	$7.00797360 \times 10^{-1}$
	0	1	3/2	+	0.0543	1	$7.00797369 \times 10^{-1}$
						2	$7.13360391 \times 10^{-1}$
	0	1	1/2	+	0.1876	0	$3.19052022 \times 10^{-1}$
						1	$9.47737204 \times 10^{-1}$
H <sub>2</sub>	0	1	2		–0.0853		
	0	1	1		–0.0299		
	0	1	0		0.5165		
D <sub>2</sub>	0	2	2	–	–0.0690	0	$7.92215947 \times 10^{-1}$
						2	$6.10240848 \times 10^{-1}$
	0	2	4		–0.0631		
	0	2	0		–0.0455		
	0	2	1		–0.0052		
	0	2	3		0.0560		
	0	2	2	+	0.1163	0	$6.10240849 \times 10^{-1}$
						2	$-7.92215947 \times 10^{-1}$

results [25] and the results reported in Refs. [26] to the possible differences in the calculated nuclear spin-rotation curve. We note, however, that the discrepancy between the position of hyperfine levels reported in Ref. [25] and Ref. [26] is, on average, 400 Hz, which is within the combined uncertainty of our results (300 Hz) and those reported in Ref. [26] (100 Hz), and is of an order of magnitude smaller than the uncertainty of the most accurate measurement of the rovibrational line frequency in HD [10]. Here, for the sake of consistency, we use the data reported by us in the previous paper [25].

Matrix elements of the effective hyperfine Hamiltonian are determined using coupling scheme which is suitable for the heteronuclear molecules. The rotational angular momentum of the molecule,  $\mathbf{N}$ , is coupled to the nuclear spin of the deuteron,  $\mathbf{I}_D$ , to form the intermediate angular momentum,  $\mathbf{F}_1$ . The intermediate angular momentum is in turn coupled to the nuclear spin angular momentum of the proton,  $\mathbf{I}_H$ , to form the total angular momentum,  $\mathbf{F}$ . The coupled basis vector is denoted as  $|v; ((N I_D) F_1 I_H) F m_F\rangle$ , where  $m_F$  is the projection of the total angular momentum on the space-fixed z-axis.

The hyperfine Hamiltonian does not couple states with different values of the total angular momentum  $F$ . Energy levels were obtained from diagonalization of each  $(2I_D + 1)(2I_H + 1) \times (2I_D + 1)(2I_H + 1) = 6 \times 6$  blocks, and the eigenvectors of the hyperfine Hamiltonian are denoted as  $|v; N F m_F(\pm)\rangle$ . The  $\pm$  labels denote the eigenstates for given  $N$  and  $F$  which are of higher (+) or lower (–) energies. The relation between the eigenbasis and the coupled basis is given by:

$$|v; N F m_F(\pm)\rangle = \sum_{F_1=|F-I_H|}^{F+I_H} \sum_{N'=|F_1-I_D|}^{F_1+I_D} a_{N'F_1}^{vNF(\pm)} |v; ((N' I_D) F_1 I_H) F m_F\rangle, \quad (1)$$

where  $a_{N'F_1}^{vNF(\pm)}$  denote the mixing coefficients. Since the mixing between different rotational levels is negligibly small, we can disregard the sum over  $N'$  and simplify the notation by putting  $a_{N'=NF_1}^{vNF(\pm)} = a_{F_1}^{vNF(\pm)}$ .

### 3. Intensities of hyperfine components of rovibrational quadrupole transitions

The intensity of each quadrupole transition between two degenerate states, in the SI units, is given [37–39] as:

$$S_{fi} = \frac{2\pi^4}{15hc^3\epsilon_0} \nu_0^3 C_{N_i, N_f} P_{fi}(T) |\mathcal{Q}_{fi}|^2, \quad (2)$$

where  $\nu_0$  is the transition frequency and the electric quadrupole transition moment is denoted by  $\mathcal{Q}_{fi}$ .  $h$ ,  $c$  and  $\epsilon_0$  are Planck's constant, the speed of light in vacuum and vacuum permittivity, respectively.  $C_{N_i, N_f}$  is an algebraic coefficient, which depends on the initial and final rotational quantum number:

$$C_{N_i, N_f} = (2N_f + 1) \begin{pmatrix} N_f & 2 & N_i \\ 0 & 0 & 0 \end{pmatrix}^2. \quad (3)$$

Here, we give the direct formulas for:

1. the O branch ( $N_f = N_i - 2$ ):

$$C_{N_i, N_f} = \frac{3N_i(N_i - 1)}{2(2N_i - 1)(2N_i + 1)}, \quad (4)$$

2. the Q branch ( $N_f = N_i$ ):

$$C_{N_i, N_f} = \frac{N_i(N_i + 1)}{(2N_i - 1)(2N_i + 3)}, \quad (5)$$

3. the S branch ( $N_f = N_i + 2$ ):

$$C_{N_i, N_f} = \frac{3(N_i + 1)(N_i + 2)}{2(2N_i + 1)(2N_i + 3)}. \quad (6)$$

The temperature-dependent term,  $P_{fi}(T)$ , is given as

$$P_{fi}(T) = w_i(2N_i + 1) \frac{(e^{-E_i/k_B T} - e^{-E_f/k_B T})}{Q(T)}, \quad (7)$$

with the partition function,  $Q(T)$ , defined as:

$$Q(T) = \sum_k w_k(2N_k + 1) e^{-E_k/k_B T}. \quad (8)$$

$w_k$  is the degeneracy factor due to nuclear spin statistics and equals 6 for each rovibrational state of HD.  $E_k$  is the energy of the

$k$ -th rovibrational state,  $k_B$  denotes the Boltzmann constant and  $T$  is the temperature.

Line intensity of each hyperfine component of a rovibrational quadrupole transition is given as [29,30]:

$$S_{fi}^{HF} = \frac{2\pi^4}{15hc^3\epsilon_0} \nu_0^3 \frac{1}{w_i(2N_i + 1)} P_{fi}(T) |\mathcal{Q}_{fi}^{HF}|^2, \quad (9)$$

where  $\mathcal{Q}_{fi}^{HF}$  is the reduced matrix element of the quadrupole moment spherical tensor, evaluated using Eq. (1):

$$\begin{aligned} |\mathcal{Q}_{fi}^{HF}|^2 &= \left| \langle \nu_f; N_f F_f(\pm) \| T^{(2)}(Q) \| \nu_i; N_i F_i(\pm) \rangle \right|^2 = \\ &= \left| \sum_{F_i=|F_i-I_H|}^{F_i+I_H} \sum_{N_i'=|F_i-I_D|}^{F_i+I_D} \sum_{F_i=|F_i-I_H|}^{F_i+I_H} \sum_{N_i'=|F_i-I_D|}^{F_i+I_D} \right. \\ &\quad \left. a_{N_i'F_i}^{\nu_f N_f F_f(\pm)} a_{N_i'F_i}^{\nu_i N_i F_i(\pm)} \right. \\ &\quad \times \langle \nu_f; (N_f' I_D) F_i I_H \| T^{(2)}(Q) \| \nu_i; (N_i' I_D) F_i I_H \rangle \left. \right|^2. \end{aligned} \quad (10)$$

The latter term can be related to the quadrupole transition moment of the rovibrational transition

$$\mathcal{Q}_{fi} = \int dR \chi_f^*(R) \mathcal{Q}(R) \chi_i(R), \quad (11)$$

where  $\mathcal{Q}(R)$  is the quadrupole moment function [37–39]:

$$\mathcal{Q}(R) = e \left( \frac{R^2}{2} - \frac{1}{2} \langle \phi | \sum_i 3z_i^2 - r_i^2 | \phi \rangle \right). \quad (12)$$

Here,  $z_i$  and  $r_i$  denote the coordinates of the  $i$ th electron and  $|\phi\rangle$  is the electronic wavefunction, which is parametrically dependent on the internuclear coordinate,  $R$ . The relation between Eq. (10) and the quadrupole transition moment is given as:

$$\begin{aligned} &\langle \nu_f; (N_f' I_D) F_i I_H \| T^{(2)}(Q) \| \nu_i; (N_i' I_D) F_i I_H \rangle \\ &= (-1)^{F_i+I_H+F_i+F_i+I_D+N_i'} \sqrt{(2F_i+1)(2F_i+1)} \\ &\quad \times \sqrt{(2F_i+1)(2F_i+1)} \begin{Bmatrix} I_H & F_i & F_i \\ 2 & F_i & F_i \end{Bmatrix} \\ &\quad \times \begin{Bmatrix} I_D & F_i & N_i \\ 2 & N_f & F_i \end{Bmatrix} \langle \nu_f N_f \| T^{(2)}(Q) \| \nu_i N_i \rangle. \end{aligned} \quad (13)$$

For a  $^1\Sigma$  state, the last term in Eq. (13) is given as:

$$\begin{aligned} &\langle \nu_f N_f \| T^{(2)}(Q) \| \nu_i N_i \rangle \\ &= (-1)^{N_f} \sqrt{(2N_f+1)(2N_i+1)} \begin{pmatrix} N_f & 2 & N_i \\ 0 & 0 & 0 \end{pmatrix} \mathcal{Q}_{fi}. \end{aligned} \quad (14)$$

In this work, we use the quadrupole transition moment function reported in Ref. [29], to evaluate the quadrupole transition matrix for all quadrupole transitions in the ground state of the HD molecule.

## 4. Example of the complete dataset record

### 4.1. Hyperfine components of rovibrational quadrupole transitions

We calculate the positions and intensities of the hyperfine components of all quadrupole transitions in the ground  $^1\Sigma^+$  electronic state of the HD isotopologue. Our calculations result in 185 631 hyperfine components of 7 251 transitions from the O, Q and S branches. Following our previous papers [25,28–30] we estimate the uncertainty of the determined transition frequencies to be approximately 0.4 kHz and the uncertainty of the transition moment and line intensity to be of an order of  $10^{-3}$ .

Table 1 presents an example of the calculated parameters for the Q(1) and S(3) lines from the first overtone (2-0) band, which were investigated by Kassi and Campargue [11]. The central frequency of the rovibrational transition is taken from the H2Spectre code [1,40]. The 2-0 Q(1) line consists of 21 hyperfine components spread over a range of almost 500 kHz. The 2-0 S(3)

line consists of 23 hyperfine components spread over a range of over 900 kHz.

We note that every  $\nu_f - \nu_i$  O(2) and S(0) lines in HD consist of 10 hyperfine components, every O(3) and S(1) lines involve 22 hyperfine components, while all the remaining rovibrational lines from these two branches involve 23 components. In the case of the Q branch, the Q(1) and Q(2) lines involve 21 and 33 hyperfine components, respectively, while all the remaining lines involve 34 components.

### 4.2. List of hyperfine splittings

We also provide a list of hyperfine splittings of all bound states in the six isotopologues of hydrogen which we have considered in the previous papers [25,28–30]. Such a list should be a practical tool for the spectroscopic community and a more convenient way to determine hyperfine splittings of a given state than using the hyperfine coupling constants and diagonalizing the effective Hamiltonian. Example lists of the hyperfine splittings for the chosen states in HD, H<sub>2</sub> and D<sub>2</sub> are given in Table 2. The complete dataset can be found in Supplementary Material [41]. We recall that the uncertainty of the determined energy of each hyperfine level is approximately 300 Hz.

Apart from the energy levels of the hyperfine states, we provide values of the mixing coefficients for the heteronuclear isotopologues and for *ortho*-D<sub>2</sub>. The hyperfine states in these isotopologues can be expressed as a linear combination of the coupled basis vectors (Eq. (1)). For example, the  $|\nu = 0, N = 1, F = 1/2^+\rangle$  state in HD is a linear combination of the coupled basis vectors with  $F_1 = 0$  and  $F_1 = 1$ , with mixing coefficients of approximately –0.948 and 0.319, respectively (see the two last columns of the first entry in Table 2). Similarly, the  $|\nu = 0, N = 2, F = 2^-\rangle$  state in D<sub>2</sub> is a combination of coupled basis vectors (see Eq. (16) in Ref. [29]) with  $I = 0$  and  $I = 2$  with mixing coefficients of approximately 0.792 and 0.610, respectively.

## 5. Conclusion

We provide a comprehensive list of positions and intensities of the 185 631 hyperfine components of 7 251 rovibrational quadrupole transitions from the O, Q and S branches in HD. We also report a list of hyperfine splittings of all bound states in the six isotopologues of hydrogen which we analyzed in our previous papers. The results presented here can serve as a reference data for future accurate measurements of transition frequencies in the HD isotopologue, which could be useful for testing the quantum electrodynamics for molecules and searching for new physics beyond the Standard Model.

### Declaration of Competing Interest

The authors declare that they have no known competing financial interests or personal relationships that could have appeared to influence the work reported in this paper.

### CRediT authorship contribution statement

**Hubert Jóźwiak:** Conceptualization, Methodology, Software, Investigation, Writing - original draft, Writing - review & editing, Funding acquisition. **Hubert Cybulski:** Software, Investigation, Writing - original draft, Writing - review & editing. **Piotr Wcisło:** Conceptualization, Methodology, Validation, Writing - original draft, Writing - review & editing.



## Acknowledgements

The research is financed from the budgetary funds on science projected for 2019–2023 as a research project under the “Diamen-towy Grant” program. P.W. is supported by the National Science Centre in Poland, Project no. 2019/35/B/ST2/01118. The research is a part of the program of the National Laboratory FAMO in Toruń, Poland.

## References

- [1] Komasa J, Puchalski M, Czachorowski P, Łach G, Pachucki K. Rovibrational energy levels of the hydrogen molecule through nonadiabatic perturbation theory. *Phys Rev A* 2019;100:032519. doi:10.1103/PhysRevA.100.032519.
- [2] Ubachs W, Koelemeij JC, Eikema KSE, Salumbides EJ. Physics beyond the Standard Model from hydrogen spectroscopy. *J Mol Spectrosc* 2016;320:1–12. doi:10.1016/j.jms.2015.12.003.
- [3] Salumbides EJ, Koelemeij JC, Komasa J, Pachucki K, Eikema KSE, Ubachs W. Bounds on fifth forces from precision measurements on molecules. *Phys Rev D* 2013;87:112008. doi:10.1103/PhysRevD.87.112008.
- [4] Salumbides EJ, Schellekens AN, Gato-Rivera B, Ubachs W. Constraints on extra dimensions from precision molecular spectroscopy. *New J Phys* 2015;17(3):033015. doi:10.1088/1367-2630/17/3/033015.
- [5] Tao L-G, Liu A-W, Pachucki K, Komasa J, Sun YR, Wang J, Hu SM. Toward a determination of the proton-electron mass ratio from the Lamb-dip measurement of HD. *Phys Rev Lett* 2018;120:153001. doi:10.1103/PhysRevLett.120.153001.
- [6] Cozijn FMJ, Dupré P, Salumbides EJ, Eikema KSE, Ubachs W. Sub-Doppler frequency metrology in HD for tests of fundamental physics. *Phys Rev Lett* 2018;120:153002. doi:10.1103/PhysRevLett.120.153002.
- [7] Diouf ML, Cozijn FMJ, Darquié B, Salumbides EJ, Ubachs W. Lamb-dips and Lamb-peaks in the saturation spectrum of HD. *Opt Lett* 2019;44(19):4733–6. doi:10.1364/OL.44.004733.
- [8] Diouf ML, Cozijn FMJ, Lai K-F, Salumbides EJ, Ubachs W. Lamb-peak spectrum of the HD (2-0) P(1) line. *Phys Rev Res* 2020;2:023209. doi:10.1103/PhysRevResearch.2.023209.
- [9] Hua T-P, Sun YR, Hu SM. Dispersion-like lineshape observed in cavity-enhanced saturation spectroscopy of HD at 14  $\mu\text{m}$ . *Opt Lett* 2020;45(17):4863. doi:10.1364/OL.401879.
- [10] Fast A, Meek SA. Sub-ppb measurement of a fundamental band rovibrational transition in HD. *Phys Rev Lett* 2020;125:023001. doi:10.1103/PhysRevLett.125.023001.
- [11] Kassi S, Campargue A. Electric quadrupole and dipole transitions of the first overtone band of HD by CRDS between 1.45 and 1.33  $\mu\text{m}$ . *J Mol Spectrosc* 2011;267(1):36–42. doi:10.1016/j.jms.2011.02.001.
- [12] Fasci E, Castrillo A, Dinesan H, Gravina S, Moretti L, Gianfrani L. Precision spectroscopy of HD at 1.38  $\mu\text{m}$ . *Phys Rev A* 2018;98:022516. doi:10.1103/PhysRevA.98.022516.
- [13] Castrillo A, Fasci E, Gianfrani L. Doppler-limited precision spectroscopy of HD at 1.4  $\mu\text{m}$ : an improved determination of the R(1) center frequency. *Phys Rev A* 2021;103:022828. doi:10.1103/PhysRevA.103.022828.
- [14] Wcisło P, Gordon IE, Cheng C-F, Hu S-M, Ciuryło R. Collision-induced line-shape effects limiting the accuracy in doppler-limited spectroscopy of H<sub>2</sub>. *Phys Rev A* 2016;93:022501. doi:10.1103/PhysRevA.93.022501.
- [15] Mondelain D, Kassi S, Sala T, Romanini D, Gatti D, Campargue A. Sub-MHz accuracy measurement of the S(2) 2-0 transition frequency of D<sub>2</sub> by comb-assisted cavity ring down spectroscopy. *J Mol Spectrosc* 2016;326:5–8. doi:10.1016/j.jms.2016.02.008.
- [16] Wcisło P, Thibault F, Zaborowski M, Wójtewicz S, Cygan A, Kowzan G, Masłowski P, Komasa J, Puchalski M, Pachucki K, Ciuryło R, Lisak D. Accurate deuterium spectroscopy for fundamental studies. *J Quant Spectrosc Radiat Transf* 2018;213:41–51. doi:10.1016/j.jqsrt.2018.04.011.
- [17] Zaborowski M, Słowiński M, Stankiewicz K, Thibault F, Cygan A, Jóźwiak H, Kowzan G, Masłowski P, Nishiyama A, Stolarczyk N, Wójtewicz S, Ciuryło R, Lisak D, Wcisło P. Ultrahigh finesse cavity-enhanced spectroscopy for accurate tests of quantum electrodynamics for molecules. *Opt Lett* 2020;45(7):1603–6. doi:10.1364/OL.389268.
- [18] Wójtewicz S, Gatti D, Lamperti M, Laporta P, Jóźwiak H, Thibault F, Wcisło P, Marangoni M. Accurate deuterium spectroscopy and comparison with ab initio calculations. *Phys Rev A* 2020;101:052504. doi:10.1103/PhysRevA.101.052504.
- [19] Mondelain D, Kassi S, Campargue A. Transition frequencies in the (2-0) band of D<sub>2</sub> with MHz accuracy. *J Quant Spectrosc Radiat Transf* 2020;253:107020. doi:10.1016/j.jqsrt.2020.107020.
- [20] Brannon PJ, Church CH, Peters CW. Electric field induced spectra of molecular hydrogen, deuterium and deuterium hydride. *J Mol Spectrosc* 1968;27(1-4):44–54. doi:10.1016/0022-2852(68)90018-0.
- [21] McKellar ARW. Intensities of the dipole and quadrupole rotation-vibration spectra of HD. *Can J Phys* 1974;52(13):1144–51. doi:10.1139/p74-152.
- [22] Rich NH, Johns JWC, McKellar ARW. Frequency and intensity measurements in the fundamental infrared band of HD. *J Mol Spectrosc* 1982;95(2):432–8. doi:10.1016/0022-2852(82)90141-2.
- [23] Vasilchenko S, Mondelain D, Kassi S, Čermák P, Chomet B, Garnache A, Denet S, Lecocq V, Campargue A. The HD spectrum near 2.3  $\mu\text{m}$  by CRDS-VECSEL: electric quadrupole transition and collision-induced absorption. *J Mol Spectrosc* 2016;326:9–16. doi:10.1016/j.jms.2016.04.002.
- [24] Dupré P. Hyperfine transitions in the first overtone mode of hydrogen deuteride. *Phys Rev A* 2020;101:022504. doi:10.1103/PhysRevA.101.022504.
- [25] Jóźwiak H, Cybulski H, Wcisło P. Positions and intensities of hyperfine components of all rovibrational dipole lines in the HD molecule. *J Quant Spectrosc Radiat Transf* 2020;253:107171. doi:10.1016/j.jqsrt.2020.107171.
- [26] Komasa J, Puchalski M, Pachucki K. Hyperfine structure in the HD molecule. *Phys Rev A* 2020;102. doi:10.1103/physreva.102.012814.
- [27] Puchalski M, Komasa J, Pachucki K. Hyperfine structure of the first rotational level in H<sub>2</sub>, D<sub>2</sub> and HD molecules and the deuteron quadrupole moment. *Phys Rev Lett* 2020;125:253001. doi:10.1103/PhysRevLett.125.253001.
- [28] Jóźwiak H, Cybulski H, Wcisło P. Hyperfine components of rovibrational dipole transitions in HT and DT. *J Quant Spectrosc Radiat Transf* 2021;270:107662. doi:10.1016/j.jqsrt.2021.107662. accepted in
- [29] Jóźwiak H, Cybulski H, Wcisło P. Hyperfine components of all rovibrational quadrupole transitions in the H<sub>2</sub> and D<sub>2</sub> molecules. *J Quant Spectrosc Radiat Transf* 2020;253:107186. doi:10.1016/j.jqsrt.2020.107186.
- [30] Jóźwiak H, Cybulski H, Wcisło P. Hyperfine structure of quadrupole rovibrational transitions in tritium-bearing hydrogen isotopologues. *J Quant Spectrosc Radiat Transf* 2020;256:107255. doi:10.1016/j.jqsrt.2020.107255.
- [31] Carr HY, Purcell EM. Interaction between nuclear spins in HD gas. *Phys Rev* 1952;88:415–16. doi:10.1103/PhysRev.88.415.2.
- [32] Ramsey NF, Purcell EM. Interactions between nuclear spins in molecules. *Phys Rev* 1952;85:143–4. doi:10.1103/PhysRev.85.143.
- [33] Code RF, Ramsey NF. Molecular-beam magnetic resonance studies of HD and D<sub>2</sub>. *Phys Rev A* 1971;4:1945–59. doi:10.1103/PhysRevA.4.1945.
- [34] Puchalski M, Komasa J, Pachucki K. Nuclear spin-spin coupling in HD, HT, and DT. *Phys Rev Lett* 2018;120:083001. doi:10.1103/PhysRevLett.120.083001.
- [35] Schwenke DW. Calculations of rate constants for the three-body recombination of H<sub>2</sub> in the presence of H<sub>2</sub>. *J Chem Phys* 1988;89(4):2076–91. doi:10.1063/1.455104.
- [36] Pachucki K. Born-Oppenheimer potential for H<sub>2</sub>. *Phys Rev A* 2010;82:032509. doi:10.1103/PhysRevA.82.032509.
- [37] Campargue A, Kassi S, Pachucki K, Komasa J. The absorption spectrum of H<sub>2</sub>: CRDS measurements of the (2-0) band, review of the literature data and accurate ab initio line list up to 35,000  $\text{cm}^{-1}$ . *Phys Chem Chem Phys* 2012;14:802–15. doi:10.1039/C1CP22912E.
- [38] Kassi S, Campargue A, Pachucki K, Komasa J. The absorption spectrum of D<sub>2</sub>: ultrasensitive cavity ring down spectroscopy of the (2-0) band near 1.7  $\mu\text{m}$  and accurate ab initio line list up to 24,000  $\text{cm}^{-1}$ . *J Chem Phys* 2012;136(18):184309. doi:10.1063/1.4707708.
- [39] Karl G, Poll JD. On the quadrupole moment of the hydrogen molecule. *J Chem Phys* 1967;46(8):2944–50. doi:10.1063/1.1841160.
- [40] H2SPECTRE ver. 7.0. Fortran source code, 2019; P. Czachorowski, Ph.D. thesis, University of Warsaw, Poland, 2019. <https://www.fuw.edu.pl/~krcp/codes.html>; [http://qcg.home.amu.edu.pl/qcg/public\\_html/H2Spectre.html](http://qcg.home.amu.edu.pl/qcg/public_html/H2Spectre.html).
- [41] Jóźwiak H, Cybulski H, Wcisło P, “Supplementary material for hyperfine splittings, line positions and intensities”, Mendeley Data, v1. 2021. doi:10.17632/79dppwdw4f.1



# Hyperfine structure of the $EF^1\Sigma_g^+$ state in $H_2$

Hubert Jóźwiak<sup>1,\*</sup>, Hubert Cybulski<sup>2</sup>, Antoni Grabowski<sup>1</sup> and Piotr Wcisło<sup>1</sup>

<sup>1</sup>*Institute of Physics, Faculty of Physics, Astronomy and Informatics,*

*Nicolaus Copernicus University in Torun, Grudziadzka 5, 87-100 Torun, Poland*

<sup>2</sup>*Institute of Physics, Kazimierz Wielki University, ul. Powstańców Wielkopolskich 2, 85-090 Bydgoszcz, Poland*



(Received 27 May 2021; accepted 28 June 2021; published 16 July 2021)

Calculations of hyperfine splittings in  $H_2$  are needed for an accurate experimental determination of frequencies of rovibrational transitions and the dissociation energy in  $H_2$ , which are used for experimental tests of quantum electrodynamics for molecules and for searches for new physics beyond the standard model. While the hyperfine structure of the ground electronic  $X^1\Sigma_g^+$  state in  $H_2$  has been studied in detail, there are no theoretical or experimental data regarding the excited electronic  $^1\Sigma_g^+$  states. Here, we report the first investigation of the hyperfine structure of rovibrational levels in the excited double-well  $EF^1\Sigma_g^+$  state in the hydrogen molecule. We provide hyperfine splittings and coupling constants for several low-lying rovibrational levels. The hyperfine splittings in the inner well are approximately 1 order of magnitude larger than those in the outer well and 2 times smaller than those in the ground electronic state.

DOI: [10.1103/PhysRevA.104.012808](https://doi.org/10.1103/PhysRevA.104.012808)

## I. INTRODUCTION

The hydrogen molecule, the simplest neutral chemically bound system, constitutes a perfect benchmark system for testing *ab initio* quantum-mechanical calculations. Its ground electronic  $X^1\Sigma_g^+$  state has been a subject of extensive experimental and theoretical studies for almost a century [1]. Studies of the ionization and dissociation energies [2–9] and the rovibrational structure [10–19] have already achieved a sub-MHz accuracy. An accurate comparison between experimental results and theoretical predictions allows for tests of quantum electrodynamics for molecules [9,10,13]. It can also be used in searches for physics beyond the standard model [20] by putting constraints on hypothetical new forces [21] or higher dimensions [22]. Improvement in the accuracy of calculated and measured dissociation energies and frequencies of rovibrational transitions in the hydrogen molecule would also yield an independent determination of the proton-charge radius or the electron-to-proton mass ratio [10,23,24]. Thus, spectroscopy of molecular hydrogen could complement the accurate studies of the hydrogen molecular ion, which has recently led to the determination of the proton-to-electron mass ratio with a parts-per-trillion relative uncertainty [25,26].

In terms of the excited electronic states of  $H_2$ , particular attention has been paid to the double-well  $EF^1\Sigma_g^+$  state, which is the first excited singlet state of the *gerade* symmetry. On the theoretical side, the state was studied extensively by *ab initio* methods [27–35]. Very recently, Siłkowski *et al.* [36] published a set of state-of-the-art Born-Oppenheimer (BO) potential energy curves for several excited electronic  $n\Sigma^+$  states (up to  $n = 7$ ), for both singlet and triplet states and the *gerade* and *ungerade* symmetries. The authors reached a relative accuracy of  $10^{-10}$ , improving the previous most

accurate results (see Refs. [33,34] for the  $EF^1\Sigma_g^+$  state) by 6 orders of magnitude. On the experimental side, the EF state has been used as an intermediate state in multiphoton transitions, which are used to determine the dissociation energy of *para*- and *ortho*- $H_2$ . As discussed in Refs. [3,6–8], the dissociation energy of  $H_2$  can be determined from a multistep thermodynamic cycle, which involves the ionization of  $H_2$ , the dissociation of hydrogen ion ( $H_2^+$ ) and the ionization of atomic hydrogen. The ionization energy of  $H_2$  can be obtained from a series of experiments, which involve the measurement of the energy of a two-photon transition to the inner (*E*) well of the EF state, the measurement of the energy interval from the  $E$  ( $\nu = 0, N = 1$ ) state to one of the highly excited Rydberg states, and the extrapolation to the ionization energy of  $H_2$ , using the multichannel quantum defect theory (MQDT). We note that this sequence can involve either the ground vibrational level of the inner well of the EF state [3,6,8] or the ground vibrational level from the inner (*G*) well from the next double-well  $GK^1\Sigma_g^+$  electronic state [7]. Similar multistep experiments involving the two-photon transition to the excited electronic states were used to determine the energy interval between the first two vibrational states, ( $\nu = 0, N = 0$ ) and ( $\nu = 1, N = 0$ ) [37], and the energy interval between the ground states of *ortho*- and *para*- $H_2$  [15].

The bound states of the outer (*F*) well of the EF state are used as intermediate states in the experimental studies of highly excited ( $\nu = 11$ –14) vibrational levels of the ground electronic state [38–41]. Two-photon spectroscopy of the *F*-*X* transition offers a perfect way to test *ab initio* calculations for these highly excited levels in the ground electronic state. It might also be used in studies of the exotic ( $\nu = 14, N = 4$ ) state, which is speculated to be rotationally predissociative [42], bound by the nonadiabatic effects [10], or a quasibound state that exists due to hyperfine interactions [43].

A remarkable accuracy of both theoretical and experimental studies of the ground electronic state of  $H_2$  and

\*hubert.jozwiak@doktorant.umk.pl

its isotopologues has recently driven an increased interest in the underlying hyperfine structure of the rovibrational levels [44–51]. On the one hand, accurate spectroscopy of the molecular hydrogen ion [25] stimulated a parallel progress in the analysis of the hyperfine structure of the  $\text{H}_2^+$ ,  $\text{HD}^+$  [52,53], and  $\text{D}_2^+$  ions [54]. On the other hand, there are no available experimental or theoretical data on the hyperfine structure of the excited states of neutral molecular hydrogen. A lack of knowledge about the underlying hyperfine structure of the  $(\nu = 0, N = 1)$  level in the inner well of the  $EF$  state is one of the factors limiting the accuracy of the recent experimental determination of the dissociation energy of *ortho*- $\text{H}_2$  [8]. This quantity was retrieved from the three-step sequence (*vide supra*) which involved a two-photon excitation from the  $(\nu = 0, N = 1) X^1\Sigma_g^+$  state to the  $(\nu = 0, N = 1) EF^1\Sigma_g^+$  state, a subsequent two-photon excitation to the  $54p1_1$  Rydberg state, and the determination of the ionization energy of the hydrogen molecule from the MQDT. As pointed out by the authors, while the hyperfine structure of the  $(\nu = 0, N = 1) X^1\Sigma_g^+$  state could be estimated from the paper of Ramsey [55] and the hyperfine structure of the Rydberg  $54p1_1$  state was known from the combination of millimeter spectroscopy and MQDT [56,57], the influence of hyperfine interactions on the structure of the first double-well state has remained unknown.

Here we report the hyperfine structure of rovibrational levels in the excited  $EF^1\Sigma_g^+$  state of the hydrogen molecule. Following our previous papers [45–49], we analyze the leading hyperfine interactions in  $\text{H}_2$ , we report the spin-rotation coefficient for the  $EF$  state, and we provide the hyperfine splittings of the first three rotational states of the *ortho*- $\text{H}_2$  ( $N = 1, 3$ , and  $5$ ) from the first seven ( $\nu = 0$ – $6$ ) vibrational levels, which lie below the barrier that separates the inner and outer wells of the  $EF$  state. In Sec. II, we provide some basic information about the excited  $EF$  state and rovibrational levels considered in this work. In Sec. III, we recall the information about the hyperfine interactions in  $\text{H}_2$  and we provide formulas for the matrix elements of the effective hyperfine Hamiltonian. In Sec. IV, we report a list of rovibrationally averaged spin-rotation and dipole-dipole coupling constants for the 21 states in  $\text{H}_2$ . The hyperfine splittings are discussed in Sec. V, where we compare the structure of the first rotational states of the first vibrational states from the  $E$  and  $F$  wells of the excited state with the splitting of the first rovibrational level in the  $X^1\Sigma_g^+$  state. In Sec. VI, we conclude our results.

## II. $EF^1\Sigma_g^+$ STATE IN $\text{H}_2$

The  $EF^1\Sigma_g^+$  state is the first excited singlet state of the *gerade* manifold, which involves two minima separated by a barrier of approximately  $6700 \text{ cm}^{-1}$ . The characteristic double-well structure originates from the avoided crossing of two diabatic  $E$  and  $F$  states [58]. As the internuclear distance tends to infinity, the  $EF^1\Sigma_g^+$  state dissociates into the  $\text{H}(1s)$  and  $\text{H}(2s)$  states. Due to a significant height of the barrier, the lowest bound states in the inner and outer wells behave like for two separated  $E$  and  $F$  states. This is the reason for the often used distinct labeling system for the states from the  $E$  and  $F$  wells [59]. The vibrational spacing and the rotational

constant for the states in the  $E$  well (approximately  $2330$  and  $63 \text{ cm}^{-1}$ , respectively) are significantly larger than the corresponding values in the  $F$  well (approximately  $1195$  and  $12 \text{ cm}^{-1}$ , respectively) [59].

According to Ref. [30], the  $EF^1\Sigma_g^+$  state involves vibrational levels up to  $\nu = 33$ . We note that states as high as  $\nu = 32$  were observed [60,61]. However, as both  $\nu$  and  $N$  increase, the assignment of the levels from the experimental spectra becomes difficult and might lead to some ambiguities [59,62]. Here, we focus on the seven vibrational states which lie below the barrier that separates the  $E$  and  $F$  wells and we study the hyperfine structure of the first three rotational states from each vibrational manifold (see Fig. 1). The rovibrational levels with  $N \leq 5$  were studied in detail by Yu and Dressler [32] using *an initio* BO potential energy curve, while adiabatic corrections and nonadiabatic coupling functions were studied by Ross and Jungen using the MQDT [62,63]. We also recall a recent study by Ferenc and Mátyus [35] of the  $(\nu = 0, N \leq 5)$  states from the inner well, where the  $EF$  states were obtained as resonances within the four-body problem. Energy intervals between the states considered in this work were also studied experimentally [40,59,62,64].

Figure 1 presents the structure of the rovibrational levels considered in this paper. The square modulus of each rovibrational wave function is plotted against the BO potential energy curve of the  $EF^1\Sigma_g^+$  state [36] summed with the contribution from the centrifugal term,  $N(N+1)/2\mu R^2$ ;  $\mu$  denotes the reduced mass of the  $\text{H}_2$  molecule and  $R$  is the internuclear distance. The position of each wave function on the energy scale corresponds to the energy of the rovibrational level. For clarity, the graphical representations of the wave function curves shown in Fig. 1 are restricted to the respective well of the potential, except for the  $\nu = 6$  states, where the values of the wave functions are non-negligible also in the outer well. The energy of both inner- and outer-well rovibrational levels increases with  $N$  due to the contribution from the centrifugal term. This effect is more significant for the inner well states, as shown in Fig. 1. As a result, for  $N > 3$ , the energy of the  $(\nu = 0, N)$  state is higher than the energy of the  $(\nu = 1, N)$  state.

Following other studies of the  $EF^1\Sigma_g^+$  state [59,62], we use two labeling systems for the rovibrational levels: a combined numbering of levels in the double-well potential,  $EF\nu, N$ , and an alternative, separate numbering for the  $E$  and  $F$  states,  $E\nu, N$ , and  $F\nu, N$ , respectively. We note, however, that the combined numbering becomes misleading as  $N$  increases: the  $EF0/E0, N = 5$  state is of higher energy than the  $EF1/F0, N = 5$  state.

## III. HYPERFINE INTERACTIONS IN THE $\text{H}_2$ MOLECULE

The hyperfine structure of rovibrational levels in the  $\text{H}_2$  molecule originates from two leading hyperfine interactions: nuclear spin-rotation interaction and nuclear dipole-dipole interaction. The former is the interaction of the nuclear magnetic dipoles with the magnetic field that originates from the overall rotation of the molecule (both the electrons and the nuclei) [65] and the latter is the magnetic dipole interaction between the two nuclear magnetic moments. We recall that these two hyperfine interactions can be expressed in terms of

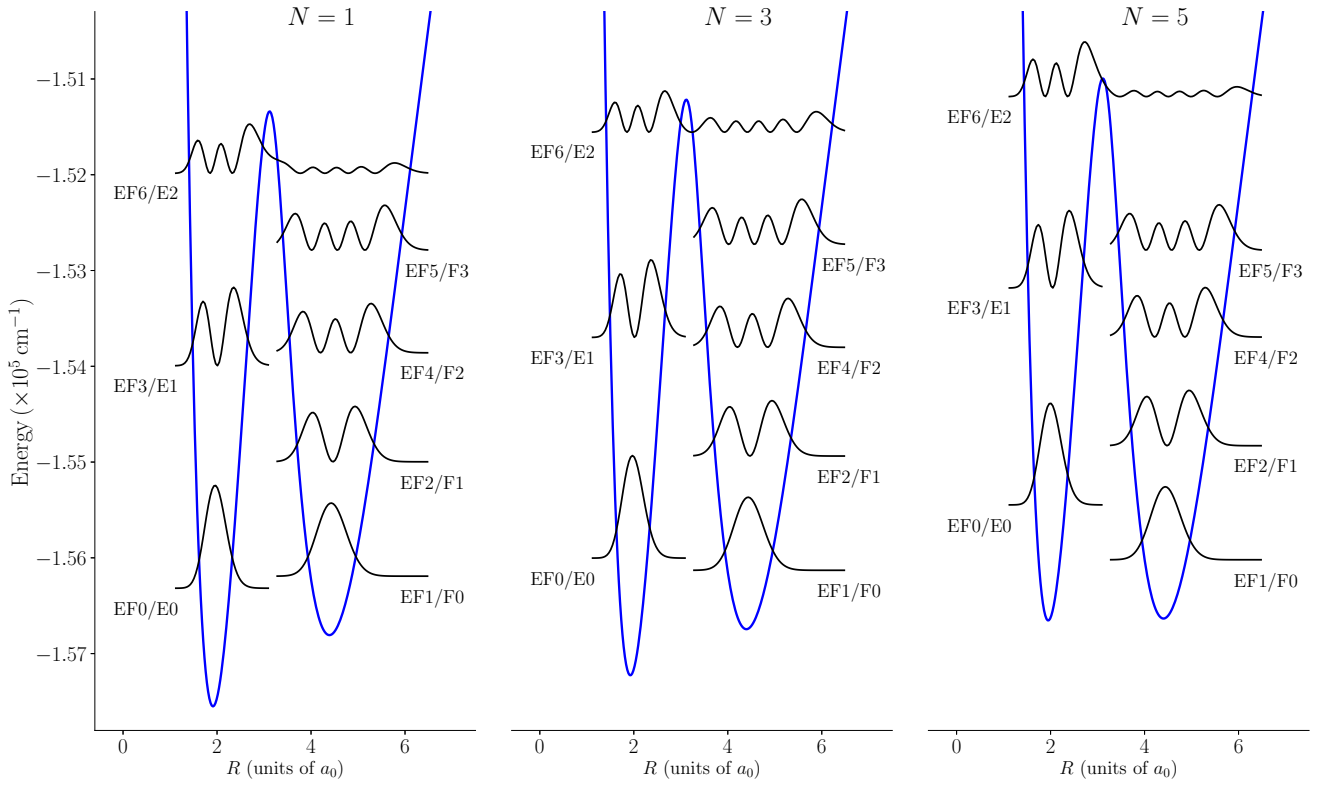


FIG. 1. The square modulus of the  $EF \ ^1\Sigma_g^+$  rovibrational ( $\nu = 0-6$ ,  $N = 1-5$ ) wave functions of *ortho*- $H_2$  considered in this work. The blue (gray) curves represent the potential energy for the  $EF \ ^1\Sigma_g^+$  state taken from Ref. [36] with the additional contribution from the centrifugal term for each  $N$ .

the three angular momenta: the nuclear spin angular momenta of the two nuclei,  $\mathbf{I}_1$  and  $\mathbf{I}_2$ , and the rotational angular momentum of the nuclei,  $\mathbf{N}$ . We construct a coupled basis set out of the three sets of eigenvectors of  $\mathbf{I}_1^2$ ,  $\mathbf{I}_2^2$ , and  $\mathbf{N}^2$ . First, we couple the two nuclear spins to form the total nuclear spin angular momentum  $\mathbf{I}$ , which, then, is coupled to the rotational angular momentum  $\mathbf{N}$  to form the total angular momentum  $\mathbf{F}$ . The coupled basis vectors are given as

$$\begin{aligned}
 |\nu; (NI)Fm_F\rangle &= \sum_{m_N=-N}^N \sum_{m_I=-I}^I \langle Nm_N Im_I | Fm_F \rangle \\
 &\quad \times |\nu; Nm_N\rangle |I_1 I_2 Im_I\rangle \\
 &= \sum_{m_N=-N}^N \sum_{m_I=-I}^I \sum_{m_{I_1}=-I_1}^{I_1} \sum_{m_{I_2}=-I_2}^{I_2} \\
 &\quad \times \langle Nm_N Im_I | Fm_F \rangle \langle I_1 m_{I_1} I_2 m_{I_2} | Im_I \rangle \\
 &\quad \times |\nu; Nm_N\rangle |I_1 m_{I_1}\rangle |I_2 m_{I_2}\rangle, \quad (1)
 \end{aligned}$$

where  $\langle \dots | \dots \rangle$  is a Clebsch-Gordan coefficient;  $|I_1 m_{I_1}\rangle$  and  $|I_2 m_{I_2}\rangle$  are the eigenvectors of  $\mathbf{I}_1^2$  and  $\mathbf{I}_2^2$ , respectively; and  $|\nu; Nm_N\rangle = |\nu, N\rangle |Nm_N\rangle$  is a shorthand notation for the rovibrational state, which, in position representation, corresponds to the product of a nuclear wave function (a solution of the nuclear Schrödinger equation in the BO approximation) and a spherical harmonic:

$$\langle \hat{\mathbf{R}} | \nu; Nm_N \rangle = \chi_{\nu, N}(R) Y_{Nm_N}(\hat{\mathbf{R}}). \quad (2)$$

Here,  $\hat{\mathbf{R}} = (R, \hat{\mathbf{R}})$  is a position vector, which describes the internuclear axis.  $\nu$  and  $N$  denote the vibrational and rotational quantum numbers, respectively.

Following our previous works [45–49], we construct an effective hyperfine Hamiltonian,  $\mathcal{H}_{H_2}^{\text{HF}}$ , which involves the two leading hyperfine interactions: the nuclear dipole-dipole interaction and the nuclear spin-rotation interaction:

$$\mathcal{H}_{H_2}^{\text{HF}} = \mathcal{H}_{\text{dip}} + \mathcal{H}_{\text{nsr}}. \quad (3)$$

We refer the reader to our previous paper regarding the hyperfine structure of rovibrational levels in the  $X \ ^1\Sigma_g^+$  state of  $H_2$ , where the form of each term in the effective Hamiltonian [46] is discussed. Here, we only write the forms of the leading hyperfine interactions using spherical tensor operators [66,67], and we recall the formulas for the matrix elements of the hyperfine Hamiltonian in the coupled basis.

The nuclear dipole-dipole interaction can be represented as a scalar product of two spherical tensors of rank 2 [67]:

$$\mathcal{H}_{\text{dip}} = -g_1 g_2 \mu_N^2 \frac{\mu_0}{4\pi} \sqrt{6} T^{(2)}(\mathbf{C}) \cdot T^{(1,1,2)}(\mathbf{I}_1, \mathbf{I}_2), \quad (4)$$

where  $T^{(2)}(\mathbf{C})$  is the rank-2 spherical tensor corresponding to the spherical harmonic associated with the transformation of the molecular wave function from the laboratory-fixed to the molecule-fixed frame of reference.  $T^{(1,1,2)}(\mathbf{I}_1, \mathbf{I}_2)$  is a spherical tensor resulting from the coupling of two spherical tensors of rank 1,  $T^{(1)}(\mathbf{I}_1)$  and  $T^{(1)}(\mathbf{I}_2)$ , which describe the two nuclear spins.  $g_1 = g_2 = g_H$  is the  $g$  factor of the proton,  $\mu_N$  is the nuclear magneton, and  $\mu_0$  is the vacuum permeability.

TABLE I. Rovibrationally averaged nuclear dipole-dipole coupling constants  $c_{\text{dip}}^{v,N}$  (in kHz) for several lowest rovibrational levels in the  $EF^1\Sigma_g^+$  state. The estimated relative uncertainty of the data reported here is of an order of  $10^{-3}$ .

$N$	$EF0/E0$ $v=0$	$EF1/F0$ $v=1$	$EF2/F1$ $v=2$	$EF3/E1$ $v=3$	$EF4/F2$ $v=4$	$EF5/F3$ $v=5$	$EF6/E2$ $v=6$
1	112.87	9.500	9.370	105.45	9.964	10.055	69.07
3	110.56	9.470	9.337	102.66	10.259	9.857	59.82
5	106.56	9.418	9.277	99.17	9.258	9.771	71.85

Matrix elements of the dipole-dipole interaction in a  $^1\Sigma$  state are given as

$$\begin{aligned}
 & \langle v'; (N'(I'_1 I'_2) I') F' m'_F | \mathcal{H}_{\text{dip}} | v; (N(I_1 I_2) I) F m_F \rangle \\
 &= -\delta_{vv'} \delta_{F'F} \delta_{m'_F m_F} \delta_{I'_1 I'_2} \delta_{I_1 I_2} \\
 & \times c_{\text{dip}}^{v,N} \sqrt{30} (-1)^{N+N'+I'+F'} \\
 & \times \begin{pmatrix} N' & 2 & N \\ 0 & 0 & 0 \end{pmatrix} \begin{Bmatrix} N' & N & 2 \\ I & I' & F' \end{Bmatrix} \begin{Bmatrix} I_1 & I_1 & 1 \\ I_2 & I_2 & 1 \\ I' & I & 2 \end{Bmatrix} \\
 & \times \sqrt{(2N+1)(2N'+1)(2I'+1)(2I+1)} \\
 & \times \sqrt{I_1(I_1+1)(2I_1+1)I_2(I_2+1)(2I_2+1)}, \quad (5)
 \end{aligned}$$

where the coupling constant is given as

$$c_{\text{dip}}^{v,N} = g_H^2 \mu_N^2 \frac{\mu_0}{4\pi} \int dR |\chi_{v,N}(R)|^2 R^{-3}. \quad (6)$$

The nuclear spin-rotation term can be represented as a scalar product of spherical tensors of rank 1<sup>1</sup>:

$$\mathcal{H}_{\text{nsr}} = -c_{\text{nsr}}(R) T^{(1)}(\mathbf{I}) \cdot T^{(1)}(\mathbf{N}), \quad (7)$$

which describe the total nuclear spin and the nuclear angular momentum, respectively. The strength of the spin-rotation interaction is determined by the nuclear spin-rotation coefficient  $c_{\text{nsr}}(R)$ , which involves the contributions to the molecular magnetic field from both the electrons and the nuclei, and is a function of the internuclear distance  $R$ . Matrix elements of the spin-rotation interaction are obtained using spherical tensor algebra [67]:

$$\begin{aligned}
 & \langle v'; (N'I') F' m'_F | \mathcal{H}_{\text{nsr}} | v; (NI) F m_F \rangle \\
 &= -\delta_{FF'} \delta_{m'_F m_F} \delta_{I'I} \delta_{NN'} \frac{c_{\text{nsr}}^{v,N}}{2} \\
 & \times [F(F+1) - I(I+1) - N(N+1)]. \quad (8)
 \end{aligned}$$

Here,  $c_{\text{nsr}}^{v,N}$  is the rovibrationally averaged spin-rotation coefficient:

$$c_{\text{nsr}}^{v,N} = \int dR |\chi_{v,N}(R)|^2 c_{\text{nsr}}(R). \quad (9)$$

The effective Hamiltonian is, thus, diagonal with respect to the total angular momentum  $F$  and its projection on the space-fixed  $Z$  axis,  $m_F$ . The dipole-dipole interaction introduces a weak coupling between different rotational states,  $N' = N \pm 2$ . However, these off-diagonal terms in the hyperfine Hamiltonian are approximately 10 orders of magnitude smaller than the energy difference between rovibrational levels. This allows us to neglect any possible coupling between different rotational states. In such a case, the coupled basis vectors constitute the eigenbasis of the effective hyperfine Hamiltonian, and the hyperfine splittings of the rovibrational levels are obtained immediately.

#### IV. HYPERFINE COUPLING CONSTANTS IN THE $EF^1\Sigma_g^+$ STATE

The magnitude of hyperfine splittings of each rovibrational level is determined by the hyperfine coupling constants. The nuclear dipole-dipole coupling constant depends only on the  $g$  factors of the nuclei, the nuclear magneton, and the average over the expectation value of the  $1/R^3$  term in a given rovibrational state. Here, we employ the values of  $g_H$ ,  $\mu_0$ , and  $\mu_N$  recommended by CODATA [68]. The  $\chi_{v,N}(R)$  wave functions for each rovibrational state were obtained by solving the nuclear Schrödinger equation in the BO approximation using the finite basis discrete variable representation method [69] implemented in the BIGOS package [70]. The calculations were performed for internuclear distances in a range of 0.7–20.0  $a_0$  with steps of 0.04  $a_0$ . We used the recently published BO potential energy curve for the  $EF^1\Sigma_g^+$  state [36]. The uncertainty of the nuclear dipole-dipole coupling constants originates from the neglected nonadiabatic effects, which are of an order of the ratio of the electron mass to the reduced mass of  $\text{H}_2$  [51]. The obtained coefficients are listed in Table I. We observe a significant difference between the obtained nuclear dipole-dipole coupling constants for the states from the inner well and the outer well—the former are 1 order of magnitude larger than the latter. This is due to the fact that the expectation values of the  $1/R^3$  term are clearly greater for the states from the inner well. We also note that the nuclear dipole-dipole coupling coefficients for the states from the  $E$  well of the potential exhibit a more significant dependence on the rotational quantum number and that they are approximately 2 times smaller than those of the first rovibrational levels of the  $X^1\Sigma_g^+$  state (see Table 1 in Ref. [46]). As  $v$  increases, the values of the nuclear dipole-dipole coupling constants for the states from the  $E$  well decrease, while those for the  $F$  well states increase.

<sup>1</sup>We note that in our previous papers [45–47], the sign of the spin-rotation term in the effective Hamiltonian was incorrect.



TABLE II. Rovibrationally averaged nuclear spin-rotation constants  $c_{\text{nsr}}^{v,N}$  (in kHz) for the several low-lying rovibrational levels in the  $EF^1\Sigma_g^+$  state.

$N$	$EF0/E0$ $v = 0$	$EF1/F0$ $v = 1$	$EF2/F1$ $v = 2$	$EF3/E1$ $v = 3$	$EF4/F2$ $v = 4$	$EF5/F3$ $v = 5$	$EF6/E2$ $v = 6$
1	47.37	−11.44	−11.53	44.40	−11.20	−11.29	23.06
3	46.23	−11.39	−11.47	42.99	−10.98	−11.29	19.19
5	44.28	−11.30	−11.38	41.23	−11.41	−11.15	25.93

Nuclear spin-rotation constants were calculated at the full configuration-interaction level using London orbitals [71]. The double-augmented d-aug-cc-pVQZ basis set [72] was used. The calculations were performed for the internuclear  $R$  distances in the 0.98–24.40  $a_0$  range mostly with steps of 0.04  $a_0$ . The numerical results of the  $R$ -dependent coupling constants are provided in the Supplemental Material [73]. All the calculations have been performed with Dalton, a molecular electronic structure program, Release v2020.0.beta, [74].

The convergence of the spin-rotation coupling constants with the basis set size can be estimated solely by a comparison of the d-aug-cc-pVTZ and d-aug-cc-pVQZ results. In the double-well region the spin-rotation coupling constants are 50.502 and 50.379 kHz (at  $R = 1.89 a_0$ ) or −11.763 and −11.868 kHz (at  $R = 4.35 a_0$ ) calculated with the d-aug-cc-pVTZ basis set and the d-aug-cc-pVQZ basis set, respectively. For the errors emerging from neglect of the relativistic effects, contributions beyond the Born-Oppenheimer approximation, and inaccuracies in the used potential curve, we can use the estimate of 200 Hz, which we have quoted previously [45] for the ground state of the hydrogen molecule (see Refs. [75,76] and cf. Ref. [44]). This gives the total uncertainty of the calculated spin-rotation constants at a level of ca. 350 Hz.

We note here, that the nonadiabatic contributions to the calculated  $c_{\text{nsr}}^{v,N}$  are expected to be included within the estimated uncertainty, since the low-lying rovibrational levels considered here are predominantly of the  $EF$  character (the probability of finding the  $EF$  electronic state in a given nonadiabatic rovibronic state is larger than 0.999 37) [32]. Moreover, the nonadiabatic corrections [32] to the adiabatic variational term values reported in Ref. [30] for the ( $v = 0$ –6,  $N = 0$ ) levels are, at most, 0.007%. By contrast, the nonadiabatic effects are more pronounced in the low-lying levels of the  $GK^1\Sigma_g^+$  state. For instance, the probabilities of finding the  $EF$  and  $GK$  states in the ( $v = 0$ ,  $N = 1$ ) nonadiabatic rovibronic state are 0.399 69 and 0.583 68, respectively [32].

Rovibrationally averaged spin-rotation coupling constants are listed in Table II. Similarly as in the case of the nuclear dipole-dipole interaction, we observe a significant difference between the coupling constants for the inner and outer well levels. The nuclear spin-rotation couplings for the  $E$ -well states are positive and approximately 2.5 times smaller than those calculated for the ground electronic state [46]. Conversely, the constants for the  $F$ -well states are negative and of the order of the nuclear dipole-dipole coupling coefficients. This is due to the fact that the rovibrational average [Eq. (6)] probes the long-range part of the  $c_{\text{nsr}}(R)$ , where the nuclear spin-rotation coupling is negative [see Fig. 2(b)]. The difference between the  $E$  and  $F$  states becomes less pronounced for larger values of  $v$ .

## V. HYPERFINE SPLITTINGS OF ROVIBRATIONAL LEVELS IN THE $EF^1\Sigma_g^+$ STATE

We have calculated hyperfine splittings for several low-lying rovibrational levels of the  $EF^1\Sigma_g^+$  state in  $\text{H}_2$ . We studied the three lowest rotational levels in the first seven vibrational states, which lie below the barrier that separates the two minima on the BO potential energy curve. Following the discussion in the previous section, we estimate the uncertainty of determined hyperfine energy levels to be approximately 0.35 kHz, if not less. A complete table containing the values of the energies of the hyperfine levels is provided in the Supplemental Material [73].

In this section, we discuss an example of the hyperfine splittings in the first two rovibrational levels of *ortho*- $\text{H}_2$ , i.e.,  $EF0/E0$ ,  $N = 1$  and  $EF1/F0$ ,  $N = 1$ , from the inner and outer wells of the BO potential energy curve. Moreover, we compare the hyperfine splittings with the ( $v = 0$ ,  $N = 1$ ) level of the ground  $X^1\Sigma_g^+$  electronic state (see Fig. 2), analyzed in previous papers [46,49]. We recall that the vibrationally averaged nuclear spin-rotation constant and the nuclear dipole-dipole constant for this level are  $c_{\text{nsr}}^{v,N} = 114.16$  kHz and  $c_{\text{dip}}^{v,N} = 288.22$  kHz, respectively [46].

The first rotational state is split into three hyperfine states with  $F = 0, 1$ , and 2. The energy of each state is given as

$$\begin{aligned}
 E_{v,N=1,F} &= (-1)^F 3c_{\text{dip}}^{v,N} \begin{Bmatrix} 1 & 1 & 2 \\ 1 & 1 & F \end{Bmatrix} \\
 &\quad - \frac{c_{\text{nsr}}^{v,N}}{2} [F(F+1) - 4] \\
 &= \begin{cases} c_{\text{dip}}^{v,N} + 2c_{\text{nsr}}^{v,N} & \text{if } F = 0, \\ -\frac{1}{2}c_{\text{dip}}^{v,N} + c_{\text{nsr}}^{v,N} & \text{if } F = 1, \\ \frac{1}{10}c_{\text{dip}}^{v,N} - c_{\text{nsr}}^{v,N} & \text{if } F = 2, \end{cases} \quad (10)
 \end{aligned}$$

which can be verified by a careful examination of Eqs. (5) and (8). The hyperfine splittings of these states are presented in Fig. 2(c). The hyperfine splittings of the  $E0$  state are of an order of several hundreds of kHz, quite similar to those of the ground state. In contrast, the splittings in the first vibrational state in the outer well are 1 order of magnitude smaller than those for the inner well. We also note that the ordering of the hyperfine states in this level is different than that observed for the inner well or for the ground electronic state. This follows from the change of the sign of the nuclear spin-rotation coupling and the fact that its absolute value is close to the value of the nuclear dipole-dipole coupling constant [see Fig. 2(b)].

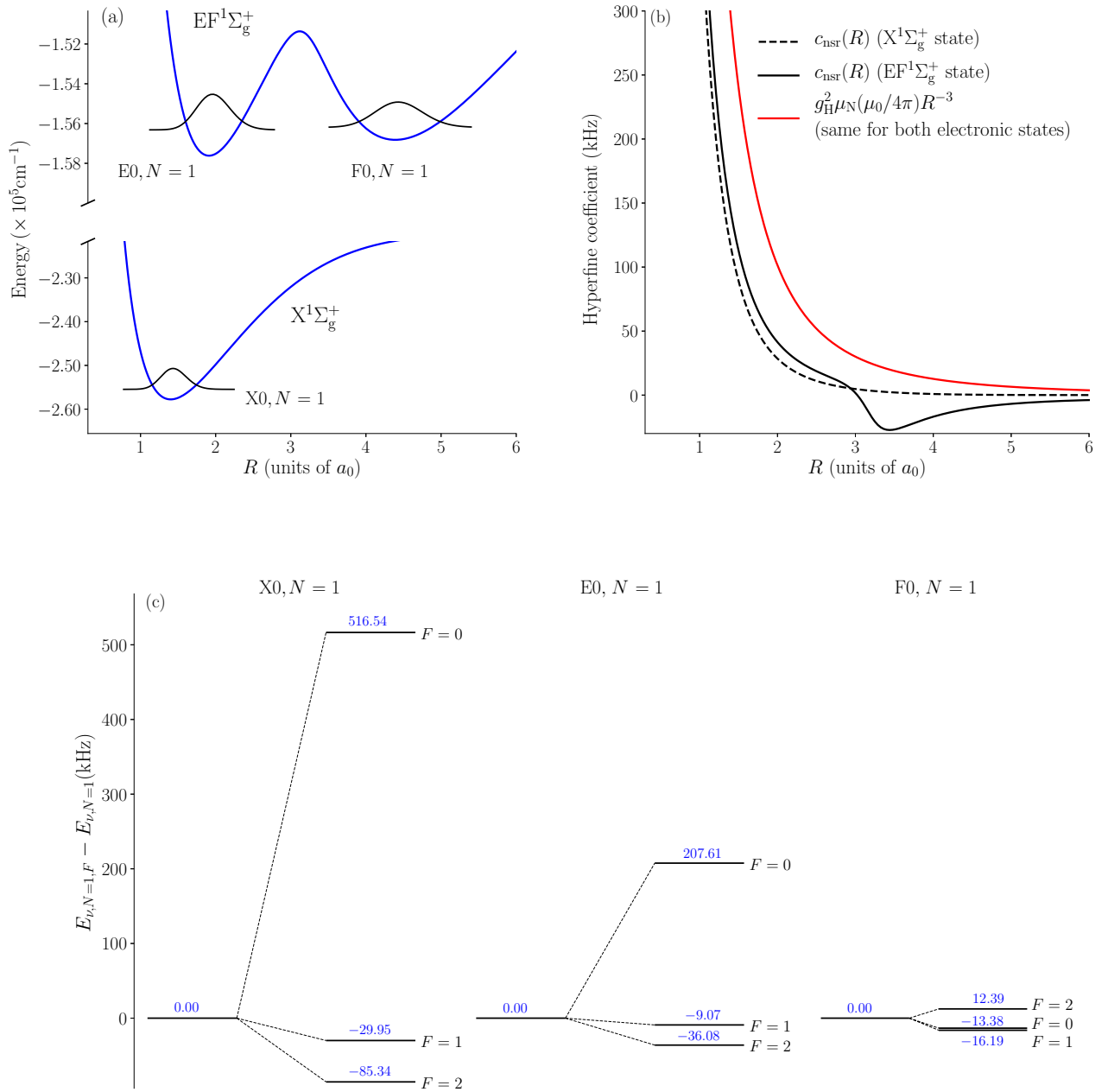


FIG. 2. Hyperfine structure of the first rovibrational levels in *ortho*-H<sub>2</sub> in the  $X^1\Sigma_g^+$  state and the  $E$  and  $F$  wells of the  $EF^1\Sigma_g^+$  state. Panel (a) presents the BO potential energy curves for the two electronic states [36,77] and the wave functions of the three considered rovibrational levels. Panel (b) presents the hyperfine coefficients for the excited states (solid lines) and the ground electronic state (dashed lines). We note that the nuclear dipole-dipole coupling constants are independent of the electronic state. Panel (c) presents a direct comparison between the hyperfine splittings in the three states: the  $X^1\Sigma_g^+$  (left) state and the  $E$  (center) and  $F$  (right) wells of the  $EF^1\Sigma_g^+$  state.

## VI. CONCLUSION

We have analyzed the hyperfine structure of the excited double-well  $EF^1\Sigma_g^+$  state in the H<sub>2</sub> molecule. Similarly as in the case of the ground electronic state, the hyperfine splittings originate mostly from the nuclear spin-rotation and nuclear dipole-dipole interactions. Hyperfine splitting of the  $N=1$  rotational state in the inner well is approximately 2 times smaller than that of the first rotational level in the ground electronic state. Furthermore, the outer-well levels exhibit a

hyperfine structure which is approximately 1 order of magnitude smaller than the one from the inner well. The magnitude of the coupling constants and the resulting hyperfine splittings in the  $EF^1\Sigma_g^+$  state decrease as the vibrational and rotational quantum numbers increase.

The results presented here are of significant importance for the ultra-accurate spectroscopies of H<sub>2</sub>. Knowledge about the hyperfine structure of the  $EF^1\Sigma_g^+$  state would reduce the uncertainty of several physical quantities determined from the



Doppler-free spectroscopy, such as the dissociation energy of *ortho*-H<sub>2</sub>. Improved accuracy of spectroscopic measurements of molecular hydrogen could in turn lead to even more stringent tests of quantum electrodynamics for molecules and physics beyond the standard model. A methodology similar to that presented here can be used to study the  $EF^1\Sigma_g^+$  state in the HD and D<sub>2</sub> molecules. However, for these two isotopologues, an additional influence of the interaction between the electric quadrupole moment of the deuteron and the electric field gradient has to be taken into account.

## ACKNOWLEDGMENTS

The research is financed from the budgetary funds on science projected for 2019–2023 as a research project under the “Diamentowy Grant” program. P.W. is supported by the National Science Centre in Poland, Project No. 2019/35/B/ST2/01118. Calculations have been carried out using resources provided by the Wrocław Centre for Networking and Supercomputing (see Ref. [78]), Grant No. 294. The research is a part of the program of the National Laboratory FAMO in Toruń, Poland.

- [1] D. Sprecher, C. Jungen, W. Ubachs, and F. Merkt, Towards measuring the ionisation and dissociation energies of molecular hydrogen with sub-MHz accuracy, *Faraday Discuss.* **150**, 51 (2011).
- [2] K. Piszczatowski, G. Łach, M. Przybytek, J. Komasa, K. Pachucki, and B. Jeziorski, Theoretical determination of the dissociation energy of molecular hydrogen, *J. Chem. Theory Comput.* **5**, 3039 (2009).
- [3] J. Liu, E. J. Salumbides, U. Hollenstein, J. C. J. Koelemeij, K. S. E. Eikema, W. Ubachs, and F. Merkt, Determination of the ionization and dissociation energies of the hydrogen molecule, *J. Chem. Phys.* **130**, 174306 (2009).
- [4] M. Puchalski, A. Spyszkiewicz, J. Komasa, and K. Pachucki, Nonadiabatic Relativistic Correction to the Dissociation Energy of H<sub>2</sub>, D<sub>2</sub>, and HD, *Phys. Rev. Lett.* **121**, 073001 (2018).
- [5] L. M. Wang and Z.-C. Yan, Relativistic corrections to the ground state of H<sub>2</sub> calculated without using the Born-Oppenheimer approximation, *Phys. Rev. A* **97**, 060501 (2018).
- [6] R. K. Altmann, L. S. Dreissen, E. J. Salumbides, W. Ubachs, and K. S. E. Eikema, Deep-Ultraviolet Frequency Metrology of H<sub>2</sub> for Tests of Molecular Quantum Theory, *Phys. Rev. Lett.* **120**, 043204 (2018).
- [7] C.-F. Cheng, J. Hussels, M. Niu, H. L. Bethlem, K. S. E. Eikema, E. J. Salumbides, W. Ubachs, M. Beyer, N. Hölsch, J. A. Agner, F. Merkt, L.-G. Tao, S.-M. Hu, and C. Jungen, Dissociation Energy of the Hydrogen Molecule at 10<sup>−9</sup> Accuracy, *Phys. Rev. Lett.* **121**, 013001 (2018).
- [8] N. Hölsch, M. Beyer, E. J. Salumbides, K. S. E. Eikema, W. Ubachs, C. Jungen, and F. Merkt, Benchmarking Theory with an Improved Measurement of the Ionization and Dissociation Energies of H<sub>2</sub>, *Phys. Rev. Lett.* **122**, 103002 (2019).
- [9] M. Puchalski, J. Komasa, P. Czachorowski, and K. Pachucki, Nonadiabatic QED Correction to the Dissociation Energy of the Hydrogen Molecule, *Phys. Rev. Lett.* **122**, 103003 (2019).
- [10] J. Komasa, K. Piszczatowski, G. Łach, M. Przybytek, B. Jeziorski, and K. Pachucki, Quantum electrodynamics effects in rovibrational spectra of molecular hydrogen, *J. Chem. Theory Comput.* **7**, 3105 (2011).
- [11] P. Wcisło, F. Thibault, M. Zaborowski, S. Wójtewicz, A. Cygan, G. Kowzan, P. Masłowski, J. Komasa, M. Puchalski, K. Pachucki, R. Ciuryło, and D. Lisak, Accurate deuterium spectroscopy for fundamental studies, *J. Quant. Spectrosc. Radiat. Transfer* **213**, 41 (2018).
- [12] E. Fasci, A. Castrillo, H. Dinesan, S. Gravina, L. Moretti, and L. Gianfrani, Precision spectroscopy of HD at 1.38 μm, *Phys. Rev. A* **98**, 022516 (2018).
- [13] J. Komasa, M. Puchalski, P. Czachorowski, G. Łach, and K. Pachucki, Rovibrational energy levels of the hydrogen molecule through nonadiabatic perturbation theory, *Phys. Rev. A* **100**, 032519 (2019).
- [14] M. L. Diouf, F. M. J. Cozijn, B. Darquié, E. J. Salumbides, and W. Ubachs, Lamb-dips and Lamb-peaks in the saturation spectrum of HD, *Opt. Lett.* **44**, 4733 (2019).
- [15] M. Beyer, N. Hölsch, J. Hussels, C.-F. Cheng, E. J. Salumbides, K. S. E. Eikema, W. Ubachs, C. Jungen, and F. Merkt, Determination of the Interval between the Ground States of Para- and Ortho-H<sub>2</sub>, *Phys. Rev. Lett.* **123**, 163002 (2019).
- [16] T.-P. Hua, Y. R. Sun, and S.-M. Hu, Dispersion-like lineshape observed in cavity-enhanced saturation spectroscopy of HD at 1.4 μm, *Opt. Lett.* **45**, 4863 (2020).
- [17] M. Zaborowski, M. Słowiński, K. Stankiewicz, F. Thibault, A. Cygan, H. Jóźwiak, G. Kowzan, P. Masłowski, A. Nishiyama, N. Stolarczyk, S. Wójtewicz, R. Ciuryło, D. Lisak, and P. Wcisło, Ultrahigh finesse cavity-enhanced spectroscopy for accurate tests of quantum electrodynamics for molecules, *Opt. Lett.* **45**, 1603 (2020).
- [18] A. Fast and S. A. Meek, Sub-ppb Measurement of a Fundamental Band Rovibrational Transition in HD, *Phys. Rev. Lett.* **125**, 023001 (2020).
- [19] M. L. Diouf, F. M. J. Cozijn, K.-F. Lai, E. J. Salumbides, and W. Ubachs, Lamb-peak spectrum of the HD (2-0) P(1) line, *Phys. Rev. Res.* **2**, 023209 (2020).
- [20] W. Ubachs, J. Koelemeij, K. Eikema, and E. Salumbides, Physics beyond the standard model from hydrogen spectroscopy, *J. Mol. Spectrosc.* **320**, 1 (2016).
- [21] E. J. Salumbides, J. C. J. Koelemeij, J. Komasa, K. Pachucki, K. S. E. Eikema, and W. Ubachs, Bounds on fifth forces from precision measurements on molecules, *Phys. Rev. D* **87**, 112008 (2013).
- [22] E. J. Salumbides, A. N. Schellekens, B. Gato-Rivera, and W. Ubachs, Constraints on extra dimensions from precision molecular spectroscopy, *New J. Phys.* **17**, 033015 (2015).
- [23] M. Puchalski, J. Komasa, P. Czachorowski, and K. Pachucki, Complete  $\alpha^6 m$  Corrections to the Ground State of H<sub>2</sub>, *Phys. Rev. Lett.* **117**, 263002 (2016).
- [24] J.-P. Karr, D. Marchand, and E. Voutier, The proton size, *Nat. Rev. Phys.* **2**, 601 (2020).
- [25] S. Patra, M. Germann, J.-P. Karr, M. Haidar, L. Hilico, V. I. Korobov, F. M. J. Cozijn, K. S. E. Eikema, W. Ubachs, and J. C. J. Koelemeij, Proton-electron mass ratio from laser spectroscopy of HD<sup>+</sup> at the part-per-trillion level, *Science* **369**, 1238 (2020).

- [26] S. Alighanbari, G. S. Giri, F. L. Constantin, V. I. Korobov, and S. Schiller, Precise test of quantum electrodynamics and determination of fundamental constants with  $\text{HD}^+$  ions, *Nature (London)* **581**, 152 (2020).
- [27] J. Gerhauser and H. S. Taylor, *Ab initio* calculation of the  $E^1\Sigma_g$  and a  $^3\Sigma_g^+$  states of the hydrogen molecule, *J. Chem. Phys.* **42**, 3621 (1965).
- [28] W. Kołos and L. Wolniewicz, Theoretical investigation of the lowest double-minimum state  $E, F^1\Sigma_g^+$  of the hydrogen molecule, *J. Chem. Phys.* **50**, 3228 (1969).
- [29] K. Dressler, R. Gallusser, P. Quadrelli, and L. Wolniewicz, The EF and GK  $^1\Sigma_g^+$  states of hydrogen, *J. Mol. Spectrosc.* **75**, 205 (1979).
- [30] L. Wolniewicz and K. Dressler, The EF, GK, and HH  $^1\Sigma_g^+$  states of hydrogen. Improved *ab initio* calculation of vibrational states in the adiabatic approximation, *J. Chem. Phys.* **82**, 3292 (1985).
- [31] P. Quadrelli, K. Dressler, and L. Wolniewicz, Nonadiabatic coupling between the  $EF+GK+H^1\Sigma_g^+, I^1\Pi_g$ , and  $J^1\Delta_g$  states of the hydrogen molecule. Calculation of rovibronic structures in  $\text{H}_2$ , HD, and  $\text{D}_2$ , *J. Chem. Phys.* **92**, 7461 (1990).
- [32] S. Yu and K. Dressler, Calculation of rovibronic structures in the lowest nine excited  $^1\Sigma_g^+ + ^1\Pi_g + ^1\Delta_g$  states of  $\text{H}_2$ ,  $\text{D}_2$ , and  $\text{T}_2$ , *J. Chem. Phys.* **101**, 7692 (1994).
- [33] T. Orlikowski, G. Staszewska, and L. Wolniewicz, Long range adiabatic potentials and scattering lengths for the EF,  $e$  and  $h$  states of the hydrogen molecule, *Mol. Phys.* **96**, 1445 (1999).
- [34] J. Komasa and C. Wojciech, Exponentially correlated Gaussian functions in variational calculations. The  $EF^1\Sigma_g^+$  state of hydrogen molecule, *Comput. Methods Sci. Technol.* **9**, 79 (2003).
- [35] D. Ferenc and E. Mátyus, Computation of rovibronic resonances of molecular hydrogen:  $EF^1\Sigma_g^+$  inner-well rotational states, *Phys. Rev. A* **100**, 020501 (2019).
- [36] M. Silkowski, M. Zientkiewicz, and K. Pachucki, Accurate Born-Oppenheimer potentials for excited  $\Sigma^+$  states of the hydrogen molecule (2021), [arXiv:2104.03174](https://arxiv.org/abs/2104.03174).
- [37] G. D. Dickenson, M. L. Niu, E. J. Salumbides, J. Komasa, K. S. E. Eikema, K. Pachucki, and W. Ubachs, Fundamental Vibration of Molecular Hydrogen, *Phys. Rev. Lett.* **110**, 193601 (2013).
- [38] M. Niu, E. Salumbides, G. Dickenson, K. Eikema, and W. Ubachs, Precision spectroscopy of the  $X^1\Sigma_g^+, v=0 \rightarrow 1(J=0-2)$  rovibrational splittings in  $\text{H}_2$ , HD and  $\text{D}_2$ , *J. Mol. Spectrosc.* **300**, 44 (2014).
- [39] T. M. Trivikram, M. L. Niu, P. Wcisło, W. Ubachs, and E. J. Salumbides, Precision measurements and test of molecular theory in highly excited vibrational states of  $\text{H}_2$  ( $v=11$ ), *Appl. Phys. B* **122**, 294 (2016).
- [40] T. M. Trivikram, E. J. Salumbides, C. Jungen, and W. Ubachs, Excitation of  $\text{H}_2$  at large internuclear separation: Outer well states and continuum resonances, *Mol. Phys.* **117**, 2961 (2019).
- [41] K.-F. Lai, M. Beyer, E. J. Salumbides, and W. Ubachs, Photolysis production and spectroscopic investigation of the highest vibrational states in  $\text{H}_2$  ( $X^1\Sigma_g^+ v=13, 14$ ), *J. Phys. Chem. A* **125**, 1221 (2021).
- [42] R. J. L. Roy and R. B. Bernstein, Shape resonances and rotationally predissociating levels: The atomic collision time-delay functions and quasibound level properties of  $\text{H}_2(X^1\Sigma_g^+)$ , *J. Chem. Phys.* **54**, 5114 (1971).
- [43] M. Selg, A quasi-bound rovibrational state of hydrogen molecule resulting from hyperfine proton-electron spin-spin interaction, *Europhys. Lett.* **96**, 10009 (2011).
- [44] P. Dupré, Hyperfine transitions in the first overtone mode of hydrogen deuteride, *Phys. Rev. A* **101**, 022504 (2020).
- [45] H. Jóźwiak, H. Cybulski, and P. Wcisło, Positions and intensities of hyperfine components of all rovibrational dipole lines in the HD molecule, *J. Quant. Spectrosc. Radiat. Transfer* **253**, 107171 (2020).
- [46] H. Jóźwiak, H. Cybulski, and P. Wcisło, Hyperfine components of all rovibrational quadrupole transitions in the  $\text{H}_2$  and  $\text{D}_2$  molecules, *J. Quant. Spectrosc. Radiat. Transfer* **253**, 107186 (2020).
- [47] H. Jóźwiak, H. Cybulski, and P. Wcisło, Hyperfine structure of quadrupole rovibrational transitions in tritium-bearing hydrogen isotopologues, *J. Quant. Spectrosc. Radiat. Transfer* **256**, 107255 (2020).
- [48] H. Jóźwiak, H. Cybulski, and P. Wcisło, Hyperfine components of rovibrational dipole transitions in HT and DT, *J. Quant. Spectrosc. Radiat. Transfer* **270**, 107662 (2021).
- [49] H. Jóźwiak, H. Cybulski, and P. Wcisło, Hyperfine components of rovibrational quadrupole transitions in HD, *J. Quant. Spectrosc. Radiat. Transfer* **272**, 107753 (2021).
- [50] J. Komasa, M. Puchalski, and K. Pachucki, Hyperfine structure in the HD molecule, *Phys. Rev. A* **102**, 012814 (2020).
- [51] M. Puchalski, J. Komasa, and K. Pachucki, Hyperfine Structure of the First Rotational Level in  $\text{H}_2$ ,  $\text{D}_2$  and HD Molecules and the Deuteron Quadrupole Moment, *Phys. Rev. Lett.* **125**, 253001 (2020).
- [52] J.-P. Karr, M. Haidar, L. Hilico, Z.-X. Zhong, and V. I. Korobov, Higher-order corrections to spin-spin scalar interactions in  $\text{HD}^+$  and  $\text{H}_2^+$ , *Phys. Rev. A* **102**, 052827 (2020).
- [53] V. I. Korobov, J.-P. Karr, M. Haidar, and Z.-X. Zhong, Hyperfine structure in the  $\text{H}_2^+$  and  $\text{HD}^+$  molecular ions at order  $m\alpha^6$ , *Phys. Rev. A* **102**, 022804 (2020).
- [54] P. Danev, D. Bakalov, V. I. Korobov, and S. Schiller, Hyperfine structure and electric quadrupole transitions in the deuterium molecular ion, *Phys. Rev. A* **103**, 012805 (2021).
- [55] N. F. Ramsey, Theory of molecular hydrogen and deuterium in magnetic fields, *Phys. Rev.* **85**, 60 (1952).
- [56] A. Osterwalder, A. Wüest, F. Merkt, and C. Jungen, High-resolution millimeter wave spectroscopy and multichannel quantum defect theory of the hyperfine structure in high Rydberg states of molecular hydrogen  $\text{H}_2$ , *J. Chem. Phys.* **121**, 11810 (2004).
- [57] D. Sprecher, C. Jungen, and F. Merkt, Determination of the binding energies of the  $np$  Rydberg states of  $\text{H}_2$ , HD, and  $\text{D}_2$  from high-resolution spectroscopic data by multi-channel quantum-defect theory, *J. Chem. Phys.* **140**, 104303 (2014).
- [58] E. R. Davidson, First excited  $^1\Sigma_g^+$  state of the hydrogen molecule, *J. Chem. Phys.* **35**, 1189 (1961).
- [59] D. Bailly, E. Salumbides, M. Vervloet, and W. Ubachs, Accurate level energies in the  $EF^1\Sigma_g^+, GK^1\Sigma_g^+, H^1\Sigma_g^+, B^1\Sigma_u^+, C^1\Pi_u, B'^1\Sigma_u^+, D^1\Pi_u, I^1\Pi_g, J^1\Delta_g$  states of  $\text{H}_2$ , *Mol. Phys.* **108**, 827 (2010).
- [60] K. Tsukiyama, S. Shimizu, and T. Kasuya, Identification of the  $EF^1\Sigma_g^+(v'=31 \text{ and } 32)$  states of  $\text{H}_2$  by XUV-VIS double-resonance spectroscopy, *J. Mol. Spectrosc.* **155**, 352 (1992).

- [61] E. Reinhold, A. de Lange, W. Hogervorst, and W. Ubachs, Observation of the  $I'^1\Pi_g$  outer well state in  $H_2$  and  $D_2$ , *J. Chem. Phys.* **109**, 9772 (1998).
- [62] G. D. Dickenson, E. J. Salumbides, M. Niu, C. Jungen, S. C. Ross, and W. Ubachs, Precision spectroscopy of high rotational states in  $H_2$  investigated by Doppler-free two-photon laser spectroscopy in the  $EF\ ^1\Sigma_g^+-X\ ^1\Sigma_g^+$  system, *Phys. Rev. A* **86**, 032502 (2012).
- [63] S. C. Ross and C. Jungen, Multichannel quantum-defect theory of  $n = 2$  and 3 gerade states in  $H_2$ : Rovibronic energy levels, *Phys. Rev. A* **50**, 4618 (1994).
- [64] M. S. Quinn, K. Nauta, and S. H. Kable, Disentangling the  $H_2E, F\ (^1\Sigma_g^+)$  ( $v' = 0 - 18$ )  $\leftarrow X(^1\Sigma_g^+)$  ( $v'' = 3 - 9$ ) ( $2 + 1$ ) REMPI spectrum via 2D velocity-mapped imaging, *Mol. Phys.* **119**, e1836412 (2021).
- [65] W. H. Flygare, Spin-rotation interaction and magnetic shielding in molecules, *J. Chem. Phys.* **41**, 793 (1964).
- [66] U. Fano and G. Racah, *Irreducible Tensorial Sets* (Academic, New York, 1959).
- [67] J. M. Brown and A. Carrington, *Rotational Spectroscopy of Diatomic Molecules* (Cambridge University, Cambridge, England, 2003).
- [68] See <http://physics.nist.gov/cuu/Constants> for CODATA 2018 recommended values of the fundamental constants (CODATA 2018) (last accessed May, XXth, 2021).
- [69] J. Lill, G. Parker, and J. Light, Discrete variable representations and sudden models in quantum scattering theory, *Chem. Phys. Lett.* **89**, 483 (1982).
- [70] H. Jóźwiak, M. Gancewski, A. Grabowski, K. Stankiewicz, and P. Wcisło, BIGOS computer code, to be published.
- [71] J. Gauss, K. Ruud, and T. Helgaker, Perturbation-dependent atomic orbitals for the calculation of spin-rotation constants and rotational  $g$  tensors, *J. Chem. Phys.* **105**, 2804 (1996).
- [72] T. H. Dunning, Jr., Gaussian basis sets for use in correlated molecular calculations. I. The atoms boron through neon and hydrogen, *J. Chem. Phys.* **90**, 1007 (1989).
- [73] H. Jóźwiak, H. Cybulski, and P. Wcisło, See supplemental Material at <http://link.aps.org/supplemental/10.1103/PhysRevA.104.012808> for the hyperfine splittings and hyperfine coupling constants.
- [74] K. Aidas, C. Angeli, K. L. Bak, V. Bakken, R. Bast, L. Boman, O. Christiansen, R. Cimiraglia, S. Coriani, P. Dahle, E. K. Dalskov, U. Ekström, T. Enevoldsen, J. J. Eriksen, P. Ettenhuber, B. Fernández, L. Ferrighi, H. Fliegl, L. Frediani, K. Hald *et al.*, The Dalton quantum chemistry program system, *WIREs Comput. Mol. Sci.* **4**, 269 (2014); see also <http://daltonprogram.org>.
- [75] D. Sundholm and J. Gauss, Isotope and temperature effects on nuclear magnetic shieldings and spin-rotation constants calculated at the coupled-cluster level, *Mol. Phys.* **92**, 1007 (1997).
- [76] J. Gauss and D. Sundholm, Coupled-cluster calculations of spin-rotation constants, *Mol. Phys.* **91**, 449 (1997).
- [77] K. Pachucki, Born-Oppenheimer potential for  $H_2$ , *Phys. Rev. A* **82**, 032509 (2010).
- [78] <http://wcss.pl>.

# Lack of hyperfine shifts in Doppler-limited spectra of molecular hydrogen

Hubert Jóźwiak<sup>✉\*</sup> and Piotr Wcisło<sup>†</sup>

*Institute of Physics, Faculty of Physics, Astronomy and Informatics, Nicolaus Copernicus University in Toruń,  
Grudziądzka 5, 87-100 Toruń, Poland*



(Received 4 November 2022; accepted 9 December 2022; published 3 January 2023)

Accurate spectroscopy of molecular hydrogen isotopologues is used for testing quantum electrodynamics and searching for physics beyond the standard model. Recent measurements of energies of rovibrational resonances in the ground electronic state have reached a level of uncertainty lower than the magnitude of the hyperfine splitting. The underlying hyperfine components of the resonance clearly perturb sub-Doppler saturation spectra. The extent to which hyperfine structure influences the Doppler-limited spectra is not fully understood, as there are two contradicting experimental works that show either a 350 kHz shift or lack of any deviation from the central frequency of the resonance in the HD molecule. Here, we address this problem theoretically. Using the spherical tensor approach, we prove that the barycenter of all hyperfine-resolved spectra corresponds to the unperturbed transition frequency (the first moment of the hyperfine-resolved spectra vanishes). This property is directly transferred to Doppler-limited spectra: we show that there is no detectable shift due to the hyperfine structure unless the ratio of the Doppler width to the root-mean-square hyperfine splitting is less than 50.

DOI: [10.1103/PhysRevA.107.012802](https://doi.org/10.1103/PhysRevA.107.012802)

## I. INTRODUCTION

Precise spectroscopic studies of simple atomic and molecular systems allow for the performance of accurate tests of quantum theory [1,2], determination of fundamental constants [3,4], and search for physics beyond the standard model [5,6]. Molecular hydrogen, the simplest neutral diatomic molecule, possesses a large number of ultralong-living rovibrational states [7]. The electric dipole transitions between these states are either very weak in heteronuclear isotopologues (HD, HT, and DT) or forbidden in homonuclear isotopologues ( $H_2$ ,  $D_2$ , and  $T_2$ ). In the latter case, the transitions are electric quadrupole [8] or magnetic dipole [9] in nature. These resonances are extremely narrow—the largest transition probabilities for spontaneous emission in  $H_2$  are of the order of  $10^{-6} \text{ s}^{-1}$  [10]. The presence of these narrow transitions stimulates accurate spectroscopic measurements in molecular hydrogen and its isotopologues for fundamental studies [11–16]. The most accurate determination of the central frequency of a rovibrational transition in the HD isotopologue has reached the level of 13 kHz, which corresponds to the 0.12 ppb relative uncertainty [11]. Further essential experimental progress requires trapping a cold  $H_2$  sample in either a magnetic trap or an optical dipole trap; the latter seems to be the most promising one as recently a magic wavelength (in infrared) for one of the rovibrational lines was identified in  $H_2$  [17].

The hyperfine structure (HFS) of rovibrational states in molecular hydrogen and its isotopologues has recently gained significant attention from the spectroscopic community [18–25]. Theoretical studies of hyperfine interactions are driven by remarkably accurate experimental studies of the frequencies of rovibrational transitions [11,12,14,26–36]

and dissociation energies [37–39]. The importance of the hyperfine structure in the saturation spectra of the 2-0 R(1) transition in HD was recognized by Diouf *et al.* [34], who attributed an outstanding discrepancy between the transition frequencies measured by the Hefei [30] and Amsterdam [31] groups, to crossover resonances between hyperfine components of this line. Hyperfine components of rovibrational transitions should also be carefully analyzed in accurate experiments performed using Doppler-limited spectroscopy [14,28,32,35]. We recall that measurements using cavity-enhanced techniques have achieved the accuracy of 75 kHz [15] for the dipole transition in HD and 117 kHz for the weaker electric quadrupole transition in  $D_2$  [14]. Although unresolved, the hyperfine structure of the R(1) 2-0 line measured by the group in Caserta led to the 350 kHz shift in the determined transition frequency [15]. Since the Doppler width of this transition is, at room temperature, of an order of GHz, it remains an open question whether the hyperfine structure, which spans over the range of hundreds of kHz, could influence the determined transition frequency or whether the inclusion of a large number of components (21) could lead to numerical problems in the fitting procedure. Interestingly, the recent studies, by the group in Grenoble, of the 2-0 R(0) and R(1) lines in HD, performed using Doppler-limited spectroscopy at 80 K, showed no deviation of the apparent line center from the HFS-free transition frequency [40]. The lack of hyperfine shift of the same line, which is almost two times narrower at 80 K than at room temperature, casts a doubt on the conclusions of Ref. [15]. Hence, there is a need for theoretical work that could explain the apparent discrepancy between Refs. [15,40].

The positions and intensities of hyperfine components of dipole and quadrupole transitions in hydrogen isotopologues were recently studied by several authors [18–25]. In particular, the authors of this manuscript reported hyperfine coupling constants, positions and intensities of all rovibrational electric

\*hubert.jozwiak@doktorant.umk.pl

†piotr.wcislo@umk.pl



dipole transitions in HD [19], HT, and DT [24], and electric quadrupole transitions in H<sub>2</sub>, D<sub>2</sub> [20], HD [25], and the three tritium-bearing isotopologues [22]. In some cases, hyperfine components seem to be spread almost symmetrically around the central frequency (as in the case of the Q lines), while in others, several blue- or red-detuned components dominate the spectrum. In this work, we analyze theoretically the first moment (the barycenter) of the hyperfine structure of all rovibrational transitions studied in Refs. [19,20,22,24,25]. First, we provide a rigorous proof that the barycenter vanishes for the stick hyperfine spectra (i.e., when each component is an infinitely sharp line). Second, we analyze the first moment of the Doppler-broadened spectra, which is based on a well-known property of Gaussian functions and a discussion of the global maximum of the sum of  $N$ -Gaussian functions, which is provided in Appendix D. Finally, we discuss the implication of the results derived here for accurate Doppler-limited measurements of rovibrational transitions in hydrogen isotopologues [14,15,32,40], providing a theoretical input to the discussion about a presence or lack of hyperfine shift in this kind of spectroscopy. This work can also be considered as an extension of our recent analysis of relative intensities of hyperfine components of rovibrational transitions in the six isotopologues of hydrogen [41]. Since the relative intensity can be viewed as the zeroth moment of the hyperfine spectrum, we take this analysis a step further and we study the first moments of this spectrum. Thus, we use the notation introduced in Ref. [41] throughout the article.

## II. THE FIRST DISTRIBUTION MOMENT (THE BARYCENTER) OF THE HYPERFINE STICK SPECTRA

We consider hyperfine components of rovibrational transition between the  $(\nu_i, N_i)$  and  $(\nu_f, N_f)$  states, where,  $\nu$  and  $N$  are the vibrational and rotational quantum numbers, respectively. Due to hyperfine interactions, both levels are split into states which, following Refs. [19,20,22,24,25,41], we label as  $|\nu_i; N_i F_i m_{F_i}(\pm)_i\rangle$  and  $|\nu_f; N_f F_f m_{F_f}(\pm)_f\rangle$ , respectively [42]. Here,  $F$  is the total angular momentum quantum number (the eigenvalue of the square of the total angular momentum,  $\mathbf{F}$ ) which originates from the coupling of three angular momenta: the rotational angular momentum  $\mathbf{N}$  and the nuclear spin angular momenta of the two nuclei,  $\mathbf{I}_1$  and  $\mathbf{I}_2$ .  $m_F$  denotes the projection of the total angular momentum on the space-fixed axis of quantization. The meaning of the  $(\pm)$  label, as well as a summary of the coupling schemes, coupled basis, and the eigenstates of the hyperfine Hamiltonian, is provided in Appendix A.

In the first step, we assume that each hyperfine component (HF) of the rovibrational transition is infinitely sharp. Such a spectrum is referred to as the stick spectrum [18]. The first distribution moment of the hyperfine spectrum is defined as a

sum of products of position and intensity of each (HF-labeled) hyperfine component,

$$\mathcal{M}_{\text{fi}}^{(1)} = \sum_{\text{HF}} (\nu_{\text{fi}}^{\text{HF}} - \nu_{\text{fi}}) \frac{S_{\text{fi}}^{\text{HF}}}{S_{\text{fi}}^n}, \quad (1)$$

where  $(\nu_{\text{fi}}^{\text{HF}} - \nu_{\text{fi}})$  is the position of a single HF component with respect to the central frequency of a rovibrational transition, and  $S_{\text{fi}}^{\text{HF}}/S_{\text{fi}}^n$  is the ratio of the intensity of a HF component to the intensity of the HF-unresolved transition. The top index denotes the rank of the spectroscopic transition:  $n = 1$  corresponds to the electric dipole transition and  $n = 2$  corresponds to the electric quadrupole transition. The formulas for  $S_{\text{fi}}^{\text{HF}}$  and  $S_{\text{fi}}^n$  depend on the rank of the transition and the considered branch. We proposed a generic form of the  $S_{\text{fi}}^{\text{HF}}/S_{\text{fi}}^n$  ratio in Ref. [41], which we refer to as the relative intensity of a given HF component,

$$\frac{S_{\text{fi}}^{\text{HF}}}{S_{\text{fi}}^n} = \frac{|\langle \nu_f; N_f F_f(\pm)_f | T^{(n)}(\mathbf{M}) | \nu_i; N_i F_i(\pm)_i \rangle|^2}{w_I f_n(N_i, N_f) |\mathbf{M}_{\text{fi}}^n|^2}. \quad (2)$$

Here,  $\mathbf{M}^n$  is the multipole moment of the rovibrational transition and corresponds to the electric dipole moment  $\mathbf{d}$  ( $n = 1$ ) and for the electric quadrupole moment  $\mathcal{Q}$  for ( $n = 2$ ). The reader is referred to Ref. [41] for the explicit formulas for  $S_{\text{fi}}^{\text{HF}}$  and  $S_{\text{fi}}^n$  for electric dipole and quadrupole transitions. In the following part of the derivation, we use the formalism of spherical tensor algebra [43]. We introduce  $T^{(n)}(\mathbf{M})$ , an irreducible spherical tensor of rank  $n$ , which describes the proper multipole moment.  $w_I$  is the nuclear degeneracy factor of the initial rovibrational state, which equals  $(2I_1 + 1)(2I_2 + 1)$  for the heteronuclear isotopologues and  $(2I + 1)$  for the homonuclear species. The  $f_n(N_i, N_f)$  term depends on the rank of the transition and the branch considered and originates from the transformation of the multipole moment between the molecule-fixed and the space-fixed frame of reference (see Appendix A of Ref. [41]).

The position of each hyperfine component with respect to the central frequency of a rovibrational transition,  $(\nu_{\text{fi}}^{\text{HF}} - \nu_{\text{fi}})$ , is given by a difference between the energies of the initial and final hyperfine levels. This can be represented as the difference between the eigenvalues of the effective hyperfine Hamiltonian  $\mathcal{H}^{\text{HF}}$ ,

$$(\nu_{\text{fi}}^{\text{HF}} - \nu_{\text{fi}}) = \frac{1}{h} (\langle \nu_f; N_f F_f m_{F_f}(\pm)_f | \mathcal{H}^{\text{HF}} | \nu_f; N_f F_f m_{F_f}(\pm)_f \rangle - \langle \nu_i; N_i F_i m_{F_i}(\pm)_i | \mathcal{H}^{\text{HF}} | \nu_i; N_i F_i m_{F_i}(\pm)_i \rangle). \quad (3)$$

Assuming a lack of strong hyperfine couplings between different rotational levels, it can be shown (see Appendix B 1) that the first distribution moment corresponds to the difference between the sum of the diagonal elements of the effective hyperfine Hamiltonian in the two rovibrational states. For the coupling scheme suitable for homonuclear diatomics, this is given as

$$\mathcal{M}_{\text{fi}}^{(1)} = \frac{1}{hw_I} \left\{ \frac{1}{2N_f + 1} \sum_{I_i, F_i, m_{F_i}} \langle \nu_f; [N_f(I_1 I_2) I_f] F_f m_{F_f} | \mathcal{H}^{\text{HF}} | \nu_f; [N_f(I_1 I_2) I_f] F_f m_{F_f} \rangle - \frac{1}{2N_i + 1} \sum_{I_i, F_i, m_{F_i}} \langle \nu_i; [N_i(I_1 I_2) I_i] F_i m_{F_i} | \mathcal{H}^{\text{HF}} | \nu_i; [N_i(I_1 I_2) I_i] F_i m_{F_i} \rangle \right\}. \quad (4)$$

TABLE I. Tensorial form of the leading hyperfine interactions in the homo- and heteronuclear isotopologues of molecular hydrogen. For a discussion of the hyperfine interactions, as well as for formulas of matrix elements of the hyperfine Hamiltonian, see Refs. [19,20,22].

Hyperfine interaction	Homonuclear case	Heteronuclear case
Nuclear spin-rotation	$c_{\text{nsr}} T^{(1)}(\mathbf{N}) \cdot T^{(1)}(\mathbf{I})$	$\sum_j c_{\text{nsr}_j} T^{(1)}(\mathbf{N}) \cdot T^{(1)}(\mathbf{I}_j)$
Nuclear spin–nuclear spin dipole	$c_{\text{dip}} T^{(2)}(\mathbf{C}) \cdot T^{(2)}(\mathbf{I}_1, \mathbf{I}_2)$	$c_{\text{dip}} T^{(1)}(\mathbf{I}_2) \cdot T^{(1)}(\mathbf{C}, \mathbf{I}_1)$
Electric quadrupole	$\sum_j T^{(2)}(\nabla \mathbf{E}_j) \cdot T^{(2)}(\mathbf{Q}_j)$	$\sum_j T^{(2)}(\nabla \mathbf{E}_j) \cdot T^{(2)}(\mathbf{Q}_j)$

The corresponding formula for the coupling scheme suitable for heteronuclear species is provided in Appendix B 2. The effective hyperfine Hamiltonian can be represented as a series expansion of spherical tensor operators which represent (electric or magnetic) nuclear moments,  $T^{(k)}(\mathcal{A})$ , and (electric or magnetic) fields generated by the electrons and nuclei and derivatives of these fields,  $T^{(k)}(\mathcal{B})$  [43–46],

$$\mathcal{H}^{\text{HF}} = \sum_{k \geq 1} T^{(k)}(\mathcal{A}) \cdot T^{(k)}(\mathcal{B}). \quad (5)$$

Each term in this expansion is, in fact, a scalar product of spherical tensor operators, defined as

$$T^{(k)}(\mathcal{A}) \cdot T^{(k)}(\mathcal{B}) = \sum_{q=-k}^k T_q^{(k)}(\mathcal{A}) T_{-q}^{(k)}(\mathcal{B}), \quad (6)$$

where  $q$  denotes the  $(2k+1)$  components of the spherical tensors. For the hydrogen molecule, the leading hyperfine interactions involve the nuclear spin-rotation interaction, the nuclear spin–nuclear spin dipole interaction, and, for the deuterium-bearing species, the interaction of the nuclear electric quadrupole moment with molecular electric field gradient (see Table I). We note that the notation in Eq. (5) (which stems from Ref. [43]) might be ambiguous in this context, as the hyperfine Hamiltonian can contain more than one term of rank  $k$ , i.e., in the homonuclear case, we consider two terms of rank  $k=2$ , while in the heteronuclear case, we have two terms of rank  $k=1$  (see Table I).

Matrix elements of the effective hyperfine Hamiltonian in Eq. (4), which has a generic form introduced in Eq. (5), are evaluated using spherical tensor algebra. For the two irreducible spherical operators which act on two distinct components of the coupled basis, matrix elements are given as [47]

$$\begin{aligned} & \langle \nu; (j_1 j_2) j m | T^{(k)}(\mathcal{A}) \cdot T^{(k)}(\mathcal{B}) | \nu; (j_1 j_2) j m \rangle \\ &= (-1)^{j_1+j+j_2} \begin{Bmatrix} j_2 & j_1 & j \\ j_1 & j_2 & k \end{Bmatrix} \\ & \times \langle \nu; j_1 | T^{(k)}(\mathcal{A}) | \nu; j_1 \rangle \langle \nu; j_2 | T^{(k)}(\mathcal{B}) | \nu; j_2 \rangle. \quad (7) \end{aligned}$$

Putting  $j_1 = N$ ,  $j_2 = I$ ,  $j = F$ , and  $m = m_F$  and summing over  $I$ ,  $F$ , and  $m_F$  leads to (see Appendix C)

$$\begin{aligned} & \sum_{I, F, m_F} \langle \nu; (NI) F m_F | T^{(k)}(\mathcal{A}) \cdot T^{(k)}(\mathcal{B}) | \nu; (NI) F m_F \rangle \\ &= \delta_{k0} [\sqrt{(2N+1)} \langle \nu; N | T^{(k)}(\mathcal{A}) | \nu; N \rangle] \\ & \times \left[ \sum_I \sqrt{(2I+1)} \langle I | T^{(k)}(\mathcal{B}) | I \rangle \right], \quad (8) \end{aligned}$$

which means that the sum vanishes unless  $k=0$ . As mentioned earlier, each hyperfine interaction is represented by a scalar product of two spherical tensors of rank at least 1. This means that both sums in Eq. (4) vanish and, as a consequence, the first distribution moment of the hyperfine stick spectrum is zero,

$$\mathcal{M}_{\text{fi}}^{(1)} = 0. \quad (9)$$

A similar derivation can be performed for the heteronuclear isotopologues, although some of the tensorial forms recalled in Table I do not fulfill the condition (7) immediately. Indeed, the nuclear spin rotation associated with the  $I_2$  nuclear spin, as well as the dipole interaction, involve the product of two spherical tensors which act either on the subspace of the  $\mathbf{I}_2$  or the coupled subspace of the  $\mathbf{F}_1$  angular momentum. The detailed analysis is presented in Appendix B 2.

We have numerically confirmed Eq. (9) for all 86 105 electric dipole and electric quadrupole transitions in the six isotopologues of hydrogen, which were studied in Refs. [19,20,20,22,24]. The result derived here is based on an assumption that the hyperfine-induced coupling between different rotational levels is negligible in comparison to the energy difference between rotational states. This condition is fulfilled by diatomic molecules in the  $^1\Sigma$  state and, in particular, by molecular hydrogen. The isotopologues of hydrogen possess large rotational constants ( $B = 60.853 \text{ cm}^{-1}$  for  $\text{H}_2$  [48]) and are characterized by hyperfine interactions that are several orders of magnitude smaller than the rotational energy intervals. The result derived here should be of interest to the accurate spectroscopy of the light hydrogen halides, such as HF and HCl, or isotopologues of carbon monoxide that possess hyperfine structure ( $^{13}\text{C}^{16}\text{O}$  or  $^{12}\text{C}^{17}\text{O}$ ). For heavier  $^1\Sigma$  diatomics, the ratio of the largest hyperfine coupling constant to the rotational constant grows considerably, and the inclusion of the  $N$  and  $N' = N \pm 2$  couplings is necessary for an accurate description of the molecular spectra [see the discussion after Eq. (A3) in Appendix A].

### III. DOPPLER-BROADENED SPECTRA

The shape of the spectrum is a result of various physical processes that perturb molecular transitions. Thermal motion of molecules gives rise to the Doppler broadening, while collisions lead to the pressure broadening and shift of the spectral lines [49]. Shapes of optical resonances in molecular hydrogen deviate considerably from the commonly used Voigt profile [50,51]. An accurate description of beyond-Voigt line-shape effects is crucial for determining the central frequency of the observed transition [14].

Here, we analyze the spectra in the low-pressure regime, where collisional broadening and shift of spectral lines are



negligible, and the primary broadening mechanism stems from the Doppler effect. In such a case, the shape of an isolated line is described by the Gaussian function. Here, we acknowledge the presence of the underlying hyperfine structure of the resonance and we consider the spectrum which involves the sum of  $N$  Gaussian functions, which are centered at frequencies of respective hyperfine components. However, unless the experimental spectra are collected at temperatures low enough to distinguish between single components, the hyperfine components are blended into a single line.

The position of the maximum of such spectrum can be determined as follows. First, one can fit the experimental data with the sum of  $N$  Gaussian functions. The number of hyperfine components can be large and, as they are spread on a relatively small range of frequencies, numerical problems might lead to incorrect determination of the maximum. Second, one might calculate the first moment of the measured spectra  $[f_{\text{exp}}(\nu)]$  numerically,

$$\mathcal{M}_{\text{fi}}^{(1)} = \int_{\nu_{\min}}^{\nu_{\max}} d\nu \nu f_{\text{exp}}(\nu), \quad (10)$$

where  $\nu_{\min}$  and  $\nu_{\max}$  denote the range of the experimental frequency scan. However, as this procedure involves numerical integration over a wide range of frequencies, large experimental noise, which is present at frequencies far from  $\nu_{\text{fi}}$ , might lead to an incorrect determination of the resulting central frequency. Ultimately, in certain cases, one can determine the central frequency as the numerical derivative of the measured spectra and look for  $\nu$ , for which the derivative vanishes (see Appendix D). This corresponds to the position of the maximum of the measured spectra. We discuss this approach at the end of the following section.

### A. Analytical considerations

We consider the spectrum which involves  $N$  Gaussian functions of the form

$$f^{\text{HF}}(\nu) = \frac{A^{\text{HF}}}{\sqrt{\pi} \nu_D} e^{-(\nu - \nu_{\text{fi}}^{\text{HF}})^2 / \nu_D^2}, \quad (11)$$

where  $\nu_D = \frac{\nu_{\text{fi}}^{\text{HF}}}{c} \sqrt{2k_B T / m}$  is related to the half width at half maximum (HWHM) of the Doppler profile,  $\Gamma_D = \sqrt{\ln 2} \nu_D$ , and  $A^{\text{HF}} = S_{\text{fi}}^{\text{HF}} / S_{\text{fi}}$  is the relative (unitless) intensity of each hyperfine component, defined in Eq. (2). Since hyperfine components are distributed in close vicinity (of the order of  $10^6$  Hz or less) of the central frequency of the rovibrational transition (which is of the order of  $10^{12}$ – $10^{15}$  Hz), we can approximate  $\nu_{\text{fi}}^{\text{HF}} \approx \nu_{\text{fi}}$  and we can assume that each hyperfine component has the same Doppler width. The latter assumption is well justified since the Doppler width of rovibrational lines in molecular hydrogen with frequencies ranging from  $10^{12}$  (for pure rotational transitions) to  $10^{15}$  Hz (for the highest overtones) is modified by less than  $10^{-6}$  on a narrow range of frequencies of the order of  $10^6$  Hz. In such a case, the first distribution moment of the total spectrum is given by

$$\mathcal{M}_{\text{fi}}^{(1)} = \int_{-\infty}^{\infty} d\nu \nu \sum_{\text{HF}} f^{\text{HF}}(\nu) = \sum_{\text{HF}} A^{\text{HF}} \nu_{\text{fi}}^{\text{HF}}, \quad (12)$$

where the symbol HF denotes the sum of all hyperfine components of the spectrum. Here, we used the fact that the first moment of a Gaussian distribution centered at  $\nu_{\text{fi}}$  is simply  $\nu_{\text{fi}}$ . As shown in the previous section, the result is exactly zero for *all* rovibrational transitions in the hydrogen molecule. This means that when the spectrum is measured in the low-pressure regime, where the shape of the spectral transition is determined by a Gaussian function, the presence of the hyperfine structure does not affect the central frequency of the Doppler-limited rovibrational transition.

We briefly discuss finding the maximum of the spectrum through the derivative of the spectrum. One has to realize the obvious limitation of this approach: if the hyperfine components can at least be partially resolved, roots of the numerical derivative will point to the various local maxima and minima of the spectrum, and not to the barycenter of the transition. Careful analysis of the derivative of the spectrum consisting of  $N$  Gaussians might indicate the range of validity of the results presented in this work.

In Appendix D, we prove that the maximum of the spectrum consisting of  $N$  Gaussians of the same width  $\nu_D$ , which are spread over the narrow range of frequencies (significantly smaller than  $\nu_D$ ), is

$$\nu^{\max(N)} \approx \sum_{i=1}^N \nu_{0i} \bar{C}_i, \quad (13)$$

where  $\nu_{0i}$  and  $\bar{C}_i = C_i / (\sum_j C_j)$  denote the center and the relative height of the  $i$ th Gaussian, respectively. This corresponds to the barycenter of the resulting spectrum, which, for the case of rovibrational transitions with hyperfine structure, is 0 [Eq. (9)].

### B. Numerical confirmation—four rovibrational transitions in molecular hydrogen

We numerically test the range of validity of the obtained results on four rovibrational transitions in the three isotopologues of hydrogen. First, similar to Ref. [52], we define a dimensionless overlapping parameter of the hyperfine components as the ratio between the HWHM of the line profile (here  $\Gamma_D$ ) and the mean-square hyperfine splitting,

$$\Omega = \frac{\Gamma_D}{\sqrt{\sum_i (A_i^{\text{HF}} \nu_i^{\text{HF}})^2}}. \quad (14)$$

We note that the root-mean-square hyperfine splitting is of the order of  $10^1$  kHz for most of the rovibrational transitions in  $\text{H}_2$ , HD, and  $\text{D}_2$ . In the next step, we simulate four chosen rovibrational transitions as a sum of Gaussian functions  $[\sum_{\text{HF}} f^{\text{HF}}(\nu)]$ , with  $f^{\text{HF}}(\nu)$  defined in Eq. (11) and we look for the maximum of the spectrum,  $\nu^{\max}$ . When the hyperfine components are well resolved,  $\nu^{\max}$  corresponds to the position of the hyperfine component with the largest intensity. We analyze the 2-0 R(1) line in HD, studied by Doppler-limited spectroscopy in Refs. [15,32,40], the 1-0 R(0) line in HD, which has the lowest absolute uncertainty of all rovibrational transitions in molecular hydrogen [11], the 2-0 S(2) line in  $\text{D}_2$ , analyzed by cavity-enhanced techniques in Refs. [14,28,29,35], and the 1-0 Q(1) line in  $\text{H}_2$ , investigated

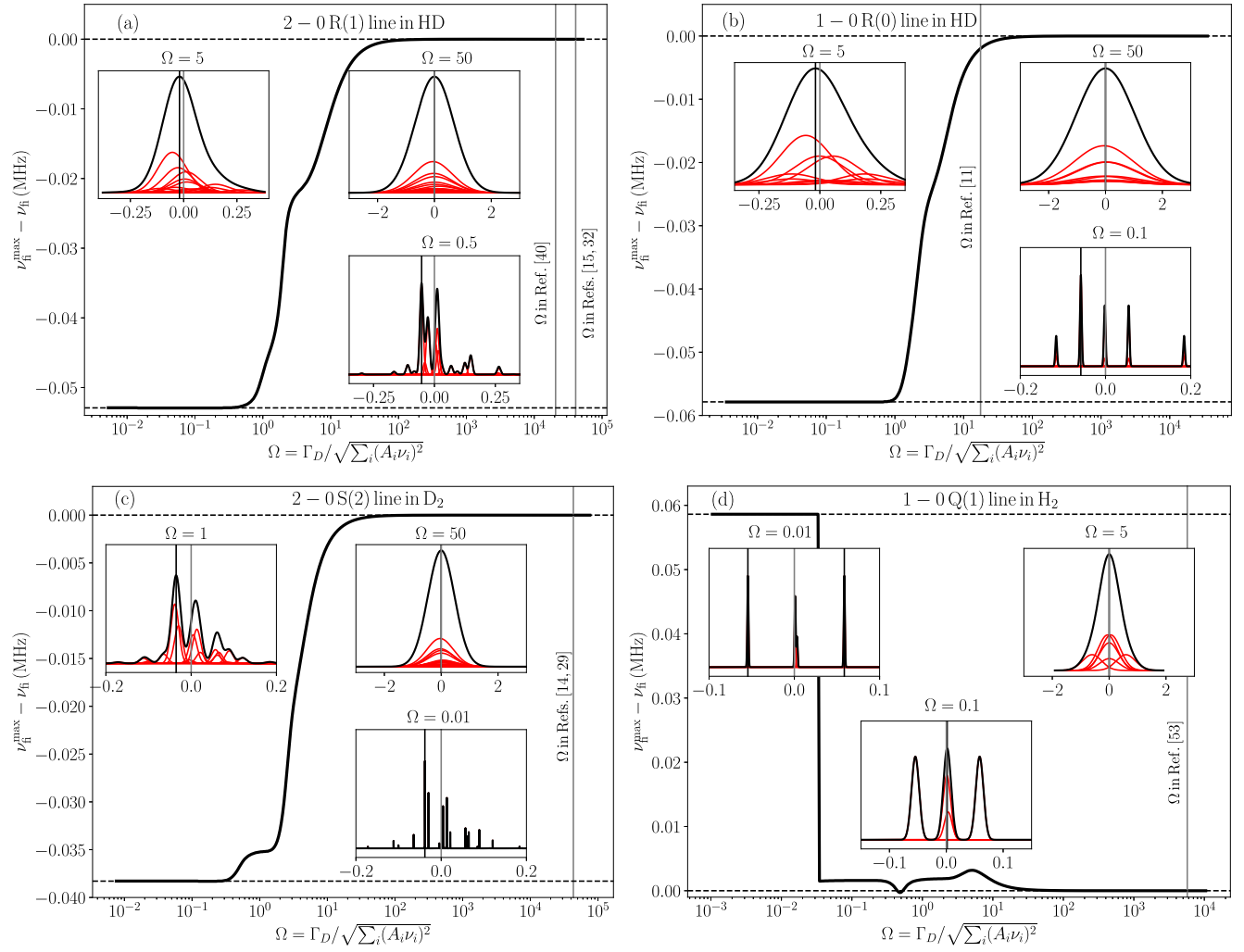


FIG. 1. Position of the maximum of rovibrational spectra,  $\nu_h^{\max}$ , with respect to the HFS-free transition frequency  $\nu_h$ , as a function of the dimensionless hyperfine overlapping parameter  $\Omega$  [defined in Eq. (14)], for the four chosen transitions in molecular hydrogen. The gray vertical lines correspond to values of  $\Omega$  in selected recent experiments (see the main text for details). The black vertical dashed lines in each panel correspond to the low- and high- $\Omega$  limits of  $\nu_h^{\max}$ , i.e., the position of the strongest hyperfine component and the HFS-free transition frequency, respectively. The inset figures present the Doppler-broadened spectra for the fixed  $\Omega$ —the red curves correspond to individual hyperfine components, while the black curve is the total spectrum, resulting from summing individual components. We put two vertical lines in each inset plot—the gray line corresponds to the HFS-free frequency and the black line denotes  $\nu_h^{\max}$ .

recently using stimulated Raman spectroscopy [53]. The results are presented in Fig. 1.

Both transitions in HD exhibit a typical  $\nu_h^{\max}(\Omega)$  dependence: at low values of  $\Omega$  (well-resolved hyperfine components), the maximum of the spectrum simply corresponds to the position of the hyperfine component with the largest intensity [ $\nu_h^{\max} = -52.9$  kHz and  $-57.8$  kHz for the 2-0 R(1) and 1-0 R(0) line, respectively]. As  $\Omega$  increases, the components blend into one line and the position of the maximum shifts towards the HFS-free frequency, which is achieved for  $\Omega \approx 50$ . The gray vertical lines in each panel correspond to the value of  $\Omega$  in respective experiments. For the 2-0 R(1) line, Doppler HWHM at room temperature is 775 MHz, which [since  $\sqrt{\sum_i (A_i^{\text{HF}} \nu_i^{\text{HF}})^2} \approx 19$  kHz for this line] gives  $\Omega \approx 4 \times 10^4$ . Thus, the underlying 21 hyperfine components have no visible effect on the position of the

maximum of the 2-0 R(1) line, not only at room temperature [15,32] but also at 80 K, as reported by Kass *et al.* [40] ( $\Omega \approx 2 \times 10^4$  at 80 K). We note here that collisional effects had a significant impact on the measurements performed by the Caserta group, and thus the Gaussian model analyzed here may not be directly applicable to the interpretation of the spectra studied in Refs. [15,32].

The experiment of Fast and Meek was performed in a different, low-density regime, using a supersonic molecular beam [11] that offers much lower effective transverse temperature, resulting in a sub-MHz Doppler broadening. The gray vertical line in the top right panel of Fig. 1 corresponds to  $\Omega \approx 18$  since the mean-square hyperfine splitting is approximately 30 kHz for the 1-0 R(0) line and the authors of Ref. [11] assumed that the underlying Gaussians have equal HWHMs of 400–500 kHz. We note here that the analysis of

the hyperfine structure in Ref. [11] was more complex than the one presented here, due to the double-resonance nature of the experimental technique—a subsequent two-photon UV excitation from the  $\nu = 1, N = 1$  state influenced the relative intensities of the hyperfine components of the 1-0 R(0) transition.

A slightly different dependence of  $\nu_{\text{fi}}^{\text{max}}$  on  $(\Omega)$  is seen for the 2-0 S(2) line in D<sub>2</sub>. For  $\Omega \sim 10^{-2}$ ,  $\nu_{\text{fi}}^{\text{max}}$  corresponds to the position of the largest hyperfine component ( $\nu_{\text{fi}}^{\text{max}} = -38.3$  kHz). As  $\Omega$  increases,  $\nu_{\text{fi}}^{\text{max}}$  shifts towards  $-35$  kHz (the plateau near  $\Omega = 1$ ), due to the vicinity of the second most intense hyperfine component at  $-29.7$  kHz. Then, as  $\Omega$  becomes larger than 1, the 22 components blend into a single line. The gray vertical line denotes  $\Omega \approx 4.3 \times 10^4$  in Refs. [14,29] [ $\Gamma_D \approx 570$  GHz and  $\sqrt{\sum_i (A_i^{\text{HF}} \nu_i^{\text{HF}})^2} \approx 13$  kHz].

Finally, we present an atypical example of  $\nu_{\text{fi}}^{\text{max}}(\Omega)$  dependence—the case of the 1-0 Q(1) line in H<sub>2</sub>, recently studied by Lamperti *et al.* [53]. This transition involves six hyperfine components which are spread almost symmetrically with respect to the HFS-free frequency (the remaining two components at  $-600$  kHz and  $587$  kHz are not visible on the inset plots in the bottom right panel of Fig. 1). The two components located at  $-54$  and  $59$  kHz have the same relative intensity (on the bottom right panel of Fig. 1, we associate  $\nu_{\text{fi}}^{\text{max}}$  with the  $59$  kHz component). As  $\Omega$  increases, the two, less intense peaks located in the vicinity of the HFS-free frequency blend into one line, which is more intense than the other components—this corresponds to the sudden drop of  $\nu_{\text{fi}}^{\text{max}}(\Omega)$  for  $\Omega \approx 3 \times 10^{-2}$ . For larger values of  $\Omega$ ,  $\nu_{\text{fi}}^{\text{max}}$  remains within the 3 kHz distance from the central frequency and tends to HFS free for  $\Omega > 10$ . This is the case for the study of Lamperti *et al.* [53], where  $\Omega \approx 5.7 \times 10^3$  justifies neglecting the hyperfine structure in the experimental analysis.

The four spectroscopic transitions considered here confirm that if the hyperfine components are spread over a narrow range of frequencies compared to the Doppler width, there is no significant shift of the resulting spectrum. Using the overlapping parameter  $\Omega$  to quantify the ratio of  $\nu_D$  to the mean-square hyperfine splitting indicates that no visible hyperfine shift is present if  $\Omega > 50$ . For instance, for the case of the 1-0 R(0) line in HD,  $\Omega = 50$  corresponds to the temperature of approximately 4 mK. In some cases, such as the Q lines in H<sub>2</sub>, this condition is obeyed for even smaller values of  $\Omega$ .

#### IV. CONCLUSION

We analyzed the first distribution moment of the hyperfine stick spectra. Based on a well-justified assumption about the form of the hyperfine Hamiltonian and the negligible mixing between rotational states, we showed that the barycenter is related to a difference between the sum of diagonal elements of the hyperfine Hamiltonian in the initial and final spectroscopic states, respectively. Additionally, we showed that the sum of diagonal elements of a scalar product of two spherical tensors vanishes unless the two tensors are of rank 0. This allowed us to state that the first distribution moment of the hyperfine spectra vanishes.

In the next step, we analyzed the barycenter of the Doppler-broadened spectra. We assumed that each hyperfine

component is described by the Gaussian function of the same width and we have shown that the formula depends on exactly the same factor as in the case of the hyperfine stick spectrum. We also calculated the maximum of the resulting spectra (by searching for roots of the derivative of the total spectrum) for the case in which the Doppler width is significantly larger than the underlying hyperfine structure. The resulting formula involved the first distribution moment of the stick spectrum, and thus vanishes.

Finally, we tested the extent to which the results derived here are applicable to the four selected rovibrational transitions in the three isotopologues of hydrogen. By introducing a dimensionless overlapping parameter  $\Omega$  (the ratio of  $\Gamma_D$  to the mean-square hyperfine splitting), we confirmed that there is no net hyperfine shift for  $\Omega > 50$ . This allowed us to conclude that in the accurate experimental spectra performed in the low-pressure regime, there should be no significant shift due to the underlying, unresolved hyperfine spectra. This result should be of particular importance for the recent Doppler-limited studies of the rovibrational structure of hydrogen [14,15,32]. We note that the formulas derived here should be valid for any diatomic molecule for which the hyperfine-induced mixing is negligible. Molecular hydrogen, with its exceptionally large rotational constant, fulfills this condition particularly well.

The work presented here is a stepping stone toward a deeper understanding of the influence of hyperfine structure on accurate molecular spectra, which are used to study quantum electrodynamics and put constraints on physics beyond the standard model. However, the majority of Doppler-limited studies suffer from collisional effects, which are not considered here. A natural extension of this work would be to study the existence of a net hyperfine shift in collision-perturbed spectra. For instance, a limiting case, opposite to the one presented here, could be considered: at high pressure and low temperature, the total spectrum should be a sum of Lorentzian functions corresponding to individual hyperfine components. We can immediately state that the results obtained here are not applicable to the Lorentzian case. We recall that one of the assumptions used here is that the hyperfine components have the same width. This is not fulfilled in the collision-perturbed case since the individual hyperfine components of molecular transitions are known to have different pressure broadening and shift coefficients. For instance, Buffa *et al.* [54] reported a significant variability ( $\approx 30\%$ ) of the pressure-broadening coefficients in the hyperfine structure of the rotational transition in CH<sub>3</sub>I. Interestingly, the hyperfine collisional effects are expected to be less pronounced in linear molecules, as explained by Belli *et al.* [55], and confirmed numerically by Green for He-perturbed rotational lines in HCN [56] and by Buffa and Tarini for He-perturbed DCO<sup>+</sup> lines [52,57]. Collisional effects in the hyperfine structure of molecular hydrogen seem to be particularly interesting: hydrogen lines are known to have an exceptionally large pressure shift [50], which can exceed pressure broadening [58]. If a significant variability in the pressure-shift coefficients is found for individual hyperfine components, the order of the particular components could be different than in the Doppler-broadened case. Moreover, line coupling between different hyperfine components, which has been detected in the rotational spectrum of HI [59], could lead

to a severe deterioration of the total shape of the spectrum, at least in the intermediate range of  $\Omega$  (for pressures large enough to induce overlapping of the components, but not large enough to blend them into a single line). The study of collisional effects in the hyperfine structure of molecular hydrogen will be the subject of upcoming papers.

### ACKNOWLEDGMENTS

The research is financed from the budgetary funds on science projected for 2019–2023 as a research project un-

der the “Diamontowy Grant” program. P.W. is supported by the National Science Centre in Poland, Project No. 2019/35/B/ST2/01118. The research is a part of the program of the National Laboratory FAMO in Toruń, Poland. Calculations have been partially carried out using resources provided by the Wrocław Centre for Networking and Supercomputing [60], Grant No. 546. We gratefully acknowledge Poland's high-performance computing infrastructure PLGrid (HPC Centers: ACK Cyfronet AGH, PCSS, CI TASK) for providing computer facilities and support within computational Grant No. PLG/2022/015576.

### APPENDIX A: COUPLING SCHEMES AND HYPERFINE EIGENSTATES

The effective hyperfine Hamiltonian for a given electronic state in the six isotopologues was discussed in Refs. [19,20,22,24,25]. Here, we discuss only the parts relevant for this paper, namely, the coupled basis used in the derivation, and the relation between the coupled basis and the eigenbasis of the hyperfine Hamiltonian.

Throughout the paper, we use the eigenbasis of the square of the total angular momentum,  $\mathbf{F}$ , which is constructed by coupling eigenvectors of the three angular momenta:  $\mathbf{I}_1$ ,  $\mathbf{I}_2$ , and  $\mathbf{N}$ . For the homonuclear isotopologues of hydrogen, we couple the two nuclear spin angular momenta to form the total nuclear spin angular momentum  $\mathbf{I}$ , which is coupled to the rotational angular momentum  $\mathbf{N}$  to form the total angular momentum  $\mathbf{F}$ . The resulting state vector is denoted as  $|v; [N(I_1 I_2) I] F m_F\rangle$  and is given by

$$\begin{aligned} |v; [N(I_1 I_2) I] F m_F\rangle &= \sum_{m_N=-N}^N \sum_{m_1=-I}^I \langle N m_N I m_1 | F m_F \rangle |v; N m_N\rangle |(I_1 I_2) I m_1\rangle \\ &= \sum_{m_N=-N}^N \sum_{m_1=-I}^I \langle N m_N I m_1 | F m_F \rangle \sum_{m_1=-I_1}^{I_1} \sum_{m_2=-I_2}^{I_2} \langle I_1 m_1 I_2 m_2 | I m_1 \rangle |v; N m_N\rangle |I_1 m_1\rangle |I_2 m_2\rangle, \end{aligned} \quad (\text{A1})$$

where  $\langle \cdot | \cdot \rangle$  is the Clebsch-Gordan coefficient,  $|I_1 m_1\rangle$  and  $|I_2 m_2\rangle$  are the eigenvectors of  $\mathbf{I}_1^2$  and  $\mathbf{I}_2^2$ , respectively, and  $|v; N m_N\rangle = |\nu N\rangle |N m_N\rangle$  denotes the rovibrational level. In position representation,  $|v; N m_N\rangle$  is given as

$$\langle \vec{\mathbf{R}} | v; N m_N \rangle = \chi_{v,N}(R) Y_{N m_N}(\hat{\mathbf{R}}). \quad (\text{A2})$$

$\vec{\mathbf{R}}$  denotes the position vector of the internuclear axis,  $\chi_{v,N}(R)$  is the solution of the nuclear radial Schrödinger equation, and  $Y_{N m_N}$  is the spherical harmonic.

In the heteronuclear case, one of the nuclear spin angular momenta,  $\mathbf{I}_1$ , is coupled to the rotational angular momentum to form the intermediate angular momentum  $\mathbf{F}_1$ . The latter is coupled to the remaining nuclear spin angular momentum  $\mathbf{I}_2$  to form the total angular momentum  $\mathbf{F}$ . The resulting vector is denoted as  $|v; [(N I_1) F_1 I_2] F m_F\rangle$ ,

$$\begin{aligned} |v; [(N I_1) F_1 I_2] F m_F\rangle &= \sum_{m_{F_1}=-F_1}^{F_1} \sum_{m_2=-I_2}^{I_2} \langle F_1 m_{F_1} I_2 m_2 | F m_F \rangle |v; (N I_1) F_1 m_{F_1}\rangle |I_2 m_2\rangle \\ &= \sum_{m_{F_1}=-F_1}^{F_1} \sum_{m_2=-I_2}^{I_2} \langle F_1 m_{F_1} I_2 m_2 | F m_F \rangle \sum_{m_N=-N}^N \sum_{m_1=-I_1}^{I_1} \langle N m_N I_1 m_1 | F_1 m_{F_1} \rangle |v; N\rangle |I_1 m_1\rangle |I_2 m_2\rangle. \end{aligned} \quad (\text{A3})$$

The effective hyperfine Hamiltonian is diagonal with respect to  $F$  and  $m_F$ . In the case of homonuclear molecules, the nuclear spin–nuclear spin dipole and, in the case of  $\text{D}_2$ , the quadrupole interaction introduce a weak coupling between the  $N$  and  $N' = N \pm 2$  states. This coupling is, however, at least seven orders of magnitude smaller than the energy interval between the  $N$  and  $N' = N \pm 2$  states, and is therefore neglected in the analysis. The relative weakness of this coupling with respect to the rotational constant is particularly pronounced in hydrogen isotopologues, but it should also hold for light hydrogen halides, such as HF and HCl, as well as for the less abundant isotopologues of carbon monoxide. The ratio of the largest hyperfine coupling constant in the  $v = 0, N = 1$  state to the rotational constant, hereafter referred to as  $\gamma$ , is of the order of  $10^{-7}$  for  $\text{H}^{19}\text{F}$  [61],  $10^{-5}$  for  $^{12}\text{C}^{17}\text{O}$  and  $^{13}\text{C}^{17}\text{O}$  [62,63], and  $10^{-4}$  for  $\text{H}^{35}\text{Cl}$  and  $\text{H}^{37}\text{Cl}$  [64]. Indeed, in the analysis of hyperfine-resolved rotational spectra [62,64] or molecular-beam electric resonance spectra [61,65] of these species, the couplings between the  $N$  and  $N' = N \pm 2$  levels were neglected. Moving down the periodic table, we note that  $\gamma \sim 10^{-3}$  for  $\text{H}^{79}\text{Br}$  and  $\text{H}^{81}\text{Br}$  [66], and  $\gamma \sim 10^{-2}$  for the  $\text{H}^{127}\text{I}$  [67,68]. In these cases, couplings between different rotational levels are crucial for accurate analysis of the hyperfine spectra [66,67]. While in the case of Doppler-limited spectroscopy large  $\gamma$  is undesirable, strong hyperfine

coupling might enhance the hypothetical Feshbach resonances in collisions of two  $^1\Sigma$  molecules, as predicted by Wallis and Krems for  $^{87}\text{Rb } ^{133}\text{Cs}$  ( $\gamma \sim 10^{-3}$ ) [69].

In the homonuclear case, the nuclear spin–nuclear spin and the electric quadrupole interaction also couple the  $I$  and  $I' = I \pm 2$  states. In the case of hydrogen molecules, considered here, this coupling is only of relevance for *ortho*-D<sub>2</sub>. In this case, to obtain the hyperfine eigenstates, the  $F$ -labeled blocks should be diagonalized. The relation between the hyperfine eigenstates and the coupled basis vectors is

$$|v; NFm_F(\pm)\rangle = \sum_I a_I^{vNF(\pm)} |v; [N(I_1 I_2)I]Fm_F\rangle. \quad (\text{A4})$$

Here,  $a_I^{vNF(\pm)}$  is a mixing coefficient obtained from diagonalization, which is related to the hyperfine coupling constants. For *ortho*-H<sub>2</sub>, *para*-D<sub>2</sub>, and *ortho*-T<sub>2</sub> ( $I = 1$ ), the sum is trivial and the coupled basis vectors are the eigenstates of the effective hyperfine Hamiltonian. Note that this leads to an interesting consequence, as the relative intensities of rovibrational transitions in these isotopologues are independent of  $v$  [41]. In the case of *ortho*-D<sub>2</sub>, two out of six hyperfine states for a given rovibrational level are a superposition of the coupled basis vectors introduced in Eq. (A1). In order to distinguish these states, we use  $(\pm)$  labels, which denote states with higher (+) and lower (−) energy.

For heteronuclear isotopologues, the nuclear spin-rotation interaction associated with nuclear spin  $\mathbf{I}_1$  (which was directly coupled with  $\mathbf{N}$ ) is fully diagonal with respect to all quantum numbers. Coupling between different  $F_1$  states occurs due to the nuclear spin rotation associated with the  $\mathbf{I}_2$  spin, the nuclear spin–nuclear spin dipole interaction, and, in deuterated species, the quadrupole interaction. This imposes the necessity to diagonalize the  $F$ -labeled blocks. The hyperfine eigenstates are related to the coupled basis vectors as

$$|v; NFm_F(\pm)\rangle = \sum_{F_1=|F-I_2|}^{F+I_2} a_{F_1}^{vNF(\pm)} |v; [(N I_1)F_1 I_2]Fm_F\rangle, \quad (\text{A5})$$

where  $a_{F_1}^{vNF(\pm)}$  is the mixing coefficient appropriate for the heteronuclear case. Similarly to the homonuclear case, we use the  $(\pm)$  labels to distinguish between the superposition states which correspond to the same values of  $v$ ,  $N$ , and  $F$ , but differ in energy.

## APPENDIX B: DERIVATION OF EQ. (4)

We begin with the analysis of the first distribution moment of the following form:

$$\mathcal{M}_{\text{fi}}^{(1)} = \frac{1}{h} \sum_{\text{HF}} \left( \langle v_f; N_f F_f m_{F_f}(\pm)_f | \mathcal{H}^{\text{HF}} | v_f; N_f F_f m_{F_f}(\pm)_f \rangle - \langle v_i; N_i F_i m_{F_i}(\pm)_i | \mathcal{H}^{\text{HF}} | v_i; N_i F_i m_{F_i}(\pm)_i \rangle \right) \frac{S_{\text{fi}}^{\text{HF}}}{S_{\text{fi}}^{\text{H}}}. \quad (\text{B1})$$

We consider the two terms separately. The first one is rewritten as [Eq. (2)]

$$\begin{aligned} & \sum_{F_i, (\pm)_i} \sum_{F_f, (\pm)_f} \langle v_f; N_f F_f m_{F_f}(\pm)_f | \mathcal{H}^{\text{HF}} | v_f; N_f F_f m_{F_f}(\pm)_f \rangle \frac{S_{\text{fi}}^{\text{HF}}}{S_{\text{fi}}^{\text{H}}} \\ &= \frac{1}{w_I f_n(N_i, N_f) |\mathbf{M}_{\text{fi}}^n|^2} \sum_{F_i, (\pm)_i} \sum_{F_f, (\pm)_f} \langle v_f; N_f F_f m_{F_f}(\pm)_f | \mathcal{H}^{\text{HF}} | v_f; N_f F_f m_{F_f}(\pm)_f \rangle \langle v_f; N_f F_f(\pm)_f | T^{(n)}(\mathbf{M}) | v_i; N_i F_i(\pm)_i \rangle^2. \end{aligned} \quad (\text{B2})$$

We express all the terms in Eq. (B2) in the coupled basis set introduced in Eqs. (A1) and (A3) in the next two paragraphs, respectively.

### 1. Homonuclear case

We focus on the reduced matrix element of the transition operator. We explicitly write the modulus square of the reduced matrix element of the transition operator in the coupled basis using Eq. (A4),

$$\begin{aligned} & \sum_{F_i, (\pm)_i} \sum_{F_f, (\pm)_f} \langle v_f; N_f F_f m_{F_f}(\pm)_f | \mathcal{H}^{\text{HF}} | v_f; N_f F_f m_{F_f}(\pm)_f \rangle \frac{S_{\text{fi}}^{\text{HF}}}{S_{\text{fi}}^{\text{H}}} \\ &= \frac{1}{w_I f_n(N_i, N_f) |\mathbf{M}_{\text{fi}}^n|^2} \sum_{F_i, (\pm)_i} \sum_{F_f, (\pm)_f} \langle v_f; N_f F_f m_{F_f}(\pm)_f | \mathcal{H}^{\text{HF}} | v_f; N_f F_f m_{F_f}(\pm)_f \rangle \\ & \quad \times \sum_{I'=|F_f-N_f|}^{F_f+N_f} a_{I'}^{(\pm)_f *} \sum_{I''=|F_i-N_i|}^{F_i+N_i} a_{I''}^{(\pm)_i} \langle v_f; [N_f(I_1 I_2)I']F_f | T^{(n)}(\mathbf{M}) | v_i; [N_i(I_1 I_2)I'']F_i \rangle \sum_{I'''=|F_f-N_f|}^{F_f+N_f} a_{I'''}^{(\pm)_f} \sum_{I''''=|F_i-N_i|}^{F_i+N_i} a_{I''''}^{(\pm)_i *} \\ & \quad \times \langle v_f; [N_f(I_1 I_2)I''']F_f | T^{(n)}(\mathbf{M}) | v_i; [N_i(I_1 I_2)I''''']F_i \rangle^*. \end{aligned} \quad (\text{B3})$$



The sum over  $(\pm)_i$  involves only the two mixing coefficients. We note that the following orthogonality relations hold:

$$\sum_{\pm} a_{I'}^{(\pm)*} a_{I''}^{(\pm)} = \delta_{I'I''}, \quad (\text{B4})$$

$$\sum_I a_I^{(\pm)*} a_I^{(\pm)} = \delta_{+-}. \quad (\text{B5})$$

In the present case, the sum over  $(\pm)_i$  results in the Kronecker delta  $\delta_{I'I''}$ , which makes the last sum in Eq. (B3) trivial. In the next step, we simplify the two reduced matrix elements using the following property of spherical tensor operators [47]:

$$\begin{aligned} & \langle \nu_f; [N_f(I_1 I_2) I_f] F_f || T^{(n)}(\mathbf{M}) || \nu_i; [N_i(I_1 I_2) I_i] F_i \rangle \\ &= \delta_{I_f I_i} (-1)^{F_i + N_f + n + I_f} \sqrt{[F_i, F_f]} \begin{Bmatrix} F_f & F_i & n \\ N_i & N_f & I_i \end{Bmatrix} \langle \nu_f; N_f || T^{(n)}(\mathbf{M}) || \nu_i; N_i \rangle, \end{aligned} \quad (\text{B6})$$

where  $[x_1, x_2, \dots, x_n] = (2x_1 + 1)(2x_2 + 1) \cdots (2x_n + 1)$ . This reduction is justified by the fact that the transition operator acts only on the subspace associated with rotational angular momentum and does not modify the nuclear spins.

These two operations lead to

$$\begin{aligned} & \sum_{F_i, (\pm)_i} \sum_{F_f, (\pm)_f} \langle \nu_f; N_f F_f m_{F_f}(\pm)_f | \mathcal{H}^{\text{HF}} | \nu_f; N_f F_f m_{F_f}(\pm)_f \rangle \frac{S_{\text{fi}}^{\text{HF}}}{S_{\text{fi}}} \\ &= (-1)^{2(F_i + N_f + n)} \frac{|\langle \nu_f; N_f || T^{(n)}(\mathbf{M}) || \nu_i; N_i \rangle|^2}{w_I f_n(N_i, N_f) |\mathbf{M}_{\text{fi}}^n|^2} \sum_{F_i, F_f, (\pm)_f} [F_i, F_f] \langle \nu_f; N_f F_f m_{F_f}(\pm)_f | \mathcal{H}^{\text{HF}} | \nu_f; N_f F_f m_{F_f}(\pm)_f \rangle \\ &\quad \times \sum_{I'=|F_i-N_f|}^{F_i+N_f} a_{I'}^{(\pm)*} \sum_{I''=|F_i-N_i|}^{F_i+N_i} \delta_{I'I''} (-1)^{I'} \begin{Bmatrix} F_f & F_i & n \\ N_i & N_f & I'' \end{Bmatrix} \sum_{I'''=|F_i-N_f|}^{F_i+N_f} a_{I'''}^{(\pm)} \delta_{I''I'''} (-1)^{I'''} \begin{Bmatrix} F_f & F_i & n \\ N_i & N_f & I''' \end{Bmatrix}. \end{aligned} \quad (\text{B7})$$

The Kronecker deltas reduce the sums over  $I'''$  and  $I''$ . Using Eq. (A12) in Ref. [41],

$$\frac{|\langle \nu_f; N_f || T^{(n)}(\mathbf{M}) || \nu_i; N_i \rangle|^2}{f_n(N_i, N_f) |\mathbf{M}_{\text{fi}}^n|^2} = 1, \quad (\text{B8})$$

we obtain

$$\begin{aligned} & \sum_{F_i, (\pm)_i} \sum_{F_f, (\pm)_f} \langle \nu_f; N_f F_f m_{F_f}(\pm)_f | \mathcal{H}^{\text{HF}} | \nu_f; N_f F_f m_{F_f}(\pm)_f \rangle \frac{S_{\text{fi}}^{\text{HF}}}{S_{\text{fi}}} \\ &= (-1)^{2(F_i + N_f + n)} \frac{1}{w_I} \sum_{F_i, F_f, (\pm)_f} [F_i, F_f] \langle \nu_f; N_f F_f m_{F_f}(\pm)_f | \mathcal{H}^{\text{HF}} | \nu_f; N_f F_f m_{F_f}(\pm)_f \rangle \sum_{I'=|F_i-N_f|}^{F_i+N_f} (-1)^{2I'} |a_{I'}^{(\pm)_f}|^2 \begin{Bmatrix} F_f & F_i & n \\ N_i & N_f & I' \end{Bmatrix}^2. \end{aligned} \quad (\text{B9})$$

The sum over  $F_i$  involves only the  $[F_i]$  term and the 6- $j$  symbol. This allows us to use the orthogonality of the 6- $j$  symbols,

$$\sum_{F_i} [F_i] \begin{Bmatrix} F_f & F_i & n \\ N_i & N_f & I' \end{Bmatrix}^2 = \frac{1}{[N_f]}, \quad (\text{B10})$$

which leads to

$$\begin{aligned} & \sum_{F_i, (\pm)_i} \sum_{F_f, (\pm)_f} \langle \nu_f; N_f F_f m_{F_f}(\pm)_f | \mathcal{H}^{\text{HF}} | \nu_f; N_f F_f m_{F_f}(\pm)_f \rangle \frac{S_{\text{fi}}^{\text{HF}}}{S_{\text{fi}}} \\ &= (-1)^{2(F_i + N_f + n)} \frac{1}{w_I [N_f]} \sum_{F_f, (\pm)_f} [F_f] \langle \nu_f; N_f F_f m_{F_f}(\pm)_f | \mathcal{H}^{\text{HF}} | \nu_f; N_f F_f m_{F_f}(\pm)_f \rangle \sum_{I'=|F_f-N_f|}^{F_f+N_f} (-1)^{2I'} |a_{I'}^{(\pm)_f}|^2. \end{aligned} \quad (\text{B11})$$

Both phase factors can be reduced:  $N$ ,  $n$ , and the sum  $F_i + I'$  are always integers. As a consequence, the sum over  $I'$  gives 1, according to Eq. (B5),

$$\sum_{F_i, (\pm)_i} \sum_{F_f, (\pm)_f} \langle \nu_f; N_f F_f m_{F_f}(\pm)_f | \mathcal{H}^{\text{HF}} | \nu_f; N_f F_f m_{F_f}(\pm)_f \rangle \frac{S_{\text{fi}}^{\text{HF}}}{S_{\text{fi}}} = \frac{1}{w_I [N_f]} \sum_{F_f, (\pm)_f} [F_f] \langle \nu_f; N_f F_f m_{F_f}(\pm)_f | \mathcal{H}^{\text{HF}} | \nu_f; N_f F_f m_{F_f}(\pm)_f \rangle. \quad (\text{B12})$$

We recall that in the absence of an external magnetic field, the hyperfine Hamiltonian is diagonal with respect to the projection of the total angular momentum on the space-fixed  $z$  axis,  $m_F$ . We note that this approach is applicable to experimental techniques



in which the laser field does not considerably shift the hyperfine components (in the extreme case of cavity-enhanced saturation experiments, the dynamical AC Stark shift can be of the order of a few kHz; see Refs. [17,31]). Using

$$\sum_{m_{F_f}} \langle \nu_f; N_f F_f m_{F_f}(\pm)_f | \mathcal{H}^{\text{HF}} | \nu_f; N_f F_f m_{F_f}(\pm)_f \rangle = [F_f] \langle \nu_f; N_f F_f m_{F_f}(\pm)_f | \mathcal{H}^{\text{HF}} | \nu_f; N_f F_f m_{F_f}(\pm)_f \rangle, \quad (\text{B13})$$

we obtain

$$\sum_{F_i, (\pm)_i} \sum_{F_f, (\pm)_f} \langle \nu_f; N_f F_f m_{F_f}(\pm)_f | \mathcal{H}^{\text{HF}} | \nu_f; N_f F_f m_{F_f}(\pm)_f \rangle \frac{S_{\text{fi}}^{\text{HF}}}{S_{\text{fi}}} = \sum_{F_i, m_{F_i}, (\pm)_i} \frac{\langle \nu_f; N_f F_f m_{F_f}(\pm)_f | \mathcal{H}^{\text{HF}} | \nu_f; N_f F_f m_{F_f}(\pm)_f \rangle}{w_1[N_f]}. \quad (\text{B14})$$

Finally, we transform the matrix element to the coupled basis using Eq. (A4) and summing over the  $(\pm)$  labels, given by Eq. (B4), we obtain the first term in Eq. (4). Using exactly the same procedure for the second term in Eq. (B1), we obtain the second term in Eq. (4),

$$\sum_{F_i, (\pm)_i} \sum_{F_f, (\pm)_f} \langle \nu_i; N_i F_i m_{F_i}(\pm)_i | \mathcal{H}^{\text{HF}} | \nu_i; N_i F_i m_{F_i}(\pm)_i \rangle \frac{S_{\text{fi}}^{\text{HF}}}{S_{\text{fi}}} = \sum_{F_i, m_{F_i}, (\pm)_i} \frac{\langle \nu_i; (N_i I_i) F_i m_{F_i} | \mathcal{H}^{\text{HF}} | \nu_i; (N_i I_i) F_i m_{F_i} \rangle}{w_1[N_i]}. \quad (\text{B15})$$

## 2. Heteronuclear case

We express the reduced matrix elements in Eq. (B1) of the transition moment in the coupled basis using Eq. (A5),

$$\begin{aligned} & \sum_{F_i, (\pm)_i} \sum_{F_f, (\pm)_f} \langle \nu_f; N_f F_f m_{F_f}(\pm)_f | \mathcal{H}^{\text{HF}} | \nu_f; N_f F_f m_{F_f}(\pm)_f \rangle \frac{S_{\text{fi}}^{\text{HF}}}{S_{\text{fi}}} \\ &= \frac{1}{w_I f_n(N_i, N_f) |\mathbf{M}_{\text{fi}}^n|^2} \sum_{F_i, (\pm)_i} \sum_{F_f, (\pm)_f} \langle \nu_f; N_f F_f m_{F_f}(\pm)_f | \mathcal{H}^{\text{HF}} | \nu_f; N_f F_f m_{F_f}(\pm)_f \rangle \\ & \times \sum_{F'_1=|F_i-I_2|}^{F_i+I_2} a_{F'_1}^{(\pm)_f *} \sum_{F''_1=|F_i-I_2|}^{F_i+I_2} a_{F''_1}^{(\pm)_i} \langle \nu_f; ((N_f I_f) F'_1 I_2) F_f || T^{(n)}(\mathbf{M}) || \nu_i; ((N_i I_i) F''_1 I_2) F_i \rangle \\ & \times \sum_{F'''_1=|F_i-I_2|}^{F_i+I_2} a_{F'''_1}^{(\pm)_f} \sum_{F''''_1=|F_i-I_2|}^{F_i+I_2} a_{F''''_1}^{(\pm)_i *} \langle \nu_f; ((N_f I_f) F'''_1 I_2) F_f || T^{(n)}(\mathbf{M}) || \nu_i; ((N_i I_i) F''''_1 I_2) F_i \rangle^*. \end{aligned} \quad (\text{B16})$$

We note that the sum over  $(\pm)_i$  involves only the two mixing coefficients. Similar to Eqs. (B4) and (B5), we can formulate the orthogonality relations for the heteronuclear basis,

$$\sum_{(\pm)} a_{F'_1}^{(\pm)*} a_{F''_1}^{(\pm)} = \delta_{F'_1 F''_1}, \quad (\text{B17})$$

$$\sum_{F_1} a_{F'_1}^{(\pm)*} a_{F''_1}^{(\pm)} = \delta_{+-}. \quad (\text{B18})$$

Using Eq. (B17) leads to the reduction of the sum over  $F''''_1$  due to the presence of  $\delta_{F'' F''''_1}$ . Since the transition operator acts only on the subspace of the eigenvectors of  $\mathbf{N}^2$ , we apply Eq. (B6) twice. Finally, we reduce the  $f_n(N_i, N_f)$  coefficients using Eq. (B8). After applying these three operations, the expression looks as follows:

$$\begin{aligned} & \sum_{F_i, (\pm)_i} \sum_{F_f, (\pm)_f} \langle \nu_f; N_f F_f m_{F_f}(\pm)_f | \mathcal{H}^{\text{HF}} | \nu_f; N_f F_f m_{F_f}(\pm)_f \rangle \frac{S_{\text{fi}}^{\text{HF}}}{S_{\text{fi}}} \\ &= \frac{1}{w_I} \sum_{F_i, F_f, (\pm)_f} \langle \nu_f; N_f F_f m_{F_f}(\pm)_f | \mathcal{H}^{\text{HF}} | \nu_f; N_f F_f m_{F_f}(\pm)_f \rangle \sum_{F'_1, F''_1, F'''_1} a_{F'_1}^{(\pm)_f *} a_{F''_1}^{(\pm)_i} (-1)^{2(F_i+2n+I_1+I_2+N_f+F''_1)} \\ & \times (-1)^{F'_1+F'''_1} [F_i, F_f, F'_1] \sqrt{[F'_1, F'''_1]} \begin{Bmatrix} F_f & F_i & n \\ F''_1 & F'_1 & I_2 \end{Bmatrix} \begin{Bmatrix} F'_1 & F''_1 & n \\ N_i & N_f & I_1 \end{Bmatrix} \begin{Bmatrix} F_f & F_i & n \\ F'''_1 & F''_1 & I_2 \end{Bmatrix} \begin{Bmatrix} F'''_1 & F''_1 & n \\ N_i & N_f & I_1 \end{Bmatrix}. \end{aligned} \quad (\text{B19})$$

The first phase factor is reduced immediately:  $N$ ,  $n$ , and the sum  $I_1 + F_1, I_2 + F$  are always integers. The  $F_i$  symbol occurs only in the  $[F_i]$  term and the two 6- $j$  symbols. Using orthonormality of the 6- $j$  symbols,

$$\sum_{F_i} [F_i] \begin{Bmatrix} F_f & F_i & n \\ F''_1 & F'_1 & I_2 \end{Bmatrix} \begin{Bmatrix} F_f & F_i & n \\ F'_1 & F''_1 & I_2 \end{Bmatrix} = \frac{\delta_{F'_1 F''_1}}{[F'_1]}, \quad (\text{B20})$$

we further simplify the expression for the first distribution moment,

$$\begin{aligned} & \sum_{F_i, (\pm)_i} \sum_{F_f, (\pm)_f} \langle \nu_f; N_f F_f m_{F_f}(\pm)_f | \mathcal{H}^{\text{HF}} | \nu_f; N_f F_f m_{F_f}(\pm)_f \rangle \frac{S_{\text{fi}}^{\text{HF}}}{S_{\text{fi}}} \\ &= \frac{1}{w_I} \sum_{F_f, (\pm)_f} \langle \nu_f; N_f F_f m_{F_f}(\pm)_f | \mathcal{H}^{\text{HF}} | \nu_f; N_f F_f m_{F_f}(\pm)_f \rangle \sum_{F'_f} (-1)^{2F'_f} |a_{F'_f}^{(\pm)_f}|^2 [F_f] \sum_{F''_f} [F''_f] \left\{ \begin{matrix} F'_f & F''_f & n \\ N_i & N_f & I_1 \end{matrix} \right\}^2. \end{aligned} \quad (\text{B21})$$

The remaining phase factor depends on whether the nuclear spin  $I_1$  is an integer  $[(-1)^{2F'_f} = (-1)^{2I_1} = 1]$  or a half integer  $[(-1)^{2F'_f} = (-1)^{2I_1} = -1]$ . We substitute  $(-1)^{2F'_f}$  with  $(-1)^{2I_1}$ , and reduce the sum over  $F''_f$  using Eq. (B20). The remaining sum over  $F'_f$ , which includes only the mixing coefficient, equals 1, according to Eq. (B18),

$$\begin{aligned} & \sum_{F_i, (\pm)_i} \sum_{F_f, (\pm)_f} \langle \nu_f; N_f F_f m_{F_f}(\pm)_f | \mathcal{H}^{\text{HF}} | \nu_f; N_f F_f m_{F_f}(\pm)_f \rangle \frac{S_{\text{fi}}^{\text{HF}}}{S_{\text{fi}}} \\ &= \frac{(-1)^{2I_1}}{w_I [N_f]} \sum_{F_f, (\pm)_f} [F_f] \langle \nu_f; N_f F_f m_{F_f}(\pm)_f | \mathcal{H}^{\text{HF}} | \nu_f; N_f F_f m_{F_f}(\pm)_f \rangle. \end{aligned} \quad (\text{B22})$$

Finally, we use Eq. (B13) and substitute the relation between the eigenvectors of the hyperfine Hamiltonian and the coupled basis vectors from Eq. (A3). This leads to the expected result,

$$\sum_{F_i, (\pm)_i} \sum_{F_f, (\pm)_f} \langle \nu_f; N_f F_f m_{F_f}(\pm)_f | \mathcal{H}^{\text{HF}} | \nu_f; N_f F_f m_{F_f}(\pm)_f \rangle \frac{S_{\text{fi}}^{\text{HF}}}{S_{\text{fi}}} = (-1)^{2I_1} \sum_{F_f, m_{F_f} F_{I_f}} \frac{\langle \nu_f; [(N_f I_1) F_{I_f} I_2] F_f m_{F_f} | \mathcal{H}^{\text{HF}} | \nu_f; [(N_f I_1) F_{I_f}] F_f m_{F_f} \rangle}{w_I [N_f]}. \quad (\text{B23})$$

The same mathematical operations can be applied to the second term in Eq. (B1), which results in

$$\sum_{F_i, (\pm)_i} \sum_{F_f, (\pm)_f} \langle \nu_i; N_i F_i m_{F_i}(\pm)_i | \mathcal{H}^{\text{HF}} | \nu_i; N_i F_i m_{F_i}(\pm)_i \rangle \frac{S_{\text{fi}}^{\text{HF}}}{S_{\text{fi}}} = (-1)^{2I_1} \sum_{F_i, m_{F_i} F_{I_i}} \frac{\langle \nu_i; [(N_i I_1) F_{I_i} I_2] F_i m_{F_i} | \mathcal{H}^{\text{HF}} | \nu_i; [(N_i I_1) F_{I_i}] F_i m_{F_i} \rangle}{w_I [N_i]}. \quad (\text{B24})$$

Subtracting the two terms leads to an analog of Eq. (4) for heteronuclear molecules,

$$\begin{aligned} \mathcal{M}_{\text{fi}}^{(1)} &= \frac{(-1)^{2I_1}}{h w_I} \left( \sum_{F_f, m_{F_f} F_{I_f}} \frac{\langle \nu_f; [(N_f I_1) F_{I_f} I_2] F_f m_{F_f} | \mathcal{H}^{\text{HF}} | \nu_f; [(N_f I_1) F_{I_f}] F_f m_{F_f} \rangle}{[N_f]} \right. \\ &\quad \left. - \sum_{F_i, m_{F_i} F_{I_i}} \frac{\langle \nu_i; [(N_i I_1) F_{I_i} I_2] F_i m_{F_i} | \mathcal{H}^{\text{HF}} | \nu_i; [(N_i I_1) F_{I_i}] F_i m_{F_i} \rangle}{[N_i]} \right). \end{aligned} \quad (\text{B25})$$

### APPENDIX C: PROOF OF EQ. (8)

We seek a general formula for the trace of the scalar product of two tensors of rank  $k$ . Using a formula for matrix elements of the scalar product of two spherical tensors which act on two distinct parts of the coupled basis [47], we obtain

$$\begin{aligned} & \sum_{v, j_1, j_2, j, m} \langle v; (j_1 j_2) j m | T^{(k)}(\mathbf{A}) \cdot T^{(k)}(\mathbf{B}) | v; (j_1 j_2) j m \rangle \\ &= \sum_{v, j_1, j_2} (-1)^{j_1+j_2} \left( \sum_j (-1)^j (2j+1) \left\{ \begin{matrix} j_2 & j_1 & j \\ j_1 & j_2 & k \end{matrix} \right\} \right) \langle v; j_1 || T^{(k)}(\mathbf{A}) || v; j_1 \rangle \langle v; j_2 || T^{(k)}(\mathbf{B}) || v; j_2 \rangle. \end{aligned} \quad (\text{C1})$$

Here, we intentionally distinguish a part of the formula in a bracket. In order to reduce this term, we start with the general orthogonality rule for the 6- $j$  symbols,

$$\sum_{j_3} (2j_3+1) \left\{ \begin{matrix} j_1 & j_2 & j_3 \\ j_4 & j_5 & k \end{matrix} \right\} \left\{ \begin{matrix} j_1 & j_2 & j_3 \\ j_4 & j_5 & k' \end{matrix} \right\} = \frac{\delta_{kk'}}{2k+1}, \quad (\text{C2})$$

and we put  $k' = 0$ . We recall that in this case, the second 6- $j$  symbol is simplified as follows:

$$\left\{ \begin{matrix} j_1 & j_2 & j_3 \\ j_4 & j_5 & 0 \end{matrix} \right\} = \frac{\delta_{j_1 j_5} \delta_{j_2 j_4}}{\sqrt{(2j_1+1)(2j_2+1)}} (-1)^{j_1+j_2+j_3}. \quad (\text{C3})$$

This leads to

$$\sum_{j_3} (-1)^{j_3} (2j_3 + 1) \begin{Bmatrix} j_1 & j_2 & j_3 \\ j_2 & j_1 & k \end{Bmatrix} = \delta_{k0} (-1)^{-j_1-j_2} \sqrt{(2j_1+1)(2j_2+1)}. \quad (\text{C4})$$

This result, inserted into Eq. (C1) with  $j_4 = j_1$ ,  $j_5 = j_2$ , and  $j_3 = j$ , leads to

$$\sum_{v, j_1, j_2, j, m} \langle v; (j_1 j_2) jm | T^{(k)}(\mathbf{A}) \cdot T^{(k)}(\mathbf{B}) | v; (j_1 j_2) jm \rangle = \delta_{k0} \sqrt{(2j_1+1)(2j_2+1)} \langle v; j_1 | T^{(k)}(\mathbf{A}) | v; j_1 \rangle \langle v; j_2 | T^{(k)}(\mathbf{B}) | v; j_2 \rangle. \quad (\text{C5})$$

#### APPENDIX D: DERIVATIVE OF THE $N$ -GAUSSIAN SPECTRUM

The central frequency of the  $N$ -Gaussian spectrum can be determined by calculating the derivative of the sum of  $N$  Gaussians, and searching for  $\nu$ , for which the derivative vanishes. Here, we prove that if the centers of the Gaussians are spread over a narrow range of frequencies, significantly smaller than their widths, the barycenter of the sum of  $N$  Gaussians of the same width is given by the formula

$$\nu_{\text{fi}}^{\text{max}} \approx \sum_{\text{HF}} A^{\text{HF}} \nu_{\text{fi}}^{\text{HF}}. \quad (\text{D1})$$

We begin with a simple case of the spectrum which involves two Gaussian functions of different heights, but the same width. The resulting spectrum is

$$f(\nu) = \frac{C}{\sqrt{\pi} \nu_D} e^{-(\nu-a)^2/\nu_D^2} + \frac{C'}{\sqrt{\pi} \nu_D} e^{-(\nu-b)^2/\nu_D^2}. \quad (\text{D2})$$

The two Gaussians are centered around  $\nu = a$  and  $\nu = b$  and are of  $C$  and  $C'$  heights, respectively. We slightly modify this equation by introducing the following variables:

$$\begin{aligned} \delta &= \frac{1}{2} \ln \frac{C}{C'}, \\ \alpha &= a + b, \\ \beta &= a - b, \\ \xi(\nu) &= e^{\alpha \nu / \nu_D^2 - (a^2 + b^2) / 2 \nu_D^2}, \end{aligned} \quad (\text{D3})$$

which allows us to rewrite Eq. (D2) as

$$f(\nu) = \frac{2\sqrt{CC'}}{\sqrt{\pi} \nu_D} e^{-\nu^2/\nu_D^2} \xi(\nu) \cosh \left[ \frac{\beta}{\nu_D^2} (\nu - \alpha) + \delta \right]. \quad (\text{D4})$$

The extrema of the spectrum occur at  $\nu$  for which  $f'(\nu) = 0$ . This leads to a nonlinear equation on  $\nu$ ,

$$\nu = \frac{\beta}{2} \tanh \left[ \frac{\beta}{\nu_D^2} (\nu - \alpha) + \delta \right] + \frac{\alpha}{2}. \quad (\text{D5})$$

An approximate solution can be found using Taylor expansion. First, we use the formula for the sum of arguments of the hyperbolic tangent,

$$\tanh(a+b) = \frac{\tanh(a) + \tanh(b)}{1 + \tanh(a) \tanh(b)}, \quad (\text{D6})$$

we rewrite the resulting equation using a new variable,  $x = \frac{\beta}{\nu_D^2} (\nu - \alpha)$ , and we expand the right-hand side of Eq. (D5)

for  $x \ll 1$ , keeping only the terms that are linear in  $x$ ,

$$\nu^{\text{max}} \approx \frac{\beta}{2} \frac{\tanh(\delta) + \frac{\beta}{\nu_D^2} (\nu - \alpha)}{1 + \tanh(\delta) \frac{\beta}{\nu_D^2} (\nu - \alpha)} + \frac{\alpha}{2}. \quad (\text{D7})$$

The remaining hyperbolic tangent is simply

$$\tanh \delta = \frac{C - C'}{C + C'}. \quad (\text{D8})$$

If  $x \ll 1$ , then  $\frac{C-C'}{C+C'} x \ll 1$  too. Thus, in the next step, we expand the denominator and we neglect all terms smaller than the linear term on the right-hand side of the equation. This leads to

$$\nu^{\text{max}} \approx \frac{\frac{1}{2} \frac{\beta(C-C') + \alpha(C+C')}{C+C'} - \frac{\alpha\beta}{\nu_D^2} \left(1 - \frac{(C-C')^2}{(C+C')^2}\right)}{1 - \frac{\beta^2}{2\nu_D^2} \left(1 - \frac{(C-C')^2}{(C+C')^2}\right)}, \quad (\text{D9})$$

which is drastically simplified if  $\beta/\nu_D \ll 1$ . Substituting  $a$  and  $b$  for  $\alpha$  and  $\beta$  from Eq. (D3) results in

$$\nu^{\text{max}} \approx a\bar{C} + b\bar{C}', \quad (\text{D10})$$

where  $\bar{C} = C/(C+C')$  and  $\bar{C}' = C'/(C+C')$  are relative intensities of the two components. This result resembles the form anticipated in Eq. (D1). We thus have provided a position of the maximum of Eq. (D2) for  $\beta/\nu_D \ll 1$ .

Additionally, we can show that if  $a/\nu_D \ll 1$  and  $b/\nu_D \ll 1$ , the general formula from Eq. (D2) is simplified into a single Gaussian, centered at  $\nu^{\text{max}}$  with the height of  $C+C'$ . We approximate the exponents involving  $a$  and  $b$  as  $e^x \approx 1+x$  in Eq. (D2), and we keep only the terms that are linear in  $a/\nu_D$  and  $b/\nu_D$ . This leads to

$$f(\nu) \approx \frac{(C+C')}{\sqrt{\pi} \nu_D} e^{-\nu^2/\nu_D^2} \left(1 + 2 \frac{\nu}{\nu_D} \frac{aC + bC'}{C+C'}\right), \quad (\text{D11})$$

which corresponds to the approximation of

$$f(\nu) = \frac{(C+C')}{\sqrt{\pi} \nu_D} e^{-(\nu-\nu^{\text{max}})^2/\nu_D^2} \quad (\text{D12})$$

for  $\nu^{\text{max}}/\nu_D \ll 1$ . We write, symbolically, that

$$f(\nu) = f(\nu; a, C) + f(\nu; b, C') \approx f(\nu; \nu^{\text{max}(2)}, C^{(2)}), \quad (\text{D13})$$

which means that the sum of two Gaussians of the same width, centered around  $a$  and  $b$ , leads to another Gaussian, centered around  $\nu^{\text{max}} = \nu^{\text{max}(2)}$  [the (2) superscript denotes the number of summed Gaussians], given by Eq. (D10). The resulting

profile is of the height which is the sum of the two Gaussian functions,  $C^{(2)} = C + C'$ .

We apply the same procedure to another Gaussian, centered around  $c$  and of the height given by  $C''$ . Using the same arguments as in the two-Gaussian case, the central frequency of the profile resulting from summing *three* Gaussians is given as

$$\nu^{\max(3)} \approx a\bar{C} + b\bar{C}' + c\bar{C}''.$$
 (D14)

This iterative approach can be used for the  $N$ -Gaussian case. If all conditions introduced throughout the derivation remain fulfilled, the central frequency of the set of  $N$ -Gaussian func-

tions,  $f(\nu; \nu_{0i}, C_i)$  is given by

$$\nu^{\max(N)} \approx \sum_{i=1}^N \nu_{0i} \bar{C}_i.$$
 (D15)

Thus, the maximum of the profile resulting from summing  $N$ -Gaussian functions involves the first moment, defined in Sec. II. If all Gaussians fulfill the condition,

$$\sum_{i=1}^N \nu_{0i} \bar{C}_i = 0,$$
 (D16)

the maximum of the resulting profile corresponds to the zero frequency.

- 
- [1] S. Alighanbari, G. S. Giri, F. L. Constantin, V. I. Korobov, and S. Schiller, Precise test of quantum electrodynamics and determination of fundamental constants with  $\text{HD}^+$  ions, *Nature (London)* **581**, 152 (2020).
  - [2] S. Patra, M. Germann, J.-P. Karr, M. Haidar, L. Hilico, V. I. Korobov, F. M. J. Cozijn, K. S. E. Eikema, W. Ubachs, and J. C. J. Koelemeij, Proton-electron mass ratio from laser spectroscopy of  $\text{HD}^+$  at the part-per-trillion level, *Science* **369**, 1238 (2020).
  - [3] A. Beyer, L. Maisenbacher, A. Matveev, R. Pohl, K. Khabarova, A. Grinin, T. Lamour, D. C. Yost, T. W. Hänsch, N. Kolachevsky, and T. Udem, The Rydberg constant and proton size from atomic hydrogen, *Science* **358**, 79 (2017).
  - [4] R. Pohl, A. Antognini, F. Nez, F. D. Amaro, F. Biraben, J. M. R. Cardoso, D. S. Covita, A. Dax, S. Dhawan, L. M. P. Fernandes *et al.*, The size of the proton, *Nature (London)* **466**, 213 (2010).
  - [5] W. Ubachs, J. Koelemeij, K. Eikema, and E. Salumbides, Physics beyond the Standard Model from hydrogen spectroscopy, *J. Mol. Spectrosc.* **320**, 1 (2016).
  - [6] M. S. Safronova, D. Budker, D. DeMille, Derek F. Jackson Kimball, A. Derevianko, and C. W. Clark, Search for new physics with atoms and molecules, *Rev. Mod. Phys.* **90**, 025008 (2018).
  - [7] L. Wolniewicz, I. Simbotin, and A. Dalgarno, Quadrupole transition probabilities for the excited rovibrational states of  $\text{H}_2$ , *Astrophys. J., Suppl. Ser.* **115**, 293 (1998).
  - [8] A. Campargue, S. Kass, K. Pachucki, and J. Komasa, The absorption spectrum of  $\text{H}_2$ : CRDS measurements of the (2-0) band, review of the literature data and accurate *ab initio* line list up to  $35000 \text{ cm}^{-1}$ , *Phys. Chem. Chem. Phys.* **14**, 802 (2012).
  - [9] K. Pachucki and J. Komasa, Magnetic dipole transitions in the hydrogen molecule, *Phys. Rev. A* **83**, 032501 (2011).
  - [10] E. Roueff, H. Abgrall, P. Czachorowski, K. Pachucki, M. Puchalski, and J. Komasa, The full infrared spectrum of molecular hydrogen, *Astron. Astrophys.* **630**, A58 (2019).
  - [11] A. Fast and S. A. Meek, Sub-ppb Measurement of a Fundamental Band Rovibrational Transition in HD, *Phys. Rev. Lett.* **125**, 023001 (2020).
  - [12] M. L. Diouf, F. M. J. Cozijn, K.-F. Lai, E. J. Salumbides, and W. Ubachs, Lamb-peak spectrum of the HD (2-0) P(1) line, *Phys. Rev. Res.* **2**, 023209 (2020).
  - [13] T.-P. Hua, Y. Sun, and S.-M. Hu, Dispersion-like lineshape observed in cavity-enhanced saturation spectroscopy of HD at  $1.4 \mu\text{m}$ , *Opt. Lett.* **45**, 4863 (2020).
  - [14] M. Zaborowski, M. Słowiński, K. Stankiewicz, F. Thibault, A. Cygan, H. Jóźwiak, G. Kowzan, P. Masłowski, A. Nishiyama, N. Stolarczyk, S. Wójtewicz, R. Ciuryło, D. Lisak, and P. Wcisło, Ultrahigh finesse cavity-enhanced spectroscopy for accurate tests of quantum electrodynamics for molecules, *Opt. Lett.* **45**, 1603 (2020).
  - [15] A. Castrillo, E. Fasci, and L. Gianfrani, Doppler-limited precision spectroscopy of HD at  $1.4 \mu\text{m}$ : An improved determination of the R(1) center frequency, *Phys. Rev. A* **103**, 022828 (2021).
  - [16] A. Fast and S. A. Meek, Precise measurement of the  $\text{D}_2\text{S}_1(0)$  vibrational transition frequency, *Mol. Phys.* **120**, e1999520 (2021).
  - [17] H. Jóźwiak and P. Wcisło, Magic wavelength for a rovibrational transition in molecular hydrogen, *Sci. Rep.* **12**, 14529 (2022).
  - [18] P. Dupré, Hyperfine transitions in the first overtone mode of hydrogen deuteride, *Phys. Rev. A* **101**, 022504 (2020).
  - [19] H. Jóźwiak, H. Cybulski, and P. Wcisło, Positions and intensities of hyperfine components of all rovibrational dipole lines in the HD molecule, *J. Quant. Spectrosc. Radiat. Transfer* **253**, 107171 (2020).
  - [20] H. Jóźwiak, H. Cybulski, and P. Wcisło, Hyperfine components of all rovibrational quadrupole transitions in the  $\text{H}_2$  and  $\text{D}_2$  molecules, *J. Quant. Spectrosc. Radiat. Transfer* **253**, 107186 (2020).
  - [21] J. Komasa, M. Puchalski, and K. Pachucki, Hyperfine structure in the HD molecule, *Phys. Rev. A* **102**, 012814 (2020).
  - [22] H. Jóźwiak, H. Cybulski, and P. Wcisło, Hyperfine structure of quadrupole rovibrational transitions in tritium-bearing hydrogen isotopologues, *J. Quant. Spectrosc. Radiat. Transfer* **256**, 107255 (2020).
  - [23] M. Puchalski, J. Komasa, and K. Pachucki, Hyperfine Structure of the First Rotational Level in  $\text{H}_2$ ,  $\text{D}_2$  and HD Molecules and the Deuteron Quadrupole Moment, *Phys. Rev. Lett.* **125**, 253001 (2020).
  - [24] H. Jóźwiak, H. Cybulski, and P. Wcisło, Hyperfine components of rovibrational dipole transitions in HT and DT, *J. Quant. Spectrosc. Radiat. Transfer* **270**, 107662 (2021).
  - [25] H. Jóźwiak, H. Cybulski, and P. Wcisło, Hyperfine components of rovibrational quadrupole transitions in HD, *J. Quant. Spectrosc. Radiat. Transfer* **272**, 107753 (2021).

- [26] G. D. Dickenson, M. L. Niu, E. J. Salumbides, J. Komasa, K. S. E. Eikema, K. Pachucki, and W. Ubachs, Fundamental Vibration of Molecular Hydrogen, *Phys. Rev. Lett.* **110**, 193601 (2013).
- [27] M. Niu, E. Salumbides, G. Dickenson, K. Eikema, and W. Ubachs, Precision spectroscopy of the  $X^1\Sigma_g^+, v=0 \rightarrow 1(J=0-2)$  rovibrational splittings in  $H_2$ , HD and  $D_2$ , *J. Mol. Spectrosc.* **300**, 44 (2014).
- [28] D. Mondelain, S. Kass, T. Sala, D. Romanini, D. Gatti, and A. Campargue, Sub-MHz accuracy measurement of the  $S(2) 2-0$  transition frequency of  $D_2$  by Comb-Assisted Cavity Ring Down spectroscopy, *J. Mol. Spectrosc.* **326**, 5 (2016).
- [29] P. Wcisło, F. Thibault, M. Zaborowski, S. Wójtewicz, A. Cygan, G. Kowzan, P. Masłowski, J. Komasa, M. Puchalski, K. Pachucki, R. Ciuryło, and D. Lisak, Accurate deuterium spectroscopy for fundamental studies, *J. Quant. Spectrosc. Radiat. Transfer* **213**, 41 (2018).
- [30] L.-G. Tao, A.-W. Liu, K. Pachucki, J. Komasa, Y. R. Sun, J. Wang, and S.-M. Hu, Toward a Determination of the Proton-Electron Mass Ratio from the Lamb-Dip Measurement of HD, *Phys. Rev. Lett.* **120**, 153001 (2018).
- [31] F. M. J. Cozijn, P. Dupré, E. J. Salumbides, K. S. E. Eikema, and W. Ubachs, Sub-Doppler Frequency Metrology in HD for Tests of Fundamental Physics, *Phys. Rev. Lett.* **120**, 153002 (2018).
- [32] E. Fasci, A. Castrillo, H. Dinesan, S. Gravina, L. Moretti, and L. Gianfrani, Precision spectroscopy of HD at  $1.38 \mu m$ , *Phys. Rev. A* **98**, 022516 (2018).
- [33] M. Beyer, N. Hölsch, J. Hussels, C.-F. Cheng, E. J. Salumbides, K. S. E. Eikema, W. Ubachs, C. Jungen, and F. Merkt, Determination of the Interval Between the Ground States of Para- and Ortho- $H_2$ , *Phys. Rev. Lett.* **123**, 163002 (2019).
- [34] M. L. Diouf, F. M. J. Cozijn, B. Darquié, E. J. Salumbides, and W. Ubachs, Lamb-dips and lamb-peaks in the saturation spectrum of HD, *Opt. Lett.* **44**, 4733 (2019).
- [35] D. Mondelain, S. Kass, and A. Campargue, Transition frequencies in the  $(2-0)$  band of  $D_2$  with MHz accuracy, *J. Quant. Spectrosc. Radiat. Transfer* **253**, 107020 (2020).
- [36] S. Wójtewicz, R. Gotti, D. Gatti, M. Lamperti, P. Laporta, H. Jóźwiak, F. Thibault, P. Wcisło, and M. Marangoni, Accurate deuterium spectroscopy and comparison with *ab initio* calculations, *Phys. Rev. A* **101**, 052504 (2020).
- [37] J. Liu, E. J. Salumbides, U. Hollenstein, J. C. J. Koelemeij, K. S. E. Eikema, W. Ubachs, and F. Merkt, Determination of the ionization and dissociation energies of the hydrogen molecule, *J. Chem. Phys.* **130**, 174306 (2009).
- [38] C.-F. Cheng, J. Hussels, M. Niu, H. L. Bethlem, K. S. E. Eikema, E. J. Salumbides, W. Ubachs, M. Beyer, N. Hölsch, J. A. Agner, F. Merkt, L.-G. Tao, S.-M. Hu, and C. Jungen, Dissociation Energy of the Hydrogen Molecule at  $10^{-9}$  Accuracy, *Phys. Rev. Lett.* **121**, 013001 (2018).
- [39] N. Hölsch, M. Beyer, E. J. Salumbides, K. S. E. Eikema, W. Ubachs, C. Jungen, and F. Merkt, Benchmarking Theory with an Improved Measurement of the Ionization and Dissociation Energies of  $H_2$ , *Phys. Rev. Lett.* **122**, 103002 (2019).
- [40] S. Kass, C. Lauzin, J. Chaillot, and A. Campargue, The  $(2-0) R(0)$  and  $R(1)$  transition frequencies of HD determined to a  $10^{-10}$  relative accuracy by Doppler spectroscopy at 80 K, *Phys. Chem. Chem. Phys.* **24**, 23164 (2022).
- [41] H. Jóźwiak and P. Wcisło, Relative intensities of hyperfine components of rovibrational transitions in molecular hydrogen, *Phys. Rev. A* **105**, 062812 (2022).
- [42] This is not the case for *para*- $H_2$  and *para*- $T_2$ , which do not exhibit hyperfine structure, since the total nuclear spin is 0.
- [43] U. Fano and G. Racah, *Irreducible Tensorial Sets*, Cambridge Molecular Science (Academic Press, Cambridge, MA, 1959).
- [44] R. L. Cook and F. C. D. Lucia, Application of the theory of irreducible tensor operators to molecular hyperfine structure, *Am. J. Phys.* **39**, 1433 (1971).
- [45] E. Arimondo, M. Inguscio, and P. Violino, Experimental determinations of the hyperfine structure in the alkali atoms, *Rev. Mod. Phys.* **49**, 31 (1977).
- [46] M. Broyer, J. Vigué, and J. Lehmann, Effective hyperfine Hamiltonian in homonuclear diatomic molecules. Application to the B state of molecular iodine, *J. Phys. France* **39**, 591 (1978).
- [47] J. M. Brown and A. Carrington, *Rotational Spectroscopy of Diatomic Molecules*, Cambridge Molecular Science (Cambridge University Press, Cambridge, 2003).
- [48] G. Herzberg and L. Howe, The Lyman bands of molecular hydrogen, *Can. J. Phys.* **37**, 636 (1959).
- [49] J.-M. Hartmann, C. Boulet, and D. Robert, *Collisional Effects on Molecular Spectra* (Elsevier, Amsterdam, 2021).
- [50] P. Wcisło, I. Gordon, H. Tran, Y. Tan, S.-M. Hu, A. Campargue, S. Kass, D. Romanini, C. Hill, R. Kochanov, and L. Rothman, The implementation of non-Voigt line profiles in the HITRAN database:  $H_2$  case study, *J. Quant. Spectrosc. Radiat. Transfer* **177**, 75 (2016).
- [51] P. Wcisło, I. E. Gordon, C.-F. Cheng, S.-M. Hu, and R. Ciuryło, Collision-induced line-shape effects limiting the accuracy in Doppler-limited spectroscopy of  $H_2$ , *Phys. Rev. A* **93**, 022501 (2016).
- [52] G. Buffa and O. Tarrini, Hyperfine effects on spectral line shape. II. The case  $DCO^+-He$ , *J. Chem. Phys.* **134**, 174310 (2011).
- [53] M. Lamperti, L. Rutkowski, D. Ronchetti, D. Gatti, R. Gotti, G. Cerullo, F. Thibault, H. Jóźwiak, S. Wójtewicz, P. Masłowski, P. Wcisło, D. Polli, and M. Marangoni, Stimulated-Raman-scattering metrology, [arXiv:2207.03998](https://arxiv.org/abs/2207.03998).
- [54] G. Buffa, A. Di Lieto, P. Minguzzi, O. Tarrini, and M. Tonelli, Nuclear-quadrupole effects in the pressure broadening of molecular lines, *Phys. Rev. A* **37**, 3790 (1988).
- [55] S. Belli, G. Buffa, and O. Tarrini, Collisional coupling between hyperfine and Stark components of molecular spectra, *Phys. Rev. A* **55**, 183 (1997).
- [56] S. Green, Effect of nuclear hyperfine structure on microwave spectral pressure broadening, *J. Chem. Phys.* **88**, 7331 (1988).
- [57] G. Buffa and O. Tarrini, Hyperfine effects on collisional line shape. I. A self-consistent set of equations, *J. Chem. Phys.* **134**, 174309 (2011).
- [58] M. Słowiński, F. Thibault, Y. Tan, J. Wang, A.-W. Liu, S.-M. Hu, S. Kass, A. Campargue, M. Konefał, H. Jóźwiak *et al.*,  $H_2$ -He collisions: *Ab initio* theory meets cavity-enhanced spectra, *Phys. Rev. A* **101**, 052705 (2020).
- [59] P.-M. Flaud, J. Orphal, C. Boulet, and J.-M. Hartmann, Measurements and analysis of collisional line-mixing within nuclear hyperfine components of helium broadened HI lines, *J. Mol. Spectrosc.* **235**, 149 (2006).
- [60] Wrocław Centre for Networking and Supercomputing, <https://wcss.pl>.

- [61] J. Muentner and W. Klemperer, Hyperfine structure constants of HF and DF, *J. Chem. Phys.* **52**, 6033 (1970).
- [62] G. Cazzoli, L. Dore, C. Puzzarini, and S. Beninati, Millimeter- and submillimeter-wave spectrum of C<sup>17</sup>O. Rotational hyperfine structure analyzed using the Lamb-dip technique, *Phys. Chem. Chem. Phys.* **4**, 3575 (2002).
- [63] G. Klapper, L. Surin, F. Lewen, H. S. Müller, I. Pak, and G. Winnewisser, Laboratory precision measurements of the rotational spectrum of <sup>12</sup>C<sup>17</sup>O and <sup>13</sup>C<sup>17</sup>O, *Astrophys. J.* **582**, 262 (2003).
- [64] G. Cazzoli and C. Puzzarini, Hyperfine structure of the J = 1 ← 0 transition of H<sup>35</sup>Cl and H<sup>37</sup>Cl: Improved ground state parameters, *J. Mol. Spectrosc.* **226**, 161 (2004).
- [65] E. W. Kaiser, Dipole moment and hyperfine parameters of H<sup>35</sup>Cl and D<sup>35</sup>Cl, *J. Chem. Phys.* **53**, 1686 (1970).
- [66] D. W. Johnson and N. F. Ramsey, Stark hyperfine structure of hydrogen bromide, *J. Chem. Phys.* **67**, 941 (1977).
- [67] F. Van Dijk and A. Dymanus, Hyperfine structure of the rotational spectrum of HI in the submillimeter region, *Chem. Phys. Lett.* **2**, 235 (1968).
- [68] F. C. De Lucia, P. Helminger, and W. Gordy, Submillimeter-wave spectra and equilibrium structures of the hydrogen halides, *Phys. Rev. A* **3**, 1849 (1971).
- [69] A. O. G. Wallis and R. V. Krems, Magnetic Feshbach resonances in collisions of nonmagnetic closed-shell <sup>1</sup>Σ molecules, *Phys. Rev. A* **89**, 032716 (2014).



# Relative intensities of hyperfine components of rovibrational transitions in molecular hydrogen

Hubert Jóźwiak<sup>\*</sup> and Piotr Wcisło<sup>†</sup>

*Institute of Physics, Faculty of Physics, Astronomy and Informatics, Nicolaus Copernicus University in Toruń,  
Gudzińska 5, 87-100 Toruń, Poland*



(Received 7 April 2022; accepted 27 May 2022; published 21 June 2022)

We provide an analytical formula for the relative intensities of hyperfine components of rovibrational transitions in the  $H_2$ ,  $T_2$ , and *para*- $D_2$  isotopologues of hydrogen. The resulting expression is essentially an algebraic factor independent of vibrational quantum numbers. For other molecular hydrogen isotopologues, we show that it is possible to distinguish a certain class of hyperfine components which hold a similar property. The results presented here can be used as an approximation for rovibrational transitions in other diatomic molecules in a  $^1\Sigma$  electronic state with smaller rotational constant.

DOI: [10.1103/PhysRevA.105.062812](https://doi.org/10.1103/PhysRevA.105.062812)

## I. INTRODUCTION

Theoretical interest in hyperfine interactions in diatomic molecules is driven by remarkable precision of the experimental studies of rovibrational resonances [1–4] and increasing number of optically cooled and trapped species [5–7]. Careful analysis of the hyperfine splittings and Zeeman sublevels of ground and electronically excited states is crucial for preparing an efficient cooling cycle. This is due to the fact that hyperfine interactions mix different rotational states which might lead to losses from the optical cycling transition [8,9]. Hyperfine-resolved electronic transitions in molecular iodine are commonly used as frequency reference for the laser stabilization [10,11].

Apart from positions of hyperfine components of molecular resonances, knowledge about hyperfine intensity factors in molecular spectra is equally important. More than 40 years ago, careful analysis of intensity ratios in the spectra of LaO allowed for a determination of a spin-rotation interaction constant [12]. Based on a theory applicable to various Hund's coupling cases by Féménias [13], Merer *et al.* explained an unexpected intensity cancellation effect in hyperfine-resolved electronic transition in NbO [14]. Hyperfine intensity factors were also used in the analysis of two-color saturation spectroscopy of CN [15] and are of significant importance in high-resolution photoelectron spectroscopy [16].

Both positions and intensities of hyperfine components of rovibrational transitions in hydrogen molecular ions and neutral hydrogen isotopologues are crucial in the experimental studies of the rovibrational structure of their ground electronic states [1–4,17–20]. Comparison of the experimentally determined transition frequencies with calculations from first principles [21,22] opens the possibility to test the quantum electrodynamics for molecules [22–25] and to search for the physics beyond the standard model [26], such as extra dimensions [27] or new forces [28].

The need for careful analysis of hyperfine interactions in molecular hydrogen sparked several recent theoretical investigations. Dupré [29] reported hyperfine coupling constants for the first three vibrational levels ( $v = 0, 1, 2$ ,  $N = 1$ ) and studied hyperfine components of the 2-0 P(1) and R(1) lines in the HD isotopologue. In a series of papers [30–34] we reported hyperfine coupling constants for all bound states in the six isotopologues of hydrogen ( $H_2$ , HD,  $D_2$ , HT, DT, and  $T_2$ ) and we provided lists of positions and intensities of hyperfine components of all rovibrational electric dipole and quadrupole transitions within the ground electronic  $^1\Sigma$  state. At the same time, Komasa *et al.* [35] calculated coupling constants for several rovibrational states and analyzed the relative intensities of the hyperfine components of the P(1) and R(1) transitions from the first overtone and of the R(0) line from the fundamental band. In another paper [36], the authors determined the value of the hyperfine coupling constants for the  $v = 0$ ,  $N = 1$  level in HD,  $H_2$  and  $D_2$ , taking into account the nonadiabatic effects, which led to the most accurate determination of the quadrupole moment of the deuteron. Recently we have studied the hyperfine structure of several low-lying rovibrational levels of the excited double-well  $EF^1\Sigma_g^+$  electronic state of  $H_2$  [37].

Here, we analyze the vibrational dependence of the relative intensities of hyperfine components reported in Refs. [30–34]. We show analytically, that for the homonuclear isotopologues of hydrogen (except for the *ortho*- $D_2$ ), relative intensities are independent of both the initial and final vibrational quantum numbers. The relative intensity in this case is given by a simple algebraic factor which involves Wigner 6- $j$  symbols. For the remaining isotopologues of molecular hydrogen, we show that it is possible to distinguish a class of hyperfine transitions which also do not depend on the vibrational quantum numbers.

## II. RELATIVE INTENSITIES OF HYPERFINE COMPONENTS OF ROVIBRATIONAL TRANSITIONS

We consider hyperfine components of rovibrational transition between the initial ( $v_i, N_i$ ) and final ( $v_f, N_f$ ) rovibrational

<sup>\*</sup>hubert.jozwiak@doktorant.umk.pl

<sup>†</sup>piotr.wcislo@umk.pl

states. Here,  $\nu$  and  $N$  denote the vibrational and rotational quantum numbers, respectively. Following Refs. [30–34], we label the initial and final hyperfine states (the eigenstates of the effective hyperfine Hamiltonian) as  $|\nu_i; N_i F_i m_{F_i}(\pm)_i\rangle$  and  $|\nu_f; N_f F_f m_{F_f}(\pm)_f\rangle$ , respectively. The  $(\pm)$  label is defined in Sec. II B. The eigenstates  $|\nu; N F m_F(\pm)\rangle$  are related to the coupled basis vectors suitable for the homonuclear

$$|\nu; N F m_F(\pm)\rangle = \sum_I \sum_{N'=|F-I|}^{F+I} a_{N'I}^{\nu N F(\pm)} |\nu; (N'I) F m_F\rangle, \quad (1)$$

and the heteronuclear isotopologues

$$|\nu; N F m_F(\pm)\rangle = \sum_{F_1=|F-I_2|}^{F+I_2} \sum_{N'=|F_1-I_1|}^{F_1+I_1} a_{N'F_1}^{\nu N F(\pm)} |\nu; [(N'I_1) F_1 I_2] F m_F\rangle. \quad (2)$$

We recall that in the former case the two nuclear spin angular momenta are coupled to form the total nuclear spin angular momentum,  $\mathbf{I}$ , which is coupled to the rotational angular momentum,  $\mathbf{N}$ , to form the total angular momentum,  $\mathbf{F}$ . In the heteronuclear case one of the nuclear spin angular momenta,  $\mathbf{I}_1$ , is coupled to the rotational angular momentum, to form the intermediate angular momentum,  $\mathbf{F}_1$ . The latter is coupled to the remaining nuclear spin angular momentum,  $\mathbf{I}_2$ , to form the total angular momentum,  $\mathbf{F}$ . In both cases  $m_F$  denotes the projection of the total angular momentum on the laboratory-fixed frame.

In Eqs. (1) and (2),  $a_{N'I}^{\nu N F(\pm)}$  and  $a_{N'F_1}^{\nu N F(\pm)}$  denote the mixing coefficients which, in general, depend on the vibrational quantum number. Following Refs. [30–34] we neglect a very weak coupling between different rotational levels (the off-diagonal terms in the effective hyperfine Hamiltonian, which couple  $N$  and  $N' = N \pm 2$  levels are almost ten orders of magnitude smaller than the energy difference between the two rotational levels) and we simplify the notation:

$$a_{N'I}^{\nu N F(\pm)} = \delta_{NN'} a_{NI}^{\nu N F(\pm)} = \delta_{NN'} a_I^{\nu N F(\pm)}, \quad (3)$$

$$a_{N'F_1}^{\nu N F(\pm)} = \delta_{NN'} a_{NF_1}^{\nu N F(\pm)} = \delta_{NN'} a_{F_1}^{\nu N F(\pm)}. \quad (4)$$

For  $\text{H}_2$ , *para*- $\text{D}_2$ , and  $\text{T}_2$ , the remaining sum over  $I$  is trivial ( $a_I^{\nu N F(\pm)} = \delta_{I,1}$ ) and the coupled basis vectors are the eigenvectors of the effective hyperfine Hamiltonian:

$$|\nu; N F m_F(\pm)\rangle = |\nu; (NI) F m_F\rangle. \quad (5)$$

Relative intensities of hyperfine components of rovibrational transitions of rank  $n$  are given by the following formula (see Appendix A for a detailed discussion):

$$\frac{S_{\text{fi}}^{\text{HF}}}{S_{\text{fi}}^n} = \frac{|\langle \nu_f; N_f F_f(\pm)_f \| \mathbf{T}^n(\mathbf{M}) \| \nu_i; N_i F_i(\pm)_i \rangle|^2}{w_I f_n(N_i, N_f) |\mathbf{M}_{\text{fi}}^n|^2}, \quad (6)$$

where  $\mathbf{M}^n$  denotes the molecule-fixed multipole moment of the rovibrational transition and corresponds to the electric dipole moment,  $\mathbf{d}$ , for  $n = 1$  and to the electric quadrupole moment,  $\mathcal{Q}$ , for  $n = 2$ .  $\mathbf{T}^n(\mathbf{M})$  is a spherical tensor of rank  $n$  which describes the proper multipole moment.  $w_I$  is the nuclear degeneracy factor of the initial rotational state which equals  $(2I_1 + 1) \times (2I_2 + 1)$  for the heteronuclear isotopologues and  $(2I + 1)$  for the homonuclear species. The

$f_n(N_i, N_f)$  factor depends on the rank of the transition and the considered branch and is associated with the transformation of the multipole moment from the space-fixed frame, where the intensity of the transition is measured to the molecule-fixed frame, where the  $\mathbf{M}_{\text{fi}}^n$  is defined. For instance, for electric dipole transitions  $f_n(N_i, N_f)$  reduces to  $N_i + 1$  and to  $N_f$  for the transitions from the R ( $N_f = N_i + 1$ ) and P ( $N_f = N_i - 1$ ) branches, respectively (see Appendix A).

### A. Homonuclear isotopologues

The homonuclear isotopologues (except for the *ortho*- $\text{D}_2$  molecule) are well described by the set of quantum numbers which is proper for the coupled basis—the rotational quantum number,  $N$ , the total nuclear spin quantum number,  $I$ , and the total angular momentum quantum number,  $F$  [see Eq. (5)]. In this case, Eq. (6) reduces to (see Appendix B for the proof)

$$\frac{S_{\text{fi}}^{\text{HF}}}{S_{\text{fi}}^n} = \frac{(2F_f + 1)(2F_i + 1)}{2I + 1} \left\{ \begin{matrix} N_i & F_i & I \\ F_f & N_f & n \end{matrix} \right\}^2. \quad (7)$$

The quantities on the right-hand side of Eq. (7) do not depend on any vibrational quantum number. Thus, we conclude that for homonuclear isotopologues (except for *ortho*- $\text{D}_2$ ), the relative intensities of hyperfine components of rovibrational transitions are essentially the same for all vibrational bands. We note that Cook and De Lucia [38] derived a similar formula for the case of electric dipole ( $n = 1$ ) transitions as a first approximation of the relative intensities of hyperfine spectra. The authors neglected possible coupling between different intermediate quantum numbers (here: the total nuclear spin,  $I$ ), and, hence, they did not consider the vibrational dependence of hyperfine components in Ref. [38].

A formula similar to Eq. (7) was used by Korobov *et al.* [39] as an approximation of the relative intensities of hyperfine components of rovibrational quadrupole transitions ( $n = 2$ ) in  $\text{H}_2^+$  [see Eq. (22) therein]. The general formula used by the authors involved the mixing coefficients (see the discussion in Appendix B), which, in zeroth-order perturbation theory could be approximated as Dirac deltas. The difference between Eq. (7) and the formulas used in Ref. [39] stems from the presence of a nonzero electronic spin and a more complex coupling scheme used by the authors. We stress that, contrary to  $\text{H}_2^+$ , the result presented here is exact for the homonuclear isotopologues of hydrogen molecule (except for the *ortho*- $\text{D}_2$ ), since the hyperfine coupling between the rotational level is negligibly small [see Eqs. (3) and (4)].

Interestingly, Eq. (7) remains valid for heteronuclear molecules involving only one nuclei with nonzero spin, for which  $\mathbf{I}_1 = \mathbf{I}$  and  $\mathbf{I}_2 = 0$ . For such cases, the coupled basis vectors are the eigenvectors of the effective Hamiltonian, as in Eq. (5). In fact, the same formula (with  $n = 1$ ) was used in the interpretation of the hyperfine-resolved  $B^4\Pi-X^4\Sigma^-$  electronic transition in NbO [see Eq. (2) in Ref. [14]]. We recall that the spin of the  $^{93}\text{Nb}$  nucleus is  $I_1 = 9/2$  and that the spin of the most abundant isotope of oxygen,  $^{16}\text{O}$ , is  $I_2 = 0$ . Similarly, the intensity of hyperfine components of the electric dipole ( $n = 1$ ) transitions from the  $A^2\Sigma^+-X^2\Pi_{3/2}$  band in the  $^{32}\text{S}^1\text{H}$  molecule were approximated by a factor proportional to Eq. (7) [40] (the spins of the  $^1\text{H}$  and  $^{32}\text{S}$  nuclei are  $I_1 = 1/2$  and  $I_2 = 0$ , respectively). We note that the authors use this

term as a first approximation, due to the fact that hyperfine coupling between different  $J$  levels in the SH molecule is non-negligible. We conclude that Eq. (7) describes properly the relative intensities of hyperfine components of molecular transitions whenever the coupled basis from Eq. (5) is the eigenbasis of the effective hyperfine Hamiltonian.

### B. Heteronuclear isotopologues and *ortho*-D<sub>2</sub>

For the heteronuclear isotopologues each rovibrational level is split into  $(2I_1 + 1) \times (2I_2 + 1)$  hyperfine levels. The exception is the  $N = 0$ , which is degenerate (provided that one neglects the electron-coupled nuclear spin-spin interaction [41–44]), and the  $N = 1$  state for the HD and DT molecules, which has five hyperfine components. The *ortho*-D<sub>2</sub> isotopologue, which was not considered in Sec. II A, involves  $2I + 1$  hyperfine components for each rovibrational level, except for the  $N = 0$  level, which is also assumed to be degenerate.

Each hyperfine level is a superposition of the coupled basis vectors [Eqs. (1) and (2)]. However, a more detailed analysis shows that some (one—for the case of the  $N = 1$  level in HD and DT; two—for the remaining levels in these two isotopologues and for each rotational state in HT; and four—for each rotational state in *ortho*-D<sub>2</sub>) of the hyperfine states are well described by the coupled basis vectors,  $|\nu; [(NI_1)F_1I_2]Fm_F\rangle$  (or  $|\nu; (NI)Fm_F\rangle$  in the case of *ortho*-D<sub>2</sub>) and the linear combination [Eqs. (1) and (2)] becomes trivial. Other states (two—for all rotational states in HT and *ortho*-D<sub>2</sub> and four—for all rotational states in HD and DT) are superpositions of two coupled basis vectors [Eqs. (1) and (2)] which correspond to the same  $(N, F)$  quantum numbers. In order to distinguish between the nontrivial superposition states, we use the  $(\pm)$  labels, which denote the eigenstates with higher (+) and lower (−) energy. Therefore, one can distinguish four classes of possible hyperfine components of rovibrational transitions:

- (1) Class 1: transitions between hyperfine states described by coupled basis vectors.
- (2) Class 2: transitions from a state described by a coupled basis vector to a hyperfine superposition state.
- (3) Class 3: transitions from hyperfine superposition state to a state described by a coupled basis vector.
- (4) Class 4: transitions between hyperfine superposition states.

The number of transitions which belong to each class depends on the isotopologue, rank of the transition, and the considered rovibrational branch. Relative intensities of the hyperfine components from the first class of transitions exhibit no dependence on vibrational quantum numbers and are given by Eq. (7) for the case of *ortho*-D<sub>2</sub> and by (see Appendix B)

$$\frac{S_{\text{fi}}^{\text{HF}}}{S_{\text{fi}}^n} = \frac{(2F_f + 1)(2F_i + 1)(2F_{i_1} + 1)(2F_{i_2} + 1)}{(2I_1 + 1)(2I_2 + 1)} \times \left\{ \begin{matrix} F_{i_1} & F_i & I_2 \\ F_f & F_{i_1} & n \end{matrix} \right\}^2 \left\{ \begin{matrix} N_i & F_{i_1} & I_1 \\ F_{i_1} & N_f & n \end{matrix} \right\}^2 \quad (8)$$

for the heteronuclear isotopologues.

Relative intensities of the class-2 transitions do not depend on the initial vibrational quantum number. Similarly, relative intensities of the class-3 transitions do not depend on the final vibrational quantum number (see the central and bottom panel

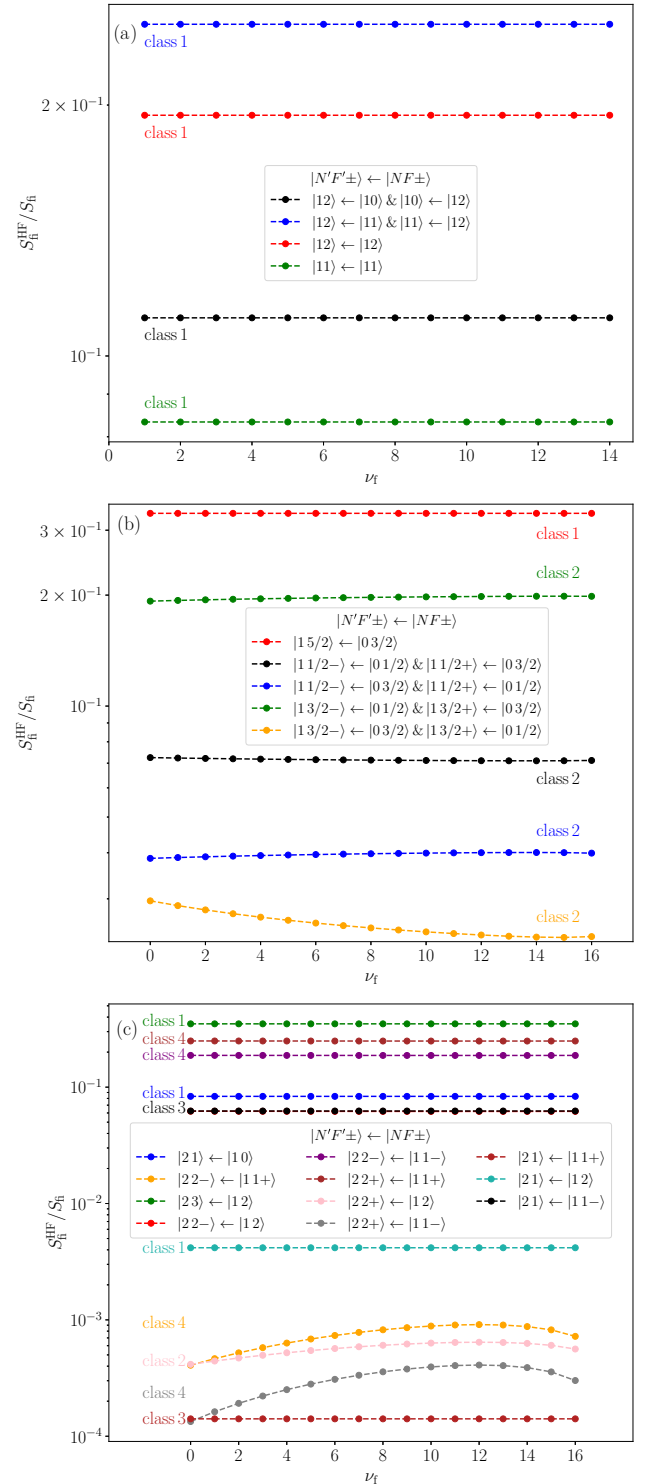


FIG. 1. Relative intensities of the 6 hyperfine components of the  $\nu_f=0$  Q(1) transitions in H<sub>2</sub> (top panel), 9 hyperfine components of the  $\nu_f=0$  R(0) transitions in HD (central panel), and 11 hyperfine components of the  $\nu_f=0$  R(1) transitions in HT (bottom panel).

in Fig. 1 and the discussion in the next section). Relative intensities of hyperfine transitions from the fourth class depend on both the initial and final quantum numbers through

the mixing coefficients, which are related to the hyperfine coupling constants in a nontrivial way.

### III. EXAMPLES OF THE CALCULATED RELATIVE INTENSITIES OF HYPERFINE COMPONENTS

An example of the values of relative intensities for different  $\nu_f=0$  Q(1) lines in  $H_2$  are shown in the top panel in Fig. 1. A quick inspection of Eq. (7) reveals that the six possible components have the relative intensity of 1/4, 7/36, 1/9, and 1/12. We note that the  $|12\rangle \leftarrow |10\rangle$  and  $|10\rangle \leftarrow |12\rangle$  transitions (as well as  $|12\rangle \leftarrow |11\rangle$  and  $|11\rangle \leftarrow |12\rangle$  transitions) have the same relative intensities.

We also provide an example for the heteronuclear isotopologues. The dependence of relative intensities of hyperfine components for the  $\nu_f=0$  R(0) lines in HD is presented in the central panel in Fig. 1. In this particular case, each rovibrational transition involves nine components: one class-1 component of relative intensity 1/3 (the top red line in the central panel in Fig. 1) and eight components of class 2. The relative intensity of class-2 transitions depends on the vibrational quantum number  $\nu_f$  through the mixing coefficients which slightly differ between vibrational bands.

Finally, the bottom panel in Fig. 1 presents relative intensities of 11 hyperfine components of the  $\nu_f=0$  R(1) lines in HT. The relative intensities of the three class-1 components are 7/20 (the top green line), 1/12 [the blue (dark gray) line], and 1/240 [the light-blue line in the center of Fig. 1(c)]. The R(1) transitions involve two class-2 and two class-3 components, out of which only one (the lower pink line) exhibits a significant dependence on  $\nu_f$ . Out of four class-4 hyperfine components of the R(1) transitions, only the two least intense [the gray and the orange at the bottom of Fig. 1(c)], that involve a change in the  $(\pm)$  sign, significantly depend on  $\nu_f$ .

### IV. CONCLUSIONS

We provided an analytical formula for the relative intensities of hyperfine transitions in the homonuclear isotopologues of hydrogen (except for the *ortho*- $D_2$  isotopologue). The formula is independent of both the initial and final vibrational quantum numbers. For the remaining isotopologues we distinguish a class of hyperfine transitions which share a similar property. The analytical formula remains valid for all diatomic molecules for which the coupled basis vectors are the eigenvectors of the effective hyperfine Hamiltonian. In particular, this condition is fulfilled by heteronuclear molecules involving only one nuclei with a nonzero spin. The results presented here are important for the accurate rovibrational spectroscopy of the six isotopologues of hydrogen, which is used for testing the quantum electrodynamics for molecules and searching for new physics beyond the standard model.

### ACKNOWLEDGMENTS

The research is financed from budget funds on science for years 2019–2023, as a research project under the “Diamen-towy Grant” program. P.W. is supported by the National Science Centre in Poland, Project No. 2019/35/B/ST2/01118. The research is a part of the program of the National Labora-

tory FAMO in Toruń, Poland. Calculations have been carried out using resources provided by Wrocław Centre for Network-ing and Supercomputing [45], Grant No. 546.

### APPENDIX A: INTENSITIES OF ROVIBRATIONAL TRANSITIONS AND THEIR HYPERFINE COMPONENTS

In this Appendix we justify the form of Eq. (6). We recall the most common formula for the intensities of rovibrational electric dipole and quadrupole transitions found in the literature [46–49]:

$$S_{fi}^{n=1} = \frac{2\pi^2}{3hc\epsilon_0} \nu_0 \frac{m}{2N_i + 1} P_{fi}(T) |d_{fi}|^2, \quad (A1)$$

$$S_{fi}^{n=2} = \frac{2\pi^4}{15hc^3\epsilon_0} \nu_0^3 C_{N_i} P_{fi}(T) |Q_{fi}|^2, \quad (A2)$$

where  $\nu_0$  is the transition frequency and  $d_{fi}$  or  $Q_{fi}$  denotes the matrix elements of the electric dipole and quadrupole moment operator, respectively.  $h$ ,  $c$ , and  $\epsilon_0$  are the Planck’s constant, the speed of light in vacuum, and vacuum permittivity, respectively. Although this is not relevant for the following discussion, we recall that the temperature-dependent factor,  $P_{fi}(T)$ , is given as

$$P_{fi}(T) = w_i(2N_i + 1) \frac{(e^{-E_i/k_B T} - e^{-E_f/k_B T})}{Q(T)}, \quad (A3)$$

with the partition function,  $Q(T)$ , defined as

$$Q(T) = \sum_k w_k (2N_k + 1) e^{-E_k/k_B T}. \quad (A4)$$

$w_k$  is the degeneracy factor of each rovibrational level due to nuclear spin statistics,  $E_k$  is the energy of the  $k$ th rovibrational state,  $k_B$  is the Boltzmann constant and  $T$  is the temperature.

The  $m$  factor in Eq. (A1) is simply  $N_i + 1$  for the R branch and  $N_i$  for the P branch. The  $C_{N_i}$  in Eq. (A2) takes the following form for the O branch:

$$C_{N_i} = \frac{3N_i(N_i - 1)}{2(2N_i + 1)(2N_i - 1)}; \quad (A5)$$

for the Q branch:

$$C_{N_i} = \frac{N_i(N_i + 1)}{(2N_i - 1)(2N_i + 3)}; \quad (A6)$$

and for the S branch:

$$C_{N_i} = \frac{3(N_i + 1)(N_i + 2)}{2(2N_i + 1)(2N_i + 3)}. \quad (A7)$$

The  $m$  and  $C_{N_i}$  factors are directly related to the transformation between the space-fixed frame of reference, where the intensity is measured, and the molecule frame of reference, where the transition moment (dipole or quadrupole) is defined. The formulas for the  $m$  and  $C_{N_i}$  factors can be justified by the relation between the reduced matrix elements of the spherical tensor of rank  $n$  (associated with the transition moment of rank  $n$ ) with the molecule-fixed transition moment [50]. Let us remind the transformation of a spherical tensor of rank  $n$  between the space-fixed ( $p$ ) and molecule-fixed ( $q$ ) frame of



reference:

$$T_p^{(n)}(\mathbf{M}) = \sum_{q=-n}^n \mathcal{D}_{pq}^{(n)}(\zeta)^* T_q^{(n)}(\mathbf{M}), \quad (\text{A8})$$

where  $\mathcal{D}$  is the rotational matrix and  $\zeta$  denotes the set of angles which describe the transformation from the space-fixed to molecule-fixed frame of reference. For transition moments which couple different rovibrational levels in a given electronic state, the space-fixed reduced matrix elements are transformed as follows [50]:

$$\begin{aligned} & \langle \nu_f; N_f || T^{(n)}(\mathbf{M}) || \nu_i; N_i \rangle \\ &= \langle \nu_f; N_f || \sum_{q=-n}^n \mathcal{D}_{.q}^{(n)*} T_q^{(n)}(\mathbf{M}) || \nu_i; N_i \rangle \\ &= (-1)^{N_f} \sqrt{(2N_i + 1)(2N_f + 1)} \begin{pmatrix} N_f & n & N_i \\ 0 & 0 & 0 \end{pmatrix} \mathbf{M}_{\text{fi}}^n, \end{aligned} \quad (\text{A9})$$

where the dot in the subscript in the second line of this equation comes from the fact that the reduced matrix element is independent of the space-fixed projection quantum numbers.

Using the tabulated values of the 3- $j$  coefficients for  $n = 1$  and  $n = 2$  (see, e.g., Appendix C in Ref. [50]) we obtain the following relations:

$$|\langle \nu_f; N_f || T^{(n=1)}(\mathbf{d}) || \nu_i; N_i \rangle|^2 = m |\mathbf{d}_{\text{fi}}|^2, \quad (\text{A10})$$

$$|\langle \nu_f; N_f || T^{(n=2)}(\mathcal{Q}) || \nu_i; N_i \rangle|^2 = (2N_i + 1) C_{N_i} |\mathcal{Q}_{\text{fi}}|^2. \quad (\text{A11})$$

In order to introduce a general formula for the relative intensities that could hold for both the electric dipole and quadrupole interactions, we introduce the factor  $f_n(N_i, N_f)$ , defined as

$$|\langle \nu_f; N_f || T^{(n)}(\mathbf{M}) || \nu_i; N_i \rangle|^2 = f_n(N_i, N_f) |\mathbf{M}_{\text{fi}}^n|^2. \quad (\text{A12})$$

In the case of hyperfine components of each rovibrational transition, we used in Refs. [30–34] the following formulas:

$$S_{\text{fi}}^{\text{HF}} = \frac{2\pi^2}{3hc\epsilon_0} \nu_0 \frac{1}{w_I(2N_i + 1)} P_{\text{fi}}(T) |d_{\text{fi}}^{\text{HF}}|^2, \quad (\text{A13})$$

$$S_{\text{fi}}^{\text{HF}} = \frac{2\pi^4}{15hc^3\epsilon_0} \nu_0^3 \frac{1}{w_I(2N_i + 1)} P_{\text{fi}}(T) |\mathcal{Q}_{\text{fi}}^{\text{HF}}|^2, \quad (\text{A14})$$

where the matrix elements of the transition moment between hyperfine levels are simply the matrix elements of the relevant spherical tensor operator:

$$d_{\text{fi}}^{\text{HF}} = \langle \nu_f; N_f F_f(\pm) || T^{(1)}(\mathbf{d}) || \nu_i; N_i F_i(\pm) \rangle, \quad (\text{A15})$$

$$\mathcal{Q}_{\text{fi}}^{\text{HF}} = \langle \nu_f; N_f F_f(\pm) || T^{(2)}(\mathcal{Q}) || \nu_i; N_i F_i(\pm) \rangle, \quad (\text{A16})$$

which we can write in general form as

$$\mathbf{M}_{\text{fi}}^{n\text{HF}} = \langle \nu_f; N_f F_f(\pm) || T^{(n)}(\mathbf{M}) || \nu_i; N_i F_i(\pm) \rangle. \quad (\text{A17})$$

Once again,  $n$  denotes the rank of the spectroscopic transition and equals  $n = 1$  for electric dipole and  $n = 2$  for electric quadrupole transitions.

This form allows us to write the relative intensity of hyperfine components of rovibrational transition of rank  $n$ , using

Eqs. (A1), (A2), (A12), (A13), and (A14) as

$$\frac{S_{\text{fi}}^{n\text{HF}}}{S_{\text{fi}}^n} = \frac{|\langle \nu_f; N_f F_f(\pm) || T^{(n)}(\mathbf{M}) || \nu_i; N_i F_i(\pm) \rangle|^2}{w_I f_n(N_i, N_f) |\mathbf{M}_{\text{fi}}^n|^2}. \quad (\text{A18})$$

## APPENDIX B: PROOF OF EQS. (7) AND (8)

### 1. Homonuclear case

Let us explicitly write Eq. (6) for the homonuclear case:

$$\begin{aligned} \frac{S_{\text{fi}}^{n\text{HF}}}{S_{\text{fi}}^n} &= \frac{1}{w_I f_n(N_i, N_f) |\mathbf{M}_{\text{fi}}^n|^2} \left( \sum_{I', I''} a_{I'}^{v_f N_f F_f(\pm)_f} a_{I''}^{v_i N_i F_i(\pm)_i} \right. \\ &\quad \times \langle \nu_f; (N_f I'_f) F_f || T^{(n)}(\mathbf{M}) || \nu_i; (N_i I'_i) F_i \rangle \\ &\quad \times \left( \sum_{I', I''} a_{I'}^{v_f N_f F_f(\pm)_f} a_{I''}^{v_i N_i F_i(\pm)_i} \right. \\ &\quad \times \langle \nu_f; (N_f I'_f) F_f || T^{(n)}(\mathbf{M}) || \nu_i; (N_i I''_i) F_i \rangle \left. \right)^*. \end{aligned} \quad (\text{B1})$$

The multipole moment operator does not modify either of the nuclear spins. Instead, it acts on the subspace of the eigenvectors of the rotational angular momentum. Making use of the well-known properties of the reduced matrix elements of the spherical tensor operators [50,51]

$$\begin{aligned} & \langle \nu_f; (N_f I'_f) F_f || T^{(n)}(\mathbf{M}) || \nu_i; (N_i I'_i) F_i \rangle \\ &= \delta_{I', I''} (-1)^{F_i + N_i + n + I'_i} \sqrt{(2F_f + 1)(2F_i + 1)} \\ &\quad \times \begin{Bmatrix} N_i & F_i & I'_i \\ F_f & N_f & n \end{Bmatrix} \langle \nu_f; N_f || T^{(n)}(\mathbf{M}) || \nu_i; N_i \rangle \end{aligned} \quad (\text{B2})$$

we obtain

$$\begin{aligned} \frac{S_{\text{fi}}^{n\text{HF}}}{S_{\text{fi}}^n} &= (-1)^{2(F_i + N_i + n)} \frac{(2F_f + 1)(2F_i + 1)}{w_I f_n(N_i, N_f) |\mathbf{M}_{\text{fi}}^n|^2} \\ &\quad \times \left( \sum_{I', I''} a_{I'}^{v_f N_f F_f(\pm)_f} a_{I''}^{v_i N_i F_i(\pm)_i} a_{I''}^{v_f N_f F_f(\pm)_f} a_{I'}^{v_i N_i F_i(\pm)_i} \right. \\ &\quad \times (-1)^{I' + I''} \begin{Bmatrix} N_i & F_i & I' \\ F_f & N_f & n \end{Bmatrix} \begin{Bmatrix} N_i & F_i & I'' \\ F_f & N_f & n \end{Bmatrix} \\ &\quad \times |\langle \nu_f; N_f || T^{(n)}(\mathbf{M}) || \nu_i; N_i \rangle|^2 \left. \right). \end{aligned} \quad (\text{B3})$$

Note that we simplified the notation by putting  $I' = I'_i = I'_f$  and  $I'' = I''_i = I''_f$ . In the next step we make use of the definition of the  $f_n(N_i, N_f)$  factor [Eq. (A12)] and we recall that  $F_i, N_f$ , and  $n$  are integers, which allows us to reduce the phase factor. Equation (B3) can now be written as

$$\begin{aligned} \frac{S_{\text{fi}}^{n\text{HF}}}{S_{\text{fi}}^n} &= \frac{(2F_f + 1)(2F_i + 1)}{w_I} \left( \sum_{I', I''} (-1)^{I' + I''} \right. \\ &\quad \times a_{I'}^{v_f N_f F_f(\pm)_f} a_{I''}^{v_i N_i F_i(\pm)_i} a_{I''}^{v_f N_f F_f(\pm)_f} a_{I'}^{v_i N_i F_i(\pm)_i} \\ &\quad \times \begin{Bmatrix} N_i & F_i & I' \\ F_f & N_f & n \end{Bmatrix} \begin{Bmatrix} N_i & F_i & I'' \\ F_f & N_f & n \end{Bmatrix} \left. \right). \end{aligned} \quad (\text{B4})$$



This formula is a generalization of Eqs. (14)–(51) in Ref. [52] to spectral transitions of rank  $n$  (the authors considered electric dipole transitions).

For the case of *ortho*-H<sub>2</sub>, *para*-D<sub>2</sub>, and *ortho*-T<sub>2</sub>, there is only one total nuclear spin  $I = I' = I'' = 1$  and mixing coefficients become trivial. This allows us to obtain Eq. (7):

$$\frac{S_{fi}^{nHF}}{S_{fi}^n} = \frac{(2F_f + 1)(2F_i + 1)}{(2I + 1)} \left\{ \begin{matrix} N_i & F_i & I \\ F_f & N_f & n \end{matrix} \right\}^2. \quad (B5)$$

For the case of *ortho*-D<sub>2</sub>, Eq. (B4) gives a general formula for the relative intensity of each component. For class-1 transitions it is easy to see that Eq. (B5) holds. For transitions of class 2 (or 3)  $I'_i = I''_i$  (or  $I'_f = I''_f$ ), the delta function from Eq. (B2) reduces both sums in Eq. (B4) ( $I' = I'' = I$ ) and additionally  $a_{I'}^{v_f N_i F_i(\pm)_i} = 1$  (or  $a_{I'}^{v_f N_f F_f(\pm)_f} = 1$ ). The relative intensities are given by [53]

$$\frac{S_{fi}^{nHF}}{S_{fi}^n} = \frac{(2F_f + 1)(2F_i + 1)}{w_I} \times |a_{I'}^{v_f N_f F_f(\pm)_f}|^2 \left\{ \begin{matrix} N_i & F_i & I \\ F_f & N_f & n \end{matrix} \right\}^2. \quad (B6)$$

This proves that transitions from class 2 (or class 3) do not depend on the initial (or final) vibrational quantum number.

A relation similar to Eq. (B4) was used in Ref. [39] in the analysis of the hyperfine components of electric quadrupole transitions in the hydrogen molecular ion [see Eq. (20) therein]. Since the H<sub>2</sub><sup>+</sup> involves a nonzero electronic spin, the analog of Eq. (B4) in Ref. [39] involves different angular momenta. As mentioned in Sec. II A, the authors recover a simplified formula for the relative intensities, Eq. (B5), by approximating the mixing coefficients as Dirac deltas in the zeroth-order perturbation theory.

## 2. Heteronuclear case

For the heteronuclear isotopologues, Eq. (6) takes the following form:

$$\begin{aligned} \frac{S_{fi}^{nHF}}{S_{fi}^n} = & \frac{1}{w_{I,f_n}(N_i, N_f) |\mathbf{M}_{fi}^n|^2} \left( \sum_{F'_{I_f}, F'_{I_i}} a_{F'_{I_f}}^{v_f N_f F_f(\pm)_f} a_{F'_{I_i}}^{v_i N_i F_i(\pm)_i} \right. \\ & \times \langle v_f; [(N_f I_f) F'_{I_f} I_2] F_f \| T^{(n)}(\mathbf{M}) \| v_i; [(N_i I_i) F'_{I_i} I_2] F_i \rangle \\ & \times \left( \sum_{F''_{I_f}, F''_{I_i}} a_{F''_{I_f}}^{v_f N_f F_f(\pm)_f} a_{F''_{I_i}}^{v_i N_i F_i(\pm)_i} \right. \\ & \times \langle v_f; [(N_f I_f) F''_{I_f} I_2] F_f \| T^{(n)}(\mathbf{M}) \| v_i; [(N_i I_i) F''_{I_i} I_2] F_i \rangle \left. \right)^* \end{aligned} \quad (B7)$$

Using the same arguments as those that lead from Eq. (B1) to Eq. (B3) we apply Eq. (B2) twice, along with Eq. (A12), which leads to

$$\begin{aligned} \frac{S_{fi}^{nHF}}{S_{fi}^n} = & (-1)^{2(N_f + 2n + F_i + I_1 + I_2)} \frac{(2F_f + 1)(2F_i + 1)}{w_I} \\ & \times \left( \sum_{F'_{I_f}, F'_{I_i}, F''_{I_f}, F''_{I_i}} (-1)^{F'_{I_i} + F'_{I_f} + F''_{I_i} + F''_{I_f}} \right. \\ & \times a_{F'_{I_f}}^{v_f N_f F_f(\pm)_f} a_{F'_{I_i}}^{v_i N_i F_i(\pm)_i} a_{F''_{I_f}}^{v_f N_f F_f(\pm)_f} a_{F''_{I_i}}^{v_i N_i F_i(\pm)_i} \\ & \times \sqrt{(2F'_{I_f} + 1)(2F'_{I_i} + 1)(2F''_{I_f} + 1)(2F''_{I_i} + 1)} \\ & \times \left\{ \begin{matrix} F'_{I_i} & F_i & I_2 \\ F_f & F'_{I_f} & n \end{matrix} \right\} \left\{ \begin{matrix} N_i & F'_{I_i} & I_1 \\ F_f & N_f & n \end{matrix} \right\} \\ & \times \left. \left\{ \begin{matrix} F''_{I_i} & F_i & I_2 \\ F_f & F''_{I_f} & n \end{matrix} \right\} \left\{ \begin{matrix} N_i & F''_{I_i} & I_1 \\ F_f & N_f & n \end{matrix} \right\} \right). \end{aligned} \quad (B8)$$

Note that the first phase factor is reduced to 1, since  $N_f$  and  $n$  are always integers, and

(1) if the two nuclear spins are integers (which is apparently not the case for any of the heteronuclear isotopologues of hydrogen), the total quantum number is also an integer, and the exponent is an even integer;

(2) if  $I_1$  is a half-integer and  $I_2$  is an integer,  $F_i$  is also a half-integer and as a result, the exponent is an even integer;

(3) if  $I_1$  is an integer and  $I_2$  is a half-integer (we chose this scheme for the case of HD [30,34] and DT [32,33]), then  $F_i$  is also a half-integer; the exponent is an even integer; and

(4) if both nuclear spins are half-integers (as in the case of HT [32,34]), the total quantum number, and the exponent is an even integer.

For class-1 transitions all four mixing coefficients equal one, and there is no need to sum over possible intermediate quantum numbers, since both the initial and final hyperfine states are well described by  $N$ ,  $F_1$ , and  $F$ . Setting  $F'_{I_i} = F''_{I_i} = F_{I_i}$  and  $F'_{I_f} = F''_{I_f} = F_{I_f}$  we obtain Eq. (8):

$$\begin{aligned} \frac{S_{fi}^{nHF}}{S_{fi}^n} = & \frac{(2F_f + 1)(2F_i + 1)(2F_{I_f} + 1)(2F_{I_i} + 1)}{(2I_1 + 1)(2I_2 + 1)} \\ & \times \left\{ \begin{matrix} F_{I_i} & F_i & I_2 \\ F_f & F_{I_f} & n \end{matrix} \right\}^2 \left\{ \begin{matrix} N_i & F_{I_i} & I_1 \\ F_f & N_f & n \end{matrix} \right\}^2. \end{aligned} \quad (B9)$$

Following the discussion for the *ortho*-D<sub>2</sub>, we note that class-2 (or class-3) transitions do not depend on the initial (or final) vibrational quantum numbers since their initial (or final) states are well described by  $N$ ,  $F_1$ , and  $F$  and the mixing coefficients simply equal 1. Finally, we note that Eq. (B8) is a generalization of Eqs. (14)–(51) in Ref. [52] to spectral transitions of rank  $n$  (the authors considered electric dipole transitions) and a different coupling scheme (the authors discussed the relative intensities in the coupling scheme suitable for homonuclear diatomics).

[1] S. Patra, M. Germann, J.-P. Karr, M. Haidar, L. Hilico, V. I. Korobov, F. M. J. Cozijn, K. S. E. Eikema, W. Ubachs, and J. C. J. Koelemeij, Proton-electron mass ratio from laser spectroscopy of HD<sup>+</sup> at the part-per-trillion level, *Science* **369**, 1238 (2020).

[2] S. Alighanbari, G. S. Giri, F. L. Constantin, V. I. Korobov, and S. Schiller, Precise test of quantum electrodynamics and determination of fundamental constants with HD<sup>+</sup> ions, *Nature (London)* **581**, 152 (2020).

- [3] A. Fast and S. A. Meek, Sub-ppb Measurement of a Fundamental Band Rovibrational Transition in HD, *Phys. Rev. Lett.* **125**, 023001 (2020).
- [4] A. Fast and S. A. Meek, Precise measurement of the  $D_2$   $S_1(0)$  vibrational transition frequency, *Mol. Phys.*, e1999520 (2021).
- [5] E. S. Shuman, J. F. Barry, and D. DeMille, Laser cooling of a diatomic molecule, *Nature (London)* **467**, 820 (2010).
- [6] A. L. Collopy, S. Ding, Y. Wu, I. A. Finneran, L. Anderegg, B. L. Augenbraun, J. M. Doyle, and J. Ye, 3D Magneto-Optical Trap of Yttrium Monoxide, *Phys. Rev. Lett.* **121**, 213201 (2018).
- [7] S. Truppe, S. Marx, S. Kray, M. Doppelbauer, S. Hofsäss, H. C. Schewe, N. Walter, J. Pérez-Ríos, B. G. Sartakov, and G. Meijer, Spectroscopic characterization of aluminum monofluoride with relevance to laser cooling and trapping, *Phys. Rev. A* **100**, 052513 (2019).
- [8] O. Grasdjik, O. Timgren, J. Kastelic, T. Wright, S. Lamoreaux, D. DeMille, K. Wenz, M. Aitken, T. Zelevinsky, T. Winick, and D. Kowall, CeNTREX: A new search for time-reversal symmetry violation in the  $^{205}\text{Tl}$  nucleus, *Quantum Sci. Technol.* **6**, 044007 (2021).
- [9] S. Hofsäss, M. Doppelbauer, S. C. Wright, S. Kray, B. G. Sartakov, J. Pérez-Ríos, G. Meijer, and S. Truppe, Optical cycling of AlF molecules, *New J. Phys.* **23**, 075001 (2021).
- [10] J. Ye, L. Robertsson, S. Picard, L.-S. Ma, and J. Hall, Absolute frequency atlas of molecular  $I_2$  lines at 532 nm, *IEEE Trans. Instrum. Meas.* **48**, 544 (1999).
- [11] F.-L. Hong, Optical frequency standards for time and length applications, *Meas. Sci. Technol.* **28**, 012002 (2017).
- [12] R. Bacis, R. Collomb, and N. Bessis, Hyperfine structure of the  $B^2\Sigma \rightarrow X^2\Sigma$  transition of the LaO molecule, *Phys. Rev. A* **8**, 2255 (1973).
- [13] J. L. Féménias, Intensity factors in molecular spectra, *Phys. Rev. A* **15**, 1625 (1977).
- [14] A. J. Merer, U. Sassenberg, J.-L. Féménias, and G. Cheval, Intensity cancellation effects in the hyperfine structure of molecules with large nuclear spins: The 6500 Å system of NbO, *J. Chem. Phys.* **86**, 1219 (1987).
- [15] D. Forthomme, C. P. McRaven, T. J. Sears, and G. E. Hall, Collinear two-color saturation spectroscopy in CN A–X (1–0) and (2–0) bands, *J. Mol. Spectrosc.* **296**, 36 (2014).
- [16] M. Germann and S. Willitsch, Fine- and hyperfine-structure effects in molecular photoionization. I. General theory and direct photoionization, *J. Chem. Phys.* **145**, 044314 (2016).
- [17] M. L. Diouf, F. M. J. Cozijn, B. Darquié, E. J. Salumbides, and W. Ubachs, Lamb-dips and Lamb-peaks in the saturation spectrum of HD, *Opt. Lett.* **44**, 4733 (2019).
- [18] M. L. Diouf, F. M. J. Cozijn, K.-F. Lai, E. J. Salumbides, and W. Ubachs, Lamb-peak spectrum of the HD (2-0) P(1) line, *Phys. Rev. Research* **2**, 023209 (2020).
- [19] T.-P. Hua, Y. Sun, and S.-M. Hu, Dispersion-like lineshape observed in cavity-enhanced saturation spectroscopy of HD at 1.4  $\mu\text{m}$ , *Opt. Lett.* **45**, 4863 (2020).
- [20] A. Castrillo, E. Fasci, and L. Gianfrani, Doppler-limited precision spectroscopy of HD at 1.4  $\mu\text{m}$ : An improved determination of the  $R(1)$  center frequency, *Phys. Rev. A* **103**, 022828 (2021).
- [21] P. Czachorowski, M. Puchalski, J. Komasa, and K. Pachucki, Nonadiabatic relativistic correction in  $H_2$ ,  $D_2$ , and HD, *Phys. Rev. A* **98**, 052506 (2018).
- [22] J. Komasa, M. Puchalski, P. Czachorowski, G. Łach, and K. Pachucki, Rovibrational energy levels of the hydrogen molecule through nonadiabatic perturbation theory, *Phys. Rev. A* **100**, 032519 (2019).
- [23] M. Puchalski, J. Komasa, P. Czachorowski, and K. Pachucki, Complete  $\alpha^6 m$  Corrections to the Ground State of  $H_2$ , *Phys. Rev. Lett.* **117**, 263002 (2016).
- [24] V. I. Korobov, L. Hilico, and J.-P. Karr, Fundamental Transitions and Ionization Energies of the Hydrogen Molecular Ions with Few ppt Uncertainty, *Phys. Rev. Lett.* **118**, 233001 (2017).
- [25] M. Zaborowski, M. Słowiński, K. Stankiewicz, F. Thibault, A. Cygan, H. Jóźwiak, G. Kowzan, P. Masłowski, A. Nishiyama, N. Stolarczyk, S. Wójtecz, R. Ciuryło, D. Lisak, and P. Wcisło, Ultrahigh finesse cavity-enhanced spectroscopy for accurate tests of quantum electrodynamics for molecules, *Opt. Lett.* **45**, 1603 (2020).
- [26] W. Ubachs, J. Koelemeij, K. Eikema, and E. Salumbides, Physics beyond the Standard Model from hydrogen spectroscopy, *J. Mol. Spectrosc.* **320**, 1 (2016).
- [27] E. J. Salumbides, A. N. Schellekens, B. Gato-Rivera, and W. Ubachs, Constraints on extra dimensions from precision molecular spectroscopy, *New J. Phys.* **17**, 033015 (2015).
- [28] E. J. Salumbides, J. C. J. Koelemeij, J. Komasa, K. Pachucki, K. S. E. Eikema, and W. Ubachs, Bounds on fifth forces from precision measurements on molecules, *Phys. Rev. D* **87**, 112008 (2013).
- [29] P. Dupré, Hyperfine transitions in the first overtone mode of hydrogen deuteride, *Phys. Rev. A* **101**, 022504 (2020).
- [30] H. Jóźwiak, H. Cybulski, and P. Wcisło, Positions and intensities of hyperfine components of all rovibrational dipole lines in the HD molecule, *J. Quant. Spectrosc. Radiat. Transfer* **253**, 107171 (2020).
- [31] H. Jóźwiak, H. Cybulski, and P. Wcisło, Hyperfine components of all rovibrational quadrupole transitions in the  $H_2$  and  $D_2$  molecules, *J. Quant. Spectrosc. Radiat. Transfer* **253**, 107186 (2020).
- [32] H. Jóźwiak, H. Cybulski, and P. Wcisło, Hyperfine structure of quadrupole rovibrational transitions in tritium-bearing hydrogen isotopologues, *J. Quant. Spectrosc. Radiat. Transfer* **256**, 107255 (2020).
- [33] H. Jóźwiak, H. Cybulski, and P. Wcisło, Hyperfine components of rovibrational dipole transitions in HT and DT, *J. Quant. Spectrosc. Radiat. Transfer* **270**, 107662 (2021).
- [34] H. Jóźwiak, H. Cybulski, and P. Wcisło, Hyperfine structure of rovibrational quadrupole transitions in HD, *J. Quant. Spectrosc. Radiat. Transfer* **272**, 107753 (2021).
- [35] J. Komasa, M. Puchalski, and K. Pachucki, Hyperfine structure in the HD molecule, *Phys. Rev. A* **102**, 012814 (2020).
- [36] M. Puchalski, J. Komasa, and K. Pachucki, Hyperfine Structure of the First Rotational Level in  $H_2$ ,  $D_2$  and HD Molecules and the Deuteron Quadrupole Moment, *Phys. Rev. Lett.* **125**, 253001 (2020).
- [37] H. Jóźwiak, H. Cybulski, A. Grabowski, and P. Wcisło, Hyperfine structure of the  $EF^1\Sigma_g^+$  state in  $H_2$ , *Phys. Rev. A* **104**, 012808 (2021).
- [38] R. L. Cook and F. C. D. Lucia, Application of the theory of irreducible tensor operators to molecular hyperfine structure, *Am. J. Phys.* **39**, 1433 (1971).
- [39] V. I. Korobov, P. Danev, D. Bakalov, and S. Schiller, Laser-stimulated electric quadrupole transitions in the molecular hydrogen ion  $H_2^+$ , *Phys. Rev. A* **97**, 032505 (2018).

- [40] A. Fast and S. A. Meek, Frequency comb referenced spectroscopy of A-X 0-0 transitions in SH, *J. Chem. Phys.* **154**, 114304 (2021).
- [41] H. Y. Carr and E. M. Purcell, Interaction between nuclear spins in HD gas, *Phys. Rev.* **88**, 415 (1952).
- [42] N. F. Ramsey and E. M. Purcell, Interactions between nuclear spins in molecules, *Phys. Rev.* **85**, 143 (1952).
- [43] R. F. Code and N. F. Ramsey, Molecular-beam magnetic resonance studies of HD and D<sub>2</sub>, *Phys. Rev. A* **4**, 1945 (1971).
- [44] M. Puchalski, J. Komasa, and K. Pachucki, Nuclear Spin-Spin Coupling in HD, HT, and DT, *Phys. Rev. Lett.* **120**, 083001 (2018).
- [45] <https://wcss.pl>.
- [46] G. Karl and J. D. Poll, On the quadrupole moment of the hydrogen molecule, *J. Chem. Phys.* **46**, 2944 (1967).
- [47] N. Rich, J. Johns, and A. McKellar, Frequency and intensity measurements in the fundamental infrared band of HD, *J. Mol. Spectrosc.* **95**, 432 (1982).
- [48] S. Kassı and A. Campargue, Electric quadrupole and dipole transitions of the first overtone band of HD by CRDS between 1.45 and 1.33  $\mu\text{m}$ , *J. Mol. Spectrosc.* **267**, 36 (2011).
- [49] A. Campargue, S. Kassı, K. Pachucki, and J. Komasa, The absorption spectrum of H<sub>2</sub>: CRDS measurements of the (2-0) band, review of the literature data and accurate *ab initio* line list up to 35 000  $\text{cm}^{-1}$ , *Phys. Chem. Chem. Phys.* **14**, 802 (2012).
- [50] J. M. Brown and A. Carrington, *Rotational Spectroscopy of Diatomic Molecules*, Cambridge Molecular Science (Cambridge University Press, Cambridge, UK, 2003).
- [51] U. Fano and G. Racah, *Irreducible Tensorial Sets*, Cambridge Molecular Science (Academic, New York, 1959).
- [52] P. R. Bunker and P. Jensen, *Molecular Symmetry and Spectroscopy* (NRC Research Press, Ottawa, Ontario, Canada, 2006).
- [53] The formula for the class-3 transitions differs only in the indices of the mixing coefficients.



OPEN

# Magic wavelength for a rovibrational transition in molecular hydrogen

H. Jóźwiak<sup>✉</sup> & P. Wcisło<sup>✉</sup>

Molecular hydrogen, among other simple calculable atomic and molecular systems, possesses a huge advantage of having a set of ultralong living rovibrational states that make it well suited for studying fundamental physics. Further experimental progress will require trapping cold  $H_2$  samples. However, due to the large energy of the first electronic excitation, the conventional approach to finding a magic wavelength does not work for  $H_2$ . We find a rovibrational transition for which the AC Stark shift is largely compensated by the interplay between the isotropic and anisotropic components of polarizability. The residual AC Stark shift can be completely eliminated by tuning the trapping laser to a specific “magic wavelength” at which the weak quadrupole polarizability cancels the residual dipole polarizability.

Accurate spectroscopy of simple calculable atomic and molecular systems has proven its importance for studying fundamental physics and testing quantum theory. A particularly important role has been played by atomic hydrogen. In addition to its large contribution to the development and tests of quantum electrodynamics, accurate spectroscopy of atomic hydrogen provides the energy scale for ab initio quantum calculations (the Rydberg constant) and gives an important contribution to the global adjustment of fundamental constants<sup>1</sup>. Several other calculable systems, such as helium atom<sup>2,3</sup>,  $HD^+$  ion<sup>4,5</sup>, exotic atoms<sup>6–8</sup> or hydrogen molecule, contribute to testing quantum theory, determining fundamental constants and searching for new physics beyond the standard model<sup>9–11</sup>. When considering a long-term perspective,  $H_2$  possesses a huge advantage over other system, which is a set of a few hundred ultralong (a week) living rovibrational states<sup>12</sup>. The ratio of the natural linewidth to the optical transition frequency is on the order of  $10^{-20}$  which, for a typical ability of resolving a  $10^{-4}$  fraction of the linewidth, gives the ultimate limit on testing fundamental physics with  $H_2$  at  $10^{-24}$  relative accuracy.

Fast progress in molecular hydrogen spectroscopy was triggered by implementing optical frequency combs over a decade ago. The present most accurate measurements were obtained with infrared-ultraviolet double resonance spectroscopy in molecular beam<sup>13,14</sup> and cavity-enhanced spectroscopy: for HD, the sub-Doppler saturation technique was implemented<sup>15,16</sup>, while for homonuclear isotopologues, due to the lack of dipole transitions, Doppler-limited techniques were used<sup>17,18</sup> (the Doppler-limited technique was also used for HD<sup>19,20</sup>). The highest accuracy, 13 kHz, was obtained for the HD isotopologue<sup>13</sup>. The factors that limit the accuracy depend on the approach used. For instance, for HD molecular beam experiments, the accuracy is limited by the residual first-order Doppler shift to the 12 kHz level<sup>13</sup>.

To maintain the fast progress in  $H_2$  rovibrational spectroscopy and progress towards the fundamental limitation, a cold  $H_2$  sample has to be trapped in an optical lattice. The first attempt to manipulate the  $H_2$  velocity with a laser field was demonstrated in Ref.<sup>21</sup>. Recent progress in laser technology already gives the capability to generate a 1 mK-deep optical-dipole trap with a continuous-wave (CW) laser coupled to a high-finesse cavity<sup>22</sup>. At this point, it is important to study this problem from the theory side and check if it is possible to eliminate the AC Stark effect caused by the trapping laser field. The conventional magic-wavelength approach<sup>23</sup> is not applicable to the  $H_2$  molecule (see the next paragraph). Here, we demonstrate a new approach to finding a magic wavelength. First, we take advantage of the anisotropy of the dipole polarizability in  $H_2$  to eliminate the dominant part of the light shift by choosing an excited state with a favorable spatial orientation. Second, we calculate that the residual light shift can be completely eliminated by tuning the trap laser close to one of the rovibrational quadrupole transitions. We consider the  $S(0) 1-0$  line in the  $H_2$  isotopologue. For this line, the magic wavelength is 2413 nm (0.23 MHz red detuned from the center of the  $Q(2) 1-0$  line).

Institute of Physics, Faculty of Physics, Astronomy and Informatics, Nicolaus Copernicus University in Toruń, Grudziądzka 5, 87-100 Toruń, Poland. ✉email: hubert.jozwiak@doktorant.umk.pl; piotr.wcislo@fizyka.umk.pl

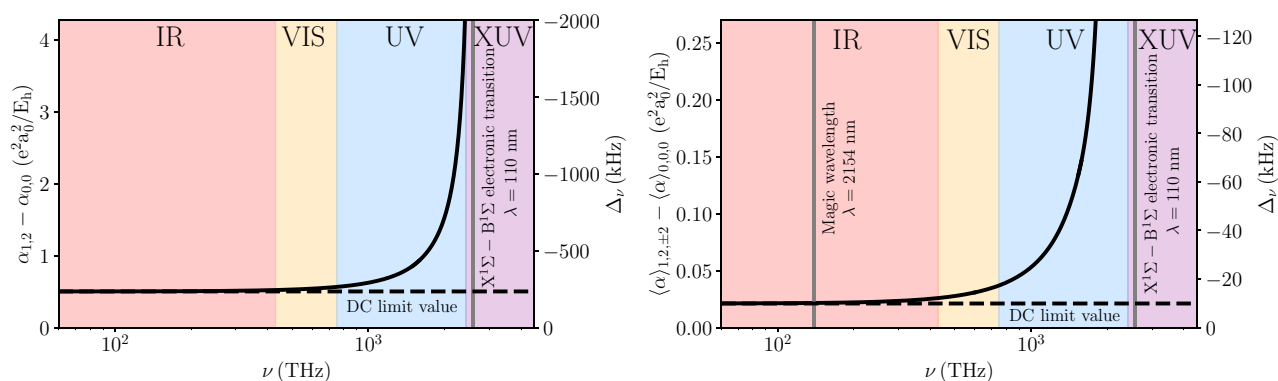


**Figure 1.** Difference between the dynamical polarizabilities in the excited,  $|v = 1, N = 2, M_N = \pm 2\rangle$ , and ground,  $|v = 0, N = 0, M_N = 0\rangle$ , states (based on the data from Ref. H<sub>2</sub><sup>24</sup>). The left panel shows the difference between the isotropic polarizabilities, while the right panel shows the difference between state-averaged polarizabilities. This plot involves only the dipole contribution to the polarizability. The secondary axis presents the light shift calculated for the trap depth of 0.12 mK, which corresponds to the trap laser intensity of 0.1 MW/mm<sup>2</sup>.

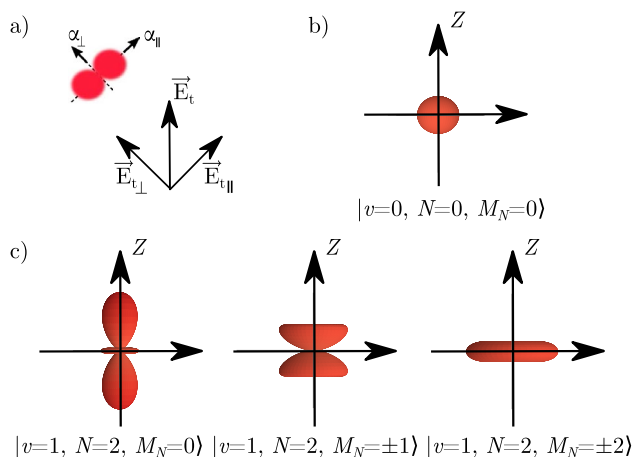


**Figure 2.** Orientation of the H<sub>2</sub> molecule with respect to the trapping field  $\vec{E}_t$  and the definition of the parallel ( $\alpha_{\parallel}$ ) and perpendicular ( $\alpha_{\perp}$ ) components of the dipole polarizability (a). Panels (b, c) show the angle distribution of the H<sub>2</sub> molecule in the ground and excited states, respectively (the squared modulus of  $Y_0^0$  and  $Y_{M_N}^2$  spherical harmonics), over which the two components of the polarizability are averaged to obtain  $\langle \alpha \rangle_{v,N,M_N}$ .

### Dipole polarizability (the interplay between the isotropic and anisotropic components)

The isotropic dipole polarizability,  $\alpha$ , of the H<sub>2</sub> molecule in its ground electronic state,  $X^1\Sigma_g^+$ , is at the level of  $5.4 e^2 a_0^2 / E_h$ <sup>24,25</sup>, which for power densities achievable with today laser technology (1 MW/mm<sup>2</sup> for a 0.4 mm laser beam waist)<sup>22</sup> gives a depth of an optical dipole trap at the level of 1 mK. However, the polarizabilities in the vibrational ground,  $v = 0$ , and first excited,  $v = 1$ , states differ by almost 10%<sup>25</sup>; hence, the enormous light shift will ultimately dominate the uncertainty budget for the determination of the energies of the rovibrational transitions (the AC Stark effect not only shifts the effective position of a resonance but also causes its inhomogeneous broadening). The conventional approach to finding a magic wavelength used in atomic spectroscopy<sup>23</sup> is not applicable to H<sub>2</sub> molecule. The two spectroscopic states share the same electronic state; hence, the difference in polarizabilities changes very slowly with laser wavelength for the infrared and visible regions and is close to its DC value. The difference increases in the UV range<sup>24,26</sup>, see the left panel in Fig. 1. One may expect it to cross zero after the first electronic line, i.e., in the XUV range ( $\lambda < 110$  nm), which is, however, difficult to access with available laser technology.

For the case of the  $X^1\Sigma_g^+$ -state H<sub>2</sub> molecule, we can benefit from the anisotropy of the dipole polarizability. When the electric field is aligned with the molecular axis, the static polarizability is larger by a quarter than  $\alpha$ , and when the field is perpendicular, it is smaller by one eighth; the corresponding polarizability components are denoted by  $\alpha_{\parallel}$  and  $\alpha_{\perp}$ ; see Fig. 2a. The relative contribution of the two components to the effective polarizability in a given rovibrational state is determined by the direction of the trap laser electric field vector,  $\vec{E}_t$ , and the distribution of the molecular orientation in the laboratory frame, which is described by a specific spherical harmonic. We assume  $\vec{E}_t$  to be directed along the Z axis in the laboratory frame. For cold *para*-H<sub>2</sub> experiments, one of the



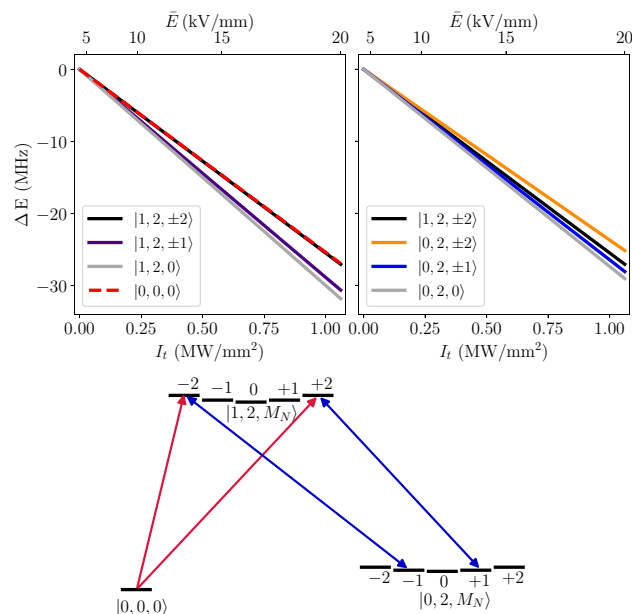


**Figure 3.** Stark shifts (the DC-limit values) of the  $|v, N, M_N\rangle$  levels in  $H_2$ :  $|0, 0, 0\rangle$ , and  $|1, 2, M_N\rangle$  (top left panel), and  $|0, 2, M_N\rangle$  and  $|1, 2, \pm 2\rangle$  (top right panel). The probe laser drives the  $\Delta M_N = \pm 2$  components of the 1–0 S(0) transition (red arrows in the bottom panel), while the trapping laser couples the  $|1, 2, \pm 1\rangle$  states with the  $|0, 2, \pm 1\rangle$  states, the two components of the 1–0 Q(2) line (blue arrows in the bottom panel).

most preferable transitions to consider is the 1–0 S(0) line that links the  $|v = 0, N = 0\rangle$  and  $|v = 1, N = 2\rangle$  states; we focus the analysis on this transition. The distribution of the molecular orientation in these two states is given by  $Y_0^0$  and  $Y_{M_N}^2$  spherical harmonics; see Fig. 2b and c, respectively. For the ground state, the angle distribution is isotropic, and the corresponding average of  $\alpha_{\parallel}$  and  $\alpha_{\perp}$  simply gives  $\alpha$ . For the excited state, the angle distribution depends on the projection of the rotational angular momentum,  $M_N$ ; see Fig. 2c. For  $M_N = 0$ , a molecule is more likely to orient along the electric field, while for  $M_N = \pm 2$ , it is more likely to be orthogonal; hence, the corresponding average polarizability,  $\langle\alpha\rangle$ , is larger for  $M_N = 0$  and smaller for  $M_N = \pm 2$ . Direct integration of the two polarizability components over the angle distribution gives a general relation

$$\langle\alpha\rangle = \alpha - \frac{2}{3}\gamma \frac{3M_N^2 - N(N+1)}{(2N-1)(2N+3)}, \quad (1)$$

where  $\alpha = \frac{1}{3}(\alpha_{\parallel} + 2\alpha_{\perp})$  and  $\gamma = \alpha_{\parallel} - \alpha_{\perp}$  are called isotropic and anisotropic dipole polarizabilities. The Supplementary Information provides a general derivation of Eq. (1) based on the time-dependent perturbation theory and irreducible spherical tensor formulation; we further use this derivation for the determination of the dynamic quadrupole polarizability. The isotropic and anisotropic polarizabilities depend on the rovibrational state; hence, we label them  $\alpha_{v,N}$  and  $\gamma_{v,N}$ . According to Eq. (1), the average value also depends on the  $M_N$  number; hence, we label it  $\langle\alpha\rangle_{v,N,M_N}$ . The isotropic components in the ground and excited states differ by 9.3%, i.e.,  $\alpha_{0,0} = 5.4179 e^2 a_0^2/E_h$  and  $\alpha_{1,2} = 5.9193 e^2 a_0^2/E_h$  (the numbers in this paragraph are the DC-limit values). It follows from Eq. (1), however, that the difference is reduced to below 0.4% when considering the  $M_N = \pm 2$  angle distribution of the excited state, i.e.,  $\langle\alpha\rangle_{0,0,0} = \alpha_{0,0} = 5.4179 e^2 a_0^2/E_h$  and  $\langle\alpha\rangle_{1,2,\pm 2} = \alpha_{1,2} - \frac{4}{21}\gamma_{1,2} = 5.4390 e^2 a_0^2/E_h$ . In Fig. 1, the right panel, shows the polarizability difference for this transition as a function of laser frequency. The upper left panel in Fig. 3, shows the corresponding Stark shifts,  $\Delta E_{v,N,M_N}^{\text{dip}} = -(\bar{E}^2/2)\langle\alpha\rangle_{v,N,M_N}$ , of the ground state and the three components of the excited state.

To drive the transitions from the ground  $M_N = 0$  to excited  $M_N = \pm 2$  states, one should properly choose the polarization of the probe laser. The 1–0 S(0) transition is a quadrupole transition (the electric dipole transitions are not allowed in  $H_2$ ); hence, the light-molecule interaction does not probe the local electric field vector but the gradients of its components. Therefore, the selection rule does not involve only the relative orientation of the polarizations of the trap and probe lasers but also the direction of the probe laser propagation. The spherical components of the electric field gradient corresponding to the  $\Delta M_N = \pm 2$  transitions are (see the Supplementary Information for details)

$$T_{\pm 2}^{(2)}(\nabla \vec{E}_p) = -\frac{(\partial_X E_{p,X} - \partial_Y E_{p,Y}) \pm i(\partial_X E_{p,Y} + \partial_Y E_{p,X})}{2\sqrt{6}}, \quad (2)$$

where  $\vec{E}_p$  is the probe laser electric field vector. Assuming that the wavelength is much shorter than the beam diameter, we can neglect the gradient components perpendicular to the direction of the probe laser propagation; hence, the  $(\partial_X E_{p,X} - \partial_Y E_{p,Y})$  term can be neglected. For the assumed  $\vec{E}_t$  directed along the Z-axis, a

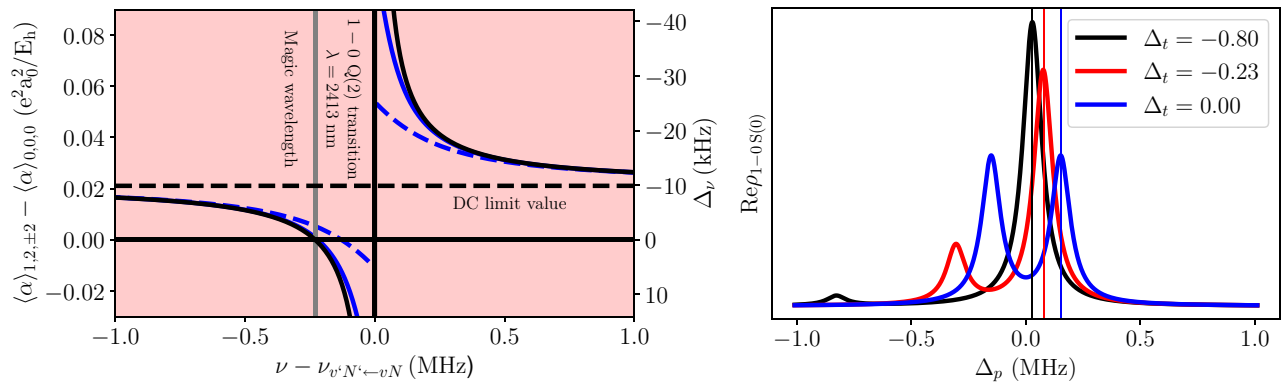


**Figure 4.** (Left panel) Difference between the average dynamical polarizabilities in the excited and ground states in  $\text{H}_2$ . This figure shows the same quantity as the right panel Fig. 1, but also includes the quadrupole contribution and is zoomed around a close neighborhood of the 1–0 Q(2) line. In the simplest approach, the quadrupole contribution was calculated using perturbation theory (Eq. (3)), see the black solid line. Full calculations show that in a close neighborhood of a resonance, the quadrupole contribution to the polarizability depends on the intensity of a trap laser; for 1 MW/mm<sup>2</sup> the actual difference between the polarizabilities considerably deviates from the perturbation approach (see the blue dashed line), while for 0.1 MW/mm<sup>2</sup> the deviation is almost negligible (see the solid blue line). (Right panel) Shape of the 1–0 S(0) transition in  $\text{H}_2$  determined by solving a full master equation for a three-level system with two laser fields (see Supplementary Information) for different values of the detuning of the trapping laser,  $\Delta_t$ , and for  $I_t = 1$  MW/mm<sup>2</sup>.

simple example of the configuration able to drive the  $\Delta M_N = \pm 2$  transitions is  $\vec{E}_p$  directed along the  $X$ -axis and propagating along the  $Y$ -axis. At this point, the selection rule does not depend on the direction of the trap laser propagation. It matters when considering the quadrupole contribution to the polarization; see the next paragraph. For that case, we assume the trap laser to propagate along the  $Y$ -axis (the same as for the probe laser).

**Quadrupole polarizability: the magic wavelength.** The difference in dynamic polarizabilities, shown in the right panel in Fig. 1, involves only the dipole contribution. Once the dominant part of the difference in dipole polarizability is eliminated by a proper choice of the ground and excited rovibrational states (see the red dashed and black solid lines in the upper left panel in Fig. 3), the quadrupole contribution is not negligible when the laser is tuned close to one of the rovibrational transitions. The dynamic quadrupole polarizability can be calculated as a sum over contributions from all rovibrational lines and electronic resonances. The electronic contribution to the quadrupole polarizability is negligible<sup>27</sup>. The quadrupole contribution to the polarizability is nonnegligible only when the trap laser is parked close to one of the rovibrational lines; in this regime, the contributions of all the other lines are completely negligible, and the full sum over the rovibrational transitions simplifies to

$$\langle \alpha^{\text{quad}}(v) \rangle_{vN} = \frac{k^2}{24h} (2N+1)(2N'+1) \left( \begin{matrix} N & 2 & N' \\ 0 & 0 & 0 \end{matrix} \right)^2 \sum_{M'_N = -|N'|}^N \frac{|\langle vN | Q(r_{\text{HH}}) | v'N' \rangle|^2}{\nu_{v'N' \leftarrow vN} - \nu} \left| \sum_{p=\pm 1} \begin{pmatrix} N & 2 & N' \\ -M_N & p & M'_N \end{pmatrix} \right|^2, \quad (3)$$

where  $k = 2\pi\nu/c$  is the magnitude of the wavevector of the trapping laser,  $h$  is the Planck constant,  $\nu_{v'N' \leftarrow vN}$  denotes the frequency of the  $v'N' \leftarrow vN$  rovibrational transition,  $Q(r_{\text{HH}})$  is the quadrupole transition moment function, which depends on the internuclear distance,  $r_{\text{HH}}$ , and  $\begin{pmatrix} j_1 & j_2 & j \\ m_1 & m_2 & m \end{pmatrix}$  is the Wigner 3- $j$  symbol. In the Supplementary Information, we give a full derivation and a detailed discussion of Eq. (3). The left panel in Fig. 4 shows a close neighborhood of the Q(2) 1–0 line (at 2413 nm) that includes not only the dipole contribution to the polarizability difference, shown in the right panel in Fig. 1, but also the quadrupole contribution [given by Eq. (3)] due to the proximity of the Q(2) 1–0 line. Effectively, the difference in polarizabilities between the ground and excited states crosses zero at the point marked by the vertical gray line in the left panel in Fig. 4. At this wavelength, the total light shift vanishes, and following Refs.<sup>23,28</sup>, we refer to it as a *magic wavelength*. A major difference from a typical magic-wavelength approach is that in our case, the trap laser must be spectrally very narrow, and its absolute frequency must be well controlled, i.e., the value and dispersion of the trap laser frequency should be much smaller than 100 kHz. This is achievable with current optical frequency comb and ultrastable laser technologies.

The magic wavelength can be achieved by tuning the frequency of the trapping laser close to any of the rovibrational transitions involving either the  $|v=0, N=0, M_N=0\rangle$  or  $|v=1, N=2, M_N=\pm 2\rangle$  levels. Taking into account the selection rules associated with the 3- $j$  symbols in Eq. (3) ( $|N-2| \leq N' \leq N+2$ ,  $N'=0 \leftrightarrow N=0$ , and  $M'_N = M_N \pm 1$ ) and the fact that there are 15 vibrational levels in  $\text{H}_2$ , we can identify 44 magic wavelengths for the 1–0 S(0) line. Table 1 lists the magic wavelengths that are the most beneficial from the perspective of experimental realization, i.e., the wavelengths are accessible with today laser technology and the magic

$\lambda_m$ (nm)	$\delta_m$ (MHz)	$\Omega$ (MHz)	Transition	$M'_N$	$\Delta_\nu$ (kHz)
1189	-0.10	0.014	2-0 S(0)	$\pm 1$	- 50
1207	0.08	0.016	3-1 S(2)	$\pm 3/\pm 1$	- 50/- 80
1318	0.04	0.012	3-1 Q(2)	$\pm 1$	70
2154	0.40	0.037	2-1 S(2)	$\pm 3/\pm 1$	- 32/- 57
2413	-0.23	0.028	1-0 Q(2)	$\pm 1$	8
2558	0.40	0.037	2-1 Q(2)	$\pm 1$	- 48
3003	-0.33	0.033	1-0 O(4)	$\pm 3/\pm 1$	- 2/14

**Table 1.** Magic wavelengths ( $\lambda_m$ ) for the 1-0 S(0) transition calculated using time-dependent perturbation theory. In the second column ( $\delta_m$ ) an accurate value of the magic wavelength is given respectively to the neighboring transition (specified in column 4).  $\Omega$  is a Rabi frequency and  $\Delta_\nu$  a light shift of the given  $\Delta M_N$  component.  $\Omega$  and  $\Delta_\nu$  are calculated for the trap depth of 10  $\mu$ K, which corresponds to the trap laser intensity of 8 kW/mm<sup>2</sup>

wavelength detunings,  $\delta_m$ , and Rabi frequencies,  $\Omega$ , are the largest. Note that for transitions involving  $N' = 4$  levels there are two  $M'_N$  components contributing to the sum in Eq. (3).

In a typical atomic dipole trap, the trap laser is far detuned from the nearest transition to avoid scattering losses<sup>29</sup>. Here this condition is followed, but the frequency regime is different. Instead of a strong and wide electronic line, we have an ultranarrow quadrupole rovibrational line; the few hundred kilohertz detuning is many orders of magnitude larger than the line width.

### The limitation of the perturbation approach

In this work, we consider very strong laser fields closely tuned to rovibrational resonance; hence, we should check if the perturbation approach [Eq. (3)] and the black curve in the left panel in Fig. 4 is applicable. We do so by solving a full master equation for a three-level system interacting with two laser fields; see the Supplementary Information. In the extreme case (opposite to the perturbation approach regime), a strong trap laser is tuned to the resonance center, and the probe laser measures an Autler-Townes doublet; see the black curve in the right panel in Fig. 4. As the trap laser is getting detuned, one of the components becomes weaker, and effectively, for larger detunings, the doublet turns into a single line shifted from the unperturbed position, which reproduces the ordinary light shift described by perturbation theory [Eq. (3)]. The right panel in Fig. 4 shows the exact results of the polarizability difference calculated from the position of a dominant component of the Autler-Townes doublet (see Supplementary Information for details). The blue solid and dashed lines are for trap laser intensities of 0.1 and 1 MW/mm<sup>2</sup>, respectively. These curves show that the resonant quadrupole contribution to the polarizability difference does not diverge to  $\pm\infty$  at the line center as predicted by the perturbation approach, and hence, the corresponding light shift cannot be arbitrarily large. Furthermore, the intensity of the trap laser is limited by a demand that the polarizability should not depend on laser intensity (otherwise, only a fraction of the trapped molecules will be tuned to a magic wavelength). The left panel in Fig. 4 shows that this condition is fulfilled for trap laser intensities of 0.1 MW/mm<sup>2</sup> but not for 1 MW/mm<sup>2</sup>. This limits the maximum depth of an optical dipole trap for which the magic wavelength can be applied; the trap depth corresponding to the intensity of 0.1 MW/mm<sup>2</sup> is 0.12 mK.

### Choice of a magic wavelength

At first glance, one could suspect that the most appropriate choice of a magic wavelength from the perspective of experimental realization would be either the 2-1 S(2) or 2-1 Q(2) line, since for these two cases the detuning of the trap laser is the largest and the strength of the trap laser-molecule coupling (expressed by the Rabi frequency  $\Omega$ ) is the largest, as shown in Table 1. In this analysis, we should, however, take into account one more factor. The position of the trap laser resonance (an example of which is shown in Fig. 4) is also shifted by the strong trap laser field, i.e., the denominator in Eq. (3) also depends on the  $M_N$  and  $M'_N$  numbers. We should ensure that the light shift of the trap laser resonance is much smaller than the magic wavelength detuning,  $\delta_m$ . The last column in Table 1 shows the light shifts for each trap laser resonance for trap laser intensity corresponding to the trap depth of 10  $\mu$ K. The table shows that the optimal choice of a magic wavelength is 2413 nm (-0.23 MHz from the 1-0 Q(2) transition). For the trap depth of 10  $\mu$ K, the light shift of the 1-0 Q(2) line (the  $M_N$  components marked with blue arrows in Fig. 3) is 8 kHz, which is over an order of magnitude smaller than the magic wavelength detuning  $\delta_m = -0.23$  MHz.

### Outlook

We demonstrate a new approach to reducing the AC Stark shift for rovibrational lines in hydrogen molecule. We analyze the *para*-H<sub>2</sub> case; we identify a magic wavelength for the 1-0 S(0) at 2413 nm (-0.23 MHz from the 1-0 Q(2) transition). Important future directions include analysis of *ortho*-H<sub>2</sub> and other molecular hydrogen isotopologues that have nonzero nuclear spin and the corresponding hyperfine structure. The hyperfine structure will make the analysis more complex, but the much richer structure of states opens a perspective for identifying a combination of levels that is more beneficial from the perspective of experimental implementation of the magic wavelength.

## Data availability

The datasets generated and analysed during the current study are available from the corresponding author on reasonable request.

Received: 25 May 2022; Accepted: 5 August 2022

Published online: 25 August 2022

## References

1. Beyer, A. *et al.* The Rydberg constant and proton size from atomic hydrogen. *Science* **358**, 79–85. <https://doi.org/10.1126/science.aah6677> (2017).
2. Zheng, X. *et al.* Measurement of the frequency of the  $2^3S - 2^3P$  transition of  $^4\text{He}$ . *Phys. Rev. Lett.* **119**, 263002. <https://doi.org/10.1103/PhysRevLett.119.263002> (2017).
3. Thomas, K. F. *et al.* Direct measurement of the forbidden  $2^3S_1 \rightarrow 3^3S_1$  atomic transition in helium. *Phys. Rev. Lett.* **125**, 013002. <https://doi.org/10.1103/PhysRevLett.125.013002> (2020).
4. Alighanbari, S., Giri, G. S., Constantin, F. L., Korobov, V. I. & Schiller, S. Precise test of quantum electrodynamics and determination of fundamental constants with  $\text{HD}^+$  ions. *Nature* **581**, 152–158. <https://doi.org/10.1038/s41586-020-2261-5> (2020).
5. Patra, S. *et al.* Proton-electron mass ratio from laser spectroscopy of  $\text{HD}^+$  at the part-per-trillion level. *Science* **369**, 1238–1241. <https://doi.org/10.1126/science.aba0453> (2020).
6. Pohl, R. *et al.* The size of the proton. *Nature* **466**, 213–216. <https://doi.org/10.1038/nature09250> (2010).
7. Hori, M. *et al.* Buffer-gas cooling of antiprotonic helium to 1.5 to 1.7 K, and antiproton-to-electron mass ratio. *Science* **354**, 610–614. <https://doi.org/10.1126/science.aaf6702> (2016).
8. Krauth, J. J. *et al.* Measuring the  $\alpha$ -particle charge radius with muonic helium-4 ions. *Nature* **589**, 527–531. <https://doi.org/10.1038/s41586-021-03183-1> (2021).
9. Salumbides, E. J., Schellekens, A. N., Gato-Rivera, B. & Ubachs, W. Constraints on extra dimensions from precision molecular spectroscopy. *New J. Phys.* **17**, 033015. <https://doi.org/10.1088/1367-2630/17/3/033015> (2015).
10. Ubachs, W., Koelemeij, J., Eikema, K. & Salumbides, E. Physics beyond the standard model from hydrogen spectroscopy. *J. Mol. Spectrosc.* **320**, 1–12. <https://doi.org/10.1016/j.jms.2015.12.003> (2016).
11. Safronova, M. S. *et al.* Search for new physics with atoms and molecules. *Rev. Mod. Phys.* **90**, 025008. <https://doi.org/10.1103/RevModPhys.90.025008> (2018).
12. Wolniewicz, L., Simbotin, I. & Dalgarno, A. Quadrupole transition probabilities for the excited rovibrational states of  $\text{H}_2$ . *Astrophys. J. Suppl. Ser.* **115**, 293–313. <https://doi.org/10.1086/313091> (1998).
13. Fast, A. & Meek, S. A. Sub-ppb measurement of a fundamental band rovibrational transition in HD. *Phys. Rev. Lett.* **125**, 023001. <https://doi.org/10.1103/PhysRevLett.125.023001> (2020).
14. Fast, A. & Meek, S. A. Precise measurement of the  $\text{D}_2$   $S_1(0)$  vibrational transition frequency. *Mol. Phys.* **1**, e1999520. <https://doi.org/10.1080/00268976.2021.1999520> (2021).
15. Cozijn, F. M. J., Dupré, P., Salumbides, E. J., Eikema, K. S. E. & Ubachs, W. Sub-Doppler frequency metrology in HD for tests of fundamental physics. *Phys. Rev. Lett.* **120**, 153002. <https://doi.org/10.1103/PhysRevLett.120.153002> (2018).
16. Tao, L.-G. *et al.* Toward a determination of the proton-electron mass ratio from the lamb-dip measurement of HD. *Phys. Rev. Lett.* **120**, 153001. <https://doi.org/10.1103/PhysRevLett.120.153001> (2018).
17. Wcislo, P. *et al.* Accurate deuterium spectroscopy for fundamental studies. *J. Quant. Spectrosc. Radiat. Transf.* **213**, 41–51. <https://doi.org/10.1016/j.jqsrt.2018.04.011> (2018).
18. Zaborowski, M. *et al.* Ultrahigh finesse cavity-enhanced spectroscopy for accurate tests of quantum electrodynamics for molecules. *Opt. Lett.* **45**, 1603–1606. <https://doi.org/10.1364/OL.389268> (2020).
19. Fasci, E. *et al.* Precision spectroscopy of HD at  $1.38\mu\text{m}$ . *Phys. Rev. A* **98**, 022516. <https://doi.org/10.1103/PhysRevA.98.022516> (2018).
20. Castrillo, A., Fasci, E. & Gianfrani, L. Doppler-limited precision spectroscopy of HD at  $1.4\mu\text{m}$ : An improved determination of the  $R(1)$  center frequency. *Phys. Rev. A* **103**, 022828. <https://doi.org/10.1103/PhysRevA.103.022828> (2021).
21. Ramirez-Serrano, J., Strecker, K. E. & Chandler, D. W. Modification of the velocity distribution of  $\text{H}_2$  molecules in a supersonic beam by intense pulsed optical gradients. *Phys. Chem. Chem. Phys.* **8**, 2985. <https://doi.org/10.1039/b603177c> (2006).
22. Turnbaugh, C. *et al.* High-power near-concentric Fabry–Perot cavity for phase contrast electron microscopy. *Rev. Sci. Instrum.* **92**, 053005. <https://doi.org/10.1063/5.0045496> (2021).
23. Katori, H., Takamoto, M., Palchikov, V. G. & Ovsiannikov, V. D. Ultrastable optical clock with neutral atoms in an engineered light shift trap. *Phys. Rev. Lett.* **91**, 173005. <https://doi.org/10.1103/PhysRevLett.91.173005> (2003).
24. Raj, A., Hamaguchi, H. & Witek, H. A. Polarizability tensor invariants of  $\text{H}_2$ , HD, and  $\text{D}_2$ . *J. Chem. Phys.* **148**, 104308. <https://doi.org/10.1063/1.5011433> (2018).
25. Kołos, W. & Wolniewicz, L. Polarizability of the hydrogen molecule. *J. Chem. Phys.* **46**, 1426–1432. <https://doi.org/10.1063/1.1840870> (1967).
26. Ford, A. L. & Browne, J. C. Direct-resolvent-operator computations on the hydrogen-molecule dynamic polarizability, Rayleigh, and Raman scattering. *Phys. Rev. A* **7**, 418–426. <https://doi.org/10.1103/physreva.7.418> (1973).
27. Miliordos, E. & Hunt, K. L. C. Dependence of the multipole moments, static polarizabilities, and static hyperpolarizabilities of the hydrogen molecule on the H–H separation in the ground singlet state. *J. Chem. Phys.* **149**, 234103. <https://doi.org/10.1063/1.5066308> (2018).
28. Kotochigova, S. & Tiesinga, E. Controlling polar molecules in optical lattices. *Phys. Rev. A* **73**, 041405. <https://doi.org/10.1103/PhysRevA.73.041405> (2006).
29. Grimm, R., Weidemüller, M. & Ovchinnikov, Y. B. Optical dipole traps for neutral atoms. *Adv. At. Mol. Opt. Phys.* **1**, 95–170. [https://doi.org/10.1016/s1049-250x\(08\)60186-x](https://doi.org/10.1016/s1049-250x(08)60186-x) (2000).

## Acknowledgements

The research is financed from the budgetary funds on science projected for 2019–2023 as a research project under the “Diamentowy Grant” program. P.W. is supported by the National Science Centre in Poland, Project No. 2019/35/B/ST2/01118. The research is a part of the program of the National Laboratory FAMO in Toruń, Poland.

## Author contributions

H.J. and P.W. both contributed to the idea conception, theory development and preparation of the manuscript. H.J. implemented the codes for finding magic wavelength and solving the master equation for the three-level system.

## Competing interests

The authors declare no competing interests.

## Additional information

**Supplementary Information** The online version contains supplementary material available at <https://doi.org/10.1038/s41598-022-18159-y>.

**Correspondence** and requests for materials should be addressed to H.J. or P.W.

**Reprints and permissions information** is available at [www.nature.com/reprints](http://www.nature.com/reprints).

**Publisher's note** Springer Nature remains neutral with regard to jurisdictional claims in published maps and institutional affiliations.






**Open Access** This article is licensed under a Creative Commons Attribution 4.0 International License, which permits use, sharing, adaptation, distribution and reproduction in any medium or format, as long as you give appropriate credit to the original author(s) and the source, provide a link to the Creative Commons licence, and indicate if changes were made. The images or other third party material in this article are included in the article's Creative Commons licence, unless indicated otherwise in a credit line to the material. If material is not included in the article's Creative Commons licence and your intended use is not permitted by statutory regulation or exceeds the permitted use, you will need to obtain permission directly from the copyright holder. To view a copy of this licence, visit <http://creativecommons.org/licenses/by/4.0/>.

© The Author(s) 2022



RESEARCH ARTICLE | MARCH 05 2024

## Hyperfine and Zeeman interactions in ultracold collisions of molecular hydrogen with atomic lithium <sup>EP</sup>

Hubert Jóźwiak  ; Timur V. Tschertbul  ; Piotr Wcisło 




*J. Chem. Phys.* 160, 094304 (2024)


<https://doi.org/10.1063/5.0193148>



CrossMark




Lock-in Amplifier



Boxcar Averager

Boost Your Optics and Photonics Measurements

 Zurich Instruments

[Find out more](#)

# Hyperfine and Zeeman interactions in ultracold collisions of molecular hydrogen with atomic lithium

Cite as: J. Chem. Phys. 160, 094304 (2024); doi: 10.1063/5.0193148

Submitted: 21 December 2023 • Accepted: 8 February 2024 •

Published Online: 5 March 2024



Hubert Jóźwiak,<sup>1,a)</sup>  Timur V. Tscherbul,<sup>2</sup>  and Piotr Wcisło<sup>1</sup> 

## AFFILIATIONS

<sup>1</sup>Institute of Physics, Faculty of Physics, Astronomy and Informatics, Nicolaus Copernicus University in Toruń, Grudziądzka 5, 87-100 Toruń, Poland

<sup>2</sup>Department of Physics, University of Nevada, Reno, Nevada 89557, USA

<sup>a)</sup>Author to whom correspondence should be addressed: [hubert.jozwiak@doktorant.umk.pl](mailto:hubert.jozwiak@doktorant.umk.pl)

## ABSTRACT

We present a rigorous quantum scattering study of the effects of hyperfine and Zeeman interactions on cold Li–H<sub>2</sub> collisions in the presence of an external magnetic field using a recent *ab initio* potential energy surface. We find that the low-field-seeking states of H<sub>2</sub> predominantly undergo elastic collisions: the ratio of elastic-to-inelastic cross sections exceeds 100 for collision energies below 100 mK. Furthermore, we demonstrate that most inelastic collisions conserve the space-fixed projection of the nuclear spin. We show that the anisotropic hyperfine interaction between the nuclear spin of H<sub>2</sub> and the electron spin of Li can have a significant effect on inelastic scattering in the ultracold regime, as it mediates two processes: the electron spin relaxation in lithium and the nuclear spin–electron spin exchange. Given the predominance of elastic collisions and the propensity of inelastic collisions to retain H<sub>2</sub> in its low-field-seeking states, our results open up the possibility of sympathetic cooling of molecular hydrogen by atomic lithium, paving the way for future exploration of ultracold collisions and high-precision spectroscopy of H<sub>2</sub> molecules.

Published under an exclusive license by AIP Publishing. <https://doi.org/10.1063/5.0193148>

## I. INTRODUCTION

Cold collisions and chemical reactions involving molecular hydrogen have been the subject of much theoretical and experimental interest due to their significance in astrochemistry and cold controlled chemistry.<sup>1,2</sup> In particular, the F + H<sub>2</sub> → HF + H reaction, despite having a high energetic barrier of ~800 K, occurs quite efficiently in cold environments (10–100 K) and is the only known source of HF in the interstellar medium.<sup>3</sup> Experiments on the Penning ionization of H<sub>2</sub> upon collisions with metastable (<sup>3</sup>S) helium revealed sub-K shape resonances,<sup>4</sup> isotopic effects,<sup>5</sup> and a significant role of molecular rotation<sup>6</sup> and anisotropy of the molecule–atom interaction<sup>7</sup> in cold reaction dynamics. Cold collisions of vibrationally excited isotopologues of molecular hydrogen (HD and D<sub>2</sub>) with D<sub>2</sub>,<sup>8,9</sup> H<sub>2</sub>,<sup>9</sup> and He<sup>10,11</sup> revealed interesting stereodynamic effects,<sup>12</sup> interference patterns, and shape resonances, which enable the quantum interference-based coherent control of the collision outcome.<sup>13,14</sup>

Previous theoretical studies of cold collisions involving molecular hydrogen and its isotopologues<sup>12,15–25</sup> neglected the effects of hyperfine interactions and Zeeman shifts on collisions with H<sub>2</sub>, which could be substantial at ultralow temperatures. For instance, the hyperfine splitting of the  $v = 0, N = 1$  state in *ortho*-H<sub>2</sub> is ~600 kHz<sup>26–28</sup> (or  $k_B$  20  $\mu$ K). The hyperfine structure of this state in an external magnetic field is quite complex, comprising nine Zeeman states.<sup>26</sup> However, ultracold collision dynamics involving these states and the mechanisms driving particular transitions (e.g., nuclear spin relaxation) remain unexplored.

An additional motivation to study the role of hyperfine and Zeeman interactions in cold collisions of H<sub>2</sub> molecules is related to high-precision spectroscopy of molecular hydrogen. Accurate determination of energy intervals between rovibrational states in hydrogen (with a relative accuracy reaching the sub-ppb level<sup>29,30</sup>) allows for performing stringent tests of quantum electrodynamics<sup>31–33</sup> and for putting constraints on the strength of hypothetical interactions beyond the standard model.<sup>34</sup> To overcome Doppler broadening

and enhance the precision of the determined transition frequencies, experimental groups employ saturation techniques,<sup>35,36</sup> molecular beams<sup>29,30</sup> or cooling of the gas sample<sup>37–39</sup> (down to 57 K). Further improvement in high-precision spectroscopy would be possible if molecular hydrogen could be cooled and trapped. Recently, we proposed a scheme for implementing a magic wavelength for the fundamental transition  $\nu = 0, N = 0 \rightarrow \nu = 1, N = 2$  in *para*-H<sub>2</sub><sup>40</sup> (which is not magnetically trappable) that has a potential to enable much higher accuracy. In contrast, magnetic trapping could be used to increase the precision spectroscopy of the fundamental transition ( $\nu = 0, N = 1 \rightarrow \nu = 1, N = 1$ ) in *ortho*-H<sub>2</sub>. Both the optical dipole and magnetic traps could reach depths of the order of 1 mK, for the laser power density of 1 MW/mm<sup>2</sup> and magnetic field strength of 0.4 T, respectively (as recently demonstrated in Ref. 41, it is possible to use strong and focused laser beams to achieve trap depths of  $\sim 3.6$  K for H<sub>2</sub>). Further progress in high-precision spectroscopy is contingent upon the ability to cool H<sub>2</sub> far below 1 mK.

One such possibility is sympathetic cooling, which relies on immersing a molecular system in a gas of coolant atoms, preferably of a similar mass.<sup>42–45</sup> Under such conditions, elastic collisions result in cooling by transferring momentum between molecules and the coolant atoms. In contrast, inelastic collisions can cause transitions to high-field-seeking (untrappable) states, which release the internal energy stored in these states, and lead to heating and trap loss.<sup>44,45</sup> For efficient sympathetic cooling, the ratio of the cross section for elastic to inelastic collisions ( $\gamma = \sigma_{\text{el}}/\sigma_{\text{inel}}$ ) should be larger than 100.<sup>46</sup>

A relatively small mass and the fact that it can be cooled down to the  $\mu\text{K}$  regime using laser cooling techniques make atomic lithium an attractive candidate for sympathetic cooling of H<sub>2</sub>. Duarte *et al.*<sup>47</sup> have demonstrated a magneto-optical trap (MOT) for <sup>6</sup>Li atoms operating on a narrow  $2S_{1/2} \rightarrow 3P_{3/2}$  transition at 323 nm, achieving temperatures as low as 59  $\mu\text{K}$ . However, the feasibility of sympathetic cooling of H<sub>2</sub> by collisions with Li remains to be determined. For instance, there is a significant mismatch in the Zeeman splittings of the two species, which could lead to losses once the lithium MOT and a hypothetical magnetic trap of H<sub>2</sub> are overlapped. Furthermore, it is unclear whether the ratio,  $\gamma$ , of the cross section for elastic to inelastic collisions of H<sub>2</sub> with Li is high enough to support the cooling process. In order to accurately calculate  $\gamma$ , it is necessary to take into account the effects of hyperfine interactions and the presence of an external magnetic field.

In this paper, we present the first rigorous theoretical study of the role of hyperfine and Zeeman interaction effects in cold atom–H<sub>2</sub> collisions. We investigate the cold collisions of *ortho*-H<sub>2</sub> ( $\nu = 0, N = 1$ ) molecules with <sup>6</sup>Li atoms using coupled-channel quantum scattering calculations based on a highly accurate *ab initio* potential energy surface (PES).<sup>48</sup> In the field-free case, we find that the three hyperfine states of H<sub>2</sub> are collisionally stable, i.e., the ratio of cross sections for elastic ( $F$ -conserving) to inelastic ( $F$ -changing) collisions exceeds 100, with the exception of a narrow range in the vicinity of a  $g$ -wave shape resonance located at  $E \approx k_B \times 1.2$  K. We find that the presence of the magnetic dipolar interaction between the nuclear magnetic moment of H<sub>2</sub> and the electron spin magnetic moment of Li manifests itself in the ultracold regime, where it drastically increases the inelastic  $F = 0 \rightarrow F' = 1$  scattering (otherwise suppressed by the selection rules for transitions driven by the H<sub>2</sub>–Li interaction potential). We also perform quantum scattering

calculations in an external magnetic field, and we analyze relaxation from the three low-field-seeking Zeeman states in H<sub>2</sub> upon collisions with <sup>6</sup>Li atoms in the trappable ( $S = 1/2, M_S = 1/2$ ) state. We find that the inelastic relaxation is dominated by collisions that conserve the space-fixed projection of the nuclear spin of H<sub>2</sub>. The magnetic dipolar interaction drives the relaxation of the electronic spin of Li, which has profound consequences on the possibility of sympathetic cooling of H<sub>2</sub> by lithium.

This article is organized as follows: In Sec. II, we outline the quantum theory of collisions between <sup>1</sup> $\Sigma$  molecules with two magnetic nuclei (such as *ortho*-H<sub>2</sub>) and <sup>2</sup>S atoms in an external magnetic field, which includes the intramolecular hyperfine interactions in the <sup>1</sup> $\Sigma$  molecules, as well as the spin-dependent (SD) interaction between the molecule and the <sup>2</sup>S atom. Next, we apply this theory to cold Li–H<sub>2</sub> collisions in Sec. III, where we present and discuss the results for the field-free case. Then, in Sec. IV, we provide the state-to-state cross sections for transitions between the Zeeman sublevels of *ortho*-H<sub>2</sub> in an external magnetic field. We discuss the kinetic energy and magnetic field dependence of the cross sections, as well as the implications of the calculated elastic-to-inelastic scattering ratio on the possibility of sympathetic cooling of H<sub>2</sub> by <sup>6</sup>Li. Section V concludes by summarizing the main results of this work. Atomic units are used throughout this article unless stated otherwise.

## II. THEORY

Here, we present the quantum theory of collisions between a <sup>1</sup> $\Sigma$  molecule and a <sup>2</sup>S atom in the presence of an external magnetic field. The theory is based on the seminal work of Krems and Dalgarno<sup>49</sup> and Volpi and Bohn,<sup>50</sup> who first considered diatom–atom collisions in a magnetic field. It is also an extension of the recent work of Hermsmeider *et al.*<sup>51</sup> (who studied nuclear spin relaxation in cold He–<sup>13</sup>C<sup>16</sup>O collisions) to the case of collisions of open-shell atoms, such as <sup>6</sup>Li, and molecules with two magnetic nuclei, such as *ortho*-H<sub>2</sub>.

We use space-fixed Jacobi coordinates to describe the scattering system: the separation vector **R** from the atom to the center of mass of the H<sub>2</sub> molecule, the internuclear vector **r**, and the angle  $\theta$  between **R** and **r**. There are six angular momenta in the H<sub>2</sub>(<sup>1</sup> $\Sigma_g^+$ )–Li(<sup>2</sup>S) system: the rotational angular momentum of the nuclei in H<sub>2</sub> (**N**); the nuclear spin angular momenta of the protons, **I**<sub>1</sub> and **I**<sub>2</sub> ( $I_i = |\mathbf{I}_i| = 1/2, i = 1, 2$ ); the total electron spin of the lithium atom, **S** ( $S = |\mathbf{S}| = 1/2$ ); the nuclear spin angular momentum of lithium, **I**<sub>Li</sub> ( $I_{\text{Li}} = |\mathbf{I}_{\text{Li}}| = 1$  for <sup>6</sup>Li and  $3/2$  for <sup>7</sup>Li); and the angular momentum operator describing the orbital motion of the collision partners, **l**. For reasons clarified below, we neglect the hyperfine structure of lithium and we exclude **I**<sub>Li</sub> from the analysis. We couple the two nuclear spins of the protons to form the total nuclear spin of H<sub>2</sub>, **I**<sub>H<sub>2</sub></sub> = **I**<sub>1</sub> + **I**<sub>2</sub>. We recall that molecular hydrogen exists in two spin isomeric forms: *para*-H<sub>2</sub> with  $I_{\text{H}_2} = |\mathbf{I}_{\text{H}_2}| = 0$  and *ortho*-H<sub>2</sub> with  $I_{\text{H}_2} = |\mathbf{I}_{\text{H}_2}| = 1$ . Because the total wave function of H<sub>2</sub> must be anti-symmetric with respect to the permutation of the protons, *para*-H<sub>2</sub> exhibits a rotational structure with only even values of  $N = |\mathbf{N}|$ , while the rotational structure of *ortho*-H<sub>2</sub> involves only odd  $N$  values. Since  $I_{\text{H}_2} = 0$  for *para*-H<sub>2</sub>, this spin isomer does not have the hyperfine structure and nuclear Zeeman shifts and interacts with the magnetic field only through its weak rotational magnetic moment (for  $N = 0$  *para*-H<sub>2</sub>, the rotational magnetic moment is strictly zero).

In contrast, *ortho*-H<sub>2</sub> does have a non-zero nuclear spin, yielding stronger Zeeman shifts that make it amenable to magnetic trapping. Thus, we focus on *ortho*-H<sub>2</sub> in what follows.

The Hamiltonian for the atom–molecule collision system is

$$\hat{H} = -\frac{1}{2\mu R} \frac{\partial^2}{\partial R^2} R + \frac{\hat{L}^2}{2\mu R^2} + \hat{V}(\mathbf{R}, \mathbf{r}) + \hat{V}_{\text{SD}}(\mathbf{R}, \mathbf{r}, \hat{\mathbf{I}}, \hat{\mathbf{S}}) + \hat{H}_{\text{as}}, \quad (1)$$

where  $\mu = m_{\text{at}}m_{\text{mol}}/(m_{\text{at}} + m_{\text{mol}})$  is the reduced mass of the collision partners (we use  $m_{\text{at}} = 6.015121$  and  $m_{\text{mol}} = 2.01565$  atomic mass units),<sup>52</sup>  $\hat{V}(\mathbf{R}, \mathbf{r})$  is the atom–molecule potential energy surface, and  $\hat{V}_{\text{SD}}(\mathbf{R}, \mathbf{r}, \hat{\mathbf{I}}, \hat{\mathbf{S}})$  denotes the spin-dependent (SD) Hamiltonian (note that the subscript in  $\hat{\mathbf{I}}_{\text{H}_2}$  is dropped for simplicity, and the nuclear spin of H<sub>2</sub> is denoted simply as  $\hat{\mathbf{I}}$ ),

$$\hat{V}_{\text{SD}}(\mathbf{R}, \mathbf{r}, \hat{\mathbf{I}}, \hat{\mathbf{S}}) = \sum_{i=1,2} A_F^i(\mathbf{R}, \mathbf{r}) \hat{\mathbf{I}}_i \cdot \hat{\mathbf{S}} + \sum_{i=1,2} \sum_{\alpha\beta} c_{\alpha\beta}^i(\mathbf{R}, \mathbf{r}) \hat{\mathbf{I}}_{i\alpha} \hat{\mathbf{S}}_{\beta}, \quad (2)$$

in which the sum over  $i$  involves the two protons in H<sub>2</sub> and  $\alpha$  and  $\beta$  run over Cartesian components of the spin operators in a molecule-fixed coordinate frame. The first term corresponds to the Fermi contact interaction between the nuclear spin angular momenta,  $\hat{\mathbf{I}}_i$  of the  $i$ th proton in H<sub>2</sub>, and the spin angular momentum,  $\hat{\mathbf{S}}$ , of the valence electron in lithium, with  $A_F^i(\mathbf{R}, \mathbf{r})$  being the coupling coefficient for the Fermi contact interaction. Due to the similarity in the interaction potentials and reduced masses, the magnitude of the Fermi contact interaction in H<sub>2</sub>–Li can be estimated from the previous work on <sup>3</sup>He–Li<sup>53</sup> and <sup>3</sup>He–K<sup>54</sup> collisions. At the zero-energy turning point of the Li–H<sub>2</sub> potential ( $R \approx 8.75a_0$ ), the Fermi contact interaction constant for <sup>3</sup>He–Li<sup>53</sup> and <sup>3</sup>He–K<sup>54</sup> is on the order of  $10^{-4} \text{ cm}^{-1}$ . Since this interaction vanishes rapidly with increasing  $R$ ,<sup>54</sup> its influence on the low-temperature Li–H<sub>2</sub> scattering is expected to be negligible. We thus exclude the Fermi contact interaction from our analysis. The second term in Eq. (2) is the intermolecular anisotropic hyperfine interaction, of which the strength is determined by the coupling tensor,  $c_{\alpha\beta}^i(\mathbf{R}, \mathbf{r})$ . Since calculating the full dependence of the coupling tensor on  $R$ ,  $\theta$ , and  $r$  is beyond the scope of this work, we use an approximate formula that is appropriate for describing the long-range part of the anisotropic hyperfine interaction. We assume that the total nuclear spin magnetic moment of H<sub>2</sub>,  $\hat{\mu}_{\text{H}_2} = g_{\text{H}}\mu_{\text{N}}\hat{\mathbf{I}}$ , and the electron spin magnetic moment of Li,  $\hat{\mu}_{\text{Li}} = g_{\text{S}}\mu_{\text{B}}\hat{\mathbf{S}}$ , are point dipoles located at the centers of mass of H<sub>2</sub> and Li, respectively. The magnetic dipole interaction between the two magnetic moments is given as<sup>54</sup>

$$\hat{V}_{\text{SD}}(\mathbf{R}, \hat{\mathbf{I}}, \hat{\mathbf{S}}) = -g_{\text{S}}\mu_{\text{B}}g_{\text{H}}\mu_{\text{N}}\sqrt{\frac{24\pi}{5}}\frac{\alpha^2}{R^3}\sum_{q=-2}^2(-1)^q Y_{2,-q}(\hat{\mathbf{R}})[\hat{\mathbf{S}} \otimes \hat{\mathbf{I}}]_q^2, \quad (3)$$

where  $g_{\text{S}}$  and  $g_{\text{H}}$  are the electron and proton  $g$ -factors, respectively,  $\mu_{\text{B}}$  and  $\mu_{\text{N}}$  denote the Bohr and nuclear magnetons, respectively, and  $\alpha$  is the fine-structure constant.  $Y_{2q}(\hat{\mathbf{R}})$  is a spherical harmonic of rank 2, which depends on the orientation of the scattering system, and  $[\hat{\mathbf{S}} \otimes \hat{\mathbf{I}}]_q^2$  is a tensorial product of  $\hat{\mathbf{S}}$  and  $\hat{\mathbf{I}}$ . We note that the general expression for the anisotropic hyperfine interactions, Eq. (2), is used in the studies of hyperfine and Zeeman effects in three-atom molecules with nonzero nuclear and electronic spins, such as

HCO,<sup>55</sup> NH<sub>2</sub>,<sup>56</sup> and Na<sub>3</sub>.<sup>57,58</sup> These interactions also play a crucial role in electron spin decoherence of alkali-metal atoms trapped in solid *para*-H<sub>2</sub> matrices.<sup>59</sup> A form similar to Eq. (3) is used to describe the long-range magnetic dipolar interaction between the electron spins of <sup>2</sup>Σ molecules and <sup>2</sup>S atoms,<sup>44,45</sup> two <sup>2</sup>Σ molecules,<sup>49</sup> and two <sup>3</sup>Σ molecules.<sup>49,60–62</sup>

The asymptotic Hamiltonian  $\hat{H}_{\text{as}}$  in Eq. (1) is given by

$$\hat{H}_{\text{as}} = \hat{H}_{\text{H}_2} + \hat{H}_{\text{Li}}, \quad (4)$$

where  $\hat{H}_{\text{H}_2}$  and  $\hat{H}_{\text{Li}}$  correspond to the Hamiltonians of the isolated molecule and atom, respectively. The effective Hamiltonian for the H<sub>2</sub> molecule in the ground electronic (<sup>1</sup>Σ<sub>g</sub><sup>+</sup>) state is

$$\hat{H}_{\text{H}_2} = \hat{H}_{\text{rot}} + \hat{H}_{\text{HF}} + \hat{H}_{\text{Zeeman}} \quad (5)$$

and involves the rotational, intramolecular hyperfine (HF), and Zeeman terms,

$$\hat{H}_{\text{rot}} = B_v \hat{\mathbf{N}}^2 - D_v \hat{\mathbf{N}}^4, \quad (6)$$

$$\hat{H}_{\text{HF}} = -c_{\text{nsr}} \hat{\mathbf{N}} \cdot \hat{\mathbf{I}} + g_{\text{H}}^2 \mu_{\text{N}}^2 \left( \frac{\mu_0}{4\pi} \right) \left( \frac{\hat{\mathbf{I}}_1 \cdot \hat{\mathbf{I}}_2}{r^3} - \frac{3(\hat{\mathbf{I}}_1 \cdot \mathbf{r})(\hat{\mathbf{I}}_2 \cdot \mathbf{r})}{r^5} \right), \quad (7)$$

$$\hat{H}_{\text{Zeeman}} = -g_{\text{r}}\mu_{\text{N}}\hat{N}_Z B_Z - g_{\text{H}}\mu_{\text{N}}I_Z B_Z(1 - \sigma). \quad (8)$$

Here,  $B_v$  and  $D_v$  are the effective rotational and centrifugal distortion constants in the vibrational state  $v$ . The intramolecular hyperfine Hamiltonian describes the two dominant hyperfine interactions in H<sub>2</sub>—the nuclear spin–rotation interaction and the dipolar interaction between the nuclear spins. The respective hyperfine coupling constants,  $c_{\text{nsr}}$  and  $c_{\text{dip}}$ , quantify the strength of these two interactions. The two terms in the Zeeman Hamiltonian correspond to the contribution of the interaction of the rotational magnetic moment and the nuclear magnetic moment with the external magnetic field, with  $g_{\text{r}}$  and  $\sigma$  being the rotational nuclear  $g$ -factor and the anisotropic part of the nuclear shielding tensor, respectively. We assume that the external magnetic field is aligned along the space-fixed  $Z$ -axis. The diamagnetic interaction parameterized by molecular susceptibility, i.e., the interaction of the magnetic field with an induced molecular magnetic moment, contributes significantly only in intense magnetic fields ( $B > 1 \text{ T}$ ),<sup>51</sup> and thus, we neglect it in the following analysis.

Because our interest here is in transitions between the hyperfine states of H<sub>2</sub>, we also neglect the internal hyperfine structure of the lithium atom. Thus, the effective Hamiltonian for the isolated lithium atom,  $\hat{H}_{\text{Li}}$ , involves only the Zeeman term,

$$\hat{H}_{\text{Li}} = -g_{\text{S}}\mu_{\text{B}}\hat{S}_Z B_Z, \quad (9)$$

where  $g_{\text{S}}$  is the electron spin  $g$ -factor.

The total wave function of the system is expanded in a complete set of uncoupled basis states in a space-fixed frame of Refs. 49 and 63,

$$|\Psi\rangle = \frac{1}{R} \sum_N \sum_{M_N=-N}^N \sum_{M_I=-1}^1 \sum_{M_S=-1/2}^{1/2} \times \sum_l \sum_{M_l=-l}^l F_{NM_N M_I M_S l M_l}(R) |NM_N\rangle |IM_I\rangle |SM_S\rangle |lM_l\rangle, \quad (10)$$

where  $M_N$ ,  $M_I$ ,  $M_S$ , and  $M_l$  are the projections of  $\hat{\mathbf{N}}$ ,  $\hat{\mathbf{I}}$ ,  $\hat{\mathbf{S}}$ , and  $\hat{\mathbf{l}}$  on the space-fixed Z-axis, respectively. The expansion (10) is appropriate for weakly anisotropic atom–molecule interaction potentials, such as the Li–H<sub>2</sub> potential used in this work.

Substitution of the total wave function from Eq. (10) to the Schrödinger equation,  $\hat{H}|\Psi\rangle = E|\Psi\rangle$ , leads to a set of coupled channel (CC) equations for the expansion coefficients,  $F_{NM_N M_I M_S l M_l}(R)$ ,

$$\left[ \frac{d^2}{dR^2} + 2\mu E - \frac{l(l+1)}{R^2} \right] F_{NM_N M_I M_S l M_l}(R) = 2\mu \sum_{N', M'_N, M'_I, M'_S, l', M'_l} F_{N' M'_N M'_I M'_S l' M'_l}(R) \times \langle NM_N | \langle IM_I | \langle SM_S | \langle lM_l | \hat{V}(\mathbf{R}, \mathbf{r}) + \hat{V}_{SD}(\mathbf{R}, \mathbf{r}, \hat{\mathbf{I}}, \hat{\mathbf{S}}) + \hat{H}_{as} | N' M'_N \rangle | l' M'_l \rangle | S' M'_S \rangle | I' M'_I \rangle, \quad (11)$$

where  $E$  is the total energy and  $\mu$  is defined in Eq. (1). The evaluation of the matrix elements on the right-hand side is described in Appendix A. Note that the CC equations are block-diagonal with respect to  $M = M_N + M_{I_{H_2}} + M_S + M_l$ , the projection of the total angular momentum,  $\hat{\mathbf{J}}$ , on the space-fixed Z-axis. This is a consequence of the fact that in the presence of an external magnetic field,  $M$ , contrary to  $J$ , is conserved.<sup>49,63</sup> This allows us to solve the CC equations for each value of  $M$  separately.

We solve the CC equations numerically (for computational details, see Sec. II A) and transform the asymptotic solution to the eigenstate basis of the asymptotic Hamiltonian (4) for H<sub>2</sub> in a magnetic field,

$$|(NI)\gamma_{H_2}\rangle = \sum_{M_N=-N}^N \sum_{M_I=-I}^I A_{M_I, M_N}^{\gamma_{H_2}}(B) |NM_N\rangle |IM_I\rangle, \quad (12)$$

where  $\gamma_{H_2}$  denotes the eigenvalue of the H<sub>2</sub> Hamiltonian (5). In principle, the asymptotic Hamiltonian involves a term that couples different rotational states of H<sub>2</sub>, but this coupling is extremely small, as shown in Appendix A, so we treat  $N$  as a good quantum number. We also note that the asymptotic Hamiltonian of the Li atom, introduced in Eq. (9), is diagonal in the basis of  $|SM_S\rangle$  states; thus,  $|SM_S\rangle$  is an approximate eigenvector for an isolated lithium atom with  $M_S = \pm 1/2$  labeling the atomic Zeeman levels. Next, we match the result to the linear combinations of the Riccati–Bessel and Neumann functions to obtain the scattering S-matrix.<sup>64</sup> The state-to-state cross sections are calculated from the S-matrix elements at a given collision energy,  $E_{\text{kin}}$ , by summing contributions from all  $M$ -blocks,<sup>49</sup>

$$\sigma_{\gamma_{H_2} M_S \rightarrow \gamma'_{H_2} M'_S}(E_{\text{kin}}) = \frac{\pi}{k_{\gamma_{H_2} M_S}^2} \sum_M \sum_{l M_l} \sum_{l' M'_l} \left| \delta_{l, l'} \delta_{M_I, M'_I} \delta_{\gamma_{H_2}, \gamma'_{H_2}} \delta_{M_S, M'_S} - S_{\gamma_{H_2} M_S l M_l \gamma'_{H_2} M'_S l' M'_l}^M \right|^2, \quad (13)$$

where  $k_{\gamma_{H_2} M_S} = \sqrt{2\mu(E - E_{\gamma_{H_2}} - E_{M_S})}$  is the collision wavevector.

Since we are interested in the collisional relaxation of the nuclear spin states of molecular hydrogen, we define a state-to-state cross section, which is summed over the final Zeeman states of the lithium atom,

$$\sigma_{\gamma_{H_2} \rightarrow \gamma'_{H_2}}(E_{\text{kin}}) = \sum_{M'_S} \sigma_{\gamma_{H_2} M_S=1/2 \rightarrow \gamma'_{H_2} M'_S}(E_{\text{kin}}), \quad (14)$$

and the related rate coefficient,

$$k_{\gamma_{H_2} \rightarrow \gamma'_{H_2}}(T) = \sqrt{\frac{8}{\pi \mu k_B^3 T^3}} \int_0^\infty \sigma_{\gamma_{H_2} \rightarrow \gamma'_{H_2}}(E_{\text{kin}}) E_{\text{kin}} e^{-E_{\text{kin}}/k_B T} dE_{\text{kin}}. \quad (15)$$

In this work, we assume that the lithium atom is initially in the trap-pable  $M_S = 1/2$  state, so we can drop the  $M_S$  symbol on the left-hand side of Eqs. (14) and (15).

When considering collisions in the absence of an external magnetic field, we expand the total wave function as follows:

$$|\Psi\rangle = \frac{1}{R} \sum_N \sum_{F=|N-1|}^{N+1} \sum_{M_S=-1/2}^{1/2} \sum_l \sum_{M_l=-l}^l F_{NFM_F M_S l M_l}(R) \times |(NI)FM_F\rangle |SM_S\rangle |lM_l\rangle, \quad (16)$$

i.e., we use the coupled basis vectors to represent the states of H<sub>2</sub>,

$$|(NI)FM_F\rangle = (-1)^{-N+1-M_F} \sum_{M_N=-N}^N \sum_{M_I=-1}^1 \sqrt{2F+1} \times \begin{pmatrix} N & 1 & F \\ M_N & M_I & -M_F \end{pmatrix} |NM_N\rangle |IM_I\rangle. \quad (17)$$

Here,  $\begin{pmatrix} \cdot & \cdot & \cdot \end{pmatrix}$  are the 3-j symbols<sup>65</sup> and  $F = |\hat{\mathbf{F}}|$  is the quantum number associated with the total angular momentum of H<sub>2</sub>, in which  $\hat{\mathbf{F}}$  is the result of coupling of  $\hat{\mathbf{N}}$  to  $\hat{\mathbf{I}}$ . This representation is convenient because  $F$  is conserved in the field-free case; see Sec. III. The rest of the procedure follows the same steps as detailed above and hence is not repeated here. The matrix elements of the PES, the spin-dependent interaction, and the asymptotic Hamiltonian in the coupled basis [see Eq. (16)] are provided in Appendix B.

## A. Computational details

The spectroscopic constants used to parameterize the Hamiltonian of H<sub>2</sub> [Eq. (5)] and Li [Eq. (9)] are listed in Table I. We use the *ab initio* H<sub>2</sub>–Li PES reported by Makrides *et al.*<sup>48</sup> This PES has recently been used in the calculations of elastic, inelastic, and glancing-angle rate coefficients for collisions of ultracold Li atoms with room-temperature H<sub>2</sub> molecules in the context of the calibration of a cold-atom vacuum standard.<sup>48,70–72</sup> For the purpose of solving the CC equations, we expand the PES in Legendre polynomials [Eq. (A1)]. Since H<sub>2</sub> is a homonuclear molecule, the expansion index takes only even values. We truncate the expansion in Eq. (A1) at  $\lambda_{\text{max}} = 4$ . The dependence of the expansion coefficients on the H<sub>2</sub> stretching coordinate,  $r$ , is averaged out by the integration over rovibrational wave functions of the isolated H<sub>2</sub> molecule in the ground vibrational state; see Eq. (A3) for details.



**TABLE I.** Spectroscopic parameters of  $\text{H}_2$  used in the calculations reported in the present work.

Constant	Value	Source
$B_v$	$59.322 \text{ cm}^{-1}$	66
$D_v$	$4.575 \times 10^{-2} \text{ cm}^{-1}$	66
$c_{\text{nsr}}$	$(3.81 \pm 0.01) \times 10^{-6} \text{ cm}^{-1}$	27
$c_{\text{dip}}$	$(9.614 \pm 0.005) \times 10^{-6} \text{ cm}^{-1}$	27
$g_r$	0.882 5	67
$g_{\text{H}}$	5.585 694 698 3	68
$\sigma$	1.76 ppm	69

We solve the CC equations using a log-derivative propagator<sup>64,73</sup> on a radial grid from  $R_{\text{min}} = 3.0a_0$  to  $R_{\text{max}} = 200a_0$  (for collisions with  $E_{\text{kin}} < 10^{-2} \text{ cm}^{-1}$ , we increase  $R_{\text{max}}$  to  $500a_0$ ) with a constant step size of  $0.05a_0$ . While this integration range is notably smaller than that used in Ref. 48, where the authors extended  $R_{\text{max}}$  to  $5000a_0$ , we validated that it is sufficient to ensure a subpercent convergence of the state-to-state cross sections. We cover the range of kinetic energies from  $10^{-9}$  to  $50 \text{ cm}^{-1}$ . Due to the weak anisotropy of the  $\text{Li}-\text{H}_2$  PES, it is sufficient to keep only the lowest two rotational levels of *ortho*- $\text{H}_2$  ( $N = 1$  and  $N = 3$ ) in the basis to obtain a subpercent convergence of the cross sections. The number of partial waves,  $l_{\text{max}}$ , included in our calculations depends

on the collision energy and varies from 6 up to 55. To verify our calculations, we compared the field-free cross sections with the previous results<sup>48</sup> and found excellent agreement. Finally, we note that the exact value of the rotational constant has no significant influence on the cross sections. For instance, switching between  $B_{v=0}$  and  $B_e$  modifies the elastic cross section for the scattering of  $\text{H}_2$  in the  $F = 0$  hyperfine state by 0.03% and the inelastic cross sections by less than 0.005%.

### III. RESULTS: FIELD-FREE $\text{H}_2$ -Li COLLISIONS

In the absence of an external magnetic field, the  $v = 0, N = 1$  state of  $\text{H}_2$  is split into three hyperfine levels, spread over a range of  $\sim 600 \text{ kHz}$ ,<sup>27</sup> as shown in the inset of Fig. 1(a). The three states are labeled by  $F$ , the total angular momentum of  $\text{H}_2$ . We present the hyperfine-resolved state-to-state cross sections of  $\text{H}_2$  ( $v = 0, N = 1$ ) colliding with  $^6\text{Li}$  in Fig. 1. The elastic ( $F$ -conserving) cross sections are shown in Fig. 1(a) as blue ( $F = 2$ ), green ( $F = 1$ ), and red ( $F = 0$ ) lines. The cross sections are almost identical, apart from kinetic energies close to the feature located at  $E_{\text{kin}} = 1.2 \text{ cm}^{-1}$ , where the largest difference between the cross sections approaches 20%. This structure was attributed to the  $g$ -wave ( $l = 4$ ) shape resonance in Ref. 48. The inelastic ( $F$ -changing) cross sections are typically orders of magnitude smaller than the elastic cross sections. However, near  $E_{\text{kin}} = 1.2 \text{ cm}^{-1}$ , this difference narrows to a factor of 2.5. The three panels [(b)–(d)] provide additional information

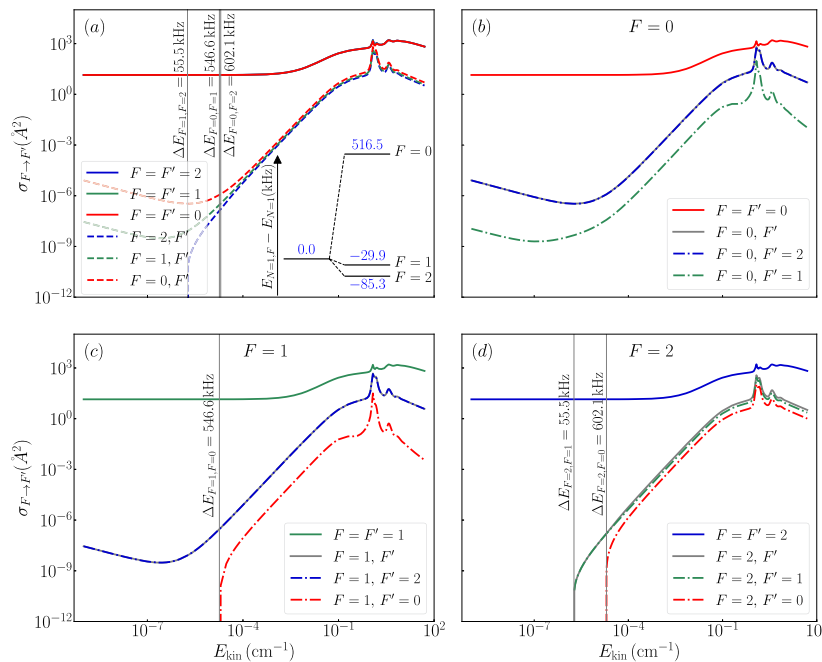


**FIG. 1.** Hyperfine-resolved state-to-state cross sections for collisions of  $\text{H}_2$  with  $^6\text{Li}$ . Panel (a) presents the elastic ( $F$ -conserving) cross sections (solid lines) and the total inelastic state-to-state cross sections (dashed lines) for a given  $F$  initial state. The gray vertical lines correspond to the energy differences between the three hyperfine states and are shown to illustrate the mechanism of channel opening. The energy diagram in the bottom right corner of panel (a) shows the hyperfine structure of the  $v = 0, N = 1$  level of  $\text{H}_2$ . In panels (b)–(d), we show the cross sections separately for each initial value of  $F$  along with the decomposition of the total inelastic cross section into the different final state,  $F'$ , contributions.

about the inelastic processes that affect each  $F$ -labeled state. Inelastic scattering from the  $F = 0$  state, which has the largest energy, is dominated by the  $F = 0 \rightarrow F' = 2$  de-excitation [the grey solid and blue dotted-dashed lines in Fig. 1(b) are almost overlapped]. This process is driven by the  $\lambda = 2$  anisotropic term of the Li–H<sub>2</sub> PES [see Eq. (B1)]. The  $F' = 1$  state is not directly coupled to the initial state by the PES (there is no  $\lambda = 1$  term in the PES expansion since H<sub>2</sub> is a homonuclear molecule), and the cross sections for the  $F = 0 \rightarrow F' = 1$  de-excitation are at least one order of magnitude smaller than those for the  $F = 0 \rightarrow F' = 2$  transition. The nuclear spin–electron spin interaction introduces a weak coupling between the  $F = 0$  and  $F = 1$  levels, which influences the cross sections only for kinetic energies smaller than  $10^{-6}$  cm<sup>-1</sup> as discussed below. Similarly, inelastic scattering from the  $F = 1$  state is dominated by the  $F = 1 \rightarrow F' = 2$  de-excitation, driven by the  $\lambda = 2$  term in the PES expansion. When the kinetic energy crosses the  $\Delta E_{F=0, F=1} = E_{F=0} - E_{F=1}$  threshold (at 546.5 kHz), the excitation to the  $F = 0$  state becomes energetically accessible. As mentioned above, since the  $F = 1$  and  $F = 0$  channels are not directly coupled by the PES, this contribution to the total inelastic cross section is significantly (two orders of magnitude) weaker than the  $F = 1 \rightarrow F' = 2$  de-excitation. For the  $F = 2$  initial state, we note that until the kinetic energy surpasses the first threshold ( $E_{F=1, F=2} = E_{F=1} - E_{F=2}$  at 54.6 kHz), the scattering is purely  $F$ -conserving. Both the  $F = 2 \rightarrow F' = 1$  and  $F = 2 \rightarrow F' = 0$  excitations are driven by the  $\lambda = 2$  term (with a weak contribution from the spin-dependent interaction).

Overall, the magnetic dipole–dipole interaction, Eq. (3), has a negligible influence on the state-to-state cross sections for collisions of H<sub>2</sub> with <sup>6</sup>Li in the absence of an external magnetic field. The only significant effect that we observe is an enhancement of the  $\Delta F = 1$  de-excitation in the ultracold regime (below  $10^{-6}$  cm<sup>-1</sup>)—the dashed and solid lines in Fig. 2 represent the values of  $\sigma_{F \rightarrow F'=F+1}$  calculated with and without the spin-dependent H<sub>2</sub>–Li interaction, respectively. Interestingly, the inclusion of this weak interaction is necessary to obtain the Wigner threshold behavior<sup>74</sup> of the  $\sigma_{F=0 \rightarrow F'=1}$  cross section ( $\sigma \sim E_{\text{kin}}^{-1/2}$ ) at  $E_{\text{kin}} \approx 10^{-6}$  cm<sup>-1</sup>. We observe a slight alternation of the  $\Delta F = -1$  excitation cross sections near the thresholds ( $\Delta E_{F=0, F=1} = 546.5$  kHz and  $E_{F=1, F=2} = 54.6$  kHz), which is not shown in Fig. 2. In the remaining field-free cases (larger relative kinetic energies and other scattering processes), the nuclear spin–electron

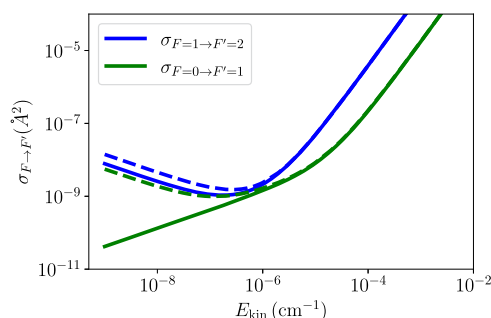


**FIG. 2.** Influence of the nuclear spin–electron spin interaction on the hyperfine-structure resolved state-to-state cross sections for collisions of H<sub>2</sub> with <sup>6</sup>Li. The dashed and solid lines present the cross sections calculated including and neglecting the spin-dependent interaction, respectively.

spin interaction has a negligible influence on the state-to-state cross sections.

#### IV. RESULTS: H<sub>2</sub>–Li COLLISIONS IN AN EXTERNAL MAGNETIC FIELD

Before proceeding to discuss the results of scattering calculations, we briefly consider the energy structure of the H<sub>2</sub> molecule in an external magnetic field. Figure 3(a) shows the Zeeman energy levels in the  $v = 0, N = 1$  rovibrational manifold of *ortho*-H<sub>2</sub> obtained by diagonalization of the Hamiltonian in Eq. (5) with the spectroscopic parameters of H<sub>2</sub> gathered in Table I. At large field strengths, the nine levels are grouped into sets of three states, which share the same projection of the nuclear spin,  $M_I$ . This reflects the relative strength of the nuclear Zeeman term with respect to the rotational Zeeman term—for  $N = 1$ , the first term in Eq. (8) is approximately six times smaller than the second term. Within each group of states, the order of states (starting from states with the largest energy) is  $M_N = -1, 0$ , and  $1$ . At high fields, the top three low-field-seeking Zeeman states, which are amenable to magnetic trapping, correspond to  $M_I = -1$ .

While we use the  $M_I$  and  $M_N$  quantum numbers to describe the Zeeman states at high fields, it is important to acknowledge that at lower fields, the eigenstates undergo significant mixing due to the nuclear spin–rotation and nuclear spin–nuclear spin interactions. This situation requires us to use a more general approach for labeling and referencing the Zeeman states throughout the entire range of magnetic fields. To this end, we introduce a “state index” (SI) that uniquely identifies each eigenstate, ranging from 1 to 9, as shown in Fig. 3(a). The three trappable states thus have SI = 1, 2, and 3.

We perform quantum scattering calculations at magnetic field strengths ranging from  $10^{-4}$  to 1 T. As an example, we discuss the kinetic energy dependence of the state-to-state cross sections for H<sub>2</sub>–Li collisions at  $B = 0.3$  T, which corresponds to a magnetic trap depth of  $\sim 0.8$  mK for the SI = 1 state. We consider the collisions of H<sub>2</sub> and Li in their low-field seeking states (SI = 1, 2, and 3 for H<sub>2</sub> and  $M_S = 1/2$  for Li, respectively). Panels (b)–(d) in Fig. 3 show the cross sections for elastic and all inelastic transitions in H<sub>2</sub>–Li collisions at  $B = 0.3$  T. The color of each curve matches that of the corresponding Zeeman level plotted in Fig. 3(a).

The elastic cross sections are consistently larger than the total inelastic cross sections by at least two orders of magnitude, except in the vicinity of  $E_{\text{kin}} = 1.2$  cm<sup>-1</sup>, where  $\gamma$  decreases to  $\sim 3$ . For the sake of discussion, we distinguish two specific regimes, namely, the ultralow collision energy regime ( $E_{\text{kin}} < 10^{-5}$  cm<sup>-1</sup>), the low collision energy regime ( $E_{\text{kin}} > 10^{-2}$  cm<sup>-1</sup>), and an intermediate regime.

##### A. Ultralow collision energy regime

At ultralow collision energies, inelastic cross sections follow the  $\sim E_{\text{kin}}^{-1/2}$  behavior predicted by Wigner’s threshold law.<sup>74</sup> For the low-field-seeking state with the largest internal energy [SI = 1, panel (b) in Fig. 3], two key events contribute to the total inelastic cross section. The first is the  $\Delta M_I = \Delta M_N = 0, \Delta M_S = -1$  transition, i.e., the relaxation of lithium’s electron spin, with H<sub>2</sub> remaining in the same Zeeman state. Although this process clearly does not lead to the transition of H<sub>2</sub> to an untrappable state, it involves the release of a

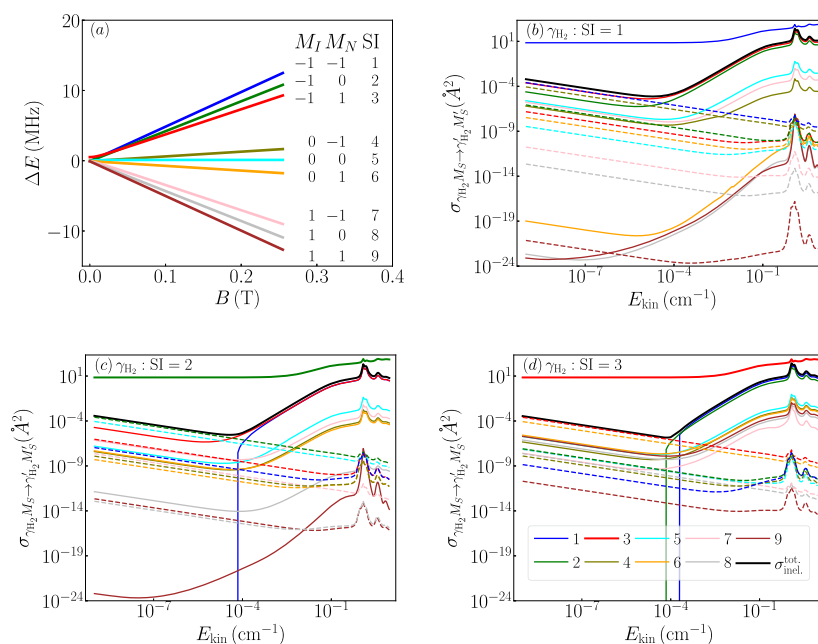


**FIG. 3.** Panel (a): Zeeman sublevels of the  $v = 0, N = 1$  rovibrational state of  $H_2$  as a function of magnetic field  $B$ . Panels (b)–(d): Cross sections for  $H_2$ -Li collisions in an external magnetic field  $B = 0.3$  T. The three panels correspond to different initial levels of  $H_2$ : the first [panel (b)], second [panel (c)], and third states [panel (d)], according to the state labels in panel (a). The solid lines correspond to the collisional events, in which the electron spin of  $^6Li$  is conserved, and the dashed lines correspond to those, in which the electron spin is flipped ( $M_S = 1/2 \rightarrow M_S' = -1/2$ ).

large amount of energy ( $g_S \mu_B B_Z \approx 0.4$  K), which will induce  $H_2$  loss. The second is a nuclear-spin-conserving  $\Delta M_I = 0, \Delta M_N = 2$  transition ( $\Delta M_S = 0$ , see the solid red curve). While this process leads to the loss of  $H_2$  population from the  $SI = 1$  state, the molecule remains in one of the low-field seeking states after the collision. The process releases  $\sim 0.1$  mK of energy. The third most prominent contribution, albeit smaller by a factor of 2.5, is the spin-exchange collision that involves a simultaneous change in the nuclear spin of  $H_2$ ,  $\Delta M_I = +1$ , and relaxation of lithium's electron spin,  $\Delta M_S = -1$ , while conserving the projection of rotational angular momentum,  $\Delta M_N = 0$ ; see the olive dashed curve in Fig. 3(b). Note that this process is driven directly by the spin-dependent  $H_2$ -Li interaction [Eq. (3)].

For the second low-field-seeking initial state of  $H_2$  [ $SI = 2$ , panel (c) in Fig. 3], the two most significant contributions to the total inelastic cross sections stem from lithium's spin-flipping transitions ( $\Delta M_S = -1$ ), with either no change of the  $H_2$  quantum numbers ( $\Delta M_I = \Delta M_N = 0$ ) or a simultaneous change of  $\Delta M_I = +1$  (with  $\Delta M_N = 0$ ); see the green and blue dashed lines in Fig. 3(c), respectively. While the first transition is essentially elastic for  $H_2$ , it releases an energy of  $g_S \mu_B B_Z \approx 0.4$  K. The second one is another example of nuclear spin-electron spin exchange driven by the spin-dependent interaction [Eq. (3)]. In both cases, the released energy will remove the  $H_2$  molecule from the magnetic trap. The third most important contribution (four-times smaller than the nuclear spin-electron spin exchange) comes from a nuclear spin-conserving ( $\Delta M_I = 0$ ) relaxation to the  $SI = 3$  state (with  $\Delta M_N = +1$ ), with no change in lithium's electron spin ( $\Delta M_S = 0$ ). Note that the transition to the  $SI = 1$  low-field-seeking state of  $H_2$  is only energetically accessible

through a simultaneous spin-flip of lithium and provides a negligible ( $10^{-3}$ ) contribution to the total inelastic cross section.

For the third low-field-seeking initial state of  $H_2$  [ $SI = 3$ , panel (d) in Fig. 3], two processes make up 99% of the total inelastic cross section. The first process conserves the Zeeman state of  $H_2$  ( $\Delta M_N = \Delta M_I = 0$ ) but involves a spin flip ( $\Delta M_S = -1$ ) accompanied by an energy release. The second process is a nuclear spin-electron spin exchange ( $\Delta M_S = -1, \Delta M_I = +1$ ), which conserves  $M_N$ . Note that  $M_I$ -conserving transitions that do not involve a simultaneous spin flip in lithium are not energetically accessible at  $E_{kin} \lesssim 10^{-4} \text{ cm}^{-1}$ .

In all three cases discussed so far, although the  $M_I$ ,  $M_N$ , or  $M_S$ -changing processes lead to undesirable energy release and loss of  $H_2$  population from the trap, the cross sections for these processes are over four orders of magnitude smaller than the elastic cross section at collision energies below  $10^{-5} \text{ cm}^{-1}$ . This suggests excellent prospects for sympathetic cooling of  $H_2$  in the low-field-seeking states ( $SI = 1$ –3) via collisions with spin-polarized Li atoms in a magnetic trap.

## B. Low collision energy regime

The second regime involves kinetic energies larger than  $10^{-2} \text{ cm}^{-1}$ . Interestingly, for all three initial low-field-seeking states of  $H_2$ , the cross sections fall into three distinct categories. The dominant contribution (at the level of 99.9%) to the inelastic cross section always comes from  $M_I$ -conserving transitions. The second category provides the contribution at the level of  $10^{-3}$ – $10^{-5}$ . For the

SI = 1 low-field-seeking state [panel (b) in Fig. 3], the second category involves two transitions that alter  $M_I$  by +1 and either conserve  $M_N$  or change  $M_N$  by +1 and one  $\Delta M_I = +2$ ,  $\Delta M_N = 0$  transition. For the SI = 2 low-field-seeking state [panel (c) in Fig. 3], the second category involves three  $\Delta M_I = +1$  transitions (with  $\Delta M_N = -1, 0, 1$ ) and one  $\Delta M_I = +2$ ,  $\Delta M_N = -1$  transition. Finally, the second category for the SI = 3 trappable state [panel (d) in Fig. 3] involves all  $\Delta M_I = +1, +2$  transitions. In all three cases, the third group encompasses all transitions, which affect the electronic spin of lithium ( $\Delta M_S = -1$ ). It additionally involves the two  $M_S$ -conserving transitions with  $\Delta M_I = +2$  for the SI = 1 ( $1 \rightarrow 8$  and  $1 \rightarrow 9$ ) and SI = 2 ( $2 \rightarrow 8$  and  $2 \rightarrow 9$ ) low-field-seeking states and a  $\Delta M_I = +1$ ,  $\Delta M_N = +2$  transition from the SI = 1 state ( $1 \rightarrow 6$ ).

Our results indicate a clear tendency in favor of  $M_I$ - and  $M_S$ -conserving transitions in an external magnetic field. Similar propensity rules were observed for  $M_S$  in cold collisions of  $^{40}\text{CaH}(X^2\Sigma^+, v=0, N=1, M_N=1, M_S=1/2)$  molecules with  $^4\text{He}^{75}$  and for  $M_I$  in collisions of  $^{13}\text{CO}(X^1\Sigma^+, v=0, N=1)$  with  $^4\text{He}^{51}$ . The strong suppression of  $M_I$ - and  $M_S$ -changing collisions in the external magnetic field can be compared to the electron and nuclear spin selection rules in spectroscopy,  $\Delta S = 0$ , and  $\Delta I = 0$ .<sup>76</sup>

An intriguing feature of the  $\text{H}_2$ -Li system is the presence of  $\Delta M_I = 2$  transitions in the second category (or “group-II” transitions, as defined in Ref. 51). In the case of transitions from the SI = 1 and 2 states, it is the  $\Delta M_I = 2$  transition to the SI = 7 state. Its relative strength can be attributed to a slight contribution of the  $|N=1, M_N=1\rangle|I=1, M_I=-1\rangle$  bare state to the SI = 7 state. The mixing of the  $|N=1, M_N=1\rangle|I=1, M_I=-1\rangle$  and  $|N=1, M_N=-1\rangle|I=1, M_I=1\rangle$  basis states is driven by the nuclear spin-spin interactions between the two protons of the  $\text{H}_2$  molecule [Eq. (A7)]. We performed additional calculations, where we excluded the intramolecular nuclear spin-nuclear spin interaction from the asymptotic Hamiltonian [Eq. (5)], and we found that the cross sections for  $\Delta M_I = 2$  transitions decreased by four orders of

magnitude. Note that this interaction is absent in the  $^{13}\text{CO}$  molecule, studied in Ref. 51.

### C. Magnetic field dependence of the cross sections

Here, we discuss the magnetic field dependence of the state-to-state cross sections across three distinct collision energy regimes: ultra-low ( $10^{-6} \text{ cm}^{-1}$ ), intermediate ( $10^{-4} \text{ cm}^{-1}$ ), and low ( $1 \text{ cm}^{-1}$ ). The discussion builds on the results in Sec. IV B, as we focus on collisions of  $\text{H}_2$  in the three magnetically trappable states, SI = 1, 2, and 3, as shown in Fig. 4. In all panels, the color of each curve corresponds directly to the color of the respective final Zeeman level (see Fig. 3).

We observe that the elastic cross sections are field-independent and by far exceed the inelastic cross sections. The dependence of the inelastic cross sections on  $B$  varies with the kinetic energy and the final Zeeman state. For instance, in the ultra-low energy regime [panels (a)–(c) in Fig. 4], we observe a systematic increase in the values of the cross sections with  $B$ . However, two distinct deviations from this pattern emerge. The first one is related to the observed resonance-like features at 0.0025 and 0.5 T for the final Zeeman states with SI = 7 and 5, respectively [see the pink and light blue curves in panels (a), (b), (d), (e), (g), and (h) in Fig. 4]. These will be discussed further in the next paragraph. The other exception is the sharp decline for excitation transitions, such as SI = 2  $\rightarrow$  1 at 0.008 T [the blue curve in panel (b)]. This is due to the closure of inelastic channels due to increasing spacing between the initial and final Zeeman sublevels with increasing magnetic field. The sharp increase in the cross sections [see, for instance, the orange, light blue, and red curves in panel (a)] corresponds to the opening of the additional inelastic channels. As the kinetic energy increases [see panels (d)–(f)], more channels become energetically accessible, even at low  $B$  field values. Meanwhile, the fields at which some of the inelastic channels become inaccessible are shifted toward larger values. Finally, in the low energy regime [panels (g)–(i)], we can categorize inelastic cross sections into two main classes. The cross sections

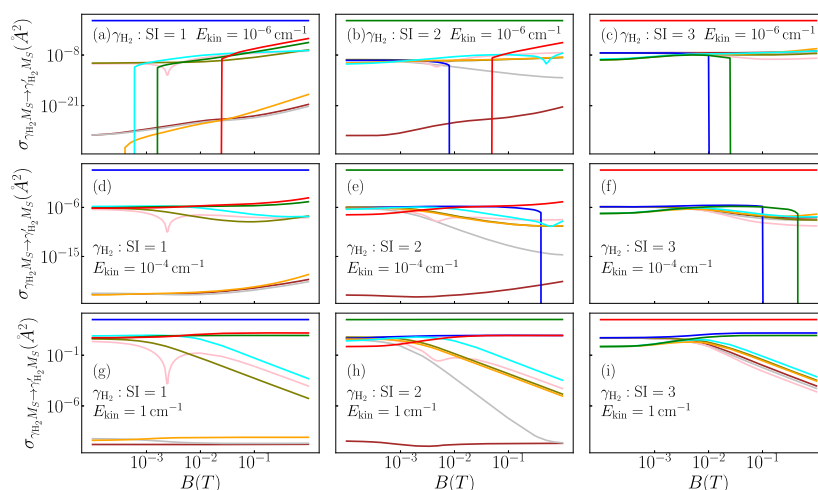


**FIG. 4.** State-to-state cross sections for cold  $\text{H}_2$ -Li collisions in the three Zeeman states amenable to magnetic trapping ( $\gamma_{\text{H}_2}$ : SI = 1, 2, and 3), as a function of the external magnetic field,  $B$ . The initial and final states of the lithium atom are fixed to  $M_S = 1/2$ . The final Zeeman states in each panel are color-coded according to Fig. 3.

from the first class exhibit a negligible field dependence. The cross sections from the second class are field-independent at low  $B$  values but decrease monotonically with increasing  $B$  for fields larger than  $10^{-2}$  T. We explain this behavior in detail below, focusing on the case of the scattering from the  $SI = 1$  state [panel (g)].

As discussed in Sec. IV B, we observe a clear propensity for  $\Delta M_I = 0$  transitions. This propensity rule is evident here too, as emphasized by the green and red curves across the considered field ranges: the cross sections for transitions to the  $SI = 2$  and 3 states are notably larger than others. Furthermore, they exhibit a weak field dependence. Transitions to the weakly coupled ( $\Delta M_I = 2$ )  $SI = 8$  and 9 states [grey and dark red lines in panel (g)] are orders of magnitude smaller. Interestingly, they are also field-independent, suggesting that the lack of strong coupling makes them less susceptible to the variations in  $B$ . Apart from these two cases, the same observation holds for the transition to the  $SI = 6$  state (orange curve): the relative weakness of this cross section is related to the admixture of the  $|N = 1, M_N = 0\rangle|I = 1, M_I = 1\rangle$  basis state. A completely different behavior of the cross sections as a function of  $B$  is observed for three other final Zeeman states. The transition to the  $SI = 4$  state (olive line) is one of the most important inelastic processes at low values of  $B$ . This is because of the admixture of the  $|N = 1, M_N = -1\rangle|I = 1, M_I = 0\rangle$  state through the nuclear spin-rotation interaction. As the field increases, so does the energy spacing between the two states, and the mixing becomes less significant. The pronounced magnetic-field dependence of the cross sections to the Zeeman eigenstates composed of strongly mixed bare states  $|NM_N\rangle|IM_I\rangle$  was observed in Ref. 51 for the  $^{13}\text{C}^{18}\text{O}$ -He system and explained in the framework of the Born approximation. For the transitions to the  $SI = 5$  and 7 states (denoted by the light blue and pink lines), the dynamics are influenced by the fact that they are composed of three strongly mixed bare states  $|NM_N\rangle|IM_I\rangle$  with  $M_N + M_I = 0$ . This mixing stems from the interplay of the nuclear spin-rotation and nuclear spin-nuclear spin interactions (the three states constitute a  $3 \times 3$  matrix of states with  $M_F = 0$ ). The mixing becomes less pronounced as the field increases, although there exists a resonant-like feature at 0.002 45 T for the  $SI = 1 \rightarrow SI = 7$  transition. We note that this feature is independent of the relative kinetic energy of the collision. The nature of this resonant-like feature and the potential for identifying such resonances in other systems will be explored in a forthcoming publication.

We note similar patterns for inelastic collisions originating from the  $SI = 2$  and 3 states. The majority of significant inelastic processes favor the  $\Delta M_I = 0$  propensity rule, showing only minor variations with increasing fields. For the  $SI = 2$  state, five distinct transitions exhibit a linear decrease with the field. This pattern traces back to the admixture of the  $|N = 1, M_N = 1\rangle|I = 1, M_I = -1\rangle$  basis state, primarily responsible for the elevated magnitudes of the inelastic cross sections at lower fields. As  $B$  increases, the mixing becomes less pronounced, leading to the decreasing magnitude of the cross sections at higher  $B$  values. Finally, the  $SI = 3$  state is somewhat special: 6 out of 9 cross sections exhibit a systematic decrease with the field. All of these are “group-II” transitions identified in Sec. IV B. Their decrease with increasing  $B$  can be understood by the decreasing admixture of the  $|N = 1, M_N = 1\rangle|I = 1, M_I = -1\rangle$  bare state to the  $SI = 5$  and 7 states (light blue and pink curves, respectively), the decreasing admixture of the  $|N = 1, M_N = 0\rangle|I = 1, M_I = -1\rangle$  bare state to the  $SI = 4$  state (olive curve), or the increasing energy separation from the rest of the Zeeman states.

#### D. Elastic-to-inelastic scattering ratio

Here, we explore the potential of atomic lithium as a sympathetic coolant for the  $\text{H}_2$  molecule. While the mismatch between Zeeman splittings of  $\text{H}_2$  and  $^6\text{Li}$  presents a challenge for the experimental realization of a two-species trap, here, we focus on estimating the efficiency of the cooling mechanism. Specifically, we determine the elastic-to-inelastic ratio and estimate the optimal lithium density that yields the most effective thermalization during collisions.

To this end, we calculate the average state-to-state cross sections for Li- $\text{H}_2$  collisions for the three initial trappable states ( $SI = 1, 2$ , and 3) of  $\text{H}_2$  [see Eq. (14)] and the corresponding rate coefficients  $k$ , given by Eq. (15). Note that the initial state of lithium is fixed to the trappable  $M_S = 1/2$  state.

The rate coefficients are presented in Fig. 5. The elastic scattering rates for the three trappable states of  $\text{H}_2$  are nearly identical to the corresponding rate coefficients calculated without the hyperfine structure and external magnetic field,  $k_{N=1}^{\text{el}}$  (black solid line in Fig. 5). The largest difference between  $k_{N=1}^{\text{el}}$  and  $k_{\gamma_{\text{H}_2}}^{\text{el}}$  is  $\sim 3\%$ . The solid lines in Fig. 5 correspond to the total inelastic rate coefficients. To check whether the sympathetic cooling of  $\text{H}_2$  by  $^6\text{Li}$  is feasible, we plot in Fig. 5 the elastic rate coefficient multiplied by  $\frac{1}{100}$  (efficient cooling requires  $k^{\text{el}}/k^{\text{inel}} \geq 100$ ). At first sight, it seems that this condition is fulfilled for temperatures below 50 mK. We recall that the proposed trap depth is  $\sim 0.8$  mK for the  $SI = 1$  state of  $\text{H}_2$ . However, the total inelastic cross section is dominated by transitions to other trappable states (transitions with  $\Delta M_I = 0$ ). Thus, the rate of inelastic scattering to states that are *not* amenable to magnetic trapping is several orders of magnitude lower (see the dashed lines in Fig. 5), and the corresponding elastic-to-inelastic scattering ratio is always larger than  $10^4$ . Transitions to other trappable states release energy ( $\sim 10$  times lower than the trap depth), which could result in heating, but not trap loss, being of minor concern for sympathetic cooling experiments.

We also estimate the rate of thermalizing collisions (in  $\text{s}^{-1}$ ) as

$$R = k_{\gamma_{\text{H}_2}}^{\text{el}} n_0. \quad (18)$$

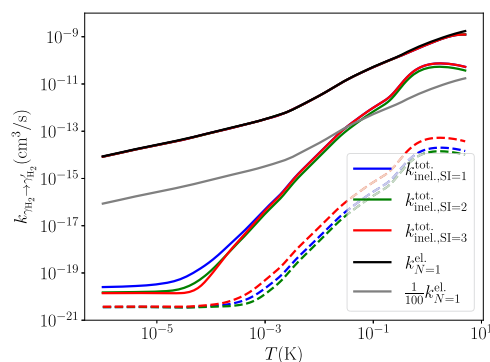


**FIG. 5.** Rate coefficients for elastic and inelastic transitions in Li- $\text{H}_2$  collisions for the three trappable Zeeman sublevels of  $\text{H}_2$  ( $v = 0, N = 1$ ) at 0.3 T. The elastic rates are almost identical to the field- and hyperfine-free elastic rate coefficients for the  $v = 0, N = 1$  state (black solid line). The total inelastic rate coefficients and the inelastic rate coefficients to the untrappable states are presented as solid and dashed lines, respectively. The gray solid line presents the elastic rate coefficient multiplied by  $\frac{1}{100}$ .



Taking the elastic rate coefficient for the  $SI = 1$  state of  $H_2$  at 1 mK ( $3.2 \times 10^{-13} \text{ cm}^3 \text{ s}^{-1}$ ) and the density of  $^6\text{Li}$  atoms in the UV MOT<sup>47</sup> operating at 59  $\mu\text{K}$  ( $n_0 = 2.9 \times 10^{10} \text{ cm}^{-3}$ ), we obtain  $R \approx 10^{-2} \text{ s}^{-1}$ . For efficient sympathetic cooling, the rate of thermalizing collisions should be higher by at least two orders of magnitude. This can be achieved by increasing the density of the lithium MOT, either by using higher magnetic field gradients or larger detunings of the UV light. The increased density is then achieved with a trade-off for an increased temperature of the Li atoms.

## V. CONCLUSIONS

We performed a rigorous quantum dynamical analysis of the effects of hyperfine and Zeeman interactions on cold and ultracold atom- $H_2$  collisions. We investigated the cold collisions of molecular hydrogen in the  $v = 0, N = 1$  rovibrational state with  $^6\text{Li}$  atoms using CC quantum scattering calculations based on an accurate *ab initio* PES. In the field-free case, we found that the three hyperfine levels of the  $v = 0, N = 1$  state in  $H_2$  predominantly undergo elastic collisions. The magnetic dipolar interaction between the electronic spin in lithium and the total nuclear spin of  $H_2$  exerts a pronounced inference on ultracold Li- $H_2$  collisions, enhancing the  $F = 0 \rightarrow F' = 1$  transitions.

We found that the collisional dynamics of  $H_2$  in low-field-seeking states in the presence of an external magnetic field is dominated by elastic, rather than inelastic, collisions. Inelastic collisions tend to conserve the space-fixed projection of the nuclear spin in  $H_2$ . The magnetic dipolar interaction between the nuclear spin of  $H_2$  and the electronic spin of Li drives the electron spin relaxation and the nuclear spin-electron spin exchange, two key inelastic processes in the ultracold regime.

Finally, we discussed the results in the context of the experimental realization of sympathetic cooling of  $H_2$  by ultracold spin-polarized Li atoms. Given the predominance of elastic collisions and the propensity of inelastic scattering to retain  $H_2$  in its low-field-seeking states, the elastic-to-inelastic collision ratio for Li- $H_2$  is favorable for sympathetic cooling ( $\gamma > 100$ ). However, to realize efficient sympathetic cooling, the current densities of Li in a MOT must be increased by at least two orders of magnitude.

## ACKNOWLEDGMENTS

This research was funded by the European Union (Grant Nos. ERC-2022-STG, H2TRAP, and 101075678). Views and opinions expressed are, however, those of the author(s) only and do not necessarily reflect those of the European Union or the European Research Council Executive Agency. Neither the European Union nor the granting authority can be held responsible for them. H.J. is supported by the Foundation for Polish Science (FNP). T.V.T. acknowledges the support from the NSF CAREER Award No. PHY-2045681. This research was financed from the budgetary funds on science projected for 2019–2023 as a research project under the “Diamantowy Grant” program. We gratefully acknowledge Polish high-performance computing infrastructure PLGrid (HPC Centers: ACK Cyfronet AGH, CI TASK) for providing computer facilities and support within computational Grant No. PLG/2023/016279. Calculations have been carried out using resources provided by Wrocław Centre for Networking and Supercomputing (<http://wcss.pl>), Grant No. 546. This research is

part of the program of the National Laboratory FAMO in Toruń, Poland.

## AUTHOR DECLARATIONS

### Conflict of Interest

The authors have no conflicts to disclose.

## Author Contributions

**Hubert Jóźwiak:** Conceptualization (equal); Funding acquisition (supporting); Investigation (lead); Methodology (equal); Software (equal); Visualization (lead); Writing – original draft (lead). **Timur V. Tscherebul:** Conceptualization (equal); Funding acquisition (supporting); Methodology (equal); Resources (supporting); Software (equal); Supervision (supporting); Validation (lead); Writing – review & editing (equal). **Piotr Wcisło:** Conceptualization (equal); Funding acquisition (lead); Resources (lead); Supervision (lead); Validation (supporting); Writing – review & editing (equal).

## DATA AVAILABILITY

The data that support the findings of this study are available from the corresponding author upon reasonable request.

## APPENDIX A: MATRIX ELEMENTS IN EQ. (11)—THE UNCOUPLED BASIS

Here, we present a derivation of the matrix elements that enter the CC equations [Eq. (11)]. Following the standard approach,<sup>49</sup> we expand the  $H_2$ -Li interaction potential in Legendre polynomials,

$$V(\mathbf{R}, \mathbf{r}) = \sum_{\lambda=0}^{\lambda_{\max}} V_{\lambda}(R, r) P_{\lambda}(\cos \theta). \quad (\text{A1})$$

Since  $H_2$  is a homonuclear molecule,  $\lambda$  takes only even values. We truncate the expansion at  $\lambda_{\max} = 4$ . The interaction potential is diagonal in all spin projections ( $M_I, M_S$ , and  $M_{I_{\text{Li}}}$ ) with matrix elements,<sup>49</sup>

$$\begin{aligned} \langle NM_N | \langle IM_I | \langle SM_S | \langle IM_I | \hat{V}(\mathbf{R}, \mathbf{r}) | N' M'_N \rangle | IM'_I \rangle | SM'_S \rangle | I' M'_I \rangle \\ = \delta_{M_S M'_S} \delta_{M_I M'_I} (-1)^{M'_I - M_N} \sqrt{[N, N', I, I']} \sum_{\lambda=0}^{\lambda_{\max}} v_{\lambda, v=0}^{N, N'}(R) \begin{pmatrix} I & \lambda & I' \\ 0 & 0 & 0 \end{pmatrix} \\ \times \begin{pmatrix} I & \lambda & I' \\ -M_I & \Delta M_I & M'_I \end{pmatrix} \begin{pmatrix} N & \lambda & N' \\ 0 & 0 & 0 \end{pmatrix} \begin{pmatrix} N & \lambda & N' \\ -M_N & \Delta M_N & M'_N \end{pmatrix}. \quad (\text{A2}) \end{aligned}$$

Here,  $\Delta M_x = M_x - M'_x$  for all angular momentum projections ( $x = I, N, S, I$ ) and  $[x_1, x_2, \dots, x_N] = (2x_1 + 1)(2x_2 + 1) \dots (2x_N + 1)$ . We note that the interaction potential mixes states with different  $M_I$  and  $M_N$ . At the same time, the interaction conserves the sum  $M_I + M_N$  and, as a result, the projection of the total angular momentum,  $M$ . The coefficients  $v_{\lambda, v=0}^{N, N'}(R)$  are obtained by taking the matrix elements of the Legendre moments in Eq. (A1),  $V_{\lambda}(R, r)$ , between the rovibrational wave functions of the  $H_2$  molecule in the  $v = 0$  state,

$$v_{\lambda, v=0}^{N, N'}(R) = \int_0^{\infty} dr \chi_{v=0, N}(r) V_{\lambda}(R, r) \chi_{v=0, N'}(r). \quad (\text{A3})$$

Rovibrational wave functions of  $H_2$ ,  $\chi_{v,N}$ , are obtained by solving the Schrödinger equation for the nuclear motion of  $H_2$  with the potential energy curve of Schwenke<sup>77</sup> using the discrete variable representation–finite basis representation method. Due to a weak dependence of the  $v_{\lambda,v=0}^{N,N'}(R)$  terms on  $N$ , we use  $N = N' = 1$  in scattering calculations.

The magnetic dipolar interaction between the nuclear spin of  $H_2$  and the electron spin of Li [see Eq. (3)] is diagonal in  $N$  and  $M_N$ ,

$$\begin{aligned} \langle NM_N | \langle IM_I | \langle SM_S | \langle IM_I | \hat{V}_{SD}(\mathbf{R}, \mathbf{r}, \hat{\mathbf{S}}) | N' M'_N \rangle | IM'_I \rangle | SM'_S \rangle | I' M'_I \rangle \\ = -\delta_{NN'} \delta_{M_N M'_N} g_S \mu_B g_H \mu_N \left( \frac{\alpha^2}{R^3} \right) \sqrt{30} (-1)^{-M_I + I - M_{H_2} + S - M_S} \\ \times \sqrt{[l, l']} \begin{pmatrix} l & 2 & l' \\ 0 & 0 & 0 \end{pmatrix} \sqrt{I(I+1)(2I+1)} \sqrt{S(S+1)(2S+1)} \\ \times \begin{pmatrix} 1 & 1 & 2 \\ \Delta M_S & \Delta M_I & \Delta M_I \end{pmatrix} \begin{pmatrix} I & 1 & I' \\ -M_I & \Delta M_I & M'_I \end{pmatrix} \\ \times \begin{pmatrix} S & 1 & S' \\ -M_S & \Delta M_S & M'_S \end{pmatrix} \begin{pmatrix} l & 2 & l' \\ -M_I & \Delta M_I & M'_I \end{pmatrix}. \end{aligned} \quad (A4)$$

This interaction mixes basis states with different  $M_S, M_I$ , and  $M_I$ , but it conserves the sum  $M_S + M_I + M_I$ . Thus, the total angular momentum,  $M$ , is also conserved.

In the next step, we consider the asymptotic Hamiltonian, Eq. (4), and we begin with the part of this operator associated with  $H_2$ . The rotational term is diagonal in all quantum numbers,

$$\begin{aligned} \langle NM_N | \langle IM_I | \langle SM_S | \langle IM_I | \hat{H}_{\text{rot}} | N' M'_N \rangle | IM'_I \rangle | SM'_S \rangle | I' M'_I \rangle \\ = \delta_{NN'} \delta_{M_N M'_N} \delta_{M_I M'_I} \delta_{M_S M'_S} \delta_{M_I M'_I} \\ \times [B_e N(N+1) - D_e N^2(N+1)^2], \end{aligned} \quad (A5)$$

and the matrix elements of the nuclear spin–rotation interaction are given as

$$\begin{aligned} -c_{\text{nsr}} \langle NM_N | \langle IM_I | \langle SM_S | \langle IM_I | \hat{\mathbf{N}} \cdot \hat{\mathbf{I}} | N' M'_N \rangle | IM'_I \rangle | SM'_S \rangle | I' M'_I \rangle \\ = -\delta_{NN'} \delta_{M_S M'_S} \delta_{I' I} \delta_{M_I M'_I} \left[ \delta_{M_I M'_I} \delta_{M_N M'_N} c_{\text{nsr}} M_N M_I \right. \\ \left. + \delta_{M_N M'_N \pm 1} \delta_{M_I M'_I \mp 1} \frac{c_{\text{nsr}}}{2} (N(N+1) - M'_N(M'_N \pm 1))^{1/2} \right. \\ \left. \times (I(I+1) - M'_I(M'_I \mp 1))^{1/2} \right]. \end{aligned} \quad (A6)$$

The intramolecular spin–spin interaction couples (very weakly) states with different rotational angular momenta,

$$\begin{aligned} g_H^2 \mu_N^2 \alpha^2 \langle NM_N | \langle IM_I | \langle SM_S | \langle IM_I | \left( \frac{\hat{\mathbf{I}}_1 \cdot \hat{\mathbf{I}}_2}{r^3} - \frac{3(\hat{\mathbf{I}}_1 \cdot \mathbf{r})(\hat{\mathbf{I}}_2 \cdot \mathbf{r})}{r^5} \right) | N' M'_N \rangle | IM'_I \rangle | SM'_S \rangle | I' M'_I \rangle \\ = \delta_{M_S M'_S} \delta_{I' I} \delta_{M_I M'_I} (-1)^{I - M_I - M'_N} \sqrt{30} c_{\text{dip}} [I] \sqrt{[N, N']} \begin{pmatrix} N & 2 & N' \\ 0 & 0 & 0 \end{pmatrix} \begin{pmatrix} N & 2 & N' \\ -M_N & \Delta M_N & M'_N \end{pmatrix} \\ \times \begin{pmatrix} I & 2 & I \\ -M_I & \Delta M_I & M'_I \end{pmatrix} \begin{pmatrix} I_1 & I_1 & 1 \\ I_2 & I_2 & 1 \\ I & I & 2 \end{pmatrix} \sqrt{I_1(I_1+1)(2I_1+1)I_2(I_2+1)(2I_2+1)}. \end{aligned} \quad (A7)$$

Here,  $\left\{ \begin{smallmatrix} . & . & . \\ . & . & . \\ . & . & . \end{smallmatrix} \right\}$  denotes the Wigner 9-j symbol. Both of the Zeeman terms in the asymptotic Hamiltonian of  $H_2$  are diagonal in all quantum numbers,

$$\begin{aligned} \langle NM_N | \langle IM_I | \langle SM_S | \langle IM_I | \hat{H}_{\text{Zeeman}} | N' M'_N \rangle | IM'_I \rangle | SM'_S \rangle | I' M'_I \rangle \\ = -\delta_{NN'} \delta_{M_N M'_N} \delta_{M_I M'_I} \delta_{M_S M'_S} \delta_{M_I M'_I} \mu_N B_Z (1 - \sigma) \\ \times (g_r M_N + g_H M_I). \end{aligned} \quad (A8)$$

The same applies to the asymptotic Hamiltonian of lithium from Eq. (9),

$$\begin{aligned} \langle NM_N | \langle IM_I | \langle SM_S | \langle IM_I | \hat{H}_{\text{Li}} | N' M'_N \rangle | IM'_I \rangle | SM'_S \rangle | I' M'_I \rangle \\ = -\delta_{NN'} \delta_{M_N M'_N} \delta_{M_I M'_I} \delta_{M_S M'_S} \delta_{M_I M'_I} g_S \mu_B B_Z M_S. \end{aligned} \quad (A9)$$

## APPENDIX B: MATRIX ELEMENTS IN EQ. (11)—THE BASIS WITH COUPLED $H_2$ VECTORS

Similarly to the uncoupled case, the  $H_2$ –Li interaction is diagonal in  $M_S$ ,

$$\begin{aligned} \langle (NI) F M_F | \langle SM_S | \langle IM_I | \langle IM_I | \hat{V}(\mathbf{R}, \mathbf{r}) | (N'I) F' M'_F \rangle | SM'_S \rangle | I' M'_I \rangle \\ = \delta_{M_S M'_S} (-1)^{M'_I - M_F + I + F + F'} \sqrt{[N, N', I, I', F, F']} \\ \times \sum_{\lambda=0}^{\lambda_{\text{max}}} v_{\lambda, v=0}^{N, N'}(R) \begin{pmatrix} l & \lambda & l' \\ 0 & 0 & 0 \end{pmatrix} \begin{pmatrix} l & \lambda & l' \\ -M_I & \Delta M_I & M'_I \end{pmatrix} \begin{pmatrix} N & \lambda & N' \\ 0 & 0 & 0 \end{pmatrix} \\ \times \begin{pmatrix} F & \lambda & F' \\ -M_F & \Delta M_F & M'_F \end{pmatrix} \begin{pmatrix} N' & F' & I \\ F & N & \lambda \end{pmatrix}. \end{aligned} \quad (B1)$$

The spin-dependent interaction is diagonal in  $N$ ,

$$\begin{aligned} & \langle (NI)FM_F | \langle SM_S | \langle IM_I | \hat{V}_{SD}(\mathbf{R}, \mathbf{r}, \hat{\mathbf{I}}, \hat{\mathbf{S}}) | (N'I)F'M'_F \rangle | SM'_S \rangle | I' M'_I \rangle \\ &= \delta_{NN'} g_S \mu_B g_H \mu_N \left( \frac{\alpha^2}{R^3} \right) \sqrt{30} (-1)^{M_I + I + N + F} \sqrt{[l, l', F, F']} \\ & \times \begin{pmatrix} l & 2 & l' \\ 0 & 0 & 0 \end{pmatrix} \sqrt{I(I+1)(2I+1)} \sqrt{S(S+1)(2S+1)} \\ & \times \begin{pmatrix} 1 & 1 & 2 \\ \Delta M_F & \Delta M_S & \Delta M_I \end{pmatrix} \begin{pmatrix} F & 1 & F' \\ -M_F & \Delta M_F & M'_F \end{pmatrix} \\ & \times \begin{pmatrix} S & 1 & S' \\ -M_S & \Delta M_S & M'_S \end{pmatrix} \begin{pmatrix} l & 2 & l' \\ -M_l & \Delta M_l & M'_l \end{pmatrix} \begin{Bmatrix} I & F' & N \\ F & I & 1 \end{Bmatrix}. \end{aligned} \quad (\text{B2})$$

The rotational part of the Hamiltonian is diagonal in all quantum numbers,

$$\begin{aligned} & \langle (NI)FM_F | \langle SM_S | \langle IM_I | \hat{H}_{\text{rot}} | (N'I)F'M'_F \rangle | SM'_S \rangle | I' M'_I \rangle \\ &= \delta_{NN'} \delta_{FF'} \delta_{M_F M'_F} \delta_{M_S M'_S} \delta_{M_I M'_I} \\ & \times (B_e N(N+1) - D_v N^2 (N+1)^2). \end{aligned} \quad (\text{B3})$$

Both hyperfine interactions are diagonal in the total angular momentum of  $\text{H}_2$  and its projection on the space-fixed Z-axis. The nuclear spin-rotation interaction is additionally diagonal in all other quantum numbers,

$$\begin{aligned} & -c_{\text{nsr}} \langle (NI)FM_F | \langle SM_S | \langle IM_I | \hat{\mathbf{N}} \cdot \hat{\mathbf{I}} | (N'I)F'M'_F \rangle | SM'_S \rangle | I' M'_I \rangle \\ &= -\delta_{NN'} \delta_{FF'} \delta_{M_F M'_F} \delta_{M_S M'_S} \delta_{M_I M'_I} \frac{c_{\text{nsr}}}{2} \\ & \times (F(F+1) - I(I+1) - N(N+1)). \end{aligned} \quad (\text{B4})$$

The spin-spin magnetic dipole interaction can, in principle, couple states with different  $N$  and  $I$ . This coupling is 11 orders of magnitude smaller than the spacing between the  $N$  and  $N' = N \pm 2$  rotational states of  $\text{H}_2$ , and we neglect it here. We additionally neglect any *ortho*-/*para*- $\text{H}_2$  coupling. The matrix elements of this interaction are

$$\begin{aligned} & g_H^2 \mu_N^2 \alpha^2 \langle (NI)FM_F | \langle SM_S | \langle IM_I | \left( \frac{\hat{\mathbf{I}}_1 \cdot \hat{\mathbf{I}}_2}{r^3} - \frac{3(\hat{\mathbf{I}}_1 \cdot \mathbf{r})(\hat{\mathbf{I}}_2 \cdot \mathbf{r})}{r^5} \right) | (N'I)F'M'_F \rangle | SM'_S \rangle | I' M'_I \rangle \\ &= -\delta_{M_S M'_S} \delta_{I I'} \delta_{F F'} \delta_{M_F M'_F} (-1)^{N+N'+I+F} \sqrt{30} c_{\text{dip}} [I] \sqrt{[N, N']} \\ & \times \begin{pmatrix} N & 2 & N' \\ 0 & 0 & 0 \end{pmatrix} \begin{pmatrix} N & N' & 2 \\ I & I & F \end{pmatrix} \begin{pmatrix} I_1 & I_1 & 1 \\ I_2 & I_2 & 1 \\ I & I & 2 \end{pmatrix} \sqrt{I_1(I_1+1)(2I_1+1)I_2(I_2+1)(2I_2+1)}. \end{aligned} \quad (\text{B5})$$

The matrix elements of the Zeeman term of the lithium atom are identical to those given by Eq. (A8). Finally, the Zeeman Hamiltonian of  $\text{H}_2$  has the following matrix elements:

$$\begin{aligned} & \langle (NI)FM_F | \langle SM_S | \langle IM_I | \hat{H}_{\text{Zeeman}} | (N'I)F'M'_F \rangle | SM'_S \rangle | I' M'_I \rangle \\ &= \delta_{NN'} \delta_{M_S M'_S} \delta_{M_I M'_I} \mu_N B_Z (1 - \sigma) (-1)^{F'-m_F+I+N'+F'} \\ & \times \begin{pmatrix} F & 1 & F' \\ -M_F & 0 & M'_F \end{pmatrix} \sqrt{[F, F']} \sqrt{I(I+1)(2I+1)} \\ & \times \left( \delta_{NN'} g_r \begin{Bmatrix} F & F' & 1 \\ I & I & N \end{Bmatrix} + g_H \begin{Bmatrix} F & F' & 1 \\ N' & N & I \end{Bmatrix} \right). \end{aligned} \quad (\text{B6})$$

## REFERENCES

- R. V. Krems, *Phys. Chem. Chem. Phys.* **10**, 4079 (2008).
- N. Balakrishnan, *J. Chem. Phys.* **145**, 150901 (2016).
- M. Tizniti, S. D. Le Picard, F. Lique, C. Berteloite, A. Canosa, M. H. Alexander, and I. R. Sims, *Nat. Chem.* **6**, 141 (2014).
- A. B. Henson, S. Gersten, Y. Shagam, J. Narevicius, and E. Narevicius, *Science* **338**, 234 (2012).
- E. Lavert-Ofir, Y. Shagam, A. B. Henson, S. Gersten, J. Kłos, P. S. Żuchowski, J. Narevicius, and E. Narevicius, *Nat. Chem.* **6**, 332 (2014).
- Y. Shagam, A. Klein, W. Skomorowski, R. Yun, V. Averbukh, C. P. Koch, and E. Narevicius, *Nat. Chem.* **7**, 921 (2015).
- A. Klein, Y. Shagam, W. Skomorowski, P. S. Żuchowski, M. Pawlak, L. M. C. Janssen, N. Moiseyev, S. Y. T. van de Meerakker, A. van der Avoird, C. P. Koch, and E. Narevicius, *Nat. Phys.* **13**, 35 (2016).
- W. E. Perreault, N. Mukherjee, and R. N. Zare, *Science* **358**, 356 (2017).
- W. E. Perreault, N. Mukherjee, and R. N. Zare, *Nat. Chem.* **10**, 561 (2018).
- H. Zhou, W. E. Perreault, N. Mukherjee, and R. N. Zare, *Science* **374**, 960 (2021).
- H. Zhou, W. E. Perreault, N. Mukherjee, and R. N. Zare, *J. Chem. Phys.* **154**, 104309 (2021).
- P. G. Jambrina, J. F. E. Croft, H. Guo, M. Brouard, N. Balakrishnan, and F. J. Aoiz, *Phys. Rev. Lett.* **123**, 043401 (2019).
- A. Devolder, T. Tschertbul, and P. Brumer, *Phys. Rev. A* **102**, 031303 (2020).
- A. Devolder, P. Brumer, and T. V. Tschertbul, *Phys. Rev. Lett.* **126**, 153403 (2021).
- N. Balakrishnan, R. Forrey, and A. Dalgarno, *Chem. Phys. Lett.* **280**, 1 (1997).
- N. Balakrishnan, R. C. Forrey, and A. Dalgarno, *Phys. Rev. Lett.* **80**, 3224 (1998).
- A. Mack, T. K. Clark, R. C. Forrey, N. Balakrishnan, T.-G. Lee, and P. C. Stancil, *Phys. Rev. A* **74**, 052718 (2006).
- G. Quémener, N. Balakrishnan, and R. V. Krems, *Phys. Rev. A* **77**, 030704 (2008).
- G. Quémener and N. Balakrishnan, *J. Chem. Phys.* **130**, 114303 (2009).
- N. Balakrishnan, G. Quémener, R. C. Forrey, R. J. Hinde, and P. C. Stancil, *J. Chem. Phys.* **134**, 014301 (2011).

- <sup>21</sup>S. F. dos Santos, N. Balakrishnan, S. Lepp, G. Quémener, R. C. Forrey, R. J. Hinde, and P. C. Stancil, *J. Chem. Phys.* **134**, 214303 (2011).
- <sup>22</sup>J. F. E. Croft, N. Balakrishnan, M. Huang, and H. Guo, *Phys. Rev. Lett.* **121**, 113401 (2018).
- <sup>23</sup>J. F. E. Croft and N. Balakrishnan, *J. Chem. Phys.* **150**, 164302 (2019).
- <sup>24</sup>M. Morita and N. Balakrishnan, *J. Chem. Phys.* **153**, 091101 (2020).
- <sup>25</sup>P. G. Jambrina, M. Morita, J. F. E. Croft, F. J. Aoiz, and N. Balakrishnan, *J. Phys. Chem. Lett.* **13**, 4064 (2022).
- <sup>26</sup>N. F. Ramsey, *Phys. Rev.* **85**, 60 (1952).
- <sup>27</sup>H. Jóźwiak, H. Cybulski, and P. Wcisło, *J. Quant. Spectrosc. Radiat. Transfer* **253**, 107186 (2020).
- <sup>28</sup>M. Puchalski, J. Komasa, and K. Pachucki, *Phys. Rev. Lett.* **125**, 253001 (2020).
- <sup>29</sup>A. Fast and S. A. Meek, *Phys. Rev. Lett.* **125**, 023001 (2020).
- <sup>30</sup>A. Fast and S. A. Meek, *Mol. Phys.* **120**, e1999520 (2021).
- <sup>31</sup>J. Komasa, M. Puchalski, P. Czachorowski, G. Łach, and K. Pachucki, *Phys. Rev. A* **100**, 032519 (2019).
- <sup>32</sup>M. Puchalski, J. Komasa, P. Czachorowski, and K. Pachucki, *Phys. Rev. Lett.* **122**, 103003 (2019).
- <sup>33</sup>M. Zaborowski, M. Słowiński, K. Stankiewicz, F. Thibault, A. Cygan, H. Jóźwiak, G. Kowzan, P. Masłowski, A. Nishiyama, N. Stolarczyk, S. Wójtewicz, R. Ciuryło, D. Lisak, and P. Wcisło, *Opt. Lett.* **45**, 1603 (2020).
- <sup>34</sup>W. Ubachs, J. Koelemeij, K. Eikema, and E. Salumbides, *J. Mol. Spectrosc.* **320**, 1 (2016).
- <sup>35</sup>M. L. Diouf, F. M. J. Cozijn, B. Darquié, E. J. Salumbides, and W. Ubachs, *Opt. Lett.* **44**, 4733 (2019).
- <sup>36</sup>T.-P. Hua, Y. R. Sun, and S.-M. Hu, *Opt. Lett.* **45**, 4863 (2020).
- <sup>37</sup>S. Kassi, C. Lauzin, J. Chaillot, and A. Campargue, *Phys. Chem. Chem. Phys.* **24**, 23164 (2022).
- <sup>38</sup>F. M. J. Cozijn, M. L. Diouf, and W. Ubachs, *Eur. Phys. J. D* **76**, 220 (2022).
- <sup>39</sup>Q.-H. Liu, Y.-N. Lv, C.-L. Zou, C.-F. Cheng, and S.-M. Hu, *Phys. Rev. A* **106**, 062805 (2022).
- <sup>40</sup>H. Jóźwiak and P. Wcisło, *Sci. Rep.* **12**, 14529 (2022).
- <sup>41</sup>A. Singh, L. Maisenbacher, Z. Lin, J. J. Axelrod, C. D. Panda, and H. Müller, *Phys. Rev. Res.* **5**, 033008 (2023).
- <sup>42</sup>M. Lara, J. L. Bohn, D. Potter, P. Soldán, and J. M. Hutson, *Phys. Rev. Lett.* **97**, 183201 (2006).
- <sup>43</sup>M. Lara, J. L. Bohn, D. E. Potter, P. Soldán, and J. M. Hutson, *Phys. Rev. A* **75**, 012704 (2007).
- <sup>44</sup>T. V. Tscherbul, J. Klos, and A. A. Buchachenko, *Phys. Rev. A* **84**, 040701(R) (2011).
- <sup>45</sup>M. Morita, J. Klos, A. A. Buchachenko, and T. V. Tscherbul, *Phys. Rev. A* **95**, 063421 (2017).
- <sup>46</sup>L. D. Carr, D. DeMille, R. V. Krems, and J. Ye, *New J. Phys.* **11**, 055049 (2009).
- <sup>47</sup>P. M. Duarte, R. A. Hart, J. M. Hitchcock, T. A. Corcovilos, T.-L. Yang, A. Reed, and R. G. Hulet, *Phys. Rev. A* **84**, 061406 (2011).
- <sup>48</sup>C. Makrides, D. S. Barker, J. A. Fedchak, J. Scherschligt, S. Eckel, and E. Tiesinga, *Phys. Rev. A* **99**, 042704 (2019).
- <sup>49</sup>R. V. Krems and A. Dalgarno, *J. Chem. Phys.* **120**, 2296 (2004).
- <sup>50</sup>A. Volpi and J. L. Bohn, *Phys. Rev. A* **65**, 052712 (2002).
- <sup>51</sup>R. Hermsmeier, X. Xing, and T. V. Tscherbul, *J. Phys. Chem. A* **127**, 4511–4525 (2023).
- <sup>52</sup>J. M. Brown and A. Carrington, *Rotational Spectroscopy of Diatomic Molecules* (Cambridge University Press, 2003).
- <sup>53</sup>T. V. Tscherbul, P. Zhang, H. R. Sadeghpour, and A. Dalgarno, *Phys. Rev. A* **79**, 062707 (2009).
- <sup>54</sup>T. V. Tscherbul, P. Zhang, H. R. Sadeghpour, and A. Dalgarno, *Phys. Rev. Lett.* **107**, 023204 (2011).
- <sup>55</sup>I. C. Bowater, J. M. Brown, and A. Carrington, *Proc. R. Soc. London, Ser. A* **333**, 265 (1973).
- <sup>56</sup>J. M. Cook, G. W. Hills, and R. F. Curl, *J. Chem. Phys.* **67**, 1450 (1977).
- <sup>57</sup>L. H. Coudert, W. E. Ernst, and O. Golonzka, *J. Chem. Phys.* **117**, 7102 (2002).
- <sup>58</sup>A. W. Hauser, J. V. Pototschnig, and W. E. Ernst, *Chem. Phys.* **460**, 2 (2015).
- <sup>59</sup>S. Upadhyay, U. Dargyte, V. D. Dergachev, R. P. Prater, S. A. Varganov, T. V. Tscherbul, D. Patterson, and J. D. Weinstein, *Phys. Rev. A* **100**, 063419 (2019).
- <sup>60</sup>A. van der Avoird and G. Brocks, *J. Chem. Phys.* **87**, 5346 (1987).
- <sup>61</sup>L. M. C. Janssen, P. S. Żuchowski, A. van der Avoird, J. M. Hutson, and G. C. Groenenboom, *J. Chem. Phys.* **134**, 124309 (2011).
- <sup>62</sup>Y. V. Suleimanov, T. V. Tscherbul, and R. V. Krems, *J. Chem. Phys.* **137**, 024103 (2012).
- <sup>63</sup>T. V. Tscherbul, J. Klos, L. Rajchel, and R. V. Krems, *Phys. Rev. A* **75**, 033416 (2007).
- <sup>64</sup>B. Johnson, *J. Comput. Phys.* **13**, 445–449 (1973).
- <sup>65</sup>R. N. Zare and W. G. Harter, *Angular Momentum: Understanding Spatial Aspects in Chemistry and Physics* (Wiley-Interscience Publication, New York, 1988).
- <sup>66</sup>K. P. Huber and G. Herzberg, *Molecular Spectra and Molecular Structure* (Springer, 1979).
- <sup>67</sup>K. Pachucki and J. Komasa, *Phys. Rev. A* **83**, 032501 (2011).
- <sup>68</sup>2018 CODATA recommended values” (2018).
- <sup>69</sup>D. Sundholm, J. Gauss, and A. Schäfer, *J. Chem. Phys.* **105**, 11051 (1996).
- <sup>70</sup>J. L. Booth, P. Shen, R. V. Krems, and K. W. Madison, *New J. Phys.* **21**, 102001 (2019).
- <sup>71</sup>P. Shen, E. Frieling, K. R. Herperger, D. Uhland, R. A. Stewart, A. Deshmukh, R. V. Krems, J. L. Booth, and K. W. Madison, *New J. Phys.* **25**, 053018 (2023).
- <sup>72</sup>J. Klos and E. Tiesinga, *J. Chem. Phys.* **158**, 014308 (2023).
- <sup>73</sup>D. E. Manolopoulos, *J. Chem. Phys.* **85**, 6425–6429 (1986).
- <sup>74</sup>E. P. Wigner, *Phys. Rev.* **73**, 1002 (1948).
- <sup>75</sup>S. Koyu, R. Hermsmeier, and T. V. Tscherbul, *J. Chem. Phys.* **156**, 034112 (2022).
- <sup>76</sup>P. Jacobs, *Group Theory with Applications in Chemical Physics* (Cambridge University Press, 2005).
- <sup>77</sup>D. W. Schwenke, *J. Chem. Phys.* **89**, 2076 (1988).



## CONCLUSIONS

The objective of this dissertation was to prove accurate reference collisional and spectroscopic data for various diatomic molecules and to address the fundamental questions at the intersection of quantum scattering and line-shape theory.

In particular, this dissertation provided:

- state-of-the-art rate coefficients for 1 059 rovibrational transitions in  $\text{H}_2$  induced by collisions with He over temperatures ranging from 20 to 8 000 K (Article **A**), enabling improved modeling of the dynamics of warm astrophysical environments,
- accurate beyond-Voigt line-shape parameters for He- and  $\text{H}_2$ -perturbed pure rotational transitions in HD (Article **B**), and the comprehensive dataset of beyond-Voigt line-shape parameters for 3 480 He-perturbed rovibrational transitions in  $\text{H}_2$  (Article **C**), which can be used in planetary atmospheric studies,
- the first *ab initio* pressure broadening coefficients for an  $\text{N}_2$ -perturbed CO line (Article **D**), relevant to terrestrial atmosphere studies,
- beyond-Voigt line-shape parameters for the self-perturbed 1-0 Q(1) (Article **E**) and S(0) transitions in  $\text{H}_2$ , which allow for reducing systematic errors in the analysis of experimental spectra and enable more stringent QED tests in  $\text{H}_2$ ,
- positions and intensities of 331 892 hyperfine components of 18 585 rovibrational dipole transitions in HT and DT molecules (Article **F**) and 185 631 hyperfine components of 7 251 quadrupole transitions in HD (Article **G**), hyperfine coupling coefficients and hyperfine splitting for low-lying rovibrational levels within the excited  $EF^1\Sigma_g^+$  state in  $\text{H}_2$  (Article **H**), serving as reference data for analysis of experimental spectra.





Apart from generating new reference data, this work has also

- demonstrated the importance of accurate PESs in determining rate coefficients for vibrationally inelastic transitions (Article **A**), and the minimal sensitivity of pressure broadening coefficients for pure rotational transitions at room temperature to fine details of the PES (Article **D**),
- demonstrated the significance of beyond-Voigt effects in hydrogen spectra at conditions relevant to conditions characteristic for giant planets, emphasizing their importance in astrophysical studies (Article **B**),
- provided an example of the first large spectroscopic dataset determined using *ab initio* calculations with efficient parameterization of speed and temperature dependencies (Article **C**), which can be used to populate line-by-line databases,
- showed proof-of-principle *ab initio* calculations of collisional width for atmospherically relevant system, demonstrating agreement with experimental results (Article **D**),
- demonstrated lack of observable shifts due to hyperfine structure in Doppler-limited spectroscopy of molecular hydrogen (Article **I**),
- showed (for a selected transition in hydrogen) that pressure broadening cross-sections can vary by up to 7% between hyperfine components,
- identified hyperfine components with relative intensities independent of vibrational quantum numbers, characteristic of molecules with large rotational constants (Article **J**),
- demonstrated that collisional broadening and shifts of a fundamental 1-0 S(0) line in H<sub>2</sub> at cryogenic conditions are dominated by a single partial wave ( $l = 2$ , d-wave),
- proposed an alternative method to achieve magic wavelengths in molecular hydrogen, designed to mitigate Stark shifts in the spectroscopy of optically trapped H<sub>2</sub> (Article **K**),
- highlighted the significant influence of hyperfine and Zeeman interactions on H<sub>2</sub> dynamics at ultralow temperatures, with a proposal for sympathetic cooling using lithium atoms (Article **L**).



The accomplishments outlined above pave the way for several future research directions.

The successful demonstration of the first comprehensive database for He-perturbed  $\text{H}_2$  lines (Article **C**), followed by a similar database for He-perturbed HD lines [112], shows the potential for creating similar datasets for other combinations of molecular hydrogen, which are critical for planetary atmosphere studies. Expanding the calculations reported in Article **B** to other pure rotational and vibrational transitions for  $\text{H}_2$ -perturbed HD is a natural next step. Similarly, the results discussed in Appendix C form the foundation for developing datasets of beyond-Voigt parameters for self-perturbed  $\text{H}_2$  lines. However, such investigations must proceed with caution. Calculations incorporating quantum indistinguishability for pure rotational transitions suggest that this effect is negligible for temperatures above 50 K and is expected to be even less pronounced for vibrational transitions. But an important discrepancy highlighted in Article **E**, where calculated pressure shifts deviated significantly from experimental data, warrants close investigation before launching a large-scale computational campaign.

The first demonstration of *ab initio* calculations for atmospherically-relevant species (Article **D**), followed by similar works in our group [121, 131, 132], provides a good starting point for large-scale calculations for  $\text{N}_2$ - and  $\text{O}_2$ -perturbed molecules of atmospheric interest. Two key challenges, currently under investigation in our group, are obtaining converged values of pressure shifts, and making calculations of line-shape parameters for transitions between highly-excited rotational levels feasible. The complexity of both problems, stemming from the large number of scattering channels involved, shows the need for either developing new approximate methods or exploring alternative approaches to solving the coupled equations [235].

Calculations similar to those presented in Article **H** could be extended to other hydrogen isotopologues and excited states, addressing the current scarcity of data on hyperfine couplings in the excited  $^1\Sigma$  states.

A comprehensive analysis of the dependence of pressure broadening and shift coefficients on hyperfine components would offer valuable insights, particularly for hydrogen deuteride lines that found significant interest in recent years [164, 171]. Additionally, line mixing effects within the hyperfine structure of single rovibrational transitions present an intriguing avenue for further study.



The unresolved mystery of asymmetric spectra observed in cavities continues to pose a significant theoretical challenge in the context of saturated absorption spectroscopy.

The methodologies outlined in Article **K** can also be extended to search for magic wavelengths in other hydrogen isotopologues. Specifically, more magic wavelengths are anticipated for heteronuclear species like HD, owing to the presence of electric dipole transitions in the infrared. While the analysis is complicated by the underlying hyperfine structure, it remains a feasible and promising area of study. Additionally, the determination of magic wavelengths due to vanishing of the electronic contribution to the dipole polarizability, though situated in the deep UV regime, is also theoretically achievable.

To maintain progress in testing quantum theory using molecular hydrogen, novel experimental strategies are essential. Trapping proposals [232] or sympathetic cooling present promising directions to push the accuracy of transition measurements towards the fundamental limit.

The direct inclusion of hyperfine and field interactions, as demonstrated in Paper **L**, paves the way for studying collisions in more complex systems involving  $^1\Sigma$  molecules. A natural next step would involve extending this approach to  $\text{H}_2\text{-H}_2$  collisions which have never been studied with a direct inclusion of hyperfine and field effects. Apart from the importance of such calculations from the viewpoint of quantifying possible losses in magnetic traps, these calculations could provide more general insights into the dynamics of ultracold  $^1\Sigma$  molecules [236]. Interestingly, to date, only a single quantum scattering study has addressed collisions between two  $^1\Sigma$  molecules (RbCs) in an external magnetic field, including hyperfine structure [237]. However, due to a restricted basis set and the absence of an accurate interaction potential, these calculations did not produce converged results. An alternative approach is to begin with ultracold collisions of smaller  $^1\Sigma$  molecules, for which accurate potential energy surfaces exist and quantum scattering calculations remain computationally feasible, and then progressively extend to heavier, many-electron species. Such incremental progress could shed light on the dynamics of heavy alkali molecules, which are of particular interest in ultracold molecular physics [236, 238].



20133 MILANO (ITALY)  
Piazza Leonardo da Vinci n.32  
Tel. 02-2399.6100  
Telex 333467 POLIMI-I  
Fax 02-2399.6126

POLITECNICO DI MILANO  
DIPARTIMENTO DI FISICA

December 12th, 2024

**Contribution statement to be included in the PhD dissertation of Hubert Jozwiak.**

Concerning my shared publication with Hubert Jozwiak:

*Stimulated Raman scattering metrology of molecular hydrogen*, Lamperti M., Rutkowski L., Ronchetti D., Gatti D., Gotti R., Cerullo G., Thibault F., Jozwiak H., Wojtewicz S., Mostowski M., Weisto P., Polli D., Marangoni M., *Communications Physics* **6**, 2023, 67  
(<https://doi.org/10.24433/CO.7913441.v1>)

In this article, I contributed to the design of the experimental setup in the Lecco laboratory and of the detection chain. I also contributed to the analysis of the measured spectra.

Regarding the manuscript, I revised and edited the draft.

With my best regards

Giulio Cerullo

Prof. Giulio Cerullo  
Socio Corrispondente, Accademia dei Lincei  
Fellow, European Physical Society  
Full Professor  
Physics Department, Politecnico di Milano  
Piazza L. da Vinci 32, 20133 Milano, Italy



Toruń, 11.12.2024

### Authorship statement

I contributed to the paper listed below.

P. Wcisło, F. Thibault, N. Stolarczyk, H. Jóźwiak, M. Słowiński, M. Gancewski, K. Stankiewicz, M. Konefał, S. Kassi, A. Campargue, Y. Tan, J. Wang, K. Patkowski, R. Ciuryło, D. Lisak, R. Kochanov, L. S. Rothman, I. E. Gordon, "The first comprehensive dataset of beyond-Voigt line-shape parameters from *ab initio* quantum scattering calculations for the HITRAN database: He-perturbed H<sub>2</sub> case study", J. Quant. Spectrosc. Radiat. Transfer **260**, 107477-10 (2021).

<https://doi.org/10.1016/j.jqsrt.2020.107477>

I helped to develop methodology for the efficient line shape description. I helped to interpret obtained results. I contributed to the correction of the final manuscript.

Prof. dr. hab. Roman Ciuryło

Head of Department of Atomic, Molecular and Optical Physics

Institute of Physics,  
Nicolaus Copernicus University,  
ul. Grudziądzka 5  
87-100 Toruń,  
e-mail: [rciurylo@fizyka.umk.pl](mailto:rciurylo@fizyka.umk.pl)





dr Hubert Cybulski, prof. UKW

Bydgoszcz, 16.12.2024

Uniwersytet Kazimierza Wielkiego, Wydział Fizyki

ul. Powstańców Wielkopolskich 2, PL-85-090 Bydgoszcz

### **Statement about research contribution**

I hereby confirm that my contribution to the research published in the papers:

*entitled:* 'Hyperfine components of rovibrational dipole transitions in HT and DT'

*by* H. Jóźwiak, H. Cybulski, and P. Wcisło

*published in:* Journal of Quantitative Spectroscopy and Radiative Transfer, Volume 270, 107662, (2021)

<https://doi.org/10.1016/j.jqsrt.2021.107662>

was to calculate the nuclear spin-rotation coupling constant and to participate in writing the final version of the manuscript;

*entitled:* 'Hyperfine structure of rovibrational quadrupole transitions in HD'

*by* H. Jóźwiak, H. Cybulski, and P. Wcisło

*published in:* Journal of Quantitative Spectroscopy and Radiative Transfer, Volume 272, 107753, (2021)

<https://doi.org/10.1016/j.jqsrt.2021.107753>

was to calculate the nuclear spin-rotation coupling constant and to participate in writing the final version of the manuscript;



*entitled:* 'Hyperfine structure of the  $EF^1\Sigma_+$  state in  $H_2$ '

*by* H. Jóźwiak, H. Cybulski, A. Grabowski, and P. Wcisło

*published in:* Physical Review A, Volume 104, 012808, (2021)

<https://doi.org/10.1103/PhysRevA.104.012808>

was to calculate the nuclear spin-rotation coupling constant and to participate in writing the final version of the manuscript;

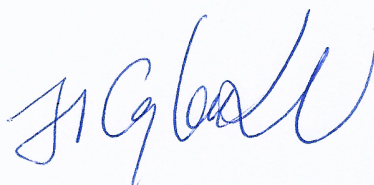
*entitled:* 'Ab initio investigation of the CO-N<sub>2</sub> quantum scattering: The collisional perturbation of the pure rotational R(0) line in CO'

*by* H. Jóźwiak, F. Thibault, H. Cybulski, and P. Wcisło

*published in:* The Journal of Chemical Physics, 154, 054314, (2021)

<https://doi.org/10.1063/5.0040438>

was to calculate the CO-N<sub>2</sub> potential energy surface and to participate in writing the final version of the manuscript.



## Statement about my contribution to the research paper

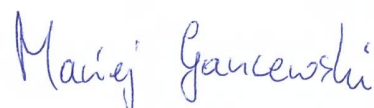
My contribution to the research paper

**Title:** The first comprehensive dataset of beyond-Voigt line-shape parameters from ab initio quantum scattering calculations for the HITRAN database: He-perturbed H<sub>2</sub> case study

**Authors:** Wcisło P., Thibault F., Stolarczyk N., Józwiak H., Słowiński M., Gancewski M., Stankiewicz K., Konefał M., Kassi S., Campargue A., Tan Y., Wang J., Patkowski K., Ciuryło R., Lisak D., Kochanov R., Rothman L. S., Gordon I. E.

**Journal:** *Journal of Quantitative Spectroscopy & Radiative Transfer*, **260**, 2021, 107477  
(<https://doi.org/10.1016/j.jqsrt.2020.107477>)

was related to performing quantum scattering calculations, and discussing the concepts and methodology with the other authors.



Maciej Gancewski



Lecco, December 12<sup>th</sup>, 2024

To whom it may concern,

I hereby declare that, as a co-author of the scientific paper “*Stimulated Raman Scattering Metrology of Molecular Hydrogen*” published in the peer-reviewed journal *Communication Physics*, I contributed to the development and testing of the FPGA algorithm implemented in a PXI system. This algorithm was implemented to acquire both the Raman signal and the frequency offset between the Stokes and the frequency comb, fundamental for frequency calibration. The beatnote frequency acquisition involved the real-time retrieval of the barycenter of the FFT.

Furthermore, I supervised the laboratory work during the hydrogen measurements and provided different contributions to the manuscript.

Sincerely,

Prof. Davide Gatti



12/16/24

**Statement about contributions of my group to the research papers.**

1. Contribution from myself and my group members Laurence Rothman and Roman Kochanov to the research published in the paper:

Wcisło, P., Thibault, F., Stolarczyk, N., Jóźwiak, H., Słowiński, M., Gancewski, M., Stankiewicz, K., Konefał, M., Kass, S., Campargue, A., Tan, Y., Wang, J., Patkowski, K., Ciuryło, R., Lisak, D., Kochanov, R., Rothman, L.S., Gordon, I.E., 2021. The first comprehensive dataset of beyond-Voigt line-shape parameters from ab initio quantum scattering calculations for the HITRAN database: He-perturbed H<sub>2</sub> case study. *J. Quant. Spectrosc. Radiat. Transf.* 260, 107477. <https://doi.org/10.1016/j.jqsrt.2020.107477>

were related to developing the parametrizations consistent with public spectroscopic databases and related software, as well as discussing the results and a way of their presentation with other co-authors, as well as contributing to writing and editing the manuscript.

2. My contribution to the research published in the paper:

Jóźwiak, H.J., Stolarczyk, N., Stankiewicz, K., Zaborowski, M., Lisak, D., Wójtewicz, S., Jankowski, P., Patkowski, K., Szalewicz, K., Thibault, F., Gordon, I.E., Wcisło, P., 2024. Accurate reference spectra of HD in an H<sub>2</sub>-He bath for planetary applications. <https://doi.org/10.1051/0004-6361/202449889>

was related to formulating the problem in the context of planetary science and discussing concepts and methodology with other co-authors and contributing to writing and editing the manuscript.

Respectfully,



Dr. Iouli E. Gordon  
*Chair of Atomic and Molecular Physics Division*  
*Director of the HITRAN project*  
 Center for Astrophysics | Harvard&Smithsonian  
 Atomic and Molecular Physics Division  
 60 Garden Street  
 Cambridge MA 02138-1516, USA  
 e-mail: [igordon@cfa.harvard.edu](mailto:igordon@cfa.harvard.edu)  
 Tel: (617) 496-2259  
[www.cfa.harvard.edu/~igordon](http://www.cfa.harvard.edu/~igordon)



For the publication "*Stimulated Raman scattering metrology of molecular hydrogen*" by Lamperti M., Rutkowski L., Ronchetti D., Gatti D., Gotti R., Cerullo G., Thibault F., Jóźwiak H., Wójtewicz S., Mastowski M., Wcisło P., Polli D., and Marangoni M., published in *Communications Physics* 6, 2023, 67 (<https://doi.org/10.1038/s42005-023-01187-z>), Riccardo Gotti served as one of the supervisors of the research activity. His primary role involved implementing the real-time program on the PXle-7961 FPGA board for acquiring and digitizing the beat-note frequency of the Stokes signal, in collaboration with Marco Lamperti and Davide Gatti. Additionally, Riccardo participated in selecting the HD target line for the study and actively contributed to discussions regarding the experimental results and fitting procedures.

Date and location:

12 / 12 / 2024 , Pavia ;

Signature:

Riccardo Gotti

## Statement about my contribution to the research paper

In the research paper:

**Title:** Hyperfine structure of the  $EF1\Sigma+g$  state in  $H_2$ ,

**Authors:** Jóźwiak H., Cybulski H., Grabowski A., Wcisło P.

**Journal:** Physical Review A, **104**, 2021, 012808,

(<https://doi.org/10.1103/physreva.104.012808>)

I was responsible for calculating energies and wave functions of rovibrational levels in the  $EF1\Sigma+g$  state of  $H_2$  within the Born-Oppenheimer approximation.

A. Grabowski  
Antoni Grabowski

30.12.2024



**Authorship Contribution Statement in the following work:**

**The first comprehensive dataset of beyond-Voigt line-shape parameters from ab initio quantum scattering calculations for the HITRAN database:**

**He-perturbed H<sub>2</sub> case study, Wcisło P., Thibault F., Stolarczyk N., Józwiak H., Słowiński M., Gancewski M., Stankiewicz K., Konefal M., Kassi S., Campargue A., Tan Y., Wang J., Patkowski K., Ciuryło R., Lisak D., Kochanov R., Rothman L. S., Gordon I.E.**

**Journal of Quantitative Spectroscopy & Radiative Transfer, 260, 2021, 107477**

**<https://doi.org/10.1016/j.jqsrt.2020.107477>**

All authors have made significant contributions to the conception, design, execution, and interpretation of the study. The specific contributions are as follows:

**Dr Yan Tan:** Managed and coordinated the laboratory in Hefei, led the spectroscopic measurements of the hydrogen molecule 3-0 band S1 spectral line, and participated in data analysis and manuscript preparation.

**Dr Jin Wang:** Involved in the experimental design, primarily responsible for operating the spectroscopic measurement of the hydrogen molecule 3-0 band S1 spectral line, and assisted Dr. **Yan Tan** in data analysis.

All authors have read and approved the final version of the manuscript and are accountable for its content.



Dec 13, 2024.

dr hab. Piotr Jankowski, prof. UMK  
Department of Quantum Chemistry  
and Atomic Spectroscopy  
Faculty of Chemistry  
Nicolaus Copernicus University in Toruń  
ul. Gagarina 7, 87-100 Toruń

Toruń, 16 December 2024

### Statement

Mr. Hubert Jóźwiak plans to include the following paper in his doctoral dissertation

„Accurate reference spectra of HD in H<sub>2</sub>–He bath for planetary applications”,  
H. Jóźwiak, N. Stolarczyk, K. Stankiewicz, M. Zaborowski, D. Lisak, S. Wójtewicz,  
P. Jankowski, K. Patkowski, K. Szalewicz, F. Thibault, I. E. Gordon, P. Wcisło  
Astronomy & Astrophysics 687, A69, 2024, <https://doi.org/10.1051/0004-6361/202449889>.

I am a co-author of this publication, and I declare that my contribution to it is as follows:

- I co-authored a new interaction energy surface for the H<sub>2</sub>–H<sub>2</sub> dimer used in the paper;
- I participated in writing the manuscript, specifically the part describing the interaction energy surface.

Sincerely,



Piotr Jankowski



## Laboratoire Interdisciplinaire de Physique

[www-liphy.ujf-grenoble.fr](http://www-liphy.ujf-grenoble.fr)

Unité Mixte de Recherche 5588

CNRS – Université Joseph Fourier

BP 87 – 38402 ST MARTIN D'HERES Cedex FRANCE

Alain Campargue Senior researcher CNRS

tél. +33 4 76 51 43 19

fax. +33 4 76 63 54 95

Grenoble

Wednesday, December 18, 2024

**Statement about the contribution of Samir KASSI and Alain CAMPARGUE to a research paper co-authored with Hubert JÓŹWIĄK**

Our contribution to the paper referenced below was mainly the recording of the high sensitivity cavity ring down spectra of the 2-0 Q1 line of  $H_2$  broadened by helium. These CRDS spectra provided experimental data to analyze collisional line-shape effects described in the paper:

*The first comprehensive dataset of beyond-Voigt line-shape parameters from ab initio quantum scattering calculations for the HITRAN database: He-perturbed  $H_2$  case study*

Piotr Wcisło, Franck Thibault, N Stolarczyk, H Józwiak, M Słowiński, M Gancewski, K Stankiewicz, M Konefał, Samir Kassi, Alain Campargue, Y Tan, J Wang, K Patkowski, R Ciuryło, D Lisak, R Kochanov, Laurence S Rothman, Iouli E Gordon.

<https://doi.org/10.1016/j.jqsrt.2020.107477>

Yours faithfully,

Samir Kassi

Alain Campargue





UNIVERSITÀ DEGLI STUDI  
DELL'INSUBRIA

DIPARTIMENTO DI SCIENZA  
E ALTA TECNOLOGIA  
- DISAT

### Contribution statement for the PhD dissertation of H. Józwiak

To whom it may concern,

I am co-author of one publication with H. Józwiak published during his PhD: Lamperti, M., Rutkowski, L., Ronchetti, D., Gatti, D., Gotti, R., Cerullo, G., Thibault, F., Józwiak, H., Wójtewicz, S., Masłowski, P. and Wcisło, P., 2023. Stimulated Raman scattering metrology of molecular hydrogen. *Communications Physics*, 6(1), p.67.

I contributed to the study by co-developing the spectrometer, performing the experimental measurements, and conceiving the line center extrapolation strategy to zero pressure. Additionally, I participated in the multi-pressure HTP fitting, drafted and reviewed the manuscript.

Yours sincerely,

Como, December 15th, 2024

Dr. Marco Lamperti



Dr. Marco Lamperti  
Senior assistant professor (RTDB)  
Dipartimento di Scienza e Alta Tecnologia – DiSAT  
Via Valleggio, 11 – 22100 Como (CO) – Italia  
Email: [marco.lamperti@uninsubria.it](mailto:marco.lamperti@uninsubria.it)  
*Chiaramente Insubria!*

François LIQUE

IPR - Université de Rennes

Bât 11b, Campus de Beaulieu, 263 avenue du Général Leclerc

35042 Rennes Cedex, France

Mail : francois.lique@univ-rennes.fr

Web : <https://sites.google.com/site/francoislique/>

Rennes, 11 December 2024

### Statement of coauthorship

I hereby declare that my contribution to the following research paper listed below involves:

- Revisiting the rovibrational (de-)excitation of molecular hydrogen by helium, *H. Józwiak, F. Thibault, A. Viel, P. Wcisło and F. Lique*, Astronomy and Astrophysics **685**, A113 (2024)

Performing the radiative transfer calculations simulating the excitation of H<sub>2</sub> in different astrophysical environment; Comparing the efficiency of He projectile vs. H, H<sub>2</sub>, H<sup>+</sup> for exciting H<sub>2</sub> in astrophysical media; writing the astrophysical application section.

Prof. dr hab. Daniel Lisak  
Uniwersytet Mikołaja Kopernika w Toruniu  
Instytut Fizyki, Grudziądzka 5/7, 87-100 Toruń

Toruń, 12.12.2024

### Statement about my contribution to the research papers

My contribution to the research published in the paper:

P. Wcisło, F. Thibault, N. Stolarczyk, H. Jóźwiak, M. Słowiński, M. Gancewski, K. Stankiewicz, M. Konefał, S. Kass, A. Campargue, Y. Tan, J. Wang, K. Patkowski, R. Ciuryło, D. Lisak, R. Kochanov, L.S. Rothman, I.E. Gordon, "*The first comprehensive dataset of beyond-Voigt line-shape parameters from ab initio quantum scattering calculations for the HITRAN database: He-perturbed H<sub>2</sub> case study*", Journal of Quantitative Spectroscopy & Radiative Transfer **260**, 107477 (2021), <https://doi.org/10.1016/j.jqsrt.2020.107477>

was related to discussing the results and a way of their presentation with other co-authors, as well as contributing to writing and editing the manuscript.

My contribution to the research published in the paper:

H. Jóźwiak, N. Stolarczyk, K. Stankiewicz, M. Zaborowski, D. Lisak, S. Wójtewicz, P. Jankowski, K. Patkowski, K. Szalewicz, F. Thibault, I. E. Gordon, P. Wcisło, "*Accurate reference spectra of HD in H<sub>2</sub>-He bath for planetary applications*", Astronomy & Astrophysics **687**, A69 (2024), <https://doi.org/10.1051/0004-6361/202449889>

was related to discussing concepts and methodology with other co-authors and contributing to writing and editing the manuscript.





POLITECNICO DI MILANO  
DIPARTIMENTO DI FISICA

Milan, December 12th 2024

**Contribution statement to be included in the PhD dissertation of Hubert Jozwiak.**

I share one publication with Hubert Jozwiak:

**Stimulated Ramon scattering metrology of molecular hydrogen**, Lamperti M., Rutkowski L., Ronchetti D., Gatti D., Gotti R., Cerullo G., Thibault F., Jozwiak H., Wojtowicz S., Maslowski P., Wcisto P., Polli D., Marangoni M., Communications Physics 6, 2023, 67  
(<https://doi.org/10.24433/CO.7913441.v1>.)

In this article, I conceived the experiment and wrote the manuscript together with M. Lamperti, and I gathered funding for it

*Prof. Marco Marangoni*



Prof. Konrad Patkowski  
Department of Chemistry and Biochemistry  
Auburn University  
179 Chemistry Building  
Auburn, Alabama 36849  
United States  
patkowski@auburn.edu

December 23, 2024

Dear Sir/Madam:

At the request of Mr. Hubert Jóźwiak, I declare that my personal contribution to our two joint publications was as follows:

1. Jóźwiak H., Stolarczyk N., Stankiewicz K., Zaborowski M., Lisak D., Wójtewicz S., Jankowski P., Patkowski K., Szalewicz K., Thibault F., Gordon I. E., Wcisło P., *Accurate reference spectra of HD in an H<sub>2</sub>—He bath for planetary applications*, *Astronomy & Astrophysics* 687, A69, **2024**  
My role in this manuscript was computing the data points for the HD–H<sub>2</sub> six-dimensional potential energy surface, used in turn by Prof. Piotr Jankowski to generate the analytical form of the potential, subsequently used in the line shape calculations. I also made minor contributions to the writing of the manuscript.
2. Wcisło P., Thibault F., Stolarczyk N., Jóźwiak H., Słowiński M., Gancewski M., Stankiewicz K., Konefał M., Kassi S., Campargue A., Tan Y., Wang J., Patkowski K., Ciuryło R., Lisak D., Kochanov R., Rothman L. S., Gordon I. E., *The first comprehensive dataset of beyond-Voigt line-shape parameters from ab initio quantum scattering calculations for the HITRAN database: He-perturbed H<sub>2</sub> case study*, *Journal of Quantitative Spectroscopy and Radiative Transfer* 260, 107477, **2021**

My role in this manuscript was computing and fitting the analytical He–H<sub>2</sub> potential energy surface that was used as input in the calculation of line shape parameters. I also made minimal contributions to the writing of the manuscript.

Yours sincerely,

Dr. Konrad Patkowski  
Professor of Chemistry and Physics





**POLITECNICO DI MILANO**  
**DIPARTIMENTO DI FISICA**

Milan, December 27th 2024

**Contribution statement to be included in the PhD dissertation of Hubert Jozwiak.**

I share one publication with Hubert Jozwiak:

**Stimulated Raman scattering metrology of molecular hydrogen**, Lamperti M., Rutkowski L., Ronchetti D., Gatti D., Gotti R., Cerullo G., Thibault F., Jozwiak H., Wojtewicz S., Maslowski P., Weisto P., Polli D., Marangoni M., Communications Physics 6, 2023, 67  
(<https://doi.org/10.24433/CO.7913441.v1>.)

In this article, I contributed in the design of the experiment, discussed the results and contributed in gathering the funds, and revised the manuscript.

*Prof. Dario Polli*

I Daniele Ronchetti contributed to the work *Stimulated Raman scattering metrology of molecular hydrogen* (Lamperti *et al.*, *Communications Physics* 6, 67 (2023), <https://doi.org/10.1038/s42005-023-01187-z>) by performing the measurements that enabled the study.

Hamburg, 16.12.2024

Daniele Ronchetti

A handwritten signature in black ink, appearing to read 'Daniele Ronchetti', with a stylized flourish at the end.

December 11<sup>th</sup>, 2024

**Contribution statement to be included in the PhD dissertation of Hubert Jóźwiak.**

I share one publication with Hubert Jóźwiak:

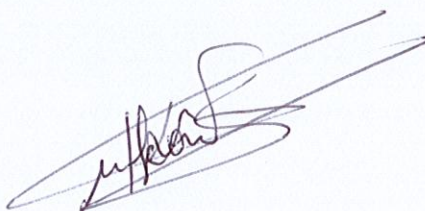
Stimulated Raman scattering metrology of molecular hydrogen, Lamperti M., Rutkowski L., Ronchetti D., Gatti D., Gotti R., Cerullo G., Thibault F., Jóźwiak H., Wójtewicz S., Maślowski M., Wcisło P., Polli D., Marangoni M., Communications Physics 6, 2023, 67  
(<https://doi.org/10.24433/CO.7913441.v1>)

In this article, I built the first iteration of the experimental setup in the Lecco laboratory, and achieved the first detection of the H<sub>2</sub> transition. I designed the Raman part of the setup, took active part in the discussions surrounding technical improvements and data treatment. I contributed to the experimental upgrade, and to the analysis of the measured spectra. Regarding the manuscript, I revised and edited the draft.

Yours respectfully,

Lucile Rutkowski

CNRS researcher, Institute of Physics of Rennes  
Department of Molecular Physics  
Campus Beaulieu, University of Rennes 1, France



Toruń 03.01.2024

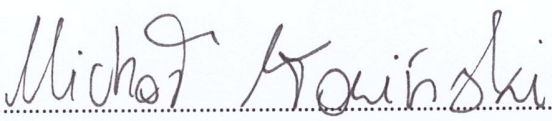
Dr inż. Michał Słowiński  
Instytut Fizyki UMK  
ul. Grudziądzka 5/7  
87-100 Toruń

## Statement of coauthorship

I hereby declare that my contribution to the paper:

*The first comprehensive dataset of beyond-Voigt line-shape parameters from ab initio quantum scattering calculations for the HITRAN database: He-perturbed H<sub>2</sub> case study*, Wcisło P., Thibault F., Stolarczyk N., Jóźwiak H., Słowiński M., Gancewski M., Stankiewicz K., Konefał M., Kassi S., Campargue A., Tan Y., Wang J., Patkowski K., Ciuryło R., Lisak D., Kochanov R., Rothman L. S., Gordon I.E. Journal of Quantitative Spectroscopy & Radiative Transfer, **260**, 2021, 107477, DOI: 10.1016/j.jqsrt.2020.107477,

was conducting a full line-shape analysis for two exemplar hydrogen transitions, concluded in Fig. 5. I calculated the ab initio speed dependencies for line-shape parameters, concluded in Fig. 4, from generalized cross-sections, presented in Fig. 2. All three figures were prepared by me. I was also responsible for debugging and correcting the database.

  
.....  
(signature)



## Authorship statement

I declare that my contribution to the publications listed below was as follows:

**The first comprehensive dataset of beyond-Voigt line-shape parameters from ab initio quantum scattering calculations for the HITRAN database: He-perturbed H<sub>2</sub> case study,**

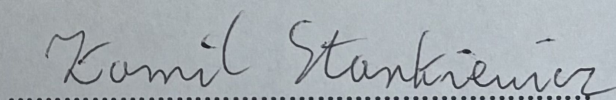
Piotr Wcisło, Franck Thibault, N Stolarczyk, H Jóźwiak, M Słowiński, M Gancewski, K Stankiewicz, M Konefał, Samir Kassi, Alain Campargue, Y Tan, J Wang, K Patkowski, R Ciuryło, D Lisak, R Kochanov, Laurence S Rothman, Iouli E Gordon  
<https://doi.org/10.1016/j.jqsrt.2020.107477>

**Contribution:** Conducting part of the scattering calculations, data validation, collaboration in manuscript preparation.

**Accurate reference spectra of HD in an H<sub>2</sub>-He bath for planetary applications,**

H Jóźwiak, N Stolarczyk, K Stankiewicz, M Zaborowski, D Lisak, S Wójtewicz, P Jankowski, K Patkowski, K Szalewicz, F Thibault, I E Gordon, P Wcisło  
<https://doi.org/10.1051/0004-6361/2022449889>

**Contribution:** Preparation of part of the experimental setup, conducting part of the scattering calculations.



Signature



Toruń, 18.12.2024

dr Nikodem Stolarczyk  
Wydział Fizyki, Astronomii i Informatyki Stosowanej  
Uniwersytet Mikołaja Kopernika w Toruniu  
ul Grudziądzka 5  
87-100 Toruń

## Statement of coauthorship

I hereby declare that my contribution to the two research articles listed below involves:

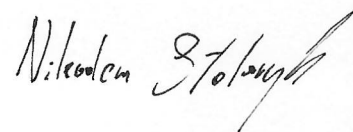
1. Accurate reference spectra of HD in an H<sub>2</sub>-He bath for planetary applications  
Jóźwiak H., Stolarczyk N., Stankiewicz K., Zaborowski M., Lisak D., Wójtewicz S., Jankowski P.,  
Patkowski K., Szalewicz K., Thibault F., Gordon I.E., Wcisło P.  
Astronomy & Astrophysics 687, A69, 2024  
[doi.org/10.1051/0004-6361/202449889](https://doi.org/10.1051/0004-6361/202449889)

providing the coefficients of the DPL temperature dependence representation for the spectral line-shape parameters, simulating the spectra and assessing the discrepancies between spectroscopic models for thermodynamic conditions found across Solar System giant planets, performing the experimental measurements and comparing the *ab initio* results with the laboratory and literature data.

2. The first comprehensive dataset of beyond-Voigt line-shape parameters from *ab initio* quantum scattering calculations for the HITRAN database: He-perturbed H<sub>2</sub> case study,  
Wcisło P., Thibault F., Stolarczyk N., Jóźwiak H., Słowiński M., Gancewski M., Stankiewicz K.,  
Konefał M., Kassi S., Campargue A., Tan Y., Wang J., Patkowski K., Ciuryło R., Lisak D.,  
Kochanov R., Rothman L. S., Gordon I.E.  
Journal of Quantitative Spectroscopy & Radiative Transfer, 260, 2021, 107477  
[doi.org/10.1016/j.jqsrt.2020.107477](https://doi.org/10.1016/j.jqsrt.2020.107477)

calculating the spectral line-shape parameters from the generalized spectroscopic cross sections, interpolating and extrapolating the database and providing the DPL coefficients for each transition.

Respectfully,





DEPARTMENT OF PHYSICS  
AND ASTRONOMY

University of Delaware  
Newark, Delaware 19716-2570  
Ph: 302/831-2661  
Fax: 302/831-1637

December 28, 2024

### **Declaration concerning coauthorship**

I declare that my contributions to the paper

“Accurate reference spectra of HD in an H<sub>2</sub>–He bath for planetary applications”, H Józwiak, N Stolarczyk, K Stankiewicz, M Zaborowski, D Lisak, S Wójtewicz, P Jankowski, K Patkowski, K Szalewicz, F Thibault, IE Gordon, P Wcisło; <https://doi.org/10.1051/0004-6361/202449889>

are as follows: *(i)* Conceptual development of the methods for calculations of the interaction potential between two H<sub>2</sub> molecules; *(ii)* Analysis of the results of such calculations and of the potential accuracy; *(iii)* Participation in the writing of the manuscript.

A handwritten signature in black ink, reading "Krzysztof Szalewicz".

Krzysztof Szalewicz  
Profesor of Physics and Chemistry

15th December 2024

Object: Hubert JOZWIAK's doctoral dissertation, Nicolaus Copernicus University in Torun

Dr Franck THIBAUT, Institut de Physique, Université de Rennes, contribution statement

Dear colleagues,

Over the past ten years, I have visited the group in Torun, led by Roman Ciurylo, four times. During this time, Hubert has also been invited to Rennes on three occasions. These visits have provided numerous opportunities for fruitful exchanges on the calculation of generalized spectroscopic cross-sections, including topics such as computational codes, quantum indistinguishability, and developing formulas for cross-sections within the coupled state approximation. Discussions with Hubert are always highly stimulating and insightful.

Hubert is not only a serious and talented researcher but also remarkably efficient in his work. I have had the pleasure of coauthoring 15 articles with him, and below, I provide a brief overview of my contributions to each of them.

1. *Revisiting the rovibrational (de-)excitation of molecular hydrogen by helium*

Jóźwiak H., Thibault F., Viel A., Wcisło P., Lique F.

Astronomy & Astrophysics 685, A113, 2024

<https://doi.org/10.1051/0004-6361/202348645>

Preparation with Hubert of the potential energy surface for the scattering calculations.

Preparation of job arrays on Rennes's cluster. Running a few complementary test calculations.

Conceptualization, Methodology, Software, Validation, Writing - original draft, Writing - review & editing

2. *Accurate reference spectra of HD in an H<sub>2</sub>-He bath for planetary applications*

Jóźwiak H., Stolarczyk N., Stankiewicz K., Zaborowski M., Lisak D., Wójtewicz S., Jankowski P., Patkowski K., Szalewicz K., Thibault F., Gordon I.E., Wcisło P.,

Astronomy & Astrophysics 687, A69, 2024

<https://doi.org/10.1051/0004-6361/202449889>

Preparation with Hubert of the potential energy surface for the scattering calculations.

Preparation of job arrays on Rennes's cluster. Running a few complementary test calculations with Molscat code.

Conceptualization, Methodology, Software, Validation, Writing - original draft, Writing - review & editing

3. *Stimulated Raman scattering metrology of molecular hydrogen*

Lamperti M., Rutkowski L., Ronchetti D., Gatti D., Gotti R., Cerullo G., Thibault F., Jóźwiak H., Wójtewicz S., Masłowski M., Wcisło P., Polli D., Marangoni M.

Communications Physics 6, 2023, 67

<https://doi.org/10.1038/s42005-023-01187-z>

Preparation with Hubert of the potential energy surface for the scattering calculations.

Preparation of job arrays on Rennes's cluster. Running a few complementary test calculations.

Conceptualization, Methodology, Software, Validation, Writing - original draft, Writing - review & editing

#### 4. Collisional line-shape effects in accurate He-perturbed $H_2$ spectra

Słowiński M., Jóźwiak H., Gancewski M., Stankiewicz K., Stolarczyk N., Tan Y., Wang J., Liu A.-W., Hu S.-M., Kassı S., Campargue A., Patkowski K., Żuchowski P. S., Ciuryło R., Thibault F., Wcisło P.

Journal of Quantitative Spectroscopy & Radiative Transfer 277 (2022) 10795

<https://doi.org/10.1016/j.jqsrt.2021.107951>

Preparation of the potential energy surface for the scattering calculations. Calculations of generalized spectroscopic cross sections.

Conceptualization, Methodology, Software, Validation

#### 5. Ab initio investigation of the CO-N<sub>2</sub> quantum scattering: the collisional perturbation of the pure rotational R(0) line in CO

Jóźwiak H., Thibault F., Cybulski H., Wcisło P.

Journal of Chemical Physics 154, 2021, 054314

<https://doi.org/10.1063/5.0040438>

Preparation with Hubert of the potential energy surface for the scattering calculations.

Preparation of job arrays on Rennes's cluster. Running a few complementary test calculations with Molscat.

Conceptualization, Methodology, Software, Validation, Writing - original draft, Writing - review & editing

#### 6. Collisional line broadening and mixing in the Raman spectrum of CO perturbed by N<sub>2</sub> : Experimental measurements and theoretical calculations

Paredes-Roibás D., Martínez R. Z., Jóźwiak H., Thibault F.

Journal of Quantitative Spectroscopy & Radiative Transfer 275 (2021) 107868

<https://doi.org/10.1016/j.jqsrt.2021.107868>

Preparation with Hubert of the potential energy surface for the scattering calculations.

Preparation of job arrays on Rennes's cluster.

Conceptualization, Methodology, Software, Validation, Writing - original draft, Writing - review & editing

#### 7. The first comprehensive dataset of beyond-Voigt line-shape parameters from ab initio quantum scattering calculations for the HITRAN database: He-perturbed H<sub>2</sub> case study

Wcisło P., Thibault F., Stolarczyk N., Jóźwiak H., Słowiński M., Gancewski M., Stankiewicz K., Konefał M., Kassı S., Campargue A., Tan Y., Wang J., Patkowski K., Ciuryło R., Lisak D., Kochanov R., Rothman L. S., Gordon I.E.

Journal of Quantitative Spectroscopy & Radiative Transfer, 260, 2021, 107477

<https://doi.org/10.1016/j.jqsrt.2020.107477>

Preparation with Hubert of the potential energy surface for the scattering calculations.

Preparation of job arrays on Rennes's cluster. Running a few complementary test calculations with Molscat.

Conceptualization, Methodology, Software, Validation, Writing - original draft, Writing - review & editing

#### 8. Accurate calculations of beyond-Voigt line-shape parameters from first principles for the He-perturbed HD rovibrational lines: A comprehensive dataset in the HITRAN DPL format

Stankiewicz K., Stolarczyk N., Jóźwiak H., Thibault F., Wcisło P.

Journal of Quantitative Spectroscopy & Radiative Transfer 276 (2021) 10791

<https://doi.org/10.1016/j.jqsrt.2021.107911>

Preparation of the potential energy surface for the scattering calculations. Calculations of generalized spectroscopic cross sections.

Conceptualization, Methodology, Software, Resources, Writing – review & editing.

#### 9. Fully quantum calculations of O<sub>2</sub>-N<sub>2</sub> scattering using a new potential energy surface: Collisional perturbations of the oxygen 118 GHz fine structure line

Gancewski M., Jóźwiak H., Quintas-Sanchez E., Dawes R., Thibault F., Wcisło P.,

J. Chem. Phys. **155**, 124307 (2021)

<https://doi.org/10.1063/5.0063006>

Conceptualization, Methodology, Software, Resources, Writing – review & editing.

10. *Evaluation of different parameterizations of temperature dependences of the line-shape parameters based on ab initio calculations: Case study for the HITRAN database*

Stolarczyk N., [Thibault F.](#), Cybulski H., [Jóźwiak H.](#), Kowzan G., Vispoel B., Gordon I.E., Rothman L.S., Gamache R.R., Wcisło P.

Journal of Quantitative Spectroscopy & Radiative Transfer 240 (2020) 106676

<https://doi.org/10.1016/j.jqsrt.2019.106676>

Conceptualization, Methodology, Software, Resources, Writing – review & editing.

11. *Ab initio calculations of collisional line-shape parameters and generalized spectroscopic cross-sections for rovibrational dipole lines in HD perturbed by He*

Stankiewicz K., [Jóźwiak H.](#), Gancewski M., Stolarczyk N., [Thibault F.](#), Wcisło P.

Journal of Quantitative Spectroscopy & Radiative Transfer 254 (2020) 107194

<https://doi.org/10.1016/j.jqsrt.2020.107194>

Conceptualization, Methodology, Software, Resources, Writing – review & editing.

12. *Accurate deuterium spectroscopy and comparison with ab initio calculations*

Wójtewicz S., Gotti R., Gatti D., Lamperti M., Laporta P., [Jóźwiak H.](#), [Thibault F.](#), Wcisło P., Marangoni M.

Physical Review A 101, 052504 (2020)

<https://doi.org/10.1103/PhysRevA.101.052504>

Conceptualization, Methodology, Software, Resources, Writing – review & editing.

13. *Ultrahigh finesse cavity-enhanced spectroscopy for accurate tests of quantum electrodynamics for molecules*

Zaborowski M., Słowiński M., Stankiewicz K., [Thibault F.](#), Cygan A., [Jóźwiak H.](#), Kowzan G., Masłowski P., Nishiyama A., Stolarczyk N., Wójtewicz S., Ciuryło R., Lisak D., Wcisło P.

Optics Letters 45 (2020) 1603-1606

<https://doi.org/10.1364/OL.389268>

Conceptualization, Methodology, Software, Resources, Writing – review & editing.

14. *Ab initio line-shape calculations for the S and O branches of H<sub>2</sub> perturbed by He*

[Jóźwiak H.](#), [Thibault F.](#), Stolarczyk N., Wcisło P.

Journal of Quantitative Spectroscopy & Radiative Transfer 219 (2018) 313–322

<https://doi.org/10.1016/j.jqsrt.2018.08.023>

Preparation of the potential energy surface for the scattering calculations. Calculations of generalized spectroscopic cross sections.

Conceptualization, Methodology, Software, Resources, Writing – review & editing.

15. *Rovibrational line-shape parameters for H<sub>2</sub> in He and new H<sub>2</sub>-He potential energy surface*

[Thibault F.](#), Patkowski K., Zuchowski P.S., [Jóźwiak H.](#), Ciuryło R., Wcisło P.

Journal of Quantitative Spectroscopy & Radiative Transfer 202 (2017) 308–320

<http://dx.doi.org/10.1016/j.jqsrt.2017.08.014>

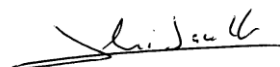
Preparation of the potential energy surface for the scattering calculations. Calculations of generalized spectroscopic cross sections.

Conceptualization, Methodology, Software, Resources, Writing – review & editing.

Sincerely yours,

Dr F. Thibault

Email : [franck.thibault@univ-rennes.fr](mailto:franck.thibault@univ-rennes.fr)







University of Nevada, Reno

Department of Physics  
College of Science  
1664 N. Virginia Street  
University of Nevada, Reno/220  
Reno, Nevada 89557-0220  
(775) 784-6792 office  
(775) 784-1398 fax  
<http://www.physics.unr.edu>

Prof. Timur V. Tscherbul  
Tel: (775) 219-5831

December 18, 2024

**Re: Co-author contribution statement**

Dear Sir or Madam:

The purpose of this letter is to outline my contributions to our joint work with Hubert Jóźwiak recently published in the Journal of Chemical Physics [H. Jóźwiak, T. V. Tscherbul, and P. Wcisło, Hyperfine and Zeeman interactions in ultracold collisions of molecular hydrogen with atomic lithium, *J. Chem. Phys.* **160**, 094304 (2024)].

As stated in this paper, my contributions to it included Conceptualization (equal); Funding acquisition (supporting), Methodology (equal); Resources (supporting); Software (equal); Supervision (supporting); Validation (lead); Writing –review & editing (equal).

With best regards,  
Dr. Timur V. Tscherbul

*Timur Tscherbul*



---

**Object: Co-author statement on a publication of Hubert Józwiak for his dissertation**

I, Alexandra Viel, list below my contributions to the work

*Revisiting the rovibrational (de-)excitation of molecular hydrogen by helium,*  
Astronomy & Astrophysics **685**, A113, 2024  
<https://doi.org/10.1051/0004-6361/202348645>

authored by

**Hubert Józwiak**, Franck Thibault, Alexandra Viel, Piotr Wcisło, and François Lique.

My contributions to the research work presented in this paper are:

- participation to general discussions about this project studying the  $\text{He}+\text{H}_2$  collision system as well as those on the results obtained by Hubert,
- providing Hubert with results of test calculations (input/output) using an in-house code we have in my laboratory in Rennes to assess and confirm the validity of the BIGOS code used and published in this publication,
- participation in editing pre- and post- submission of the manuscript.

Rennes, on December the 12th 2024

Alexandra Viel

Senior CNRS Researcher

Institute of Physics of Rennes

France



### Author contribution statement

1. Revisiting the rovibrational (de-)excitation of molecular hydrogen by helium

Hubert Józwiak, Franck Thibault, Alexandra Viel, Piotr Wcisło, François Lique

Astronomy & Astrophysics 685, A113 (2024)

DOI: 10.1051/0004-6361/202348645

My role in this research was: contribution to research in setting the research strategy, supervising the work of the PhD student, participation and supervision over the manuscript preparation.

**I would like to emphasize that Mr Hubert Józwiak was the main and leading contributor to this work.**

2. Accurate reference spectra of HD in an H<sub>2</sub>-He bath for planetary applications

Hubert Józwiak, Nikodem Stolarczyk, Kamil Stankiewicz, Mikołaj Zaborowski, Daniel Lisak, Szymon Wójtewicz, Piotr Jankowski, Konrad Patkowski, Krzysztof Szalewicz, Franck Thibault, Iouli E. Gordon, Piotr Wcisło

Astronomy & Astrophysics 687, A69 (2024)

DOI: 10.1051/0004-6361/202449889

My role in this research was: initiator of this research direction, coordination of work and international cooperation, contribution to research in setting the research strategy and supporting the project at technical level, supervising the work of PhD students, participation and supervision over the manuscript preparation.

**I would like to emphasize that Mr Hubert Józwiak was the main and leading contributor to this work.**

3. The first comprehensive dataset of beyond-Voigt line-shape parameters from ab initio quantum scattering calculations for the HITRAN database: He-perturbed H<sub>2</sub> case study

Piotr Wcisło, Franck Thibault, Nikodem Stolarczyk, Hubert Józwiak, Michał Słowiński, Maciej Gancewski, Kamil Stankiewicz, Magdalena Konefał, Samir Kassi, Alain Campargue,



Yan Tan, Jin Wang, Konrad Patkowski, Roman Ciuryło, Daniel Lisak, Roman Kochanov,  
Laurence S. Rothman, Iouli E. Gordon

Journal of Quantitative Spectroscopy and Radiative Transfer 260, 107477 (2021)

DOI: 10.1016/j.jqsrt.2020.107477

My role in this research was: initiator of this research direction, coordination of work and international cooperation, contribution to research in setting the research strategy and supporting the project at technical level, supervising the work of PhD students, participation and supervision over the manuscript preparation.

Additionally, due to a lack of contact with M. Konefał, as the first author, I declare that the contribution of M. Konefał to this work was small and related to supporting the data analysis.

4. Ab initio investigation of the CO–N<sub>2</sub> quantum scattering: The collisional perturbation of the pure rotational R(0) line in CO

Hubert Jóźwiak, Franck Thibault, Hubert Cybulski, Piotr Wcisło

The Journal of Chemical Physics 154, 054314 (2021)

DOI: 10.1063/5.0040438

My role in this research was: initiator of this research direction, coordination of work and international cooperation, contribution to research in setting the research strategy and supporting the project at technical level, supervising the work of the PhD student, participation and supervision over the manuscript preparation.

**I would like to emphasize that Mr Hubert Jóźwiak was the main and leading contributor to this work.**





5. Stimulated Raman scattering metrology of molecular hydrogen

Marco Lamperti, Lucile Rutkowski, Daniele Ronchetti, Davide Gatti, Riccardo Gotti, Giulio Cerullo, Franck Thibault, Hubert Jóźwiak, Szymon Wójtewicz, Piotr Masłowski, Piotr Wcisło, Dario Polli, Marco Marangoni

Communications Physics 6, 67 (2023)

DOI: 10.1038/s42005-023-01187-z

My contribution was: developing concept for the analysis of experimental data and comparing them with *ab initio* calculations, support in solving detailed technical problems in the analysis of measurement data and simulations of optical resonances disturbed by collisions, direct supervision of the PhD student, participation in the preparation of the manuscript.

6. Hyperfine components of rovibrational dipole transitions in HT and DT

Hubert Jóźwiak, Hubert Cybulski, Piotr Wcisło

Journal of Quantitative Spectroscopy and Radiative Transfer 270, 107662 (2021)

DOI: 10.1016/j.jqsrt.2021.107662

My role in this research was: initiator of this research direction, coordination of work, contribution to research in setting the research strategy and supporting the project at technical level, supervising the work of the PhD student, participation and supervision over the manuscript preparation.

**I would like to emphasize that Mr Hubert Jóźwiak was the main and leading contributor to this work.**

7. Hyperfine structure of rovibrational quadrupole transitions in HD

Hubert Jóźwiak, Hubert Cybulski, Piotr Wcisło

Journal of Quantitative Spectroscopy and Radiative Transfer 272, 107753 (2021)

DOI: 10.1016/j.jqsrt.2021.107753

My role in this research was: initiator of this research direction, coordination of work, contribution to research in setting the research strategy and supporting the project at technical level, supervising the work of the PhD student, participation and supervision over the manuscript preparation.





I would like to emphasize that Mr Hubert Jóźwiak was the main and leading contributor to this work.

8. Hyperfine structure of the  $EF^1\Sigma_g^+$  state in  $H_2$

Hubert Jóźwiak, Hubert Cybulski, Antoni Grabowski, Piotr Wcisło

Physical Review A 104, 012808 (2021)

DOI: 10.1103/PhysRevA.104.012808

My role in this research was: initiator of this research direction, coordination of work, contribution to research in setting the research strategy and supporting the project at technical level, supervising the students' work, participation and supervision over the manuscript preparation.

I would like to emphasize that Mr Hubert Jóźwiak was the main and leading contributor to this work.

9. Lack of hyperfine shifts in Doppler-limited spectra of molecular hydrogen

Hubert Jóźwiak, Piotr Wcisło

Physical Review A 107, 012802 (2023)

DOI: 10.1103/PhysRevA.107.012802

My role in this research was: coordination of work, contribution to research in setting the research strategy, supervising the work of the PhD student, participation and supervision over the manuscript preparation.

I would like to emphasize that Mr Hubert Jóźwiak was the main and leading contributor to this work.

10. Relative intensities of hyperfine components of rovibrational transitions in molecular hydrogen

Hubert Jóźwiak, Piotr Wcisło

Physical Review A 105, 062812 (2022)

DOI: 10.1103/PhysRevA.105.062812

My role in this research was: initiator of this research direction, coordination of work, contribution to research in setting the research strategy, supervising the work of the PhD student, participation and supervision over the manuscript preparation.



**I would like to emphasize that Mr Hubert Józwiak was the main and leading contributor to this work.**

11. Magic wavelength for a rovibrational transition in molecular hydrogen

Hubert Józwiak, Piotr Wcisło

Scientific Reports 12, 14529 (2023)

DOI: 10.1038/s41598-022-18159-y

My role in this research was: initiator of this research direction, coordination of work, contribution to research in setting the research strategy and supporting the project at technical level, supervising the work of the PhD student, participation and supervision over the manuscript preparation.

**I would like to emphasize that Mr Hubert Józwiak was the main and leading contributor to this work.**

12. Hyperfine and Zeeman interactions in ultracold collisions of molecular hydrogen with atomic lithium

Hubert Józwiak, Timur V. Tscherbul, Piotr Wcisło

The Journal of Chemical Physics 160, 094304 (2024)

DOI: 10.1063/5.0193148

My role in this research was: initiator of this research direction, coordination of work and international cooperation, contribution to research in setting the research strategy, supervising the work of the PhD student, participation and supervision over the manuscript preparation.

**I would like to emphasize that Mr Hubert Józwiak was the main and leading contributor to this work.**

## AUTHORSHIP STATEMENT

I declare that in the paper:

- H. Jóźwiak, N. Stolarczyk, K. Stankiewicz, M. Zaborowski, D. Lisak, S. Wójtewicz, P. Jankowski, K. Patkowski, K. Szalewicz, F. Thibault, I. E. Gordon, P. Wcisło, *Accurate reference spectra of HD in an H<sub>2</sub>-He bath for planetary applications*, *Astronomy & Astrophysics* **687**, A69, 2024

my contribution consisted in preparing the CRDS spectrometer for measurements and in performing measurements of the spectral lines of D<sub>2</sub>,

- M. Lamperti, L. Rutkowski, D. Ronchetti, D. Gatti, R. Gotti, G. Cerullo, F. Thibault, H. Jóźwiak, S. Wójtewicz, P. Masłowski, P. Wcisło, D. Polli, M. Marangoni, *Stimulated Raman scattering metrology of molecular hydrogen*, *Communications Physics* **6**, 67, 2023

my contribution consisted in performing the multispectrum fits using the Hartmann-Tran profile and in discussing the uncertainty analysis.

Szymon Wójtewicz

Toruń, 17.12.2024

## Statement of coauthorship

I hereby declare that my contribution to the paper:

*Accurate reference spectra of HD in an H<sub>2</sub>-He bath for planetary applications*

Jóźwiak H., Stolarczyk N., Stankiewicz K., Zaborowski M., Lisak D., Wójtewicz S., Jankowski P., Patkowski K., Szalewicz K., Thibault F., Gordon I.E., Wcisło P., *Astronomy & Astrophysics* **687**, A69, 2024, <https://doi.org/10.1051/0004-6361/202449889>

included taking part in the measurements (S(2) 2-0 line in H<sub>2</sub>-perturbed D<sub>2</sub>) and contributing to the software used for measurements.

Statement sent by Mikołaj Zaborowski  
from [zaborowski.mikolaj@gmail.com](mailto:zaborowski.mikolaj@gmail.com)  
on December 17, 2024, 16:02



# ALL PUBLISHED ARTICLES

INCLUDING THOSE NOT SUBMITTED  
WITHIN THIS DISSERTATION

1. Heterodyne dispersive cavity ring-down spectroscopy exploiting eigenmode frequencies for high-fidelity measurements

Agata Cygan, Szymon Wójtewicz, **Hubert Jóźwiak**, Grzegorz Kowzan, Nikodem Stolarczyk, Katarzyna Bielska, Piotr Wcisło, Roman Ciuryło, Daniel Lisak

accepted in *Science Advances*

DOI: 10.48550/arXiv.2403.01961

2. Accurate reference spectra of HD in an H<sub>2</sub>–He bath for planetary applications

**Hubert Jóźwiak**, Nikodem Stolarczyk, Kamil Stankiewicz, Mikołaj Zaborowski, Daniel Lisak, Szymon Wójtewicz, Piotr Jankowski, Konrad Patkowski, Krzysztof Szalewicz, Franck Thibault, Iouli E. Gordon, Piotr Wcisło

*Astronomy & Astrophysics* 687, A69 (2024)

DOI: 10.1051/0004-6361/202449889

3. Revisiting the rovibrational (de-)excitation of molecular hydrogen by helium

**Hubert Jóźwiak**, Franck Thibault, Alexandra Viel, Piotr Wcisło, François Lique

*Astronomy & Astrophysics* 685, A113 (2024)

DOI: 10.1051/0004-6361/202348645





4. Hyperfine and Zeeman interactions in ultracold collisions of molecular hydrogen with atomic lithium

**Hubert Jóźwiak**, Timur V. Tscherbul, Piotr Wcisło

*The Journal of Chemical Physics* 160, 094304 (2024)

DOI: 10.1063/5.0193148

5. *Ab initio* quantum scattering calculations and a new potential energy surface for the  $\text{HCl}(X^1\Sigma^+)-\text{O}_2(X^3\Sigma_g^-)$  system: Collision-induced line shape parameters for  $\text{O}_2$ -perturbed R(0) 0-0 line in  $\text{H}^{35}\text{Cl}$ ,

Artur Olejnik, **Hubert Jóźwiak**, Maciej Gancewski, Ernesto Quintas-Sánchez, Richard Dawes, Piotr Wcisło

*The Journal of Chemical Physics* 159, 13401 (2023)

DOI: 10.1063/5.0169968

6. Stimulated Raman scattering metrology of molecular hydrogen

Marco Lamperti, Lucile Rutkowski, Daniele Ronchetti, Davide Gatti, Riccardo Gotti, Giulio Cerullo, Franck Thibault, **Hubert Jóźwiak**, Szymon Wójtewicz, Piotr Masłowski, Piotr Wcisło, Dario Polli, Marco Marangoni

*Communications Physics* 6, 67 (2023)

DOI: 10.1038/s42005-023-01187-z

7. Lack of hyperfine shifts in Doppler-limited spectra of molecular hydrogen

**Hubert Jóźwiak**, Piotr Wcisło

*Physical Review A* 107, 012802 (2023)

DOI: 10.1103/PhysRevA.107.012802

8. Magic wavelength for a rovibrational transition in molecular hydrogen

**Hubert Jóźwiak**, Piotr Wcisło

*Scientific Reports* 12, 14529 (2023)

DOI: 10.1038/s41598-022-18159-y



9. Relative intensities of hyperfine components of rovibrational transitions in molecular hydrogen

**Hubert Jóźwiak**, Piotr Wcisło

*Physical Review A* 105, 062812 (2022)

DOI: 10.1103/PhysRevA.105.062812

10. Collisional line-shape effects in accurate He-perturbed H<sub>2</sub> spectra

Michał Słowiński, **Hubert Jóźwiak**, Maciej Gancewski, Kamil Stankiewicz, Nikodem Stolarczyk, Yan Tan, Jin Wang, An-Wen Liu, Shui-Ming Hu, Samir Kassi, Alain Campargue, Konrad Patkowski, Piotr Żuchowski, Roman Ciuryło, Franck Thibault, Piotr Wcisło

*Journal of Quantitative Spectroscopy & Radiative Transfer* 277, 107951 (2022)

DOI: 10.1016/j.jqsrt.2021.107951

11. *Ab initio* quantum scattering calculations for the CO-O<sub>2</sub> system and a new CO-O<sub>2</sub> potential energy surface: O<sub>2</sub> and air broadening of the R(0) line in CO,

Adam Zadrozny, **Hubert Jóźwiak**, Ernesto Quintas-Sánchez, Richard Dawes, Piotr Wcisło

*The Journal of Chemical Physics* 157, 174310 (2022)

DOI: 10.1063/5.0115654

12. Fully quantum calculations of O<sub>2</sub>-N<sub>2</sub> scattering using a new potential energy surface: Collisional perturbations of the oxygen 118 GHz fine structure line

Maciej Gancewski, **Hubert Jóźwiak**, Ernesto Quintas-Sánchez, Richard Dawes, Franck Thibault, Piotr Wcisło

*The Journal of Chemical Physics* 155, 124307 (2021)

DOI: 10.1063/5.0063006



13. *Ab initio* investigation of the CO–N<sub>2</sub> quantum scattering: The collisional perturbation of the pure rotational R(0) line in CO  
**Hubert Jóźwiak**, Franck Thibault, Hubert Cybulski, Piotr Wcisło  
*The Journal of Chemical Physics* 154, 054314 (2021)  
DOI: 10.1063/5.0040438
  
14. Hyperfine components of rovibrational dipole transitions in HT and DT  
**Hubert Jóźwiak**, Hubert Cybulski, Piotr Wcisło  
*Journal of Quantitative Spectroscopy and Radiative Transfer* 270, 107662 (2021)  
DOI: 10.1016/j.jqsrt.2021.107662
  
15. Hyperfine structure of rovibrational quadrupole transitions in HD  
**Hubert Jóźwiak**, Hubert Cybulski, Piotr Wcisło  
*Journal of Quantitative Spectroscopy and Radiative Transfer* 272, 107753 (2021)  
DOI: 10.1016/j.jqsrt.2021.107753
  
16. Hyperfine structure of the  $EF^1\Sigma_g^+$  state in H<sub>2</sub>  
**Hubert Jóźwiak**, Hubert Cybulski, Antoni Grabowski, Piotr Wcisło  
*Physical Review A* 104, 012808 (2021)  
DOI: 10.1103/PhysRevA.104.012808
  
17. Collisional line broadening and mixing in the Raman spectrum of CO perturbed by N<sub>2</sub>: Experimental measurements and theoretical calculations  
Dennís Paredes-Roibás, Raul Martínez, **Hubert Jóźwiak**, Franck Thibault  
*Journal of Quantitative Spectroscopy and Radiative Transfer* 275, 107868 (2021)  
DOI: 10.1016/j.jqsrt.2021.107868



18. Accurate calculations of beyond-Voigt line-shape parameters from first principles for the He-perturbed HD rovibrational lines: A comprehensive dataset in the HITRAN DPL format

Kamil Stankiewicz, Nikodem Stolarczyk, **Hubert Jóźwiak**,  
Franck Thibault, Piotr Wcisło

*Journal of Quantitative Spectroscopy and Radiative Transfer* 276, 107911  
(2021)

DOI: 10.1016/j.jqsrt.2021.107911

19. The first comprehensive dataset of beyond-Voigt line-shape parameters from *ab initio* quantum scattering calculations for the HITRAN database: He-perturbed H<sub>2</sub> case study

Piotr Wcisło, Franck Thibault, Nikodem Stolarczyk, **Hubert Jóźwiak**,  
Michał Słowiński, Maciej Gancewski, Kamil Stankiewicz, Magdalena  
Konefał, Samir Kassi, Alain Campargue, Yan Tan, Jin Wang, Konrad  
Patkowski, Roman Ciuryło, Daniel Lisak, Roman Kochanov, Laurence  
S. Rothman, Iouli E. Gordon

*Journal of Quantitative Spectroscopy and Radiative Transfer* 260, 107477  
(2021)

DOI: 10.1016/j.jqsrt.2020.107477

20. Hyperfine structure of quadrupole rovibrational transitions in tritium-bearing hydrogen isotopologues

**Hubert Jóźwiak**, Hubert Cybulski, Piotr Wcisło

*Journal of Quantitative Spectroscopy and Radiative Transfer* 255, 107255  
(2020)

DOI: 10.1016/j.jqsrt.2020.107255



21. Hyperfine components of all rovibrational quadrupole transitions in the  $H_2$  and  $D_2$  molecules

**Hubert Jóźwiak**, Hubert Cybulski, Piotr Wcisło

*Journal of Quantitative Spectroscopy and Radiative Transfer* 253, 107186 (2020)

DOI: 10.1016/j.jqsrt.2020.107186

22. Positions and intensities of hyperfine components of all rovibrational dipole lines in the HD molecule

**Hubert Jóźwiak**, Hubert Cybulski, Piotr Wcisło

*Journal of Quantitative Spectroscopy and Radiative Transfer* 253, 107171 (2020)

DOI: 10.1016/j.jqsrt.2020.107171

23.  $H_2$ -He collisions: *Ab initio* theory meets cavity-enhanced spectra

Michał Słowiński, Franck Thibault, Yan Tan, Jin Wang, An-Wen Liu, Shui-Ming Hu, Samir Kassi, Alain Campargue, Magdalena Konefał,

**Hubert Jóźwiak**, Konrad Patkowski, Piotr Żuchowski, Roman Ciuryło, Daniel Lisak, Piotr Wcisło

*Physical Review A* 101, 052705 (2020)

DOI: 10.1103/PhysRevA.101.052705

24. *Ab initio* calculations of collisional line-shape parameters and generalized spectroscopic cross-sections for rovibrational dipole lines in HD perturbed by He

Kamil Stankiewicz, **Hubert Jóźwiak**, Maciej Gancewski, Nikodem Stolarczyk, Franck Thibault, Piotr Wcisło

*Journal of Quantitative Spectroscopy and Radiative Transfer* 254, 107194 (2020)

DOI: 10.1016/j.jqsrt.2020.107194





25. Evaluation of different parameterizations of temperature dependences of the line-shape parameters based on ab initio calculations: case study for the HITRAN database

Nikodem Stolarczyk, Franck Thibault, Hubert Cybulski,

**Hubert Jóźwiak**, Grzegorz Kowzan, Bastian Vispoel, Iouli E. Gordon, Laurence Rothman, Robert R. Gamache, Piotr Wcisło

*Journal of Quantitative Spectroscopy and Radiative Transfer* 240, 106676 (2020)

DOI: 10.1016/j.jqsrt.2019.106676

26. Accurate deuterium spectroscopy and comparison with *ab initio* calculations

Szymon Wójtewicz, Riccardo Gotti, Davide Gatti, Marco Lamperti, Paolo Laporta, **Hubert Jóźwiak**, Franck Thibault, Piotr Wcisło, Marco Marangoni

*Physical Review A* 101, 052504 (2020)

DOI: 10.1103/PhysRevA.101.052504

27. Ultrahigh finesse cavity-enhanced spectroscopy for accurate tests of quantum electrodynamics for molecules

Mikołaj Zaborowski, Michał Słowiński, Kamil Stankiewicz,

Franck Thibault, Agata Cygan, **Hubert Jóźwiak**, Grzegorz Kowzan, Piotr Masłowski, Nikodem Stolarczyk, Szymon Wójtewicz, Roman Ciuryło, Daniel Lisak, Piotr Wcisło

*Optics Letters* 45, 1603 (2020)

DOI: 10.1364/OL.389268

28. Ab initio line-shape calculations for the S and O branches of H<sub>2</sub> perturbed by He

**Hubert Jóźwiak**, Franck Thibault, Nikodem Stolarczyk, Piotr Wcisło

*Journal of Quantitative Spectroscopy and Radiative Transfer* 219, 313 (2018)

DOI: 10.1016/j.jqsrt.2018.08.023



29. Rovibrational line-shape parameters for  $H_2$  in He and new  $H_2$ -He potential energy surface

Franck Thibault, Konrad Patkowski, Piotr Żuchowski, **Hubert Jóźwiak**, Roman Ciuryło, Piotr Wcisło

*Journal of Quantitative Spectroscopy and Radiative Transfer* 202, 308 (2017)

DOI: 10.1016/j.jqsrt.2017.08.014



# NOTATION

This section clarifies the notation conventions adopted in the Introduction and Appendices.

## General Conventions

- **Operators and Vectors:**

- Operators are denoted by hats, e.g.,  $\hat{H}$  for the Hamiltonian.
- Vectors are represented in bold font, e.g.,  $\mathbf{R}$  for the intermolecular separation vector.
- In some cases, vectors are expressed in spherical coordinates, where their magnitude (e.g.,  $R = |\mathbf{R}|$ ) and angular part (denoted by a unit vector, e.g.,  $\hat{\mathbf{R}}$ ) are used separately. Note that the hat ( $\hat{\cdot}$ ) symbol is also used to denote operators, which might lead to ambiguity. In such cases, the context makes the distinction clear, and specific details are clarified in the text.

- **Notation in two-body systems:**

- For quantum scattering and spectral line shape theory, the two colliding species (molecules or atoms) are typically labeled as:
  - \* **A**: The *active* molecule that undergoes a spectral transition.
  - \* **P**: The *perturber*—the molecule or atom that collides with the active molecule but does not undergo a transition.
- This notation follows conventions used in line shape theory [11]. In ordinary scattering theory, the two molecules are commonly referred to as *target* and *projectile* [239]. However, this dissertation consistently uses the labels **A** and **P** to avoid confusion.

- **Indexing for Molecules:**

- Quantities related to the active molecule ( $A$ ) and perturber ( $P$ ) are denoted with uppercase indices  $A$  and  $P$  when describing operators, and lowercase indices  $a$  and  $p$  for quantum numbers. For example:



- \*  $\hat{H}_A, \hat{H}_P$ : Internal Hamiltonians of molecules  $A$  and  $P$ .
- \*  $E_a, E_p$ : Energies of states in molecules  $A$  and  $P$ .
- When discussing spectral transitions involving molecule  $A$ , the states are labeled:
  - \*  $a$ : Ground state.
  - \*  $b$ : Excited state.
- Spectral transitions are written in standard spectroscopic notation, e.g.,  $b \leftarrow a$ . This differs from ordinary scattering theory, where pre-collisional and post-collisional states are written left to right using  $a' \rightarrow a$ . This notation is used in Appendix A (see Eq. (A.14)).
- In Appendices, primed quantum numbers ( $N'_a, N'_p$ ) represent pre-collisional states, while unprimed ( $N_a, N_p$ ) denote post-collisional states.

## Spectroscopic Notation

Spectral transitions are denoted using standard spectroscopic conventions. If  $v_a$  and  $v_b$  are the ground and excited vibrational quantum numbers, and  $N_a$  and  $N_b$  are the ground and excited rotational quantum numbers, transitions are written as

$$v_b - v_a \text{ LETTER}(N_a),$$

where **LETTER** corresponds to  $\Delta N = N_b - N_a$  according to the table below:

<b>LETTER</b>	$O$	$P$	$Q$	$R$	$S$
$\Delta N$	−2	−1	0	+1	+2

For example, the transition  $1 - 0 \text{ S}(0)$  refers to

$$v_b = 1, N_b = 2 \leftarrow v_a = 0, N_a = 0.$$



## List of acronyms

Acronym	Description
ALMA	Atacama Large Millimeter/submillimeter Array
AMO	atomic, molecular and optical
BSP	Bakr, Smith and Patkowski ( $\text{H}_2$ -He PES [109])
CC	coupled channel
CP	charge conjugation and parity transformation
CPT	charge conjugation, parity transformation and time reversal
CSA	coupled states approximation
EDM	electric dipole moment
FWHM	full-width at half maximum
HAPI	HITRAN Application Programming Interface [94]
HC	hard collision (profile)
HT	Hartmann-Tran (profile)
HWHM	half-width at half maximum
ISM	interstellar medium
JWST	the James Webb Space Telescope
LTE	local thermodynamic equilibrium
mHT	modified Hartmann-Tran (profile)
MQDT	multichannel quantum defect theory
MR	Muchnick and Russek ( $\text{H}_2$ -He PES [51])
ODT	optical dipole trap
PBXS	pressure broadening cross section
PES	potential energy surface
PSXS	pressure shift cross section
QED	quantum electrodynamics
qSDHC	quadratic speed-dependent hard collision (profile)
SDBB	speed-dependent billiard ball (profile)
SM	the Standard Model
SOFIA	Stratospheric Observatory for Infrared Astronomy
SRS	stimulated Raman scattering
VC	velocity-changing collisions





## APPENDIX

### A. Quantum scattering calculations of collisional rate coefficients

This Appendix provides a concise overview of the fundamental theory used to solve the quantum scattering problem involving two molecules or a molecule and an atom, as applied in Articles **A–E** and Article **L**.

The quantum mechanical description of molecular scattering begins with the full Hamiltonian, which involves both electronic and nuclear degrees of freedom. Detailed discussions on the separation of the center-of-mass motion of the collision complex, fixing the origin of the space-fixed coordinate frame at the center of mass of the scattering system, as well as the separation of the electronic and nuclear parts of the problem, can be found in standard references [33,240]. Here, we assume that the scattering occurs on a single potential energy surface (PES) computed within the Born-Oppenheimer approximation. This treatment is valid for non-reactive collisions where non-adiabatic effects are negligible.

Consider two colliding species (molecules or atoms), referred to, as  $A$  and  $P$  (following the terminology used in line-shape theory for the active molecule  $A$  molecule and the perturber  $P$ ), each described by their internal Hamiltonian operators

$$\hat{H}_A|a\rangle = E_a|a\rangle, \quad \hat{H}_P|p\rangle = E_p|p\rangle. \quad (\text{A.1})$$

Here,  $E_a$  and  $E_p$  correspond to the internal energies of molecules  $A$  and  $P$ , while  $|a\rangle$  and  $|p\rangle$  represent their respective eigenstates, which remain unspecified for now. The Hamiltonian of the two colliding species in the space-fixed frame, with the origin placed at the center of mass of the system, is given by

$$\hat{H}(\mathbf{R}, \mathbf{r}_A, \mathbf{r}_P) = -\frac{\hbar^2}{2\mu}\hat{\Delta}_{\mathbf{R}} + V(\mathbf{R}, \mathbf{r}_A, \mathbf{r}_P) + \hat{H}_A + \hat{H}_P. \quad (\text{A.2})$$

Here,  $\mathbf{R}$  is the vector connecting the center of mass  $A$  to that of  $P$ . The first term



represents the kinetic energy operator of the relative motion of the colliding pair

$$-\frac{\hbar^2}{2\mu}\hat{\Delta}_{\mathbf{R}} = -\frac{\hbar^2}{2\mu}R^{-2}\frac{\partial}{\partial R}R^2\frac{\partial}{\partial R} + \frac{\hbar^2\hat{l}^2}{2\mu R^2}, \quad (\text{A.3})$$

where  $R = |\mathbf{R}|$ , and  $\hat{l}$  is the relative orbital angular momentum of the colliding pair. The eigenstates of  $\hat{l}$

$$\hat{l}|lm_l\rangle = l(l+1)|lm_l\rangle, \quad (\text{A.4})$$

describing the end-over-end rotation of the complex, are called *partial waves*.  $V(\mathbf{R}, \mathbf{r}_A, \mathbf{r}_P)$  is the potential energy surface of the colliding system, which vanishes as  $R \rightarrow \infty$ .

The goal of quantum scattering calculations is to determine the eigenstates of the Hamiltonian in Eq. (A.2), that satisfy the time-independent Schrödinger equation

$$\hat{H}|\Psi\rangle = E|\Psi\rangle, \quad (\text{A.5})$$

for a given total energy  $E$ . To achieve this, the unknown eigenstate  $\Psi$  is expanded in a suitable basis

$$|\Psi\rangle = \sum_{\xi} \frac{F_{\xi}(R)}{R} |\xi\rangle, \quad (\text{A.6})$$

where  $F_{\xi}(R)$  are radial expansion coefficients, functions of  $R$ , which is the only variable that is not covered by the basis states. The basis states  $|\xi\rangle$  define the collision (scattering) *channels*. Substituting this expansion into the Schrödinger equation and projecting onto  $\langle\xi'|$  results in a set of coupled second-order differential equations for the expansion coefficients

$$\frac{d^2}{dR^2}F_{\xi}(R) = \sum_{\xi'} \langle\xi|\hat{W}(\mathbf{R}, \mathbf{r}_A, \mathbf{r}_P)|\xi'\rangle F_{\xi'}(R), \quad (\text{A.7})$$

where I have swapped the primed and unprimed symbols for convenience. These equations are *coupled* because the radial expansion coefficients  $F_{\xi'}(R)$  are interdependent through the matrix elements of  $\hat{W}$

$$\hat{W}(\mathbf{R}, \mathbf{r}_A, \mathbf{r}_P) = \frac{l^2}{R^2} + \frac{2\mu}{\hbar^2} \left( V(\mathbf{R}, \mathbf{r}_A, \mathbf{r}_P) + \hat{H}_A + \hat{H}_P - E \right), \quad (\text{A.8})$$

The actual form of the matrix elements of  $\hat{W}$  depends on the chosen basis. In principle, Eq. (A.7) represents an infinite set of coupled equations. In practice, the expansion is truncated at some number of scattering channels,  $N$ , which



may depend on the chosen basis.

The most straightforward choice of the basis functions, formed by the direct product of the eigenstates of the operators forming  $\hat{W}$ —that is

$$|\Psi\rangle = \sum_{a,p,l,m_l} \frac{F_{apl m_l}(R)}{R} |apl m_l\rangle, \quad (\text{A.9})$$

where  $|apl m_l\rangle = |a\rangle \otimes |p\rangle \otimes |l m_l\rangle$ . In this case matrix elements of  $\hat{W}$  are given as

$$\begin{aligned} \langle apl m_l | \hat{W}(\mathbf{R}, \mathbf{r}_A, \mathbf{r}_P) | a' p' l' m'_l \rangle &= \delta_{aa'} \delta_{pp'} \delta_{ll'} \delta_{m_l m'_l} \left( \frac{l(l+1)}{R^2} - k_r^2 \right) \\ &+ \frac{2\mu}{\hbar^2} \langle apl m_l | V(\mathbf{R}, \mathbf{r}_A, \mathbf{r}_P) | a' p' l' m'_l \rangle, \end{aligned} \quad (\text{A.10})$$

where  $k_r^2$  is the wave vector quantifying the relative kinetic energy ( $E_{\text{kin}}$ ) of the colliding pair

$$k_r^2 = \frac{2\mu}{\hbar^2} (E - E_a - E_p) = \frac{2\mu}{\hbar^2} E_{\text{kin}}. \quad (\text{A.11})$$

Matrix elements of the PES are then calculated depending on the specific form of  $|a\rangle$  and  $|p\rangle$ .

It is not, however, sufficient, to find a numerical solution of Eq. (A.7); the solution must also have a particular behavior as  $R$  goes to zero and infinity [241]. At short range the radial coefficients should vanish due to the repulsive wall of the PES

$$\lim_{R \rightarrow 0} F_{apl m_l}(R) \rightarrow 0, \quad (\text{A.12})$$

for all scattering channels. At large  $R$ , the expansion coefficients should behave as

$$F_{apl m_l}(R) \sim \delta_{a,\tilde{a}} \delta_{p,\tilde{p}} \delta_{l,\tilde{l}} \delta_{m_l,\tilde{m}_l} e^{-ik_r R - \pi l/2} - S_{\tilde{a}\tilde{p}\tilde{l}\tilde{m}_l, apl m_l} e^{i(k_r R - \pi l/2)}. \quad (\text{A.13})$$

This expression represents a combination of the incoming wave, describing the pre-collisional state of the system in channel  $|\tilde{a}\tilde{p}\tilde{l}\tilde{m}_l\rangle$  and the outgoing wave, representing the post-collisional state in a different channel,  $|apl m_l\rangle$ . The transition between these channels is encoded in the  $S$ -matrix element, which quantifies the probability amplitude for the system to transition between the incoming and outgoing states. For a detailed discussion of the boundary conditions in quantum scattering, the reader is referred to Refs. [241, 242].

The scattering  $S$ -matrix elements determine the *cross section* for the



collision-induced transition  $|\tilde{a}\tilde{p}\rangle \rightarrow |ap\rangle$ , defined as

$$\sigma_{\tilde{a}\tilde{p} \rightarrow ap}(E_{\text{kin}}) = \frac{\pi}{k_r^2} \sum_{l, m_l, l', m'_l} |\delta_{ll'} \delta_{m_l m'_l} \delta_{\tilde{a}a} \delta_{\tilde{p}p} - S_{\tilde{a}\tilde{p}lm_l, aplm_l}|^2, \quad (\text{A.14})$$

which depends on the relative collision energy,  $E_{\text{kin}}$ , not only through  $k_r$  but also through the energy dependence of the  $S$ -matrix.

While molecular beam experiments can measure the cross sections directly, they are often not accessible in other experimental techniques. Instead, the experimentally measurable quantity is the *rate coefficient*, which averages the cross-sections over a Maxwellian distribution of relative collision energies

$$k_{\tilde{a}\tilde{p} \rightarrow ap}(T) = \langle v_r \rangle \left( \frac{1}{k_B T} \right)^2 \int_0^\infty \sigma_{\tilde{a}\tilde{p} \rightarrow ap}(E_{\text{kin}}) E_{\text{kin}} e^{-E_{\text{kin}}/k_B T} dE_{\text{kin}}, \quad (\text{A.15})$$

where  $\langle v_r \rangle = \sqrt{8k_B T / (\pi \mu)}$  is the mean relative speed of colliding species,  $k_B$  is the Boltzmann constant,  $T$  is the temperature, and  $\mu$  is the reduced mass of the system.

The direct product basis defined in Eq. (A.9) was applied in Paper **L**, in which I studied collisions of molecular hydrogen with atomic lithium in the presence of an external magnetic field. In this study, the internal Hamiltonian of the  $\text{H}_2$  molecule ( $\hat{H}_A$ ) included the rotational, hyperfine and Zeeman terms. Consequently, the internal state  $|a\rangle$  was constructed as a direct product of the eigenstates of the rotational angular momentum of the  $\text{H}_2$  molecule,  $\hat{N}|NM_N\rangle = N(N+1)|NM_N\rangle$  and the total nuclear spin,  $\hat{I}|IM_I\rangle = I(I+1)|IM_I\rangle$ , such that  $|a\rangle = |NM_N\rangle|IM_I\rangle$ . For the lithium atom, the internal Hamiltonian ( $\hat{H}_P$ ) included the Zeeman interaction describing the coupling of the electronic spin magnetic moment to the external magnetic field. Accordingly, the eigenstate  $|p\rangle$  was defined as  $|SM_S\rangle$ , the eigenstate of the total electron spin operator in Li,  $\hat{S}|SM_S\rangle = S(S+1)|SM_S\rangle$ . Details about the matrix elements of  $\hat{W}$  and additional interactions involved are provided in Paper **L**.

It is always beneficial to exploit any symmetries present in the scattering system, as doing so can simplify the quantum scattering problem considerably. In the absence of external fields, the total angular momentum of the scattering system is conserved. This principle underlies the alternative choice of basis functions proposed by Arthurs and Dalgarno [119], initially developed for the scattering of a rigid rotor molecule and a structureless atom.

The basis in this representation still involves products of the eigenstates of



$\hat{H}_A$ ,  $\hat{H}_P$ , and  $\hat{l}$ , but it uses linear combinations of these states to take advantage of the conservation of total angular momentum. For the specific case of scattering between two molecules modeled as rigid rotors, such as in Paper **D**, the internal Hamiltonians are given by

$$\hat{H}_A = B_e \hat{N}_A, \quad \hat{H}_P = B_e \hat{N}_P, \quad (\text{A.16})$$

where  $\hat{N}_A$  and  $\hat{N}_P$  are the rotational angular momentum operators for molecules  $A$  and  $P$ , respectively, with the eigenstates

$$\hat{N}_A |N_a M_{N_a}\rangle = N_a(N_a + 1) |N_a M_{N_a}\rangle, \quad \hat{N}_P |N_p M_{N_p}\rangle = N_p(N_p + 1) |N_p M_{N_p}\rangle. \quad (\text{A.17})$$

The basis states are constructed by coupling the eigenstates of  $\hat{N}_A$ ,  $\hat{N}_P$ , and  $\hat{l}$  into a total angular momentum,  $\hat{J}$ , eigenstate

$$\begin{aligned} & |((N_a N_p) N_{ap} l) J M\rangle = \\ & = (-1)^{-N_{ap} + l - M} \sqrt{[J]} \sum_{M_{N_{ap}}, M_l} \begin{pmatrix} N_{ap} & I & J \\ M_{N_{ap}} & M_l & -M \end{pmatrix} |(N_a N_p) N_{ap} M_{N_{ap}}\rangle |l M_l\rangle \\ & = (-1)^{-N_{ap} + l - M - N_a + N_p - M_{N_{ap}}} \sqrt{[J, N_{ap}]} \sum_{M_{N_a}, M_{N_p}, M_{N_{ap}}, M_l} \begin{pmatrix} N_{ap} & I & J \\ M_{N_{ap}} & M_l & -M \end{pmatrix} \\ & \quad \times \begin{pmatrix} N_a & N_p & N_{ap} \\ M_{N_a} & M_{N_p} & -M_{N_{ap}} \end{pmatrix} |N_a M_{N_a}\rangle |N_p M_{N_p}\rangle |l M_l\rangle. \end{aligned} \quad (\text{A.18})$$

Here,  $[x_1, x_2, \dots, x_n] = (2x_1 + 1)(2x_2 + 1) \cdots (2x_n + 1)$ .  $|(N_a N_p) N_{ap} M_{N_{ap}}\rangle$  represents the eigenstate of  $\hat{N}_{AP}$ , the intermediate angular momentum resulting from coupling  $\hat{N}_A$  and  $\hat{N}_P$  (sometimes referred to as the *total rotational angular momentum*). The order in which the three angular momenta are coupled (the *coupling scheme*) can be written symbolically as

$$\hat{N}_A + \hat{N}_P = \hat{N}_{AP}, \quad \hat{N}_{AP} + \hat{l} = \hat{J}. \quad (\text{A.19})$$

This choice, referred to here as the *scattering coupling scheme*, is not unique, and alternative schemes are discussed in Appendix B.

The states defined above are also eigenfunctions of the spatial inversion operator,  $\hat{P}_{\text{inv}}$ , which maps the spatial coordinates as [243]

$$\mathbf{R}, \mathbf{r}_A, \mathbf{r}_P \rightarrow -\mathbf{R}, -\mathbf{r}_A, -\mathbf{r}_P. \quad (\text{A.20})$$





Under this operation, the basis states transform as

$$\hat{P}_{\text{inv}}|((N_a N_p)N_{ap}l)JM\rangle = (-1)^{N_a+N_b+l}|((N_a N_p)N_{ap}l)JM\rangle. \quad (\text{A.21})$$

The use of this basis significantly simplifies the quantum scattering problem compared to the direct product basis set introduced in Eq. (A.9). Since the total angular momentum and its projection on the space-fixed  $Z$ -axis commute with the Hamiltonian, the coupled equations are block-diagonal with respect to  $J$  and  $M$ . Furthermore, it can be shown that the equations do not explicitly depend on  $M$ , and this index is often omitted. Similarly, because the spatial inversion operator commutes with the Hamiltonian, each  $J$ -block of equations further splits into two uncoupled sub-blocks corresponding to even and odd eigenstates of  $\hat{P}_{\text{inv}}$ .

For the purposes of the upcoming discussion, let me provide the explicit formula for the matrix elements of the  $\hat{W}$  matrix [244]

$$\begin{aligned} &\langle((N_a N_p)N_{ap}l)JM|\hat{W}(\mathbf{R}, \mathbf{r}_A, \mathbf{r}_P)|((N'_a N'_p)N'_{ap}l)J'M'\rangle = \\ &= \delta_{JJ'}\delta_{MM'} \left( \delta_{N_a N'_a} \delta_{N_p N'_p} \delta_{N_{ap} N'_{ap}} \delta_{ll'} \left( \frac{l(l+1)}{R^2} - k_r^2 \right) \right. \\ &\quad \left. + \frac{2\mu}{\hbar^2} \langle((N_a N_p)N_{ap}l)JM|V(\mathbf{R}, \mathbf{r}_A, \mathbf{r}_P)|((N'_a N'_p)N'_{ap}l)J'M'\rangle \right). \end{aligned} \quad (\text{A.22})$$

The  $\hat{W}$ -matrix is diagonal in the total angular momentum and its projection on the space-fixed  $Z$  axis. The centrifugal term provides a diagonal contribution, and  $k_r$  has been defined in Eq. (A.11). The last term represents the contribution from the PES of the scattering system, which is given by [243, 245]

$$\begin{aligned} &\langle((N_a N_p)N_{ap}l)JM|V(\mathbf{R}, \mathbf{r}_A, \mathbf{r}_P)|((N'_a N'_p)N'_{ap}l')J'M'\rangle = \\ &= \delta_{JJ'}\delta_{MM'} \sum_{\lambda_a \lambda_p \lambda_{ap}} A_{\lambda_a \lambda_p \lambda_{ap}}(R) f_{\lambda_a \lambda_p \lambda_{ap}}(N_a, N_p, N_{ap}, l, N'_a, N'_p, N'_{ap}, l'; J). \end{aligned} \quad (\text{A.23})$$

Here,  $A_{\lambda_a \lambda_p \lambda_{ap}}(R)$  are the radial expansion terms of the interaction potential

$$V(\mathbf{R}, \mathbf{r}_A, \mathbf{r}_P) = \sum_{\lambda_a \lambda_p \lambda_{ap}} A_{\lambda_a \lambda_p \lambda_{ap}}(R) I_{\lambda_a \lambda_p \lambda_{ap}}(\hat{\mathbf{R}}, \hat{\mathbf{r}}_A, \hat{\mathbf{r}}_P). \quad (\text{A.24})$$

In this particular context, the hat symbols in  $\hat{\mathbf{R}}$ ,  $\hat{\mathbf{r}}_A$  and  $\hat{\mathbf{r}}_P$  are used to denote the unit vectors of  $\mathbf{R} = R\hat{\mathbf{R}}$ ,  $\mathbf{r}_A = r_A\hat{\mathbf{r}}_A$  and  $\mathbf{r}_P = r_P\hat{\mathbf{r}}_P$ , defining the orientation



of these vectors in space. The angular part of the expansion,  $I_{\lambda_a \lambda_p \lambda_{ap}}(\hat{\mathbf{R}}, \hat{\mathbf{r}}_A, \hat{\mathbf{r}}_P)$ , is defined as

$$\begin{aligned}
 I_{\lambda_a \lambda_p \lambda_{ap}}(\hat{\mathbf{R}}, \hat{\mathbf{r}}_A, \hat{\mathbf{r}}_P) &= \\
 &= (-1)^{\lambda_a + \lambda_p - m_{ap}} \sqrt{[\lambda_{ap}]} \sum_{m_a, m_p, m_{ap}} \begin{pmatrix} \lambda_a & \lambda_p & \lambda_{ap} \\ m_a & m_p & -m_{ap} \end{pmatrix} Y_{\lambda_a, m_a}(\hat{\mathbf{r}}_A) Y_{\lambda_p, m_p}(\hat{\mathbf{r}}_P) Y_{\lambda_{ap}, m_{ap}}(\hat{\mathbf{R}})^*.
 \end{aligned}
 \tag{A.25}$$

This expansion conveniently separates variables, with the dependence of the matrix elements in Eq. (A.23) on the magnitude of the intermolecular separation  $R$  encoded only in the radial expansion coefficients,  $A_{\lambda_a \lambda_p \lambda_{ap}}(R)$ . Each coefficient can be interpreted in terms of distinct electrostatic contributions to the interaction energy [246]. For instance,  $A_{000}$  is the isotropic van der Waals term, which originates from a combination of the short-range repulsion and a long-range dispersion attraction, related to the spherical polarizabilities of the two molecules. The  $A_{\lambda_a 0 \lambda_a}$  (and  $A_{0 \lambda_p \lambda_p}$ ) terms describe the interaction of the nonspherical charge distribution of molecule  $A$  (or  $P$ ), with the other molecule approximated as a spherical target. Higher-order terms involve corrections related to the mutual orientation of molecules or can be directly related to the electrostatic interactions between multipole moments.

In principle, the sums over  $\lambda_a$  and  $\lambda_p$  are infinite. The third index,  $\lambda_{ap}$ , is determined by the triangular condition,  $|\lambda_a - \lambda_p| \leq \lambda_{ap} \leq \lambda_a + \lambda_p$ . In practice, the expansion is truncated at certain maximum values,  $\lambda_a^{(\max)}$ ,  $\lambda_p^{(\max)}$ ,  $\lambda_{ap}^{(\max)}$ , based on a suitable convergence criterion. In the papers constituting this dissertation, the truncation indices were chosen to ensure that the expansion coefficients allow for a satisfactory reconstruction of the original *ab initio* datapoints.

The  $R$ -independent algebraic coefficients in Eq. (A.23) are given as

$$\begin{aligned}
 f_{\lambda_a \lambda_p \lambda_{ap}}(N_a, N_p, N_{ap}, l, N'_a, N'_p, N'_{ap}, l'; J) &= (4\pi)^{-3/2} (-1)^{N_a + N_p + N'_{ap} + J} [\lambda_{ap}] \\
 &\times \sqrt{[\lambda_a, \lambda_p, N_a, N_p, N_{ap}, l, N'_a, N'_p, N'_{ap}, l']} \begin{pmatrix} N_a & N'_a & \lambda_a \\ 0 & 0 & 0 \end{pmatrix} \begin{pmatrix} N_p & N'_p & \lambda_p \\ 0 & 0 & 0 \end{pmatrix} \begin{pmatrix} l & l' & \lambda_{ap} \\ 0 & 0 & 0 \end{pmatrix} \\
 &\times \begin{Bmatrix} l & l' & \lambda_{ap} \\ N'_{ap} & N_{ap} & J \end{Bmatrix} \begin{Bmatrix} l & l' & \lambda_{ap} \\ N'_{ap} & N_{ap} & J \end{Bmatrix} \begin{Bmatrix} N'_{ap} & N'_p & N'_a \\ N_{ap} & N_p & N_a \\ \lambda_{ap} & \lambda_p & \lambda_a \end{Bmatrix}.
 \end{aligned}
 \tag{A.26}$$



This expression serves as a source of *selection rules*, linking specific radial expansion coefficients to particular collision processes. The Wigner 3-j symbols in this formula impose constraints on the allowed changes in quantum numbers during collisions, for instance

$$\begin{aligned} |N'_a - \lambda_a| &\leq N_a \leq N'_a + \lambda_a, \\ |N'_p - \lambda_p| &\leq N_p \leq N'_p + \lambda_p. \end{aligned} \quad (\text{A.27})$$

If the primed symbols represent pre-collisional values and the unprimed symbols post-collisional values, these selection rules show that, for instance, the isotropic  $A_{000}$  term contributes only to the elastic processes, where  $N'_a = N_a$  and  $N'_p = N_p$ . The  $A_{202}$  term contributes to inelastic processes that change  $N_a$  up to  $\Delta N_a = N_a - N'_a = 2$ , while keeping  $N_p$  unchanged.<sup>9</sup>

An additional selection rule arises from the properties of the 3-j symbols: since the projections in the symbols are 0, the sums  $N_a + N'_a + \lambda_a$ ,  $N_p + N'_p + \lambda_p$  and  $l + l' + \lambda_{ap}$  must be even integers. This has significant implications for homonuclear molecules. If a molecule  $A$  (or  $P$ ) is homonuclear, the PES should be invariant under spatial inversion of the respective molecular coordinates,  $\mathbf{r}_A \rightarrow -\mathbf{r}_A$  (or  $\mathbf{r}_P \rightarrow -\mathbf{r}_P$ ). As implied by Eq. (A.25), in this case  $\lambda_a$  (or  $\lambda_p$ ) must be even. Combining this with the condition that  $N_a + N'_a + \lambda_a$  (or  $N_p + N'_p + \lambda_p$ ) must be an even integer, implies that the rotational quantum number  $N_a$  (or  $N_p$ ) can only change by an even value. Transitions between odd and even  $N$  values are thus forbidden.

The scattering  $S$ -matrix elements are determined using boundary conditions analogous to those in Eq. (A.13). For two molecules modeled as rigid rotors, the integral cross-section in the basis introduced in Eq. (A.18) is given by

$$\begin{aligned} \sigma_{\tilde{N}_a \tilde{N}_p \rightarrow N_a N_p}(E_{\text{kin}}) &= \frac{\pi}{k_r^2 (2\tilde{N}_a + 1)(2\tilde{N}_p + 1)} \sum_J (2J + 1) \\ &\times \sum_{\substack{\tilde{N}_a + \tilde{N}_p \\ \tilde{N}_{ap} = |\tilde{N}_a - \tilde{N}_p|}} \sum_{\substack{N_a + N_p \\ N_{ap} = |N_a - N_p|}} \sum_{\substack{J + \tilde{N}_{ap} \\ l = |J - \tilde{N}_{ap}|}} \sum_{\substack{J + N_{ap} \\ l' = |J - N_{ap}|}} |\delta_{\tilde{N}_a N_a} \delta_{\tilde{N}_p N_p} \delta_{\tilde{N}_{ap} N_{ap}} \delta_{ll'} - S_{\tilde{N}_a \tilde{N}_p \tilde{N}_{ap} l, N_a N_p N_{ap} l}^J|^2, \end{aligned} \quad (\text{A.28})$$

where the superscript in the  $S$ -matrix,  $S^J$ , indicates that it was calculated within a specific  $J$ -block. The  $(2J + 1)$  factor arises from the independence of

<sup>9</sup>Similar selection rules can be deduced for  $l$  and  $N_{ap}$ .



the coupled equations on  $M$ . Similarly, the  $(2\tilde{N}_a + 1)(2\tilde{N}_p + 1)$  factor accounts for the degeneracy of the initial rotational states of the two molecules in the absence of external fields.

The corresponding rate coefficients can be calculated by averaging the integral cross-sections over a Maxwellian distribution of relative collision energies, as defined in Eq. (A.15).

The basis set defined in Eq. (A.18) is implemented in the commonly-used quantum scattering codes, such as MOLSCAT [128] and HIBRIDON [247]. It was used in the quantum scattering calculations reported in Papers **D** and **E**.

A different choice of the basis set allows for a more convenient representation of the matrix element of  $\hat{W}$  [243, 248]

$$\begin{aligned} & |(N_a N_p) N_{ap} \bar{\Omega} J M \epsilon\rangle \\ &= \frac{1}{\sqrt{2(1 + \epsilon \zeta \delta_{\bar{\Omega}, 0})}} \left( |(N_a N_p) N_{ap} \Omega J M\rangle + \epsilon \zeta |(N_a N_p) N_{ap} - \Omega J M\rangle \right) \end{aligned} \quad (\text{A.29})$$

where  $|(N_a N_p) N_{ap} \Omega J M\rangle = |(N_a N_p) N_{ap} \Omega\rangle |J M \Omega\rangle$ . In this case,  $|(N_a N_p) N_{ap} \Omega\rangle$  are the eigenvectors of the total rotational angular momentum,  $\hat{N}_{AP}^2 |(N_a N_p) N_{ap} \Omega\rangle = N_{ap}(N_{ap} + 1) |(N_a N_p) N_{ap} \Omega\rangle$ , and its projection along the  $R$ -axis,  $\hat{N}_{APR} |(N_a N_p) N_{ap} \Omega\rangle = \Omega |(N_a N_p) N_{ap} \Omega\rangle$ .  $|J M \Omega\rangle$  are the symmetric-top eigenvectors, being the eigenvectors of the total angular momentum operator,  $\hat{J}^2 |J M \Omega\rangle = J(J + 1) |J M \Omega\rangle$ , its space-fixed  $Z$ -axis projection  $J_Z |J M \Omega\rangle = M |J M \Omega\rangle$ , and its projection on the  $R$ -axis  $J_R |J M \Omega\rangle = \Omega |J M \Omega\rangle$ . The basis functions in Eq. (A.29) are also eigenvectors of the spatial inversion operator, satisfying  $\hat{P}_{\text{inv}} |(N_a N_p) N_{ap} \bar{\Omega} J M\rangle = \epsilon |(N_a N_p) N_{ap} \bar{\Omega} J M\rangle$ , where  $\epsilon = \pm 1$ . Additionally,  $\bar{\Omega} = |\Omega| \in \langle 0, \min(N_{ab}, J) \rangle$ , and  $\zeta = (-1)^{N_a + N_p + J - N_{ap}}$ .

This basis, often referred to as the body-fixed basis, is related to the basis introduced in Eq. (A.18) by the following transformation

$$\begin{aligned} & |((N_a N_p) N_{ap} l) J M\rangle = (-1)^{-N_{ap} + l} \sum_{\bar{\Omega}} (-1)^{\bar{\Omega}} \\ & \times \sqrt{\frac{2(2l + 1)}{(1 + \epsilon p \delta_{\Omega, 0})}} \begin{pmatrix} N_{ap} & l & J \\ \bar{\Omega} & 0 & -\bar{\Omega} \end{pmatrix} |(N_a N_p) N_{ap} \bar{\Omega} J M \epsilon\rangle. \end{aligned} \quad (\text{A.30})$$

The most significant advantage of the body-fixed basis is the resulting



### structure of the $\hat{W}$ -matrix

$$\begin{aligned}
 & \langle (N_a N_p) N_{ap} \bar{\Omega} J M \epsilon | \hat{W}(\mathbf{R}, \mathbf{r}_A, \mathbf{r}_P) | (N'_a N'_p) N'_{ap} \bar{\Omega}' J' M' \epsilon' \rangle = \\
 & = \delta_{JJ'} \delta_{MM'} \delta_{\epsilon\epsilon'} \left( \delta_{N_a N'_a} \delta_{N_p N'_p} \delta_{N_{ap} N'_{ap}} \left( \frac{1}{R^2} \langle (N_a N_p) N_{ap} \bar{\Omega} J M | \hat{\mathbf{l}}^2 | (N'_a N'_p) N'_{ap} \bar{\Omega}' J' M' \rangle \right. \right. \\
 & \quad \left. \left. - \delta_{\bar{\Omega}\bar{\Omega}'} k_r^2 \right) + \delta_{\bar{\Omega}\bar{\Omega}'} \frac{2\mu}{\hbar^2} \langle (N_a N_p) N_{ap} \bar{\Omega} J M | V(\mathbf{R}, \mathbf{r}_A, \mathbf{r}_P) | (N'_a N'_p) N'_{ap} \bar{\Omega}' J' M' \rangle \right). \tag{A.31}
 \end{aligned}$$

The contribution from the PES is diagonal with respect to  $\bar{\Omega}$

$$\begin{aligned}
 & \langle (N_a N_p) N_{ap} \bar{\Omega} J M \epsilon | V(\mathbf{R}, \mathbf{r}_A, \mathbf{r}_P) | (N'_a N'_p) N'_{ap} \bar{\Omega}' J' M' \epsilon' \rangle = \\
 & = \delta_{JJ'} \delta_{MM'} \delta_{\epsilon\epsilon'} \delta_{\bar{\Omega}\bar{\Omega}'} \sum_{\lambda_a \lambda_p \lambda_{ap}} A_{\lambda_a \lambda_p \lambda_{ap}}(R) g_{\lambda_a \lambda_p \lambda_{ap}}(N_a, N_p, N_{ap}, N'_a, N'_p, N'_{ap}; \bar{\Omega}, J), \tag{A.32}
 \end{aligned}$$

where the radial expansion coefficients,  $A_{\lambda_a \lambda_p \lambda_{ap}}(R)$  were previously defined in Eq. (A.24). The algebraic coefficients are given as

$$\begin{aligned}
 & g_{\lambda_a \lambda_p \lambda_{ap}}(N_a, N_p, N_{ap}, N'_a, N'_p, N'_{ap}; \bar{\Omega}, J) \\
 & = (4\pi)^{-3/2} (-1)^{N_a + N_p + N'_{ap} + \bar{\Omega}} [\lambda_{ap}] \sqrt{[\lambda_a, \lambda_p, N_a, N_p, N_{ap}, N'_a, N'_p, N'_{ap}]} \\
 & \times \begin{pmatrix} N_a & N'_a & \lambda_a \\ 0 & 0 & 0 \end{pmatrix} \begin{pmatrix} N_p & N'_p & \lambda_p \\ 0 & 0 & 0 \end{pmatrix} \begin{pmatrix} N_{ap} & N'_{ap} & \lambda_{ap} \\ \bar{\Omega} & -\bar{\Omega} & 0 \end{pmatrix} \begin{Bmatrix} N'_{ap} & N'_p & N'_a \\ N_{ap} & N_p & N_a \\ \lambda_{ap} & \lambda_p & \lambda_a \end{Bmatrix}. \tag{A.33}
 \end{aligned}$$

This property leads to a sub-block structure within each  $J$  and  $\epsilon$  block, corresponding to distinct values of  $\bar{\Omega}$ . These sub-blocks are interconnected only by the centrifugal terms

$$\begin{aligned}
 & \langle (N_a N_p) N_{ap} \bar{\Omega} J M \epsilon | \hat{\mathbf{l}}^2 | (N'_a N'_p) N'_{ap} \bar{\Omega}' J' M' \epsilon' \rangle \\
 & = \delta_{JJ'} \delta_{MM'} \delta_{\epsilon\epsilon'} \delta_{N_a N'_a} \delta_{N_p N'_p} \delta_{N_{ap} N'_{ap}} \left( \delta_{\bar{\Omega}\bar{\Omega}'} \left( J(J+1) + N_{ap}(N_{ap}+1) - 2\bar{\Omega}^2 \right) \right. \\
 & \quad \left. - \delta_{\bar{\Omega}\bar{\Omega} \pm 1} \sqrt{(1 + \delta_{\bar{\Omega}0})(1 + \delta_{\bar{\Omega} \pm 1, 0})} \sqrt{(J(J+1) - \bar{\Omega}(\bar{\Omega} \pm 1))(N_{ap}(N_{ap}+1) - \bar{\Omega}(\bar{\Omega} \pm 1))} \right). \tag{A.34}
 \end{aligned}$$

The body-fixed basis reduces memory requirements significantly. Instead of storing all non-zero algebraic coefficients for the space-fixed basis, only the much smaller subset of coefficients relevant to the body-fixed representation





is needed.

This approach has been implemented in the scattering code developed as part of the `BIGOS` package, created by our group and used in the calculations reported in Papers **A**, **B**, and **C**. Coupled equations were solved numerically using either the log-derivative Johnson method [249] or the renormalized Numerov propagator [250]. At large intermolecular separations, where the radial expansion terms of the PES become negligible compared to the centrifugal terms, the solution (or its log-derivative) is transformed to the basis introduced in Eq. (A.18) using Eq. (A.30). Integral cross-sections are then calculated as described in Eq. (A.28). For further details, readers are referred to the specific papers and the manual of the scattering code, available on GitHub [130], published alongside Paper **A**.

Finally, the body-fixed basis is the natural starting point for approximate methods of solving the coupled equations. One such method is the coupled-states approximation (CSA) [126], which simplifies the centrifugal distortion terms by neglecting off-diagonal contributions in  $\bar{\Omega}$

$$\begin{aligned} & \langle (N_a N_p) N_{ap} \bar{\Omega} J M \epsilon | \hat{I}_{\text{CSA}}^2 | (N'_a N'_p) N'_{ap} \bar{\Omega}' J' M' \epsilon' \rangle \\ & \approx \delta_{JJ'} \delta_{MM'} \delta_{\epsilon\epsilon'} \delta_{N_a N'_a} \delta_{N_p N'_p} \delta_{N_{ap} N'_{ap}} \delta_{\bar{\Omega} \bar{\Omega}'} \left( J(J+1) + N_{ap}(N_{ap}+1) - 2\bar{\Omega}^2 \right). \end{aligned} \quad (\text{A.35})$$

This approximation allows the coupled equations to be solved independently for each combination of  $J$ , parity, and  $\bar{\Omega}$ . CSA was applied in Paper **D** to study the CO-N<sub>2</sub> system. For a detailed discussion of this approximation and its variants, see Paper **D** and Ref. [251].



## B. *Ab initio* description of the spectral line shape

It was mentioned in the Introduction that, contrary to phenomenological models, *ab initio* line-shape models eliminate the reliance on adjustable parameters determined from fitting spectra. Instead, they provide a direct link between observed spectra and interaction energy surfaces, providing a rigorous test for quantum theory. While a full derivation of the collision-perturbed spectral line shape is beyond the scope of this Appendix, the key concepts underlying the approach used in the papers comprising this dissertation are outlined here.

For interested readers, the seminal work of Fano [252] established the first rigorous connection between pressure broadening and the  $t$  (or  $S$ ) matrix of scattering theory using Liouville space formalism. Ben-Reuven [198, 253] later introduced angular momentum techniques to simplify Fano's formulas within the impact approximation. Comprehensive reviews by Ben-Reuven [254], Breene [74], and Rayer [255] provide further details on this approach.

It is important to note that these methods do not account for the motional effects of the active molecule and are therefore restricted to the high-density regime. To include motional effects, such as Dicke narrowing, a framework based on kinetic theory [256] is more appropriate. The key elements of this approach are summarized here, drawing on the works of Hess [75], Monchick [76], and Blackmore [257]. For a more contemporary review, readers may consult Ref. [258].

The underlying physical picture has already been introduced earlier: the entire system consists of a single *active* molecule  $A$ , capable of undergoing spectroscopic transitions induced by electromagnetic radiation, immersed in a thermal bath of  $N_P$  *perturbers*. These perturbers are optically inert—meaning they do not absorb or emit electromagnetic radiation and thus cannot undergo spectroscopic transitions. The total number of particles in the system,  $N = N_P + 1$ , remains constant.

The Hamiltonian for the entire system,  $\hat{H}^{(N)}$ , involves all  $N$  single-particle Hamiltonians, and the two-body interaction terms between the active molecule and a perturber, and interactions among perturbers. Note that while this Hamiltonian theoretically involves all interactions within the  $N$ -particle system, its practical use is limited by the enormous complexity and the vast number of degrees of freedom involved.



The spectral line shape problem for a single active molecule immersed in a thermal bath of perturbers is often formulated through the autocorrelation function,  $\phi(t)$ , of the spectral transition operator—usually the dipole moment operator,  $\hat{\mu}$ —belonging to the active molecule, and acting only on its subspace [11, 252]

$$\begin{aligned} S(\omega) &= \frac{1}{\pi} \text{Re} \int_0^\infty dt e^{i\omega t} \phi(t) = \frac{1}{\pi} \text{Re} \int_0^\infty dt e^{i\omega t} \langle \hat{\mu}(0) \cdot \hat{\mu}(t) \rangle_{\text{eq}} \\ &\equiv \frac{1}{\pi} \text{Re} \int_0^\infty dt e^{i\omega t} \text{Tr} \left( \hat{\mu} \cdot \hat{\mu}(t) \hat{\rho}_{\text{eq}}^{(N)} \right), \end{aligned} \quad (\text{B.1})$$

where  $\omega = 2\pi\nu$  is the angular frequency of the electromagnetic field,  $\hat{\mu}(t) = e^{i\hat{H}^{(N)}t} \hat{\mu}(0) e^{-i\hat{H}^{(N)}t}$  represents the dipole moment operator in the Heisenberg picture and  $\hat{\rho}_{\text{eq}}^{(N)}$  is the equilibrium density matrix of the entire system. The trace is taken over all quantum states of the entire system. The spectral function,  $S(\omega)$ , is interpreted as a statistical average of the equilibrium fluctuations of the dipole moment operator.

This formula can be reexpressed using the cyclic property of the trace and a change to the Schrödinger picture

$$S(\omega) = \frac{1}{\alpha\pi} \text{Re} \int_0^\infty dt e^{i\omega t} \text{Tr} \left( \hat{\mu} \cdot \hat{\rho}_{\text{neq}}^{(N)}(t) \right), \quad (\text{B.2})$$

which offers an alternative interpretation of  $S(\omega)$  [252]. The spectral function is given as an expectation value of the dipole moment operator in the *non-equilibrium state*,  $\hat{\rho}_{\text{neq}}^{(N)}(t) = e^{-i\hat{H}^{(N)}t} (\alpha \hat{\rho}_{\text{eq}}^{(N)} \hat{\mu}) e^{i\hat{H}^{(N)}t}$ , evolving from the initial perturbation of  $\hat{\rho}_{\text{eq}}^{(N)}$  induced by an interaction with electromagnetic radiation. Here,  $\alpha$  is the normalization constant that ensures that the non-equilibrium density operator is dimensionless.

Since Papers **C** and **E** focus on transitions in  $\text{H}_2$  molecule, which lacks a permanent dipole moment, a more generalized approach is required. This can be achieved by replacing  $\hat{\mu}$  with a spectral transition operator of arbitrary rank  $q$ ,  $\hat{X}^{(q)}$ , which has  $2q + 1$  spherical components. In the case of electric dipole transitions,  $\hat{X}^{(q)}$  is the molecule's electric dipole moment—an operator of rank  $q = 1$  with components  $p = -1, 0, +1$ . In cases where the molecule lacks a permanent electric dipole moment,  $\hat{X}^{(q)}$  may correspond to an electric quadrupole moment, represented by an operator of rank  $q = 2$  with five spherical



components. The spectral function is thus expressed as

$$\begin{aligned} S^{(q)}(\omega) &= \frac{1}{\alpha\pi} \text{Re} \int_0^\infty dt e^{i\omega t} \text{Tr} \left( \hat{X}^{(q)} \cdot \hat{\rho}_{\text{neq}}^{(N)(q)}(t) \right) \\ &= \frac{1}{\alpha\pi} \text{Re} \int_0^\infty dt e^{i\omega t} \text{Tr} \left( \sum_{p=-q}^q (-1)^p \hat{X}^{(q,-p)} \cdot \hat{\rho}_{\text{neq}}^{(N)(q,p)}(t) \right), \end{aligned} \quad (\text{B.3})$$

where the second line provides explicit expression for the scalar product of the two operators of rank  $q$  in terms of their spherical components (see, for instance, Sec. 5 in Ref. [240]). The two indices in the superscript of the optical coherence,  $(q, p)$ , indicate that the density operator evolves from the initial state defined at time  $t_0$  as the product of the equilibrium distribution multiplied by the  $p$ -th spherical component of the multipole moment operator  $\hat{\rho}_{\text{neq}}^{(N)(q,p)}(t_0) = \alpha \hat{\rho}_{\text{eq}}^{(N)} \hat{X}^{(q,p)}$ .

Since  $\hat{X}^{(q)}$  acts only on the subspace of the active molecule, the trace over the entire system can be decomposed into a trace over the quantum states of the active molecule and a trace over quantum states of all the perturbers. This yields

$$S^{(q)}(\omega) = \frac{1}{\alpha\pi} \text{Re} \int_0^\infty dt e^{i\omega t} \text{Tr}_A \left( \sum_{p=-q}^q (-1)^p \hat{X}^{(q,-p)} \cdot \hat{\rho}^{(1)(q,p)}(t) \right), \quad (\text{B.4})$$

where  $\hat{\rho}^{(1)}$  is the *reduced density matrix*—a single-particle density operator pertinent to the active molecule, obtained from  $\hat{\rho}_{\text{neq}}^{(N)(q,p)}$  by taking the partial trace over quantum states of all the perturbers

$$\hat{\rho}^{(1)(q,p)}(t) = \frac{1}{N_P!} \text{Tr}_{N_P} \hat{\rho}_{\text{neq}}^{(N)(q,p)}(t). \quad (\text{B.5})$$

Finally, Eq. (B.4) can be generalized by introducing the spatial degrees of freedom through the spatial Fourier transform. This step is essential for accounting for motional effects in line-shape theory—an aspect absent in the treatment of pressure broadening developed by Fano [252] and Ben-Reuven [198, 253]. The resulting formula for the spectral function pertinent to the transition of rank  $q$ ,  $S^{(q)}(\mathbf{k}, \omega)$ , is the starting point of the standard kinetic theory approaches [75] to the spectral line shape problem

$$S^{(q)}(\mathbf{k}, \omega) = \frac{1}{\alpha\pi} \text{Re} \int dt e^{i\omega t} \int d^3\mathbf{r}_A e^{-i\mathbf{k} \cdot \mathbf{r}_A} \langle \hat{X}^{(q)} \rangle_{\text{neq}}, \quad (\text{B.6})$$



where  $\langle \hat{X}^{(q)} \rangle_{\text{neq}}$  is the non-equilibrium average of the multipole operator

$$\langle \hat{X}^{(q)} \rangle_{\text{neq}} = \langle \mathbf{r}_A | \text{Tr}_A \left( \sum_{p=-q}^q (-1)^p \hat{X}^{(q,-p)} \hat{\rho}^{(1)(q,p)}(\mathbf{x}_A, t) \right) | \mathbf{r}_A \rangle. \quad (\text{B.7})$$

Here,  $\mathbf{x}_A = (\mathbf{r}_A, \boldsymbol{\xi}_A)$  is a shorthand notation for the combination of the translational ( $\mathbf{r}_A$ ) and internal ( $\boldsymbol{\xi}_A$ ) coordinates of the active molecule.  $\mathbf{k}$  is the angular wave vector of the electromagnetic radiation, related to its frequency,  $\nu$ , through  $|\mathbf{k}| = 2\pi\nu/c$

The task is then to derive an equation for the evolution of the single-particle density operator (or specifically, its  $p$ -th spherical component,  $\hat{\rho}^{(1)(q,p)}(\mathbf{x}_A, t)$  that describes the relaxation of the system after being driven out of equilibrium, *independent of further influence from the radiation field*, with the initial condition  $\hat{\rho}^{(1)(q,p)}(\mathbf{x}_A, t_0) = \alpha \hat{\rho}_{\text{eq}}^{(1)} \hat{X}^{(q,p)}$ . This approach is appropriate for linear spectroscopy, where the molecule-field coupling is weak. Extensions of this model that incorporate the electromagnetic field in the density operator's evolution [259] provide a robust framework for addressing *non-linear phenomena* like saturated absorption spectroscopy.

Within the kinetic theory, the translational aspects of the density operator are treated classically, similar to the Boltzmann equation [256]. In classical physics, the Boltzmann equation describes the evolution of a thermodynamic system in a non-equilibrium state through the probability distribution function  $f(\mathbf{r}, \mathbf{p}, t)$ . This function represents the likelihood that a typical particle will be found within a specific phase space volume element  $(\mathbf{r}, \mathbf{r} + d\mathbf{r})$  and  $(\mathbf{p}, d\mathbf{p})$  at time  $t$ .

A quantum mechanical analogue of  $f(\mathbf{r}, \mathbf{p}, t)$  is the Wigner distribution function [260]. This function effectively describes the translational motion of the active molecule as a function of position  $\mathbf{r}_A$  and linear momentum  $\mathbf{p}_A$ . Wigner distribution function acts as an *operator* in the internal coordinates of the active molecule,  $\boldsymbol{\xi}_A$ , and a *function* in the position and momentum space. The mathematical definition of the Wigner distribution function is given by

$$\rho_{ba}(\mathbf{r}_A, \mathbf{p}_A, t) = \frac{1}{(2\pi\hbar)^3} \int d^3\mathbf{q} \exp\left(\frac{i}{\hbar} \mathbf{q} \cdot \mathbf{r}_A\right) \rho_{b, \mathbf{p}_A + \frac{1}{2}\mathbf{q}; a, \mathbf{p}_A - \frac{1}{2}\mathbf{q}}(t), \quad (\text{B.8})$$

$$\rho_{b, \tilde{\mathbf{p}}_A; a, \mathbf{p}_A}(t) = \int d^3\mathbf{r}_A \exp\left(-\frac{i}{\hbar} (\tilde{\mathbf{p}}_A - \mathbf{p}_A) \cdot \mathbf{r}_A\right) \rho_{ba}(\mathbf{r}_A, \frac{1}{2}(\tilde{\mathbf{p}}_A + \mathbf{p}_A), t). \quad (\text{B.9})$$





The role of  $q$  in the context of line-shape theory will be clarified shortly.

It can be shown that the spectral function can be expressed through the Wigner distribution as follows

$$S^{(q)}(\mathbf{k}, \omega) = \frac{1}{\alpha\pi} \text{Re} \int dt e^{i\omega t} \int d^3\mathbf{r}_A e^{-i\mathbf{k}\cdot\mathbf{r}_A} \sum_{a,b} \sum_{p=-q}^q (-1)^p X_{ab}^{(q,-p)} \times \left( \int d^3\mathbf{p}_A \rho_{ba}^{(q,p)}(\mathbf{r}_A, \mathbf{p}_A, t) \right), \quad (\text{B.10})$$

where  $X_{ab}^{(q,-p)}$  is the matrix element of the  $p$ -th component of the multipole moment operator between the states participating in the transition  $b \leftarrow a$ , and  $\rho_{ba}^{(q,p)}(\mathbf{r}_A, \mathbf{p}_A, t)$  represents the distribution of the of the *optical coherence*—the off-diagonal elements of the density operator—between states  $a$  and  $b$  of the active molecule at the specified phase-space point  $(\mathbf{r}_A, \mathbf{p}_A)$ .

The line-shape problem reduces to deriving an equation for the time evolution of optical coherence,  $\rho_{ab}^{(q,p)}(\mathbf{r}_A, \mathbf{p}_A, t)$ , represented through the Wigner distribution function. This requires *a quantum analog of the classical Boltzmann equation*.

The first extension of the Boltzmann equation to quantum systems with non-degenerate internal energy states was proposed by Wang Chang and Uhlenbeck [261]. However, their model does not apply to molecules due to the degeneracy of rotational levels. Subsequent adaptations of the Boltzmann equation to account for molecules with degenerate internal states were achieved by Waldmann [262, 263] and Snider [264], who first explicitly employed the Wigner distribution function as a quantum analog of the classical  $f(\mathbf{r}, \mathbf{p}, t)$ . These authors focused on the evolution of the distribution function *diagonal* in internal states,  $\rho_{aa}(\mathbf{r}_A, \mathbf{p}_A, t)$ . The equation of interest for this chapter, describing the time evolution of an off-diagonal element,  $\rho_{ba}(\mathbf{r}, \mathbf{p}, t)$ , was first derived by Tip [265] and is referred to as the *generalized Waldmann-Snider equation*.

Derivations of this equation can be found elsewhere [258, 265]. Starting from the Liouville-von Neumann equation for the  $N$ -particle density matrix,  $\hat{\rho}^{(N)}$ , this approach involves applying the Bogliubov-Born-Green-Kirkwood-Yvon (BBKGY) hierarchy to obtain two key equations: one for the reduced, single-particle density matrix and another for the two-particle density matrix describing interactions between the active molecule and a perturber.

To simplify the equations further, the three-particle terms are neglected



under the *binary approximation*. Additional assumptions include factorization of the two-particle density matrix into single-particle terms at the initial time, long before the collision; and the *impact approximation*, which allows to describe the evolution of the factorized density matrices between the initial time and the time of collisions occurs as there is no interaction at all. The impact approximation essentially decouples the dynamics of individual collisions from the broader temporal evolution of the system.

The perturber's density operator is approximated as diagonal in internal states, with populations governed by the Boltzmann distribution, and diagonal in linear momenta, with a Maxwell-Boltzmann distribution. By setting the initial time to  $-\infty$  the derivation connects time evolution of the density matrices to time-independent scattering theory. The Møller wave operator is introduced, expressed in terms of Green's function, and the transition  $t$ -matrix known from time-independent quantum scattering theory.

Recall that the spectral function has been expressed in terms of the Wigner distribution, which, by definition involves density matrix elements coupling the states involved in the spectral transition  $b \leftarrow a$ . To account for the Doppler effect, the matrix elements are off-diagonal in *linear momenta*, differing by the photon momentum,  $\mathbf{q}$ :  $\rho_{b, \mathbf{p}_A + \frac{1}{2}\mathbf{q}; a, \mathbf{p}_A - \frac{1}{2}\mathbf{q}}(t)$ . By invoking the definition of the Wigner distribution, Eq. (B.8), the generalized Waldmann-Snider equation is obtained

$$\left( \frac{\partial}{\partial t} + i\omega_{ba} + \mathbf{v}_A \cdot \nabla_{\mathbf{r}_A} + \mathcal{R} \right) \rho_{ba}(\mathbf{r}_A, \mathbf{p}_A, t) = 0. \quad (\text{B.11})$$

Here,  $\omega_{ba}$  is the transition frequency, the  $\mathbf{v}_A \cdot \nabla_{\mathbf{r}_A}$  term is going to provide the Doppler term, and  $\mathcal{R}\rho_{ba}(\mathbf{r}_A, \mathbf{p}_A, t)$  is the collision term

$$\begin{aligned} \left( \mathcal{R}[\rho(\mathbf{r}_A, \mathbf{p}_A, t)] \right)_{ba} = \\ - \sum_{a'b'} \rho_{b'a'}(\mathbf{r}_A, \mathbf{p}_A, t) \mathcal{A}_{ba\mathbf{p}_A; b'a'\mathbf{p}_A}^{\text{loss}} + \sum_{a'b'} \int d^3\mathbf{p}'_A \rho_{b'a'}(\mathbf{r}_A, \mathbf{p}'_A, t) \mathcal{B}_{ba\mathbf{p}_A; b'a'\mathbf{p}'_A}^{\text{gain}}. \end{aligned} \quad (\text{B.12})$$

The loss term

$$\begin{aligned} \mathcal{A}_{ba\mathbf{p}_A; b'a'\mathbf{p}_A}^{\text{loss}} = 2\pi\hbar^2 n_b \sum_p n_p \int d^3\mathbf{p}_P f_{\text{MB}}^p(\mathbf{p}_P) \\ \times \left( \langle b, p, \mathbf{p}_r | t | b', p, \mathbf{p}_r \rangle \delta_{a'a} - \delta_{b'b} \langle a', p, \mathbf{p}_r | t | a, p, \mathbf{p}_r \rangle^* \right), \end{aligned} \quad (\text{B.13})$$

quantifies the rate of collisional loss (or decay) of  $\rho_{ba}(\mathbf{r}_A, \mathbf{p}_A, t)$  to all other cohe-



rences,  $\rho_{b'a'}$ . Here,  $n_b$  is the number density of perturbers, the sum runs over the internal states of the perturber,  $p$ ,  $n_p$  is the population of the perturbers in each  $p$ -th internal state, and  $f_{\text{MB}}^P(\mathbf{p}_P)$  is the Maxwell-Boltzmann distribution for perturber's momenta. The second term

$$\begin{aligned} \mathcal{B}_{ba\mathbf{p}_A;b'a'\mathbf{p}'_A}^{\text{gain}} &= \frac{4\pi^2\hbar^2}{i} n_b \sum_{p,p'} n_{p'} \int d^3\mathbf{p}_P \int d^3\mathbf{p}'_P f_{\text{MB}}^P(\mathbf{p}'_P) \delta(\mathbf{P} - \mathbf{P}') \\ &\times \delta(E^{\text{tot}} - E^{\text{tot}'}) \langle b, p, \mathbf{p}_r | t | b', p', \mathbf{p}'_r \rangle \langle a, p, \mathbf{p}_r | t | a', p', \mathbf{p}'_r \rangle^* \end{aligned} \quad (\text{B.14})$$

quantifies the gain of coherence  $\rho_{ba}(\mathbf{r}_A, \mathbf{p}_A, t)$  from all other coherences with *arbitrary* momentum  $\mathbf{p}'_A$ .

In both terms, the  $t$ -matrix elements are evaluated in the relative momentum-internal state basis,  $|a, p, \mathbf{p}_r\rangle$  [266], which includes product states of the active molecule and perturber,  $|a, p\rangle = |a\rangle \otimes |p\rangle$ . The momentum distribution,  $f_{\text{MB}}^P(\mathbf{p}_P)$ , is given as (compare with Eq. (6))

$$f_{\text{MB}}^P(\mathbf{p}_P) = \left( \frac{1}{\sqrt{\pi} p_{m_P}} \right)^2 \exp\left( -\frac{\mathbf{p}_P^2}{p_{m_P}^2} \right), \quad (\text{B.15})$$

where  $p_{m_P} = \sqrt{2m_P k_B T}$  and  $m_P$  denote the most probable momentum of the perturber and its mass, respectively. It is noted that in deriving the collision term, the dependence on the photon momentum,  $\mathbf{q}$ , is neglected [258].

Given that the spectral function can be alternatively represented as

$$S^{(q)}(\mathbf{k}, \omega) = \frac{1}{\alpha\pi} \text{Re} \sum_{a,b} \sum_{p=-q}^q (-1)^p \hat{X}_{ab}^{(q,-p)} \int d^3\mathbf{p}_A \tilde{\rho}_{ba}^{(q,p)}(\mathbf{k}, \mathbf{p}_A, \omega), \quad (\text{B.16})$$

where  $\tilde{\rho}_{ba}^{(q,p)}(\mathbf{k}, \mathbf{p}_A, \omega)$  represents the Laplace-Fourier transform of the optical coherence

$$\tilde{\rho}_{ba}^{(q,p)}(\mathbf{k}, \mathbf{p}_A, \omega) = \int dt \int d^3\mathbf{r}_A e^{i(\omega t - \mathbf{k} \cdot \mathbf{r}_A)} \rho_{ba}^{(q,p)}(\mathbf{r}_A, \mathbf{p}_A, t), \quad (\text{B.17})$$

kinetic theory considerations often discuss the transformed version of the generalized Waldmann-Snider equation [76]

$$\left( -i\omega + i\omega_{ba} + i\mathbf{k} \cdot \mathbf{v}_A + \mathcal{R} \right) \tilde{\rho}_{ba}^{(q,p)}(\mathbf{k}, \mathbf{p}_A, \omega) = f_{\text{MB}}(\mathbf{p}_A) \alpha X_{ba}^{(q,p)}, \quad (\text{B.18})$$

Here,  $f_{\text{MB}}(\mathbf{p}_A) \alpha X_{ba}^{(q,p)}$  is the (space) Fourier transform of the *initial* distribution of optical coherence,  $\rho_{ba}^{(q,p)}(\mathbf{r}_A, \mathbf{p}_A, t_0) = \delta(\mathbf{r}_A) f_{\text{MB}}(\mathbf{p}_A) \alpha X_{ba}^{(q,p)}$ , corresponding to the product of the Maxwell-Boltzmann distribution of the active molecule's mo-



menta,  $f_{\text{MB}}^A(\mathbf{p}_A)$ , and the  $p$ -th spherical component of the multipole moment operator  $\hat{X}^{(q,p)}$ , localized at  $\mathbf{r}_A$ .

The primary goal is thus achieved: the generalized Waldmann-Snider equation establishes a link between the spectral function and the  $t$ -matrix (or equivalently,  $S$ -matrix), which can be obtained from *ab initio* quantum scattering calculations (Appendix A). A significant simplification of the equations can be achieved by employing angular momentum theory. To proceed, let us define the states  $a$  and  $b$  involved in the spectral transition. Since Papers **B**, **C**, **D**, and **E** focus on transitions within a single (ground) electronic state of each molecule, these states are specified as

$$|a\rangle \equiv |v_a j_a M_{j_a}\rangle, \quad |b\rangle \equiv |v_b j_b M_{j_b}\rangle, \quad (\text{B.19})$$

where  $v$  is the vibrational quantum number, while  $j$  and  $M_j$  represent the *total angular momentum* of the active molecule and its projection on the space-fixed  $Z$  axis.

In  $^1\Sigma$  molecules such as  $\text{H}_2$  and  $\text{CO}$ , if hyperfine interactions are neglected,  $j$  corresponds to the rotational quantum number  $N$ . If the hyperfine interactions are included, as discussed in Appendix D,  $j$  represents  $F$ , the total angular momentum resulting from coupling of  $N$  with the nuclear spin  $I$ . For molecules in  $^{2S+1}\Sigma$  states, such as the ground electronic state of  $\text{O}_2$  studied in Ref. [132],  $j$  results from coupling of  $N$  to the non-zero electronic spin,  $S$ .

The sum over  $a$  and  $b$  in Eq. (B.16) thus looks like this

$$\begin{aligned} & \sum_{a,b,p} (-1)^p \hat{X}_{ab}^{(q,-p)} \tilde{\rho}_{ba}^{(q,p)}(\mathbf{k}, \mathbf{p}_A, \omega) \\ &= \sum_{v_a, j_a, v_b, j_b, p} (-1)^p \sum_{M_{j_a}, M_{j_b}} \langle v_a j_a M_{j_a} | \hat{X}^{(q,-p)} | v_b j_b M_{j_b} \rangle \tilde{\rho}_{v_b j_b M_{j_b}, v_a j_a M_{j_a}}^{(q,p)}(\mathbf{k}, \mathbf{p}_A, \omega), \end{aligned} \quad (\text{B.20})$$

which reveals a new layer of complexity: for each  $v_b j_b \leftarrow v_a j_a$  transition,  $(2j_a + 1) \times (2j_b + 1)$  coherences, corresponding to various magnetic quantum numbers  $M_{j_a}$  and  $M_{j_b}$ , must be determined. A major simplification can be obtained through the Wigner-Eckart theorem, which, for instance, simplifies the calculations of the matrix elements of the multipole moment operator

$$\langle v_a j_a M_{j_a} | \hat{X}^{(q,-p)} | v_b j_b M_{j_b} \rangle = (-1)^{j_a - M_{j_a}} \begin{pmatrix} j_a & q & j_b \\ -M_{j_a} & -p & M_{j_b} \end{pmatrix} X_{v_b j_b, v_a j_a}^{(q)}, \quad (\text{B.21})$$



where  $X_{v_b j_b, v_a j_a}^{(q)} = \langle v_b j_b | \hat{X}^{(q)} | v_a j_a \rangle$  is the *reduced* matrix element of the multipole moment operator, independent from magnetic quantum numbers. For a detailed discussion of the Wigner-Eckart theorem, readers are referred to Refs. [240, 267].

In the initial formulation of the problem, the non-equilibrium state of the gas (Eq. (B.2)), the single-particle density matrix (Eq. (B.6)), and the distribution of optical coherence (Eq. (B.10)), all incorporate the multipole moment operator,  $\hat{X}^{(q,p)}$ . Consequently, the matrix elements of  $\tilde{\rho}^{(q,p)}$  must transform in the same manner as those of the multipole moment operator

$$\tilde{\rho}_{v_b j_b M_{j_b}, v_a j_a M_{j_a}}^{(q,p)}(\mathbf{k}, \mathbf{p}_A, \omega) = (-1)^{j_b - M_{j_b}} \begin{pmatrix} j_b & q & j_a \\ -M_{j_b} & p & M_{j_a} \end{pmatrix} \tilde{\rho}_{v_b j_b, v_a j_a}^{(q)}(\mathbf{k}, \mathbf{p}_A, \omega), \quad (\text{B.22})$$

where  $\tilde{\rho}_{v_b j_b, v_a j_a}^{(q)}$  represents the *spherically-averaged* optical coherence, independent of the projection quantum numbers.

Inserting Eqs. (B.21) and (B.22) to (B.16), summing over the projection quantum numbers and using the orthogonality of the 3-j symbols leads to

$$S^{(q)}(\mathbf{k}, \omega) = \frac{1}{\alpha\pi} \text{Re} \int d^3 \mathbf{p}_A \sum_{v_a j_a, v_b j_b} X_{v_b j_b, v_a j_a}^{(q)*} \tilde{\rho}_{v_b j_b, v_a j_a}^{(q)}(\mathbf{k}, \mathbf{p}_A, \omega), \quad (\text{B.23})$$

where the complex conjugation property of the reduced matrix element is used,  $X_{v_b j_b, v_a j_a}^{(q)*} = (-1)^{j_a + j_b} X_{v_a j_a, v_b j_b}^{(q)}$  [240]. The formula for the spectral function involves now only *one* spherically-averaged distribution of the optical coherence per one  $v_b j_b \leftarrow v_a j_a$  transition.

Similarly, one can develop an equation on the spherically-averaged optical coherence  $\tilde{\rho}_{v_b j_b, v_a j_a}^{(q)}$ . To achieve this, we interpret these as coefficients of the expansion of the optical coherence in a complete basis of operators referred to as *state multipoles* [76, 266]

$$\tilde{\rho}^{(q,p)}(\mathbf{k}, \mathbf{p}_A, \omega) = \sum_{v_a j_a, v_b j_b} \tilde{\rho}_{v_b j_b, v_a j_a}^{(q)}(\mathbf{k}, \mathbf{p}_A, \omega) \mathcal{T}_{ba}^{(q)p}, \quad (\text{B.24})$$

where the state multipoles,  $\mathcal{T}_{ab}^{(q)p}$ , are defined as

$$\mathcal{T}_{ba}^{(q)p} = \sum_{m_a, m_b} (-1)^{j_b - m_b} \begin{pmatrix} j_b & q & j_a \\ -m_b & p & m_a \end{pmatrix} |v_b j_b m_b\rangle \langle v_a j_a m_a|, \quad (\text{B.25})$$

and normalized through the trace taken over internal states of the active mo-





leucule, Eq. (B.19)

$$\sum_{p=-q}^q \text{Tr}_A \left[ \mathcal{T}_{b'a'}^{(q)p\dagger} \mathcal{T}_{ba}^{(q)p} \right] = \delta_{aa'} \delta_{bb'}. \quad (\text{B.26})$$

The equation on the spherically-averaged optical coherence is given as

$$\left( -i\omega + i\omega_{ba} + i\mathbf{k} \cdot \mathbf{v}_A + \bar{\mathcal{R}}_{v_b j_b, v_a j_a} \right) \tilde{\rho}_{v_b j_b, v_a j_a}^{(q,p)}(\mathbf{k}, \mathbf{p}_A, \omega) = f_{\text{MB}}(\mathbf{p}_A) \alpha X_{v_b j_b, v_a j_a}^{(q)}. \quad (\text{B.27})$$

The spherically-averaged form of the collision operator,  $\bar{\mathcal{R}}$ , retains a similar structure to Eq. (B.12)

$$\begin{aligned} \bar{\mathcal{R}}_{v_b j_b, v_a j_a} \tilde{\rho}_{v_b j_b, v_a j_a}^{(q,p)}(\mathbf{r}, \mathbf{p}_A, t) &= \sum_{p=-q}^q \text{Tr}_A \left( \mathcal{T}_{ba}^{(q)p\dagger} \bar{\mathcal{R}}_{v_b j_b, v_a j_a} \tilde{\rho}_{v_b j_b, v_a j_a}^{(q,p)} \mathcal{T}_{ba}^{(q)p} \right) \\ &= - \sum_{\substack{v'_b j'_b v'_a j'_a \\ v'_a j'_a v'_b j'_b}} \tilde{\rho}_{v'_b j'_b v'_a j'_a}^{(q,p)}(\mathbf{r}, \mathbf{p}_A, t) \mathcal{A}_{v_b j_b v_a j_a \mathbf{p}_A; v'_b j'_b v'_a j'_a \mathbf{p}_A}^{\text{loss}} \\ &\quad + \sum_{v'_a j'_a v'_b j'_b} \int d^3 \mathbf{p}'_A \rho_{v'_a j'_a v'_b j'_b}^{(q,p)}(\mathbf{r}, \mathbf{p}'_A, t) \mathcal{B}_{v_b j_b v_a j_a \mathbf{p}_A; v'_b j'_b v'_a j'_a \mathbf{p}'_A}^{\text{gain}}, \end{aligned} \quad (\text{B.28})$$

with the loss term given by

$$\begin{aligned} \mathcal{A}_{v_b j_b v_a j_a \mathbf{p}_A; v'_b j'_b v'_a j'_a \mathbf{p}_A}^{\text{loss}} &= 2\pi h^2 n_b \sum_{m_a, m_b, m'_a, m'_b} (-1)^{j'_b - m'_b + j_b - m_b} \\ &\times \begin{pmatrix} j'_b & q & j'_a \\ -m'_b & p & m'_a \end{pmatrix} \begin{pmatrix} j_b & q & j_a \\ -m_b & p & m_a \end{pmatrix} \sum_{v_p j_p m_p} n_{v_p j_p} \int d^3 \mathbf{p}_P f_{\text{MB}}^P(\mathbf{p}_P) \\ &\times \left( \langle v_b j_b m_b, v_p j_p m_p, \mathbf{p}_r | t | v'_b j'_b m'_b, v'_p j'_p m'_p, \mathbf{p}_r \rangle \delta_{aa'} \right. \\ &\quad \left. - \delta_{b'b} \langle v'_a j'_a m'_a, v_p j_p m_p, \mathbf{p}_r | t | v_a j_a m_a, v_p j_p m_p, \mathbf{p}_r \rangle^* \right), \end{aligned} \quad (\text{B.29})$$

where  $\delta_{aa'} = \delta_{v'_a v_a} \delta_{j'_a j_a} \delta_{m'_a m_a}$  and  $\delta_{bb'} = \delta_{v'_b v_b} \delta_{j'_b j_b} \delta_{m'_b m_b}$ . The gain term is given as

$$\begin{aligned} \mathcal{B}_{v_b j_b v_a j_a \mathbf{p}_A; v'_b j'_b v'_a j'_a \mathbf{p}'_A}^{\text{gain}} &= \frac{4\pi^2 h^2}{i} n_b \sum_{m_a, m_b, m'_a, m'_b} (-1)^{j'_b - m'_b + j_b - m_b} \\ &\times \begin{pmatrix} j'_b & q & j'_a \\ -m'_b & p & m'_a \end{pmatrix} \begin{pmatrix} j_b & q & j_a \\ -m_b & p & m_a \end{pmatrix} \sum_{v_p j_p m_p v'_p j'_p m'_p} n_{v'_p} \int d^3 \mathbf{p}_P \int d^3 \mathbf{p}'_P f_{\text{MB}}^p(\mathbf{p}'_P) \\ &\times \delta(E^{\text{tot}} - E^{\text{tot}'}) \delta(\mathbf{p}_A + \mathbf{p}_P - \mathbf{p}'_A - \mathbf{p}'_P) \langle v_b j_b m_b, v_p j_p m_p, \mathbf{p}_r | t | v'_b j'_b m'_b, v'_p j'_p m'_p, \mathbf{p}'_r \rangle \\ &\times \langle v_a j_a m_a, v_p j_p m_p, \mathbf{p}_r | t | v'_a j'_a m'_a, v'_p j'_p m'_p, \mathbf{p}'_r \rangle^*. \end{aligned} \quad (\text{B.30})$$

To facilitate solving Eq. (B.27), it is assumed that the system is only slightly



deviated from the global equilibrium. The *spherically-averaged* distribution of the optical coherence evolves from the initial state  $\delta(\mathbf{r}_A)f_{\text{MB}}(\mathbf{p}_A)\alpha X_{v_b j_b, v_a j_a}^{(q)}$ , and retains the proportionality to the *reduced* matrix element of the multipole moment operator of rank  $q$ . The distribution of the optical coherence is thus approximated as [202, 259]

$$\tilde{\rho}_{v_b j_b, v_a j_a}^{(q,p)}(\mathbf{k}, \mathbf{p}_A, \omega) \approx f_{\text{MB}}(\mathbf{p}_A) \tilde{\Phi}(\mathbf{k}, \mathbf{p}_A, \omega) \alpha X_{v_b j_b, v_a j_a}^{(q)}, \quad (\text{B.31})$$

where  $\tilde{\Phi}(\mathbf{k}, \mathbf{p}, \omega)$  is understood as the deviation of the distribution of the active molecule momenta from the equilibrium.

Next, since the dissertation was only concerned with *isolated* rovibrational transitions, we neglect the collisional transfer of optical coherences between different rovibrational resonances (the line mixing or line coupling effect [268]). The collision term no longer couples different pair of coherences  $(v'_a j'_a, v'_b j'_b)$  and the loss and gain terms are simplified accordingly. The spectral function is now given as

$$S^{(q)}(\mathbf{k}, \omega) = \frac{1}{\pi} \sum_{v_a j_a, v_b j_b} |X_{v_b j_b, v_a j_a}^{(q)}|^2 \text{Re} \int d^3 \mathbf{p}_A f_{\text{MB}}(\mathbf{p}_A) \tilde{\Phi}(\mathbf{k}, \mathbf{p}_A, \omega), \quad (\text{B.32})$$

where  $\tilde{\Phi}$  fulfills the *linearized* version of Eq. (B.27)

$$\left(-i\omega + i\omega_{ba} + i\mathbf{k} \cdot \mathbf{v} + \bar{\mathcal{R}}^{(L)}\right) \tilde{\Phi}(\mathbf{k}, \mathbf{p}_A, \omega) = 1, \quad (\text{B.33})$$

and where  $\bar{\mathcal{R}}^{(L)}$  denotes the *linearized* version of the reduced Waldmann-Snider collision operator

$$\begin{aligned} \bar{\mathcal{R}}^{(L)} \tilde{\Phi}(\mathbf{k}, \mathbf{p}_A, \omega) &= \sum_{p=-q}^q \text{Tr}_A \left( \mathcal{T}_{ba}^{(q)p \dagger} \bar{\mathcal{R}}^{(L)} \tilde{\rho}_{v_b j_b, v_a j_a}^{(q,p)} \mathcal{T}_{ba}^{(q)p} \right) \\ &= -\tilde{\Phi}(\mathbf{k}, \mathbf{p}_A, \omega) \mathcal{A}_{v_b j_b v_a j_a, \mathbf{p}}^{\text{loss}} + \int d^3 \mathbf{p}' \tilde{\Phi}(\mathbf{k}, \mathbf{p}'_A, \omega) \mathcal{B}_{v_b j_b v_a j_a, \mathbf{p}, \mathbf{p}'}^{\text{gain}}, \end{aligned} \quad (\text{B.34})$$



with the following version of the loss and gain terms

$$\begin{aligned}
\mathcal{A}_{v_b j_b v_a j_a, \mathbf{p}}^{\text{loss}} &= 2\pi h^2 n_b \sum_{v_p j_p m_p} n_{v_p j_p} \int d^3 \mathbf{p}_P f_{\text{MB}}^P(\mathbf{p}_P) \\
&\times \left( \frac{1}{2j_b + 1} \sum_{m_b} \langle v_b j_b m_b, v_p j_p m_p, \mathbf{p}_r | t | v_b j_b m_b, v_p j_p m_p, \mathbf{p}_r \rangle \right. \\
&\left. - \frac{1}{2j_a + 1} \sum_{m_a} \langle v_a j_a m_a, v_p j_p m_p, \mathbf{p}_r | t | v_a j_a m_a, v_p j_p m_p, \mathbf{p}_r \rangle^* \right),
\end{aligned} \tag{B.35}$$

$$\begin{aligned}
\mathcal{B}_{v_b j_b v_a j_a, \mathbf{p}_A, \mathbf{p}'_A}^{\text{gain}} &= \frac{4\pi^2 h^2}{i} n_b (f_{\text{MB}}^A(\mathbf{p}_A))^{-1} f_{\text{MB}}^A(\mathbf{p}'_A) \sum_{m_a, m_b, m'_a, m'_b} (-1)^{-m'_b - m_b} \\
&\times \begin{pmatrix} j_b & q & j_a \\ -m'_b & p & m'_a \end{pmatrix} \begin{pmatrix} j_b & q & j_a \\ -m_b & p & m_a \end{pmatrix} \sum_{v_p j_p m_p v'_p j'_p m'_p} n_{p'} \int d^3 \mathbf{p}_P \int d^3 \mathbf{p}'_P f_{\text{MB}}^p(\mathbf{p}'_P) \\
&\times \delta(E^{\text{tot}} - E^{\text{tot}'}) \delta(\mathbf{p}_A + \mathbf{p}_P - \mathbf{p}'_A - \mathbf{p}'_P) \\
&\times \langle v_b j_b m_b, v_p j_p m_p, \mathbf{p}_r | t | v_b j_b m'_b, v'_p j'_p m'_p, \mathbf{p}'_r \rangle \langle v_a j_a m_a, v_p j_p m_p, \mathbf{p}_r | t | v_a j_a m'_a, v'_p j'_p m'_p, \mathbf{p}'_r \rangle^*.
\end{aligned} \tag{B.36}$$

The challenge in solving Eq. (B.33) lies in the competing Doppler ( $\mathbf{k} \cdot \mathbf{v}_A$ ) and collision terms, which dominate in the low- and high-density regimes, respectively. In an attempt to provide a solution valid across the entire pressure domain, Hess [75], approximated the collision term by the sum of two complex frequencies

$$\bar{\mathcal{R}}^{(L)} \tilde{\Phi}(\mathbf{k}, \mathbf{p}_A, \omega) = \omega_a \langle \tilde{\Phi} \rangle_{\mathbf{p}_A} + \omega_r (\tilde{\Phi}(\mathbf{k}, \mathbf{p}_A, \omega) - \langle \tilde{\Phi} \rangle_{\mathbf{p}_A}) + \mathcal{W}(\tilde{\Phi}), \tag{B.37}$$

where  $\langle \tilde{\Phi} \rangle_{\mathbf{p}_A}$  is the momentum-averaged value of  $\tilde{\Phi}(\mathbf{k}, \mathbf{p}_A, \omega)$

$$\langle \tilde{\Phi} \rangle_{\mathbf{p}_A} = \int d^3 \mathbf{p}_A f_{\text{MB}}(\mathbf{p}_A) \tilde{\Phi}(\mathbf{k}, \mathbf{p}_A, \omega) \tag{B.38}$$

and  $\mathcal{W}(\tilde{\Phi})$  is the remainder of  $\bar{\mathcal{R}}^{(L)} \tilde{\Phi}$ . The spectral function can now be succinctly expressed as

$$S^{(q)}(\mathbf{k}, \omega) = \frac{1}{\pi} \sum_{v_a, j_a, v_b, j_b} |X_{v_b j_b, v_a j_a}^{(q)}|^2 \text{Re} \langle \tilde{\Phi} \rangle_{\mathbf{p}_A}. \tag{B.39}$$

In Hess's theory,  $\omega_a$  is defined as the speed-averaged collision operator acting on the identity—a complex quantity (in the units of  $\text{rad} \cdot \text{s}^{-1}$ ) which coincides



with the speed-averaged pressure broadening ( $\Gamma_0$ ) and shift ( $\Delta_0$ ) coefficients of the spectral line at high densities

$$\omega_a = \langle \bar{\mathcal{R}}^{(L)}(1) \rangle_{pA} = \sum_{p=-q}^q \text{Tr}_A \left( \mathcal{T}_{ba}^{(q)p\dagger} \mathcal{R}^{(L)} \mathcal{T}_{ba}^{(q)p} \right) = 2\pi(\Gamma_0 - i\Delta_0). \quad (\text{B.40})$$

To express  $\Gamma_0$  and  $\Delta_0$  explicitly, a few steps need to be done, and they are only mentioned here in brief. First, one should express the active molecule's and the perturber's momentum using the relative and center-of-mass momenta. Next, the relative angular momenta should be decomposed into spherical harmonics describing partial waves (Eq. (A.4))—individual quanta of the *relative* (end-over-end) rotational angular momenta of the colliding system [266], and choose the appropriate angular momenta coupling scheme, to couple the angular momenta of the active molecule,  $\hat{j}_A$ , the perturber ( $\hat{j}_P$ ) and the partial wave ( $\hat{l}$ ) to form the total angular momentum ( $\hat{J}$ ). The two most commonly chosen options here are the scheme used by Ben-Reuven [198], referred to here as the *spectroscopic* coupling scheme, within which

$$\hat{j}_P + \hat{l} = \hat{L}, \quad \hat{j}_A + \hat{L} = \hat{J}. \quad (\text{B.41})$$

The other one is more natural from the view point of quantum scattering theory, it referred to here as the *scattering* coupling scheme (see Eq. (A.19))

$$\hat{j}_A + \hat{j}_P = \hat{j}_{AP}, \quad \hat{j}_{AP} + \hat{l} = \hat{J}. \quad (\text{B.42})$$

More on the choice of the coupling scheme in the context of line-shape theory can be found in Refs. [76, 269, 270].

Eventually,  $\Gamma_0$  and  $\Delta_0$  are expressed as<sup>10</sup>

$$\Gamma_0 - i\Delta_0 = \frac{1}{2\pi c} \frac{p}{k_B T} \langle v_r \rangle \int_0^\infty dx x e^{-x} \sigma_{\lambda=0}^q(v_b, j_b, v_a, j_a, x = E_{\text{kin}}/kT), \quad (\text{B.43})$$

where  $\langle v_r \rangle = \sqrt{8kT/(\pi\mu)}$  is the mean relative speed of the colliding molecules, and  $\sigma_{\lambda=0}^q$  is the complex cross-section, expressed in terms of the scattering

<sup>10</sup>The speed of light  $c$  in the denominator allows for conversion of the collisional width and shift from  $\text{s}^{-1}$  to the reciprocal lengths units, customary used in line shape theory, as in Papers **B-E**.



## $S$ -matrices [76]

$$\begin{aligned}
 \sigma_{\lambda=0}^q(v_b, j_b, v_a, j_a, E_{\text{kin}}) &= \frac{\pi}{k_r^2} \sum_{v_p, j_p} n_p(T) \sum_{v'_p, j'_p} (-1)^{j_p+j'_p} \sum_{l=0}^{\infty} \sum_{l'=0}^{\infty} (-1)^{l+l'} \\
 &\times \sum_{j_{bp}=|j_b-j_p|}^{j_b+j_p} \sum_{j_{ap}=|j_a-j_p|}^{j_a+j_p} \sum_{j_{bp'}=|j_b-j'_p|}^{j_b+j'_p} \sum_{j_{ap'}=|j_a-j'_p|}^{j_a+j'_p} \sqrt{[j_{ap}, j_{ap'}, j_{bp}, j_{bp'}]} \sum_{J=|j_{bp}-l|}^{j_{bp}+l} \sum_{\bar{J}=|j_{ap}-l|}^{j_{ap}+l} [J, \bar{J}] \\
 &\times \begin{Bmatrix} j_{ap} & q & j_{bp} \\ j_b & j_p & j_a \end{Bmatrix} \begin{Bmatrix} j_{ap'} & q & j_{bp'} \\ j_b & j'_p & j_a \end{Bmatrix} \begin{Bmatrix} J & q & \bar{J} \\ j_{ap} & l & j_{bp} \end{Bmatrix} \begin{Bmatrix} J & q & \bar{J} \\ j_{ap'} & l' & j_{bp'} \end{Bmatrix} \\
 &\times \left( \delta_{j_p, j'_p} \delta_{j_{ap}, j_{ap'}} \delta_{j_{bp}, j_{bp'}} \delta_{l, l'} - S_{v_b v_p, (j_b j_p) j_{bp} l; v_b v'_p, (j_b j'_p) j_{bp'} l'}^{J, J} (E_{v_b, j_b} + E_{v_p, j_p} + E^{\text{kin}}) \right. \\
 &\quad \left. \times S_{v_a v_p, (j_a j_p) j_{ap} l; v_a v'_p, (j_a j'_p) j_{ap'} l'}^{J, J} (E_{v_a, j_a} + E_{v_p, j_p} + E^{\text{kin}}) \right). \tag{B.44}
 \end{aligned}$$

The real and imaginary parts of  $\sigma_{\lambda=0}^q$  are referred to as the pressure broadening (PBXS) and pressure shift cross-sections (PSXS), respectively. Here,  $k_r = \sqrt{2\mu E_{\text{kin}}/\hbar^2}$  is the wave vector related to the relative kinetic energy of the colliding molecules and  $[x_1, x_2, \dots, x_n] = (2x_1 + 1)(2x_2 + 1) \cdots (2x_n + 1)$ . The pre- and post-collisional quantum numbers are denoted with primed and unprimed symbols. Coupling schemes for the ground ( $a$ ) and excited ( $b$ ) spectroscopic states can be deduced from  $S$ -matrix descriptors and Wigner symbols.

Contrary to the cross-sections discussed in Appendix A (Eq. (A.28)), one needs to determine *two*  $S$ -matrices, that describe scattering of the active molecule in states  $v_a, j_a$  and  $v_b, j_b$ . The  $S$ -matrices are determined at two distinct *total* energies but at the same *kinetic* energy.

The second complex frequency in Hess's theory is chosen to minimize an error introduced by this approximation. This is achieved by substituting Eq. (B.37) into Eq. (B.33) and multiplying the result by

$$\mathcal{G} = (-i\omega + i\omega_{ba} + i\mathbf{k} \cdot \mathbf{v}_A + \omega_r)^{-1}, \tag{B.45}$$

which leads to

$$\tilde{\Phi}(\mathbf{k}, \mathbf{p}_A, \omega) = \left(1 + (\omega_r - \omega_a) \langle \tilde{\Phi} \rangle_{\mathbf{p}_A}\right) \left(\mathcal{G} - \mathcal{G}\mathcal{W}(\mathcal{G})\right) + \mathcal{G}\mathcal{W}(\mathcal{W}(\tilde{\Phi})). \tag{B.46}$$

To minimize the effect of  $\mathcal{W}$  on the line shape, Hess required that the term linear in  $\mathcal{W}$  does not affect the spectrum, i.e.  $\langle \mathcal{G}\mathcal{W}(\mathcal{G}) \rangle_{\mathbf{p}_A} = 0$ . This condition





leads a nonlinear equation on  $\omega_r$

$$\omega_r = \langle g^2 \rangle_{p_A}^{-1} \langle g \bar{\mathcal{R}}^{(L)}(g) \rangle_{p_A}, \quad (\text{B.47})$$

where  $g = \beta(\mathcal{G} - \langle \mathcal{G} \rangle_{p_A})$ , and  $\beta$  is a constant that is reduced in the formula for  $\omega_r$ . Note that  $\omega_r$  depends on the frequency  $\omega$  and  $k$  and is not, in general, proportional to the number density. The relation of  $\omega_r$  to the exact collision term is found by considering the high-density limit, where the Doppler term,  $i\mathbf{k} \cdot \mathbf{v}_A$  is significantly smaller than the collision term. In this regime,  $\mathcal{G}$  and  $\langle \mathcal{G} \rangle_p$  are expanded in powers of  $k \cdot \mathbf{v}_A$ . Neglecting terms involving higher than second power of  $k = |\mathbf{k}|$ , Eq. (B.47) leads to

$$\omega_r \approx \omega_b - k^2 v_{m_A}^2 (-i\omega + i\omega_{ba} + \omega_r)^{-2} (\omega_c - \omega_b), \quad (\text{B.48})$$

where  $v_{m_A} = \sqrt{2kT/m_A}$  is the most probable speed of the active molecule, and

$$\begin{aligned} \omega_b &= \frac{2}{v_{m_A}^2} \langle (\hat{k} \cdot \mathbf{v}_A) \bar{\mathcal{R}}^{(L)}(\hat{k} \cdot \mathbf{v}_A) \rangle_{p_A}, \\ \omega_c &= \frac{2}{v_{m_A}^4} \langle \left( (\hat{k} \cdot \mathbf{v}_A)^2 - \frac{v_{m_A}^2}{2} \right) \bar{\mathcal{R}}^{(L)} \left( (\hat{k} \cdot \mathbf{v}_A)^2 - \frac{v_{m_A}^2}{2} \right) \rangle_p. \end{aligned} \quad (\text{B.49})$$

In the lowest order, the effective relaxation coefficient is approximated as  $\omega_r \approx \omega_b$ . Using the condition  $\langle \mathcal{GW}(\mathcal{G}) \rangle_{p_A} = 0$  and neglecting terms quadratic in  $W$ , we obtain the spectral line shape profile

$$S^{(q)}(\mathbf{k}, \omega) = \frac{1}{\pi} \sum_{v_a, j_a, v_b, j_b} |X_{v_b j_b, v_a j_a}^{(q)}|^2 \text{Re} \frac{\langle \mathcal{G} \rangle_p}{1 - (\omega_b - \omega_a) \langle \mathcal{G} \rangle_p}. \quad (\text{B.50})$$

Similarly to  $\omega_a$ ,  $\omega_b$  and  $\omega_c$  can be explicitly expressed using scattering  $S$ -matrix elements. Using a modern notation (see Paper **C**), we introduce  $\nu_{\text{opt}}$ —the complex Dicke parameter—defined as<sup>11</sup>

$$\begin{aligned} \nu_{\text{opt}} &= \nu_{\text{opt}}^r - i\nu_{\text{opt}}^i = \frac{1}{2\pi} (\omega_b - \omega_a) \\ &= \frac{1}{2\pi c} \frac{p}{k_B T} M_P \langle v_r \rangle \int_0^\infty dx x e^{-x} \left( x \frac{2}{3} \sigma_{\lambda=1}^q(v_b, j_b, v_a, j_a, x) - \sigma_{\lambda=0}^q(v_b, j_b, v_a, j_a, x) \right), \end{aligned} \quad (\text{B.51})$$

<sup>11</sup>See the footnote regarding Eq. (B.43).



where  $M_P = m_P/(m_A + m_P)$ ,  $x$  and  $\sigma_{\lambda=0}^q$  were defined in Eq. (B.44), and  $\sigma_{\lambda=1}^q$  [76]

$$\begin{aligned}
 \sigma_{\lambda=1}^q(v_b, j_b, v_a, j_a, E^{\text{kin}}) &= \frac{\pi}{k_r^2} \sum_{v_p, j_p} n_p(T) \sum_{v'_p, j'_p} (-1)^{j_p+j'_p} \sum_{l=0}^{\infty} \sum_{l'=0}^{\infty} \sum_{\bar{l}=0}^{\infty} \sum_{\bar{l}'=0}^{\infty} i^{l-l'-\bar{l}+\bar{l}'} \sqrt{[l, l', \bar{l}, \bar{l}']} \\
 &\times \begin{pmatrix} l & \bar{l} & 1 \\ 0 & 0 & 0 \end{pmatrix} \begin{pmatrix} l' & \bar{l}' & 1 \\ 0 & 0 & 0 \end{pmatrix} \sum_{j_{bp}=|j_b-j_p|}^{j_b+j_p} \sum_{j_{ap}=|j_a-j_p|}^{j_a+j_p} \sum_{j_{bp'}=|j_b-j'_p|}^{j_b+j'_p} \sum_{j_{ap'}=|j_a-j'_p|}^{j_a+j'_p} \sqrt{[j_{ap}, j_{ap'}, j_{bp}, j_{bp'}]} \\
 &\times \sum_{J=|j_{bp}-l|}^{j_{bp}+l} \sum_{\bar{J}=|j_{ap}-\bar{l}|}^{j_{ap}+\bar{l}} [J, \bar{J}] \left\{ \begin{matrix} j_{ap} & q & j_{bp} \\ j_b & j_p & j_a \end{matrix} \right\} \left\{ \begin{matrix} j_{ap'} & q & j_{bp'} \\ j_b & j_{p'} & j_a \end{matrix} \right\} \begin{bmatrix} j_{bp} & j'_{bp} & \bar{l} & \bar{l}' \\ j_{ap} & l & j'_{ap} & l' \\ q & \bar{J} & J & 1 \end{bmatrix} \\
 &\times \left( \delta_{j_p, j'_p} \delta_{j_{ap}, j_{ap'}} \delta_{j_{bp}, j_{bp'}} \delta_{l, l'} \delta_{\bar{l}, \bar{l}'} - S_{v_b v_p, (j_b j_p) j_{bp} l; v_b v'_p, (j_b j'_p) j_{bp'} l'}^J (E_{v_b, j_b} + E_{v_p, j_p} + E^{\text{kin}}) \right. \\
 &\quad \left. \times S_{v_a v_p, (j_a j_p) j_{ap} \bar{l}; v_a v'_p, (j_a j'_p) j_{ap'} \bar{l}'}^{J*} (E_{v_a, j_a} + E_{v_p, j_p} + E^{\text{kin}}) \right), \tag{B.52}
 \end{aligned}$$

is another complex cross-section, referred to as the Dicke cross-section. Here the symbol in large brackets is a 12-j symbol of the second kind [271]. The coupling scheme can be deduced from the subscripts denoting the  $S$ -matrices and Wigner symbols. Similarly to the  $\sigma_{\lambda=0}^q$  cross-section in Eq. (B.44), one needs to perform two series of quantum scattering calculations, to the  $S$ -matrices, that describe the scattering of the active molecule in states  $v_a, j_a$  and  $v_b, j_b$ .

The spectral line-shape function can ultimately be written in modern notation (see Appendix D of Paper **B**) as

$$\begin{aligned}
 S^{(q)}(\nu) &= \sum_{v_a, j_a, v_b, j_b} |X_{v_b j_b, v_a j_a}^{(q)}|^2 \text{Re} \frac{I_V(\nu)}{1 - (\nu_{\text{opt}}^r - i\nu_{\text{opt}}^i) \pi I_V(\nu)}, \\
 I_V(\nu) &= \frac{1}{\pi} \int d^3 \mathbf{v}_a \frac{f_{\text{MB}}(\mathbf{v}_a)}{\Gamma_0 + \nu_{\text{opt}}^r - i(\nu - \nu_{ba} - \nu_D v_{z_A}/v_m + \Delta_0 + \nu_{\text{opt}}^i)}. \tag{B.53}
 \end{aligned}$$

Here, the "V" subscript indicates that  $I_V$  can be interpreted as the Voigt profile (Eq. (10)) with  $\nu_{\text{opt}}^r + \Gamma_0$  as the collisional width and  $\nu_{\text{opt}}^i + \Delta_0$  as the collisional shift. Since the four collisional line-shape parameters ( $\Gamma_0$ ,  $\Delta_0$ ,  $\nu_{\text{opt}}^r$  and  $\nu_{\text{opt}}^i$ ) are proportional to pressure, the spectral line shape recovers the familiar Doppler-broadened (Gaussian) profile in the zero-pressure limit.

The spectral function in Eq. (B.53) is mathematically identical to the phenomenological hard collision (HC) profiles [72, 73] (see Appendix A of Ref. [55]). This demonstrates the key benefit of the Hess profile: it links commonly used



line-shape models with parameters derived *ab initio*.

An important limitation of the Hess approach and its generalizations by Monchick [76, 202] is the neglect of speed dependence in collisional broadening and shift. Speed-dependent effects are well-documented experimentally and can also be derived from *ab initio* calculations. To address this, speed dependence is introduced at the final stage of derivation by replacing the speed-averaged collisional broadening ( $\Gamma_0$ ) and shift ( $\Delta_0$ ) with their speed-dependent counterparts, evaluated as

$$\Gamma(v) - i\Delta(v) = \frac{1}{2\pi c} \frac{p}{k_B T} \frac{2}{\sqrt{\pi} v v_{m_p}} \int_0^\infty dv_r v_r^2 e^{-\frac{v^2 + v_r^2}{v_{m_p}^2}} \sinh\left(\frac{2vv_r}{v_{m_p}^2}\right) \sigma_{\lambda=0}^q(v_b, j_b, v_a, j_a, E_{\text{kin}}), \quad (\text{B.54})$$

where  $v$  is the speed of the active molecule,  $v_{m_p}$  is the most probable speed of the perturber, and  $v_r$  is the relative speed of the colliding pair.

The modified Hartmann-Tran (mHT) profile approximates the speed dependence of  $\Gamma$  and  $\Delta$  by a quadratic function (see Eq. (12)). While formulas for the speed-averaged values have been provided, the coefficients for the quadratic term are given as

$$\begin{aligned} \Gamma_2 - i\Delta_2 &= \frac{1}{2\pi c} \frac{p}{k_B T} \frac{\langle v_r \rangle \sqrt{M_a}}{2} e^{-y^2} \\ &\times \int_0^\infty \left( 2\bar{x} \cosh(2\bar{x}y) - \left( \frac{1}{y} + 2y \right) \sinh(2\bar{x}y) \right) \bar{x}^2 e^{-\bar{x}^2} \sigma_0^1(\bar{x}v_p) d\bar{x}, \end{aligned} \quad (\text{B.55})$$

where  $\bar{x} = \frac{2v_r}{\sqrt{\pi M_a} \langle v_r \rangle}$ , and  $y = \sqrt{\frac{m_p}{m_a}}$ . The explicit form of the mHT profile is thus obtained by substituting  $\Gamma_0$  and  $\Delta_0$  with the quadratic approximation of the speed-dependent collisional width and shift (Eqs. (12) and (B.55)).

The complex cross-sections in Eqs. (B.44) and (B.52) are examples from a broader family of generalized cross-sections used in kinetic theory for spectral line shapes, nuclear magnetic resonance, and depolarized light scattering. Detailed discussions on their properties can be found in Refs. [266, 270].

The Hess method extends the Bhatnagar-Gross-Krook (BGK) approximation from classical Boltzmann equations for light scattering by gases without internal degrees of freedom [272]. Hess's approach involves two relaxation terms,  $\omega_a$  and  $\omega_r$ , with  $\omega_r$  approximated to lowest order in the Doppler term expansion at high densities. Further generalizations of this approach could



include adding the  $\omega_c$  term (Eq. (B.49)), or expand the collision term into additional relaxation terms. However, such extensions remain unexplored.

The spectral line shape function presented here describes the *isolated lines*. Monchick and Hunter [76] extended Hess's method to account for collisional coupling of optical resonances (line mixing) [268], known as the generalized Hess method (GHM). GHM has been further generalized to incorporate collisions between active molecules (self-broadening) and to include effects beyond the impact approximations by Monchick [202].

Alternative methods for solving Waldmann-Snider equations have been developed (see, for instance Ref. [273]). Specifically, Blackmore [257] developed a computational method known as the collision kernel method, which expands the optical coherence in a complete and orthonormal basis of spherical tensors resulting from the coupling of state multipoles with spherical harmonics describing the linear momentum of active molecules. This approach transforms Eq. (B.33) into a set of coupled algebraic equations that can be solved numerically. An extension of the CK method that includes collisions between active molecules has been developed in Ref. [274]. These methods, have, however, not been used on a wider scale.



## C. The role of quantum indistinguishability in spectral line shape theory

The approach outlined in the previous appendix made a clear distinction between the *active* molecule undergoing a spectral transition and the surrounding *perturbers* which are incapable of doing so. If perturbors can undergo spectral transitions themselves, an additional *resonant contribution* must be included alongside the standard formulas discussed earlier [199, 201, 254]. This resonant contribution is significant when the energy level spacings of the perturber closely match those of the active molecule, and can occur *regardless* of whether the perturber is the same species as the active molecule.

When the perturber and active molecule *are* identical, additional symmetry considerations must be incorporated. Specifically, the *S*- or *t*-matrices must be determined using a properly symmetrized basis. Consider the case of *rigid*  $^1\Sigma$  molecules, where the total angular momentum of each molecule,  $j$ , is equivalent to the rotational angular momentum,  $N$ . The Pauli exclusion principle requires the *total wave function* of the scattering system to be either symmetric or antisymmetric under the exchange of the two molecules. This exchange operation, denoted by  $\hat{P}_{\text{exch}}$ , transforms the molecular coordinates as

$$\hat{\mathbf{R}}, \hat{\mathbf{r}}_A, \hat{\mathbf{r}}_P \rightarrow -\hat{\mathbf{R}}, \hat{\mathbf{r}}_P, \hat{\mathbf{r}}_A. \quad (\text{C.1})$$

To incorporate this symmetry, the basis set from Eq. (A.18) is replaced by the *symmetrized* basis

$$\begin{aligned} & |((N_a N_p) N_{ap} l) J M \eta\rangle \\ &= \frac{1}{\sqrt{2(1 + \delta_{N_a N_p})}} \left( |((N_a N_p) N_{ap} l) J M\rangle + \eta (-1)^{N_a + N_p - N_{ap} + l} |((N_p N_a) N_{ap} l) J M\rangle \right), \end{aligned} \quad (\text{C.2})$$

where  $\eta = \pm 1$  determines whether the basis function is symmetric or antisymmetric with respect to the exchange of the two molecules. Note that not all symmetrized basis functions are independent

$$|((N_p N_a) N_{ap} l) J M \eta\rangle = \eta (-1)^{N_a + N_p - N_{ap} + l} |((N_a N_p) N_{ap} l) J M \eta\rangle.$$

To obtain a linearly independent set,  $N_p$  and  $N_a$  must satisfy a restriction, such





as  $N_p \leq N_a$ . The scattering wave function is then expanded as

$$|\Psi\rangle = \sum_{N_p N_a N_{ap} l J M \eta} \frac{F_{N_p N_a N_{ap} l}^{JM\eta}(R)}{R} |((N_p N_a) N_{ap} l) J M \eta\rangle, \quad (\text{C.3})$$

where the sum goes over restricted set of quantum numbers.

The interpretation of  $\eta$  becomes clearer when considering the nuclear spin states of the molecules. First, note that collisions between molecules with different nuclear spins  $I_A$  and  $I_P$  (e.g., *para*-H<sub>2</sub> and *ortho*-H<sub>2</sub>) are distinguishable, as the potential energy surface does not alter nuclear spins. However, for collisions of identical molecules ( $I_A = I_P = I$ ) the *total* wave function, combining spatial and nuclear spin components, must be symmetric or antisymmetric under exchange, depending on whether  $I$  is integer or half-integer.

The basis functions in Eq. (C.2) specify the spatial exchange symmetry, while the nuclear spin functions, arising from the coupling of  $I_A$  and  $I_P$ , must conform to the same symmetry. According to angular momentum addition rules, there are  $(2I + 1)^2$  nuclear spin functions, of which  $(I + 1)(2I + 1)$  are symmetric ( $\eta = +1$ ) and  $I(2I + 1)$  are antisymmetric ( $\eta = -1$ ). This gives rise to statistical weights for symmetric and antisymmetric states used in scattering experiments that do not resolve nuclear hyperfine structure [275]

$$W^{\eta=+1} = \frac{I + 1}{2I + 1}, \quad W^{\eta=-1} = \frac{I}{2I + 1}. \quad (\text{C.4})$$

For two *para*-H<sub>2</sub> molecules, where  $I = 0$ , we get  $W^{+1} = 1$  and  $W^{-1} = 0$ . This indicates that the total wave function is entirely symmetric, and only  $\eta = +1$  basis functions are allowed. Furthermore, since  $N_a$  and  $N_p$  are even, the relative orbital angular momentum  $l$  must also be, as previously shown in Fig. 6.

In contrast, for two *ortho*-H<sub>2</sub> molecules ( $I = 1$ ), the weights are  $W^{+1} = 2/3$  and  $W^{-1} = 1/3$ , meaning that both symmetric ( $\eta = +1$ ) and antisymmetric ( $\eta = -1$ ) basis functions contribute to the scattering process. Consequently, both even and odd partial waves are allowed.

A few notable considerations of quantum indistinguishability in line-shape theory have been pursued, most prominently by Ben-Reuven [199, 254], and later within the framework of kinetic theory by Liu [201] and Monchick [202]. For the purpose of this appendix, I focus on the case of pressure broadening and shift cross-sections. The symmetry-adapted result, including the resonant



contribution, is given by

$$\begin{aligned}
\sigma_{\lambda=0}^q(N_b, N_a, E_{\text{kin}}) &= \frac{\pi}{k_r^2} \sum_{N_p} n_p(T) \sum_{N'_p} (-1)^{N_p+N'_p} \frac{1}{8\mathcal{N}_{ap}\mathcal{N}_{ap'}\mathcal{N}_{bp}\mathcal{N}_{bp'}} \\
&\times \sum_{l,l'} (-1)^{l+l'} \sum_{N_{bp}, N_{ap}, N_{bp'}, N_{ap'}} \sqrt{[N_{ap}, N_{ap'}, N_{bp}, N_{bp'}]} \\
&\times \sum_{\bar{J}, J} \begin{Bmatrix} N_{ap} & q & N_{bp} \\ N_b & N_p & N_a \end{Bmatrix} \begin{Bmatrix} N_{ap'} & q & N_{bp'} \\ N_b & N_{p'} & N_a \end{Bmatrix} \begin{Bmatrix} J & q & \bar{J} \\ N_{ap} & l & N_{bp} \end{Bmatrix} \begin{Bmatrix} J & q & \bar{J} \\ N_{ap'} & l' & N_{bp'} \end{Bmatrix} \quad (\text{C.5}) \\
&\times \sum_{\eta=\pm 1} W^\eta \left( \delta_{(N_b N_p) N'_{bp} l' | (N_b N_p) N_{bp} l}^{\bar{J}\eta} \delta_{(N_a N_p) N'_{ap} l' | (N_a N_p) N_{ap} l}^{J\eta} \right. \\
&\quad \left. - S_{(N_b N_p) N_{bp} l; (N_b N_p) N_{bp'} l'}^{\bar{J}\eta} S_{(N_a N_p) N_{ap} l; (N_a N_p) N_{ap'} l'}^{J\eta *} \right).
\end{aligned}$$

Here,  $\mathcal{N}_{12}$  denotes the normalization factor

$$\mathcal{N}_{12} = \frac{1}{\sqrt{2(1 + \delta_{N_1 N_2})}}, \quad (\text{C.6})$$

the  $\delta^{\bar{J}\eta} \delta^{J\eta}$  term is given as

$$\begin{aligned}
\delta_{(N_b N_p) N'_{bp} l' | (N_b N_p) N_{bp} l}^{\bar{J}\eta} \delta_{(N_a N_p) N'_{ap} l' | (N_a N_p) N_{ap} l}^{J\eta} &= 4\mathcal{N}_{a'p'}\mathcal{N}_{b'p'}\mathcal{N}_{ap}\mathcal{N}_{bp} \delta_{N_{ap} N'_{ap}} \delta_{N_{bp} N'_{bp}} \delta_{ll'} \delta_{N_p N'_p} \\
&\times \left( 1 + (-1)^{N_a+N_p+N_{ap}+l+N_b+N_p+N_{bp}+l} \delta_{N_a N_b} \right. \\
&\quad \left. + \eta \left( (-1)^{N_a+N_p+N_{ap}+l} \delta_{N_a N_p} + (-1)^{N_b+N_p+N_{bp}+l} \delta_{N_b N_p} \right) \right). \quad (\text{C.7})
\end{aligned}$$

The  $S$ -matrix elements in this formula are evaluated in the symmetrized basis introduced in Eq. (C.2).

Interestingly, this formula has never been employed in actual quantum scattering calculations.

To test its applicability, I conducted quantum scattering calculations for a set of pure rotational  $S(N)$  lines in molecular hydrogen, using the state-of-the-art PES developed in Paper **B**. Figure 7 compares the pressure broadening and shift coefficients for the  $S(0)$  and  $S(1)$  lines, calculated by treating colliding molecules as distinguishable (Eq. (B.44)) and indistinguishable molecules (Eq. (C.5)).

Pressure broadening coefficients for the  $S(0)$  line exhibit the largest differences between the distinguishable and indistinguishable approaches at tem-

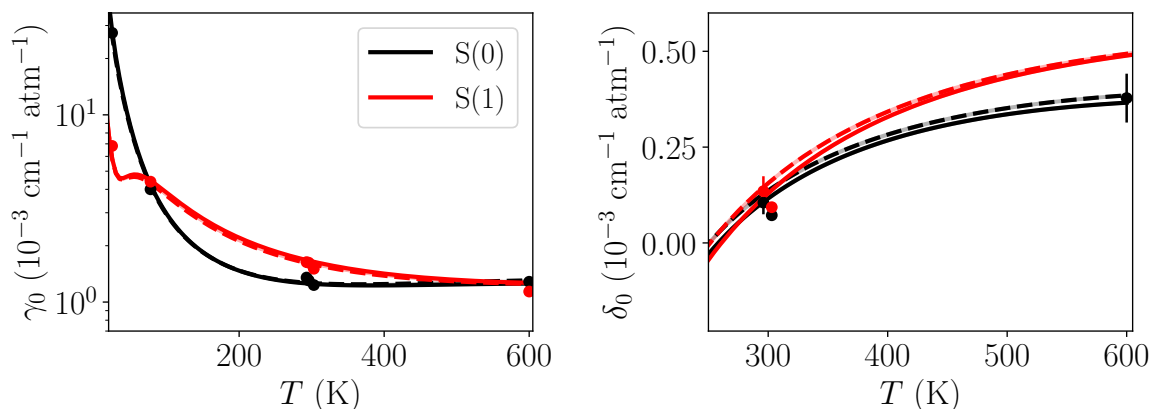


Figure 7: Temperature dependence of the speed-averaged pressure broadening coefficient ( $\gamma_0$ , left panel) and pressure shift coefficient ( $\delta_0$ , right panel) for the self-perturbed 0-0 S(0) (black lines) and S(1) (red lines) transitions in  $\text{H}_2$ . Solid lines represent calculations treating colliding molecules as indistinguishable, while dashed lines correspond to distinguishable treatments. Experimental results at 24.8 K and 77.8 K are taken from Ref. [276]. The values of  $\gamma_0$  were extrapolated to the pure *ortho*- and pure *para* limits and then adjusted for the equilibrium *ortho*-*para* distribution at these temperatures. The pure *ortho*- and *para* values of  $\delta_0$  were not determined in Ref. [276]. Results at 296 K and 600 K are from Ref. [277], and the value at 303 K is from Ref. [278].

peratures below 50 K. In this regime, the majority of  $\text{H}_2$  molecules occupy the  $N = 0$  state—the ground state of *para*- $\text{H}_2$ —which is also the spin isomer involved in the S(0) transition. As the temperature increases, the *ortho*-to-*para*- $\text{H}_2$  ratio increases, and more molecules occupy the  $N = 1$  state. Consequently, most collisions perturbing the 0-0 S(0) line become distinguishable (i.e., *para*- $\text{H}_2$  colliding with *ortho*- $\text{H}_2$ ).

For the S(1) line, the situation is reversed. The most significant differences between the indistinguishable and distinguishable treatments occur near room temperature, where the majority of perturbers occupy the  $N = 1$  state, which also participates in the S(1) transition.

Unfortunately, due to the limited accuracy of the calculated values of  $\gamma_0$  and  $\delta_0$ , and their close agreement in the two treatments, it is challenging to unambiguously validate the inclusion of quantum indistinguishability effects. An intriguing opportunity for experimental validation lies in measuring the pressure shift at temperatures where  $\delta_0$  crosses zero. Calculations including or neglecting quantum indistinguishability predict different temperatures at which the pressure shift changes sign from negative to positive. Spectral me-



asurements near these transition temperatures could provide a direct test of the theory.

An alternative approach to validate the theoretical framework involves simulating the entire line shape profile and comparing it to high-accuracy spectra. In the Introduction, calculations for the 1-0 S(0) transition were briefly discussed. A detailed comparison of these calculations with spectra obtained under cryogenic conditions is currently in preparation.



## D. Pressure broadening and shift coefficients for hyperfine components of rovibrational transitions

The goal of this Appendix is to derive formulas for the generalized spectroscopic cross-sections analogous to those provided in Appendix B, but extended to account for the individual hyperfine components of a chosen rovibrational transition.

It is assumed that the nuclear spins of the active molecule couple to form the total nuclear spin  $\hat{I}$ , which remains unchanged during the spectroscopic transition. For simplicity, it is further assumed that the eigenvectors of the hyperfine Hamiltonian are also eigenvectors of the total angular momentum  $\hat{F}^2$ , resulting from the coupling of the rotational angular momentum  $\hat{N}$  to  $\hat{I}$ , such that  $\hat{F} = \hat{N} + \hat{I}$ . This gives rise to the basis states:

$$|(NI)Fm_F\rangle = \sum_{m_N, m_I} (-1)^{-N+I-M_F} \sqrt{2F+1} \begin{pmatrix} N & I & F \\ m_N & m_I & m_F \end{pmatrix} |Nm_N\rangle |Im_I\rangle, \quad (\text{D.1})$$

where  $|Nm_N\rangle$  and  $|Im_I\rangle$  are the eigenvectors of  $\hat{N}^2$  and  $\hat{I}^2$ , respectively. The results derived here can be easily generalized to cases where the states in Eq. (D.1) are not eigenvectors of the hyperfine Hamiltonian. In such cases, the true eigenvectors can always be represented as linear combinations of the basis vectors defined in Eq. (D.1). Similarly, these results can accommodate alternative coupling schemes, such as those discussed in Papers **F** and **G**.

Let me consider the collisional perturbation of the  $(N_b, I)F_b \leftarrow (N_a, I)F_a$  transition. The perturber is assumed to have a zero nuclear spin. Eq. (B.44), adapted to the case considered here, is given as [76]

$$\begin{aligned} \sigma_{\lambda=0}^q(F_a, F_b, F'_a, F'_b; E_{\text{kin}}) &= \frac{\pi}{k_r^2} \sum_{N_p} n_p(T) \sum_{l, l', J, \bar{J}, L, L', N'_p} (-1)^{F_a - F'_a} \\ &\times ([J, \bar{J}]) (-1)^{L+L'} \begin{Bmatrix} J & q & \bar{J} \\ F_a & L & F_b \end{Bmatrix} \begin{Bmatrix} J & q & \bar{J} \\ F'_a & L' & F'_b \end{Bmatrix} \\ &\left( \delta_{F_a F'_a} \delta_{F_b F'_b} \delta_{N_p N'_p} \delta_{ll'} \delta_{LL'} - S_{F_b L(N_p l); F'_b L'(N'_p l')}^J S_{F_a L(N_p l); F'_a L'(N_p l)}^{\bar{J}*} \right). \end{aligned} \quad (\text{D.2})$$

This cross-section provides additional information than the standard pressure broadening and shift cross-sections (Eq. (B.44)). It allows to describe *line mixing* [268] between  $(N_b, I)F_b \leftarrow (N_a, I)F_a$  and  $(N_b, I)F'_b \leftarrow (N_a, I)F'_a$  two hyperfine





components of the  $N_b \leftarrow N_a$  transition.

The angular momentum coupling scheme used here is given by

$$\hat{N}_A + \hat{I}_A = \hat{F}_A, \quad \hat{N}_P + \hat{l} = \hat{L}, \quad \hat{F}_A + \hat{L} = \hat{J}. \quad (\text{D.3})$$

By setting  $N_p = 0$ , and consequently  $L = l$  and  $L' = l'$ , the case of a hyperfine component of the chosen rovibrational line perturbed by a structureless collision partner is recovered

$$\begin{aligned} \sigma^q(F_a, F_b, F'_a, F'_b; E_{\text{kin}}) &= \frac{\pi}{k_r^2} \sum_{l, l', J, \bar{J}} (-1)^{F_a - F'_a} [J, \bar{J}] (-1)^{l+l'} \begin{Bmatrix} J & q & \bar{J} \\ F_a & l & F_b \end{Bmatrix} \begin{Bmatrix} J & q & \bar{J} \\ F'_a & l' & F'_b \end{Bmatrix} \\ &\times \left( \delta_{F_a F'_a} \delta_{F_b F'_b} \delta_{ll'} - S_{F_b l; F'_b l'}^J S_{F_a l; F'_a l'}^{\bar{J}*} \right). \end{aligned} \quad (\text{D.4})$$

This formula was originally derived by Green [279] for He-perturbed hyperfine components of pure rotational lines in HCN and later revisited by Buffa and Tarini [280]. Buffa and Tarini noted a crucial inconsistency in Green's treatment: the sign convention used by Green for hyperfine line amplitudes ( $A_{ab}$ ) leads to an incorrect sign of the product  $A_{ab} \sigma^q(a, b, a', b') A_{a'b'}$ . This drastically impacts the line shape when the line width significantly exceeds the hyperfine splitting, preventing the recovery of the hyperfine-free result [76].

Buffa and Tarini resolved this issue by introducing a corrected phase convention for the hyperfine line amplitudes. Using their approach, the proper formula for the line amplitudes becomes

$$A_{ab} = (-1)^{F_b + N_a + I + q} \frac{\sqrt{[F_a, F_b]}}{[I]} \begin{Bmatrix} N_b & F_b & I \\ F_a & N_a & q \end{Bmatrix}, \quad (\text{D.5})$$

which involves the additional phase factor that was missing in Green's formula. Indeed this phase convention is widely adopted in literature (see for instance Chapter 5 in Ref. [240]) and in this dissertation (see, for instance, Eq. (B2) in Article **J**).

The S-matrices in Eqs. (D.2) and (D.4) are expressed in the coupled basis (Eq. (D.1)), which explicitly incorporates nuclear spin. How can one get such S-matrices? There are essentially two options.

First, the entire quantum scattering problem can be defined in this basis by coupling the eigenvectors of the relative angular momentum and/or the eigenvectors of the rotational states of the perturber. The coupled equations



are then solved directly in this basis. This approach was employed in Paper **L**, where the other colliding species was a  $^2S$  (lithium) atom. In this case,  $N_p = 0$ , but the electronic spin  $S = 1$  introduces additional coupling. Rigorous inclusion of nuclear spins is crucial when the collision energy is comparable to hyperfine or Zeeman interactions.

Alternatively, if the collision energy is significantly larger than the hyperfine or Zeeman interaction energies, angular momenta can be coupled in a different order

$$\hat{N}_A + \hat{N}_P = \hat{N}_{AP}, \quad \hat{N}_{AP} + \hat{l} = \hat{\mathcal{J}}, \quad \hat{\mathcal{J}} + \hat{I}_A = \hat{J}, \quad (\text{D.6})$$

and all interactions that couple nuclear spins and its projection on the space-fixed  $Z$ -axis are neglected. In this approximation, nuclear spin acts as a spectator, decoupled from all other angular momenta modified during the collision. This simplifies the scattering problem, reducing it to the scattering of two spin-free diatomic molecules (or a spin-free diatomic molecule and an atom), as described in Appendix A. Expanding the scattering wave function in this basis and imposing standard boundary conditions yields spin-free scattering matrices,  $S_{(N_a N_p)N_{ap}l; (N'_a N'_p)N'_{ap}l'}^{\mathcal{J}}$ . To establish the relation between the spin-free and spin-including  $S$ -matrices, one can use the transformation between the two basis sets, given by

$$\begin{aligned} |(N_a I)F_a, (N_p l)L; JM\rangle &= (-1)^{F+L+N_a+N_p+l+I} \\ &\times \sum_{\mathcal{J}, N_{ap}} \sqrt{[N_{ap}, L, \mathcal{J}, F]} \begin{Bmatrix} L & N_a & \mathcal{J} \\ I & J & F \end{Bmatrix} \begin{Bmatrix} N_a & N_p & N_{ap} \\ l & \mathcal{J} & L \end{Bmatrix} |((N_a N_p)N_{ap}l)\mathcal{J}I; JM\rangle. \end{aligned} \quad (\text{D.7})$$

Since no couplings involving nuclear spins are included in this approximation, the  $S$ -matrix remains diagonal in  $I$ , and the spin-including  $S$ -matrices required for Eqs. (D.2) and (D.4) can be derived algebraically using the transformation

$$\begin{aligned} S_{(N_a I)F_a(N_p l)L; (N'_a I)F'_a(N'_p l')L'}^J &= (-1)^{F+F'+L+L'+N_a+N'_a+N_p+N'_p+l+l'+2I} \\ &\times \sqrt{[L, L', F, F']} \sum_{\mathcal{J}, N_{ap}, N'_{ap}} [\mathcal{J}] \sqrt{[N_{ap}, N'_{ap}]} \begin{Bmatrix} L & N_a & \mathcal{J} \\ I & J & F_a \end{Bmatrix} \begin{Bmatrix} N_a & N_p & N_{ap} \\ l & \mathcal{J} & L \end{Bmatrix} \\ &\times \begin{Bmatrix} L' & N'_a & \mathcal{J} \\ I & J & F'_a \end{Bmatrix} \begin{Bmatrix} N'_a & N'_p & N'_{ap} \\ l' & \mathcal{J} & L' \end{Bmatrix} S_{(N_a N_p)N_{ap}l; (N'_a N'_p)N'_{ap}l'}^{\mathcal{J}}. \end{aligned} \quad (\text{D.8})$$



Substituting this to Eq. (D.2) and taking  $N'_a = N_a$  and  $N'_b = N_b$  leads to

$$\begin{aligned}
 \sigma^q(F_a, F_b, F'_a, F'_b; E_{\text{kin}}) &= (-1)^{F_b - F'_b} \frac{\pi}{k_r^2} \sqrt{[F_a, F'_a, F_b, F'_b]} \\
 &\times \sum_{N_p} n_p(T) \sum_{N'_p, l, l'} \sum_{J, \bar{J}, L, L'} (-1)^{L+L'} [J, \bar{J}, L, L'] \begin{Bmatrix} J & q & \bar{J} \\ F_a & L & F_b \end{Bmatrix} \begin{Bmatrix} J & q & \bar{J} \\ F'_a & L & F'_b \end{Bmatrix} \\
 &\times \sum_{\mathcal{J}, \bar{\mathcal{J}}, N_{ap}, N'_{ap}, N_{bp}, N'_{bp}} [\mathcal{J}, \bar{\mathcal{J}}] \sqrt{[N_{ap}, N'_{ap}, N_{bp}, N'_{bp}]} \begin{Bmatrix} L & N_a & \bar{\mathcal{J}} \\ I & J_a & F_a \end{Bmatrix} \begin{Bmatrix} L & N_b & \mathcal{J} \\ I & J_b & F_b \end{Bmatrix} \\
 &\times \begin{Bmatrix} N_a & N_p & N_{ap} \\ l & \bar{\mathcal{J}} & L \end{Bmatrix} \begin{Bmatrix} N_b & N_p & N_{bp} \\ l & \mathcal{J} & L \end{Bmatrix} \begin{Bmatrix} L' & N_a & \bar{\mathcal{J}} \\ I & \bar{J} & F'_a \end{Bmatrix} \\
 &\times \begin{Bmatrix} L' & N_b & \bar{\mathcal{J}} \\ I & \bar{J} & F'_b \end{Bmatrix} \begin{Bmatrix} N_a & N'_p & N'_{ap} \\ l' & \bar{\mathcal{J}} & L' \end{Bmatrix} \begin{Bmatrix} N_b & N'_p & N'_{bp} \\ l' & \mathcal{J} & L' \end{Bmatrix} \\
 &[\delta_{N_p N'_p} \delta_{ll'} \delta_{N_{ap} N'_{ap}} \delta_{N_{bp} N'_{bp}} - S_{(N_b N_p) N_{bp} l; (N_b N'_p) N'_{bp} l'} S_{(N_a N_p) N_{ap} l}^*] (N_a N'_p) N'_{ap} l'].
 \end{aligned} \tag{D.9}$$

The approach of obtaining S-matrices that incorporate nuclear spins through algebraic transformations is known as the *recoupling technique*. [281]. Though originally developed for studying scattering of molecules with non-zero *electronic* spin, it has since then been mostly used in studies of hyperfine-resolved rate coefficients [244, 282, 283]. For the detailed discussion of the recoupling approach, applied to the case of pressure broadening of the molecule with a non-zero electronic spin, see Ref. [132].

To validate whether Eq. (D.9) is correct, one can follow the method outlined by Buffa and Tarini [280], verifying that the following sum recovers the nuclear spin-free result

$$\begin{aligned}
 \sum_{ab, a'b'} A_{ab} \sigma_{ab, a'b'}^q A_{a'b'} &= \frac{1}{(2I+1)} \sum_{F_a, F_b, F'_a, F'_b} \sigma^q(F_a, F_b, F'_a, F'_b; E_{\text{kin}}) \\
 &\times (-1)^{F_b + F'_b} \sqrt{[F_a, F'_a, F_b, F'_b]} \begin{Bmatrix} N_b & F_b & I \\ F_a & N_a & q \end{Bmatrix} \begin{Bmatrix} N_b & F'_b & I \\ F'_a & N_a & q \end{Bmatrix}.
 \end{aligned} \tag{D.10}$$

The validation begins by summing over  $F_a$  and  $F'_a$ , reducing the terms associated with the active molecule's nuclear spin states. This is followed by summing over  $F_b$  and  $F'_b$ , consolidating the contributions from the perturber states, using sum rules discussed in Appendix A of Ref. [229]. Subsequently, the sums over  $\bar{J}$  and  $J$  are performed, further simplifying the expression. Finally, a transition is made from the coupling scheme typically employed in quantum scattering



calculations

$$\hat{N}_A + \hat{N}_P = \hat{N}_{AP}, \quad \hat{N}_{AP} + \hat{l} = \hat{\mathcal{J}}, \quad (\text{D.11})$$

to the coupling scheme more natural for line-shape theory

$$\hat{N}_P + \hat{l} = \hat{L}, \quad \hat{N}_A + \hat{L} = \hat{\mathcal{J}}, \quad (\text{D.12})$$

resulting in the nuclear spin-free expression

$$\begin{aligned} & \sum_{ab,a'b'} A_{ab} \sigma_{ab,a'b'}^q A_{a'b'} = \sigma^q(N_a, N_b; E_{\text{kin}}) = \frac{\pi}{k_r^2} \\ & \times \sum_{N_p} n_p(T) \sum_{N'_p, l, l'} \sum_{\mathcal{J}, \bar{\mathcal{J}}, L, L'} (-1)^{L+L'} [\mathcal{J}, \bar{\mathcal{J}}, L, L'] \begin{Bmatrix} \bar{\mathcal{J}} & N_a & L' \\ N_b & \mathcal{J} & q \end{Bmatrix} \begin{Bmatrix} \bar{\mathcal{J}} & N_a & L \\ N_b & \mathcal{J} & q \end{Bmatrix} \quad (\text{D.13}) \\ & \times [\delta_{N_p N'_p} \delta_{ll'} \delta_{N_{ap} N'_{ap}} \delta_{N_{bp} N'_{bp}} - S_{N_b(N_p l) L; N_b(N'_p l') L'}^{\mathcal{J}} S_{N_a(N_p l) L; N_a(N'_p l') L'}^{\bar{\mathcal{J}}*}]. \end{aligned}$$

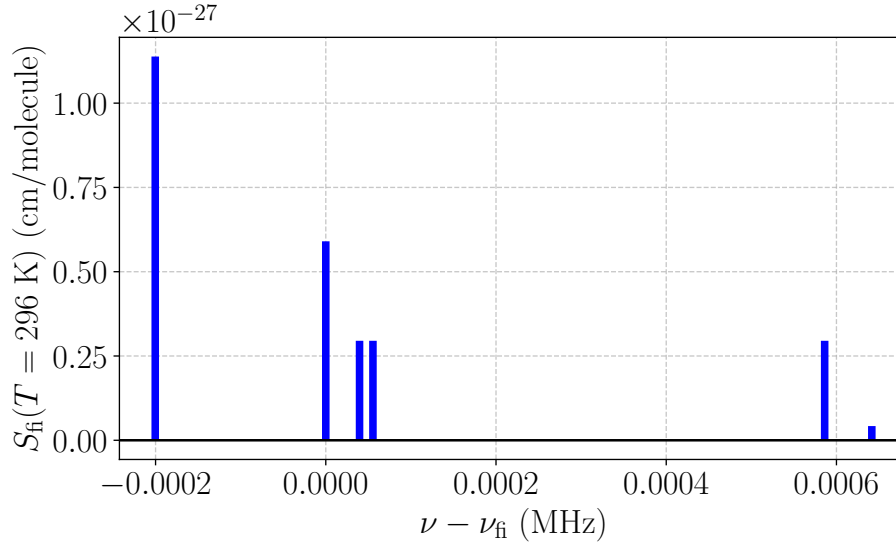


Figure 8: Hyperfine components of the 0-0 S(1) line in  $\text{H}_2$ , shown relative to the hyperfine-free transition frequency ( $\nu_f$ ). Line intensities ( $S_f$ ) are calculated at  $T = 296$  K. Data is taken from Ref. [192].

As an example, consider the collisional perturbation of the 0-0 S(1) line in  $\text{H}_2$ , analyzed in detail in Appendix C. This transition exhibits hyperfine structure due to the non-zero nuclear spin ( $I = 1$ ) of the *ortho*- $\text{H}_2$  isomer. Consequently, both the ground ( $v_a = 0, N_a = 1$ ) and excited ( $v_b = 0, N_b = 3$ ) rotational states are split into three hyperfine levels each. A full list of hyperfine levels for all six hydrogen isotopologues can be found in the Supplementary Materials of Paper **G**. The S(1) line is a quadrupole transition ( $q = 2$ ), with selection rules



$\Delta F = F_b - F_a = 0, \pm 1, \pm 2$ . As a result, six hyperfine components are allowed (see Supplementary Materials of Ref. [192] and Fig.8).

The perturber state is fixed to be the hyperfine-free *para*-H<sub>2</sub> molecule in the  $N_p = 2$  state. If the hyperfine structure of the 0-0 S(1) line in *ortho*-H<sub>2</sub> is neglected, the pressure broadening and shift cross-sections calculated at  $E_{\text{kin}} = 200 \text{ cm}^{-1}$  are

$$\sigma^{q=2}(E_{\text{kin}}) = (0.414 + i0.1028) \text{ Å}^2.$$

Now, using Eq. (D.9), we calculate the cross-sections for all hyperfine components of the transition, *including* hyperfine structure, setting  $N_a = 1$ ,  $N_b = 3$ , and  $N_p = 2$ . The results are presented in Tabs. 2 and 3.

		$(F'_a, F'_b)$					
		(0,2)	(1,2)	(1,3)	(2,2)	(2,3)	(2,4)
$(F_a, F_b)$	(0,2)	0.439	-0.004	-0.001	-0.014	-0.010	-0.002
	(1,2)	-0.004	0.428	-0.006	-0.014	-0.001	0.002
	(1,3)	-0.001	-0.006	0.443	0.008	-0.017	-0.010
	(2,2)	-0.015	-0.014	0.008	0.440	0.008	-0.001
	(2,3)	-0.010	-0.001	-0.017	0.008	0.431	0.007
	(2,4)	-0.002	0.002	-0.010	-0.001	0.007	0.417

Table 2: Real part of the generalized cross-sections (in Å<sup>2</sup>) for the six hyperfine components of the 0-0 S(1) line in H<sub>2</sub>. Each component is labeled by the total angular momentum in the ground ( $F_a$ ) and excited ( $F_b$ ) spectroscopic states. Diagonal elements on the table correspond to the pressure-broadening cross-sections for each of the six hyperfine components.

		$(F'_a, F'_b)$					
		(0,2)	(1,2)	(1,3)	(2,2)	(2,3)	(2,4)
$(F_a, F_b)$	(0,2)	0.1036	-0.0004	-0.0002	-0.0001	-0.0001	0
	(1,2)	-0.0004	0.1034	0.0001	-0.0003	-0.0001	0
	(1,3)	-0.0002	0.0001	0.1033	0.0001	-0.0003	-0.0002
	(2,2)	-0.0001	-0.0003	0.0001	0.1033	0.0002	0
	(2,3)	-0.0001	-0.0001	-0.0003	0.0002	0.1031	0.0001
	(2,4)	0	0	-0.0002	-0.00001	0.0001	0.1029

Table 3: Imaginary part of the generalized cross-sections (in Å<sup>2</sup>) for the six hyperfine components of the S(1) 0-0 line in H<sub>2</sub>. Each component is labeled by the total angular momentum in the ground ( $F_a$ ) and excited ( $F_b$ ) spectroscopic states. Diagonal elements on the table correspond to the pressure-shift cross-sections for each of the six hyperfine components.

As shown in the tables, pressure broadening cross-sections for individual hyperfine components can deviate by up to 7% compared to the hyperfine-free case, while pressure shift cross-sections differ by less than 1%. The off-





diagonal ( $F_a \neq F'_a$  and  $F_b \neq F'_b$ ) cross-sections, which govern line-mixing effects [268], reveal that real off-diagonal elements are at least an order of magnitude larger than their imaginary counterparts.

The purpose of this appendix was to provide a straightforward example demonstrating how to calculate pressure broadening and shift cross-sections for hyperfine components of rovibrational transitions. A natural extension of this work would involve performing calculations over a range of kinetic energies, averaging the cross-sections using Maxwell-Boltzmann distributions to derive pressure broadening and shift coefficients for each hyperfine component (Eq. (B.43)) and quantify line-mixing effects between these components. This approach would allow for the construction of a complete relaxation matrix, enabling the simulation of theoretical line shapes and their comparison with experimental spectra. Such detailed analysis, however, lies beyond the scope of this appendix.



## BIBLIOGRAPHY

- [1] A. D. Ludlow, M. M. Boyd, J. Ye, E. Peik, and P. O. Schmidt. Optical atomic clocks. *Rev. Mod. Phys.*, 87:637–701, Jun 2015. URL: <https://link.aps.org/doi/10.1103/RevModPhys.87.637>, doi:10.1103/RevModPhys.87.637.
- [2] R. Pohl et al. The size of the proton. *Nature*, 466(7303):213–216, jul 2010. doi:10.1038/nature09250.
- [3] M. Hori et al. Buffer-gas cooling of antiprotonic helium to 1.5 to 1.7 K, and antiproton-to-electron mass ratio. *Science*, 354(6312):610–614, 2016. doi:10.1126/science.aaf6702.
- [4] S. Alighanbari, G. S. Giri, F. L. Constantin, V. I. Korobov, and S. Schiller. Precise test of quantum electrodynamics and determination of fundamental constants with  $\text{HD}^+$  ions. *Nature*, 581(7807):152–158, may 2020. doi:10.1038/s41586-020-2261-5.
- [5] S. Patra, M. Germann, J.-Ph. Karr, M. Haidar, L. Hilico, V. I. Korobov, F. M. J. Cozijn, K. S. E. Eikema, W. Ubachs, and J. C. J. Koelemeij. Proton-electron mass ratio from laser spectroscopy of  $\text{HD}^+$  at the part-per-trillion level. *Science*, 369(6508):1238–1241, sep 2020. doi:10.1126/science.aba0453.
- [6] J. J. Krauth, K. Schuhmann, M. A. Ahmed, F. D. Amaro, P. Amaro, F. Biraben, T. L. Chen, D. S. Covita, A. J. Dax, M. Diepold, et al. Measuring the  $\alpha$ -particle charge radius with muonic Helium-4 ions. *Nature*, 589(7843):527–531, jan 2021. doi:10.1038/s41586-021-03183-1.
- [7] E. J. Salumbides, A. N. Schellekens, B. Gato-Rivera, and W. Ubachs. Constraints on extra dimensions from precision molecular spectroscopy. *New. J. Phys.*, 17(3):033015, mar 2015. doi:10.1088/1367-2630/17/3/033015.
- [8] W. Ubachs, J.C.J. Koelemeij, K.S.E. Eikema, and E.J. Salumbides. Physics beyond the Standard Model from hydrogen spectroscopy. *J. Mol.*



- Spectrosc.*, 320:1–12, February 2016. URL: <http://dx.doi.org/10.1016/j.jms.2015.12.003>, doi:10.1016/j.jms.2015.12.003.
- [9] M. S. Safronova, D. Budker, D. DeMille, D. F. Jackson Kimball, A. Derevianko, and C. W. Clark. Search for new physics with atoms and molecules. *Rev. Mod. Phys.*, 90:025008, Jun 2018. URL: <https://link.aps.org/doi/10.1103/RevModPhys.90.025008>, doi:10.1103/RevModPhys.90.025008.
- [10] D. DeMille, N. R. Hutzler, A. M. Rey, and T. Zelevinsky. Quantum sensing and metrology for fundamental physics with molecules. *Nat. Phys.*, 20(5):741–749, May 2024. URL: <http://dx.doi.org/10.1038/s41567-024-02499-9>, doi:10.1038/s41567-024-02499-9.
- [11] J.-M. Hartmann, C. Boulet, and D. Robert. *Collisional effects on molecular spectra*. Elsevier, 2008. doi:10.1016/b978-0-444-52017-3.x0001-5.
- [12] B. M. Hays, D. Gupta, T. Guillaume, Omar Abdelkader K., I. R. Cooke, F. Thibault, F. Lique, and I. R. Sims. Collisional excitation of HNC by He found to be stronger than for structural isomer HCN in experiments at the low temperatures of interstellar space. *Nat. Chem.*, 14(7):811–815, May 2022. URL: <http://dx.doi.org/10.1038/s41557-022-00936-x>, doi:10.1038/s41557-022-00936-x.
- [13] Z. D. Reed, H. Tran, H. N. Ngo, J.-M. Hartmann, and J. T. Hodges. Effect of non-Markovian collisions on measured integrated line shapes of CO. *Phys. Rev. Lett.*, 130:143001, Apr 2023. URL: <https://link.aps.org/doi/10.1103/PhysRevLett.130.143001>, doi:10.1103/PhysRevLett.130.143001.
- [14] F. Thibault, P. Wcisło, and R. Ciuryło. A test of H<sub>2</sub>-He potential energy surfaces. *EPJD*, 70(11), nov 2016. doi:10.1140/epjd/e2016-70114-9.
- [15] M. Słowiński, F. Thibault, Y. Tan, J. Wang, A.-W. Liu, S.-M. Hu, S. Kassı, A. Campargue, M. Konefał, H. Jóźwiak, K. Patkowski, P. Żuchowski, R. Ciuryło, D. Lisak, and P. Wcisło. H<sub>2</sub>-He collisions: Ab initio theory meets cavity-enhanced spectra. *Phys. Rev. A*, 101:052705,



- May 2020. URL: <https://link.aps.org/doi/10.1103/PhysRevA.101.052705>, doi:10.1103/PhysRevA.101.052705.
- [16] J. Tennyson. *Astronomical Spectroscopy: An Introduction to the Atomic and Mol. Phys. of Astronomical Spectroscopy*. World Scientific, 2019.
- [17] J. Hartmann. Investigations on the spectrum and orbit of delta Orionis. *ApJ*, 19:268, May 1904. URL: <http://dx.doi.org/10.1086/141112>, doi:10.1086/141112.
- [18] H. W. Kroto. The spectra of interstellar molecules. *Int. Rev. Phys. Chem.*, 1(3):309–376, December 1981. URL: <http://dx.doi.org/10.1080/01442358109353324>, doi:10.1080/01442358109353324.
- [19] Jr. Dunham, T. Interstellar neutral potassium and neutral calcium. *Publ. Astron. Soc. Pac.*, 49:26, February 1937. URL: <http://dx.doi.org/10.1086/124759>, doi:10.1086/124759.
- [20] P. Swings and L. Rosenfeld. Considerations regarding interstellar molecules. *ApJ*, 86:483, November 1937. URL: <http://dx.doi.org/10.1086/143880>, doi:10.1086/143880.
- [21] A. E. Douglas and G. Herzberg. Note on  $\text{CH}^+$  in interstellar space and in the laboratory. *ApJ*, 94:381, September 1941. URL: <http://dx.doi.org/10.1086/144342>, doi:10.1086/144342.
- [22] W. S. Adams. Some results with the COUDÉ spectrograph of the Mount Wilson Observatory. *ApJ*, 93:11, January 1941. URL: <http://dx.doi.org/10.1086/144237>, doi:10.1086/144237.
- [23] A. McKellar. The structure of the  $\lambda$  3883 CN band in the spectrum of comet Cunningham (1940 c). *Publ. Astron. Soc. Pac.*, 53:235, August 1941. URL: <http://dx.doi.org/10.1086/125324>, doi:10.1086/125324.
- [24] A. Wootten and A.R. Thompson. The Atacama Large Millimeter/Submillimeter Array. *Proc. IEEE*, 97(8):1463–1471, August 2009. URL: <http://dx.doi.org/10.1109/jproc.2009.2020572>, doi:10.1109/jproc.2009.2020572.
- [25] ALMA Science Portal. Alma overview. <https://www.almaobservatory.org>, 2024. Accessed: 2024-12-10.



- [26] E. T. Young, E. E. Becklin, P. M. Marcum, T. L. Roellig, J. M. De Buizer, T. L. Herter, R. Güsten, E. W. Dunham, P. Temi, B.-G. Andersson, D. Backman, M. Burgdorf, L. J. Caroff, S. C. Casey, J. A. Davidson, E. F. Erickson, R. D. Gehrz, D. A. Harper, P. M. Harvey, L. A. Helton, S. D. Horner, C. D. Howard, R. Klein, A. Krabbe, I. S. McLean, A. W. Meyer, J. W. Miles, M. R. Morris, W. T. Reach, J. Rho, M. J. Richter, H.-P. Roeser, G. Sandell, R. Sankrit, M. L. Savage, E. C. Smith, R. Y. Shuping, W. D. Vacca, J. E. Vaillancourt, J. Wolf, and H. Zinnecker. Early science with SOFIA, the stratospheric observatory for infrared astronomy. *ApJ*, 749(2):L17, March 2012. URL: <http://dx.doi.org/10.1088/2041-8205/749/2/L17>, doi:10.1088/2041-8205/749/2/L17.
- [27] NASA and USRA. SOFIA Science Center. <https://science.nasa.gov/mission/sofia/>, 2024. Accessed: 2024-12-10.
- [28] J. P. and others Gardner. The James Webb Space Telescope. *Space Sci. Rev.*, 123(4):485–606, April 2006. URL: <http://dx.doi.org/10.1007/s11214-006-8315-7>, doi:10.1007/s11214-006-8315-7.
- [29] NASA. James Webb Space Telescope. <https://science.nasa.gov/mission/webb/>, 2024. Accessed: 2024-12-10.
- [30] T. P. Snow and B. J. McCall. Diffuse atomic and molecular clouds. *Annu. Rev. Astron. Astrophys.*, 44(1):367–414, September 2006. URL: <http://dx.doi.org/10.1146/annurev.astro.43.072103.150624>, doi:10.1146/annurev.astro.43.072103.150624.
- [31] F. F. S. van der Tak, J. H. Black, F. L. Schöier, D. J. Jansen, and E. F. van Dishoeck. A computer program for fast non-LTE analysis of interstellar line spectra: With diagnostic plots to interpret observed line intensity ratios. *A&A*, 468(2):627–635, April 2007. URL: <http://dx.doi.org/10.1051/0004-6361:20066820>, doi:10.1051/0004-6361:20066820.
- [32] E. Roueff and F. Lique. Molecular excitation in the interstellar medium: Recent advances in collisional, radiative, and chemical processes. *Chem. Rev.*, 113(12):8906–8938, October 2013. URL: <http://dx.doi.org/10.1021/cr400145a>, doi:10.1021/cr400145a.



- [33] D. Flower. *Molecular collisions in the interstellar medium*, volume 42. Cambridge University Press, 2007.
- [34] A. Faure, P. J. Dagdigian, C. Rist, R. Dawes, E. Quintas-Sánchez, F. Lique, and M. Hochlaf. Interaction of chiral propylene oxide ( $\text{CH}_3\text{CHCH}_2\text{O}$ ) with Helium: Potential energy surface and scattering calculations. *ACS Earth Space Chem.*, 3(6):964–972, April 2019. URL: <http://dx.doi.org/10.1021/acsearthspacechem.9b00069>, doi:10.1021/acsearthspacechem.9b00069.
- [35] S. Demes, C. T. Bop, M. Ben Khalifa, and F. Lique. First close-coupling study of the excitation of a large cyclic molecule: collision of c- $\text{C}_5\text{H}_6$  with He. *Phys. Chem. Chem. Phys.*, 26(23):16829–16837, 2024. URL: <http://dx.doi.org/10.1039/d4cp01380h>, doi:10.1039/d4cp01380h.
- [36] F. Lique and J. Kłos. Quantum scattering of SiS with  $\text{H}_2$ : Potential energy surface and rate coefficients at low temperature. *J. Chem. Phys.*, 128(3), January 2008. URL: <http://dx.doi.org/10.1063/1.2820770>, doi:10.1063/1.2820770.
- [37] M. Żóltowski, F. Lique, A. Karska, and P. S. Żuchowski. Rotational excitation of highly excited  $\text{H}_2\text{O}$  by  $\text{H}_2$ . *MNRAS*, 502(4):5356–5361, February 2021. URL: <http://dx.doi.org/10.1093/mnras/stab453>, doi:10.1093/mnras/stab453.
- [38] M. Ben Khalifa and J. Loreau. Rotational excitation of interstellar benzonitrile by helium atoms. *MNRAS*, 527(1):846–854, 10 2023. arXiv:<https://academic.oup.com/mnras/article-pdf/527/1/846/52829177/stad3201.pdf>, doi:10.1093/mnras/stad3201.
- [39] A. Semenov, B. Mandal, and D. Babikov. MQCT: User-ready program for calculations of inelastic scattering of two molecules. *Comput. Phys. Commun.*, 252:107155, July 2020. URL: <http://dx.doi.org/10.1016/j.cpc.2020.107155>, doi:10.1016/j.cpc.2020.107155.
- [40] B. Mandal, A. Semenov, and D. Babikov. Adiabatic trajectory approximation within the framework of mixed quantum/classical theory. *J. Phys. Chem. A*, 124(47):9877–9888, November 2020. URL: <http://dx.doi.org/10.1021/acs.jpca.0c07547>, doi:10.1021/acs.jpca.0c07547.





- [41] B. Mandal, C. Joy, A. Semenov, and D. Babikov. Mixed quantum/classical theory for collisional quenching of PAHs in the interstellar media. *ACS Earth Space Chem.*, 6(3):521–529, February 2022. URL: <http://dx.doi.org/10.1021/acsearthspacechem.1c00418>, doi:10.1021/acsearthspacechem.1c00418.
- [42] J. Loreau, F. Lique, and A. Faure. An efficient statistical method to compute molecular collisional rate coefficients. *ApJ Letters*, 853(1):L5, January 2018. URL: <http://dx.doi.org/10.3847/2041-8213/aaa5fe>, doi:10.3847/2041-8213/aaa5fe.
- [43] M. Konings, B. Desrousseaux, F. Lique, and J. Loreau. Benchmarking an improved statistical adiabatic channel model for competing inelastic and reactive processes. *J. Chem. Phys.*, 155(10), September 2021. URL: <http://dx.doi.org/10.1063/5.0062388>, doi:10.1063/5.0062388.
- [44] F. Lique. Revisited study of the ro-vibrational excitation of  $H_2$  by H: towards a revision of the cooling of astrophysical media. *MNRAS*, 453(1):810–818, August 2015. URL: <http://dx.doi.org/10.1093/mnras/stv1683>, doi:10.1093/mnras/stv1683.
- [45] B. Desrousseaux, C. M. Coppola, M. V. Kazandjian, and F. Lique. Rotational excitation of HD by hydrogen revisited. *J. Phys. Chem. A*, 122(42):8390–8396, October 2018. URL: <http://dx.doi.org/10.1021/acs.jpca.8b08618>, doi:10.1021/acs.jpca.8b08618.
- [46] Y. Wan, N. Balakrishnan, B. H. Yang, R. C. Forrey, and P. C. Stancil. Rotational quenching of HD induced by collisions with  $H_2$  molecules. *MNRAS*, 488(1):381–386, June 2019. URL: <http://dx.doi.org/10.1093/mnras/stz1735>, doi:10.1093/mnras/stz1735.
- [47] D. R. Flower and G. Pineau des Forêts. The thermal balance of the first structures in the primordial gas. *MNRAS*, 323(3):672–676, may 2001. doi:10.1046/j.1365-8711.2001.04240.x.
- [48] C. Cecchi-Pestellini, S. Casu, and A. Dalgarno.  $H_2$  excitation in turbulent interstellar clouds. *MNRAS*, 364(4):1309–1314, dec 2005. doi:10.1111/j.1365-2966.2005.09652.x.



- [49] M. Ruaud. H<sub>2</sub> rovibrational excitation in protoplanetary disks and its effects on the chemistry. *ApJ*, 916(2):103, aug 2021. doi:10.3847/1538-4357/abe712.
- [50] D. R. Flower, E. Roueff, and C. J. Zeippen. Rovibrational excitation of molecules by He atoms. *J. Phys. B-At. Mol. Opt.*, 31(5):1105–1113, mar 1998. doi:10.1088/0953-4075/31/5/017.
- [51] P. Muchnick and A. Russek. The HeH<sub>2</sub> energy surface. *J. Chem. Phys.*, 100(6):4336–4346, mar 1994. doi:10.1063/1.466316.
- [52] T.-G. Lee, C. Rochow, R. Martin, T. K. Clark, R. C. Forrey, N. Balakrishnan, P. C. Stancil, D. R. Schultz, A. Dalgarno, and Gary J. Ferland. Close-coupling calculations of low-energy inelastic and elastic processes in <sup>4</sup>He collisions with H<sub>2</sub>: A comparative study of two potential energy surfaces. *J. Chem. Phys.*, 122(2):024307, jan 2005. doi:10.1063/1.1833351.
- [53] G. Tejeda, F. Thibault, J. M. Fernández, and S. Montero. Low-temperature inelastic collisions between hydrogen molecules and helium atoms. *J. Chem. Phys.*, 128(22):224308, jun 2008. doi:10.1063/1.2938366.
- [54] M. Słowiński, H. Jóźwiak, M. Gancewski, K. Stankiewicz, N. Stolarczyk, Y. Tan, J. Wang, A.-W. Liu, S.-M. Hu, S. Kassı, A. Campargue, K. Patkowski, P. S. Żuchowski, R. Ciuryło, F. Thibault, and P. Wcisło. Collisional line-shape effects in accurate He-perturbed H<sub>2</sub> spectra. *J. Quant. Spectrosc. Radiat. Transf.*, 277:107951, jan 2022. doi:10.1016/j.jqsrt.2021.107951.
- [55] F. Thibault, K. Patkowski, P. S. Żuchowski, H. Jóźwiak, R. Ciuryło, and P. Wcisło. Rovibrational line-shape parameters for H<sub>2</sub> in He and new H<sub>2</sub>-He potential energy surface. *J. Quant. Spectrosc. Radiat. Transf.*, 202:308–320, nov 2017. doi:10.1016/j.jqsrt.2017.08.014.
- [56] N. Balakrishnan, R. C. Forrey, and A. Dalgarno. Quantum-mechanical study of ro-vibrational transitions in H<sub>2</sub> induced by He atoms. *ApJ*, 514(1):520, mar 1999. URL: <https://dx.doi.org/10.1086/306922>, doi:10.1086/306922.



- [57] N. Balakrishnan, M. Vieira, J. F. Babb, A. Dalgarno, R. C. Forrey, and S. Lepp. Rate coefficients for ro-vibrational transitions in  $\text{H}_2$  due to collisions with He. *ApJ*, 524(2):1122, oct 1999. URL: <https://dx.doi.org/10.1086/307846>, doi:10.1086/307846.
- [58] P. Wcisło, I.E. Gordon, H. Tran, Y. Tan, S.-M. Hu, A. Campargue, S. Kassı, D. Romanini, C. Hill, R.V. Kochanov, and L.S. Rothman. The implementation of non-Voigt line profiles in the HITRAN database:  $\text{H}_2$  case study. *J. Quant. Spectrosc. Radiat. Transf.*, 177:75–91, July 2016. URL: <http://dx.doi.org/10.1016/j.jqsrt.2016.01.024>, doi:10.1016/j.jqsrt.2016.01.024.
- [59] H.A. Lorentz. The absorption and emission lines of gaseous bodies. In *Proceedings of the Royal Academy of Sciences at Amsterdam*, volume 8, pages 1905–1906, 1906.
- [60] W. Voigt. Über das gesetz der intensitätsverteilung innerhalb der linien eines gasspektrums. *Sitzungsber. Math.-Phys. Cl. Königl. Bayer. Akad. Wiss. München*, 1912.
- [61] P. R. Berman. Speed-dependent collisional width and shift parameters in spectral profiles. *J. Quant. Spectrosc. Radiat. Transf.*, 12(9):1331–1342, September 1972. URL: [http://dx.doi.org/10.1016/0022-4073\(72\)90189-6](http://dx.doi.org/10.1016/0022-4073(72)90189-6), doi:10.1016/0022-4073(72)90189-6.
- [62] A. T. Mattick, A. Sanchez, N. A. Kurnit, and A. Javan. Velocity dependence of collision-broadening cross section observed in an infrared transition of  $\text{NH}_3$  gas at room temperature. *Appl. Phys. Lett.*, 23(12):675–678, December 1973. URL: <http://dx.doi.org/10.1063/1.1654787>, doi:10.1063/1.1654787.
- [63] S. L. Coy. Speed dependence of microwave rotational relaxation rates. *J. Chem. Phys.*, 73(11):5531–5555, December 1980. URL: <http://dx.doi.org/10.1063/1.440073>, doi:10.1063/1.440073.
- [64] R. H. Dicke. The effect of collisions upon the Doppler width of spectral lines. *Phys. Rev.*, 89(2):472–473, January 1953. URL: <http://dx.doi.org/10.1103/physrev.89.472>, doi:10.1103/physrev.89.472.



- [65] A. Henry, D. Hurtmans, M. Margottin-Maclou, and A. Valentin. Confinement narrowing and absorber speed dependent broadening effects on CO lines in the fundamental band perturbed by Xe, Ar, Ne, He and N<sub>2</sub>. *J. Quant. Spectrosc. Radiat. Transf.*, 56(5):647–671, November 1996. URL: [http://dx.doi.org/10.1016/s0022-4073\(96\)00118-5](http://dx.doi.org/10.1016/s0022-4073(96)00118-5), doi:10.1016/s0022-4073(96)00118-5.
- [66] D. H. Rank and T. A. Wiggins. Collision narrowing of spectral lines. H<sub>2</sub> quadrupole spectrum. *J. Chem. Phys.*, 39(5):1348–1349, September 1963. URL: <http://dx.doi.org/10.1063/1.1734441>, doi:10.1063/1.1734441.
- [67] R.S. Eng, A.R. Calawa, T.C. Harman, P.L. Kelley, and A. Javan. Collisional narrowing of infrared water-vapor transitions. *Appl. Phys. Lett.*, 21(7):303–305, October 1972. URL: <http://dx.doi.org/10.1063/1.1654387>, doi:10.1063/1.1654387.
- [68] A.S. Pine. Collisional narrowing of HF fundamental band spectral lines by neon and argon. *J. Mol. Spectrosc.*, 82(2):435–448, August 1980. URL: [http://dx.doi.org/10.1016/0022-2852\(80\)90127-7](http://dx.doi.org/10.1016/0022-2852(80)90127-7), doi:10.1016/0022-2852(80)90127-7.
- [69] D. Ramachandra Rao and T. Oka. Dicke narrowing and pressure broadening in the infrared fundamental band of HCl perturbed by Ar. *J. Mol. Spectrosc.*, 122(1):16–27, March 1987. URL: [http://dx.doi.org/10.1016/0022-2852\(87\)90215-3](http://dx.doi.org/10.1016/0022-2852(87)90215-3), doi:10.1016/0022-2852(87)90215-3.
- [70] J. P. Wittke and R. H. Dicke. Redetermination of the hyperfine splitting in the ground state of atomic hydrogen. *Phys. Rev.*, 103(3):620–631, August 1956. URL: <http://dx.doi.org/10.1103/physrev.103.620>, doi:10.1103/physrev.103.620.
- [71] L. Galatry. Simultaneous effect of doppler and foreign gas broadening on spectral lines. *Phys. Rev.*, 122(4):1218–1223, May 1961. URL: <http://dx.doi.org/10.1103/physrev.122.1218>, doi:10.1103/physrev.122.1218.



- [72] M. Nelkin and A. Ghatak. Simple binary collision model for Van Hove's  $G_s(r, t)$ . *Phys. Rev.*, 135:A4–A9, Jul 1964. URL: <https://link.aps.org/doi/10.1103/PhysRev.135.A4>, doi:10.1103/PhysRev.135.A4.
- [73] S. G. Rautian and Il. I. Sobel'man. The effect of collisions on the Doppler broadening of spectral lines. *Sov. Phys. Usp.*, 9(5):701, 1967.
- [74] R. G. Breene Jr and H. R. Zaidi. *Theories of spectral line shape*. Wiley, New York, 1981.
- [75] S. Hess. Kinetic theory of spectral line shapes. The transition between doppler broadening and collisional broadening. *Physica*, 61(1):80–94, September 1972. URL: [http://dx.doi.org/10.1016/0031-8914\(72\)90035-3](http://dx.doi.org/10.1016/0031-8914(72)90035-3), doi:10.1016/0031-8914(72)90035-3.
- [76] L. Monchick and L. W. Hunter. Diatomic–diatomic molecular collision integrals for pressure broadening and Dicke narrowing: A generalization of Hess's theory. *J. Chem. Phys.*, 85(2):713–718, July 1986. URL: <http://dx.doi.org/10.1063/1.451277>, doi:10.1063/1.451277.
- [77] N.H. Ngo, D. Lisak, H. Tran, and J.-M. Hartmann. An isolated line-shape model to go beyond the Voigt profile in spectroscopic databases and radiative transfer codes. *J. Quant. Spectrosc. Radiat. Transf.*, 129:89–100, November 2013. URL: <http://dx.doi.org/10.1016/j.jqsrt.2013.05.034>, doi:10.1016/j.jqsrt.2013.05.034.
- [78] J. Tennyson, P. F. Bernath, A. Campargue, A. G. Császár, L. Daumont, R. R. Gamache, J. T. Hodges, D. Lisak, O. V. Naumenko, L. S. Rothman, Ha Tran, N. F. Zobov, J. Buldyreva, C. D. Boone, M.D. De Vizia, L. Gianfrani, J.-M. Hartmann, R. McPheat, D. Weidmann, J. Murray, N. H. Ngo, and O. L. Polyansky. Recommended isolated-line profile for representing high-resolution spectroscopic transitions (IUPAC technical report). *Pure Appl. Chem.*, 86(12):1931–1943, December 2014. URL: <http://dx.doi.org/10.1515/pac-2014-0208>, doi:10.1515/pac-2014-0208.
- [79] B. Lance, G. Blanquet, J. Walrand, and J.-P. Bouanich. On the speed-dependent hard collision lineshape models: Application to  $C_2H_2$  perturbed by Xe. *J. Mol. Spectrosc.*, 185(2):262–271, October 1997. URL:



- <http://dx.doi.org/10.1006/jmsp.1997.7385>, doi:10.1006/jmsp.1997.7385.
- [80] A.S. Pine. Asymmetries and correlations in speed-dependent Dicke-narrowed line shapes of argon-broadened HF. *J. Quant. Spectrosc. Radiat. Transf.*, 62(4):397–423, July 1999. URL: [http://dx.doi.org/10.1016/s0022-4073\(98\)00112-5](http://dx.doi.org/10.1016/s0022-4073(98)00112-5), doi:10.1016/s0022-4073(98)00112-5.
- [81] M. Konefał, M. Słowiński, M. Zaborowski, R. Ciuryło, D. Lisak, and P. Wcisło. Analytical-function correction to the Hartmann–Tran profile for more reliable representation of the Dicke-narrowed molecular spectra. *J. Quant. Spectrosc. Radiat. Transf.*, 242:106784, February 2020. URL: <http://dx.doi.org/10.1016/j.jqsrt.2019.106784>, doi:10.1016/j.jqsrt.2019.106784.
- [82] R. Ciuryło, D. A. Shapiro, J. R. Drummond, and A. D. May. Solving the line-shape problem with speed-dependent broadening and shifting and with Dicke narrowing. II. Application. *Phys. Rev. A*, 65:012502, Dec 2001. URL: <https://link.aps.org/doi/10.1103/PhysRevA.65.012502>, doi:10.1103/PhysRevA.65.012502.
- [83] P. Wcisło, H. Tran, S. Kassı, A. Campargue, F. Thibault, and R. Ciuryło. Velocity-changing collisions in pure H<sub>2</sub> and H<sub>2</sub>-Ar mixture. *J. Chem. Phys.*, 141(7), August 2014. URL: <http://dx.doi.org/10.1063/1.4892414>, doi:10.1063/1.4892414.
- [84] P. Wcisło, F. Thibault, H. Cybulski, and R. Ciuryło. Strong competition between velocity-changing and phase- or state-changing collisions in H<sub>2</sub> spectra perturbed by Ar. *Phys. Rev. A*, 91:052505, May 2015. URL: <https://link.aps.org/doi/10.1103/PhysRevA.91.052505>, doi:10.1103/PhysRevA.91.052505.
- [85] G. Herzberg and L. L. Howe. The Lyman bands of molecular hydrogen. *Can. J. Phys.*, 37(5):636–659, May 1959. URL: <http://dx.doi.org/10.1139/p59-070>, doi:10.1139/p59-070.
- [86] R. L. Farrow, L. A. Rahn, G. O. Sitz, and G. J. Rosasco. Observation of a speed-dependent collisional inhomogeneity in H<sub>2</sub> vibrational line profiles. *Phys. Rev. Lett.*, 63:746–749, Aug 1989. URL: <https://link.aps.org/doi/10.1103/PhysRevLett.63.746>, doi:10.1103/PhysRevLett.63.746.





---

[//link.aps.org/doi/10.1103/PhysRevLett.63.746](https://link.aps.org/doi/10.1103/PhysRevLett.63.746), doi:10.1103/PhysRevLett.63.746.

- [87] J. Ph. Berger, R. Saint-Loup, H. Berger, J. Bonamy, and D. Robert. Measurement of vibrational line profiles in H<sub>2</sub>-rare-gas mixtures: Determination of the speed dependence of the line shift. *Phys. Rev. A*, 49:3396–3406, May 1994. URL: <https://link.aps.org/doi/10.1103/PhysRevA.49.3396>, doi:10.1103/PhysRevA.49.3396.
- [88] S. Green, D. W. Schwenke, and W. M. Huo. Raman q-branch line shapes as a test of a H<sub>2</sub>-Ar intermolecular potential. *J. Chem. Phys.*, 101(1):15–19, July 1994. URL: <http://dx.doi.org/10.1063/1.468188>, doi:10.1063/1.468188.
- [89] D. Robert and L. Bonamy. Memory effects in speed-changing collisions and their consequences for spectral lineshape: I. Collision regime. *EPJD*, 2(3):245, 1998. URL: <http://dx.doi.org/10.1007/s100530050137>, doi:10.1007/s100530050137.
- [90] F. Chaussard, X. Michaut, R. Saint-Loup, H. Berger, P. Joubert, B. Lance, J. Bonamy, and D. Robert. Collisional effects on spectral line shape from the Doppler to the collisional regime: A rigorous test of a unified model. *J. Chem. Phys.*, 112(1):158–166, January 2000. URL: <http://dx.doi.org/10.1063/1.480570>, doi:10.1063/1.480570.
- [91] L. Bonamy, H. Tran Thi Ngoc, P. Joubert, and D. Robert. Memory effects in speed-changing collisions and their consequences for spectral line shape: II. From the collision to the Doppler regime. *EPJD*, 31(3):459–467, December 2004. URL: <http://dx.doi.org/10.1140/epjd/e2004-00148-5>, doi:10.1140/epjd/e2004-00148-5.
- [92] H. Tran, F. Thibault, and J.-M. Hartmann. Collision-induced velocity changes from molecular dynamic simulations in H<sub>2</sub>-Ar: A test of the Keilson-Storer model and of line-broadening/shifting calculations for the Q(1) Raman line. *J. Quant. Spectrosc. Radiat. Transf.*, 112(6):1035–1042, April 2011. URL: <http://dx.doi.org/10.1016/j.jqsrt.2010.12.004>, doi:10.1016/j.jqsrt.2010.12.004.
- [93] I.E. Gordon et al. The HITRAN2020 molecular spectroscopic database. *J. Quant. Spectrosc. Radiat. Transf.*, 277:107949, January 2022. URL:



- <http://dx.doi.org/10.1016/j.jqsrt.2021.107949>, doi:10.1016/j.jqsrt.2021.107949.
- [94] R.V. Kochanov, I.E. Gordon, L.S. Rothman, P. Wcisło, C. Hill, and J.S. Wilzewski. HITRAN Application Programming Interface (HAPI): A comprehensive approach to working with spectroscopic data. *J. Quant. Spectrosc. Radiat. Transf.*, 177:15–30, July 2016. URL: <http://dx.doi.org/10.1016/j.jqsrt.2016.03.005>, doi:10.1016/j.jqsrt.2016.03.005.
- [95] K. Pachucki and J. Komasa. Electric dipole rovibrational transitions in the HD molecule. *Phys. Rev. A*, 78:052503, Nov 2008. URL: <https://link.aps.org/doi/10.1103/PhysRevA.78.052503>, doi:10.1103/PhysRevA.78.052503.
- [96] E. Lellouch, B. Bézard, T. Fouchet, H. Feuchtgruber, T. Encrenaz, and T. de Graauw. The deuterium abundance in Jupiter and Saturn from ISO-SWS observations. *A &A*, 370(2):610–622, may 2001. doi:10.1051/0004-6361:20010259.
- [97] J. Geiss and G. Gloeckler. Abundances of Deuterium and Helium-3 in the protosolar cloud. *Space Sci. Rev.*, 84:239–250, 1998. doi:10.1007/978-94-011-5116-0\_24.
- [98] J. L. Linsky. *Space Sci. Rev.*, 84(1/2):285–296, 1998. doi:10.1023/a:1005048124341.
- [99] T. Guillot. A comparison of the interiors of Jupiter and Saturn. *P&SS*, 47(10-11):1183–1200, oct 1999. doi:10.1016/s0032-0633(99)00043-4.
- [100] J. D. R. Pierel, C. A. Nixon, E. Lellouch, L. N. Fletcher, G. L. Bjoraker, R. K. Achterberg, B. Bézard, B. E. Hesman, P. G. J. Irwin, and F. M. Flasar. D/H ratios on Saturn and Jupiter from *Cassini* CIRS. *ApJ*, 154(5):178, oct 2017. doi:10.3847/1538-3881/aa899d.
- [101] H. Feuchtgruber, E. Lellouch, G. Orton, T. de Graauw, B. Vandenbusche, B. Swinyard, R. Moreno, C. Jarchow, F. Billebaud, T. Cavalié, S. Sidher, and P. Hartogh. The D/H ratio in the atmospheres of Uranus and Neptune from *Herschel*-PACS observations. *A&A*, 551:A126, mar 2013. doi:10.1051/0004-6361/201220857.



- [102] H. Wiesemeyer, R. Güsten, P. Hartogh, Y. Okada, O. Ricken, and J. Stutzki. Revisiting Jupiter's deuterium fraction in the rotational ground-state line of HD at high spectral resolution. *A&A*, 688:A222, August 2024. URL: <http://dx.doi.org/10.1051/0004-6361/202450115>, doi:10.1051/0004-6361/202450115.
- [103] C. Hedges and N. Madhusudhan. Effect of pressure broadening on molecular absorption cross sections in exoplanetary atmospheres. *MNRAS*, 458(2):1427–1449, February 2016. URL: <http://dx.doi.org/10.1093/mnras/stw278>, doi:10.1093/mnras/stw278.
- [104] C. L. Renaud, K. Cleghorn, L. Hartmann, B. Vispoel, and R. R. Gamache. Line shape parameters for the H<sub>2</sub>O–H<sub>2</sub> collision system for application to exoplanet and planetary atmospheres. *Icarus*, 306:275–284, May 2018. URL: <http://dx.doi.org/10.1016/j.icarus.2017.10.016>, doi:10.1016/j.icarus.2017.10.016.
- [105] P. Niraula, J. de Wit, I. E. Gordon, R. J. Hargreaves, C. Sousa-Silva, and R. V. Kochanov. The impending opacity challenge in exoplanet atmospheric characterization. *Nat. Astron.*, 6(11):1287–1295, September 2022. URL: <http://dx.doi.org/10.1038/s41550-022-01773-1>, doi:10.1038/s41550-022-01773-1.
- [106] K. L. Chubb et al. Data availability and requirements relevant for the Ariel space mission and other exoplanet atmosphere applications. *RAS Techniques and Instruments*, 3(1):636–690, January 2024. URL: <http://dx.doi.org/10.1093/rasti/rzae039>, doi:10.1093/rasti/rzae039.
- [107] L. Wiesenfeld, P. Niraula, J. de Wit, N. Jaïdane, I. E. Gordon, and R. J. Hargreaves. Ab initio quantum dynamics as a scalable solution to the exoplanet opacity challenge: A case study of CO<sub>2</sub> in hydrogen atmosphere, 2024. URL: <https://arxiv.org/abs/2409.04439>, arXiv:2409.04439.
- [108] J. Tennyson et al. The 2024 release of the ExoMol database: Molecular line lists for exoplanet and other hot atmospheres. *J. Quant. Spectrosc. Radiat. Transf.*, 326:109083, November 2024. URL:



- <http://dx.doi.org/10.1016/j.jqsrt.2024.109083>, doi:10.1016/j.jqsrt.2024.109083.
- [109] B. W. Bakr, D. G. A. Smith, and K. Patkowski. Highly accurate potential energy surface for the He–H<sub>2</sub> dimer. *J. Chem. Phys.*, 139(14), October 2013. URL: <http://dx.doi.org/10.1063/1.4824299>, doi:10.1063/1.4824299.
- [110] H. Jóźwiak, F. Thibault, N. Stolarczyk, and P. Wcisło. Ab initio line-shape calculations for the S and O branches of H<sub>2</sub> perturbed by He. *J. Quant. Spectrosc. Radiat. Transf.*, 219:313–322, November 2018. URL: <http://dx.doi.org/10.1016/j.jqsrt.2018.08.023>, doi:10.1016/j.jqsrt.2018.08.023.
- [111] F. Thibault, R. Z. Martínez, D. Bermejo, and P. Wcisło. Line-shape parameters for the first rotational lines of HD in He. *Mol. Astrophys.*, 19:100063, June 2020. URL: <http://dx.doi.org/10.1016/j.molap.2020.100063>, doi:10.1016/j.molap.2020.100063.
- [112] K. Stankiewicz, H. Jóźwiak, M. Gancewski, N. Stolarczyk, F. Thibault, and P. Wcisło. Ab initio calculations of collisional line-shape parameters and generalized spectroscopic cross-sections for rovibrational dipole lines in HD perturbed by He. *J. Quant. Spectrosc. Radiat. Transf.*, 254:107194, October 2020. URL: <http://dx.doi.org/10.1016/j.jqsrt.2020.107194>, doi:10.1016/j.jqsrt.2020.107194.
- [113] R. Z. Martínez, Di. Bermejo, F. Thibault, and P. Wcisło. Testing the ab initio quantum-scattering calculations for the D<sub>2</sub>–He benchmark system with stimulated Raman spectroscopy. *J. Raman Spectrosc.*, 49(8):1339–1349, June 2018. URL: <http://dx.doi.org/10.1002/jrs.5391>, doi:10.1002/jrs.5391.
- [114] M. Morita and N. Balakrishnan. Stereodynamics of rotationally inelastic scattering in cold He + HD collisions. *J. Chem. Phys.*, 153(9), September 2020. URL: <http://dx.doi.org/10.1063/5.0022190>, doi:10.1063/5.0022190.
- [115] P. G. Jambrina, M. Morita, J. F. E. Croft, F. J. Aoiz, and N. Balakrishnan. Role of low energy resonances in the stereodynamics of cold He + D<sub>2</sub> collisions. *J. Phys. Chem. Letters*, 13(18):4064–4072, May 2022. URL:



- <http://dx.doi.org/10.1021/acs.jpcclett.2c00587>, doi:10.1021/acs.jpcclett.2c00587.
- [116] R. R. Gamache and B. Vispoel. On the temperature dependence of half-widths and line shifts for molecular transitions in the microwave and infrared regions. *J. Quant. Spectrosc. Radiat. Transf.*, 217:440–452, September 2018. URL: <http://dx.doi.org/10.1016/j.jqsrt.2018.05.019>, doi:10.1016/j.jqsrt.2018.05.019.
- [117] N. Stolarczyk, F. Thibault, H. Cybulski, H. Jóźwiak, G. Kowzan, B. Vispoel, I.E. Gordon, L.S. Rothman, R.R. Gamache, and P. Wcisło. Evaluation of different parameterizations of temperature dependences of the line-shape parameters based on ab initio calculations: Case study for the HITRAN database. *J. Quant. Spectrosc. Radiat. Transf.*, 240:106676, January 2020. URL: <http://dx.doi.org/10.1016/j.jqsrt.2019.106676>, doi:10.1016/j.jqsrt.2019.106676.
- [118] C. Leforestier, K. Szalewicz, and A. van der Avoird. Spectra of water dimer from a new ab initio potential with flexible monomers. *J. Chem. Phys.*, 137(1), July 2012. URL: <http://dx.doi.org/10.1063/1.4722338>, doi:10.1063/1.4722338.
- [119] A. M. Arthurs and A. Dalgarno. The theory of scattering by a rigid rotator. *Proc. R. Soc. Lond. Ser. A*, 256(1287):540–551, July 1960. URL: <http://dx.doi.org/10.1098/rspa.1960.0125>, doi:10.1098/rspa.1960.0125.
- [120] D. G. Truhlar. Long-standing themes in computational chemical dynamics. *Comp. Phys. Comm.*, 84(1–3):78–90, November 1994. URL: [http://dx.doi.org/10.1016/0010-4655\(94\)90204-6](http://dx.doi.org/10.1016/0010-4655(94)90204-6), doi:10.1016/0010-4655(94)90204-6.
- [121] A. Olejnik, H. Jóźwiak, M. Gancewski, E. Quintas-Sánchez, R. Dawes, and P. Wcisło. Ab initio quantum scattering calculations and a new potential energy surface for the  $\text{HCl}(X^1\Sigma^+)-\text{O}_2(X^3\Sigma_g^-)$  system: Collision-induced line shape parameters for  $\text{O}_2$ -perturbed R(0) 0–0 line in  $\text{H}^{35}\text{Cl}$ . *J. Chem. Phys.*, 159(13), October 2023. URL: <http://dx.doi.org/10.1063/5.0169968>, doi:10.1063/5.0169968.



- [122] J.-M. Liu, Yu. Zhai, X.-L. Zhang, and H. Li. Intermolecular configurations dominated by quadrupole–quadrupole electrostatic interactions: explicit correlation treatment of the five-dimensional potential energy surface and infrared spectra for the CO–N<sub>2</sub> complex. *Phys. Chem. Chem. Phys.*, 20(3):2036–2047, 2018. URL: <http://dx.doi.org/10.1039/c7cp06854a>, doi:10.1039/c7cp06854a.
- [123] L. A. Surin, I. V. Tarabukin, S. Schlemmer, Y. N. Kalugina, and A. van der Avoird. Ab initio potential and rotational spectra of the CO–N<sub>2</sub> complex. *J. Chem. Phys.*, 148(4), January 2018. URL: <http://dx.doi.org/10.1063/1.5013115>, doi:10.1063/1.5013115.
- [124] H. Cybulski, C. Henriksen, R. Dawes, X.-G. Wang, N. Bora, G. Avila, T. Carrington, and B. Fernández. Ab initio study of the CO–N<sub>2</sub> complex: a new highly accurate intermolecular potential energy surface and ro-vibrational spectrum. *Phys. Chem. Chem. Phys.*, 20(18):12624–12636, 2018. URL: <http://dx.doi.org/10.1039/c8cp01373j>, doi:10.1039/c8cp01373j.
- [125] N. Nissen, J. Doose, A. Guarnieri, H. Mäder, V. N. Markov, G. Yu. Golubyatnikov, I.I. Leonov, V. N. Shanin, and A. F. Krupnov. Foreign gas broadening studies of the  $J' \rightarrow J = 1 \rightarrow 0$  rotational line of CO by frequency and time domain techniques. *Z. Naturforsch A*, 54:218 – 224, 1999. doi:10.1515/zna-1999-3-410.
- [126] P. McGuire and D. J. Kouri. Quantum mechanical close coupling approach to molecular collisions.  $j_z$ -conserving coupled states approximation. *J. Chem. Phys.*, 60(6):2488–2499, March 1974. URL: <http://dx.doi.org/10.1063/1.1681388>, doi:10.1063/1.1681388.
- [127] C. F. Roche, J. M. Hutson, and A. S. Dickinson. Calculations of line width and shift cross sections for HCl in Ar. *J. Quant. Spectrosc. Radiat. Transf.*, 53(2):153–164, February 1995. URL: [http://dx.doi.org/10.1016/0022-4073\(95\)90003-9](http://dx.doi.org/10.1016/0022-4073(95)90003-9), doi:10.1016/0022-4073(95)90003-9.
- [128] JM Hutson and S Green. MOLSCAT computer code, version 14. *Collaborative computational project*, (6), 1994.
- [129] R. V. Krems. TwoBC - Quantum Scattering Program, 2006.





- [130] H. Jóźwiak. The SCATTERING code adjusted for diatom-atom calculations. [https://github.com/hjozwiak-umk/bigos\\_h2he](https://github.com/hjozwiak-umk/bigos_h2he), 2024.
- [131] A. Zadrożny, H. Jóźwiak, E. Quintas-Sánchez, R. Dawes, and P. Wcisło. Ab initio quantum scattering calculations for the CO-O<sub>2</sub> system and a new CO-O<sub>2</sub> potential energy surface: O<sub>2</sub> and air broadening of the R(0) line in CO. *J. Chem. Phys.*, 157(17), November 2022. URL: <http://dx.doi.org/10.1063/5.0115654>, doi:10.1063/5.0115654.
- [132] M. Gancewski, H. Jóźwiak, E. Quintas-Sánchez, R. Dawes, F. Thibault, and P. Wcisło. Fully quantum calculations of O<sub>2</sub>-N<sub>2</sub> scattering using a new potential energy surface: Collisional perturbations of the oxygen 118 Ghz fine structure line. *J. Chem. Phys.*, 155(12), September 2021. URL: <http://dx.doi.org/10.1063/5.0063006>, doi:10.1063/5.0063006.
- [133] A. Cygan, D. Lisak, S. Wójtewicz, J. Domysławska, J. T. Hodges, R. S. Trawiński, and R. Ciuryło. High-signal-to-noise-ratio laser technique for accurate measurements of spectral line parameters. *Phys. Rev. A*, 85(2), February 2012. URL: <http://dx.doi.org/10.1103/physreva.85.022508>, doi:10.1103/physreva.85.022508.
- [134] H. Lin, Z.D. Reed, V.T. Sironneau, and J.T. Hodges. Cavity ring-down spectrometer for high-fidelity molecular absorption measurements. *J. Quant. Spectrosc. Radiat. Transf.*, 161:11–20, August 2015. URL: <http://dx.doi.org/10.1016/j.jqsrt.2015.03.026>, doi:10.1016/j.jqsrt.2015.03.026.
- [135] X. Fan, T. G. Myers, B. A. D. Sukra, and G. Gabrielse. Measurement of the electron magnetic moment. *Phys. Rev. Lett.*, 130:071801, Feb 2023. URL: <https://link.aps.org/doi/10.1103/PhysRevLett.130.071801>, doi:10.1103/PhysRevLett.130.071801.
- [136] A. Aepli, K. Kim, W. Warfield, M. S. Safronova, and J. Ye. Clock with  $8 \times 10^{-19}$  systematic uncertainty. *Phys. Rev. Lett.*, 133:023401, Jul 2024. URL: <https://link.aps.org/doi/10.1103/PhysRevLett.133.023401>, doi:10.1103/PhysRevLett.133.023401.
- [137] R. M. Godun, P. B. R. Nisbet-Jones, J. M. Jones, S. A. King, L. A. M. Johnson, H. S. Margolis, K. Szymaniec, S. N. Lea, K. Bongs, and P. Gill.



- Frequency ratio of two optical clock transitions in  $^{171}\text{Yb}^+$  and constraints on the time variation of fundamental constants. *Phys. Rev. Lett.*, 113:210801, Nov 2014. URL: <https://link.aps.org/doi/10.1103/PhysRevLett.113.210801>, doi:10.1103/PhysRevLett.113.210801.
- [138] N. Huntemann, B. Lipphardt, Chr. Tamm, V. Gerginov, S. Weyers, and E. Peik. Improved limit on a temporal variation of  $m_p/m_e$  from comparisons of  $\text{Yb}^+$  and Cs atomic clocks. *Phys. Rev. Lett.*, 113:210802, Nov 2014. URL: <https://link.aps.org/doi/10.1103/PhysRevLett.113.210802>, doi:10.1103/PhysRevLett.113.210802.
- [139] P. Wcisło, P. Ablewski, K. Beloy, S. Bilicki, M. Bober, R. Brown, R. Fasano, R. Ciuryło, H. Hachisu, T. Ido, J. Lodewyck, A. Ludlow, W. McGrew, P. Morzyński, D. Nicolodi, M. Schioppo, M. Sekido, R. Le Targat, P. Wolf, X. Zhang, B. Zjawin, and M. Zawada. New bounds on dark matter coupling from a global network of optical atomic clocks. *Sci. Adv.*, 4(12), December 2018. URL: <http://dx.doi.org/10.1126/sciadv.aau4869>, doi:10.1126/sciadv.aau4869.
- [140] K. Beloy, M. I. Bodine, T. Bothwell, S. M. Brewer, S. L. Bromley, J.-S. Chen, J.-D. Deschênes, S. A. Diddams, R. J. Fasano, T. M. Fortier, Y. S. Hassan, D. B. Hume, D. Kedar, C. J. Kennedy, I. Khader, A. Koepke, D. R. Leibrandt, H. Leopardi, A. D. Ludlow, W. F. McGrew, W. R. Milner, N. R. Newbury, D. Nicolodi, E. Oelker, T. E. Parker, J. M. Robinson, S. Romisch, S. A. Schäffer, J. A. Sherman, L. C. Sinclair, L. Sonderhouse, W. C. Swann, J. Yao, J. Ye, and X. Zhang. Frequency ratio measurements at 18-digit accuracy using an optical clock network. *Nature*, 591(7851):564–569, March 2021. URL: <http://dx.doi.org/10.1038/s41586-021-03253-4>, doi:10.1038/s41586-021-03253-4.
- [141] M. Pospelov and A. Ritz. CKM benchmarks for electron electric dipole moment experiments. *Phys. Rev. D*, 89:056006, Mar 2014. URL: <https://link.aps.org/doi/10.1103/PhysRevD.89.056006>, doi:10.1103/PhysRevD.89.056006.
- [142] Y. Ema, T. Gao, and M. Pospelov. Standard model prediction for paramagnetic electric dipole moments. *Phys. Rev. Lett.*, 129:231801, Nov 2022. URL: <https://link.aps.org/doi/10.1103/PhysRevLett.129.231801>, doi:10.1103/PhysRevLett.129.231801.



- [143] Improved limit on the electric dipole moment of the electron. *Nature*, 562(7727):355–360, October 2018. URL: <http://dx.doi.org/10.1038/s41586-018-0599-8>, doi:10.1038/s41586-018-0599-8.
- [144] T. S. Roussy, L. Caldwell, T. Wright, W. B. Cairncross, Y. Shagam, J. B. Ng, N. Schlossberger, S. Y. Park, A. Wang, J. Ye, and E. A. Cornell. An improved bound on the electron's electric dipole moment. *Science*, 381(6653):46–50, July 2023. URL: <http://dx.doi.org/10.1126/science.adg4084>, doi:10.1126/science.adg4084.
- [145] Various. *Annual Register: A Review of Public Events at Home and Abroad for the Year 1894*. Longmans, Green and Company, London, 1896. Contains the quote: "An eminent physicist remarked that the future truths of physical science are to be looked for in the sixth place of decimals.". URL: <https://books.google.com/books?id=HysXAAAAYAAJ&pg=PA159>.
- [146] W. E. Lamb and R. C. Retherford. Fine structure of the hydrogen atom by a microwave method. *Phys. Rev.*, 72:241–243, Aug 1947. URL: <https://link.aps.org/doi/10.1103/PhysRev.72.241>, doi:10.1103/PhysRev.72.241.
- [147] H. A. Bethe. The electromagnetic shift of energy levels. *Phys. Rev.*, 72:339–341, Aug 1947. URL: <https://link.aps.org/doi/10.1103/PhysRev.72.339>, doi:10.1103/PhysRev.72.339.
- [148] A. Beyer, L. Maisenbacher, A. Matveev, R. Pohl, K. Khabarova, A. Grinin, T. Lamour, D. C. Yost, T. W. Hänsch, N. Kolachevsky, and T. Udem. The Rydberg constant and proton size from atomic hydrogen. *Science*, 358(6359):79–85, 2017. doi:10.1126/science.aah6677.
- [149] M. Fischer, N. Kolachevsky, M. Zimmermann, R. Holzwarth, Th. Udem, T. W. Hänsch, M. Abgrall, J. Grünert, I. Maksimovic, S. Bize, H. Marion, F. Pereira Dos Santos, P. Lemonde, G. Santarelli, P. Laurent, A. Clairon, C. Salomon, M. Haas, U. D. Jentschura, and C. H. Keitel. New limits on the drift of fundamental constants from laboratory measurements. *Phys. Rev. Lett.*, 92:230802, Jun 2004. URL: <https://link.aps.org/doi/10.1103/PhysRevLett.92.230802>, doi:10.1103/PhysRevLett.92.230802.



- [150] P. G. Blunden and I. Sick. Proton radii and two-photon exchange. *Phys. Rev. C*, 72:057601, Nov 2005. URL: <https://link.aps.org/doi/10.1103/PhysRevC.72.057601>, doi:10.1103/PhysRevC.72.057601.
- [151] H. Gao and M. Vanderhaeghen. The proton charge radius. *Rev. Mod. Phys.*, 94:015002, Jan 2022. URL: <https://link.aps.org/doi/10.1103/RevModPhys.94.015002>, doi:10.1103/RevModPhys.94.015002.
- [152] G.S. Adkins, D.B. Cassidy, and J. Pérez-Ríos. Precision spectroscopy of positronium: Testing bound-state QED theory and the search for physics beyond the Standard Model. *Phys. Rep.*, 975:1–61, September 2022. URL: <http://dx.doi.org/10.1016/j.physrep.2022.05.002>, doi:10.1016/j.physrep.2022.05.002.
- [153] X. Zheng, Y. R. Sun, J.-J. Chen, W. Jiang, K. Pachucki, and S.-M. Hu. Measurement of the frequency of the  $2^3S - 2^3P$  transition of  $^4\text{He}$ . *Phys. Rev. Lett.*, 119:263002, Dec 2017. doi:10.1103/PhysRevLett.119.263002.
- [154] K. F. Thomas, J. A. Ross, B. M. Henson, D. K. Shin, K. G. H. Baldwin, S. S. Hodgman, and A. G. Truscott. Direct measurement of the forbidden  $2^3S_1 \rightarrow 3^3S_1$  atomic transition in helium. *Phys. Rev. Lett.*, 125:013002, Jul 2020. doi:10.1103/PhysRevLett.125.013002.
- [155] L. Wolniewicz, I. Simbotin, and A. Dalgarno. Quadrupole transition probabilities for the excited rovibrational states of  $\text{H}_2$ . *Astrophys. J. Suppl. Ser.*, 115(2):293–313, apr 1998. doi:10.1086/313091.
- [156] G. Herzberg. Quadrupole rotation-vibration spectrum of the hydrogen molecule. *Nature*, 163(4135):170–170, January 1949. URL: <http://dx.doi.org/10.1038/163170a0>, doi:10.1038/163170a0.
- [157] U. Fink, T.A. Wiggins, and D.H. Rank. Frequency and intensity measurements on the quadrupole spectrum of molecular hydrogen. *J. Mol. Spectrosc.*, 18(4):384–395, December 1965. URL: [http://dx.doi.org/10.1016/0022-2852\(65\)90044-5](http://dx.doi.org/10.1016/0022-2852(65)90044-5), doi:10.1016/0022-2852(65)90044-5.



- [158] S. L. Bragg, W. H. Smith, and J. W. Brault. Line positions and strengths in the  $\text{H}_2$  quadrupole spectrum. *ApJ*, 263:999, December 1982. URL: <http://dx.doi.org/10.1086/160568>, doi:10.1086/160568.
- [159] A. Campargue, S. Kassı, K. Pachucki, and J. Komasa. The absorption spectrum of  $\text{H}_2$ : CRDS measurements of the (2-0) band, review of the literature data and accurate ab initio line list up to  $35\,000\text{ cm}^{-1}$ . *Phys. Chem. Chem. Phys.*, 14(2):802–815, 2012. URL: <http://dx.doi.org/10.1039/c1cp22912e>, doi:10.1039/c1cp22912e.
- [160] P. Maddaloni, P. Malara, E. De Tommasi, M. De Rosa, I. Ricciardi, G. Gagliardi, F. Tamassia, G. Di Lonardo, and P. De Natale. Absolute measurement of the S(0) and S(1) lines in the electric quadrupole fundamental band of  $\text{D}_2$  around  $3\text{ }\mu\text{m}$ . *J. Chem. Phys.*, 133(15), October 2010. URL: <http://dx.doi.org/10.1063/1.3493393>, doi:10.1063/1.3493393.
- [161] G. D. Dickenson, M. L. Niu, E. J. Salumbides, J. Komasa, K. S. E. Eikema, K. Pachucki, and W. Ubachs. Fundamental vibration of molecular hydrogen. *Phys. Rev. Lett.*, 110:193601, May 2013. URL: <https://link.aps.org/doi/10.1103/PhysRevLett.110.193601>, doi:10.1103/PhysRevLett.110.193601.
- [162] D. Mondelain, S. Kassı, T. Sala, D. Romanini, D. Gatti, and A. Campargue. Sub-MHz accuracy measurement of the S(2) 2-0 transition frequency of  $\text{D}_2$  by Comb-Assisted Cavity Ring Down spectroscopy. *J. Mol. Spectrosc.*, 326:5–8, August 2016. URL: <http://dx.doi.org/10.1016/j.jms.2016.02.008>, doi:10.1016/j.jms.2016.02.008.
- [163] P. Weisł, F. Thibault, M. Zaborowski, S. Wójtewicz, A. Cygan, G. Kowzan, P. Masłowski, J. Komasa, M. Puchalski, K. Pachucki, R. Ciurył, and D. Lisak. Accurate deuterium spectroscopy for fundamental studies. *J. Quant. Spectrosc. Radiat. Transf.*, 213:41–51, July 2018. URL: <http://dx.doi.org/10.1016/j.jqsrt.2018.04.011>, doi:10.1016/j.jqsrt.2018.04.011.
- [164] E. Fasci, A. Castrillo, H. Dinesan, S. Gravina, L. Moretti, and L. Gianfrani. Precision spectroscopy of HD at  $1.38\text{ }\mu\text{m}$ . *Phys. Rev. A*, 98:022516, Aug 2018. URL: <https://link.aps.org/doi/10.1103/PhysRevA.98.022516>, doi:10.1103/PhysRevA.98.022516.



- [165] M. L. Diouf, F. M. J. Cozijn, B. Darquié, E. J. Salumbides, and W. Ubachs. Lamb-dips and lamb-peaks in the saturation spectrum of HD. *Opt. Lett.*, 44(19):4733, September 2019. URL: <http://dx.doi.org/10.1364/ol.44.004733>, doi:10.1364/ol.44.004733.
- [166] M. Zaborowski, M. Słowiński, K. Stankiewicz, F. Thibault, A. Cygan, H. Jóźwiak, G. Kowzan, P. Masłowski, A. Nishiyama, N. Stolarczyk, S. Wójtewicz, R. Ciuryło, D. Lisak, and P. Wcisło. Ultrahigh finesse cavity-enhanced spectroscopy for accurate tests of quantum electrodynamics for molecules. *Opt. Lett.*, 45(7):1603, March 2020. URL: <http://dx.doi.org/10.1364/ol.389268>, doi:10.1364/ol.389268.
- [167] D. Mondelain, S. Kassi, and A. Campargue. Transition frequencies in the (2-0) band of D<sub>2</sub> with MHz accuracy. *J. Quant. Spectrosc. Radiat. Transf.*, 253:107020, September 2020. URL: <http://dx.doi.org/10.1016/j.jqsrt.2020.107020>, doi:10.1016/j.jqsrt.2020.107020.
- [168] A. Fast and S. A. Meek. Sub-ppb measurement of a fundamental band rovibrational transition in HD. *Phys. Rev. Lett.*, 125:023001, Jul 2020. URL: <https://link.aps.org/doi/10.1103/PhysRevLett.125.023001>, doi:10.1103/PhysRevLett.125.023001.
- [169] M. L. Diouf, F. M. J. Cozijn, K.-F. Lai, E. J. Salumbides, and W. Ubachs. Lamb-peak spectrum of the HD (2-0) P(1) line. *Phys. Rev. Res.*, 2:023209, May 2020. URL: <https://link.aps.org/doi/10.1103/PhysRevResearch.2.023209>, doi:10.1103/PhysRevResearch.2.023209.
- [170] T.-P. Hua, Y. R. Sun, and S.-M. Hu. Dispersion-like lineshape observed in cavity-enhanced saturation spectroscopy of HD at 1.4  $\mu\text{m}$ . *Opt. Lett.*, 45(17):4863, August 2020. URL: <http://dx.doi.org/10.1364/ol.401879>, doi:10.1364/ol.401879.
- [171] A. Castrillo, E. Fasci, and L. Gianfrani. Doppler-limited precision spectroscopy of HD at 1.4  $\mu\text{m}$ : An improved determination of the  $R(1)$  center frequency. *Phys. Rev. A*, 103:022828, Feb 2021. URL: <https://link.aps.org/doi/10.1103/PhysRevA.103.022828>, doi:10.1103/PhysRevA.103.022828.





- [172] A. Fast and S. A. Meek. Precise measurement of the  $D_2$   $S_1(0)$  vibrational transition frequency. *Mol. Phys.*, 120(19–20), November 2021. URL: <http://dx.doi.org/10.1080/00268976.2021.1999520>, doi:10.1080/00268976.2021.1999520.
- [173] S. Kassi, C. Lauzin, J. Chaillot, and A. Campargue. The (2–0)  $R(0)$  and  $R(1)$  transition frequencies of HD determined to a  $10^{-10}$  relative accuracy by doppler spectroscopy at 80 K. *Phys. Chem. Chem. Phys.*, 24(38):23164–23172, 2022. URL: <http://dx.doi.org/10.1039/d2cp02151j>, doi:10.1039/d2cp02151j.
- [174] Q.-H. Liu, Y.-N. Lv, C.-L. Zou, C.-F. Cheng, and S.-M. Hu. Saturated absorption spectroscopy of HD at 76 K. *Phys. Rev. A*, 106:062805, Dec 2022. URL: <https://link.aps.org/doi/10.1103/PhysRevA.106.062805>, doi:10.1103/PhysRevA.106.062805.
- [175] F. M. J. Cozijn, M. L. Diouf, and W. Ubachs. Saturation spectroscopy of  $R(0)$ ,  $R(2)$  and  $P(2)$  lines in the (2–0) band of HD. *EPJD*, 76(11), November 2022. URL: <http://dx.doi.org/10.1140/epjd/s10053-022-00552-x>, doi:10.1140/epjd/s10053-022-00552-x.
- [176] F. M. J. Cozijn, M. L. Diouf, and W. Ubachs. Lamb dip of a quadrupole transition in  $H_2$ . *Phys. Rev. Lett.*, 131:073001, Aug 2023. URL: <https://link.aps.org/doi/10.1103/PhysRevLett.131.073001>, doi:10.1103/PhysRevLett.131.073001.
- [177] M. L. Diouf, F. M. J. Cozijn, and W. Ubachs. Hyperfine structure in a vibrational quadrupole transition of ortho- $H_2$ . *Mol. Phys.*, 122(15–16), January 2024. URL: <http://dx.doi.org/10.1080/00268976.2024.2304101>, doi:10.1080/00268976.2024.2304101.
- [178] J. Komasa, M. Puchalski, P. Czachorowski, G. Łach, and K. Pachucki. Rovibrational energy levels of the hydrogen molecule through nonadiabatic perturbation theory. *Phys. Rev. A*, 100:032519, Sep 2019. URL: <https://link.aps.org/doi/10.1103/PhysRevA.100.032519>, doi:10.1103/PhysRevA.100.032519.
- [179] K. Pachucki and J. Komasa. Nonadiabatic rotational states of the hydrogen molecule. *Phys. Chem. Chem. Phys.*, 20(1):247–255,



2018. URL: <http://dx.doi.org/10.1039/c7cp06516g>, doi:10.1039/c7cp06516g.
- [180] Q.-H. Liu, Y. Tan, C.-F. Cheng, and S.-M. Hu. Precision spectroscopy of molecular hydrogen. *Phys. Chem. Chem. Phys.*, 25(41):27914–27925, 2023. URL: <http://dx.doi.org/10.1039/d3cp03042c>, doi:10.1039/d3cp03042c.
- [181] T.L. Nicholson, S.L. Campbell, R.B. Hutson, G.E. Marti, B.J. Bloom, R.L. McNally, W. Zhang, M.D. Barrett, M.S. Safronova, G.F. Strouse, W.L. Tew, and J. Ye. Systematic evaluation of an atomic clock at  $2 \times 10^{-18}$  total uncertainty. *Nat. Comm.*, 6(1), April 2015. URL: <http://dx.doi.org/10.1038/ncomms7896>, doi:10.1038/ncomms7896.
- [182] T. Bothwell, D. Kedar, E. Oelker, J. M. Robinson, S. L. Bromley, W. L. Tew, J. Ye, and C. J. Kennedy. JILA Srl optical lattice clock with uncertainty of  $2.0 \times 10^{-18}$ . *Metrologia*, 56(6):065004, October 2019. URL: <http://dx.doi.org/10.1088/1681-7575/ab4089>, doi:10.1088/1681-7575/ab4089.
- [183] S. M. Brewer, J.-S. Chen, A. M. Hankin, E. R. Clements, C. W. Chou, D. J. Wineland, D. B. Hume, and D. R. Leibbrandt.  $^{27}\text{Al}^+$  quantum-logic clock with a systematic uncertainty below  $10^{-18}$ . *Phys. Rev. Lett.*, 123:033201, Jul 2019. URL: <https://link.aps.org/doi/10.1103/PhysRevLett.123.033201>, doi:10.1103/PhysRevLett.123.033201.
- [184] T. Bothwell, C. J. Kennedy, A. Aeppli, D. Kedar, J. M. Robinson, E. Oelker, A. Staron, and J. Ye. Resolving the gravitational redshift across a millimetre-scale atomic sample. *Nature*, 602(7897):420–424, February 2022. URL: <http://dx.doi.org/10.1038/s41586-021-04349-7>, doi:10.1038/s41586-021-04349-7.
- [185] E. J. Salumbides, J. C. J. Koelemeij, J. Komasa, K. Pachucki, K. S. E. Eikema, and W. Ubachs. Bounds on fifth forces from precision measurements on molecules. *Phys. Rev. D*, 87:112008, Jun 2013. URL: <https://link.aps.org/doi/10.1103/PhysRevD.87.112008>, doi:10.1103/PhysRevD.87.112008.
- [186] L.-G. Tao, A.-W. Liu, K. Pachucki, J. Komasa, Y. R. Sun, J. Wang, and S.-M. Hu. Toward a determination of the proton-electron mass ratio



- from the Lamb-dip measurement of HD. *Phys. Rev. Lett.*, 120:153001, Apr 2018. URL: <https://link.aps.org/doi/10.1103/PhysRevLett.120.153001>, doi:10.1103/PhysRevLett.120.153001.
- [187] K. Pachucki and J. Komasa. Magnetic dipole transitions in the hydrogen molecule. *Phys. Rev. A*, 83:032501, Mar 2011. URL: <https://link.aps.org/doi/10.1103/PhysRevA.83.032501>, doi:10.1103/PhysRevA.83.032501.
- [188] P. Wcisło, I. E. Gordon, C.-F. Cheng, S.-M. Hu, and R. Ciuryło. Collision-induced line-shape effects limiting the accuracy in Doppler-limited spectroscopy of H<sub>2</sub>. *Phys. Rev. A*, 93:022501, Feb 2016. URL: <https://link.aps.org/doi/10.1103/PhysRevA.93.022501>, doi:10.1103/PhysRevA.93.022501.
- [189] A. Cygan, S. Wójtewicz, H. Jóźwiak, G. Kowzan, N. Stolarczyk, K. Bielska, P. Wcisło, R. Ciuryło, and D. Lisak. Heterodyne dispersive cavity ring-down spectroscopy exploiting eigenmode frequencies for high-fidelity measurements, 2024. Accepted for publication in Science Advances. URL: <https://arxiv.org/abs/2403.01961>, arXiv:2403.01961.
- [190] F. M. J. Cozijn, P. Dupré, E. J. Salumbides, K. S. E. Eikema, and W. Ubachs. Sub-Doppler frequency metrology in HD for tests of fundamental physics. *Phys. Rev. Lett.*, 120:153002, Apr 2018. URL: <https://link.aps.org/doi/10.1103/PhysRevLett.120.153002>, doi:10.1103/PhysRevLett.120.153002.
- [191] H. Jóźwiak, H. Cybulski, and P. Wcisło. Positions and intensities of hyperfine components of all rovibrational dipole lines in the HD molecule. *J. Quant. Spectrosc. Radiat. Transf.*, 253:107171, 2020. doi:10.1016/j.jqsrt.2020.107171.
- [192] H. Jóźwiak, H. Cybulski, and P. Wcisło. Hyperfine components of all rovibrational quadrupole transitions in the H<sub>2</sub> and D<sub>2</sub> molecules. *J. Quant. Spectrosc. Radiat. Transf.*, 253:107186, 2020. doi:10.1016/j.jqsrt.2020.107186.
- [193] H. Jóźwiak, H. Cybulski, and P. Wcisło. Hyperfine structure of quadrupole rovibrational transitions in tritium-bearing hydrogen isotopologues. *J. Quant. Spectrosc. Radiat. Transf.*, in press.



- [194] H. Wu, N. Stolarczyk, Q.-H. Liu, C.-F. Cheng, T.-P. Hua, Y. R. Sun, and S.-M. Hu. Comb-locked cavity ring-down spectroscopy with variable temperature. *Opt. Express*, 27(26):37559, December 2019. URL: <http://dx.doi.org/10.1364/oe.376572>, doi:10.1364/oe.376572.
- [195] L. Gianfrani, S.-M. Hu, and W. Ubachs. Advances in cavity-enhanced methods for high precision molecular spectroscopy and test of fundamental physics. *Riv. Nuovo Cim.*, 47(4):229–298, April 2024. URL: <http://dx.doi.org/10.1007/s40766-024-00054-z>, doi:10.1007/s40766-024-00054-z.
- [196] M.L. Niu, E.J. Salumbides, G.D. Dickenson, K.S.E. Eikema, and W. Ubachs. Precision spectroscopy of the  $X^1\Sigma_g^+, v = 0 \rightarrow 1(J = 0 - 2)$  rovibrational splittings in  $\text{h}_2$ ,  $\text{hd}$  and  $\text{d}_2$ . *J. Mol. Spectrosc.*, 300:44–54, 2014. Spectroscopic Tests of Fundamental Physics. URL: <https://www.sciencedirect.com/science/article/pii/S0022285214000630>, doi:10.1016/j.jms.2014.03.011.
- [197] G. Garberoglio, P. Jankowski, K. Szalewicz, and A. H. Harvey. Second virial coefficients of  $\text{H}_2$  and its isotopologues from a six-dimensional potential. *J. Chem. Phys.*, 137(15), October 2012. URL: <http://dx.doi.org/10.1063/1.4757565>, doi:10.1063/1.4757565.
- [198] A. Ben-Reuven. Impact broadening of microwave spectra. *Phys. Rev.*, 145:7–22, May 1966. URL: <https://link.aps.org/doi/10.1103/PhysRev.145.7>, doi:10.1103/PhysRev.145.7.
- [199] A. Ben-Reuven. Resonance broadening of spectral lines. *Phys. Rev. A*, 4:2115–2120, Dec 1971. URL: <https://link.aps.org/doi/10.1103/PhysRevA.4.2115>, doi:10.1103/PhysRevA.4.2115.
- [200] R.A. Pasmanter and A. Ben-Reuven. Resonance-transfer contributions to resonance line broadening in the impact limit. *J. Quant. Spectrosc. Radiat. Transf.*, 13(1):57–68, January 1973. URL: [http://dx.doi.org/10.1016/0022-4073\(73\)90100-3](http://dx.doi.org/10.1016/0022-4073(73)90100-3), doi:10.1016/0022-4073(73)90100-3.
- [201] W.-K. Liu. Symmetrized Liouville basis for indistinguishable particles. Application to spectral linewidth. *J. Chem. Phys.*, 72(9):4869–4872, May



1980. URL: <http://dx.doi.org/10.1063/1.439743>, doi:10.1063/1.439743.
- [202] L. Monchick. Quantum kinetic equations incorporating the Fano collision operator: The generalized Hess method of describing line shapes. *J. Chem. Phys.*, 101(7):5566–5577, October 1994. URL: <http://dx.doi.org/10.1063/1.467344>, doi:10.1063/1.467344.
- [203] S. Green and W. M. Huo. Quantum calculations for line shapes in Raman spectra of molecular nitrogen. *J. Chem. Phys.*, 104(19):7590–7598, May 1996. URL: <http://dx.doi.org/10.1063/1.471467>, doi:10.1063/1.471467.
- [204] W. Demtröder. *Laser spectroscopy 1: basic principles*. Springer, 2014.
- [205] V. S. Letokhov and V. P. Chebotayev. *Nonlinear laser spectroscopy*, volume 4. Springer, 1977.
- [206] R. L. Cook and F. C. De Lucia. Application of the theory of irreducible tensor operators to molecular hyperfine structure. *Am. J. Phys.*, 39(12):1433–1454, dec 1971. doi:10.1119/1.1976693.
- [207] M. Broyer, J. Vigué, and J.C. Lehmann. Effective hyperfine hamiltonian in homonuclear diatomic molecules. Application to the B state of molecular iodine. *J. Phys. (Paris)*, 39(6):591–609, 1978. doi:10.1051/jphys:01978003906059100.
- [208] N. F. Ramsey. Theory of molecular hydrogen and deuterium in magnetic fields. *Phys. Rev.*, 85:60–65, Jan 1952. doi:10.1103/PhysRev.85.60.
- [209] N. J. Harrick, R. G. Barnes, P. J. Bray, and N. F. Ramsey. Nuclear radiofrequency spectra of D<sub>2</sub> and H<sub>2</sub> in intermediate and strong magnetic fields. *Phys. Rev.*, 90:260–266, Apr 1953. doi:10.1103/PhysRev.90.260.
- [210] W. E. Quinn, J. M. Baker, J. T. LaTourrette, and N. F. Ramsey. Radiofrequency spectra of hydrogen deuteride in strong magnetic fields. *Phys. Rev.*, 112:1929–1940, Dec 1958. doi:10.1103/PhysRev.112.1929.



- [211] R. F. Code and N. F. Ramsey. Molecular-beam magnetic resonance studies of HD and D<sub>2</sub>. *Phys. Rev. A*, 4:1945–1959, Nov 1971. doi:10.1103/PhysRevA.4.1945.
- [212] J. Verberne, I. Ozier, L. Zandee, and J. Reuss. Molecular beam magnetic resonance study of intra- and inter- molecular effects in H<sub>2</sub> in high rotational states. *Mol. Phys.*, 35(6):1649–1657, 1978. doi:10.1080/00268977800101231.
- [213] P. Dupré. Hyperfine transitions in the first overtone mode of hydrogen deuteride. *Phys. Rev. A*, 101:022504, Feb 2020. doi:10.1103/PhysRevA.101.022504.
- [214] J. Komasa, M. Puchalski, and K. Pachucki. Hyperfine structure in the HD molecule. *Phys. Rev. A*, 102:012814, Jul 2020. doi:10.1103/PhysRevA.102.012814.
- [215] M. Puchalski, J. Komasa, and K. Pachucki. Hyperfine structure of the first rotational level in H<sub>2</sub>, D<sub>2</sub> and HD molecules and the deuteron quadrupole moment. *Phys. Rev. Lett.*, 125:253001, Dec 2020. URL: <https://link.aps.org/doi/10.1103/PhysRevLett.125.253001>, doi:10.1103/PhysRevLett.125.253001.
- [216] F. M. J. Cozijn, M. L. Diouf, V. Hermann, E. J. Salumbides, M. Schlösser, and W. Ubachs. Rotational level spacings in HD from vibrational saturation spectroscopy. *Phys. Rev. A*, 105:062823, Jun 2022. URL: <https://link.aps.org/doi/10.1103/PhysRevA.105.062823>, doi:10.1103/PhysRevA.105.062823.
- [217] M.-Y. Yu, Q.-H. Liu, C.-F. Cheng, and S.-M. Hu. Cavity-enhanced double resonance spectroscopy of HD. *Mol. Phys.*, 121(17–18), September 2022. URL: <http://dx.doi.org/10.1080/00268976.2022.2127382>, doi:10.1080/00268976.2022.2127382.
- [218] F. M. J. Cozijn, M. L. Diouf, W. Ubachs, V. Hermann, and M. Schlösser. Precision measurement of vibrational quanta in tritium hydride. *Phys. Rev. Lett.*, 132(11), March 2024. URL: <http://dx.doi.org/10.1103/physrevlett.132.113002>, doi:10.1103/physrevlett.132.113002.





- [219] S. Kassı and A. Campargue. Electric quadrupole and dipole transitions of the first overtone band of HD by CRDS between 1.45 and 1.33  $\mu\text{m}$ . *J. Mol. Spectrosc.*, 267(1–2):36–42, May 2011. URL: <http://dx.doi.org/10.1016/j.jms.2011.02.001>, doi:10.1016/j.jms.2011.02.001.
- [220] S. Vasilchenko, D. Mondelain, S. Kassı, P. Čermák, B. Chomet, A. Garnache, S. Denet, V. Lecocq, and A. Campargue. The HD spectrum near 2.3  $\mu\text{m}$  by CRDS-VECSEL: Electric quadrupole transition and collision-induced absorption. *J. Mol. Spectrosc.*, 326:9–16, August 2016. URL: <http://dx.doi.org/10.1016/j.jms.2016.04.002>, doi:10.1016/j.jms.2016.04.002.
- [221] U. Fano. Effects of configuration interaction on intensities and phase shifts. *Phys. Rev.*, 124:1866–1878, Dec 1961. URL: <https://link.aps.org/doi/10.1103/PhysRev.124.1866>, doi:10.1103/PhysRev.124.1866.
- [222] Y.-N. Lv, A.-W. Liu, Y. Tan, C.-L. Hu, T.-P. Hua, X.-B. Zou, Y. R. Sun, C.-L. Zou, G.-C. Guo, and S.-M. Hu. Fano-like resonance due to interference with distant transitions. *Phys. Rev. Lett.*, 129:163201, Oct 2022. URL: <https://link.aps.org/doi/10.1103/PhysRevLett.129.163201>, doi:10.1103/PhysRevLett.129.163201.
- [223] P. R. Brooks, W. Lichten, and R. Reno. Metstable hydrogen molecules. III. Hyperfine structure of orthohydrogen. *Phys. Rev. A*, 4:2217–2223, Dec 1971. URL: <https://link.aps.org/doi/10.1103/PhysRevA.4.2217>, doi:10.1103/PhysRevA.4.2217.
- [224] A. Osterwalder, A. Wüest, F. Merkt, and Ch. Jungen. High-resolution millimeter wave spectroscopy and multichannel quantum defect theory of the hyperfine structure in high Rydberg states of molecular hydrogen  $\text{H}_2$ . *J. Chem. Phys.*, 121(23):11810–11838, 2004. doi:10.1063/1.1792596.
- [225] D. Sprecher, C. Jungen, and F. Merkt. Determination of the binding energies of the np Rydberg states of  $\text{H}_2$ , HD, and  $\text{D}_2$  from high-resolution spectroscopic data by multichannel quantum-defect theory. *J. Chem. Phys.*, 140(10):104303, 2014. doi:10.1063/1.4866809.



- [226] N. Hölsch, M. Beyer, E. J. Salumbides, K. S. E. Eikema, W. Ubachs, C. Jungen, and F. Merkt. Benchmarking theory with an improved measurement of the ionization and dissociation energies of  $\text{H}_2$ . *Phys. Rev. Lett.*, 122:103002, Mar 2019. doi:10.1103/PhysRevLett.122.103002.
- [227] N. Hölsch, I. Doran, F. Merkt, J. Hussels, C.-F. Cheng, E. J. Salumbides, H. L. Bethlem, K. S. E. Eikema, M. Beyer, W. Ubachs, and Ch. Jungen. Ionization and dissociation energies of HD and dipole-induced  $g/u$ -symmetry breaking. *Phys. Rev. A*, 108:022811, Aug 2023. URL: <https://link.aps.org/doi/10.1103/PhysRevA.108.022811>, doi:10.1103/PhysRevA.108.022811.
- [228] A. Castrillo, E. Fasci, and L. Gianfrani. Erratum: Doppler-limited precision spectroscopy of HD at 1.4  $\mu\text{m}$ : An improved determination of the  $R(1)$  center frequency [Phys. Rev. A 103, 022828 (2021)]. *Phys. Rev. A*, 103:069902, Jun 2021. URL: <https://link.aps.org/doi/10.1103/PhysRevA.103.069902>, doi:10.1103/PhysRevA.103.069902.
- [229] G. Buffa, A. Di Lieto, P. Minguzzi, O. Tarrini, and M. Tonelli. Nuclear-quadrupole effects in the pressure broadening of molecular lines. *Phys. Rev. A*, 37:3790–3794, May 1988. URL: <https://link.aps.org/doi/10.1103/PhysRevA.37.3790>, doi:10.1103/PhysRevA.37.3790.
- [230] M. Słowiński K. L. Sołtys B. Bednarski H. Jóźwiak N. Stolarczyk M. Narożnik D. Kierski S. Wójtewicz A. Cygan G. Kowzan P. Masłowski M. Piwiński D. Lisak P. Wcisło K. Stankiewicz, M. Makowski. Cavity-enhanced spectroscopy in a deep cryogenic regime; new hydrogen technologies for quantum sensing, in preparation.
- [231] U. Fantz and D. Wunderlich. Franck-Condon factors, transition probabilities, and radiative lifetimes for hydrogen molecules and their isotopomers. *At. Data Nucl. Data Tables*, 92(6):853–973, November 2006. URL: <http://dx.doi.org/10.1016/j.adt.2006.05.001>, doi:10.1016/j.adt.2006.05.001.
- [232] A. Singh, L. Maisenbacher, Z. Lin, J. J. Axelrod, C. D. Panda, and H. Müller. Dynamics of a buffer-gas-loaded, deep optical trap for molecules. *Phys. Rev. Res.*, 5:033008, Jul 2023. URL: <https://link.aps.org/doi/10.1103/PhysRevRes.5.033008>.



- aps.org/doi/10.1103/PhysRevResearch.5.033008, doi:10.1103/PhysRevResearch.5.033008.
- [233] W. Kołos and L. Wolniewicz. Polarizability of the hydrogen molecule. *J. Chem. Phys.*, 46(4):1426–1432, February 1967. URL: <http://dx.doi.org/10.1063/1.1840870>, doi:10.1063/1.1840870.
- [234] H. Katori, M. Takamoto, V. G. Pal’chikov, and V. D. Ovsiannikov. Ultra-stable optical clock with neutral atoms in an engineered light shift trap. *Phys. Rev. Lett.*, 91:173005, Oct 2003. URL: <https://link.aps.org/doi/10.1103/PhysRevLett.91.173005>, doi:10.1103/PhysRevLett.91.173005.
- [235] L. D. Thomas. Solution of the coupled equations of inelastic atom–molecule scattering for a single initial state. *J. Chem. Phys.*, 70(6):2979–2985, March 1979. URL: <http://dx.doi.org/10.1063/1.437836>, doi:10.1063/1.437836.
- [236] T. Karman, M. Tomza, and J. Pérez-Ríos. Ultracold chemistry as a testbed for few-body physics. *Nat. Phys.*, 20(5):722–729, May 2024. URL: <http://dx.doi.org/10.1038/s41567-024-02467-3>, doi:10.1038/s41567-024-02467-3.
- [237] A. O. G. Wallis and R. V. Krems. Magnetic feshbach resonances in collisions of nonmagnetic closed-shell  $^1\Sigma$  molecules. *Phys. Rev. A*, 89:032716, Mar 2014. URL: <https://link.aps.org/doi/10.1103/PhysRevA.89.032716>, doi:10.1103/PhysRevA.89.032716.
- [238] N. Bigagli, W. Yuan, S. Zhang, B. Bulatovic, T. Karman, I. Stevenson, and S. Will. Observation of bose–einstein condensation of dipolar molecules. *Nature*, 631(8020):289–293, June 2024. URL: <http://dx.doi.org/10.1038/s41586-024-07492-z>, doi:10.1038/s41586-024-07492-z.
- [239] M. L. Dubernet et al. BASECOL2023 scientific content. *A&A*, 683:A40, March 2024. URL: <http://dx.doi.org/10.1051/0004-6361/202348233>, doi:10.1051/0004-6361/202348233.
- [240] J. M. Brown and A. Carrington. *Rotational spectroscopy of diatomic molecules*. Cambridge university press, 2003.



- [241] R. Schinke. *Photodissociation Dynamics: Spectroscopy and Fragmentation of Small Polyatomic Molecules*. Cambridge University Press, April 1993. URL: <http://dx.doi.org/10.1017/cbo9780511586453>, doi: 10.1017/cbo9780511586453.
- [242] R. V. Krems. *Molecules in electromagnetic fields: from ultracold physics to controlled chemistry*. John Wiley & Sons, 2018.
- [243] M. H. Alexander and A. E. DePristo. Symmetry considerations in the quantum treatment of collisions between two diatomic molecules. *J. Chem. Phys.*, 66(5):2166–2172, March 1977. URL: <http://dx.doi.org/10.1063/1.434132>, doi:10.1063/1.434132.
- [244] M. H. Alexander and P. J. Dagdigan. Collision-induced transitions between molecular hyperfine levels: Quantum formalism, propensity rules, and experimental study of  $\text{CaBr}(X^2\Sigma^+)+\text{Ar}$ . *J. Chem. Phys.*, 83(5):2191–2200, September 1985. URL: <http://dx.doi.org/10.1063/1.449311>, doi:10.1063/1.449311.
- [245] S. Green. Rotational excitation in  $\text{H}_2\text{--H}_2$  collisions: Close-coupling calculations. *J. Chem. Phys.*, 62(6):2271–2277, March 1975. URL: <http://dx.doi.org/10.1063/1.430752>, doi:10.1063/1.430752.
- [246] V. Aquilanti, M. Bartolomei, D. Cappelletti, E. Carmona-Novillo, and F. Pirani. The  $\text{N}_2\text{--N}_2$  system: An experimental potential energy surface and calculated rotovibrational levels of the molecular nitrogen dimer. *J. Chem. Phys.*, 117(2):615–627, jul 2002. doi:10.1063/1.1482696.
- [247] M.H. Alexander, P.J. Dagdigan, H.-J. Werner, J. Klos, B. Desrousseaux, G. Raffy, and F. Lique. Hibridon: A program suite for time-independent non-reactive quantum scattering calculations. *Comp. Phys. Comm.*, 289:108761, August 2023. URL: <http://dx.doi.org/10.1016/j.cpc.2023.108761>, doi:10.1016/j.cpc.2023.108761.
- [248] J. M. Launay. Molecular collision processes. I. Body-fixed theory of collisions between two systems with arbitrary angular momenta. *J. Phys. B: At. Mol. Opt. Phys.*, 10(18):3665–3672, December 1977. URL: <http://dx.doi.org/10.1088/0022-3700/10/18/023>, doi:10.1088/0022-3700/10/18/023.



- [249] B.R. Johnson. The multichannel log-derivative method for scattering calculations. *J. Comput. Phys.*, 13(3):445–449, November 1973. URL: [http://dx.doi.org/10.1016/0021-9991\(73\)90049-1](http://dx.doi.org/10.1016/0021-9991(73)90049-1), doi:10.1016/0021-9991(73)90049-1.
- [250] B. R. Johnson. The renormalized Numerov method applied to calculating bound states of the coupled-channel Schroedinger equation. *J. Chem. Phys.*, 69(10):4678–4688, November 1978. URL: <http://dx.doi.org/10.1063/1.436421>, doi:10.1063/1.436421.
- [251] D. J. Kouri. *Rotational Excitation II: Approximation Methods*, page 301–358. Springer US, 1979. URL: [http://dx.doi.org/10.1007/978-1-4613-2913-8\\_9](http://dx.doi.org/10.1007/978-1-4613-2913-8_9), doi:10.1007/978-1-4613-2913-8\_9.
- [252] U. Fano. Pressure broadening as a prototype of relaxation. *Phys. Rev.*, 131:259–268, Jul 1963. URL: <https://link.aps.org/doi/10.1103/PhysRev.131.259>, doi:10.1103/PhysRev.131.259.
- [253] A. Ben-Reuven. Symmetry considerations in pressure-broadening theory. *Phys. Rev.*, 141:34–40, Jan 1966. URL: <https://link.aps.org/doi/10.1103/PhysRev.141.34>, doi:10.1103/PhysRev.141.34.
- [254] A. Ben-Reuven. Spectral line shapes in gases in the binary-collision approximation, January 1975. URL: <http://dx.doi.org/10.1002/9780470142523.ch5>, doi:10.1002/9780470142523.ch5.
- [255] P. J. Rayer. *Pressure Broadening of Spectral Lines: The Theory of Line Shape in Atmospheric Physics*. Cambridge University Press, 2020.
- [256] F.R.W. McCourt, J.J.M. Beenakker, W.E. Kohler, and I. Kuscer. *Nonequilibrium Phenomena in Polyatomic Gases: Cross Sections, Scattering, and Rarefied Gases*. Oxford University Press, 1991.
- [257] R. Blackmore. Collision kernels for the Waldmann-Snider equation. *J. Chem. Phys.*, 86(7):4188–4197, April 1987. URL: <http://dx.doi.org/10.1063/1.451878>, doi:10.1063/1.451878.
- [258] A.D. May, W.-K. Liu, F.R.W. McCourt, R. Ciuryło, J. Sanchez-Fortún Stoker, D. Shapiro, and R. Wehr. The impact theory of spectral line shapes: a paradigm shift. *Can. J. Phys.*, 91:879–895, 2013. URL: <http://dx.doi.org/10.1139/cjp-2012-0345>, doi:10.1139/cjp-2012-0345.



- [259] P.L. Roney. A theory of doppler and binary collision broadening by foreign gases-i. *J. Quant. Spectrosc. Radiat. Transf.*, 15(5):361–374, May 1975. URL: [http://dx.doi.org/10.1016/0022-4073\(75\)90053-9](http://dx.doi.org/10.1016/0022-4073(75)90053-9), doi:10.1016/0022-4073(75)90053-9.
- [260] E. Wigner. On the quantum correction for thermodynamic equilibrium. *Phys. Rev.*, 40:749–759, Jun 1932. URL: <https://link.aps.org/doi/10.1103/PhysRev.40.749>, doi:10.1103/PhysRev.40.749.
- [261] Wang Chang, C. S and Uhlenbeck, G. E. Transport phenomena in polyatomic gases. Technical report, Engineering Research Institute, University of Michigan, Ann Arbor, 1951.
- [262] L. Waldmann. Die Boltzmann-gleichung für gase mit rotierenden molekülen. *Z. Naturforsch. A*, 12(8):660–662, August 1957. URL: <http://dx.doi.org/10.1515/zna-1957-0811>, doi:10.1515/zna-1957-0811.
- [263] L. Waldmann. Die Boltzmann-gleichung für gase aus spinteilchen. *Z. Naturforsch. A*, 13(8):609–620, August 1958. URL: <http://dx.doi.org/10.1515/zna-1958-0803>, doi:10.1515/zna-1958-0803.
- [264] R. F. Snider. Quantum-mechanical modified Boltzmann equation for degenerate internal states. *J. Chem. Phys.*, 32(4):1051–1060, April 1960. URL: <http://dx.doi.org/10.1063/1.1730847>, doi:10.1063/1.1730847.
- [265] A. Tip. Transport equations for dilute gases with internal degrees of freedom. *Physica*, 52(4):493–522, April 1971. URL: [http://dx.doi.org/10.1016/0031-8914\(71\)90161-3](http://dx.doi.org/10.1016/0031-8914(71)90161-3), doi:10.1016/0031-8914(71)90161-3.
- [266] D. A. Coombe, R. F. Snider, and B. C. Sanctuary. Definitions and properties of generalized collision cross sections. *J. Chem. Phys.*, 63(7):3015–3030, October 1975. URL: <http://dx.doi.org/10.1063/1.431727>, doi:10.1063/1.431727.
- [267] R. N. Zare and W. G. Harter. Angular momentum: understanding spatial aspects in chemistry and physics. *New York*, 120, 1988.
- [268] A. Lévy, N. Lacome, and C. Chackerian. *Collisional Line Mixing*, page 261–337. Elsevier, 1992. URL: [http://dx.doi.org/10.1016/0022-4073\(92\)90053-9](http://dx.doi.org/10.1016/0022-4073(92)90053-9), doi:10.1016/0022-4073(92)90053-9.





org/10.1016/b978-0-12-580645-9.50008-3, doi:10.1016/  
b978-0-12-580645-9.50008-3.

- [269] S. Green. Rotational excitation in collisions between two rigid rotors: Alternate angular momentum coupling and pressure broadening of hcl by h<sub>2</sub>. *Chem. Phys. Lett.*, 47(1):119–122, April 1977. URL: [http://dx.doi.org/10.1016/0009-2614\(77\)85320-7](http://dx.doi.org/10.1016/0009-2614(77)85320-7), doi:10.1016/0009-2614(77)85320-7.
- [270] W. K. Liu, F. R. McCourt, and W. E. Köhler. Effective collision cross sections for the viscomagnetic effect in a pure gas of linear molecules. *J. Chem. Phys.*, 71(6):2566–2574, September 1979. URL: <http://dx.doi.org/10.1063/1.438611>, doi:10.1063/1.438611.
- [271] A. P. Yutsis, I. B. Levinson, and V. V. Vanagas. *Mathematical apparatus of the theory of angular momentum*. Academy of Sciences of the Lithuanian SS R, 1962.
- [272] C. Cercignani. *The Boltzmann Equation and Its Applications*. Springer New York, 1988. URL: <http://dx.doi.org/10.1007/978-1-4612-1039-9>, doi:10.1007/978-1-4612-1039-9.
- [273] G. C. Corey and F. R. McCourt. Dicke narrowing and collisional broadening of spectral lines in dilute molecular gases. *J. Chem. Phys.*, 81(5):2318–2329, September 1984. URL: <http://dx.doi.org/10.1063/1.447930>, doi:10.1063/1.447930.
- [274] L. Demeio and L. Monchick. Collision kernels for the Waldmann-Snider equation: generalization to gas mixtures. *Phys. A: Stat. Mech. Appl.*, 214(1):95–114, 1995.
- [275] D. L. Johnson, R. S. Grace, and J. G. Skofronick. The total scattering cross sections for H<sub>2</sub>+H<sub>2</sub>, D<sub>2</sub>+D<sub>2</sub>, and HD+HD for relative collision energies below 10 mev. *J. Chem. Phys.*, 71(11):4554–4569, December 1979. URL: <http://dx.doi.org/10.1063/1.438209>, doi:10.1063/1.438209.
- [276] K.D. Van Den Hout, P.W. Hermans, E. Mazur, and H.F.P. Knaap. The broadening and shift of the rotational Raman lines for hydrogen isotopes



- at low temperatures. *Phys. A: Stat. Mech. Appl.*, 104(3):509–547, dec 1980. doi:10.1016/0378-4371(80)90012-6.
- [277] X. Michaut, R. Saint-Loup, H. Berger, M. L. Dubernet, P. Joubert, and J. Bonamy. Investigations of pure rotational transitions of  $\text{H}_2$  self-perturbed and perturbed by He. I. Measurement, modeling, and quantum calculations. *J. Chem. Phys.*, 109(3):951–961, jul 1998. doi:10.1063/1.476638.
- [278] M. P. Le Flohic, P. Duggan, P. M. Sinclair, J. R. Drummond, and A. D. May. Collisional broadening and shifting of the pure rotational raman lines  $S_0(J = 0-4)$  of  $\text{H}_2$  at room temperature. *Can. J. Phys.*, 72(5-6):186–192, may 1994. doi:10.1139/p94-029.
- [279] S. Green. Effect of nuclear hyperfine structure on microwave spectral pressure broadening. *J. Chem. Phys.*, 88(12):7331–7336, jun 1988. URL: <https://doi.org/10.1063%2F1.454344>, doi:10.1063/1.454344.
- [280] G. Buffa and O. Tarrini. Hyperfine effects on collisional line shape. I. A self-consistent set of equations. *J. Chem. Phys.*, 134(17), may 2011. URL: <https://doi.org/10.1063%2F1.3585646>, doi:10.1063/1.3585646.
- [281] G. C. Corey and F. R. McCourt. Inelastic differential and integral cross sections for  $^{2S+1}\Sigma$  linear molecule- $^1\text{S}$  atom scattering: the use of Hund’s case b representation. *J. Phys. Chem.*, 87(15):2723–2730, July 1983. URL: <http://dx.doi.org/10.1021/j100238a009>, doi:10.1021/j100238a009.
- [282] A. R. Offer, M. C. van Hemert, and E. F. van Dishoeck. Rotationally inelastic and hyperfine resolved cross sections for  $\text{OH-H}_2$  collisions. Calculations using a new ab initio potential surface. *J. Chem. Phys.*, 100(1):362–378, January 1994. URL: <http://dx.doi.org/10.1063/1.466950>, doi:10.1063/1.466950.
- [283] A. Faure and F. Lique. The impact of collisional rate coefficients on molecular hyperfine selective excitation: Molecular hyperfine selective excitation. *MNRAS*, 425(1):740–748, July 2012. URL: [http:](http://)



[//dx.doi.org/10.1111/j.1365-2966.2012.21601.x](https://dx.doi.org/10.1111/j.1365-2966.2012.21601.x), doi:10.1111/  
j.1365-2966.2012.21601.x.